UNIVERSITY OF ADELAIDE LIBRARY SOUTH AUSTRALIA
8.9.99

EXPLORATION IMPLICATIONS PREDICTED BY THE DISTRIBUTION OF CARBON - OXYGEN - HYDROGEN GASES ABOVE AND WITHIN THE JUNCTION GOLD DEPOSIT, KAMBALDA, WESTERN AUSTRALIA

Paul A Polito B.Sc (Hons)

Department of Geology and Geophysics
The University of Adelaide
South Australia

May 1999

Thesis submitted in fulfilment required for the degree of Doctor of Philosophy in the Faculty of Science, University of Adelaide

Table of Contents

Table of Contents i
List of Figures ix
List of Tables xv
Statement of originality xvi
Abstract xvii
Acknowledgements xix
Dedication xxi

Chapter 1: Introduction 1
1.1 Rationale for the project 1
1.2 Soil-gas prospecting in deeply weathered terranes 2
1.3 Aims and significance 3
1.4 Project location and access 4
1.5 Physiography of the Junction deposit 4
1.5.1 Physical features 4
1.5.2 Climate 4
1.6 History of gold exploration in the Kambalda area 5
1.7 Previous workers 5

Chapter 2: Regional geology 8
2.1 Overview of the Yilgarn Craton 8
2.2 Stratigraphy of the Kambalda region 10
2.2.1 Red Hill Group 12
2.2.2 Kalgoorlie Group 12
2.2.2.1 Lunnon Basalt Formation 12
2.2.2.2 Kambalda Komatiite Formation 12
2.2.2.2.1 The Silver Lake Member 12
2.2.2.2.2 The Tripod Hill Member 12
2.2.2.3 Devon Consols Basalt Formation 12
2.2.2.4 Kapaii Slate Formation 13
2.2.2.5 Paringa Basalt Formation 13
2.2.3 Black Flag Group 13
2.2.3.1 The Newtown Felsic Formation 13
2.2.3.1.1 The Condensor, Junction and Golden Mile Gabbroic sills 14
2.2.3.2 Morgans Island Epiclastic Formation 14

Chapter 3: Geology and petrography of the Junction gold deposit **15**
3.1 Introduction 15
3.2 Methods and procedures 15
3.3 The Junction Gabbro 21
3.3.1 Zone one 22
3.3.2 Zone two 22
3.3.3 Zone three 23
3.3.4 Zone four 24
3.4 The late intrusives 26
3.5 Alteration associated with mineralisation 27
3.5.1 The distal-chlorite zone (DCZ) 29
3.5.2 The proximal-chlorite zone (PCZ) 31
3.5.3 The biotite-carbonate zone (BCZ) 33
3.5.3.1 Implications of the mineral assemblage in the BCZ 39
3.6 Vein styles 45
3.6.1 Pre-shearing vein assemblage 45
3.6.1.1 Molybdenite-bearing quartz veins 45
3.6.2 Syn-gold quartz veins associated with the development of the N25 surface 47
3.6.2.1 Shear veins 48
3.6.2.2 Extension veins 48
3.6.2.3 Breccia veins 51
3.6.3 Post-shearing vein assemblage 53
3.6.3.1 South dipping quartz veins 53
3.7 Proterozoic dykes 53
3.8 Tertiary sediments 53
3.9 Recent sediments 55

Chapter 4: Soil gas emissions above the Junction gold deposit **56**
4.1 Introduction to soil gas prospecting 56
4.2 Location of the soil gas survey relative to gold mineralisation 57
4.3 Characteristics of the N75 surface 59
4.3.1 Soil cover 59
4.3.2 Groundwater geochemistry 59
4.4 Methods 61
4.4.1 Active analysis of CO_2 and O_2 61
4.4.1.1 Measurement of soil O_2 and CO_2 concentrations 62
4.4.2 Light hydrocarbon analysis using passive samplers 63
4.4.2.1 Passive sampling 63

4.4.3 Occluded hydrocarbon analysis 64
4.5 Results 68
4.5.1 Traverse 6518998 68
4.5.2 Traverse 6519584 71
4.6 Discussion 74
4.6.1 Traverse 6518998 74
4.6.2 Traverse 6519584 76
4.6.3 Gas migration through the crust from its source 78
4.6.4 Origin of the carbon dioxide and oxygen 79
4.6.4.1Origin of the carbon dioxide and oxygen above sulphides 79
4.6.4.2 Bacterial production 80
4.6.4.3 Temperature and moisture levels 81
4.6.5 Origin of hydrocarbons above mineralisation 82

Chapter 5: Fluid inclusion studies 87
5.1 Introduction 87
5.1.1 Rationale 88
5.1.2 Fluid inclusion theory 89
5.1.2.1 Freezing runs 89
5.1.2.1.1 Fluid-gas components (CO_2 - CH_4) 89
5.1.2.1.2 First melt (Tfm) and eutectic temperature (Te) 89
5.1.2.2.3 Salinity estimates calculated from the melting temperature of fluid hydrates 90
5.1.2.2.4 Salinity estimates calculated from the melting temperature of CO_2 clathrates 90
5.1.2.2.5 Density calculations for two phase L + V fluid inclusions 91
5.1.2.2 Heating runs 91
5.1.2.2.1 Temperature of homogenisation (Th) 91
5.1.2.2.2 Th CO_2 94
5.2 Methods, equipment and procedures 94
5.3 Sample types and related fluid inclusions 95
5.3.1 Fluid inclusion types in pre-gold Mo-type quartz veins 97
5.3.2 Fluid inclusion types in syn-gold quartz veins 98
5.3.3 Fluid inclusion types in post-gold quartz veins 104
5.3.4 Secondary fluid inclusions 106
5.4 Rationale for layout of results and discussion 106
5.5 Understanding the formation of fluid inclusion types in late-orogenic, structurally-controlled gold deposits 106

5.5.1 The role of seismic rupture and lithostatic depressurisation in controlling phase separation in fluid inclusions 107
5.6 Results 109
5.6.1 Syn-gold quartz veins 109
5.6.1.1 Freezing runs 109
5.6.1.1.1. Fluid solutes 109
5.6.1.1.2 Daughter minerals 112
5.6.1.1.3 Fluid-gas components (CO_2 - CH_4) 113
5.6.1.1.4 Salinity estimates calculated from the melting temperature of fluid hydrates 115
5.6.1.1.5 Salinity estimates calculated from the melting temperature of CO_2 clathrates 117
5.6.1.2 Syn-gold quartz veins - Density calculations for the two phase L + V fluid inclusions. 117
5.6.1.3 Syn-gold quartz veins - homogenisation temperatures 118
5.6.1.3.1 Th CO_2 118
5.6.1.3.2 Temperature of total homogenisation and entrapment (Th and Tt) 119
5.6.2 Pre-gold, Mo-type quartz veins 124
5.6.2.1 Freezing runs 125
5.6.2.1.1 First melt (Tfm), eutectic temperature (Te) 125
5.6.2.1.1.1 Fluid solutes 125
5.6.2.1.1.2 Daughter minerals 125
5.6.2.1.1.3 Fluid-gas components (CO_2 - CH_4) 125
5.6.2.1.2 Final melt temperature (Tm) 125
5.6.1.1.2.1 Salinity estimates calculated from the melting temperature of fluid hydrates 125
5.6.1.1.2.2 Salinity estimates calculated from the melting temperature of CO_2 clathrates 125
5.6.2.2 Homogenisation temperatures 126
5.6.2.2.1 Th CO_2 126
5.6.2.2.2 Temperature of total homogenisation and entrapment (Th and Tt) 126
5.6.2.3 Summary on Mo-type fluid inclusions 126
5.6.3 Post-gold SV-type quartz veins 126
5.6.3.1 Freezing runs 127
5.6.3.1.1 First melt (Tfm), eutectic temperature (Te) 127
5.6.3.1.1.1 Fluid solutes 127
5.6.3.1.1.2 Fluid-gas components (CO_2 - CH_4) 127
5.6.3.2 Homogenisation temperatures 127

5.6.3.2.1 Th CO_2 127
5.6.3.2.2 Temperature of total homogenisation and entrapment (Th and Tt) 127
5.6.3.3 Summary on SV-type fluid inclusions 127
5.6.4 Secondary fluid inclusions 128
5.6.4.1 Freezing runs 128
5.6.4.1.1 First melt (Tfm), eutectic temperature (Te) 128
5.6.4.1.1.1 Fluid solutes 128
5.6.4.1.1.2 Fluid-gas components (CO_2 - CH_4) 129
5.6.4.2.2 Final melt temperature (Tm) 129
5.6.4.2.2.1 Salinity estimates calculated from the melting temperature of fluid hydrates 129
5.6.4.3 Homogenisation temperatures 129
5.6.4.3.1 Temperature of total homogenisation and entrapment (Th and Tt) 129
5.6.4.3.1.1 Salinity estimates calculated from the homogenisation temperature of daughter minerals 130
5.6.4.4 Discussion on secondary fluid inclusions 131
5.7 Discussion 131

Chapter 6: Laser Raman spectroscopy 135
6.1 Introduction 135
6.2 Methods, equipment and procedures 135
6.2.1 Fluid inclusion types 135
6.2.1.1 Pre-gold Mo-type quartz veins 135
6.2.1.2 Syn-gold extensional and shear veins 136
6.2.1.3 Post-gold SV-type quartz veins 136
6.2.1.4 Secondary fluid inclusions 136
6.2.2 Equipment and procedures 136
6.3 Results 137
6.3.1 Gas phases confirmed 137
6.3.1.1 Pre-gold Mo-type quartz veins 138
6.3.1.2 Syn-gold extensional and shear veins 138
6.3.1.3 Post-gold SV-type quartz veins 138
6.3.1.4 Secondary fluid inclusions 138
6.3.2 Hydrates and daughter minerals present 138
6.3.2.1 Pre-gold Mo-type quartz veins 140
6.3.2.2 Syn-gold extensional and shear veins 140
6.3.2.3 Post-gold SV-type quartz veins 140

6.3.2.4 Secondary fluid inclusions 140
6.4 Discussion 140

Chapter 7: CH_4-bearing fluid inclusions in calcite: the source for the light hydrocarbon soil-gas anomaly 145
7.1 Introduction to EDTA-gas chromatography 145
7.2 Methods and procedures 147
7.3 Results 151
7.4 Discussion 154
7.4.1 Related work and possible hydrocarbon origin 155
7.4.2 Relevance to soil gas anomaly 159

Chapter 8: Aliphatic and aromatic hydrocarbons in the biotite-carbonate zone 161
8.1 Introduction 161
8.2 Methods, procedures and materials 162
8.3 Results 163
8.4 Discussion and research into the atypical hydrocarbons detected 163

Chapter 9: Oxygen isotope analysis 165
9.1 Introduction 165
9.1.1 Application of oxygen isotopes as a geothermometer 166
9.1.1.1 Limitations on oxygen isotope geothermometry 167
9.2 Methods 168
9.3 Results 169
9.3.1 Pre-gold quartz vein samples 169
9.3.2 Syn-gold quartz vein samples 169
9.3.3 Post-gold quartz vein samples 171
9.4 Discussion 173
9.4.1 Oxygen isotope geothermometry 173
9.4.1.1 Syn-gold quartz vein samples 173
9.4.1.2 Post-gold quartz vein samples 174
9.4.2 The origin of the ore-transporting fluids 174
9.4.2.1 Pre-gold quartz vein samples 174
9.4.2.2 Syn-gold quartz vein samples 175
9.4.2.3 Post-gold quartz vein samples 176

Chapter 10: Stable isotope systematics of carbon in calcite at Junction 177
10.1 Introduction 177

10.1.1 Carbonate species evaluated at Junction 178
10.2 Methods 178
10.3 Results 179
10.3.1 $\delta^{13}C$ values for calcite sampled from the JSZ 179
10.3.2 $\delta^{13}C$ values for calcite sampled from SV-type veins 179
10.4 Discussion 180
10.4.1 The role of Rayleigh isotope stable isotope fractionation 182
10.4.2 Fluid sources 187
10.4.2.1 Fluid sources of the JSZ calcite 187
10.4.2.2 Fluid sources of the SV-type calcite 190

Chapter 11: Stable isotope evaluation of CO_2 in fluid inclusions 191
11.1 Introduction 191
11.2 Methods 192
11.3 Results 193
11.4 Discussion 193
11.4.1 Fluid inclusion CO_2 in pre-gold quartz veins 193
11.4.2 Fluid inclusion CO_2 in syn-gold quartz veins 195
11.4.3 SV-type quartz veins 200
11.4.4 Concluding remarks 200

Chapter 12: Coupled gas chromatography and stable isotope mass spectrometry 201
12.1 Introduction 201
12.1 Methods 202
12.3 Results 203
12.3.1 Pre-gold quartz vein samples 203
12.3.2 Syn-gold quartz vein samples 203
12.3.3 Post-gold quartz vein samples 203
12.4 Discussion 205
12.4.1 Interpretation of $\delta^{13}C$ values 205
12.4.1.1 Pre-gold Mo-type quartz vein samples 206
12.4.1.2 Syn-gold quartz vein samples 207
12.4.1.3 Post-gold SV-type quartz vein samples 207
12.4.2 Application of mass balance equations to the GC-MS results 207
12.4.3 Concluding remarks 210

Chapter 13: Coupled elemental analysis-mass spectrometry 212
13.1 Introduction 212
13.2 Methods 213

13.3 Results 214
13.3.1 EA-MS analyses on pre-gold Mo-type quartz veins 214
13.3.2 EA-MS analyses on syn-gold quartz veins 216
13.3.3 EA-MS analyses on post-gold SV-type quartz veins 216
13.3.4 Calculation of CO_2 and CH_4 ratios from the EA-MS $\delta^{13}C\Sigma$ values 216
13.4 Discussion 217

Chapter 14: Origin of CH_4 in the Junction gold deposit 221
14.1 Introduction: what are the currently proposed origins for the light hydrocarbons? 221
14.2 CH_4 formation by Fischer-Tropsch type synthesis 224
14.3 Application of FTTS to the Junction fluids 225

Chapter 15: Summary of the main findings and general discussion 227
15.1 The main findings 227
15.1.1 The soil-gas anomalies 227
15.1.2 The light hydrocarbon gas - gold relationship 228
15.2 Implications of this study 231

References 233

Appendix I: Sample numbers and drill hole/ drive sampled A1.1

Appendix II: Labelled SEM images A2.1

Appendix III: Electron microprobe traverse results: Sample 1074 - 50 A3.1
Electron microprobe traverse results: Sample 1074 - 91 A3.2
Electron microprobe traverse results: Sample 1074 - 226 A3.3
Electron microprobe traverse results: Sample 1074 - 237 A3.4

Appendix IV: X-ray diffraction results A4.1

Appendix V: Junction soil-gas survey results over the N75 surface A5.1

Appendix VI: Fluid inclusion database A6.1

Appendix VII: EDTA-Gas chromatography database A7.1

List of Figures

Chapter 1:
Figure 1.1. Location map of the Junction gold deposit.

Chapter 2:
Figure 2.1. Regional geology of the Yilgarn Craton, Western Australia, incorporating the geology of the southwestern Kalgoorlie Terrane.

Figure 2.2. Stratigraphic column for the Kambalda succession.

Chapter 3:
Figure 3.1. Geology of the Junction gold mine highlighting the currently mined N25 surface and the narrower, but related N75 surface.

Figure 3.2. Longitudinal cross section through the Junction Shear Zone (N25 surface) showing the zonation of the Junction Gabbro in relation to gold mineralisation.

Figure 3.3a. Vein mapping of drive 502-1-25.

Figure 3.3b. Vein mapping of drive 502-1-25.

Figure 3.4. Vein mapping of drive 405-1-54.

Figure 3.5. Drill core hand specimens showing texture characteristics of Junction Gabrro from a) Zone 1: cumulative, b) Zone 2: equigranular, c) Zone 3: granophyric, d) Zone 4: bladed.

Figure 3.6. Photomicrograph of granophyric intergrowth between quartz and albite.

Figure 3.7. Photomicrograph of ilmenite laths exsolved from titanomagnetite.

Figure 3.8. Schematic cross section through a mineralised section of the Junction shear zone showing the relationship between the biotite-carbonate zone the proximal-chlorite zone and the distal-chlorite zone.

Figure 3.9. Cathodoluminescence photomicrograph of calcite in the DCZ.

Figure 3.10. SEM image of ilmenite and chlorite in the DCZ, preserving the skeletal structure usually associated with exsolution of titanomagnetite.

Figure 3.11a and 3.11b. Transmitted light and cathodoluminescence photomicrographs showing the abundance of calcite present in the DCZ alteration matrix close (< 3 cm) to quartz veining.

Figure 3.12a and 3.12b. Cathodoluminescence photomicrograph of calcite growing along the cleavage planes of biotite and chlorite.

Figure 3.13a. Transmitted light and cathodoluminescence photomicrograph showing well developed calcite crystals growing at the edge of a quartz vein.

Figure 3.13b. Cathodoluminescence photomicrograph showing rarely observed zoned calcite forming at the edge of a quartz extension vein.

Figure 3.14. Pervasive foliation of biotite and carbonate as seen in zone three gabbro.

Figure 3.15. Elongated quartz and pyrrhotite ribbons typical of mylonite in the biotite-carbonate zone.

Figure 3.16a and 3.16b. Transmitted light and cathodoluminescence photomicrographs showing the abundance of calcite in the BCZ alteration matrix.

Figure 3.17a and 3.17b. Transmitted light and cathodoluminescence photomicrographs of radiating, intergrowing, calcite and chlorite aggregates growing in to a quartz vein from the edge of the wall rock.

Figure 3.18a, 3.18b, and 3.18 c. Transmitted light, reflected light and cathodoluminescence photomicrographs showing the replacement by calcite and rutile of ilmenite and titanomagnetite.

Figure 3.19a and 3.19b. Transmitted light and cathodoluminescence photomicrograph showing the progressive replacement of early ankerite by calcite.

Figure 3.20. SEM image showing the relationship between rutile (after ilmenite), calcite ± chlorite and pyrrhotite.

Figure 3.21a and 3.21b. Transmitted light and reflected light photomicrographs showing ilmeniteand rutile forming tattered trails with pyrrhotite enhancing the foliation developed by the biotite, chlorite, calcite assemblage.

Figure 3.22. An example of pyrrhotite rich alteration in the BCZ, Zone three.

Figure 3.23. Reflected light photomicrograph showing late euhedral pyrite replacin chalcopyrite in a pyrrhotite dominated assemblage.

Figure 3.24. Cathodoluminescence photomicrograph of a large, zoned, apatite crystal.

Figure 3.25. An example of preferential mineralisation of the Fe-rich gabbro (lower right) as opposed to the Fe-poor porphyry (upper left).

Figure 3.26. Oxygen fugasity and sulphur activity diagram (after Mickuki and Ridley, 1993), showing the estimated fields at which mineralisation occurred at Junction.

Figure 3.27a. Cathodoluminescence photomicrographs showing luminescence variations in calcite.

Figure 3.27b. Cathodoluminescence photomicrographs showing luminescence variations in calcite, ankerite and siderite.

Figure 3.28. Cathodoluminescence photomicrograph showing the progressive Fe-depletion in calcite.

Figure 3.29. An example of a Mo-type vein stretched into a boudin.

Figure 3.30 and 3.31. Reflected light photomicrographs of laminated Mo ribbons (Figure 3.30) and clusters (Figure 3.31) as they appear in the Mo-type quartz veins.

Figure 3.32. An example of a quartz-carbonate, reverse fault fill, shear vein with related extension veins forming in the footwall.

Figure 3.33. Planar extension veins exhibiting a moderate degree of rotation forming a sigmoidal en echelon vein set.

Figure 3.34. A continuous coating of albite formed mostly on the upper edge of a quartz vein in the biotite-carbonate zone.

Figure 3.35. An example of growth layering in an extension vein.

Figure 3.36. Quartz mineral fibres that have formed perpendicular to the edge of the vein wall indicating that the rate of precipitation is equal to or greater than the rate of wall-rock separation.

Figure 3.37. Chlorite-calcite-pyrrhotite mineral fibres growing perpendicular to or at a high angle to the vein wall.

Figure 3.38. Jigsaw puzzle breccia.

Figure 3.39. Angular and rounded clasts of highly altered wall rock and vein material, set in a hydrothermal matrix dominated by quartz and albite.

Figure 3.40. Typical of the SV-type veins at Junction is the large calcite crystals that grow within the quartz veins.

Figure 3.41. Transmitted light photomicrographs showing the large well formed crystal structure typical of the calcite, biotite and pyrrhotite crystals that are present in the SV-type quartz veins.

Chapter 4

Figure 4.1. Positioning of traverses 6518998 and 6519584 across the N75 surface.

Figure 4.2. Soil profile in the Junction area.

Figure 4.3. Incorporporation of Figure 4.2, showing the hand coring device used to dig the sampling holes and the PVC casing used to protect the passive sampler.

Figure 4.4. CO_2 - O_2 analyser in use by the author at another WMC Resources prospect.

Figure 4.5. Physiography and topography above the N75 surface showing the scattered salt-bush, acacia and black butt eucalyptus.

Figure 4.6. Soil-gas emission cross section along traverse 6518998.

Figure 4.7. Occluded hydrocarbon profiles for each sample point along traverse 6518998 and corresponding geochemical cross section.

Figure 4.8. Soil-gas emission cross section along traverse 6519584.

Figure 4.9. Occluded hydrocarbon profiles for each sample point along traverse 6519584 and corresponding geochemical cross section.

Figure 4.10. Schematic model showing the preferred pathway of evolved gas originating from the oxidation front of a mineralised shear zone containing sulphides and carbonate.

Chapter 5

Figure 5.1. Photomicrograph of small (<5μm), but abundant fluid inclusions in calcite.

Figure 5.2. Photomicrograph of tabular fluid inclusions in a twinned albite lath growing near the vein-wall rock margin.

Figure 5.3. Photomicrograph of naturally decrepitated single phase (?carbonic) fluid inclusions occuring at the edge of a deformed quartz grain.

Figure 5.4. Fine grained, strained quartz with sutured margins, typical of Mo-type quartz veins, occurring with co-existing foliated molybdenite.

Figure 5.5. A typical Mo-type fluid inclusion.

Figure 5.6. Mo-type fluid inclusions appear to have trapped a highly saline, H_2O-$CO_2 \geq CH_4$ fluid.

Figure 5.7. A rare vapour rich Mo-type fluid inclusion.

Figure 5.8. Photo micrograph of a carbonic-rich Mo-type fluid inclusion containing a halite daughter mineral and an unidentified carbonate.

Figure 5.9. A three dimentional cluster of fluid inclusions showing classic phase sparation in a shear vein.

Figure 5.10a and 5.10b. Photomicrographs of fluid inclusion trails in a shear vein in transmitted light and cross polarised light.

Figure 5.11 Two fluid inclusion trails at almost right angles to each other, both with different phase compositions.

Figure 5.12. Fluid inclusion trails found in a shear vein containing H_2O-CO_2 fluid inclusions.

Figure 5.13. A typical type A fluid inclusion usually found along fluid inclusion trails in extensional quartz-carbonate veins.

Figure 5.14. Photomicrograph of two adjacent syn-gold fluid inclusions containing different volumes of a carbonic phase.

Figure 5.15. Typical type B fluid inclusions displaying >50 vol. % carbonic phase.

Figure 5.16. Type C fluid inclusion at room temperature displaying liquid and vapour CO_2 $\pm CH_4$ phases.

Figure 5.17. A rare type B fluid inclusion containing > 50 vol. % carbonic phase and a prominent halite daughter mineral.

Figure 5.18. Type D fluid inclusion containing < 20 vol. % vapour phase.

Figure 5.19. Sub-horizontal fluid inclusion trails in an extensional quartz vein.

Figure 5.20. Three dimensional array of vapour rich fluid inclusions in a SV-type quartz vein.

Figure 5.21. Aqueous rich, halite bearing secondary fluid inclusions forming a three dimensional cluster.

Figure 5.22. Unusually large, but very typical equi-dimensional secondary fluid inclusion containing two daughter minerals, calcite and halite.

Figure 5.23a and 5.23b. Photomicrographs of the same fluid inclusion taken at +23°C and at -185°C.

Figure 5.24 Diagram from Boullier and Robert (1992) showing shear stress variations and fluid pressure fluctuations with time, as predicted by the fault-valve model of Sibson *et al.* (1988).

Figure 5.25. Histogram of T_{fm} for type B/C fluid inclusions and type D fluid inclusions.

Figure 5.26. Histogram of T_mCO_2 for type A, B, C and D fluid inclusions.

Figure 5.27. Histogram of T_{mICE} for type B/C fluid inclusions and type D fluid inclusions.

Figure 5.28. Salinity estimates in wt% NaCl equivalent for type B and C fluid inclusions only.

Figure 5.29. Histogram of Th_{CO_2} in °C for all syn-gold fluid inclusion types.

Figure 5.30. Homogenisation and decrepitation temperatures for all fluid inclusion types in syn-gold quartz veins.

Figure 5.31 a. Solubility of CO_2 in a 20 wt. % NaCl aqueous solution as a function of pressure and temperature (Robert and Kelly, 1987 from data by Takenouchi and Kennedy, 1965). b. Variation of lithostatic and hydrostatic pressures as a function of depth.

Figure 5.32. Tfm histogram for secondary fluid inclusions.

Figure 5.33. Histogram of Th for secondary fluid inclusions showing bimodal distribution. Higher temperature results correspond to ThNaCl.

Figure 5.34. Salinity histogram for secondary fluid inclusions combining wt% equivalent data from Tm and ThNaCl results.

Figure 5.35. Temperature vs salinity plot for type B, C and D fluid inclusions hosted in syn-gold quartz veins.

Chapter 6

Figure 6.1. An example of the Raman spectra obtained from the vapour phase in a fluid inclusion containing both CO_2 and CH_4.

Figure 6.2. An example of the Raman spectra obtained from the liquid phase in different fluid inclusions containing the stoichiometric hydrates $NaCl.2H_2O$, $CaCl_2.6H_2O$, or $MgCl_2.12H_2O$.

Figure 6.3. A schematic illustration showing the distribution of CO_2 and CH_2 across a typical quartz vein.

Chapter 7

Figure 7.1. Reaction chamber used to dissolve carbonate from whole rock sample.

Figure 7.2 Scatter plot comparing the volumes of CH_4 released from one gram of carbonate to the concentration of gold for the same sample.

Figure 7.3. Histogram showing the distribution of CH_4 in different sample types analysed from the Junction deposit.

Figure 7.4. Schematic cartoon of CH_4 distribution through the Junction shear zone.

Figure 7.5. Distribution of hydrocarbons across outcropping mineralisation at the Ashanti gold mine, Ghana.

Chapter 9

Figure 9.1. Compilation of $\delta^{18}O$ values for Mo-type, Syn-gold type and SV-type quartz - calcite veins.

Figure 9.2. Fractionation factors (indicated by dashed lines) for ^{18}O isotopes obtained from quartz and calcite samples from Junction gold mine using relationships between 1000 lna (mineral - H_2O) and $10^6/T^2$ for ^{18}O fractionations (from Kyser, 1987).

Figure 9.3. Compilation of $\delta^{18}O$ quartz and $\delta^{18}O$ of coexisting calcite for syn-gold quartz-calcite veins and SV-type quartz-calcite veins from the Junction gold mine.

Chapter 10

Figure 10.1. Compilation of $\delta^{13}C$ values for biotite-carbonate zone calcite, proximal-chlorite zone/distal-chlorite zone calcite and SV-type calcite collected from Junction.

Figure 10.2. The calcite-CO_2 fractionation factor at 385°C is 3.0‰, as illustrated by the dashed line.

Figure 10.3 The CH_4-CO_2 fractionation factor at 385°C is 20‰, as illustrated by the dashed line.

Figure 10.4. The isotopic profile of one quartz vein and its alteration halo at Mt. Charlotte shows that heavy carbon and oxygen isotope values are restricted to the pyrrhotitic interface between bleached and altered dolerite (from Golding *et al.*, 1990a).

Figure 10.5a. Schematic cartoon of CH_4 volumes and $\delta^{13}C$ values for calcite through the Junction shear zone.

Figure 10.6. The oxygen and carbon isotopic fields of specific fluid reservoirs and the isotope values of calcites from the Junction deposit (oxygen and carbon fields from [Kerrich, 1989]).

Chapter 11

Figure 11.1. Diagramatic representation of the aparatus used to extract CO_2 from the quartz.

Figure 11.2. Compilation of $\delta^{13}C$ values for Mo-type, Syn-gold type and SV-type fluid inclusion CO_2 extracted from quartz veins and trapped using cryogenic methods.

Chapter 12

Figure 12.1. Diagramatic representation of the aparatus used to extract CO_2 from the quartz.

Figure 12.2. The stable isotope fractionation factor between co-existing CO_2 and CH_4 in the one Mo-type quartz vein analysed is 30.4‰. This equates to a temperature of 220°C (dot-dash line).

Chapter 13

Figure 13.1. Compilation of $\delta^{13}C\Sigma$ values for Mo-type, Syn-gold type and SV-type carbonic fluid (CO_2 and CH_4) extracted from quartz veins by combustion in an elemental analyser and determined by mass spectrometry.

Figure 13.2. The $\delta^{13}C\Sigma$ values determined by EA-MS for syn-gold samples plotted along the equilibrium curve for CO_2 and CH_4 assuming mineralisation occurred at 385°C.

List of Tables

Chapter 3
Table 3.1. The geochemical composition of the Junction Gabbro.

Chapter 4
Table 4.1. Groundwater geochemistry above and around the Junction deposit.

Table 4.2. Soil-gas results collected from above the N75 structure, Junction gold deposit.

Table 4.3. Occluded hydrocarbon results obtained from soil samples collected above the N75 structure, Junction gold deposit.

Chapter 5
Table5.1. Synthesis of microthermometric data from the four main vein types present in the Junction mine, W.A.

Chapter 6
Table 6.1. Raman spectroscopic data for Mo-type fluid inclusions.

Table 6.2. Raman spectroscopic data for syn-gold fluid inclusions trapped in shear and extension veins.

Table 6.3. Raman spectroscopic data for SV-type and secondary fluid inclusions.

Chapter 7
Table 7.1. Summary of data collected by EDTA-GC analysis.

Chapter 9
Table 9.1. Geothermometric pairs and temperature estimates.

Chapter 11
Table 11.1. $\delta^{13}C$ values for fluid inclusion CO_2 with comparisons to coexisting $\delta^{13}C$ values for calcite.

Chapter 12
Table 12.1. $\delta^{13}C$ values of coexisting fluid inclusion CO_2 determined by off-line crushing and cryogenic trapping of CO_2 tabulated for comparison with the $\delta^{13}C$ values for CO_2 and CH_4 as determined by GC-MS methods.

Chapter 13
Table 13.1. EA-MS values ($\delta^{13}C\Sigma$) together with the estimated CO_2 and CH_4 volumes calculated using Equation 13.1 and the appropriate fractionation factors for CO_2 and CH_4 at different temperatures.

Statement of originality

This work contains no material which has been accepted for the award of any other degree or diploma in any university and that, to the best of my knowledge and belief, contains no material previously published or written by another person, except where due reference has been made in the text.

I hereby consent to this copy of my thesis, when deposited in the University library, being available for loan and photocopying.

5-5-99

Paul A Polito.

Acknowledgements

A number of great scientists, friends and family have contributed to various aspects of this thesis.

Firstly, I would like to thank the cheerful and enthusiastic input contributed by my two supervisors, Yvonne Bone and Jon Clarke. Both Yvonne and Jon were always keen for the project to do well and both were instrumental in setting up the scholarship. Thanks to you both for your time and experience in field, for your support of my ideas and for reviewing the thesis as required.

WMC Resources are thanked for their financial and logistical support of the project. Without WMC Resources, there would not have been a project and I would not have done a PhD. However, it is the people of WMC Resources who helped turn the study into a thesis. Firstly, to Jon Clarke, Megan Clark and Bob Watchorn, thank you for initiating the project, making it a reality and having the faith in me to carry out the research. Thank you Paul Taufen for your continued interest since then and for putting me in touch with TEG Rocky Mountain, USA and Actlabs, Canada. In particular, I would like to extend a big thank you to Kim Hein who became a great and treasured friend and whose encouragement and faith gave me the inspiration for so many ideas and the realisation that I might just discover something new! To Ernie Poole, thanks for your support, honesty and words of wisdom. I hope that you find this thesis more than just an academic blurb. With a bit of luck and a little faith it may help to find another Junction. To Dave Finn, Christian Holland, Travis Murphy, Ross Peden, and John Slade, the geologists I worked with at Junction, thank you all for your desk space, your patience when I needed you to take me underground or to find the right piece of drill core, and for your opinion when I needed advice. To "Old" Steve MacDonald and his farm..... of drill cores. Thanks Steve for your help in locating and uncovering deeply buried core at a time when I know you were very busy with many other requests. To Michelle Carey, thanks for your time in the field and the interest you shared in the project. Thanks also to the Mutton Clubbers of Kambalda for your friendship and the social events you organised each week. Cheers K-Neil. Finally, thank you Jacqui Chapman. You were always ready to help when I needed anything at all, from a drill log, to geochemical data, to rock samples. Nothing was too much to ask. Your support was fantastic and greatly appreciated.

Kurt "Sepo" Kyser. What can I say? I am struggling to get into only a few sentences what a huge impact you had on this project. Just when I needed the stimulation to get the most out of this project you turned up, took me under your wing and showed me what geochemistry is really about. Your enthusiasm became my excitement, your optimism became my inspiration and your friendship is treasured. Thank you for your contribution.

Indeed, to all my friends at Queen's University who contributed to this project. To Kerry Klassen and Mostafa Fayek. Thanks for your time, your patience, your expertise and your friendship in the lab, the pub and the gym. Kerry, here's to your nostrils. Will they ever recover? Thanks Christoph and Aliona for making lab work so much fun!

To all of the general and technical staff at the Department of Geology and Geophysics, a big thank you. To Sondra (who took on the extra role of looking after my apatite and general well being), Mary, Kim and Soph, you guys are an asset to the department. All of you are truly wonderful, nothing was ever too much trouble. I owe a great deal of my sanity to you all. Thanks especially to Gerald "Mr. Fixit" Buttfield for always getting things done on time and with a smile. Thanks Wayne Mussared and Geoff Trevelyan for making my thin sections of all description and for lending an ear on things football and farming. Thanks Keith for your help, advice and particularly your patience in the stable isotope labs. My persistence for your permission paid off in a big way. Thanks Liz for keeping me tidy and for proof reading my final draft (I hope this doesn't incriminate you for any errors I've failed to omit.!). Thanks Sherry for your help with all of my drafting needs, from posters to page set-up, your advice was always timely and much appreciated. Thanks Ian for all your computing assistance.

Thanks Kerri Muller, Department of Botany, for your time and the use of the Gas Chromatograph and your expert touch in getting it going each time I wandered in with some samples. Jim Villenave is also thanked for analysing the passive samplers for me in the USA.

To all of my peers that were once, or still are in the department: Garry, Jack, Bruce, Jon, Scotty M., Blob, Basim, Eike, Lal, Kathy, Jerry, Trevor, Scotty R., Sandra, Narelle, Victor, Miles, Rolf, Kirsty, Betina, and any one that I have unwittingly forgotten. Thank you for contributing your opinions, support, concerns and humour over the years. I look forward to catching up with each and everyone of you at various times in different places around the globe to reminisce about the good ol' days at Adelaide Uni.

To my fiance, Kathy. A very special thank you to you for your support, your encouragement, your belief that it will all come together one day, and for just being there and listening when I needed to talk to someone about the project when things didn't look so rosy. It takes a special someone to put up with a geologist for a partner and you are very special to me indeed.

Finally, two people have been there for me to share in the triumphs and tribulations of this PhD long before it got off the ground. Mum and Dad, you may never fully realise how grateful I am for your support of me all the way since the first time I mentioned that I might go back and study for another three or so years. I could not have done without your financial support, but it is your love, care, wisdom and advice, that I thank you the most. I could not wish to be blessed with better parents than the two of you..... Thank you.

ABSTRACT

Exploration for sulphide ore deposits is becoming increasingly difficult in areas where bedrock is concealed below transported and deeply weathered cover. The Yilgarn Craton of Western Australia, host to many Archaean gold mines, is one such area that is characterised by saprolite that is up to 50m thick and variably covered by transported alluvium. This study used the late-orogenic, structurally-controlled Junction gold deposit near Kambalda, W estern Australia, to examine the potential of soil-gas geochemistry as an exploration vector in an environment where mineralisation is present, but no ore-related trace elements are detectable in the near-surface regolith.

It was discovered that CO_2, O_2, CH_4 and other light hydrocarbon anomalies are detectable directly above the Junction gold mine. However, where as CO_2 - O_2 anomalies above sulphidic ore deposits are common, and typically attributed to the oxidation of sulphide and carbonate minerals associated with the mineralisation at depth, CH_4 and other light hydrocarbons are typically attributed to the presence of heavier aromatic and aliphatic hydrocarbons related to the buried mineralisation, or to microbiological activity in the soil above the mineralisation. No heavier hydrocarbons are visibly present at Junction, and microbiological activity fails to account for the C_2^+ hydrocarbons that have been detected in the soil. Thus, the presence of the light hydrocarbon soil-gas anomaly needs to be explained. Prior to this investigation, it was not known if late-orogenic, structurally-controlled gold deposits contained and released enough CH_4 ($\pm$ light hydrocarbons) to be detectable at the surface by gas sniffing techniques.

Fluid inclusion microthermometry and Raman spectroscopy on fluid inclusions in quartz veins indicate that CO_2, H_2O, NaCl and CH_4 were all present at the time of gold mineralisation. However, the fluid inclusions at Junction do not indicate that CH_4 was a major component in the ore forming system. Nevertheless, Raman spectroscopy shows that CH_4 is locally abundant in some fluid inclusions and that these fluid inclusions regularly contain >20% CH_4 at the quartz vein - host rock contact.

Carbonate collected from near the quartz vein - host rock contact was analysed for its gas content and revealed that the most intensely-altered and gold-rich part of the mineralised shear zone contains the highest volumes of light hydrocarbons, whereas the weakly altered samples collected from the periphery of the shear zone contain low to negligible volumes of light hydrocarbons. The results indicate that CH_4 and other light hydrocarbons are directly associated with the gold mineralisation and that the light hydrocarbon volume detected in the carbonate is only a fraction of the total light hydrocarbon budget likely to be present in the ore body given that other non-quartz minerals (albite, sulphides and scheelite) are likely to contain the same volumes of light

hydrocarbons as the calcite at the quartz vein - host rock contact.

Oxygen isotope analysis of the quartz and calcite reveals that the two minerals are in equilibrium with each other and are therefore contemporaneous. Thus, it is conceivable that the light hydrocarbons detected in the calcite are related to the gold mineralisation. However, in contrast to the oxygen isotope findings, carbon isotope analysis reveals that the CO_2 in the quartz veins is isotopically distinct from that in the calcite. Thus suggesting that the quartz and calcite may not be related at all.

Further investigations of the carbon-bearing phases indicates that Rayleigh stable isotope fractionation must have occurred at the time of mineralisation, resulting in a relatively wide range of $\delta^{13}C$ values for the ore-related calcite. That Rayleigh isotope fractionation is inferred, suggests that considerable CH_4 (± light hydrocarbons) must have been formed at the site of mineralisation by a Fischer-Tropsch type reaction to alter the parent $\delta^{13}C$ value of the CO_2-rich ore-fluid as it interacted with the Fe-rich gabbro under low fO_2 conditions.

The zonation of the CH_4-rich fluid inclusions at the quartz vein - host rock contact can be explained using this model, but the isotopically distinct calcite and fluid inclusion CO_2 cannot. Stable isotope analysis of the CO_2 and CH_4 trapped in fluid inclusions hosted in the quartz veins reveals that the CO_2 has become isotopically heavier as the CH_4 has become isotopically lighter since their entrapment 2.6 Ga. This indicates that the two gases have re-equilibrated with each other at a temperature below that at which they were trapped. Thus, it is evident why the calcite and the fluid inclusion CO_2 are isotopically distinct.

In conclusion, the CH_4 (± light hydrocarbons) trapped in the calcite and presumably trapped in the other gangue minerals is contemporaneous with the CH_4 trapped in the quartz. Thus the light hydrocarbon anomalies detected in the soil above the Junction deposit are believed to have originated from the gangue minerals associated with gold mineralisation at depth as the unaltered host rock weathers to clay, subsequently releasing the gaseous contents in the fluid inclusions. The CH_4 and light hydrocarbons are therefore a primary gas signature expressing the presence of gold mineralisation at depth. The coexistence of the CH_4 and light hydrocarbons with a prominent CO_2-O_2 anomaly enhances the use of soil-gas geochemistry as an exploration vector for similar mineral deposits on the Yilgarn Craton.

Dedication

The work contained in this thesis was made possible by my parents,

Rocco and Louise Polito.

UNIVERSITY OF ADELAIDE LIBRARY

CHAPTER ONE

Introduction

1.1 Project rationale

The Junction gold deposit, owned and operated by WMC Resources (henceforth WMC) is the focus of the project. The deposit was discovered by a gold-in-soil geochemical survey conducted in 1985 after a lengthy exploration program that began in the Kambalda area in 1979. The gold-in-soil anomaly was the precursor to the discovery of the mineralisation, thus paving the way for mine development in mid 1987. However, the discovery of a slightly smaller, but significantly mineralised shear zone only 400m east of the Junction ore body did not occur until late 1987 as a result of a structural stratigraphic drilling program. Re-examination of the soil geochemistry data revealed that no gold anomaly had been defined over this ore-body, despite the fact that this smaller ore body could be mapped for a short distance at the surface as a discontinuous line of rubbly quartz float (Balkau, 1989). Infill soil geochemistry over the N75 surface in 1988, again failed to highlight any anomaly above background values for a range of pathfinder elements including Ni, Cu, Co, Cr, Fe, Mn, Zn, Bi, As, Bo, Se, Te, Hg, Sn, W, Mo, Sb, Pb, As, Ag, and Au.

Assessment of the discovery geochemistry data showed that the peak gold-in-soil values coincided with alluvial gold mineralisation that occurred in an upper palaeochannel (Balkau, 1989). Investigations by Clarke (1988) found that the two strongest of three soil anomalies were related to Tertiary palaeochannels. Thus, it was concluded that the gold-in-soil anomaly was a reflection of near-surface alluvial mineralisation and not the primary shear zone mineralisation. Clarke (1988) revealed that the Junction ore-body may not have been discovered when it was if it were not for the presence of the shallow alluvial gold mineralisation that had formed in the upper levels of a palaeodrainage system that traversed the mineralised Junction Shear Zone. Subsequently, WMC realised that the same soil geochemistry techniques that delineated the Junction deposit by chance, possibly missed other similar deposits in the surrounding district. Thus, in 1994 WMC sought to find an alternative exploration method to detect similar styles of mineralisation to that found at Junction, given that gold-bearing palaeodrainage systems do not traverse across all of the prospective areas in the Kambalda region.

1.2 Soil-gas prospecting in deeply weathered terrains

Soil-gas prospecting for hidden reservoirs of hydrocarbons was first proposed for the petroleum industry in 1929 (Laubmeyer, 1933). By the mid 1950s, researchers in the U.S.A. and Russia regularly reported anomalous levels of hydrocarbons in soil over petroleum deposits. This is despite the primitive techniques employed which could detect only a fraction of the anomaly that was probably present (Rosaire, 1938; Horvitz, 1939, 1945, 1954, 1972; Sokolov, 1935, 1959). Soil- and rock-gas prospecting for hidden mineral deposits was not used by researchers until the late 1970s and early 1980s. However, much has been documented and published on this topic since then.

The presence of He, Mg, N_2, CO_2-O_2, Rn, Th, sulphur gases and light hydrocarbon gases above various ore-bodies has been reported by many researchers. They invariably recommend soil-gas technology as a viable mineral exploration vector (Dyck, 1976; Dunsmore and Shearman, 1977; Amanor, 1979; Taylor *et al.*, 1982; Lovell *et al.*, 1983; Carter and Cazalet, 1984, 1988; Hinkle and Dilbert, 1984; Kesler *et al.*, 1986; Kesler and Gardner, 1986; McCarthy and Reimer, 1986; Reimer, 1986; Goodman, 1987; Ferguson, 1987, 1988; McCarthy *et al.*, 1986; Oakes and Hale, 1987; Carter *et al.*, 1988; Disnar and Gauthier, 1988; Alpers *et al.*, 1990; Ball *et al.*, 1990; Disnar, 1990; Hinkle *et al.*, 1990; Kesler *et al.*, 1990; Reid and Rasmussen, 1990; Mauk and Hieshima, 1992; Mulshaw, 1996; Wood, 1996). The gases are thought to migrate from the ore deposit and can pass through weathered rock and the younger cover rocks and soils. Many of these authors argue convincingly that the soil-gas anomaly detectable at the surface is indeed sourced from the mineralisation below. However, linking the soil-gas anomalies detected at the surface to a deposit at depth is occasionally challenged by other researchers who claim, among other things that:

- soil-gas anomalies above mineralisation cannot be isotopically distinguished from background soil-gas emissions arising from unmineralised, but oxidising carbonates. Thus, soil-gas anomalies are not necessarily related to mineralisation (Alpers *et al.*, 1990),

- soil-gas anomalies are created or suppressed by daily and seasonal weather fluctuations, soil respiration and plant activity (Alpers *et al.*, 1990; Amundson and Davidson, 1990), and

- soil-gas anomalies above mineralisation are difficult to distinguish from plant and microbially mediated processes (Butt *et al.*, 1985; Amundson and Davidson, 1990).

These claims are feasible, and need to be addressed according to the area being investigated. However, soil-gas geochemistry has broad application if two and preferably three or more gases can be found to co-exist in a single area. Just as trace-element soil geochemistry uses a range

of elements to delineate a metal-in-soil anomaly, soil-gas geochemistry should aim to detect a range of gas types to define co-existing anomalies. This is especially so if the gases detected in the soil can be linked to gases found in the ore deposit or to gases that arise from the breakdown of minerals that are hosted in the deposit.

1.3 Aims and significance

Establishing the viability of soil-gas geochemistry as an exploration vector for Junction-type gold deposits in the Kambalda region and beyond, involves determining the presence of, and then the exact source for, the soil-gas emissions. Therefore the aims of this project are two-fold. Firstly, the presence of a soil-gas anomaly needs to be established using available and up-to-the-minute soil-gas detection techniques. Secondly, because soil-gas anomalies do not indicate relative concentrations of a target element in the soil (i.e. dispersion haloes of Au-As-Cu-Pb-Zn-Mo etc.), the source of the soil-gas anomaly needs to be linked to the zone of gold mineralisation by some other "finger print-type" characteristic.

The **aims** of the project are can be condensed to:

- investigate the potential of soil-gas geochemistry as a prospecting tool for Junction-style gold deposits by identifying the presence of soil-gas anomalies associated with a known gold mineralised system,
- understand how the gases detected at the surface are related to the gold mineralised system,
- understand if, how and where the gases are incorporated into the host minerals and the mechanisms that control their later release, and
- apply the understanding of the surface gas haloes to high-risk exploration in weathered and concealed terrains.

The **significance** of this project is that it will augment the conventional exploration techniques and will investigate further the potential for using various gases associated with ore deposits that are released from the mineral lattice over time, including when deep regolith weathering occurs. Indeed, this project may have far reaching repercussions across much of the Yilgarn Craton. This is because the Yilgarn terrane presents considerable problems for the exploration geologist. Australia's long, complex history of weathering and erosion (see Veevers, 1984; Smith and Anand, 1990; and Clarke, 1994a for examples in Western Australia), is characterised by widespread saprolitic bedrock (Butt, 1989; Smith and Anand, 1990), variably covered by ferricrete and a thin veneer of calcrete, silcrete, gypcrete, sheet-wash, and/or aeolian sand (Clarke, 1994a). The saprolitic bedrock in Western Australia is commonly depleted in useful trace

elements (Butt, 1981, 1989; Smith and Anand, 1990). This is compounded in the Kambalda region where saprolite thicknesses commonly exceed 30 m. Smith and Anand (1990) report that multi-element geochemistry in lateritic environments, can be useful in delineating wide-ranging dispersion haloes of trace elements. These trace elements become trapped within resistate minerals or are strongly held by Fe-oxyhydroxides that are relatively stable to further weathering. Unfortunately, these ferricretes are not widespread across the Yilgarn craton, and when present, they too may be covered by a veneer of transported material (Clarke, 1994a). The thickness of this veneer (commonly >2m) often renders multi-element geochemistry useless. Similarly, other parts of the Yilgarn Craton are transected by sediment-filled palaeovalleys that occupy up to 20% of the Yilgarn Craton in some areas, and can contain as much as 100 m of cover (Clarke, 1994b).

1.4 Project location and access

The Junction gold deposit is a large Archaean gold deposit that is currently operated by WMC as an underground mining operation. The deposit is situated approximately 670 km east of Perth, 100 km south-southeast of Kalgoorlie, and 35 km south of the Kambalda East township (Figure 1.1). Junction can be reached by a private road from Kambalda. It is located on the Widgiemooltha (SH 51-14) 1: 250, 000 scale sheet. The study area covers approximately 2.0 km^2 and incorporates the currently mined N25 surface and related hanging wall and footwall surfaces.

1.5 Physiography of the Junction deposit

1.5.1 Physical features

Physical relief in the study area is less than 5 m and outcrop density is < 1%. The deposit is typically covered by up to 30 m of leached saprolite and transported material consisting of red-yellow to brown-white coloured sandy to ferruginous clay, calcrete nodules and loamy soil. The local vegetation is dominated by scattered salt-bush (*Atriplex vesicaria*), blue-bush (*Cratystylis conocephala*), various acacia shrubs, black-butt eucalypts (*Eucalyptus le souefii*) and salmon gums (*Eucalyptus salmonophloia*).

1.5.2 Climate

Data collected by WMC, and the Bureau of Meteorology show that the Kalgoorlie area (50 km north of Kambalda) has a semi-arid environment with a mean monthly maximum temperature ranging from 33.6°C in January to 16.5°C in July. WMC records reveal that the mean annual rainfall for Kambalda is 242 mm (Clarke, 1994b). This is similar to records collected by the Bureau of Meteorology which show that the annual rainfall for Kalgoorlie is 256 mm. Both Kalgoorlie and Kambalda have a bimodal rainfall distribution with peaks occurring in January and June. However, the annual pan evaporation for Kalgoorlie is 2701 mm, with the highest evaporation occurring in January and the lowest in August.

1.6 History of gold exploration in the Kambalda area

The Junction gold mine was named after its close proximity to the Widgiemooltha - St. Ives and Paris - St. Ives roads (Figure 1.1). The history of gold exploration in the Kambalda-St. Ives area is fully described by Balkau (1989), and Roberts and Elias (1990). It is only briefly summarised here. Historically, gold was first discovered in the Kambalda-St. Ives area during 1897 at Red Hill, Victory, Orchin, Delta Island and Cooee (Roberts and Elias, 1990). There are no significant old workings in the Junction area, although a small 5 m shaft and some shallow costeans occur in oxidised dolerite 800 m west of the main ore bearing lode and a shallow, prominent costean exists 400 m east of the main lode. The shallow costean 400 m east of the main lode is thought to be very early, as it is the only feature marked on a 1925 geological map of the area (Balkau, 1989).

WMC delineated the Junction Gabbro in 1968 during a regional aeromagnetic survey searching for ultramafic lithologies that could potentially host nickel sulphide mineralisation. Basement lithologies were not intersected by drilling until 1971. In 1974 and in response to rising gold prices the 1971 drill hole was deepened and intersected a magnetite and ilmenite-bearing gabbro which hosted several thin quartz veins. Assayed core gave a range of gold grades, including 0.2 m @ 35.8 g/t, and 0.9 m @ 3.3 g/t.

No further interest was shown in the Junction area until the 1979 gold price increase. However, it was not until 1983 that a systematic gold exploration programme commenced. In early 1983 a diamond drilling programme over and around the Junction anomaly commenced, intersecting several thin structures that contained gold but lacked significant alteration. This downgraded the potential of the gabbro to host a major ore body.

A reconnaissance soil geochemistry programme at Junction in 1985 highlighted a significant gold-in-soil anomaly coincident with the magnetic high. In April 1986, the first two discovery holes were completed with assays returning grades of 11 m @ 5.6 g/t and 5 m @ 3.8 g/t. Mining of the open cut ore commenced in July 1987 (Holland, 1995).

1.7 Previous workers

The Kambalda area was first mentioned in Western Australian Mines Department reports in 1897 for minor gold production at the St Ives, Paris and Red Hill gold mines. The discovery of nickel sulphide mineralisation around the Kambalda Dome in 1966 resulted in a flourish of geological research. Numerous internal WMC reports documenting the geology of these deposits were written. This work is mostly summarised by Gresham and Loftus-Hills (1981).

The discovery of significant gold mineralisation in the Kambalda - St Ives area in 1979-85 shifted geological attention to the upper part of the Kambalda succession, which is host to most

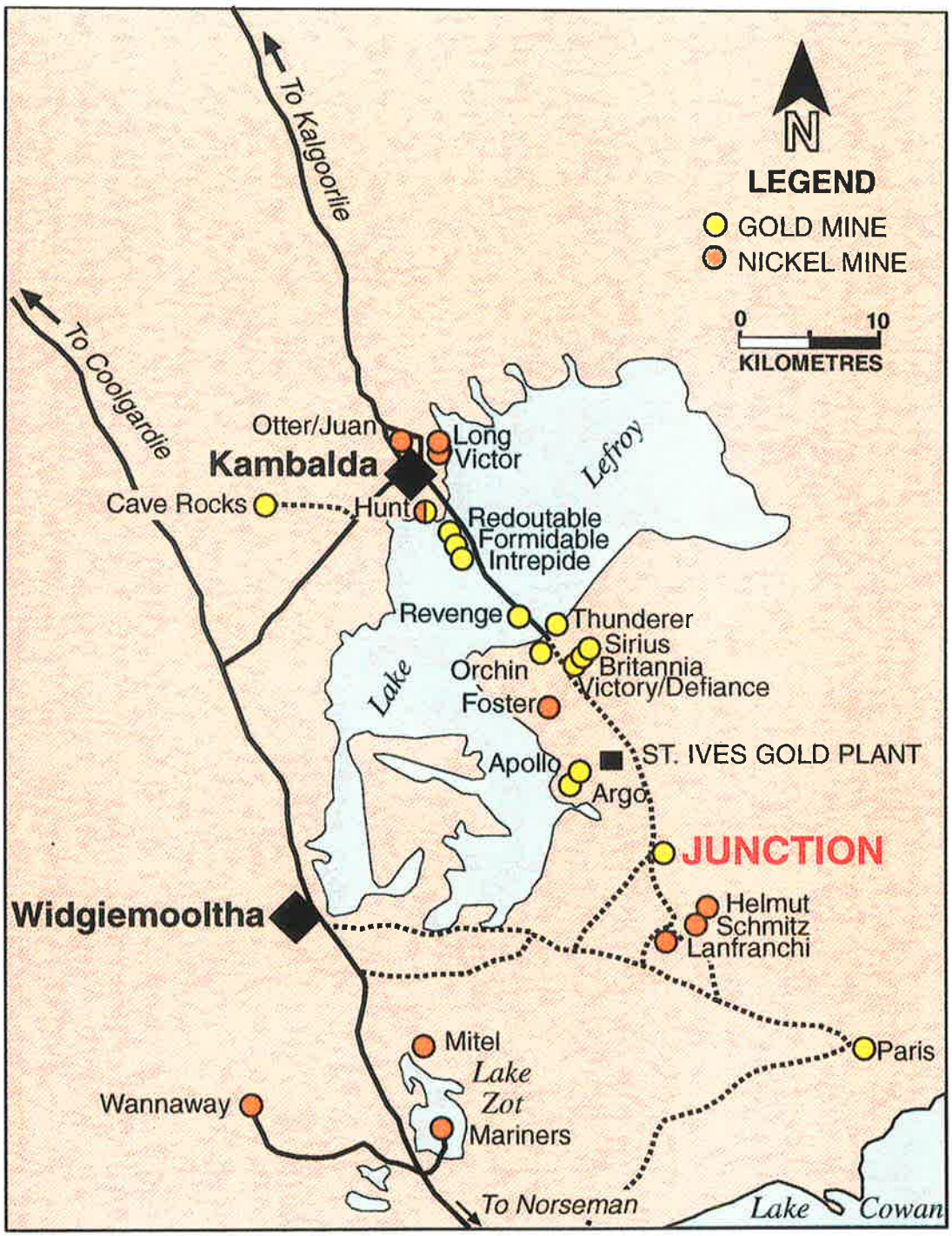


Figure 1.1. Location map of the Junction gold deposit in relation to other gold and nickel deposits in the Kambalda district (after Reddell, 1995). Solid lines indicate sealed roads. Dashed lines indicate gravel roads.

of the known gold mineralisation. The subsequent work is mostly contained in WMC internal reports. Much of this work is summarised by Roberts and Elias (1990). However, particularly detailed work on gold mineralisation at the Hunt deposit (Figure 1.1) is published by Phillips and Groves (1984) and Neall and Phillips (1987) and gold mineralisation at the nearby Victory-Defiance deposit (Figure 1.1) is published by Clark *et al.* (1986, 1989). Other selected publications that discuss various aspects of the geology of the Kambalda area include Bavington and Keays

(1978), Roddick (1984), Cowden and Archibald (1985), Campbell and Hill (1988), Cowden (1988), Perring *et al.*. (1989), Cowden and Roberts (1990), Swager and Griffen (1990), Perring and McNaughton (1992), Witt (1993) and Lesher and Arndt (1995).

The numerous publications and internal reports that cover various aspects of the geology and geochemistry in and around the Junction gold deposit are of interest to this project. The exploration history of the Junction gold deposit is summarised by Balkau (1989). This report covers the difficulties experienced by WMC geologists in locating the deposit during the early days of exploration, and the conclusions therein undoubtably highlight the need for alternative exploration methods in the Kambalda area. Clarke (1988, 1993 1994a, 1994b, 1994c) is extensive in his investigations of the geomorphological and sedimentological aspects of the palaeodrainage systems in the Kambalda to Norseman region. In particular, Clarke (1988) reports on the relationship between the 1985 soil-geochemistry anomalies above the Junction deposit and the alluvial gold mineralisation hosted by the Tertiary palaeochannel(s) that traverse the mineralised section of the Junction Gabbro. The alteration assemblage associated with gold mineralisation at Junction is discussed by Costello (1993, 1994), Carey (1994) and Gilmore (1996). These authors give a detailed account of the petrology of the alteration assemblage associated with mineralisation. These reports discuss the three distinct alteration zones that exist around the gold mineralisation. The petrography and geochemistry of the Junction, Condensor and Golden Mile gabbro sills is discussed by Carey (1994) who concludes that the high iron content found in the most differentiated part of these sills is most favourable for the desulphidisation of a gold-bearing hydrothermal fluid. Felsic intrusions that exist within the Junction Gabbro are discussed by Murphy (1995) who suggests that these intrusives were emplaced during near-peak metamorphism but prior to the gold-mineralising event. Gilmore (1996) compiled a structural and geotechnical analysis of the Junction open pit. His work is complemented by Mol *et al.* (1996), who discuss a variety of structural features that occur in the upper 300 m of the mine. Finally, Ellis and Mapleson (1997) report on the alteration assemblage around the contact aureole of a Proterozoic dolerite dyke and comment on the redistribution of gold associated with the introduction of this late-stage intrusion.

CHAPTER TWO

Regional Geology

2.1 Overview of the Yilgarn Craton

The Yilgarn Craton (Figure 2.1) is a coherent unit of Archaean continental crust that was stabilised by a late-Archaean orogenic event at approximately 2.6 Ga (Myers and Hickman, 1990 and Barley *et al.*, 1990a). It covers approximately 635,000 km^2 of south-western Western Australia (Gresham and Loftus-Hills, 1981). The Yilgarn Craton consists of a series of terrains and superterrains (formerly known as provinces). The superterrains range in age from the 3.65 Ga Narryer Gneiss of the West Yilgarn Superterrain, to the 3.3 - 2.6 Ga, upper amphibolite - granulite gneiss and greenstone complexes of the South-west Terrain of the West Yilgarn Superterrain, to the 3.0 - 2.6 Ga mostly greenschist facies granite - greenstones of the West Yilgarn Superterrain, Southern Cross Superterrain, and Eastern Goldfields Superterrain (Gee *et al.*, 1981; Gee *et al.*, 1986; Myers and Hickman, 1990; Barley *et al.*, 1990a; Witt *et al.*, 1998). The Junction gold deposit is hosted in the Kalgoorlie terrain, the western terrain of the Eastern Goldfields Superterrain (Norseman - Wiluna belt), according to the classification of Witt *et al.* (1998).

The western Eastern Goldfields Superterrain is distinguished by a composite greenstone belt, 800 km long and up to 150 km wide that runs from the northern gold town of Wiluna to the southern gold town of Norseman. The belt is dominated by volcano-sedimentary assemblages, with rare oxide facies ironstones (Barley *et al.*, 1990a). The Kalgoorlie terrain is characterised by a relatively simple and consistent stratigraphy comprising a lower mafic-ultramafic sequence overlain by felsic volcanic and volcaniclastic rocks (Swager *et al.*, 1992). Depositional ages for the greenstones of the western Eastern Goldfields Superterrain vary from 2700 to 2690 Ma for the komatiitic volcanic units to around 2680 for the felsic Black Flag Group (Claoue-Long *et al.*, 1988; Carey, 1994; Nelson, 1995).

Seismic and density profiles indicate that the Yilgarn Craton is up to 50 km thick adjacent to Proterozoic orogens (Barley *et al.*, 1990a). Interpretation of an east-west seismic traverse across the southern part of the Kalgoorlie terrain near Kambalda suggests that the greenstones bottom out against felsic crust along a flat-lying surface at around seven km (Witt *et al.*, 1997).

Traditionally, the Yilgarn Craton is known for its heterogeneous distribution of small, medium and world class gold and primary nickel deposits. As of 1990, the Norseman-Wiluna belt is

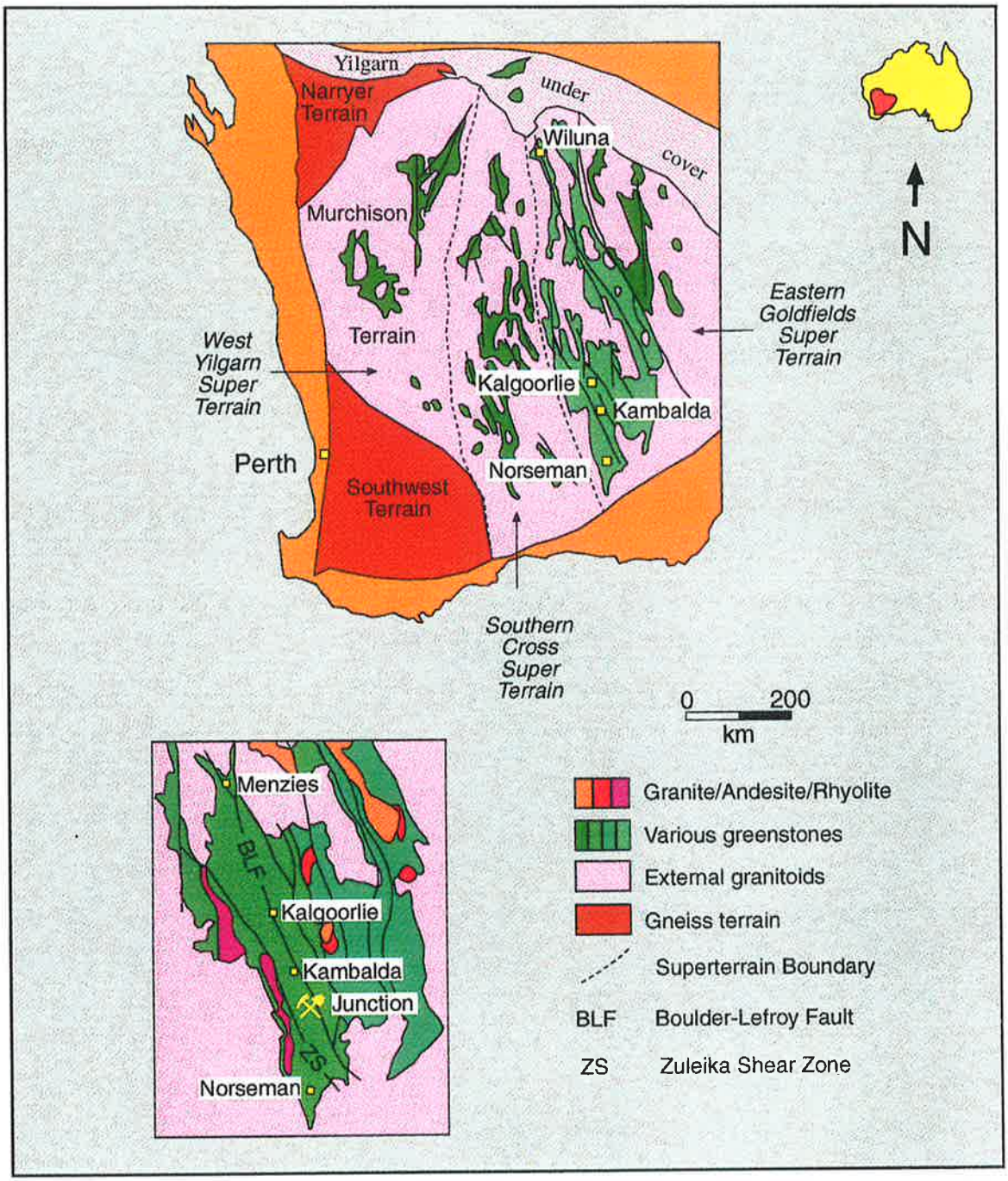


Figure 2.1. Regional geology of the Yilgarn Craton, Western Australia, incorporating the geology of the southwestern Kalgoorlie Terrain (inset). Compiled from figures presented in Phillips and Groves (1983), Barley *et al.* (1992) and Witt *et al.* (1998).

recognised as being the most highly mineralised greenstone belt in the Yilgarn Craton (Groves *et al.*, 1990). Gold is regionally and effectively controlled by craton scale, high strain, deformation structures, with the best mineralised terrains being those with a high density of anastomosing, oblique, to strike-slip transcraton deformation zones which control the geometry of adjacent, subsidiary mineralised structures (Barley *et al.*, 1990b). The Norseman-Wiluna belt is characterised by a closely spaced network of north-north-westerly trending deformation zones, including an

upright regional foliation, craton-scale shear zones, and elongate granitoid bodies (Witt, 1993).

The Kalgoorlie-Kambalda-Norseman area, which is the host area of the Junction deposit, is bound by two craton scale north-north-westerly structures: the Ida Fault to the West and the Boorara-Menzies Shear Zone to the east (Witt, 1993; Witt *et al.*, 1997). Locally, the Junction deposit is bound to the west by the Zuleika Shear Zone and to the east by the Boulder-Lefroy fault (Figure 2.1, inset).

Regional deformation of the greenstones at Kambalda consist of four separate phases of deformation (Witt *et al.*, 1997). Deformation commenced with thrust faulting and recumbent folding, layer parallel flattening and locally layer parallel shear fabrics (D1), possibly associated with an early stage of north-south compression (Archibald *et al.*, 1981; Archibald, 1985; Swager and Griffin, 1990).

The second episode of deformation involved the formation of upright asymmetric, inclined to recumbent folds with north-north-west trending fold axes (D2: Swager *et al.*, 1992; Witt *et al.*, 1997). These folds are displaced by thrust planes parallel or sub-parallel to their axial plane (Cowden and Roberts, 1990). This event is related to east-north-east/west-south-west to east-west compression (Swager *et al.*, 1992).

The third episode of deformation (D3) was the main phase of east-west shortening. The formation of north-north-west trending upright open folds with large wavelengths and low amplitudes, and a major north-north-west brittle ductile fault/shear system (Clark, 1987), were the major structures formed during this episode. The third episode of deformation coincides with peak metamorphism to amphibolite facies. Regional metamorphism in the Kambalda area peaked at the greenschist-amphibolite transition. Witt (1992) calculated the temperature of metamorphism to be 470 - 530°C and the associated pressure at 0.2 - 0.3 Gpa.

The fourth stage of deformation (D4) involved north-north-west faulting, shearing and mylonitisation, which often appears to be parallel to the axial trace of the D3 anticlines (Archibald, 1985). The faults and shear zones that developed during this period of deformation are large-scale (transcrustal), regional scale structures (Groves *et al.*, 1998). All mineralisation in the Kambalda district is hypothesised to be associated with second, third and fourth order branching structures off the Boulder-Lefroy fault, which formed during this stage of deformation. Retrograde upper greenschist metamorphism and local carbonatisation are associated with this mineralisation (Phillips and Groves, 1984; Clark, 1987; Neal and Phillips, 1987; Groves *et al.*, 1998).

2.2 Stratigraphy of the Kambalda region

There are four informal stratigraphic groups in the Kambalda area. They are the Red Hill Group, the Kalgoorlie Group, the Black Flag Group and the Merougil Beds (Figure 2.2). These groups

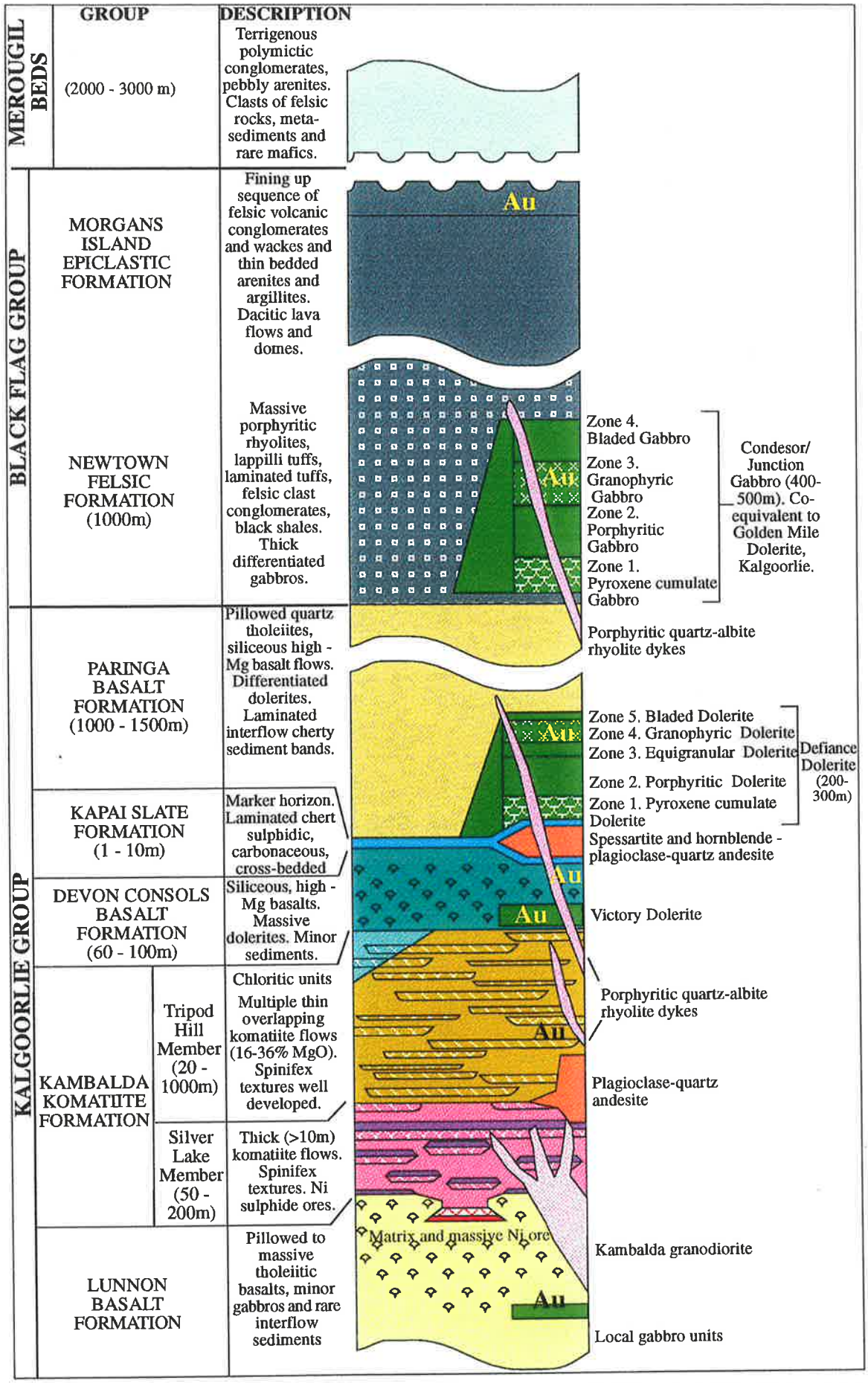


Figure 2.2. Stratigraphic column for the Kambalda succession (after Sudgen *et al.*, 1995). The basal Red Hill Group is below this section.

are further subdivided into formations and where necessary, these formations are divided into members.

2.2.1 Red Hill Group

The Red Hill Group is the lowermost of the four groups and comprises a sequence of tholeiitic basalts, gabbro-dolerites, occasional hyloclastite and rare, thin discontinuous sediment horizons (Cowden, 1986).

2.2.2 Kalgoorlie Group

The Kalgoorlie Group consists of the Lunnon Basalt Formation, the Kambalda Komatiite Formation, (sub - divided into two members, the Silver Lake Peridotite Member and the Upper Tripod Hill Komatiite Member), the Devon Consols Basalt Formation, the Kapai Slate Formation, the Paringa Basalt Formation and the Defiance Dolerite.

2.2.2.1 Lunnon Basalt Formation

The Lunnon Basalt Formation is at the base of the known 5000 m-thick Kalgoorlie Group sequence. The Lunnon Basalt Formation consists of a sequence of pillowed to massive tholeiitic basalt with inter-layered dolerites, gabbros and thin interflow sediments (Hein *et al.*, 1996).

2.2.2.2 Kambalda Komatiite Formation

The Kambalda Komatiite Formation conformably overlies the Lunnon Basalt Formation. This has been divided into two members, the Silver Lake Member and the Tripod Hill Member.

2.2.2.2.1 The Silver Lake Member

The Silver Lake Member reaches 100 m in thickness and generally consists of one or more komatiite flows. Lateral variations in composition, differentiation, and the distribution of interflow sediments within each flow, allow the Silver Lake Member to be divided into two facies; the ore environment channel-flow facies and the non ore environment sheet-flow facies (Hein *et al.*, 1996).

2.2.2.2.2 The Tripod Hill Member

The Tripod Hill Member consists of up to 700 m of thin < 0.5m to 10m komatiite flows. Thickened zones represent weakly developed channel-flow facies. The Tripod Hill Member can be distinguished from the Silver Lake Member by its much thinner flows and its lesser lateral continuity (Cowden and Roberts, 1988; Hein *et al.*, 1996).

2.2.2.3 Devon Consols Basalt Formation

The Devon Consols Basalt Formation is a pillowed and massive epidote-rich komatiitic basalt. It ranges in thickness from 60 m -100 m, and is intruded by thin differentiated dolerites, including the Victory Dolerite. The Devon Consols Basalt Formation contact with the underlying Tripod

Hill Member ranges from sharp to transitional.

2.2.2.4 Kapai Slate Formation

The Kapai Slate Formation is an important regional stratigraphic marker occurring between the Devon Consols Basalt Formation and the Paringa Basalt Formation (Clark, 1987). It consists of laminated carbonaceous, sulphidic black shales with some highly altered felsic volcanics. It ranges in thickness from 1-10m. The bands of sediment are commonly separated by albitised mafic rocks or dacite to rhyolite sills. Primary sedimentary textures are rare, apart from local cross bedding (Roberts and Elias, 1990). It can be sub-divided into five lithofacies (Hein *et al.*, 1996):

- a laminated siliceous magnetite-bearing slate or phyllite,
- a siliceous pyrrhotite-bearing slate or phyllite,
- a magnetite-bearing chert or phyllite,
- a carbonaceous pyrite-bearing slate or phyllite, and
- an iron-sulphide bearing chert.

2.2.2.5 Paringa Basalt Formation

The Paringa Basalt Formation consists of thin variolitic pillowed flows and massive basaltic flows, thin to thick differentiated dolerite units (Defiance Dolerite), and rare thin interflow shale horizons (Roberts and Elias, 1990; Balkau, 1989; Carey, 1994). The Defiance Dolerite is interpreted to have fractionated in situ to produce up to five consistent internal zones and layers. The layered dolerites within the Paringa Basalt Formation are generally 10-40 m thick. The consistent internal zonation shows basal pyroxenite to central dolerite to a massive top with randomly oriented acicular amphibole-chlorite-biotite (Roberts and Elias, 1990). The thickest of the layered dolerites is the Defiance Dolerite, which occurs at the base of the Paringa Basalt Formation and is up to 300 m thick (Archibald, 1985).

2.2.3 Black Flag Group

The Black Flag Group comprises a thick sequence of felsic volcanic and /or sedimentary units up to 2000 m thick. It is conformable on the mafic-ultramafic lavas of the Kalgoorlie Group. The Black Flag Group can be divided into two formations, the Newton Felsic Formation (including the Black Flag Beds) and the Morgans Island Epiclastic Formation.

2.2.3.1 Newtown Felsic Formation

The Newtown Felsic Formation is up to 1000 m thick. The basal 200 m are dominated by mafic conglomerates and volcanic breccias with abundant mafic clasts (Cowden and Archibald, 1987). These are known as the Black Flag Beds. Felsic volcaniclastic rocks including lapilli tuffs, laminated tuffs and related epiclastic sediments, interpreted by Balkau (1989) as being pyroclastics dominate the Newtown Felsic Formation above the predominantly mafic basal 200 m. The

felsic volcanics are overlain by calcareous greywackes and felsic conglomerates, which are in turn overlain by thin bedded sandstones and siltstones (Hand, 1996).

2.2.3.1.1 The Condensor, Junction and Golden Mile gabbroic sills

A series of stratigraphically equivalent, differentiated iron-rich tholeiitic sills intrude the Black Flag Beds just above the contact with the Paringa Basalt Formation. These are the Condensor, Junction and Golden Mile Gabbros. All three gabbros have been interpreted to be stratigraphically and geochemically equivalent to each other (Roberts, 1987; Carey, 1994). These gabbros are up to 500 m thick and contain internal zonation. Magnetite is common in the middle and upper zones of the sills and ilmenite is ubiquitous.

The Junction Gabbro is the host rock of the gold mineralisation at the Junction gold mine and is therefore an important focus in this study. Details of its textural and geochemical characteristics will be dealt with in more detail in later chapters. The Junction gabbroic sill is up to 500 m thick (Roberts and Elias, 1990) and displays textural and mineralogical zonation that allows four distinct zones to be recognised from base to top.

2.2.3.2 Morgans Island Epiclastic Formation

Three facies are recognised within the Morgans Island Epiclastic Formation (Hein *et al.*, 1996). From oldest to youngest, these are:

- interbedded massive to diffusely bedded sandstone and polymictic breccias displaying disorganised beds and weakly-developed sedimentary structures,
- interbedded massive and well bedded sandstones that display basal scouring, loaded sandstone ball structures, ripple cross beds, climbing ripples and planar laminations, and
- interbedded-interlaminated shales and siltstones that display ripples, laminations, cross bedding and soft sediment deformation.

2.2.4 Merougil Beds

The Merougil Beds are interpreted to be a series of terrigenous rudites and arenites that lie unconformably on the Black Flag Group (Cowden, 1986; Roberts and Elias, 1990). They are considered to be a late (post - tectonic) element of the Archaean stratigraphy and could be up to 3000 m thick (Roberts and Elias, 1990).

CHAPTER THREE

Geology and petrography of the Junction gold deposit

3.1 Introduction

The Junction gold mine is a late-orogenic, structurally-controlled gold deposit hosted by the Junction Gabbro (Figure 3.1). The term "late-orogenic, structurally-controlled gold deposit" is proposed by Witt and Vanderhor (1998) as one which more completely encompasses the class of mineralisation formerly termed mesothermal lode-gold deposit. Groves *et al.* (1998), announce that the term "mesothermal" is not appropriate for this deposit type because mesothermal was first applied by Lindgren (1933) for deposits that formed specifically at depths of 1.2 to 3.6 km. Witt and Vanderhor (1998) further suggest that the terms epizonal, mesozonal and hypozonal be used where appropriate to reflect the exact crustal depth of gold deposition.

3.2 Methods and procedures

The geology at Junction was investigated by mapping drives and collecting samples from throughout the deposit (Figure 3.2). Drill core, and hand specimen samples were the two principle sample types used in the investigation. Vein-type and alteration assemblage relationships were observed during detailed mapping along two underground drives. Drive 502-1-25 (Figures 3.3a and 3.3b) is representative of mineralisation within Zone 3 of the Junction gabbro, whereas drive 402-1-54 is representative of mineralisation within Zone 4 of the Junction gabbro (Figure 3.4).

The petrography of Junction deposit was investigated using:

- transmitted - reflected light microscopy,
- cathodoluminescence microscopy (CL), employing a Leitz Wetzlar microscope with a Technosyn Cold Cathode Luminoscope Model 8200 Mk2 stage,
- scanning electron microprobe (SEM) analysis, employing a Phillips XL-30 SEM fitted with an edax probe attachment,
- electron microprobe analysis, using a Cameca SX51 electron microprobe and, X-ray diffraction (XRD) analysis, employing a Siemens X-ray diffractometer.

Analytical data discussed in this chapter is presented in Appendix I, II, III, and IV.

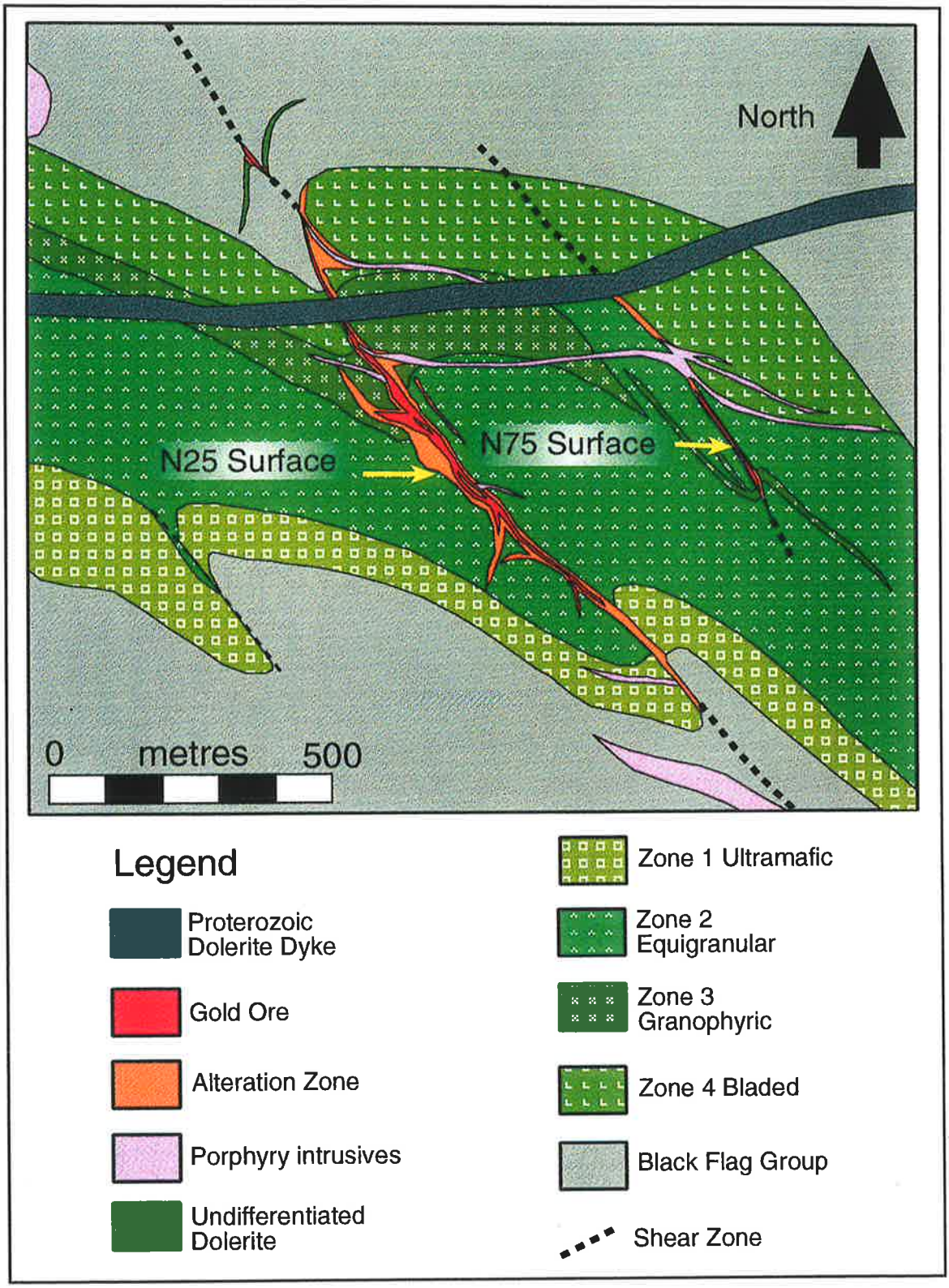


Figure 3.1. Geology of the Junction gold mine highlighting the currently mined N25 surface and the narrower, but related N75 surface (modified from Ellery and Watts, 1996).

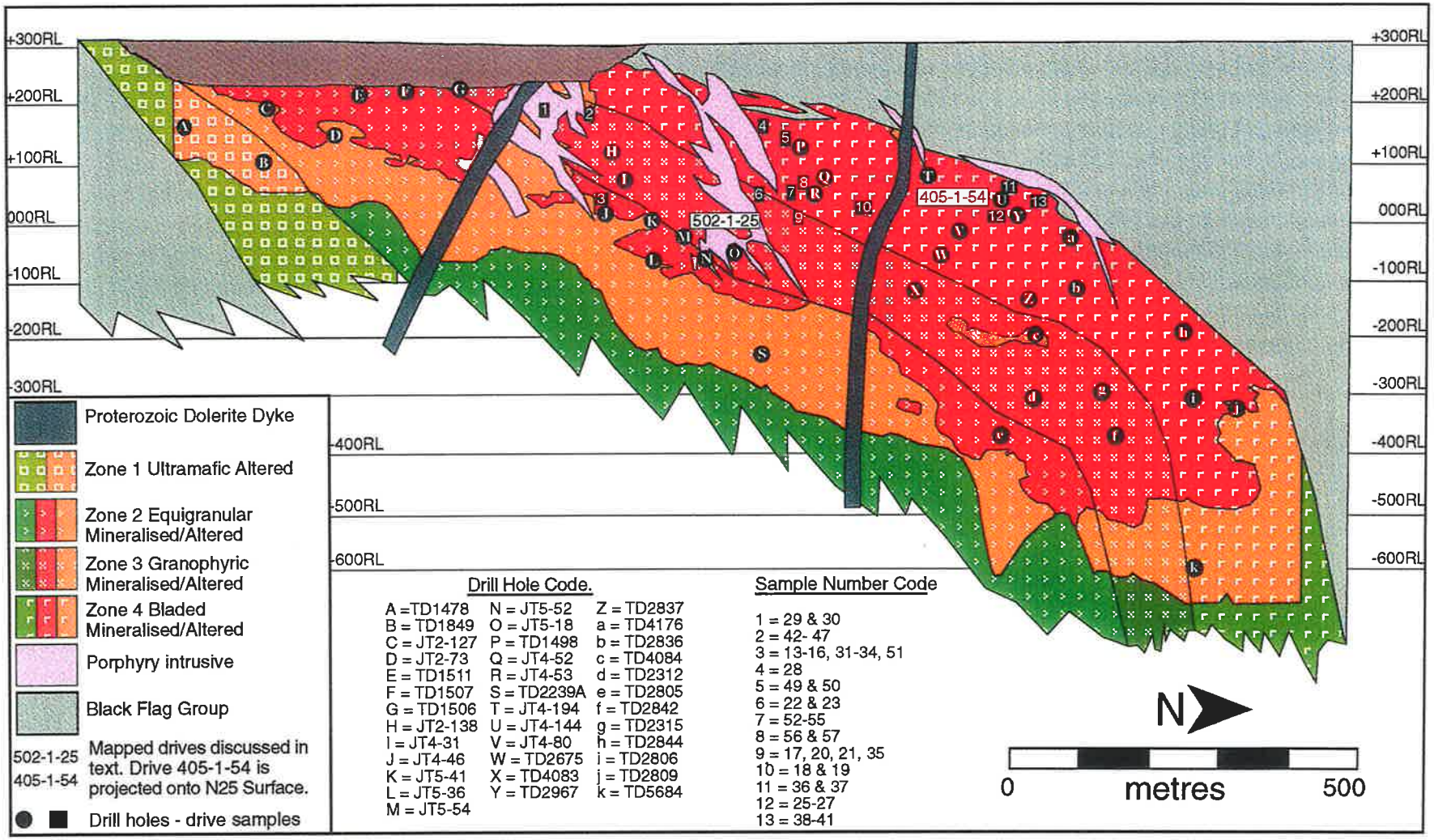


Figure 3.2. Longitudinal cross section through the Junction Shear Zone (N25 surface) showing the zonation of the Junction Gabbro in relation to gold mineralisation. For this diagram, mineralised refers to drill hole intersections that graded > 2 grams/ton Au, whereas altered refers to visible chlorite ± carbonate alteration that grades < 2 grams/ton Au. Drill holes sampled for this project are labelled and samples collected from these drill holes can be cross-referenced in Appendix I. RL is a WMC acronym for relative sea-level and is referred to in the text. Diagram modified from maps drawn by Costello (1994) and Peden (1997).

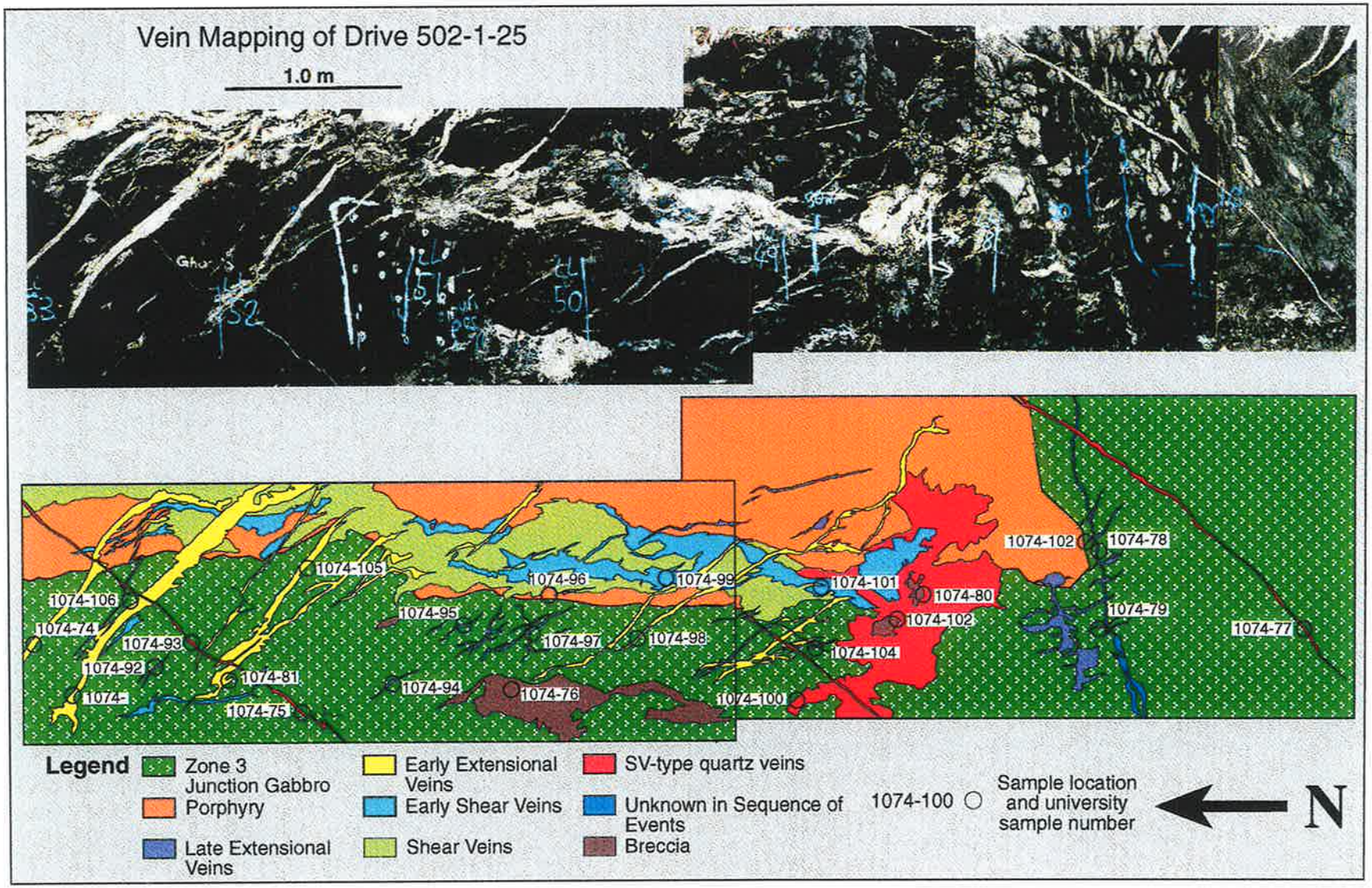


Figure 3.3a. Vein mapping of drive 502-1-25. Vein details are not included on the map, but are discussed in text (section 3.6). Joins southern end of Figure 3.3b.

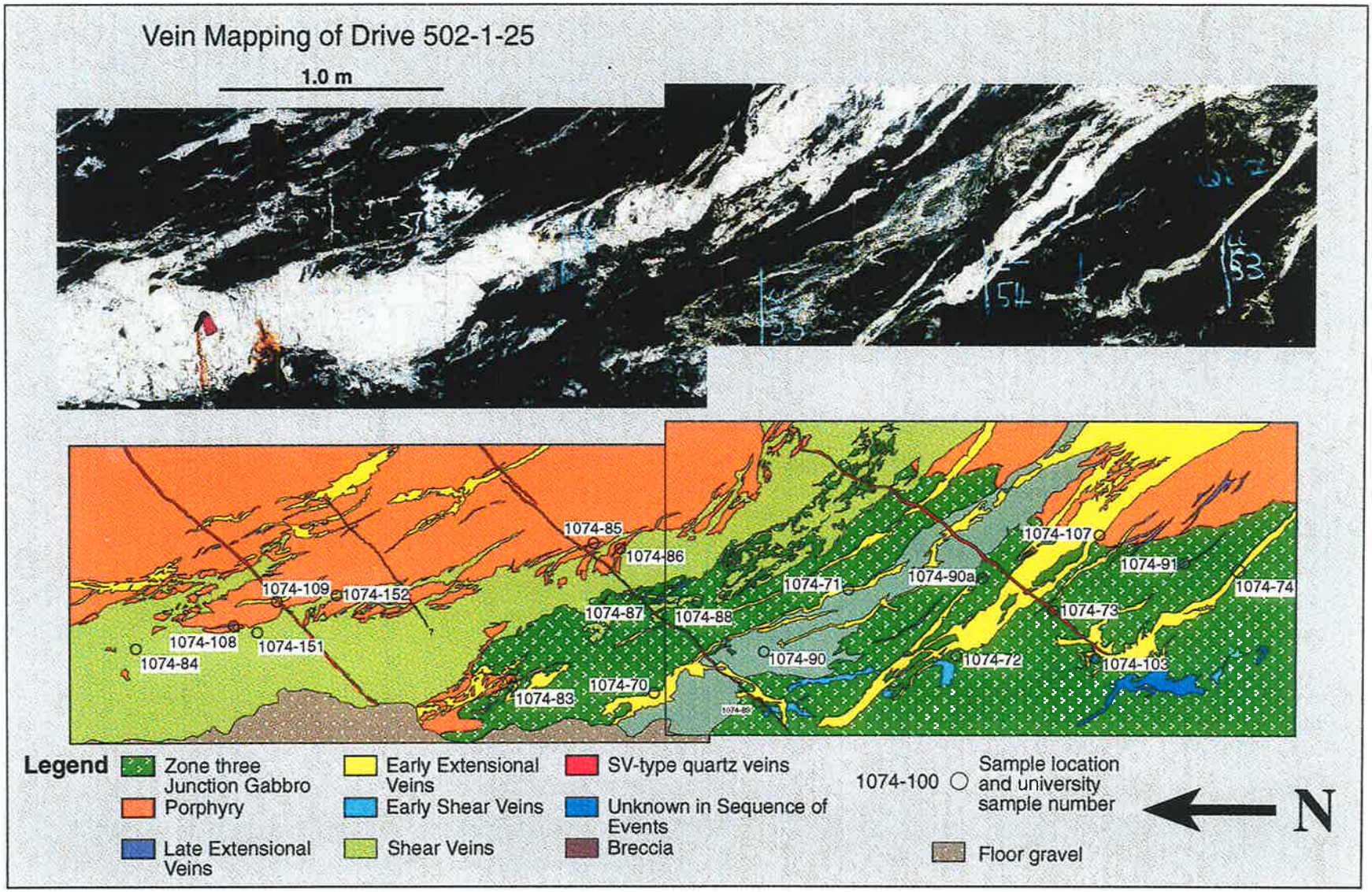


Figure 3.3b. Vein mapping of drive 502-1-25. Vein details are not included on the map, but are discussed in text (section 3.6). Joins northern end of Figure 3.3a.

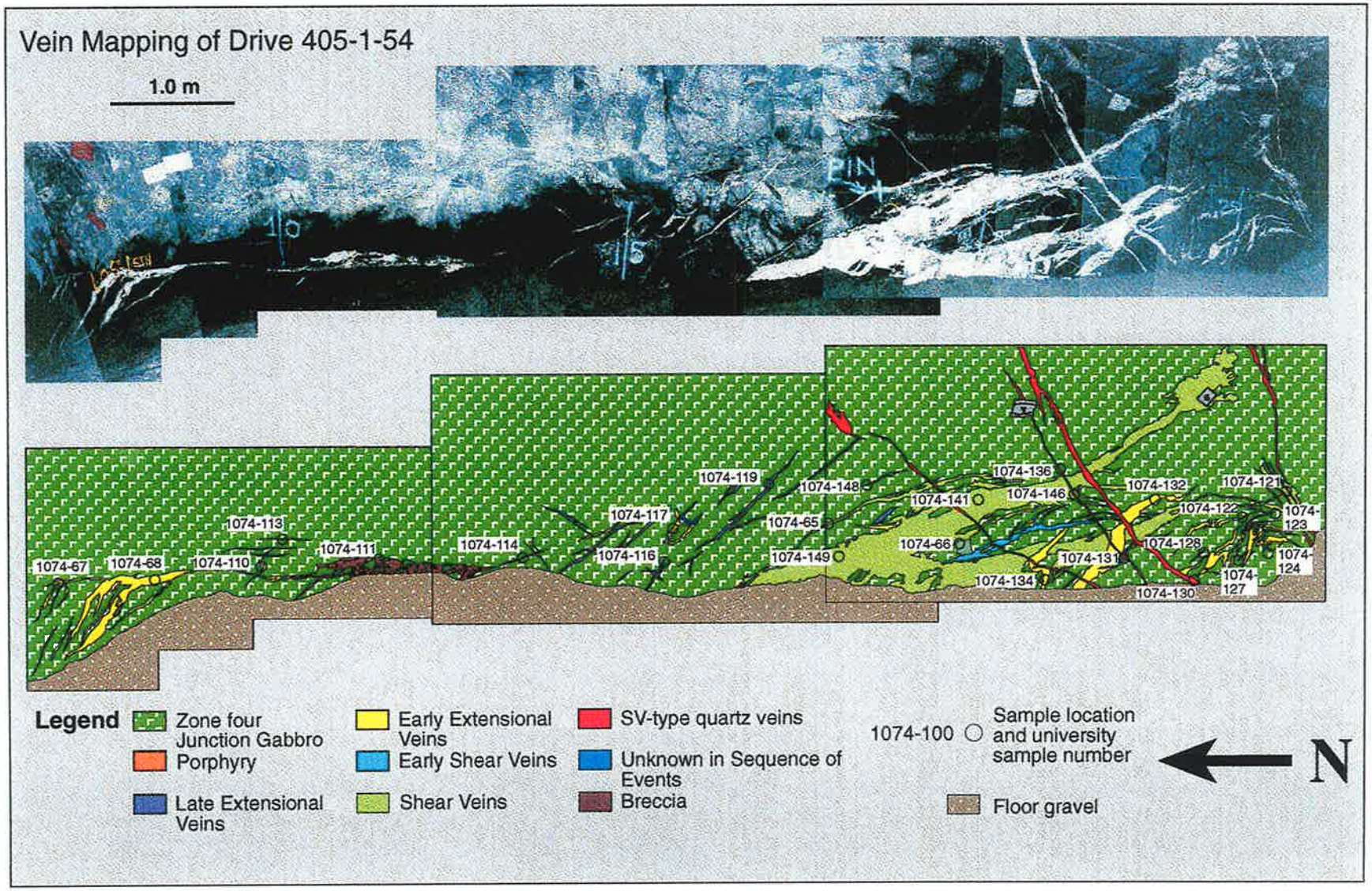


Figure 3.4. Vein mapping of drive 405-1-54. Vein details are not included on the map, but are discussed in text (section 3.6).

3.3 The Junction Gabbro

The Junction gold deposit is hosted by the Junction Gabbro (Figure 3.1) which intrudes the lower unit of the Black Flag Beds, just above its contact with the Paringa Basalt (Roberts and Elias, 1990; Carey, 1994; Holland, 1995; Hein *et al.*, 1996).

The Junction Gabbro and its co-equivalents, the Condensor Gabbro and the Golden Mile Gabbro (host of the giant Golden Mile Deposit, Kalgoorlie), represent the last mafic magma within the Kambalda succession. They are differentiated, iron-rich, tholeiitic gabbro sills. The Condensor Gabbro has been dated by Carey (1994) by U-Th-Pb analyses using a SHRIMP ion microprobe to give an age of 2680 ± 8 Ma.

The Junction Gabbro is known to be up to 500 m thick (Roberts and Elias, 1990). It is divided into four distinct zones (plus upper and lower chill margins) based on petrographical and geochemical observations. The geochemistry of the Junction Gabbro is presented in Table 3.1. Geochemical and petrographical criteria indicate that the Junction Gabbro crystallised from the bottom up, and the top down, with crystallisation from the bottom up commencing first (Hein *et al.*, 1996). This has resulted in the most evolved magma crystallising 2/3 to 3/4 the way up the sill, forming a granophyric zone.

Metamorphic reactions that occurred within the Junction Gabbro during regional metamorphism (Witt, 1992) preserved many of the original igneous textures through pseudomorphism. Carey

Geochemistry of the Junction Gabbro

	Chill Zone#	Zone 1#	Zone 2#	Zone 3#	Zone 4#	Undifferentiated Gabbro*	Undifferentiated Gabbro*
SiO_2	48.68	48.78	49.20	50.51	49.73	51.80	51.08
TiO_2	1.17	1.02	1.20	1.97	0.99	1.03	1.09
Al_2O_3	14.09	14.25	14.04	11.69	14.53	15.20	14.55
Fe_2O_3	13.81	13.09	11.70	17.81	11.44	16.42	12.26
MnO	0.23	0.19	0.17	0.19	0.17	0.18	0.17
MgO	6.92	7.81	5.76	3.90	6.34	3.33	4.69
CaO	10.22	10.35	11.06	8.31	11.33	8.07	9.64
Na_2O	2.39	1.62	2.29	2.48	2.30	3.99	4.36
K_2O	0.38	0.74	0.36	0.28	0.15	0.64	0.36
P_2O_5	0.04	0.04	0.05	0.11	0.02	0.16	0.14
S	0.52	0.25	0.52	0.03	0.01	0.25	n.d
TOTAL	99.45	98.14	96.35	97.28	97.01	100.20	98.76

* Murphy (1995), # Carey (1994).

Table 3.1. The geochemical composition of the Junction Gabbro compiled from data by Carey (1994) and Murphy (1995).

(1994) combined the petrography of the pseudomorphs with electron microprobe analyses and CIPW normative compositions to determine the nature of the original igneous petrology.

3.3.1 Zone one

Zone one represents a weak accumulation of more mafic minerals in the basal part of the sill. It consists of approximately 60% amphibole (both actinolite, hornblende ± tremolite co-exist, but actinolite predominates; Carey, 1994; Gilmore, 1996) and chlorite pseudomorphs after olivine and pyroxene in a fine grained matrix (Figure 3.5a). In some cases, both of these phases pseudomorph the same primary crystal, preserving exsolution of augite from orthopyroxene. Chlorite makes up the bulk of the pseudomorphs with the amphiboles present as thin bands parallel to the 001 plane of the crystal indicating that chlorite was an initial pseudomorphing phase rather than a later alteration product (Carey, 1994).

Saussuritic pseudomorphism of plagioclase contributes to approximately 35-40% of zone one. The saussurite assemblage is clinozoisite - epidote - calcite - albite (Carey, 1994). This saussuritic alteration is present as small irregular intergranular masses which represent the breakdown of intercumulus plagioclase.

Oxides represent less than 2% of zone one and consist predominantly of ilmenite, with up to 90% of the ilmenite breaking down to titanite. Secondary magnetite is rare and occurs as an overgrowth on the amphiboles.

3.3.2 Zone two

Zone two is a porphyritic textured dolerite marked by dark green, equant hornblende and paler elongate actinolite that are pseudomorphs after orthopyroxene and clinopyroxene respectively (Figure 3.5b; Carey, 1994; Hein *et al.*, 1996). A gradual transition from zone one to zone two is marked by a decrease in the proportion of normative mafic minerals, but an increase in the normative clinopyroxene content relative to normative orthopyroxene. The boundary is further marked by a change in the oxide species from ilmenite to titanomagnetite (Carey, 1994).

The hornblende and actinolite pseudomorphs make up 45 - 50% of zone two, with actinolite becoming slightly more abundant with increasing height within the sill. These pseudomorphs suggest that orthopyroxene was superseded by clinopyroxene towards zone three. Electron microprobe data collected by Carey (1994), provide evidence to support the presence of two igneous pyroxene populations prior to metamorphic rehydration.

Plagioclase makes up to 50% of zone two. It is present in two forms; distinct laths and as an interstitial phase. There is an increase in the size of plagioclase laths as well as an increase in the degree of elongation of the laths as the sill grades into zone three. Normative compositions suggest that the plagioclase became increasingly albitic with progressive crystallisation. The

overall textures of zone two suggest simultaneous plagioclase-pyroxene crystallisation.

Secondary actinolite exists that does not replace an igneous phase, but overprints the remainder of the mineralogy. The actinolite occurs as clumps of needle-like crystals up to 1 cm long, radiating out from a central point. Carey (1994), has subdivided zone two into two sub-zones, based on changes in the oxide species ilmenite and titanomagnetite and the amphibole content (both hornblende and actinolite) which varies between 45% and 55% within the two sub-zones.

Zone two (A) is characterised by oxides that have been totally altered to titanite ± rutile. The titanite has preserved the exsolution texture typically associated with the oxide species titanomagnetite. Zone two (A) also shows a distinct drop in the concentration of incompatible elements. This is interpreted to be due to the higher proportion of plagioclase in this zone. This hypothesis is supported by the increase in Ca and Al content and a lower amphibole content (45%) in this zone. Zone two (A) is further characterised by weak microrhythmic layering. This takes the form of amphibole rich bands alternating with saussurite rich bands.

Zone two (B) is characterised by a rapid transition from the oxide species titanomagnetite back to ilmenite. Toward the top of zone two (B), ilmenite is interpreted to have become a liquidus phase which is reflected by its large (2-3 mm) skeletal forms. Zone two (B) shows an increase in the concentration of incompatible elements and has a higher amphibole content (55%) than zone one.

3.3.3 Zone three

Zone three ranges in thickness, present where the sill is thickest, and absent where the sill thins. The boundary between zone two and zone three is often ambiguous and may appear in hand specimen to be either gradational or sharp (Carey, 1994). However, the magnetic susceptibility data usually shows a sharp change from low (0.7 SI units) to high (50 - 80 SI units) over a distance as small as 1 cm. The overall trends in mineralogy and texture across the boundary, regardless of the rate of change, are an increasing granophyric texture and plagioclase content (up to 55%), and an elongation of plagioclase and pyroxene pseudomorphs (Figure 3.5c; Carey, 1994).

Carey (1994) shows that zone three was recrystallised by late stage (deuteric) fluids released from the crystallising magma, resulting in a diffuse textural change across the boundaries of zones two and four. These late stage fluids are also thought to be responsible for the development of a granophyric intergrowth between albite and quartz (Figure 3.6) which gives the matrix an opalescent greyish-blue appearance. As a result of this re-crystallisation, hornblende and albite do not pseudomorph primary minerals. Amphibole exists as elongate acicular crystals and makes up 45% of the zone. The amphiboles are dominated by hornblende in zone three, but electron microprobe analyses indicate that a continuum between hornblende and actinolite may exist,

probably as a result of the late deuteric fluids (Carey, 1994). Larger elongate hornblende interlocks with 5-7 mm long albite laths. Epidote is present as a relatively coarse euhedral phase, as a product of igneous Ca-rich plagioclase breakdown (Carey, 1994).

The oxide phase in zone three is higher than in any other zone (10-12%). Ilmenite and magnetite coexist, either as homogeneous grains or as an exsolution of one within the other (Figure 3.7). The ilmenite - magnetite exsolution textures are not true exsolution products, but are instead a result of titanium exsolving from titanomagnetite into laths of ilmenite during temperature lowering and oxidation associated with cooling (Vaughan and Craig, 1997). The oxides show no breakdown to titanite, but some oxides are rich in silicate inclusions. The lack of retrograde breakdown, combined with the knowledge that this zone has reacted with deuteric fluids indicates that the oxides are secondary. They are either a product of hornblende breakdown, or a product of recrystalisation of primary oxide phases (Carey, 1994).

Zone three represents the last magma to crystallise in the sill, and marks the peak of the sill's differentiation trend. Therefore, it has the highest iron and incompatible element content. This is expressed by the crystallisation of a significantly higher proportion of oxides in this zone. Normative compositions suggest that olivine was a crystallising phase (Carey, 1994).

3.3.4 Zone four

Zone four is a reasonably homogeneous bladed norite (Figure 3.5d; Hein *et al.*, 1996), with a tendency towards upwardly-increasing grain size, until it passes sharply into the fine grained upper chill margin of the sill.

Zone four, like zone two, has both actinolite and hornblende pseudomorphs. The average total amphibole content of zone four is 45 - 50%. Textures indicate that plagioclase and pyroxene were crystallising simultaneously (Carey, 1994).

Saussurite replacing plagioclase and fine euhedral (secondary) quartz surrounded by fine grained albite, quartz, and actinolite with minor areas of granophyric growth makes up 45 - 50% of zone four (Carey, 1994).

Ilmenite is the dominant oxide present in zone four, occurring as a minor part (<2%) of the matrix. Larger (2 - 2.5 mm) ilmenite crystals have been reduced to small patches of ilmenite surrounded by titanite ± minor rutile.

Geochemically, zone four is moderately enriched in the incompatible elements, iron and titanium when compared to zone one or the base of zone two. This implies that the magma which crystallised at the top of the sill underwent significant evolution prior to accumulation (Carey, 1994).

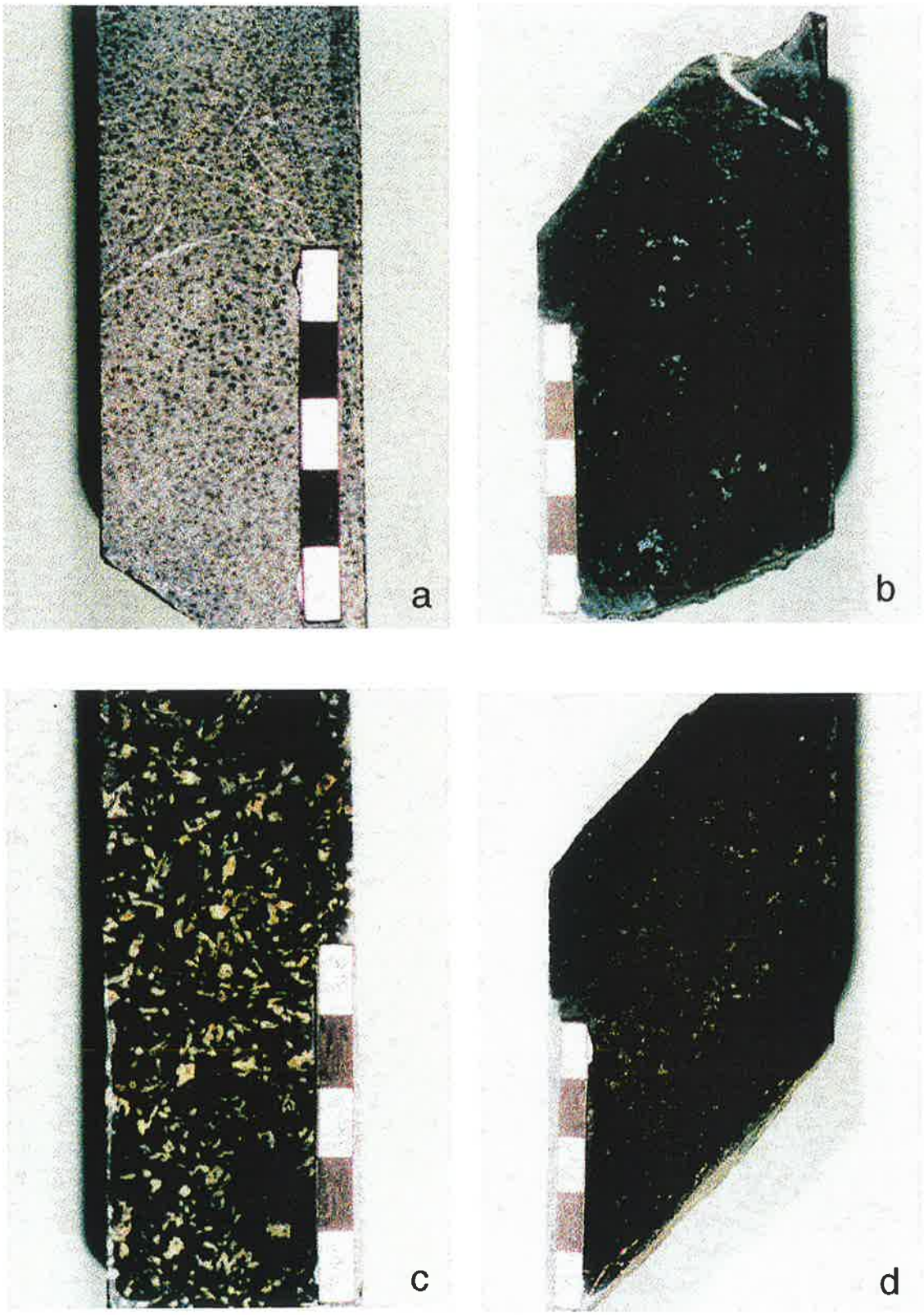


Figure 3.5. Drill core hand specimens showing texture characteristics of Junction Gabrro from a) Zone 1: cumulative, b) Zone 2: equigranular, c) Zone 3: granophyric, d) Zone 4: bladed. Scale is in cm.



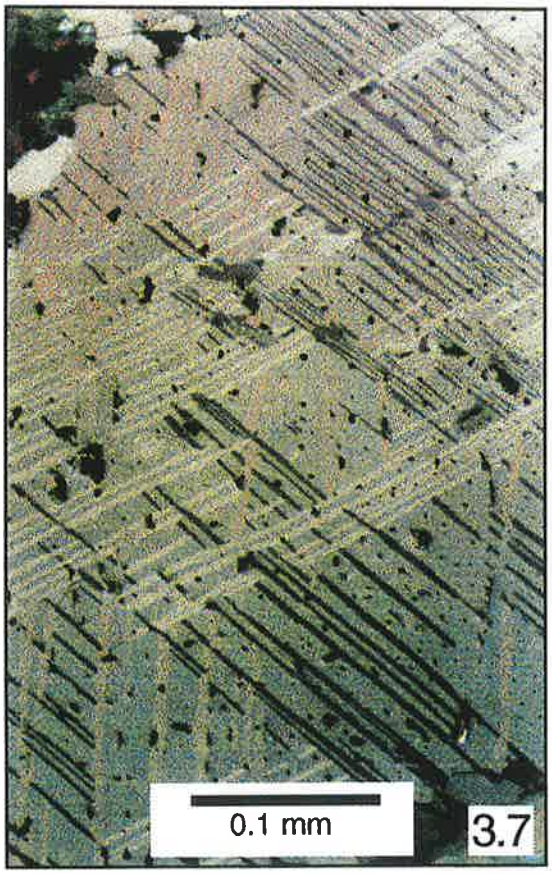


Figure 3.6. Photomicrograph of granophyric intergrowth between quartz and albite that formed in zone three of the Junction Gabbro.
Figure 3.7. Photomicrograph of ilmenite laths exsolved from titanomagnetite (now magnetite) preserving the pre-existing exsolution texture of titanomagnetite.

3.4 The late intrusives

The gold mines of the Kambalda region are characterised by a number of small to medium sized intrusions that are texturally, mineralogically and chemically diverse. Pering *et al.*. (1989) identified a suite of porphyritic dykes and sills ranging from mafic (lamprophyric) to intermediate and felsic compositions that intrude the Kambalda stratigraphy from pre-D1 to syn-D3, together with a trondhjemitic stock that forms the Kambalda Dome (see Figure 2.2). At Junction, the porphyries intruded prior to the main gold mineralisation event. Murphy (1995) classified a number of small (2-10 m wide) felsic intrusives that cross cut the Junction Gabbro into two specific rock-types. These are classified as a porphyritic micro-quartz-monzodiorite and a porphyritic hornblende-bearing micro-quartz-monzodiorite. The porphyry - gabbro contacts have insignificant chilled margins, which have been interpreted by Murphy (1995) to be due to the intrusion of the porphyry occurring at the time of peak greenschist metamorphism.

3.5 Alteration associated with mineralisation

For the purpose of this project, the term unaltered, will refer to rocks of the Junction mine area in which the only mineralogical alteration of the original igneous assemblage is due to metamorphism. Rocks that have been affected by later interaction with a hydrothermal fluid associated with mineralisation are referred to as altered.

The main gold lode at Junction is structurally controlled within the N25 shear zone, otherwise known as the Junction Shear Zone (JSZ) and the N25 surface (Figure 3.1). The N25 surface is believed to be a low-order splay off of the regional Boulder-Lefroy Shear zone which passes within 4 km of the Junction deposit. The N25 surface cross-cuts all zones of the Junction Gabbro, dipping to the north-east at approximately 40° (Roberts and Elias, 1990). However, economic gold grades (>2 grams per ton) are mostly focussed in zones three and four of the Junction Gabbro (Figure 3.2). Smaller, but economically significant shear zones, such as the N75 surface (Figure 3.1), mostly trend sub-parallel to the N25 surface. The N75 surface is a significant hanging wall surface of the larger N25 surface. The N25 surface is interpreted as a reverse-oblique shear with the east block up and north, as determined by slickenside fibres on shear surfaces (Mol *et al.*, 1996). Vertical and horizontal displacement is < 100m (Roberts and Elias, 1990).

The following section draws on the work by Costello (1993), Carey (1994) and Gilmore (1996), but emphasis is placed on the petrography of the vein types and the carbonate mineralogy within the alteration assemblage. This is because the vein material and the associated carbonate mineralogy within the N25 surface are the most likely sources for a soil-gas anomaly (Chapter 4).

Wall rock alteration at Junction is more extensive than the gold mineralisation itself. The mineralisation is inextricably linked to the chemical transfer of components into and out of the host rock. Aqueous solutions that transported the fluid solutes ± gold to the site of mineralisation are likely to have undergone various degrees of alteration themselves during interaction with the host gabbro, and these fluids would be trapped within the veins as fluid inclusions. Fluid inclusions trapped in quartz veins and alteration minerals are a potential source for the soil-gas anomalies detectable at the surface. Further to this, carbonates that precipitated with quartz during the introduction of the hydrothermal fluid are abundant within the N25 surface and their rapid dissolution at the oxidation front are often cited as the source of CO_2-O_2 anomalies in soil-gas surveys (Lovell *et al.*, 1983; Hinkle and Dilbert, 1984; McCarthy et al., 1986; Hinkle *et al.*, 1990). Carbonates are also good fluid inclusion hosts. Therefore, well preserved carbonate grains have the potential to release significant volumes of CH_4 and other light hydrocarbons that were trapped at the time of mineralisation as the mineral(s) dissolve at the oxidation front.

The alteration halo at Junction can be divided into three discrete zones (Costello, 1993: Carey, 1994; Gilmore, 1996). These zones represent the evolution of a fluid as it dispersed outward from a central conduit. The three alteration zones have been named (outward from the highly altered shear to the unaltered host rock), the biotite-carbonate zone, the proximal chlorite zone and the distal chlorite zone (Figure 3.8). Alteration assemblages diminish rapidly away from the mineralised conduit, with relatively unaltered gabbro displaying minor to negligible hydrothermal alteration typically within 5 - 10 m of the BCZ.

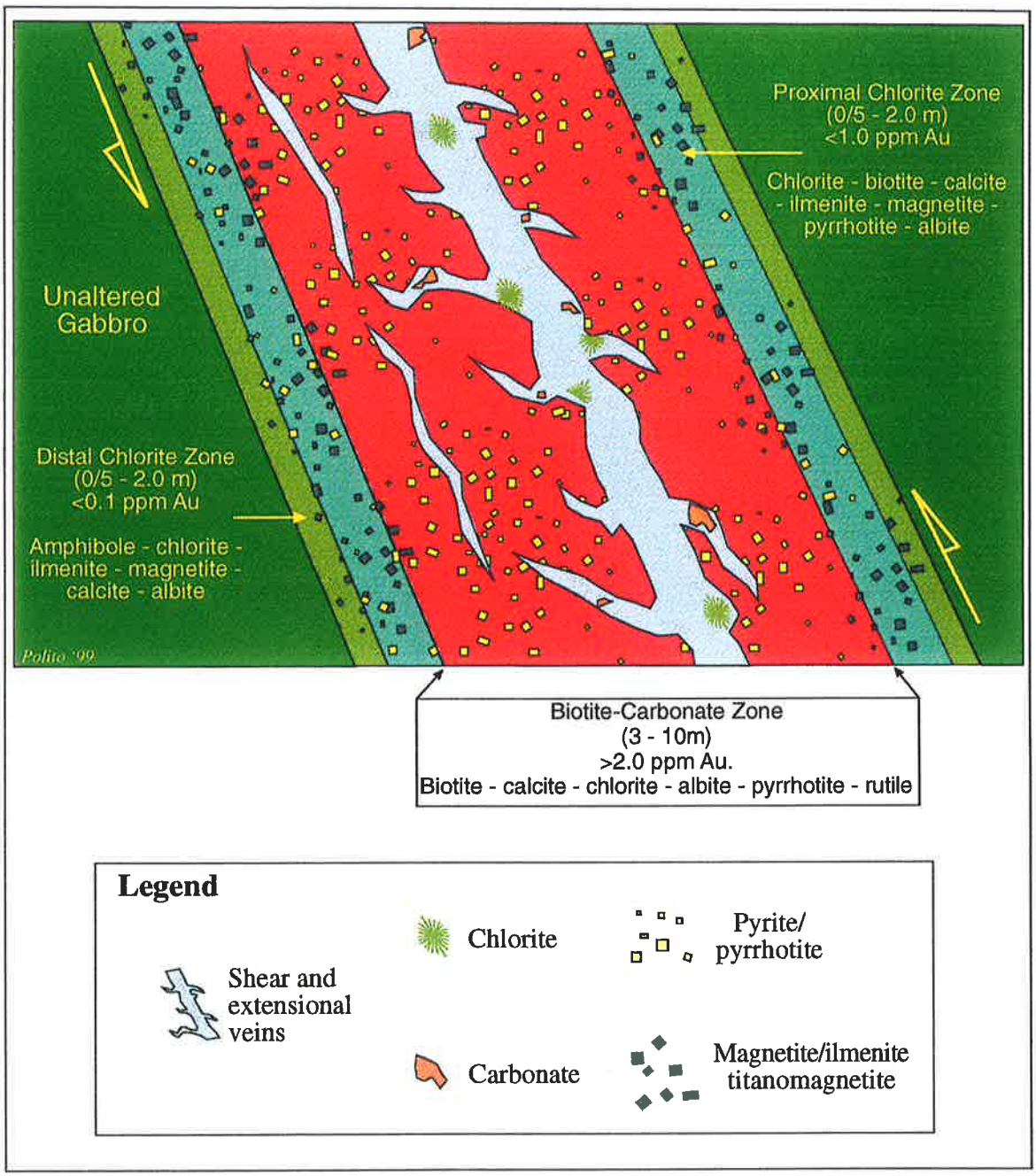


Figure 3.8. Schematic cross section through a mineralised section of the Junction shear zone (zone 3 or 4), showing the relationship between the biotite-carbonate zone (BCZ), the proximal-chlorite zone (PCZ) and the distal-chlorite zone (DCZ).

3.5.1 The distal-chlorite zone (DCZ)

The DCZ is characterised by the retention of its original unaltered "igneous" texture despite the gradual breakdown of pseudomorphic amphibole to randomly orientated chlorite and needle like amphibole. It has a gradational outer boundary extending into the unaltered gabbro, but has a sharp contact with the texturally-destructive proximal chlorite zone. The width of the DCZ varies, but generally ranges from 0.5 to 3.0 m (Costello, 1993). Gold grades are generally <0.1 ppm.

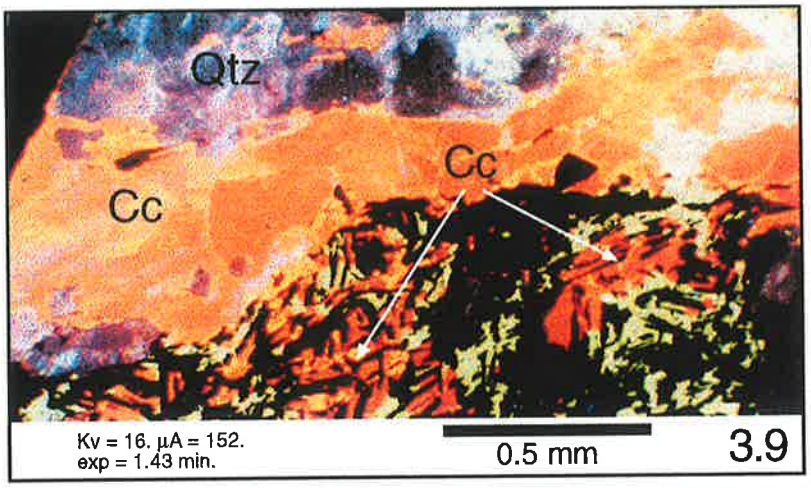
Alteration in the DCZ is dominated by the partial to complete replacement of amphibole by chlorite. Minor, fine grained biotite is observed rimming saussurite where it is in contact with altered amphibole, magnetite and ilmenite grains. Large albite laths containing solid inclusions of chlorite, biotite and amphibole are observed replacing fine grained saussurite. Minor calcite is observed as veinlets and as part of the wall rock alteration assemblage. Investigations using CL microscopy indicate that well-formed layered calcite crystals are commonly found within and at the edges of quartz veins, and in association with oxides in the host rock assemblage close to the edges of these quartz veins (Figure 3.9).

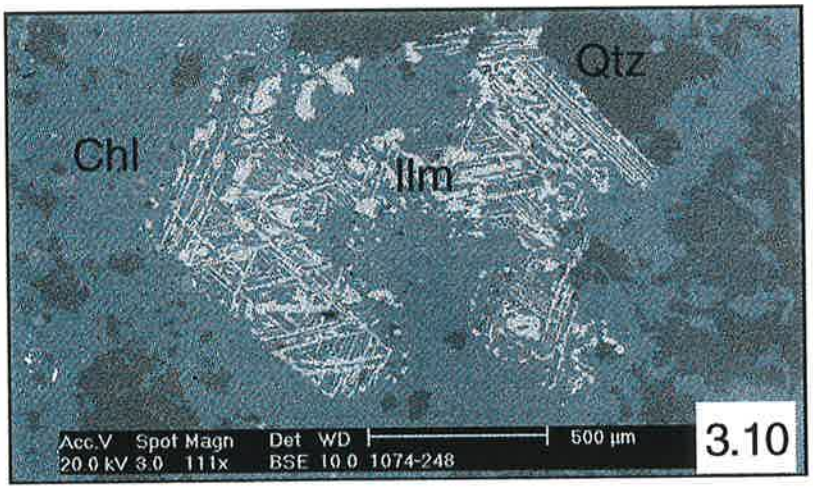
Alteration in the N25 surface is generally magnetite destructive (Costello, 1993). However, Carey (1994) reports that magnetite formed at the expense of amphibole in the DCZ. This study found that small euhedral magnetite crystals did form at the expense of amphibole at the periphery of the DCZ. However, pyrrhotite ± pyrite is observed replacing magnetite grains co-existing with ilmenite closer to the proximal chlorite zone. SEM analysis revealed that magnetite no longer existed in parts of the DCZ and only ilmenite remained relatively intact, preserving the skeletal exsolution texture typically associated with the oxide species titanomagnetite (Figure 3.10). The titanomagnetite probably exsolved its titanium content in the form of ilmenite, leaving residual magnetite which has since been replaced by either pyrrhotite or chlorite.

The DCZ mineral assemblage comprises amphibole - chlorite - albite - ilmenite - magnetite - pyrrhotite ± pyrite - biotite - calcite and can be represented by the following equation (Colvine *et al.*, 1988):

$$\underset{\text{Amphibole}}{2Ca_2(Mg,Fe^{2+})4Fe^{3+}AlSi_7O_{22}(OH)_2} + 4CO_2 + 2H_2O + 1/3O_2 \Rightarrow$$

$$\underset{\text{Chlorite}}{Mg_5Al_2Si_3O_{10}(OH)_8} + \underset{\text{Calcite}}{CaCO_3} + \underset{\text{Magnetite}}{5/3Fe_3O_4} + \underset{\text{Quartz}}{11SiO_2} \qquad \text{(Equation 3.1)}$$





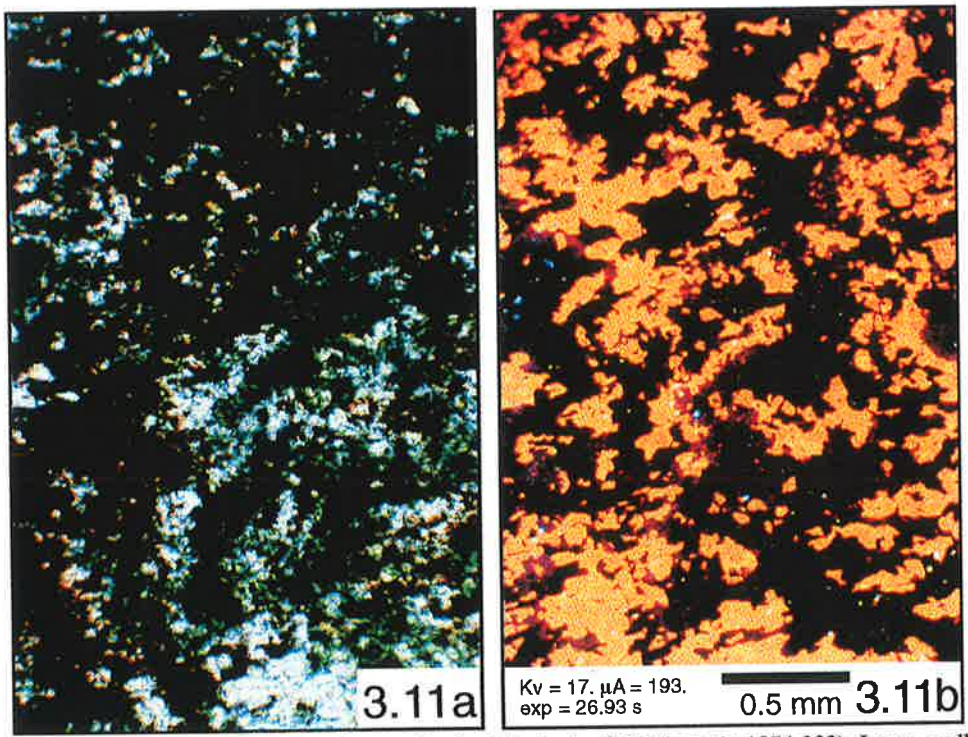


Figure 3.9. Cathodoluminescence photomicrograph of calcite in the DCZ (sample 1074-233). Large, well developed calcite crystals (Cc) are common within quartz veins (Qtz) and as a replacement of magnetite in the alteration matrix, near the edge of the quartz vein - wall rock contact. Ilmenite = black, albite = light green.

Figure 3.10. SEM image of ilmenite (Ilm) and chlorite (Chl) in the DCZ preserving the skeletal structure usually associated with exsolution of titanomagnetite. Qtz = quartz.

Figure 3.11a and 3.11b. Transmitted light and cathodoluminescence photomicrographs showing the abundance of calcite (bright yellow) present in the PCZ alteration matrix close (< 3 cm) to quartz veining.

3.5.2 The proximal-chlorite zone (PCZ)

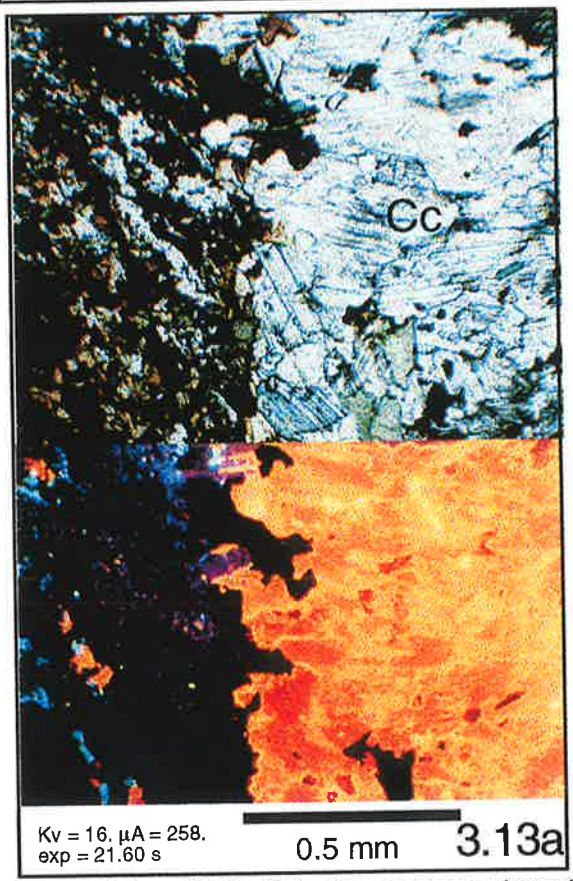
The PCZ is sharply defined from the DCZ by its total lack of igneous texture. The progressive chloritisation of amphibole results in the obliteration of the igneous texture as the fine grained chlorite is no longer restricted to within the individual amphibole crystals (Costello, 1993). The width of the PCZ ranges from 0.5 to 2.0 m (Costello, 1993). Gold values are <1.0 ppm.

The PCZ is further destinguished from the DCZ by the abundance of fine grained chlorite and biotite intergrowing with fine grained quartz, albite, calcite, magnetite and pyrrhotite (Costello, 1993; Carey, 1994; Gilmore, 1996). Biotite forms roughly 20% of the PCZ and is found with chlorite replacing magnetite and to a lesser extent, ilmenite. Magnetite displays progressive breakdown to pyrrhotite ± pyrite. Biotite may also be replaced by pyrrhotite. The albite and quartz grains appear relatively unaltered, but grain size reduction is noticeable. Costello (1993) reported that foliation is weakly and locally developed, affecting chlorite, biotite and calcite.

The abundance of calcite increases in this zone compared to the amount of calcite in the DCZ. Calcite is common within the alteration assemblage as a matrix mineral, occupying up to 20% of the alteration assemblage. CL microscopy shows that calcite regularly grows as individual crystals within the matrix (Figures 3.11a and 3.11b). Calcite is also observed growing along the cleavage planes of biotite and chlorite (Figure 3.12a and 3.12b), and is dominant at the edge of quartz veins where it forms large well formed crystals (Figure 3.13a and 3.13b). Calcite is regularly found highlighting the skeletal structure of ilmenite, rutile and magnetite, where it has grown in the consumed magnetite sites (see Figures 3.9 and 3.20 for examples).







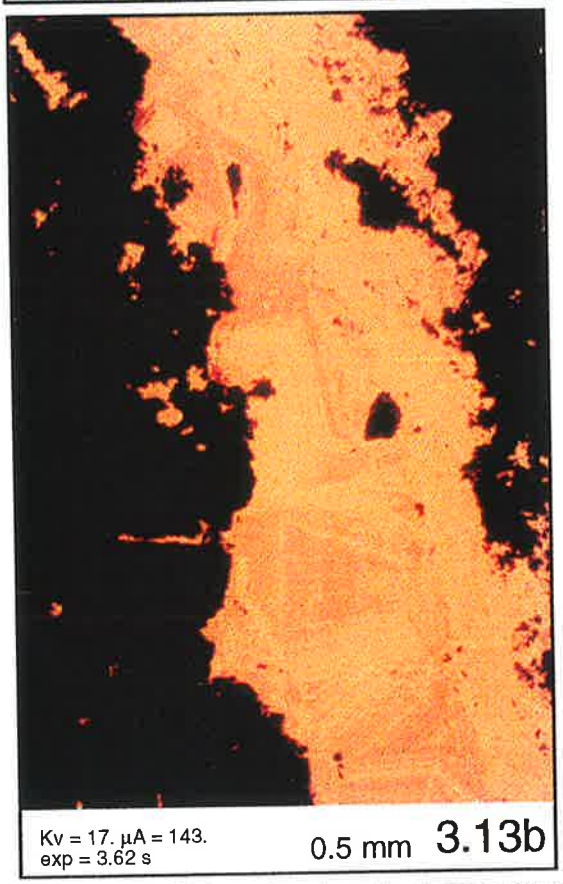


Figure 3.12a and 3.12b. Cathodoluminescence photomicrograph of calcite (Cc) growing along the cleavage planes of biotite (biot) and chlorite (chl).
Figure 3.13a. Transmitted light and cathodoluminescence photomicrograph showing well developed calcite crystals (Cc) growing at the edge of a quartz vein (quartz not seen).
Figure 3.13b. Cathodoluminescence photomicrograph showing rarely observed zoned calcite forming at the edge of a quartz extension vein. Zoned calcite like this example is good evidence for prolonged open space filling.

The alteration assemblage in the PCZ is biotite - chlorite - quartz - albite - calcite - pyrrhotite ± pyrite - actinolite - rutile - ilmenite ± apatite and can be represented by Equations 3.1 (p. 29) to 3.6 (Colvine *et al.*, 1988):

$$3(Ca,Na)Al_2Si_2O_8 + CO_2 + 1/2H_2O \Rightarrow Ca_2Al_3Si_3O_{12}(OH) + 3NaAlSi_3O_8 + CaCO_3 + 5/2O_2$$

Plagioclase — Epidote + Albite + Calcite

(Equation 3.2)

$$(Mg,Fe)_5Al_2Si_3O_{10}(OH)_8 + 1/3Fe_3O_4 + 3SiO_2 + 2K^+ \Rightarrow 2KAl(Mg,Fe)_3Si_3O_{10}(OH)_2 + H_2O + 2H^+$$

Chlorite + Magnetite + Quartz → Biotite

(Equation 3.3)

$$Fe_3O_4 + H_2S \Rightarrow FeS_2 + H_2O$$

Magnetite — Pyrite

(Equation 3.4)

$$Fe_3O_4 + H_2S \Rightarrow FeS + H_2O$$

Magnetite — Pyrrhotite

(Equation 3.5)

$$TiFeO_2 + H_2O + H_2S \Rightarrow FeS + TiO_2$$

Ilmenite — Pyrrhotite + Rutile

(Equation 3.6)

3.5.3 The biotite-carbonate zone (BCZ)

The BCZ is the principal zone of gold mineralisation. The mineralisation of the BCZ is essentially similar to the PCZ. However, the BCZ is marked by a significant increase in the amount of carbonate, biotite and pyrrhotite and an overall decrease in the chlorite and amphibole concentrations. Brittle-ductile deformation textures clearly dominate this zone. Shear, extension and breccia quartz veins highlight the brittle-ductile nature of the BCZ (discussed below). Similarly, moderate to pervasive foliation of the micas, calcite and sulphides grading into pervasive mylonite is present throughout the BCZ (Figures 3.14 and 3.15). The width of the BCZ ranges from 3 to 10 m (Costello, 1993; Costello, 1994). Gold grades are generally >2.0 ppm, but gold grades > 20 ppm are common.

Carbonate in the BCZ is dominated by calcite. Costello (1993) reported trace amounts of magnesite in the more mafic zones of the Junction Gabbro, and Carey (1994) reported appreciable amounts of ankerite and siderite in certain parts of the BCZ. However, only trace to minor dolomite was detected in most samples by XRD. Ankerite and siderite were only detected in one sample by electron microprobe analysis.

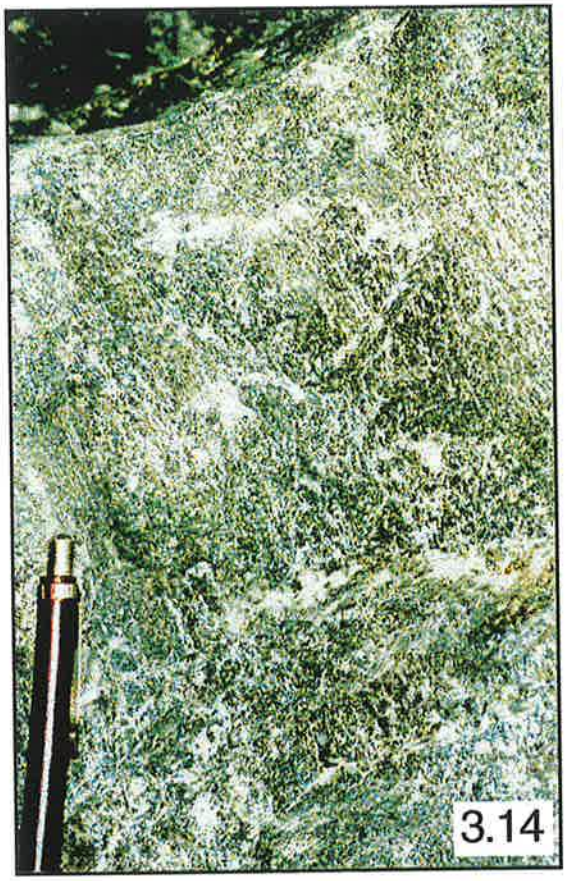
Calcite is common within the alteration assemblage as a matrix mineral, regularly occupying up to 40% of the alteration assemblage (Figure 3.16a and 3.16b). Calcite is typically ubiquitous with sulphide mineralisation and is often observed at the edge of quartz veins where it occurs as large well formed crystals (similar to Figure 3.13), or delicate, radiating aggregates with chlorite, biotite and occasionally pyrrhotite (Figure 3.17a and 3.17b). CL microscopy and SEM analyses show that calcite is regularly found occupying the sites formerly occupied by ilmenite or titanomagnetite in remnant skeletal structures and exsolution textures that are now dominated by rutile (Figure 3.18a to 3.18c). In rare cases where ankerite ± dolomite are the dominant carbonate present, they are usually observed being replaced along cleavage planes by calcite (Figure 3.19a and 3.19b).

SEM analyses show that magnetite and to a lesser extent ilmenite are rare in the BCZ having been replaced by pyrrhotite, calcite and rutile. Rutile ± ilmenite is often observed preserving the skeletal structure of the exsolution textures that are present in the unaltered gabbro (Figure 3.20). Ilmenite ± rutile also occurs as tattered trails of finer-grained crystals, helping to define the foliation through the alteration matrix (Figures 3.21a and 3.21b). These apparently are recrystallised remnants of original oxide phenocrysts (Costello, 1993).

Sulphides occur wholly or partially replacing the oxide phases and rarely as euhedral porphyroblasts. They are usually associated with biotite and calcite within the foliated lode. The sulphide content and species type vary significantly with depth in the ore body. The total sulphide content in most parts of the upper levels of the lode is <6% (i.e. above +100RL, Figure 3.2). However, with increasing depth, the total sulphide content increases to ≥20% (Figure 3.22).

Pyrite dominates over pyrrhotite above the +100RL. However, below the +100RL, pyrrhotite dominates over minor chalcopyrite and trace to negligible pyrite. Chalcopyrite is relatively common (<5% of the total sulphide species) in most parts of the deposit, often co-existing as blebs around pyrrhotite (see Figure 3.19). Pyrite, when found below the +100RL, is occasionally observed as euhedral crystals replacing pyrrhotite, chalcopyrite or pyrite (Figure 3.23). Euhedral crystals of pyrite growing over older Fe-bearing sulphides is a common observation in pyrrhotite rich ores (Vaughan and Craig, 1997). Pyrrhotite, being metastable, releases sulphur from its structure during slow cooling and this sulphur may form pyrite by exsolution or by overgrowth of pyrite on pre-existing Fe-sulphide crystals (Vaughan and Craig, 1997). In some pyrrhotite-rich ore deposits up to 30% of the total pyrite content of the ore body is late euhedral pyrite (Vaughan and Craig, 1997). The euhedral pyrite crystals in the Junction deposit indicate that this pyrite was a late phase of the mineralisation process, and unlikely is to contain gold.

The dominant minerals within the BCZ, by volume percent, are albite and quartz. Large amounts of quartz is present as vein material, but subordinate amounts are present throughout the alteration matrix. Albite is common throughout the alteration matrix and around the edges of the quartz



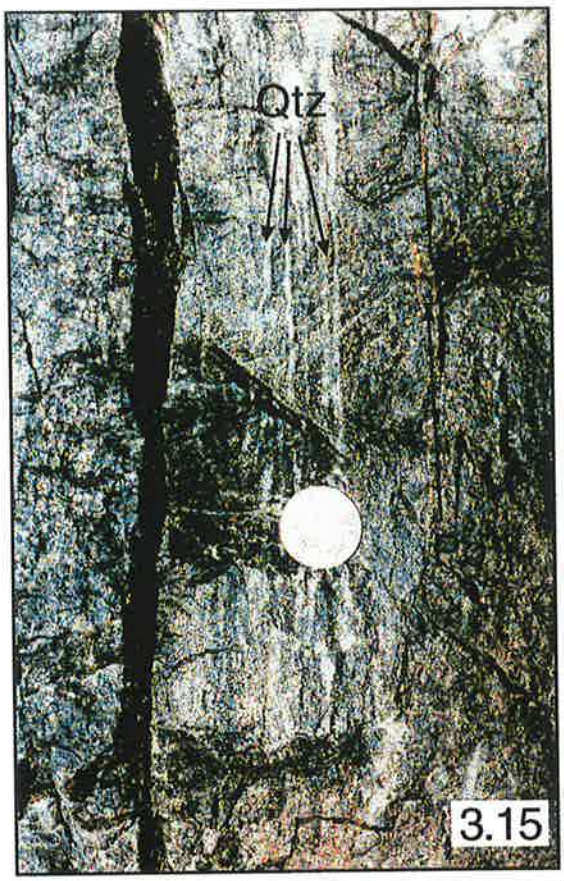
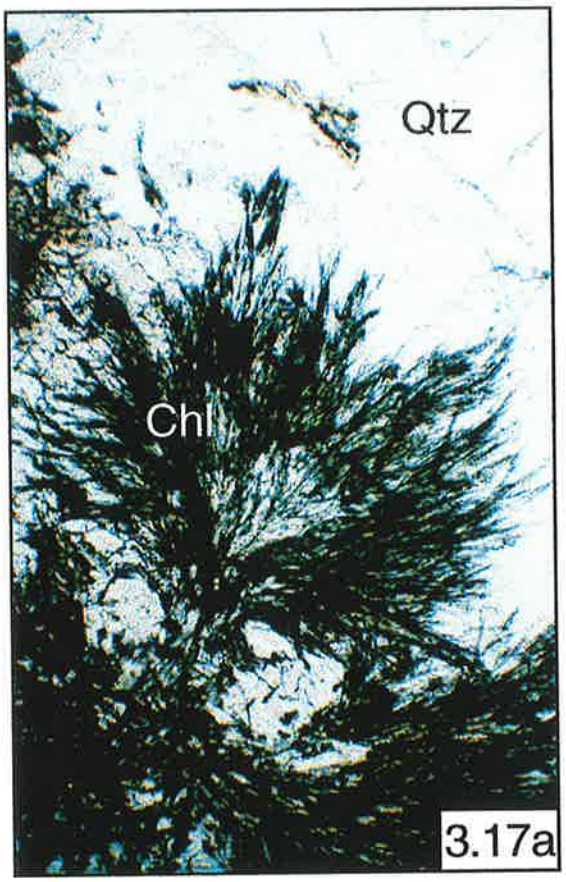


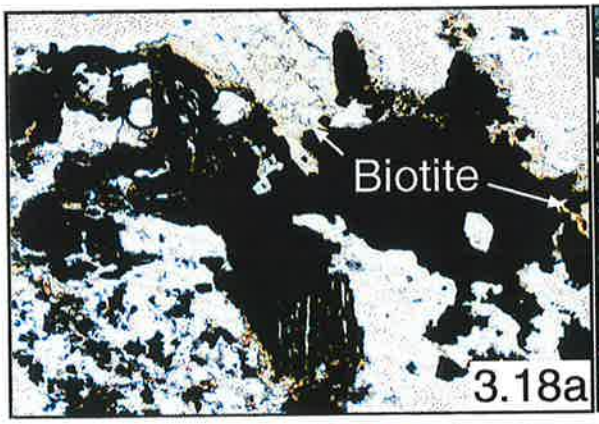


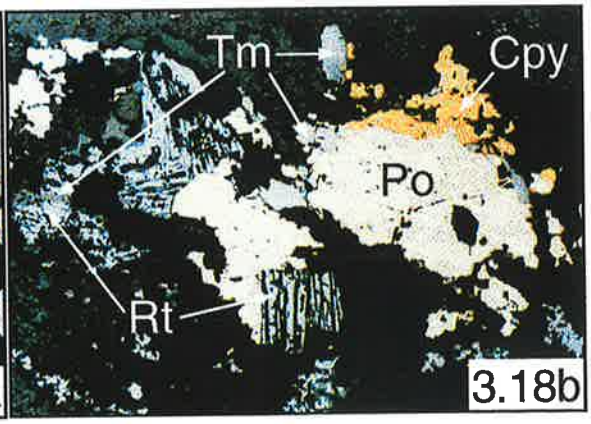


Figure 3.14. Pervasive foliation of biotite and carbonate as seen in zone three gabbro, drive 502-1-A.
Figure 3.15. Elongated quartz (Qtz) and pyrrhotite (Po) ribbons typical of mylonite in the BCZ, zone three, drive 502-1-A. Coin scale is $A 0.20.
Figure 3.16a and 3.16b. Transmitted light and cathodoluminescence photomicrographs showing the abundance of calcite in the BCZ alteration matrix. In this example approximately 60% of the matrix is calcite, but 40% is common.









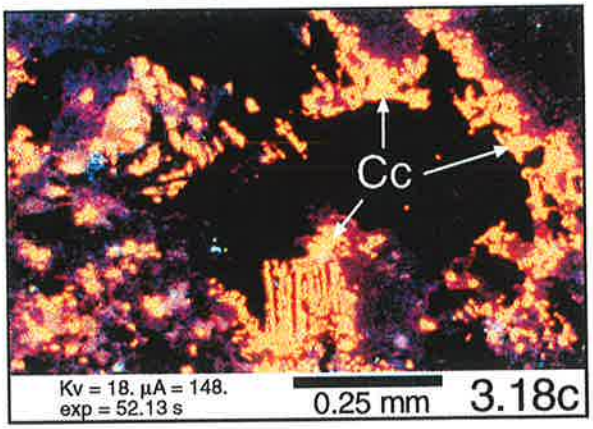
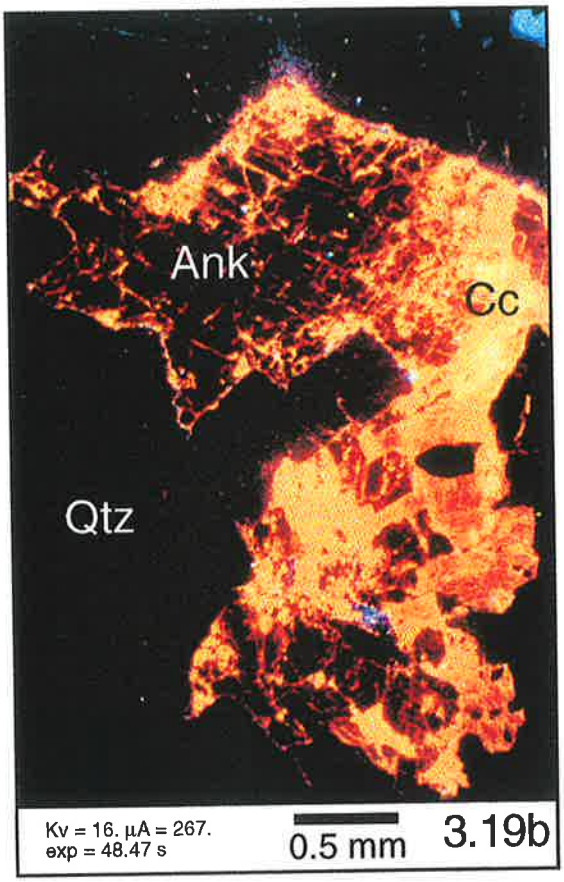


Figure 3.17a and 3.17b. Transmitted light and cathodoluminescence photomicrographs of radiating, intergrowing, calcite (Cc) and chlorite (Chl) aggregates growing into a quartz vein from the edge of the wall rock. This texture is indicative of open space filling.

Figure 3.18a, 3.18b, and 3.18 c. Transmitted light, reflected light and cathodoluminescence photomicrographs showing the replacement by calcite (Cc) and rutile (Rt) of ilmenite and titanomagnetite. In many samples, calcite is observed encrusting the pyrrhotite (Po) as seen in figure 3.18c.





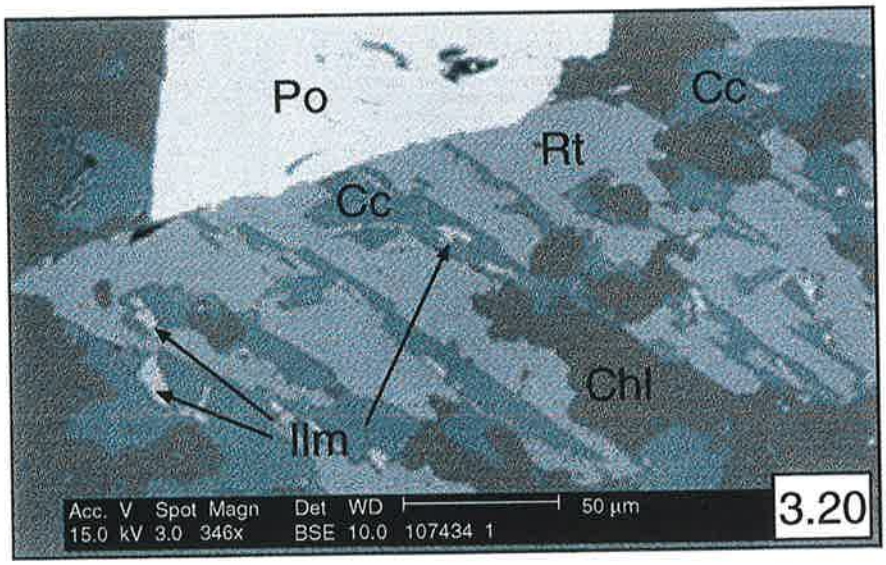
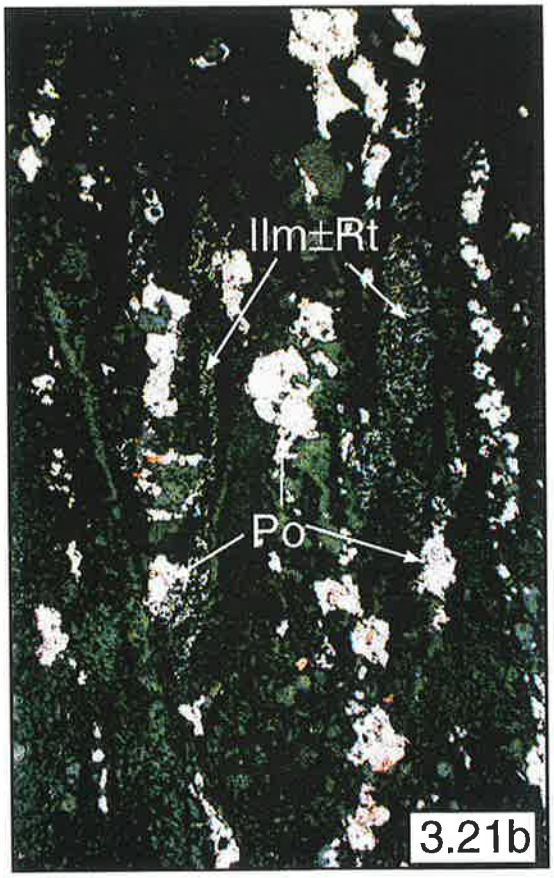


Figure 3.19a and 3.19b. Transmitted light and cathodoluminescence photomicrograph showing the progressive replacement of early ankerite (Ank) by calcite (Cc) along cleavage planes and crystal boundaries. Quartz (Qtz), Chlorite (Chl)

Figure 3.20. SEM image showing the relationship between rutile (after ilmenite), calcite ± chlorite and pyrrhotite. Calcite (Cc), ankerite (Ank), quartz (Qtz), ilmenite (Ilm), rutile (Rt), pyrrhotite (Po), chlorite (Chl)).







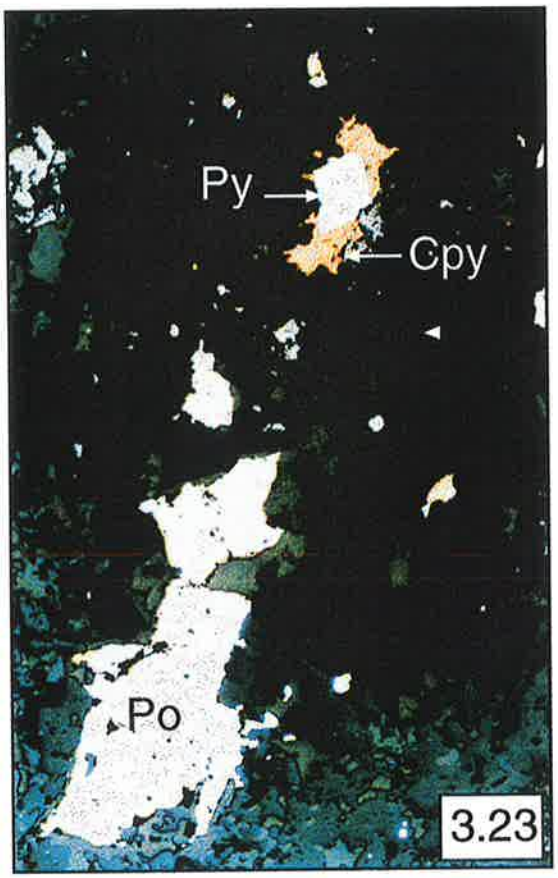


Figure 3.21a and 3.21b. Transmitted light and reflected light photomicrographs showing Ilmenite (Ilm) and rutile (Rt) forming tattered trails with pyrrhotite (Po) enhancing the foliation developed by the biotite, chlorite, calcite assemblage.
Figure 3.22. An example of pyrrhotite rich alteration in the BCZ, zone three, 502-1-25.
Figure 3.23. Reflected light photmicrograph showing late euhedral pyrite (Py) replacing chalcopyrite (Cpy) in a pyrrhotite (Po) dominated assemblage. See text for details.

veins. Albite is commonly preserved at the edge of quartz veins as large (up to 1.5 mm) euhedral crystals, and throughout the alteration matrix as much smaller (<0.3 mm) anhedral grains. Deformed albite crystals often display both brittle deformation in the form of cracking and slight rotation and ductile deformation in the form of grain elongation.

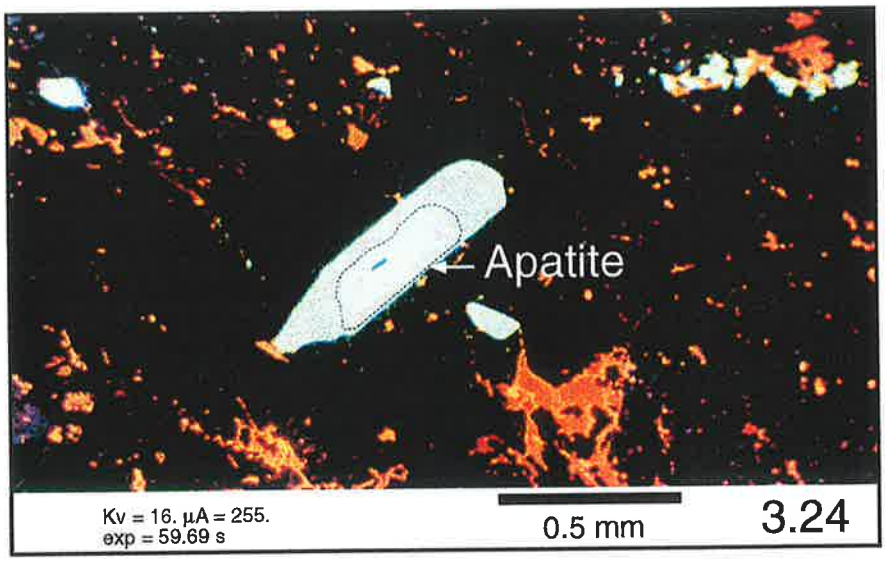
Costello (1993; 1994) reports that the amphibole content increases with depth in the BCZ (i.e. below level -300RL, Figure 3.2). The amphibole is not remnant metamorphic amphibole but occurs as small rosettes and fibrous crystals overgrowing foliation and replacing biotite and chlorite. Costello (1994) interprets the amphibole-biotite-calcite alteration assemblage at depth to infer a higher metamorphic grade. This alteration style was not investigated during this study.

Apatite is a common accessory mineral in sub-ordinate amounts within the BCZ (<1%). Apatite is easily recognisable using CL microscopy, where it has a bright light green-blue luminescence. Apatite almost always occurs as euhedral crystals overgrowing the foliation. It occurs in clusters or as individual crystals. Larger apatite crystals show weakly developed, cyclic zoning (Figure 3.24) that is assumed to reflect variations in the Mn^{2+} concentrations within the crystal (Marshall, 1989). The presence of zoned, euhedral apatite crystals in the BCZ indicates that phosphorus and fluorine(?) was introduced late in the mineralisation process. Carey (1994) reported an increase in P associated with mineralisation within the JSZ. The presence of fluorine was not determined, but fluor-apatite is by far the most common apatite found in igneous and metamorphic rocks (Deer *et al.*, 1993).

Carey (1994) has noted significant textural and mineralogical contrasts between the BCZ alteration halos in zones three and four. The textural difference is observable in hand specimen. BCZ alteration in zone four gabbro is only moderately foliated over less than one metre, whereas BCZ alteration in zone three gabbro exhibits a well developed foliated zone. Mineralogically, the BCZ alteration in zone four gabbro is marked by an increase in the amounts of biotite, chlorite and carbonate, whereas BCZ alteration in zone three gabbro is marked by the disappearance of chlorite from the alteration assemblage and a greater abundance of biotite and carbonate.

3.5.3.1 Implications of the mineral assemblage in the BCZ

The mineral assemblage of the BCZ is biotite-chlorite-calcite-quartz-albite-pyrrhotite±pyrite-actinolite-rutile±ilmenite±apatite. Alteration in the BCZ is represented by Equations 3.1 to 3.6 (Colvine *et al.*, 1988). These equations show that the alteration assemblage at Junction records a massive introduction of H_2O, CO_2, K_2O, and S. It is assumed that these compounds are the main components in the gold transporting solution. Trace element geochemistry by Carey (1994), found that there were also significant increases in Ba, Cs, Rb, Sr, K, S, Cu, Zn, Pb, Sn, Li, Si, P, Zr, Hf, V, U, W and Nb and significant losses in Co, Cr and Ni. Increases in Mo are recorded by Carey (1994), but the presence of Mo in a pre-shearing vein assemblage makes estimating the increase of Mo during mineralisation problematical.



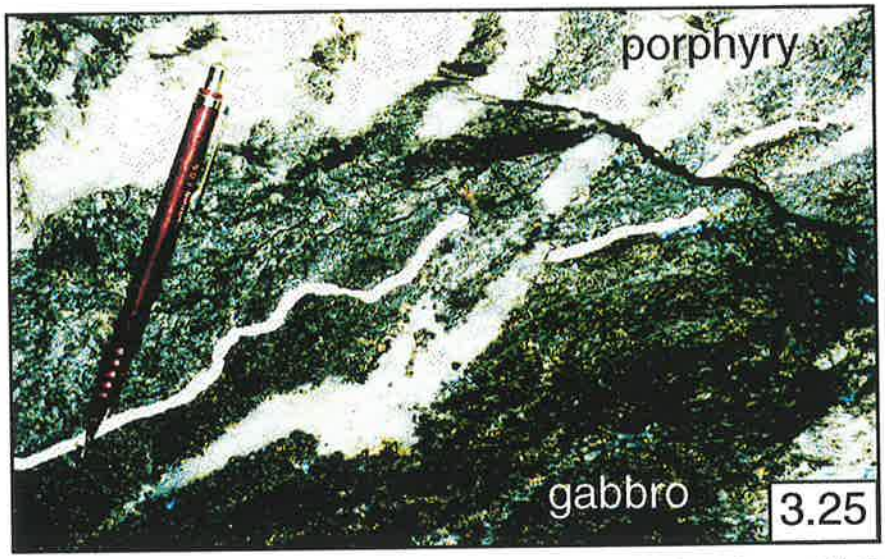


Figure 3.24. Cathodoluminescence photomicrograph of a large zoned, apatite crystal in the Biotite-Carbonate Zone assemblage. Dashed lined highlights zonation.
Figure 3.25. An example of preferential mineralisation of the Fe-rich gabbro (lower right) as opposed to the Fe-poor porphyry (upper left). Both lithologies are cross cut by the same quartz veins, but disseminated pyrrhotite (fine yellow flecks) can only be seen in the sheared gabbro.

The difference in sulphide contents and species ratios within the BCZ has been discussed by Carey (1994) and Costello (1993). Both authors note that the lower sulphide content and the dominance of pyrite in the upper levels of the lode correspond to mineralisation that occurs in zone two of the Junction Gabbro. Unaltered zone two of the Junction Gabbro contains less iron oxide than zones three and four. Carey (1994) notes that mineralisation in zone two is confined to the upper part of the zone where greater concentrations of Fe and incompatible elements are present. A good example of the preferential mineralisation of Fe-rich rocks is illustrated by the felsic porphyries within the mine that are cut by shearing, but contain no sulphides or gold (Figure 3.25). The distribution of mineralisation in zones two, three and four is shown in Figure 3.2. Reflected light petrology indicates that it is unlikely that the sulphide zoning is due to supergene replacement of pyrrhotite by pyrite in the upper levels of the deposit. Therefore, the

domination of pyrite over pyrrhotite in zone two in comparison to the pyrrhotite dominated zones three and four is probably due to the amount of Fe present in zone two.

The dominance of pyrrhotite throughout most of the deposit suggests that oxygen fugacity (fO_2) favoured the stabilisation of pyrrhotite over pyrite during precipitation. The dominance of pyrite over pyrrhotite in the upper levels of the deposit suggests that the fO_2 may have been different at this level, because pyrite is stable at higher fO_2 values than pyrrhotite (Figure 3.26). However, it is unlikely that the fO_2 changed significantly over the scale of the deposit. Similarly, pyrite is stable at higher sulphur activities ($a\Sigma S$) than pyrrhotite (Figure 3.26) (Mikucki and Ridley, 1993), but again, $a\Sigma S$ is unlikely to vary significantly over the scale of the deposit. The dominance of pyrrhotite over pyrite throughout most of the deposit (as much as 99 : 1 in the

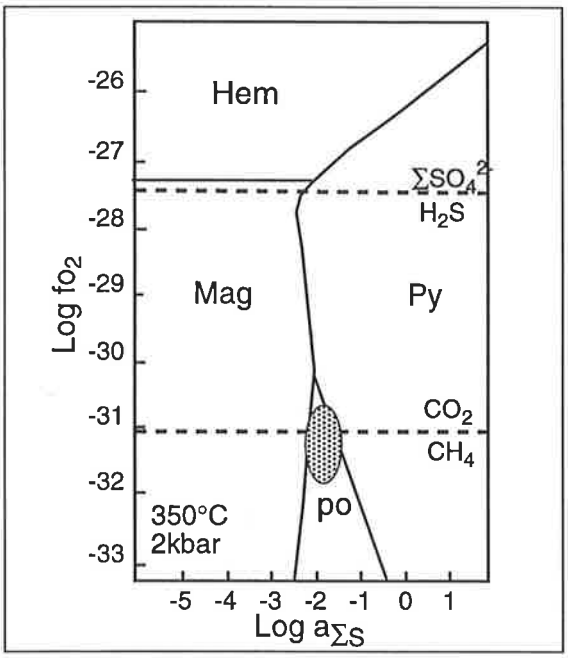


Figure 3.26. Oxygen fugacity and sulphur activity diagram from Mickuki and Ridley (1993), showing the estimated fields at which mineralisation occurred at Junction (hatched area). Hem = hematite, Mag = magnetite, Py = pyrite, Po = pyrrhotite.

BCZ of zone three, based on visual estimates) indicates that the $fO2$ and $a\Sigma S$ for the Junction deposit are likely to fall in the range depicted in Figure 3.26.

Given that as much as 30% of the pyrite present in zone three (total pyrite in zone three is <1%) formed during the cooling stages of the formation of the deposit (section 3.5.3; Vaughan and Craig, 1997), fO_2 values are hypothesised to have been at or below 10^{-31} log units, at 350°C and 2 kbars (Figure 3.26). Calculations of fO_2 and $a\Sigma S$ by Phillips and Groves (1983), Neall and Phillips (1984), Colvine *et al.* (1988) and Mikucki and Ridley (1993) indicate that sub-amphibolite late-orogenic, structurally-controlled gold deposits formed from relatively reduced ore fluids. Golding and Wilson (1983) and Cameron (1989) used $\delta^{13}C$ values to suggest that ore fluid fO_2 was just above or near that of the CO_2-CH_4 buffer (10^{-31} at 350°C and 2 kbar). These results are similar to the fO_2 estimations calculated for the Junction deposit based on the dominant mineralogy observed in zones three and four of the Junction Gabbro. Therefore, given that the fO_2 and $a\Sigma S$ of the mineralising fluid would not vary significantly across the deposit,

it can be concluded that variations in pyrrhotite to pyrite ratios in the Junction deposit are most probably due to variations in the iron content of the different zones within the Junction Gabbro. The dominance of calcite over dolomite, siderite and ankerite within the deposit is probably due to the lower melting point temperature of calcite over these minerals at the ambient temperatures rather than to fluctuations in the iron content of the hosting gabbro (Rimstidt, 1997). Witt *et al.* (1997) report that chlorite, ankerite, albite and pyrrhotite dominate the outer alteration zone associated with gold mineralisation hosted in iron-rich mafic rocks at low to mid-greenschist facies (300°C) (e.g. the co-equivalent Golden Mile Gabbro at Kalgoorlie),whereas ankerite, siderite, muscovite, pyrite and pyrrhotite dominate the inner mineralised zone. Alternatively, gold mineralisation in areas of mid to upper greenschist facies metamorphism (400°C) consist of chlorite, calcite, albite, minor pyrrhotite and biotite in the outer alteration halo, and biotite, calcite, albite, pyrrhotite and pyrite in the inner mineralised zone (Witt *et al.*, 1997). Accordingly, the Junction gold deposit with its inner alteration assemblage consisting of biotite, calcite, albite, pyrrhotite ± pyrite ± chlorite appears to have formed at mid to upper greenschist facies metamorphism.

Further to the stability of calcite over dolomite, siderite and ankerite at upper greenschist facies metamorphism, CL investigations combined with electron microprobe analyses show that the calcite in the BCZ generally contains low, but variable concentrations of Fe^{2+} in its crystal structure. Electron microprobe traverses across three calcite grains and one ankerite grain show that the darker, quenched portions of the calcite contain higher concentrations of Fe^{2+} in the crystal lattice, whereas variations in Mn^{2+} within the calcite is minimal (Figures 3.27a and 3.27b, appendix II). Variations in calcite luminescence in natural samples is generally due to variations of Mn^{2+} within the crystal (Marshall, 1989). However, it can be seen in Figures 3.27a and 3.27b that the concentration of Fe^{2+} in the crystal structure of calcite at Junction controls the intensity of the luminescence of the carbonate.

Dark orange-red to bright yellow luminescent calcite is common in all parts of the Junction shear zone. Many calcite crystals in the alteration matrix are dark orange in colour when viewed under CL. However, nearly all of these crystals have bright yellow luminescent rims (see Figures 3.11 and 3.16). Similarly, calcite crystals growing at the edge of quartz grains show repeated cycles of dissolution (or fracturing) and reprecipitation. The later calcite is increasingly Fe-deficient, but with constant Mn^{2+}, it is more luminescent (Figure 3.28). The variation in calcite luminescence at Junction is significant because it corresponds to the findings of Costello (1993; 1994) who reported that competition for Fe by sulphur to form sulphides resulted in increased pyrrhotite concentrations in the BCZ at the expense of biotite. The growth stages of the calcite observed in the BCZ, suggest that the sulphides also out-competed calcite for available iron as the mineralisation process matured. Therefore, the luminescence of the calcite in the JSZ is attributed to the competition for iron by sulphur to form sulphides.

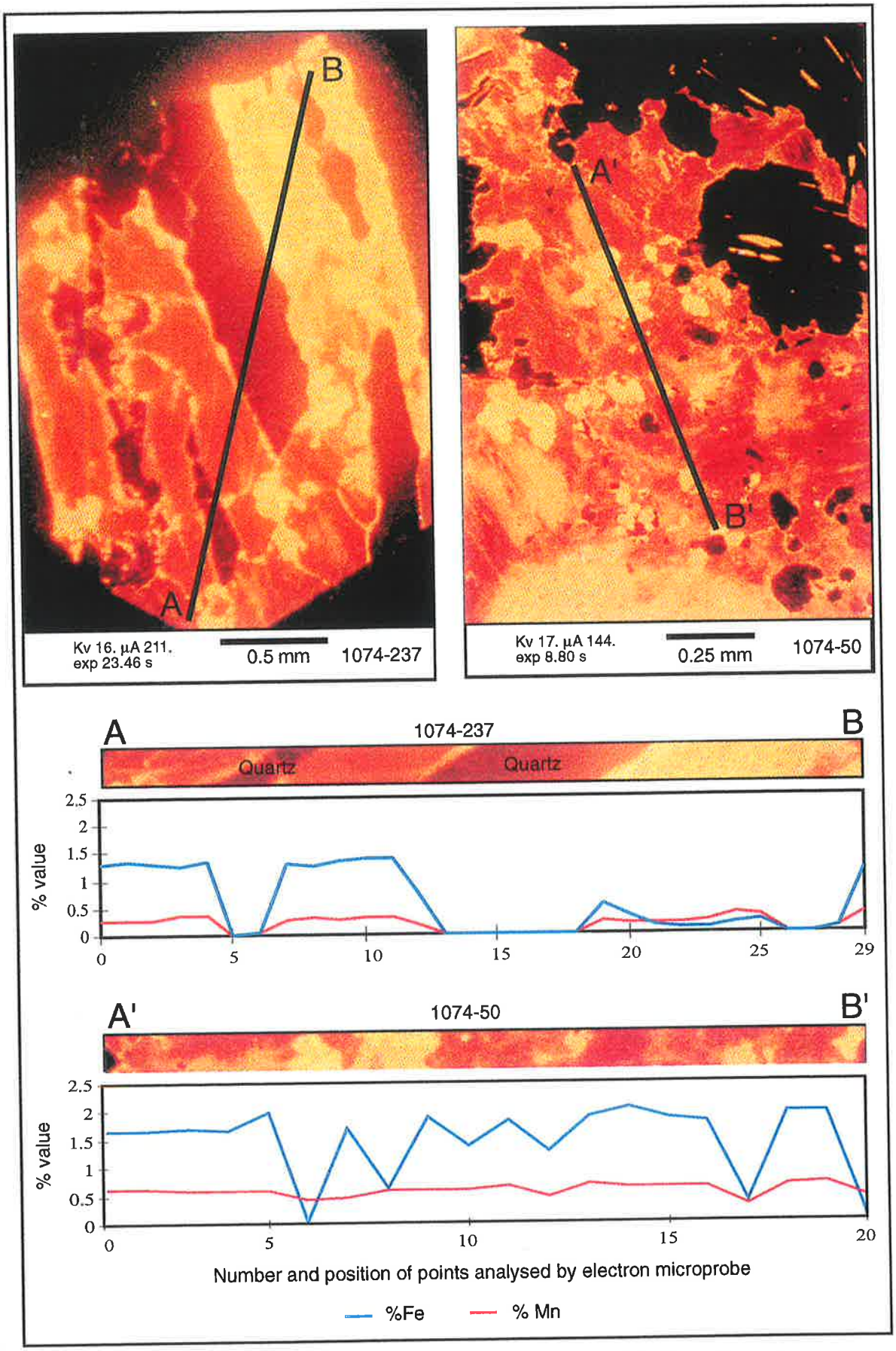


Figure 3.27a. Cathodoluminescence photomicrographs showing luminescence variations in calcite. Electron microprobe traverses (below) show that the luminescence variation is due to the concentration of Fe in the carbonate. Lines A-B and A'-B' show the traverses analysed by electron microprobe.

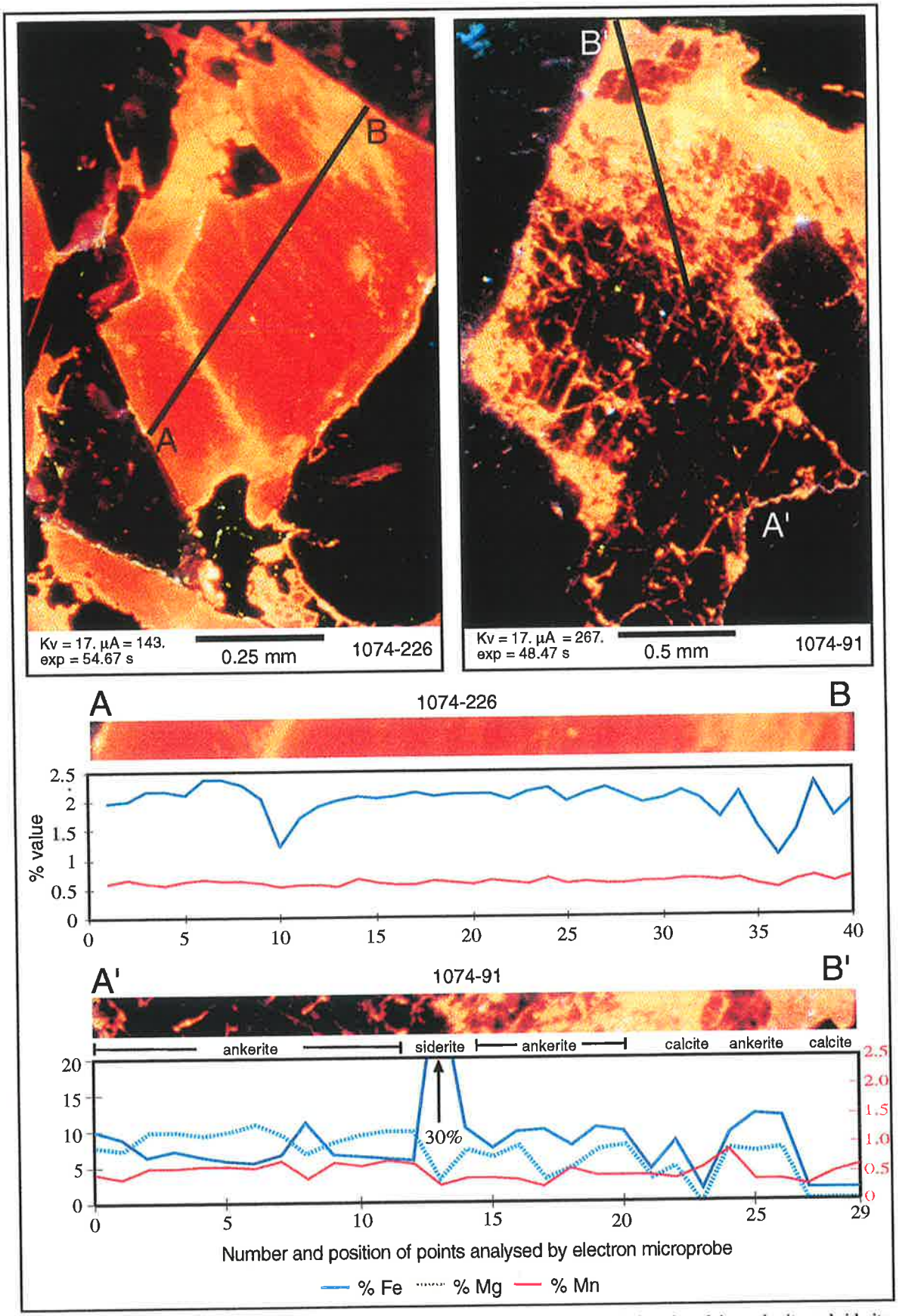


Figure 3.27b. Cathodoluminescence photomicrographs showing luminescence variations in calcite, ankerite and siderite. Electron microprobe analyses (below) show that the variations in luminescence are due to fluctuating Fe concentration within the carbonate structure and not variations in Mn concentration. In the ankerite-siderite-calcite example (1074-91), the ankerite and siderite are significantly quenched by their high Fe content (left hand side of electron microprobe traverse 1074-91), whereas the lower Fe concentrations in the replacing calcite results in bright luminescence (right hand side of electron microprobe traverse 1074-91). Mg concentrations are shown to distinguish ankerite from siderite and calcite. Lines A-B and A'-B' show the traverses analysed.

3.6 Vein styles

Veining associated with late-orogenic, structurally-controlled gold mineralisation represent an ideal case for studying the role of fluids in faulting, veining, stress cycling and wall-rock interaction (Sibson *et al.*, 1988; Boullier and Robert, 1992; Robert *et al.*, 1994, 1995). The Junction gold deposit has three main generations of quartz veins that represent three periods of tectonic activity. Gilmore (1995) detected as many as six different vein types within the Junction deposit, based on structural orientation and mineralogy. However, the following three vein generations are by far the most abundant within the area of interest:

- pre-shearing, pre-gold, molybdenite bearing quartz veins,
- syn-shearing, syn-gold, quartz-albite±carbonate±chlorite±biotite±pyrrhotite veins, and
- post-shearing, post-gold, quartz-carbonate-pyrrhotite-biotite veins.

3.6.1 Pre-shearing vein assemblage

3.6.1.1 Molybdenite-bearing quartz veins

Molybdenite-bearing quartz veins (hereon referred to as Mo-type veins) are regularly encountered in drill holes and mine drives in the upper 200 m of the Junction deposit. Current underground mining operations indicate that the Mo-type veins become less prevalent with depth. Indeed, Mo-type veins are rarely encountered in diamond drill holes below the current level of mining (-100RL, Figure 3.2; E. Poole, pers. comm., 1997). However, Costello (1994) reported clasts of layered, recrystallised and rotated quartz vein material at the -308 mRL that he interpreted to be clasts of recrystallised molybdenite vein.

The Mo-type veins formed prior to the main gold deposition event. The veins are cross cut by later shear and extensional quartz veins, and many have a distinct foliation indicative of syn-shearing deformation. Mo-type veins are occasionally stretched into boudins (Figure 3.29) indicating vertical-extension of the veins during shear related deformation. This supports the interpretation that they formed prior to the gold deposition event. Mo-type veins are typically laminated, and contain ribbons, clusters, plates or disseminations of molybdenite throughout the mostly translucent quartz (Figures 3.30 and 3.31). The molybdenite crystals give the Mo-type veins a light grey colouring when compared to other vein types in the deposit.

The quartz in the Mo-type veins is often, but not always recrystallised, having sutured boundaries with 120° triple points and undulose extinction. Where the quartz grains are not recrystallised, they are usually found in embayments, protected by layers of molybdenite and chlorite where the effects of recrystalisation were apparently minimised. These grains contain well preserved fluid inclusions that distinguish this quartz as Mo-type vein material and not syn- or post-gold

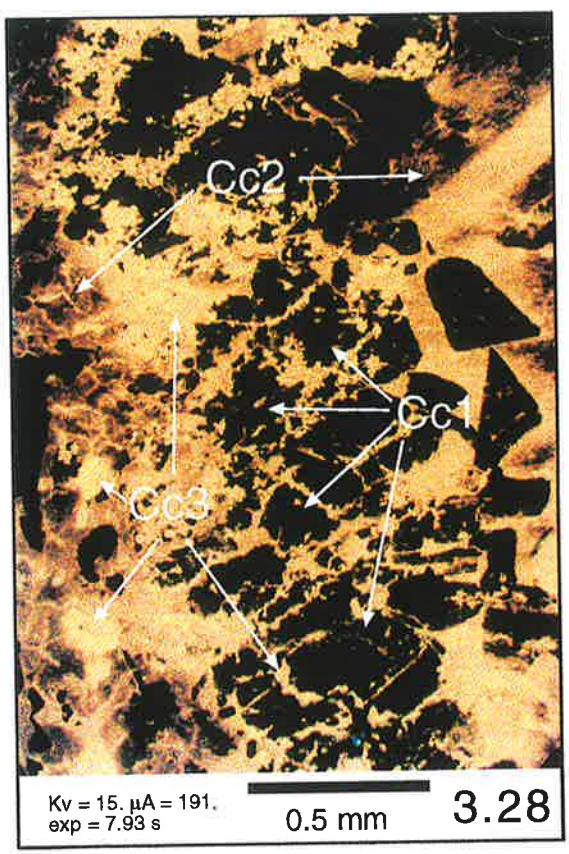








Figure 3.28. Cathodoluminescence photomicrograph showing the progressive Fe-depletion in calcite. Old, Fe-rich calcite that formed at the edge of the quartz vein - wall rock contact appears dark (Cc1). Subsequent growth periods associated with vein extension have fractured Cc1 away from the wall rock and allowed the precipitation of younger Fe-depleted calcite (Cc2) between the fractures. A third generation of calcite (Cc3) containing less Fe than Cc2, overprints parts of Cc2 and Cc1 (mostly along cleavage planes and grain boundaries).

Figure 3.29. An example of a Mo-type vein stretched into a boudin.

Figure 3.30 and 3.31. Reflected light photomicrographs of laminated Mo ribbons (Figure 3.30) and clusters (Figure 3.31) as they appear in the Mo-type quartz veins.

mineralisation quartz material. Pyrrhotite, chlorite, calcite and low gold grades (< 2 ppm Au) have been observed with the Mo-type quartz veins (Newman, 1993; Gilmore, 1996; Mol *et al.*, 1996). However, it is likely that the chlorite, calcite, pyrrhotite and minor gold observed in the Mo-type veins is associated with alteration that occurred during the main gold mineralisation event.

The origin of the Mo-type veins is enigmatic. Molybdenum mineralisation is rarely reported in or adjacent to other late-orogenic, structurally-controlled gold deposits. However, Burrows and Spooner (1987) conclude from fluid inclusion analysis and stable isotope geochemistry that molybdenite mineralisation at the Hollinger-McIntyre late-orogenic, structurally-controlled gold deposit in Canada is associated with the near-by Mink Lake Granodiorite stock. This interpretation may be applicable to the Mo-type veins found in the Junction deposit where pre-gold felsic porphyries intruded the Junction Gabbro (Murphy, 1995). Indeed, Clark *et al.* (1986) notes that there are Mo-bearing porphyry bodies in the near-by Victory gold deposit (Figure 1.1). However, Murphy (1995) does not report any Mo in the porphyry bodies at Junction. Therefore, linking the Mo-type veins directly to the felsic porphyries in the Junction deposit is untenable.

3.6.2 Syn-gold veins associated with the development of the N25 surface

The veins associated with the gold mineralisation and the related alteration assemblages discussed above occur in the steeply dipping, reverse to reverse-oblique N25 surface and related hanging-wall and footwall structures. The veins have developed incrementally in regimes of horizontal compression. The presence of overprinting shear veins, sigmoidal *en echelon* extensional veins and "jig-saw style" breccia veins throughout the N25 surface, indicate that the Junction deposit formed in the brittle-ductile transition zone in the continental crust.

All of the syn-gold quartz veins studied contain subordinate amounts of chlorite, albite, carbonate (calcite >> dolomite), pyrrhotite, scheelite, biotite, pyrite and rarely, free gold. They are all surrounded by zoned alteration envelopes dominated by carbonatisation of the wall rocks. The quartz crystals growing in the veins are present as small (<0.1 mm) to large (typically <0.8 mm) anhedral crystals and small (<0.2 mm) deformed crystals displaying significant grain size reduction, sutured grain boundaries often displaying 120° triple point junctions and undulose extinction when viewed by transmitted light microscopy under cross-polarised light. These textures are largely dependent on the degree of deformation endured by the quartz vein after precipitation.

Following the classification of Colvine *et al.* (1988), Sibson (1990) and Robert *et al.* (1994; 1995), three main types of veins are distinguished on the basis of their internal structure and the orientation of opening vectors relative to the vein walls: shear veins, extension veins and breccia veins.

3.6.2.1 Shear veins

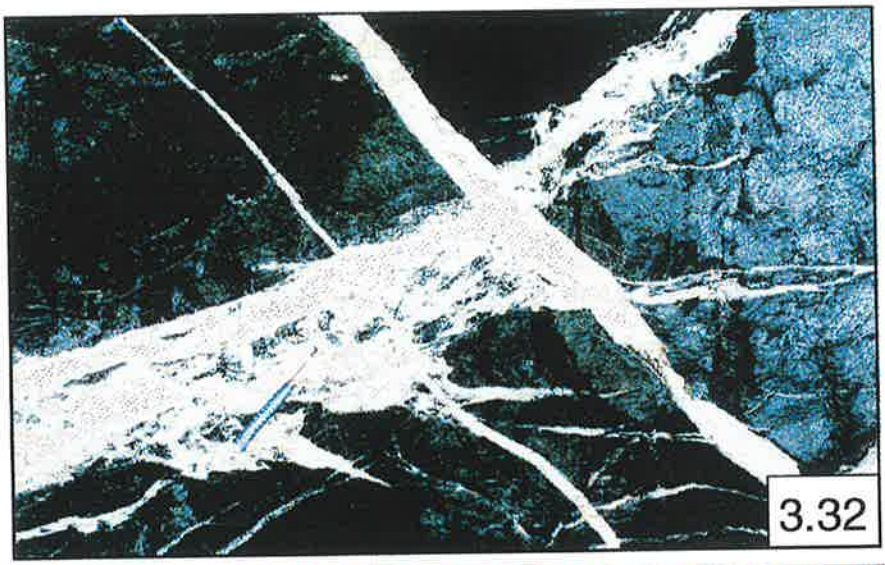
Shear veins, also termed fault fill veins by Robert *et al.* (1994; 1995), are the most common vein type at Junction. For the purpose of this project, central-shear veins, oblique-shear veins and fault fill veins whose vein boundaries are sub-parallel to or at a low angle to the shear zone foliation and the shear zone boundary (as classified by Hodgson, 1989), are henceforth known as shear veins. Shear veins form mineralised, lenticular bodies either in discrete faults or in the central part of the JSZ. They vary in thickness from <1 cm ribbons to ≥3m wide laminated structures, and can be several tens of metres in their longest dimensions.

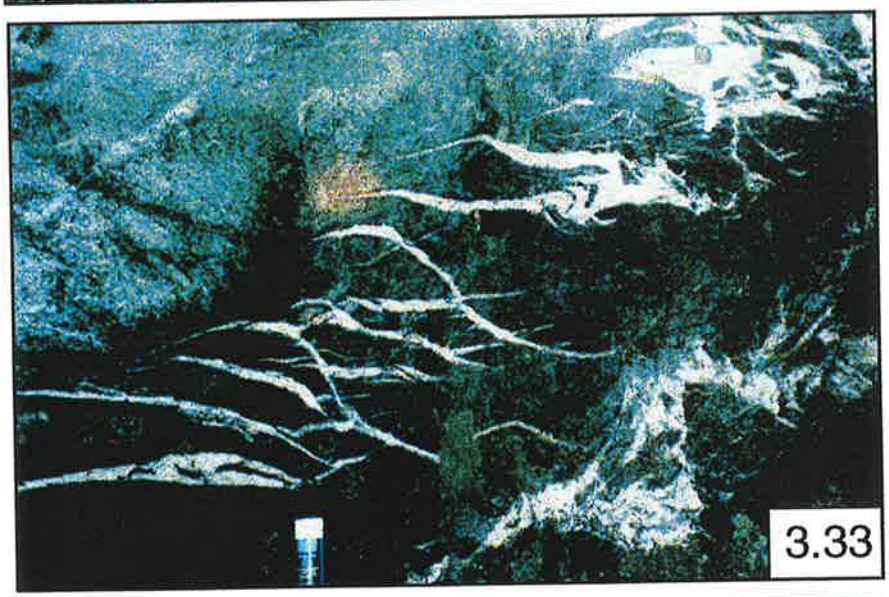
The shear veins at Junction lack diagnostic internal textures and are dominated by massive, homogeneous buck quartz (see Figures 3.3a, 3.3b and 3.4). These veins are rimmed at the contact with the altered gabbro by a thin, typically <1 cm thick layer of intergrowing albite, biotite, chlorite, calcite, minor dolomite, and pyrrhotite ± pyrite. Occasionally these minerals are euhedral in shape and chlorite, pyrrhotite and calcite have been observed forming rosettes attached to the vein walls. In one sample examined, a large (10 cm), euhedral dolomite crystal with distinctive twinning was observed 30 cm from the vein wall. These textures highlight the dilational formation of these veins and indicate that open space filling within the shear veins predominated (Boullier and Robert, 1992). Quartz laminations are most common in the large shear veins, but crack-seal structures that are usually associated with shear veins were not regularly observed in samples collected from Junction. However, this does not imply their scarcity.

3.6.2.2 Extension veins

Extension veins are common in the Junction deposit and vary in thickness from millimetres to tens of centimetres (usually less than 1 metre). These veins form normal to the maximum principle stress axis when the pore fluid pressure is greater than the sum of the tensile strength of the rock (Ramsay and Huber, 1983). Therefore, they are typically subhorizontal when initially formed, cutting across previously rotated veins and shear zone foliation. Extensional veins discussed here are those veins that formed by extensional opening of fractures at moderate to high angles to fault planes and to shear zone foliation as classified by Robert *et al.* (1994).

Extension veins at Junction are variably developed. At the macroscale, Mol *et al.* (1996), noted that sigmoidal and plannar extensional veins at Junction terminate within or at the edge of hanging-wall and footwall shears. Only late, undeformed, and relatively unmineralised plannar extension veins extend out of the JSZ into the unaltered gabbro (Holland, 1995). Sigmoidal extension veins at Junction commonly fringe shear veins and are often, but not always, restricted in lateral extent, and to one side of the shear vein (Figure 3.32). Plannar extension veins are distinguishable from sigmoidal extensional veins because they are not laterally restricted like the sigmoidal extension veins that fringe shear veins. Planar extension veins exhibit various degrees of rotation occasionally forming sigmoidal *en echelon* vein sets (Figure 3.33). Early





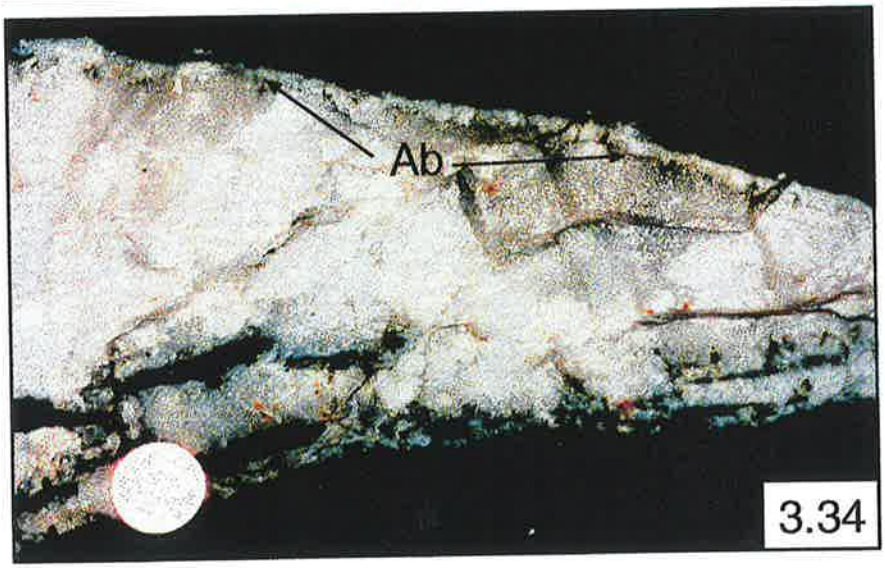


Figure 3.32. An example of a quartz-carbonate, reverse fault fill, shear vein with related extension veins forming in the footwall, drive 405-1-54.
Figure 3.33. Planar extension veins exhibiting a moderate degree of rotation forming a sigmoidal *en echelon* vein set, drive 405-1-54. Spray can is 30 cm tall.
Figure 3.34. A continuous coating of albite (Ab) formed mostly on the upper edge of a quartz vein in the BCZ, drive 502-1-25 . Note growth layering incorporating slivers of the wall rock, each with a weakly developed albite rim, running parallel to the vein wall on the lower edge of the quartz vein. Coin scale is $A0.20.

extension veins that have been rotated to form sigmoidally shaped arrays of *en echelon* vein sets are invariably cross cut by successive extensional veins that are much less deformed.

At the mesoscale, extensional veins at Junction are dominated by quartz and are regularly rimmed by a continuous coating of albite that is typically 0.5 to 1.0 cm thick, regardless of the total thickness of the quartz vein (Figure 3.34). This continuous coating of albite appears to have precluded the development of intense wall-rock alteration at the edge of some veins. Where albite does not form a continuous coating at the edge of an extensional vein, intergrowing albite, chlorite, calcite and pyrrhotite display a variety of structures near the vein wall, and wall-rock alteration is intense. Occasionally, the tips and edges of the extensional veins are dominated by the usually subordinate minerals (albite, chlorite, calcite and pyrrhotite), and have been observed consisting of up to 40% pyrrhotite, albite or a combination of the two with varying amounts of quartz, chlorite and biotite.

Extensional veins at Junction have a number of internal structures and textures that are diagnostic of this vein type and indicative of their opening vector. The most common textures and structures observed in the extensional veins at Junction were growth layering, open space filling and elongate mineral fibres.

Growth layering in extensional veins attests to the incremental development of the veins (Boullier and Robert, 1992; Robert *et al.*, 1995). Growth layering generally exhibits one or several wall-parallel ribbons of varying minerals at various scales. Growth layers correspond to major individual opening increments. They have sharp, well defined boundaries, and contain several types of internal mesostructures such as fluid inclusion bands and trails, mineral fibres and euhedral crystals (Boullier and Robert, 1992). At Junction growth layering is common and can been seen at both the mesoscale (Figure 3.35) and the microscale.

According to Boullier and Robert (1992), a significant difference exists between growth layering textures and crack-seal structures. Boullier and Robert (1992) distinguish that crack seal structures are defined by very regular lines of small crystals of wall rock assemblage matrix; albite, calcite, chlorite and biotite. The fine lines they form within the vein are parallel to each other, reproducing the delicate geometry of the vein wall. Spacing between crack-seal bands is regular, and ranges from 25μm on average for crack-seal increments formed adjacent to very fine crystals (<10μm), to 200μm for crack-seal increments formed adjacent to the host rocks containing larger phenocrysts. This description of crack-seal structures differs from the examples referred to by Colvine *et al.* (1988), who presents diagrams of crack-seal structures that resemble the growth-layering structures presented by Boullier and Robert (1992). Using the criteria set out by Boullier and Robert (1992), crack seal structures were not observed in extensional veins as commonly as growth layering structures in the same veins.

Open space filling textures are regularly observed at the mesoscale and microscale in extensional veins at Junction. The textures of open space filling are characterised by well developed euhedral and radiating aggregates of chlorite, calcite, biotite and occasionally pyrrhotite crystals (see Figure 3.17). These rosettes are typically, but not always, attached to the vein wall, indicating crystallisation in a fluid filled cavity (Boullier and Robert, 1992). These textures, indicate that the rate of fracture was greater than the rate of crystal growth and that the fracture was at least partly opened until completely filled, requiring the fluid pressure to equal that of the lithostatic load (Robert *et al.*, 1995).

Mineral fibres are common in many extensional veins at Junction. They are generally perpendicular or at a high angle to the vein wall (Figure 3.36). Mineral fibres form when the rate of mineral precipitation is equal to or greater than the rate of wall-rock separation (Robert *et al.*, 1994). Mineral fibres represent crystals that grew progressively as the fracture opened. Therefore they track the direction of opening of the veins (Robert *et al.*, 1994). At Junction quartz, chlorite and pyrrhotite mineral fibres are most common (Figure 3.37). However, albite and calcite mineral fibres are regularly observed.

The three main textures described above (growth layers, mineral fibres and open space filling) may co-exist in a single vein and occasionally in a single growth layer. Rosettes of chlorite and euhedral albite indicative of open space filling have been observed to form adjacent to chlorite - pyrrhotite mineral fibres in veins that exhibit one or more growth layers. Fluid inclusion clusters and trails are common throughout most of the veins analysed.

3.6.2.3 Breccia Veins

Two styles of breccia veins occur at Junction. The most common form of breccia veining at Junction consists of angular wall rock fragments set in a matrix of hydrothermal quartz (Figure 3.38). These "jig-saw style" or "carrot" breccia veins range in size, and are typically irregular in shape. The wall rock fragments are not unusually altered in any way (ie the alteration of these fragments is consistent with the altered wall rock associated with other vein types) thus, albite, chlorite, biotite, pyrrhotite and calcite crystals are commonly observed growing at the edge of the vein-wall rock contact. Mol *et al.* (1996) noted that this style of breccia vein appears to correlate with sites of shear bifurcation or positions of minor flexure in the shear zone.

The less common style of breccia veining observed at Junction comprises angular and rounded clasts of highly altered wall rock and vein material set in a hydrothermal matrix (Figure 3.39). The rounded clasts indicate rotation of the wall rock and existing vein material, probably due to multiple faulting episodes associated with shear vein activation nearby (Robert *et al.*, 1994). This style of breccia vein at Junction is dominated by albite > quartz > chlorite with subordinate amounts of calcite and pyrrhotite.









Figure 3.35. An example of growth layering in an extension vein from drive 405-1-54. Note the incorporation of chlorite and calcite slivers into the quartz vein upon subsequent extension and precipitation.
Figure 3.36. Quartz mineral fibres that have formed perpendicular to the edge of the vein wall indicating that the rate of precipitation is equal to or greater than the rate of wall-rock separation.
Figure 3.37. Chlorite-calcite-pyrrhotite mineral fibres growing perpendicular to or at a high angle to the vein wall are the most common mineral fibres observed at Junction.
Figure 3.38. Jigsaw puzzle breccia is the most common form of breccia observed at Junction.

3.6.3 Post-shearing vein assemblage

3.6.3.1 South dipping quartz veins

South-east dipping quartz veins (hereon known as SV-type veins) are observed throughout the Junction deposit (see Figures 3.3a, 3.3b and 3.4). These veins cut through all rock units and vein arrays in the N25 surface, but not the Proterozoic dolerite dykes. This indicates that these veins formed after activity on the N25 surface ceased but before the dolerite dykes intruded.

Two orientations of SV-type veins have been observed by Gilmore (1996), one dipping at 40° to SE and the other at 70° to the SE. However, both veins sets have the same internal mineralogy. They are regularly < 10 cm thick, but some veins can be up to 25 cm wide.

SV-type veins are commonly filled with white buck-quartz, coarse calcite (with traces of dolomite), large randomly orientated biotite and coarse pyrrhotite (Figures 3.40 and 3.41). Alteration around these veins is negligible and no selvages have been observed either in hand specimen or in microscope investigations where they cross-cut the Junction Gabbro. However, where SV-type veins cross-cut the felsic to intermediate porphyries, alteration zones up to 5 cm wide and comprised of 60% plagioclase, 25% K-feldspar, 10% muscovite, 5-10% chlorite and 5% quartz are observed (Murphy 1995). Anomalous but uneconomic gold grades are associated with the alteration (Murphy 1995). Both sets of south-dipping veins show normal sense of movement.

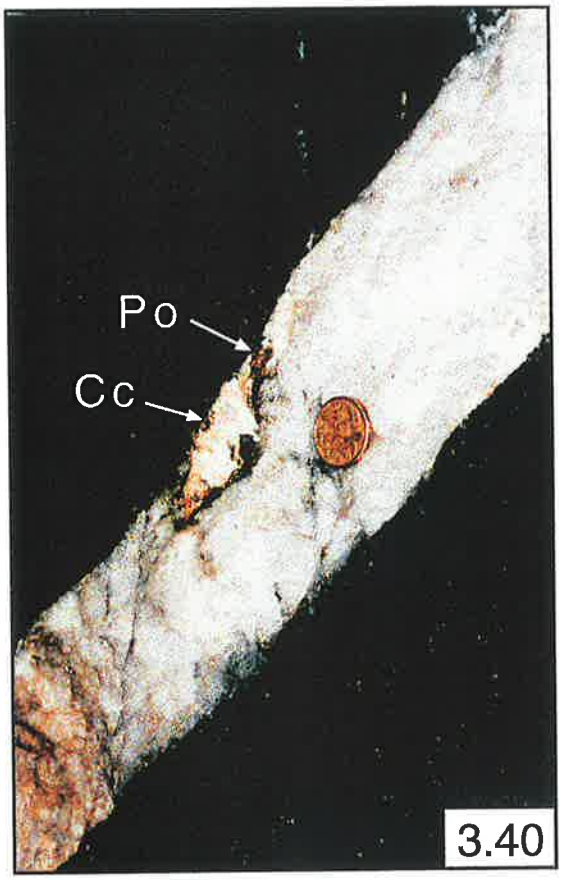
3.7 Proterozoic dykes

The Junction deposit is cross-cut by two east-west striking dolerite dykes that transect mineralisation in two separate areas within the Junction Gabbro. The dykes are 20-30 metres wide, dip steeply to the south and dextrally displace the ore lodes by up to 20 metres (Ellis and Mapleson, 1997). The dykes are Proterozoic in age and consist predominantly of calc-plagioclase, augite, hornblende, biotite, quartz and chlorite (Gilmore, 1996). The dykes exhibit chilled margins at the contact with the Junction Gabbro and have a distinct alteration assemblage observed up to 30 metres into the host rock or lode (Ellis and Mapleson, 1997). This alteration assemblage is characterised by pink-red iron enriched albite, epidote, actinolite, Fe-rich chlorite and haematite after magnetite.

3.8 Tertiary sediments

The Pre-Cambrian geology at Junction is overlain by a prominent palaeochannel that traverses in a north-east - south-west direction across the Junction Gabbro and is likely to be a related tributary of the larger Lake Lefroy palaeodrainage system further north. The channel consists of an upper 4m thick sequence of partially lithified and laterized brown alluvial sediments consisting of lithic conglomerates, quartz sands and clays incised into an earlier channel approximately 20 metres thick (Balkau, 1989). Extensive geomorphological and sedimentological





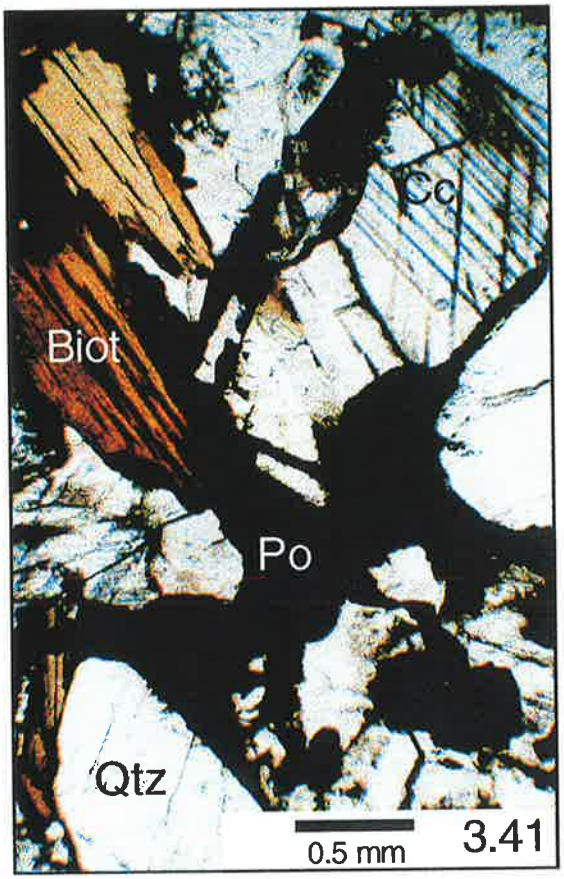


Figure 3.39. Angular and rounded clasts of highly altered wall rock and vein material, set in a hydrothermal matrix dominated by quartz and albite. This is a less common form of breccia observed at Junction.
Figure 3.40. Typical of the SV-type veins at Junction are the large calcite crystals that grow within the quartz veins. The calcite (Cc) is often in co-existence with pyrrhotite (Po) and large randomly orientated biotite crystals (Figure 3.41).
Figure 3.41. Transmitted light photomicrograph showing the large well formed crystal structure typical of the calcite (Cc), biotite (Biot) and pyrrhotite (Po) crystals that are present in the SV-type quartz (Qtz) veins.

investigations of palaeodrainage systems in the Kambalda to Norseman region (Clarke, 1993 1994a, 1994b, 1994c; Woolrich, 1994) have shown that similar nearby palaeochannels contain:

- lignitic facies comprising lignite, carbonaceous silt and white clay (absent at Junction);
- varved facies, consisting of red-brown to green silt and clay (only present in the main palaeodrainage channels);
- sandstone facies comprising fine grained to gravelly sand containing sparse to moderate marine fauna interbedded with minor silt;
- spongelite, comprising greater than 50% siliceous sponge spicules, minor quartz silt and glauconitic pellets, and
- fine and coarse grained lake facies, comprising massive to faintly bedded red-brown silty clay with varying amounts of siderite and red, iron cemented sandstone.

3.9 Recent sediments

A one to three metre thick layer of residual soil, calcrete and transported sheetwash overlies all of the aforementioned geology. It typically consists of a 0.5 m to 2 m thick ferruginous zone comprising reddish alluvial loam with rare ferric nodules. The soil becomes increasingly calcareous with depth and excavations by earth-moving equipment at a nearby prospect shows that this calcareous soil develops into massive calcrete between 1 and 2 m below the surface.

CHAPTER FOUR

Soil gas emissions above the Junction deposit

4.1 Introduction to soil gas prospecting

Soil gas geochemical exploration is increasing in popularity with some mineral explorers, because ongoing research indicates that CO_2, light hydrocarbons, nitrogenous gases, helium, radon, thoron, mercury and sulphur gases form anomalies at or near the surface above virtually all mineral deposits, either as primary components or as reaction products (Taylor *et al.*, 1982; Lovell *et al.*, 1983; Carter and Cazalet, 1984, 1988; Hinkle and Dilbert, 1984; Kesler *et al.*, 1986; Kesler and Gardner, 1986; McCarthy and Reimer, 1986; Reimer, 1986; McCarthy *et al.*, 1986, Oakes and Hale, 1987; Ball *et al.*, 1990; Disnar, 1990; Hinkle *et al.*, 1990; Kesler *et al.*, 1990; Mulshaw, 1996).

The primary assumption involved in soil gas sampling is that volatiles migrate from concealed ore bodies to produce anomalies in surface rocks and soil (Disnar, 1990). These gases eventually escape into the atmosphere. Some gases are released from within the ore-body and are known to arrive at the surface relatively unchanged, with bulk compositions similar to those at their sources. These gases are known as primary gases and form primary gas anomalies (Viellanave, 1997). In other cases, gases arrise from the breakdown of organic or inorganic material, or there are significant changes in the gases' chemistry, resulting from losses of higher molecular weight materials in transit, or due to oxidation, hydrolysis, bacterial action, solubility losses, and other factors. These gases are known as secondary gases and form secondary gas anomalies (Viellanave, 1997).

Primary and secondary soil gases have been detected at the surface despite the ore body being buried below:

- weathered basalt float (Klessig, 1984),
- glacial till (McCarthy *et al.*, 1986),
- leached saprolite and ferruginous soils (Ball *et al.*, 1990),

- younger limestones (Kesler *et al.*, 1990) and
- transported soil cover (Reid and Rasmussen, 1990).

Indeed, Reid and Rasmussen (1990), detected CO_2 anomalies above oxidising sulphides that were 200 m below the surface.

Gas anomalies associated with buried mineral deposits are typically formed by the generation of secondary gases at the site of mineralisation. These gases are generated by weathering and other geochemical processes through the interaction of the ore body with the hydrosphere, biosphere and atmosphere (McCarthy and Reimer, 1986). An example of this is when CO_2 and sulphur gases, COS and CS_2 are generated during the oxidation of sulphide bearing ore bodies. Similarly, helium and radon are generated by the radioactive decay of uranium-containing minerals.

Hydrocarbons in the soil-atmosphere have a somewhat enigmatic origin when compared to CO_2 and sulphur gases. With the exception of CH_4, hydrocarbons are not commonly associated with the alteration assemblage in igneous and metamorphic ore deposits. However, **light** hydrocarbons, (along with the anticipated CO_2, and various sulphur gases) have been detected in soil and weathered rock above many ore deposits (Lovell *et al.*, 1983; Hinkle and Dilbert, 1984; Stedman *et al.*, 1984; Peachy *et al.*, 1985; McCarthy *et al.*, 1986; McCarthy and Reimer, 1986; Ferguson, 1987, 1988; Fridman, 1990; Hinkle *et al.*, 1990; Kesler *et al.*, 1990; Reid and Rasmussen, 1990; Polito, 1993; Mulshaw, 1996), including late-orogenic, structurally-controlled gold deposits (Amanor, 1979; Ball *et al.*, 1990).

Carbon dioxide and CH_4, detectable above late-orogenic, structurally-controlled gold deposits, probably originate from fluid inclusions hosted in the gangue minerals of the deposit. CO_2 and CH_4 are regularly encountered in fluid inclusions associated with this deposit style (Roedder, 1984; Robert and Kelly, 1987; Ho *et al.*, 1990; Bray *et al.*, 1991; de Ronde *et al.*, 1992; Mernagh and Witt, 1994; Graney and Kesler, 1995; Robert *et al.*, 1995; Mernagh, 1996; Boullier *et al.*, 1998). However, the ability to distinguish between soil gas anomalies that are associated with ore mineralisation and those that are created by bacterial metabolism or soil contamination by previous anthropogenic activity, is vital and has considerable economic importance for exploration.

4.2 Location of the soil gas survey relative to gold mineralisation

A soil gas survey was conducted across two traverses over the N75 surface at the Junction deposit. The N75 surface is a narrow (<3 m) mineralised shear zone that runs sub-parallel to, and lies approximately 400 m east of, the wider and currently mined N25 surface (see Figure 3.1). The N75 surface is ideal for this type of experimental survey because its mineralogy,

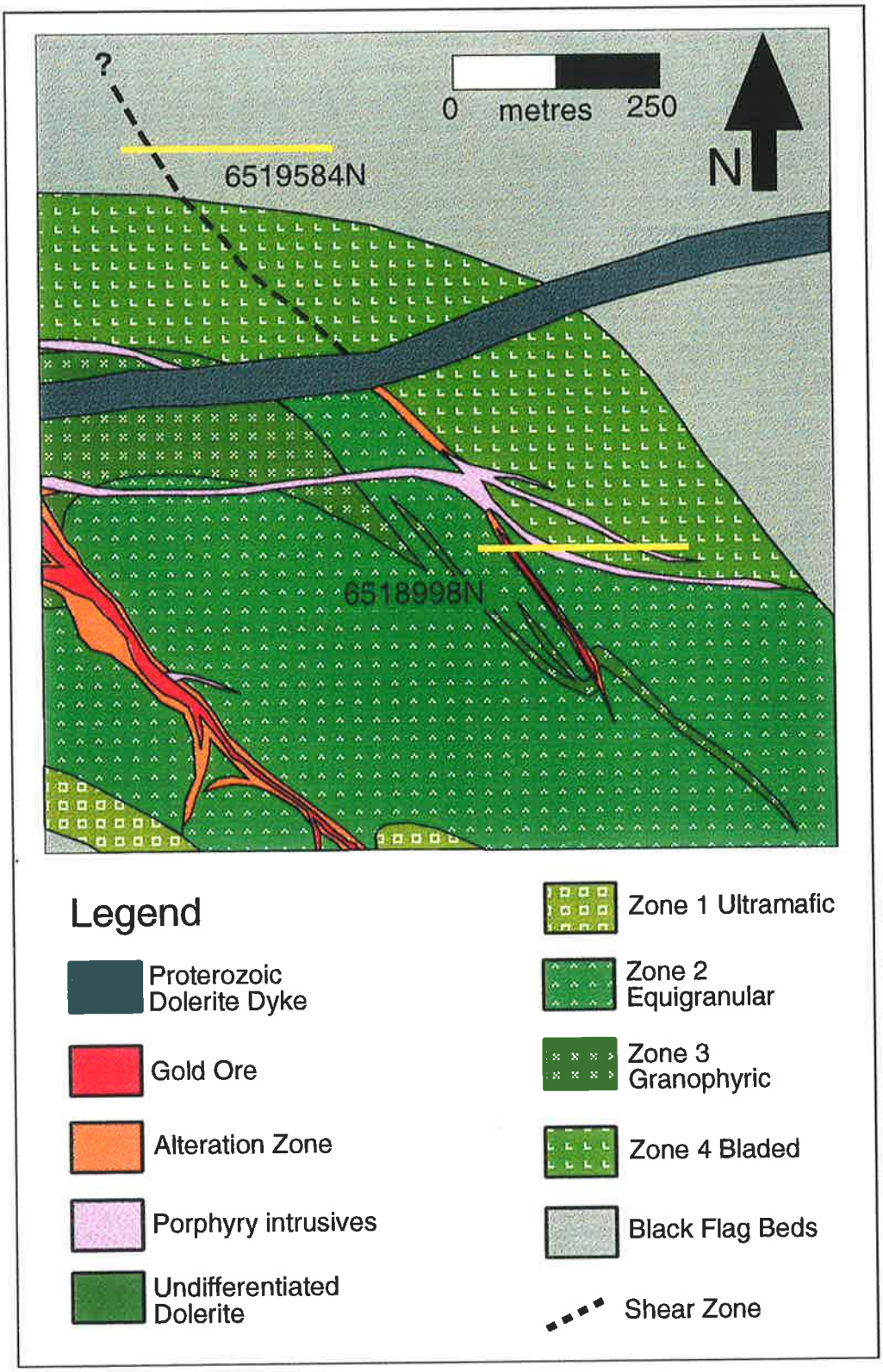


Figure 4.1. Positioning of traverses 6518998 and 6519584 across the N75 surface. Note the proximity of the much larger N25 surface, bottom left hand corner. Modified from Ellery and Watts (1996).

dimensions, and depth to oxidation are known and comparable to the larger N25 surface. Drill hole compilations show that the N75 surface shares the same orientation as the N25 surface and is part of the same mineralising system. Therefore, the results from the soil gas survey presented here are applicable to the geology and geochemistry of the N25 surface.

Traverse 6518998 lies directly above, and transects a mineralised section of the N75 surface hosted by the Junction Gabbro (Figure 4.1). The N75 surface dips toward the east at approximately 50° at this site. This traverse was pre-pegged for the survey by a WMC Resources field assistant, based on GPS co-ordinates pin pointing the location of the mineralised shear. This location probably represents the position of the N75 surface at depth (±5 m), because sub-outcropping buck quartz veining interpreted to represent the location of the N75 surface at ground level is observed approximately 8 m west of this peg.

Traverse 6519584 is north of and parallel to traverse 6518998 (Figure 4.1). It lies directly above and transects a relatively unexplored portion of the N75 surface. Drill holes targeting deep (>600m) mineralisation in the larger N25 surface to the west of the N75 surface are positioned only 150 metres east of the N75 surface. However, these drill holes are vertical to near vertical in this area of the mining lease and do not intersect any hanging wall mineralisation indicative of the N75 surface. Nevertheless, the presence of shallow mineralisation or a related alteration assemblage below this traverse cannot be dismissed. Unlike traverse 6518998, the N75 surface does not sub-outcrop or outcrop at this point. Aeromagnetic and drill hole data indicates that up to 60 m of Black Flag Group metasediments overlie the Junction Gabbro below this traverse (B. Perriam, pers. comm., 1997).

4.3 Characteristics of the N75 surface

4.3.1 Soil cover

The N75 surface sub-outcrops in part towards its southern extension, where it is expressed as white buck-quartz veining, but it is typically covered by up to 30 m of leached saprolite and transported material consisting of red-yellow to brown-white coloured sandy to ferruginous clay, calcrete nodules and loamy soil. Detailed descriptions of the soil geology for each sample site are listed in Appendix V. The top 50 - 100 cm of cover consists of creamy-brown to red-brown loamy soil interbedded with rounded ferruginous surface grains (FSGs) (Clarke and Chenoweth, 1996) and white to clear angular quartz chips at most sample sites. This is commonly underlain by indurated to nodular calcrete (Figure 4.2).

4.3.2 Groundwater geochemistry

The pH of the ground water around Junction is significant to this project, because sulphide oxidation and carbonate dissolution are two principle catalysts and sources for soil gas anomalies above sulphide bearing ore deposits. Ground water geochemistry shows that the pH of the water in the aquifer surrounding the Junction Pit and above sulphide bearing mineralisation ranges

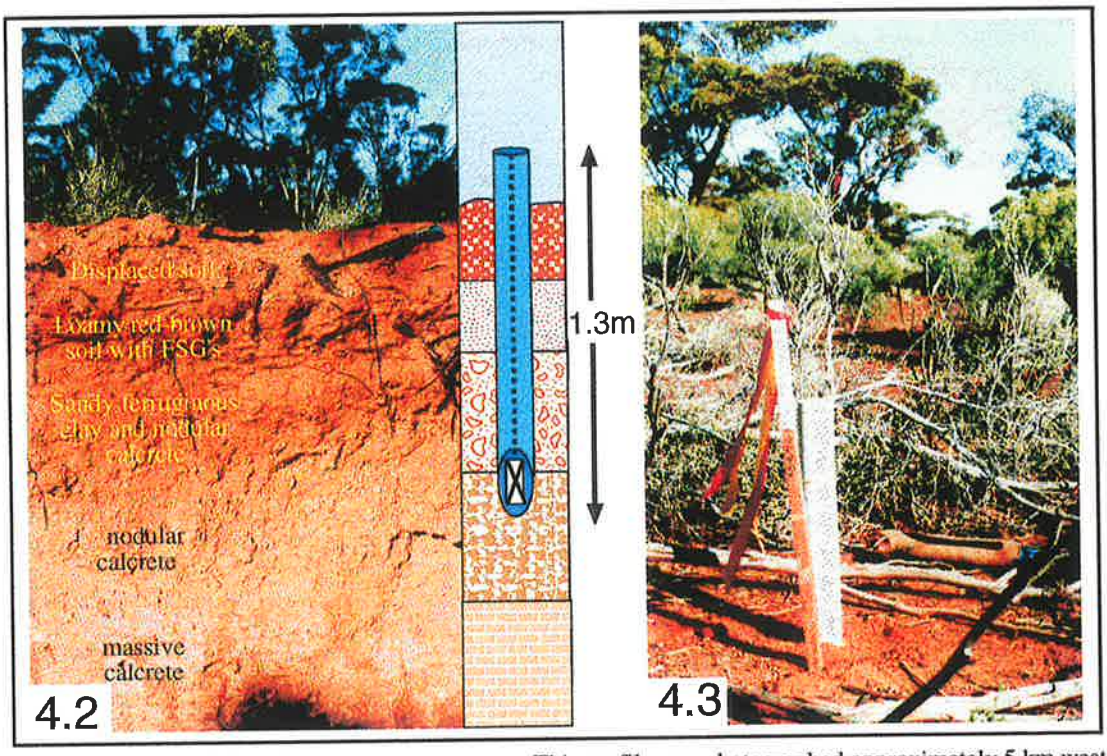


Figure 4.2. Soil profile in the Junction area. This profile was photographed approximately 5 km west of the Junction mine, but accurately reflects the soil profile at Junction. Note the relative abundance of coarse organic material near the surface (mostly roots) compared to that just 1metre below the surface.
Figure 4.3. Incorporporation of Figure 4.2, showing the hand coring device used to dig the sampling holes and the PVC casing used to protect the passive sampler. Cartoon illustration shows the passive sampler configuration when in position in the soil.

Ground-water geochemistry around the Junction deposit

Drill Hole/ Bore sampled	Date Sampled	TDS*	pH	Cl	SO_4	Na	Ca	Mg
TD2153: Junction Pit	14/8/95	49,050	3.8	28,150	1,860	16,800	270	1,290
TD2289A: Junction Pit	18/9/91	110,000	4.1	n.d	n.d	n.d	n.d	n.d
	8/8/94	122,600	5.2	67,050	11,150	40,600	340	5,570
	14/8/95	101,200	6.4	52,900	9,660	28,950	255	3,560
	28/2/96	120,000	5.5	59,000	11,000	42,000	250	710
	9/10/96	114,480	6.1	61,000	11,000	37,000	270	6,200
TD2497: Junction Pit	16/11/90	162,600	6.3	n.d	n.d	n.d	n.d	n.d
TD2600: Junction Pit	14/8/96	37,450	6.7	19,900	3,280	10,100	300	1,530
Regional Bore 2: Lake Finn	20/11/90	45,800	6.8	24,800	3,800	13,000	1,540	1,420
	24/3/91	43,720	6.8	19,700	7,288	12,400	1,320	1,300
Regional Bore 5: Lake Finn	20/11/90	61,800	6.7	33,700	3,400	16,800	2,780	1,660
	24/3/91	45,220	6.8	19,800	7,440	12,800	1,400	1,340
Regional Bore 6: Lake Finn	20/11/90	46,700	7	24,800	4,100	13,200	1,210	1,640
	24/3/91	52,350	6.5	26,730	7,280	13,800	2,000	1,540

TDS* = Total Dissolved Salts n.d. = not determined

Table 4.1. Groundwater geochemistry above and around the Junction deposit. Data supplied by WMC.

from 3.8 to 6.7 log units (average pH = 5.4 log units, Table 4.1). Similar pH values are assumed above the N75 surface. This contrasts with pH values that range from 6.5 to 7.0 log units (average pH = 6.8 log units, Table 4.1) in three bore holes regionally distributed around the Junction area. While sulphide oxidation to sulphuric acid is strongly suspected, the only evidence for sulphide oxidation in these bore holes is the higher SO_4 content in the aquifer surrounding the Junction Pit which ranges from 1860 to 11,150 ppm (average = 7991 ppm, or 9218 ppm excluding the outlier value of 1860 ppm) compared to 3,400 to 7440 ppm (average = 5551 ppm) in three bore holes regionally distributed around the Junction area (Table 4.1; J. Chapman, pers. comm., 1998).

4.4 Methods

Soil gases targeted at Junction were CO_2, O_2, light hydrocarbons (C_1 to C_{10}) and occluded aliphatic and aromatic hydrocarbons (occluded = adsorbed on to soil and clay particles). Three different gas detection methods were used to determine whether CO_2, O_2 and hydrocarbons were present.

1. CO_2 and O_2 were actively measured using a portable CO_2 - O_2 analyser.

2. Light hydrocarbons (C_1 to C_{10}) were collected passively on to an activated charcoal (Carbosol) filament and were later analysed by gas chromatography.

3. Heavier occluded hydrocarbons (C_5-C_6 aliphatic to C_{17}-C_{18} aromatic) were determined by gas chromatography after being desorbed from soil samples.

4.4.1 Active analysis of CO_2 and O_2

The concentration of CO_2 and O_2 was measured using a portable Servomex 570 Oxygen analyser and a Drager Multiwarn CO_2 analyser. The operating equipment used for the CO_2 - O_2 analysis included:-

- steel sampling probes made from 4130 tubing of CrMo steel , including sliding hammer,
- Mityvac hand pumps, attached to surgical tubing which was used as the sampling line,
- a Servomex 570 Portable Oxygen Analyser and Drager Multiwarn CO_2 Analyser, and
- a filled tube of indicator drying agent, drierite, to remove moisture from the moisture sensitive instruments.

The configuration is:
Steel Probe - Sample line - drierite - hand pump - O_2 Analyser - CO_2 Analyser (Figure 4.4).



Figure 4.4. CO_2 - O_2 analyser in use by the author at another WMC Resources prospect. The Servomex 570 Portable oxygen analyser is hidden behind the Drager Multiwarn CO_2 analyser. Small white arrows indicate flow of soil gas from steel probe to analytical equipment.

4.4.1.1 Measurement of Soil O_2 and CO_2 concentrations

After assembling the sampling lines, drierite, pump, and analysers, with the steel probe open to the atmosphere, the O_2 analyser was turned on and the hand pump was pumped to clear the instrument of gas. Pumping continued until the readings were stable. This often took >300 pumps.

A nail was inserted into the lead opening of the steel probe to prevent clogging of the hollow probe with soil and a sliding hammer was used to pound the probe into the soil. Once fully inserted, the probe was raised approximately 2 cm to lift the end of the probe above the nail. Where possible, the steel probe was hammered to a depth of 100 cm, but due to the nature of the underlying calcrete at Junction, most analyses were collected from less than 80 cm. After ensuring that a good seal between the top of the steel probe and the surrounding soil was in place, the upstream end of the surgical tubing was attached to the steel probe. The hand pump was then pumped while watching the CO_2 and O_2 reading. Once the O_2 and CO_2 readings became stable, the minimum O_2 and the maximum CO_2 readings were recorded. Barometric pressure and air temperature were measured with hand-held instruments. A completed sampling record is presented in Table 4.2.

Anomalies for O_2 and CO_2 are calculated as follows:

$$\Delta O_2 = O_2 \text{ atmosphere} - O_2 \text{ soil}$$
$$\Delta CO_2 = CO_2 \text{ soil} - CO_2 \text{ atmosphere}$$

(Expected atmospheric values: $O_2 = 20.9 + 0.5\%$; $C0_2 = 200$ to 400 ppm).

4.4.2 Light hydrocarbon analysis using passive samplers

Stimulated by the need for high quality, reproducible data, TEG Rocky Mountain, Colorado, USA, was approached for advice on analytical techniques that could be applied or adapted to resource exploration activities. TEG Rocky Mountain are a resource exploration consultancy group who specialise in soil gas methods for the detection of oil and gas reservoirs, mineral deposits and geothermal hot-spots. A sampling method, known as the passive sampling technique, was chosen as the preferred method to detect any migrating hydrocarbons. The passive sampling technique was implemented at the Junction mine during July-August 1997.

4.4.2.1 Passive Sampling

The use of passive samplers is based on the assumption that all migrating gases will attach themselves to the sorbent sites of the activated charcoal particles at levels that are in equilibrium with the source's concentration. Thus, passive samplers collect the gases that are present in the soil on to the activated charcoal particles without significantly altering the ratio of the co-existing gas species (CH_4 can occasionally be affected). The goal of the passive sampler is to avoid intrinsic organics in the near-surface soils that may have been introduced e.g. by previous anthropogenic activity, by detecting the free soil-gas which is actively migrating from the sub-surface source. Further to this, passive samplers overcome the problem of inconsistent soil-gas results caused by migration fluctuations of volatile gases due to soil characteristics, seasonal changes and daily weather patterns (Lovell *et al.*, 1983; Hinkle and Dilbert, 1984; McCarthy *et al.*, 1986; McCarthy and Reimer, 1986; Ferguson, 1987; Alpers *et al.*, 1990; Ball *et al.*, 1990; Fridman, 1990; Hinkle *et al.*, 1990; Kesler *et al.*, 1990; Mulshaw, 1996). Passive samplers smooth out the seasonal and daily variations in soil gas concentrations by continuously collecting gas over an extended period of time until all of the sorbent sites are filled or equilibrium is reached (Viellanave, 1997).

The effectiveness of sorption and the retention of the sorbed gases depend on the substrate and the compounds migrating through the soil. Experiments in controlled conditions on ground water or soils, where the precise ppb concentrations of petroleum and chlorinated hydrocarbons are known, indicate that a passive sampler can continue to collect and concentrate components 100-5000 times greater than the natural concentration.

While passive samplers do not normally alter the ratio of co-existing gas species, CH_4 may be

selectively excluded by the sorption of the C_2^+ hydrocarbons in a hydrocarbon-rich environment (Viellanave, 1997). Therefore, the gases collected by a passive sampler may be biased against CH_4 depending on the volumes of other hydrocarbons present at the various sites. However, analytical problems arising from such samples are not expected to significantly affect the detection of CH_4 at Junction. Soils at Junction are not expected to be hydrocarbon-rich, thus CH_4 should not be excluded from the sorption sites, and the gas chromatograph detector used during gas analysis can be chosen to favour light hydrocarbons (specifically C_1-C_4) over heavier C_4^+ hydrocarbons.

Passive sampling in this project was accomplished by using specially manufactured passive samplers. The passive samplers are constructed of a 120 ml glass vial containing two 8 cm long aluminium rods, coated at one end with activated charcoal absorbent. The absorbent used in the vials was specially designed to absorb light hydrocarbons. The aluminium rods are bent to restrain them within the glass vial. The unused absorbent was heat treated to 200°C to remove any pre-absorbed gas prior to sealing the vial and dispatching it to the user. The glass vial is filled with argon gas and sealed by an air tight screw-on plastic lid fitted with a teflon septum. The plastic lid is removed only at the sampling site.

This project predicated that the collectors were suspended in an inverted position a minimum of 15 cm below the surface, and optimally, at 100 cm below the surface. The holes were drilled using a hand held coring tube. Thus, the depth of each hole was determined by the depth to the calcrete below the soil. Each hole was cased with a 15 cm diameter PVC pipe (Figure 4.3). The collectors were suspended by copper-alloy wire approximately 5 cm from the bottom of each hole. Finally, the casing was sealed with plastic and Scotch tape to impede any downward influx of surface gases. The collectors were left in place for 15 days.

The hydrocarbon gas analyses were carried out by TEG Rocky Mountain, Denver, Colorado, USA. The passive sampler vials were heated to 200°C for five minutes to desorb the gases from the absorbent. This released the gas into the head space, allowing removal by plunging a syringe through the septum. This gas was then injected into a Tracor 560 gas chromatograph fitted with a packed Supel-Q PLOT column and a flame ionisation detector (FID). This instrument is capable of achieving a detection limit between 1 and 10 ppb. Hydrocarbons detected were CH_4, ethene, ethane, propene, propane, iso-butane, butane, pentane, C_6, C_7, C_8, C_9 and C_{10}.

Thirty-three sites along the two traverses over the N75 surface (east of the main N25 lode), were tested for anomalous gas emissions. Sample spacing ranged from 5 m intervals directly over the N75 surface, up to 50 m intervals 200m away from the N75 surface (Figure 4.5).

4.4.3 Occluded hydrocarbon analysis

The occluded hydrocarbon survey used soil samples that were obtained by digging holes with a hand coring device (Figure 4.3) to the soil-calcrete interface. Approximately 80 to 100 gm



Figure 4.5. Physiography and topography above the N75 surface showing the scattered salt-bush (low, pale blue shrub), acacia (short, <3m high shrub, centre right) and black butt eucalyptus (tall gum trees, centre right and background). Photo also shows spacing between the passive samplers.

of soil, free of visible organic mater, was collected from the bottom of the cored hole, placed in a 200 ml glass vial and capped with an aluminium lined, screw-top bakelite lid.

The soil samples were analysed by Actlabs, Ancastor, Ontario, Canada. Actlabs are an analytical consultancy group who have extensive experience in extracting organic hydrocarbons from soil material for oil and gas exploration. Combined gas chromatography and mass spectrometry used by Actlabs is precise to 0.1 ppb.

The soils were degassed by two methods in order to remove the low temperature fraction of the hydrocarbons first, and then the higher temperature hydrocarbons later. Approximately 2 gm of soil was placed into a glass vial capped by a plastic lid with a teflon-lined septum and heated at 70°C for 24 hours. The soil was allowed to cool before analysis. This method does not destroy the water layer that can trap gases around particles nor does it evaporate the water from the sample. Water evaporation is usually preceded by a minor, but critical water expansion which may cause the teflon septum to burst. Water vapour also impedes the efficiency of the capillary column fitted in the gas chromatograph. The head space gas was removed by syringe and analysed. Next, the glass vials containing the soils, from which the low temperature gas fraction had been removed, were opened and heated for two hours at 70°C to remove excess moisture. The vials were then closed and heated at 125°C for 24 hours to liberate any further adsorbed gases before analysis.

CO_2 - O_2 and light hydrocarbon soil gas results

Sample location	CO_2 atmosph. level ppm	O_2 atmosph. level %	CO_2 soil level ppm	O_2 soil level %	CO_2 soil anomaly %	O_2 soil anomaly %	°F	°C	Depth of sample	CH_4 ppm	C_2 ppm	$C_{2:1}$ ppm	C_3 ppm	$C_{3:1}$ ppm	iC_4 ppm	nC_4 ppm	C_5 ppm	nC_6 ppm	nC_7 ppm	nC_8 ppm	nC_8 ppm	nC_{10} ppm	CH_4 - nC_{10} total
6518998N, 050W	250	21.1	870	21.0	620	-0.10	83	28.6	70cm	11.02	0.44	5.58	0.78	11.15	0.22	0.07	0.05	1.00	0.00	0.00	0.00	0.11	30.42
6518998N, 015W																							
6518998N, 010W	230	21.1	920	21.1	790	0.00	79	26.1	10cm	114.75	8.07	85.69	10.18	252.70	3.16	0.89	1.08	0.48	1.01	0.00	0.23	0.00	478.20
6518998N, 005W	250	21.1	2260	20.8	2010	-0.30	82	27.8	90cm	10.57	0.47	5.87	0.54	9.90	0.21	0.08	0.05	0.00	0.00	0.00	0.00	0.60	28.29
6518998N, 000	250	21.1	980	21.0	730	-0.10	82	27.8	70cm	26.04	1.31	12.33	2.27	21.87	1.30	0.18	0.07	1.90	0.18	0.00	0.35	0.00	67.80
6518998N, 005E	290	21.1	1380	20.8	1070	-0.30	71	21.7	60cm	12.42	0.29	3.30	1.34	5.80	0.83	0.00	0.03	0.23	0.00	0.00	0.00	0.00	24.24
6518998N, 010E	320	21.1	990	21.0	670	-0.10	74	23.3	70cm	12.84	0.28	3.86	0.49	5.79	0.39	0.06	0.08	0.00	0.00	0.00	0.00	0.00	23.79
6518998N, 015E	330	21.1	800	21.0	470	-0.10	73	22.8	60cm	1.62	0.08	0.43	0.04	0.81	0.02	0.03	0.03	0.00	0.00	0.00	0.00	0.00	3.06
6518998N, 020E	310	21.1	970	21.0	660	-0.10	75	23.9	60cm	10.40	0.20	2.18	0.34	3.39	0.27	0.04	0.05	0.24	0.00	0.00	0.00	0.00	17.11
6518998N, 030E	310	21.1	1230	21.0	920	-0.10	73	22.8	60cm	21.53	0.68	7.91	0.96	10.36	0.53	0.12	0.09	2.63	0.87	0.00	0.00	0.00	45.68
6518998N, 040E	300	21.1	1390	21.0	1090	-0.10	74	23.3	60cm	32.63	1.26	17.50	2.27	27.84	0.90	0.24	0.20	9.72	0.00	0.00	0.00	0.00	92.56
6518998N, 050E	300	21.1	1220	21.0	920	-0.10	79	26.1	60cm	13.81	0.27	3.91	0.89	6.48	0.40	0.07	0.12	2.81	0.00	0.00	0.00	0.00	28.76
6518998N, 060E	290	21.1	720	21.0	430	-0.10	82	27.7	50cm	9.83	0.36	4.99	0.36	6.30	0.13	0.07	0.04	0.71	0.00	0.00	0.00	0.00	22.79
6518998N, 080E	290	21.1	1090	21.0	800	-0.10	81	27.2	70cm	14.14	0.35	3.27	0.46	5.69	0.24	0.15	0.14	1.38	0.00	0.00	0.00	0.00	25.82
6518998N, 100E	290	21.1	990	21.0	700	-0.10	83	28.3	70cm	7.36	0.19	1.96	0.14	2.72	0.07	0.04	0.04	0.00	0.00	0.00	0.00	0.00	12.52
6518998N, 150E	320	21.1	780	20.9	460	-0.20	77	25.0	70cm	10.38	0.17	1.77	0.09	2.21	0.02	0.03	0.03	0.00	0.00	0.00	0.00	0.00	14.70
6518998N, 200E	320	21.1	2050	20.8	1730	-0.30	79	26.1	80cm	4.89	0.11	1.93	0.11	1.91	0.03	0.03	0.00	0.00	0.00	0.00	0.00	0.00	9.01
6519584N, 50W	270	21.1	2120	20.8	1850	-0.30	76	24.4	80cm	1.79	0.00	6.71	2.36	8.59	0.02	0.02	0.01	0.00	0.00	0.00	0.00	0.00	19.50
6519584N, 30W	300	21.1	1460	20.9	1160	-0.20	75	23.9	70cm	5.41	0.32	3.12	0.46	3.86	0.08	0.35	0.35	0.32	0.14	0.00	0.00	0.00	14.41
6519584N, 15W	300	21.1	1720	20.8	1420	-0.30	73	22.8	60cm	5.25	0.26	2.62	0.39	3.56	0.09	0.25	0.22	0.12	0.00	0.00	0.00	0.11	12.87
6519584N, 10W	280	21.1	1210	20.9	930	-0.20	71	21.7	90cm	2.68	0.12	0.63	0.04	1.17	0.02	0.02	0.01	0.00	0.00	0.00	0.00	0.00	4.69
6519584N, 06W	300	21.1	1410	20.8	1110	-0.30	72	22.2	80cm	3.11	0.13	1.83	0.23	3.27	0.04	0.20	0.17	0.32	0.00	0.00	0.00	0.27	9.57
6519584N, 000	290	21.1	1490	20.8	1200	-0.30	70	21.1	80cm	3.33	0.12	1.01	0.17	2.38	0.05	0.03	0.05	0.00	0.00	0.00	0.00	0.00	7.14
6519584N, 5E	280	21.1	1460	20.9	1180	-0.20	72	22.2	60cm	7.48	0.26	2.94	0.61	6.45	0.16	0.2	0.21	1.53	0.00	0.00	0.00	0.00	19.84
6519584N, 10E	280	21.1	2840	20.7	2560	-0.40	72	22.2	90cm	5.73	0.17	1.74	0.20	3.69	0.10	0.02	0.02	0.00	0.00	0.00	0.00	0.00	11.67
6519584N, 15E	270	21.1	1950	20.8	1730	-0.30	71	21.7	90cm	3.30	0.10	0.76	0.11	1.48	0.03	0.02	0.01	0.00	1.10	0.00	0.03	0.00	6.94
6519584N, 21E	270	21.1	1650	20.7	1430	-0.40	69	20.6	90cm	70.40	3.5	41.75	9.39	98.66	1.86	0.72	0.24	0.38	1.34	0.00	0.00	0.00	228.24
6519584N, 30E	330	21.1	2010	20.8	1680	-0.30	69	20.6	80cm	23.88	1.65	23.05	3.71	36.50	0.05	1.46	0.94	0.65	0.32	0.07	0.03	0.00	92.31
6519584N, 40E	280	21.1	1270	20.9	990	-0.20	68	20.0	40cm	23.85	0.03	0.52	0.02	0.63	0.01	0.02	0.01	0.00	0.00	0.00	0.00	0.00	25.09
6519584N, 60E	280	21.1	2130	20.8	1850	-0.30	68	20.0	90cm	1.93	0.05	0.67	0.07	1.19	0.01	0.05	0.00	0.00	0.00	0.00	0.00	0.00	3.97
6519584N, 80E	400	21.1	1560	20.8	1160	-0.30	51	10.6	50cm	5.51	0.00	0.19	0.01	0.01	0.00	0.00	0.00	0.00	0.00	0.00	0.00	0.00	5.72
6519584N, 100E	470	21.1	1580	20.9	1110	-0.20	58	14.4	80cm	4.21	0.04	1.01	0.04	1.30	0.01	0.02	0.04	0.00	0.29	0.00	0.00	0.00	6.96
6519584N, 150E	450	21.1	2230	20.8	1780	-0.30	59	15.0	90cm	4.24	0.20	0.96	0.05	1.13	0.01	0.01	0.00	0.00	0.63	0.00	0.00	0.00	7.23
6519584N, 200E	480	21.1	770	20.7	290	-0.40	58	14.4	70cm	1.83	0.05	0.39	0.34	0.73	0.02	0.01	0.01	0.00	0.00	0.00	0.00	0.00	3.38

Table 4.2 Soil gas results collected from above the N75 structure, Junction gold deposit

Occluded hydrocaron soil gas results

Sample location	C_5-C_6 Aliph.	C_7-C_8 Aliph.	C_7-C_8 Arom.	C_8-C_9 Aliph.	C_8-C_9 Arom.	C_9-C_{10} Aliph.	C_9-C_{10} Arom.	C_{10}-C_{11} Aliph.	C_{10}-C_{11} Arom.	C_{11}-C_{12} Aliph.	C_{11}-C_{12} Arom.	C_{12}-C_{13} Aliph.	C_{12}-C_{13} Arom.	C_{13}-C_{13} Aliph.	C_{13}-C_{14} Arom.	C_{14}-C_{15} Aliph.	C_{14}-C_{15} Arom.	C_{15}-C_{16} Aliph.	C_{15}-C_{16} Arom.	C_{16}-C_{17} Aliph.	C_{16}-C_{17} Arom.	C_{17}-C_{18} Arom.	Sum total
6518998N, 50W	0.00	0.02	0.08	0.00	0.23	0.00	0.23	0.00	0.09	0.03	0.08	0.00	0.06	0.01	0.05	0.07	0.01	0.00	0.03	0.03	0.24	0.03	1.29
6518998N, 15 W																							
6518998N, 10W	0.00	0.2	0.11	0.00	0.3	0.00	0.19	0.00	0.03	0.05	0.25	0.00	0.05	0.03	0.02	0.04	0.04	0.00	0.03	0.04	0.22	0.03	1.63
6518998N, 05W	0.00	0.00	0.17	0.02	0.51	0.01	0.51	0.00	0.15	0.00	0.16	0.00	0.08	0.04	0.01	0.06	0.04	0.00	0.02	0.00	0.19	0.01	1.98
6518998N, 000	0.00	0.02	0.16	0.02	0.35	0.01	0.29	0.02	0.1	0.11	0.3	0.00	0.12	0.03	0.05	0.12	0.03	0.00	0.08	0.00	0.3	0.08	2.19
6518998N, 05E	0.00	0.00	0.14	0.02	0.32	0.01	0.23	0.02	0.07	0.03	0.23	0.00	0.05	0.04	0.03	0.00	0.03	0.00	0.03	0.08	0.19	0.08	1.58
6518998N, 10E	0.00	0.00	0.26	0.01	0.50	0.01	0.25	0.02	0.06	0.02	0.23	0.00	0.08	0.03	0.02	0.09	0.06	0.00	0.04	0.02	0.18	0.03	1.89
6518998N, 15E	0.00	0.02	0.11	0.00	0.02	0.01	0.17	0.01	0.07	0.09	0.33	0.10	0.22	0.32	0.21	0.00	0.42	0.00	0.19	0.01	0.64	0.23	3.18
6518998N, 20E	0.00	0.27	0.11	0.03	0.24	0.01	0.18	0.05	0.05	0.01	0.16	0.00	0.05	0.01	0.05	0.00	0.00	0.00	0.03	0.00	0.12	0.02	1.38
6518998N, 30E	0.00	0.01	0.11	0.00	0.22	0.00	0.18	0.01	0.03	0.01	0.17	0.07	0.02	0.01	0.03	0.00	0.04	0.00	0.00	0.00	0.09	0.00	1.00
6518998N, 40E	0.00	0.01	0.06	0.00	0.28	0.00	0.21	0.01	0.06	0.04	0.16	0.03	0.04	0.02	0.07	0.00	0.14	0.00	0.04	0.00	0.03	0.01	1.21
6518998N, 50E	0.00	0.00	0.09	0.00	0.28	0.00	0.18	0.00	0.10	0.14	0.13	0.04	0.02	0.10	0.06	0.01	0.06	0.11	0.01	0.02	0.07	0.00	1.43
6518998N, 60E	0.00	0.00	0.06	0.00	0.53	0.00	0.28	0.00	0.09	0.11	0.34	0.07	0.10	0.05	0.08	0.18	0.08	0.00	0.05	0.04	0.05	0.03	2.14
6518998N, 80E	0.00	0.00	0.2	0.00	0.61	0.01	0.43	0.03	0.17	0.03	0.23	0.00	0.07	0.11	0.05	0.10	0.16	0.00	0.02	0.00	0.04	0.46	2.73
6518998N, 100E	0.00	0.00	0.00	0.00	0.01	0.00	0.06	0.00	0.02	0.01	0.11	0.01	0.17	0.00	0.15	0.15	0.15	0.00	0.04	0.00	0.11	0.32	1.30
6518998N, 150E	0.00	0.00	0.02	0.00	0.01	0.00	0.04	0.01	0.02	0.05	0.10	0.07	0.10	0.02	0.12	0.00	0.09	0.06	0.09	0.00	0.17	0.10	1.07
6518998N, 200E	0.00	0.00	0.03	0.00	0.06	0.01	0.16	0.00	0.06	0.12	0.39	0.05	0.20	0.07	0.13	0.00	0.22	0.00	0.09	0.16	0.08	0.32	2.15
6519584N, 50W	0.00	0.00	0.00	0.00	0.05	0.01	1.13	0.00	0.04	0.09	0.38	0.07	0.17	0.07	0.13	0.00	0.16	0.00	0.70	0.00	0.16	0.04	3.17
6519584N, 30W	0.00	0.00	0.10	0.00	0.21	0.08	1.23	0.01	0.35	0.01	1.04	0.03	0.38	0.06	0.31	0.00	0.28	0.00	0.26	0.03	0.18	0.04	4.58
6519584N, 15W	0.00	0.00	0.19	0.00	0.46	0.04	0.73	0.00	0.47	0.07	1.20	0.06	0.45	0.05	0.31	0.00	0.23	0.00	0.14	0.02	0.21	0.07	4.73
6519584N, 10W	0.00	0.00	0.10	0.00	0.34	0.03	1.06	0.01	0.42	0.11	1.16	0.08	0.43	0.03	0.30	0.00	0.42	0.00	0.26	0.00	0.11	0.19	5.05
6519584N, 06W	0.00	0.00	0.14	0.00	0.58	0.02	0.50	0.02	0.78	0.07	2.64	0.13	0.72	0.06	0.58	0.00	0.79	0.00	0.50	0.00	0.12	0.09	7.75
6519584N, 000	0.00	0.00	0.20	0.02	0.53	0.02	0.11	0.01	0.64	0.05	1.50	0.01	0.51	0.04	0.36	0.00	0.51	0.00	0.20	0.11	0.09	0.09	5.01
6519584N, 5E	0.00	0.00	0.00	0.00	0.01	0.01	0.10	0.00	0.03	0.05	0.31	0.02	0.15	0.01	0.14	0.00	0.13	0.00	0.12	0.00	0.08	0.35	1.52
6519584N, 10E	0.00	0.00	0.16	0.00	0.52	0.01	0.75	0.00	0.43	0.04	1.52	0.16	0.37	0.01	0.30	0.11	0.21	0.00	0.26	0.09	0.06	0.28	5.28
6519584N, 15E	0.00	0.04	0.13	0.02	0.41	0.02	0.40	0.07	0.16	0.03	0.42	0.02	0.07	0.00	0.06	0.03	0.13	0.00	0.29	0.00	0.15	0.33	2.76
6519584N, 21E	0.00	0.00	0.00	0.00	0.04	0.00	0.14	0.00	0.07	0.00	0.42	0.02	0.20	0.02	0.09	0.10	0.20	0.62	0.41	0.01	0.17	0.37	2.88
6519584N, 30E	0.00	0.00	0.00	0.00	0.15	0.02	0.36	0.01	0.10	0.07	0.53	0.07	0.25	0.01	0.21	0.00	0.31	0.15	0.89	0.02	0.41	0.36	3.92
6519584N, 40E	0.00	0.02	0.00	0.00	0.11	0.11	0.28	0.00	0.09	0.05	0.65	0.12	0.10	0.00	0.18	0.31	0.22	0.00	0.51	0.00	0.14	0.40	3.30
6519584N, 60E	0.00	0.00	0.00	0.00	0.03	0.00	0.10	0.00	0.01	0.00	0.19	0.04	0.03	0.03	0.11	0.00	0.11	0.00	0.39	0.00	0.20	0.39	1.64
6519584N, 80E	0.00	0.00	0.00	0.00	0.02	0.00	0.04	0.00	0.00	0.00	0.11	0.02	0.01	0.01	0.09	0.00	0.08	0.64	0.82	0.00	0.13	0.48	2.45
6519584N, 100E	0.00	0.00	0.00	0.03	0.04	0.01	0.07	0.00	0.01	0.00	0.16	0.03	0.09	0.06	0.13	0.46	0.06	0.10	0.78	0.00	0.10	0.61	2.74
6519584N, 150E	0.00	0.00	0.00	0.00	0.03	0.00	0.09	0.00	0.00	0.00	0.18	0.04	0.02	0.00	0.09	0.00	0.08	0.00	0.33	0.00	0.13	0.34	1.32
6519584N, 200E	0.00	0.01	0.00	0.00	0.00	0.02	0.06	0.00	0.00	0.01	0.08	0.03	0.00	0.07	0.05	0.52	0.26	0.00	0.53	0.00	1.80	2.33	5.77

Table 4.3. Occluded hydrocarbon results obtained from soil samples collected above the N75 structure, Junction gold deposit. Arom = aromatic, Aliph = aliphatic.

Details of the gas chromatograph model and column were not supplied by Actlabs. However, other work completed by Actlabs for this project used a Varian gas chromatograph/mass spectrometer. Hydrocarbons detected were C_5-C_6 aliphatic to C_{16}-C_{17} aliphatic and C_7-C_8 aromatic to C_{17}-C_{18} aromatic. A complete record of the occluded hydrocarbons is presented in Table 4.3.

4.5 Results

4.5.1 Traverse 6518998

The portable O_2 - CO_2 analyser detected a strong CO_2 - O_2 anomaly above the area extending from the sub-outcropping quartz veining (point 10 west), to an area possibly representative of the oxidation front at depth, point 10 east (Figure 4.6). The gas peak occurs directly above a thinly buried portion of the mineralised shear zone between points 5 and 10 west.

The CO_2 peak occurs at point 5 west and has a strong antithetical relationship with O_2. The peak value for CO_2 is 2260 ppm, 2010 ppm above the atmospheric level of CO_2, and almost double that of the other CO_2 values measured along traverse 6518998. The corresponding value for O_2 is 20.8%, a depletion of approximately 0.3% from the atmospheric level.

Similar to the O_2 - CO_2 results, the passive samplers detected a light hydrocarbon gas anomaly that co-coincides with the O_2 - CO_2 anomaly. Geochemical cross sections plotted from the light hydrocarbon results (Figure 4.6), show that a significant rise in the levels of CH_4, C_2H_6, propane (C_3H_8) and a combined plot of CH_4 through to C_{10} are clearly present at point 10 west. Figure 4.6 shows that the C_3H_8 peak is double that of the CH_4 peak (252.7 ppm vs 114.7 ppm). However, this is possibly due to the sensitivity of the passive samplers to CH_4 (section 4.4.2.1) and not a true reflection of the CH_4 to propane ratios. Villenave (1997) highlights the fact that passive samplers are more sensitive to C_2^+ hydrocarbons than CH_4 and will out-compete CH_4 for adsorption sites if the concentration of C_2^+ hydrocarbons is high enough.

A wide, low amplitude CO_2-O_2 and light hydrocarbon anomaly is detectable between points 20 east and 50 east. This wide anomaly is not as strong as the peak anomaly at 5 and 10 west, thus it is not anticipated to be associated with mineralisation. Instead, two anastomosing porphyry bodies that intruded the Junction Gabbro near these points (Ellery and Watts, 1996) (see Figure 4.1) are the likely source of the weakly anomalous CO_2-O_2 and light hydrocarbons.

The occluded hydrocarbon survey over traverse 6518998 discloses very little about the underlying geology or mineralisation. Results are presented in Table 4.3. Close inspection of the results (Figure 4.7) shows that no single occluded hydrocarbon dominates. Further to this, a plot of individual occluded hydrocarbons against their relative sampling positions along the traverse, would result in erratic peak distributions across the entire traverse. An example of this erratic

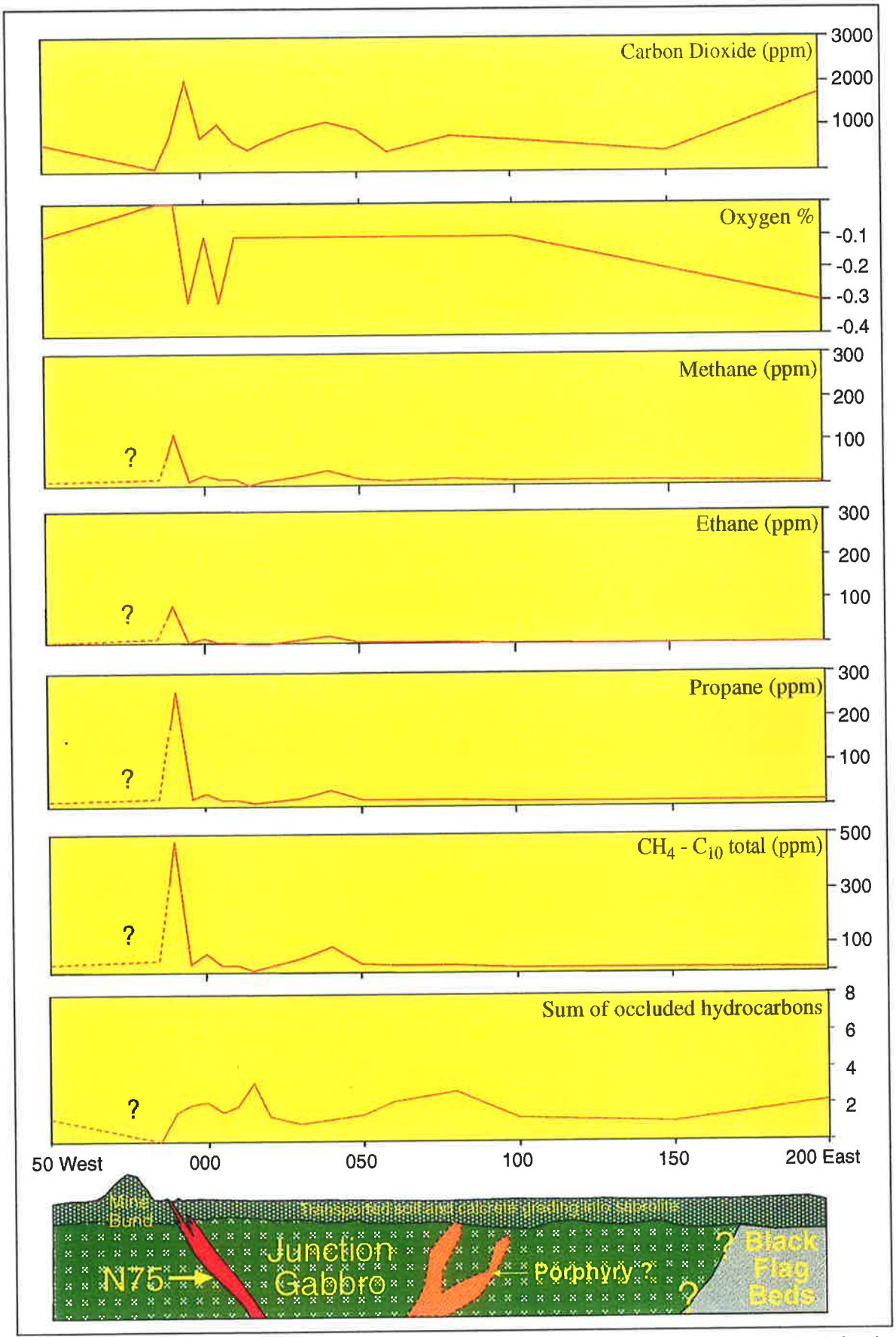


Figure 4.6. Soil-gas emission cross section along traverse 6518998. The geological cross section below is schematic for comparison to the soil-gas anomalies. It is not to scale. The geology is based on drill hole data, surface observations, aeromagnetic interpretation and soil-gas values.

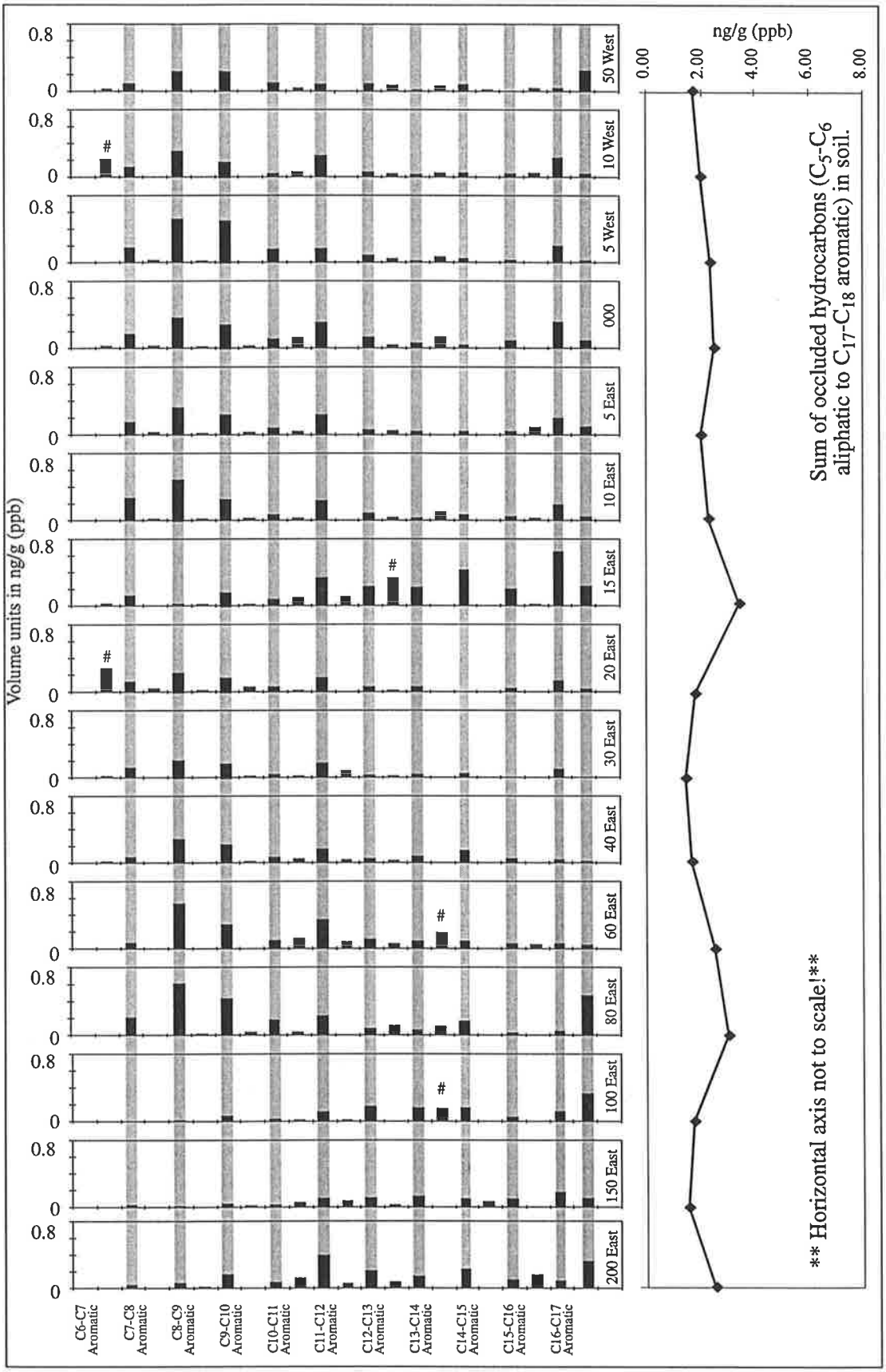


Figure 4.7. Occluded hydrocarbon profiles for each sample point along traverse 6518998 and corresponding geochemical cross section. Grey bars highlight the dominance of the aromatic hydrocarbons. Aliphatic hydrocarbons are not labelled, but are sequential between the labelled aromatic hydrocarbons. # = anomalous aliphatic volume.

peak distribution would be seen if the C_8-C_9 aromatic hydrocarbons from each sampling point were compared. Such a comparison shows that similar sized major peaks occur at 5 west, 10 east, 60 east and 80 east while minor, but again similar sized peaks occur at 10 west, 5 east and 40 east.

Plotting the combined total of all the occluded hydrocarbons at each sample point along the traverse does not greatly enhance the geochemical cross section, nor does it define a single anomalous peak (Figures 4.6 and 4.7). Instead, a combined plot of all the occluded hydrocarbons at each sample point shows low peaks occurring at point 15 east, 80 east and 200 east. Respectively, these peaks are approximately 20 m, 85 m and 205 m east of the CO_2-O_2 and light hydrocarbon anomalies detected between 5 and 10 west (Figures 4.6 and 4.7).

4.5.2 Traverse 6519584

The CO_2 - O_2 and light hydrocarbon survey response above traverse 6519584 shows a moderate, but reasonably defined gas anomaly directly above an area extending from point 10 east to an area possibly representative of the oxidation front at depth, point 30 east (Figure 4.8). None of the gas peaks occur above the area interpreted from aeromagnetic data to be the N75 surface. This is most likely due to marginal misplacement of the N75 surface caused by shear zone interpretation difficulties in the Black Flag Group metasediments (B Perrium, pers. comm., 1997), rather than a false soil-gas anomaly.

The portable O_2 - CO_2 analyser detected a more erratic and weaker CO_2 - O_2 response above traverse 6519584 than the relatively sharp anomaly observed above traverse 6518998. This is complicated by the fact that the Black Flag Group metasediments appear to produce a higher background response to that detected over the Junction Gabbro (traverse 6518998).

The CO_2 peak occurs at point 10 east and has a strong antithetical relationship with O_2. The peak value for CO_2 is 2840 ppm, 2560 ppm above the atmospheric level of CO_2, and approximately 800 ppm higher than the other CO_2 values measured along traverse 6519584. The corresponding value for O_2 is 20.7 %, a depletion of approximately 0.4% from the atmospheric level. A complete table of results is presented in Table 4.2.

Geochemical cross sections for light hydrocarbons, CH_4, C_2H_6, C_3H_8 and a combined plot of CH_4 through to C_{10}, are not so erratic and clearly show a significant rise in the levels of light hydrocarbons in soil at point 20 East (Figure 4.8). The light hydrocarbon values above traverse 6519854 are significantly smaller than the ones detected along line 6518998 (73.8 ppm CH_4 compared to 114.7 ppm CH_4, and 228.2 ppm C_1-C_{10} combined compared to 478.2 ppm C_1-C_{10} combined). However, similar to the light hydrocarbon values above traverse 6518998, the C_3H_8 peak is larger than that of the CH_4 peak (C_3H_8 = 98.7 ppm vs CH_4 = 70.4 ppm). Again, this is probably due to the adsorption properties of the passive samplers.

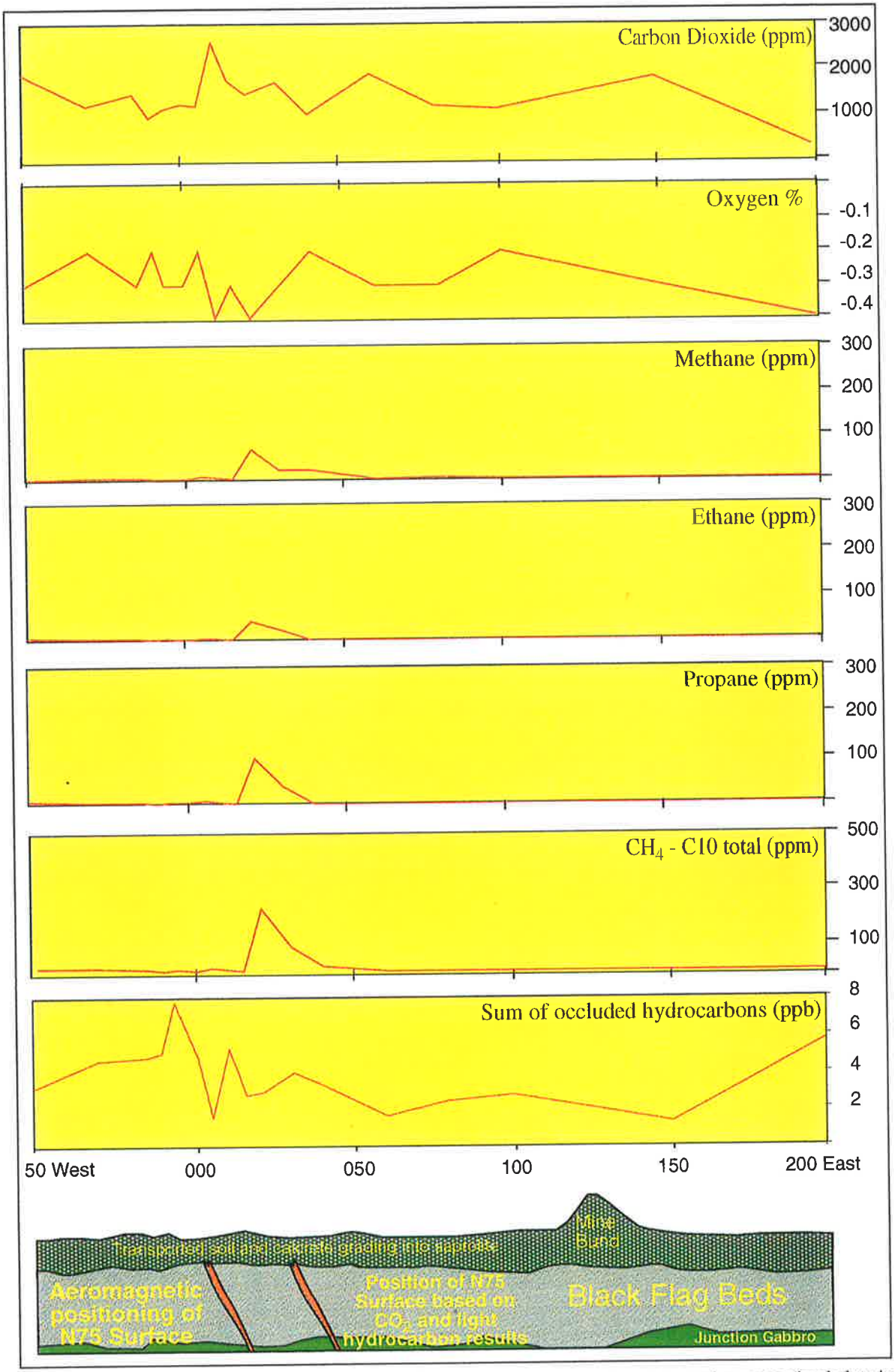


Figure 4.8. Soil-gas emission cross section along traverse 6519584. The geological cross section below is schematic for comparison to the soil-gas anomalies. It is not to scale. The geology is based on drill hole data, surface observations, aeromagnetic interpretation and soil-gas values. The depth to the Junction Gabbro is unknown, but is shown here for representation.

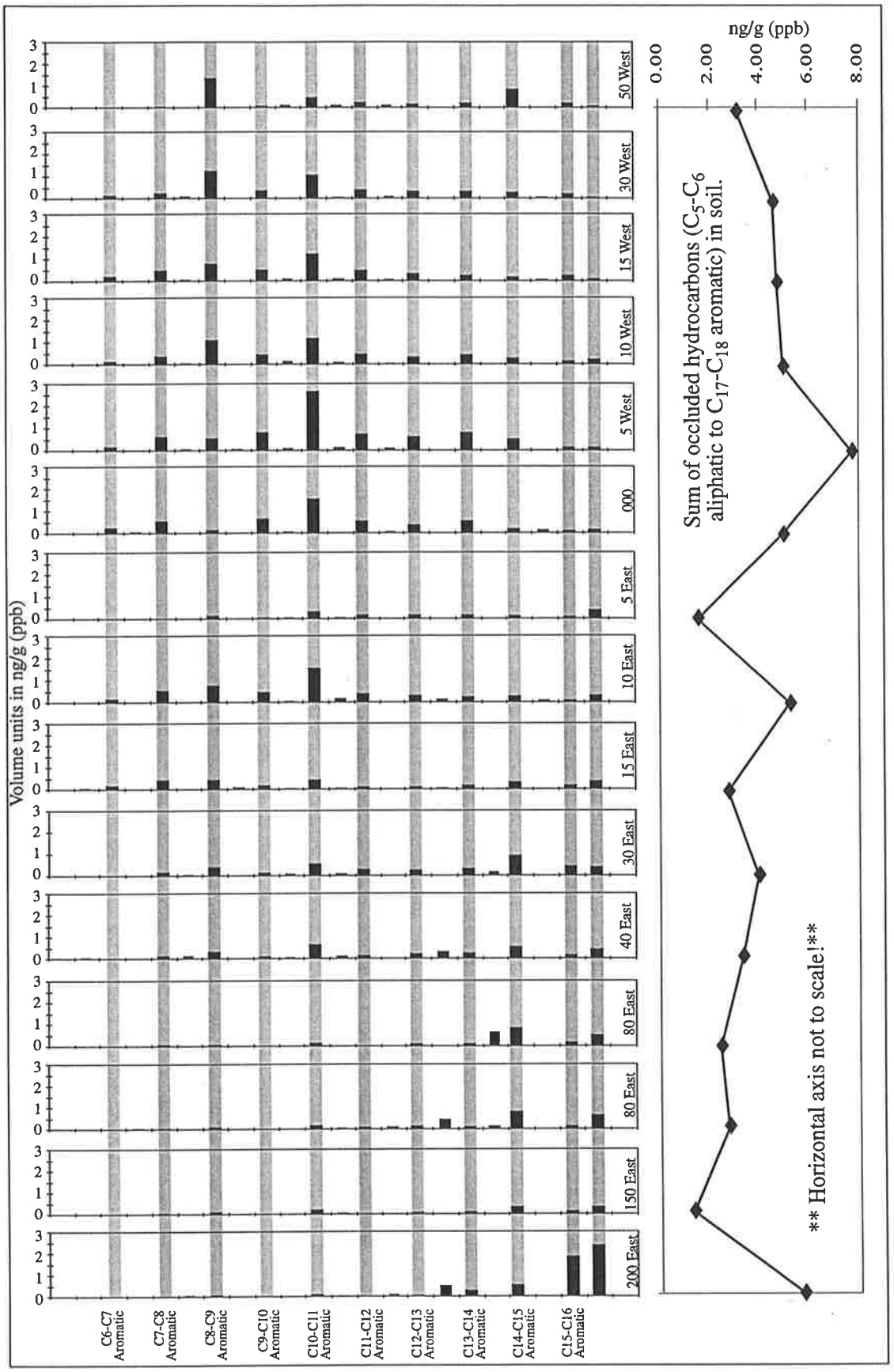


Figure 4.9. Occluded hydrocarbon profiles for each sample point along traverse 6519584 and corresponding geochemical cross section. Grey bars highlight the dominance of the aromatic hydrocarbons. Aliphatic hydrocarbons are not labelled, but are sequential between the labelled aromatic hydrocarbons.

The occluded hydrocarbon values detected above traverse 6519584 are erratic. Further to this, the background values detected above traverse 6519584 are at least double the background values detected above traverse 6518998 (Table 4.3). Owing to the erratic response and high back ground values, it could be argued that the occluded hydrocarbon anomaly spans from points 10 west to 60 east. However, plotting the combined total of all the occluded hydrocarbons at each sample point along the traverse reveals a single, clearly defined peak occurring at 5 west (Figures 4.8 and 4.9). This peak is a lone anomaly occurring 15 metres west of the CO_2-O_2 peak and 25 metres west of the light hydrocarbon peak.

4.6 Discussion

4.6.1 Traverse 6518998

One of the most important observations concerning the soil gas anomaly detected above the N75 surface is that the N75 surface is generally ≤ 3 metres wide (as indicated by drill hole logs). This is significantly less in terms of width than would be required to be considered economic. However, it is not too narrow to escape the detection of soil gas geochemistry with sampling points spaced at 5 m intervals. This suggests that the method has potential as a tool in exploration.

The detection of CO_2-O_2 and light hydrocarbon anomalies that extend from 10 west to 5 east is encouraging because they directly overlap the sub-outcropping quartz veins that occur at 8 west, (believed to be an expression of the N75 at the surface) and point 000, the position interpreted to be the N75 surface at depth. That the light hydrocarbon peaks are at point 10 west, 5 m west of the CO_2 - O_2 peaks, requires no explanation, given that the sub-outcropping quartz rubble occurs at 8 west, between the two sampling points.

The CO_2 and light hydrocarbon anomalies show a distinct waning towards the east of the main peak. This phenomenon is not unexpected in soil gas surveys above oxidising ore bodies hosted in shear zones. The waning anomaly probably reflects the fact that the oxidation front is at depth and to the east of the gas peak. It is anticipated that some of the gases generated at the oxidation front will migrate vertically from their origin to the surface. However, it appears that the majority of gas preferentially travels diagonally along steeply-dipping microfractures associated with the weathered shear zone, eventually exhausting into the atmosphere near the area where the N75 surface sub-outcrops (Figure 4.10).

The source of the wide, weakly anomalous CO_2 - O_2 and light hydrocarbon anomaly that is detectable between points 20 east and 50 east is unknown. Aeromagnetic interpretation and underground drilling, indicates that two anastomosing porphyry bodies have intruded the Junction Gabbro near these points (Ellery and Watts, 1996) (see Figure 4.1) and calcite is known to be a minor component within altered porphyries (Murphy, 1995). Calcite releases CO_2 and consumes O_2 upon dissolution (section 4.6.4). However, the source of the weakly-anomalous light

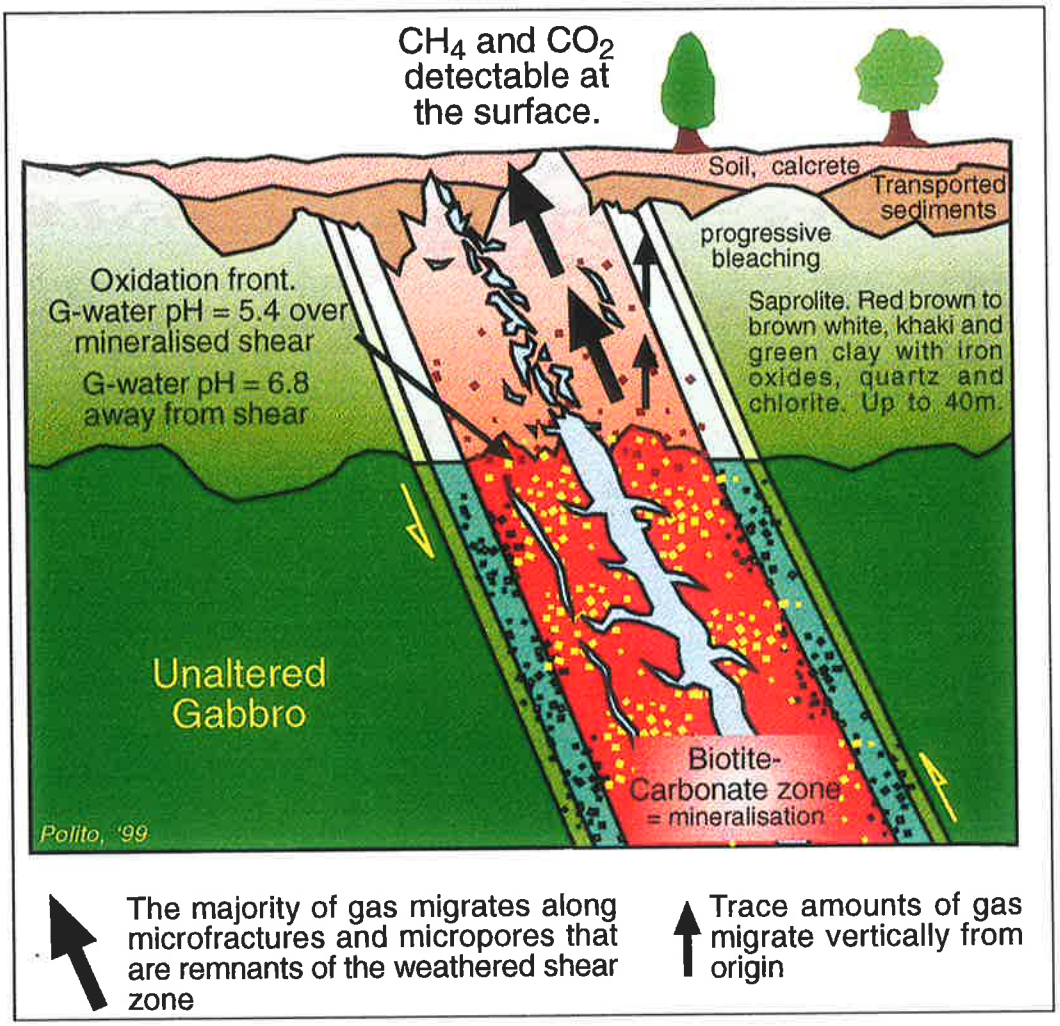


Figure 4.10. Schematic model showing the preferred pathway of evolved gas originating from the oxidation front of a mineralised shear zone containing sulphides and carbonate. Note the typical over burden that the migrating gases pass through, including saprolitic clays, transported sediments, calcrete and soil.

hydrocarbons can only be speculated. Importantly, no soil contamination was visibly observed or detected by the occluded hydrocarbon survey and no change in soil type is apparent near this anomaly. Therefore the low amplitude anomaly does not appear to be related to soil contamination by previous exploration activity and remains enigmatic.

A sharp rise in CO_2 and a corresponding depletion in O_2 occurs at point 200 East. It is interesting to note that the CO_2 value at this point approaches the peak value for CO_2 above the mineralised N75 surface (Figure 4.6). No change in soil type was observed. However, a gradational change in vegetation from black-butt to salmon gum eucalyptus trees was observed. The tall salmon gum, distinguished by its shiny, light pink coloured bark, is indicative of underlying metasediments and granitoids (Beard, 1979). It contrasts with the rough, dark brown - black coloured bark of the black-butt, which is commonly well developed on mafic and ultramafic rocks (Beard, 1979).

Aeromagnetic interpretation indicates that point 200 east lies above zone four of the Junction Gabbro. However, the occurrence of the salmon gums indicates that a thin veneer of Black Flag Group metasediments may overlie the gabbro at this point. This cannot be verified by drill hole logs, because no drill holes (testing deep mineralisation of the N25 surface) have been drilled this far east (as of late 1997). However, it is noteworthy that the other traverse, 6519584 has a higher background value than traverse 6518998, possibly because of the underlying Black Flag Group metasediments.

Significantly, there is no corresponding light hydrocarbon anomaly coinciding with the sharp rise in CO_2 and a corresponding depletion in O_2 at point 200 east. This suggests that the CO_2 anomaly is not related to the same style of mineralisation to that hosted in the N75 surface. Instead, a weak relationship between the CO_2 anomaly and the sum total of the occluded hydrocarbons exists at point 200 east, and indicates that the CO_2 anomaly could be related to bacterial degradation of hydrocarbon contamination in the soil. However, the sum total of the occluded hydrocarbons at 200 east is 2.15 ppb, whereas the peak values for the occluded hydrocarbons at points 15 east and 80 east are 3.18 and 2.73 ppb respectively and neither of these sample points co-coincides with a CO_2 anomaly.

The interpretation of the CO_2 anomaly at point 200 east is a speculative assessment of the results. The lack of light hydrocarbons, especially CH_4, indicates that the anomaly at this point is not related to and can be distinguished from the anomaly above the N75 surface. Further to this, the lack of CH_4 at 200 east suggests that if bacteria are present in the soil around Junction, they appear to be aerobic and not anaerobic micro-organisms, thus producing CO_2, from any extraneous hydrocarbon and not CH_4. This observation is important and is discussed further with regard to methanogenic generation of light hydrocarbons in anaerobic soils (section 4.6.5).

It is difficult to know if there is any relationship between the occluded hydrocarbon peaks and mineralisation at depth because the occluded hydrocarbon peaks do not coincide with the light hydrocarbon or the CO_2-O_2 anomalies. Further to this it is not possible to determine the origin of the occluded hydrocarbons along this traverse, because only compound masses were calculated by Actlabs, and no specific aromatic or aliphatic hydrocarbon has been identified (there are between three and five common compounds that have masses that fit into each of the classes $C_{11\text{-}12}$ to $C_{17\text{-}18}$ aromatic; D. McKirdy pers. comm., 1999). Interpretation of the occluded hydrocarbon survey is further complicated by the fact that no single mass compound is anomalous in every profile.

4.6.2 Traverse 6519584

Interpretation of traverse 6519584 is complicated by the higher background values for CO_2 and occluded hydrocarbons compared to the background values that were detected over the Junction Gabbro (traverse 6518998). Indeed, the outline of the CO_2-O_2 anomaly is better defined by the

depletion of O_2 between 10 east and 30 east rather than the increase of CO_2 which fluctuates across the entire traverse.

The detection of co-incident CO_2-O_2 and light hydrocarbon anomalies is once again encouraging. That the light hydrocarbon peaks are 10 m east of the CO_2 - O_2 peak is insignificant, given that the CO_2-O_2 anomaly encompasses a 25 m long section of the traverse that incorporates the area of the light hydrocarbon anomaly. The major concern for this traverse is that the CO_2-O_2 and light hydrocarbon anomalies do not directly overlie the interpreted position of the N75 surface. However, the fact that the exact position of the N75 surface below the soil cover is enigmatic (section 4.5.2), this small discrepancy is insignificant.

Similar to traverse 6518998, the light hydrocarbon anomalies show a distinct waning towards the east of the main peak. Again, the waning anomaly probably reflects the fact that the oxidation front is at depth and to the east of the gas peak (see Figure 4.10). The light hydrocarbon values above traverse 6519854 are significantly smaller than the ones detected above traverse 6518998 (73.8 ppm CH_4 compared to 114.7 ppm CH_4, and 228.2 ppm C_1-C_{10} combined compared to 478.2 ppm C_1-C_{10} combined). This may be highlighting the fact that the mineralisation below traverse 6519584 is deeper than the mineralisation below traverse 6518998. On the other hand, it may be that mineralisation, hence alteration, is less developed below traverse 6519584. These hypotheses cannot be verified due to the lack of geological data below 6519584.

The occluded hydrocarbon survey is again difficult to interpret because the anomaly, although defined by a single peak at 5 west, spans across 70 m of the traverse from 10 west to 60 east. Further to this, close inspection of Figure 4.9 reveals that the peak at 5 west, and indeed, most of the elevated values detected above traverse 6519584 appear to be determined by the concentration of C_{11}-C_{12} in the sample. This contrasts with traverse 6518998 where no single occluded hydrocarbon dominated the sampling set. Nor does any single mass compound stand out in every profile. This observation is disputable on the basis that other hydrocarbons (e.g. C_9-C_{10} aromatics and C_{15}-C_{16} aromatics) dominate over the C_{11}-C_{12} aromatics at other sample points. Again, it is difficult to know if there is any relationship between the occluded hydrocarbon peak and mineralisation at depth because the occluded hydrocarbon peak does not coincide with the light hydrocarbon peak or the CO_2 - O_2 anomaly.

The occluded hydrocarbon profiles across both traverses are largely dominated by aromatic hydrocarbons with few exceptions (highlighted by grey tinting in Figures 4.7 and 4.9). This is an unusual geochemical response for heavier hydrocarbons typically associated with light oils and petroleum. The dominance of the aromatic hydrocarbons over the aliphatic hydrocarbons is enigmatic. However, it is unlikely that the dominance by aromatic hydrocarbons is a primary signature. Instead, the dominance of the aromatic hydrocarbons in the soil above Junction is probably an artefact of microbial activity in the soil, as it is a well known fact that micro-

organisms that are able to metabolise higher molecular-sized hydrocarbons, metabolise aliphatic hydrocarbons (straight or branched open-chain hydrocarbons) faster than they do aromatic hydrocarbons (monocyclic or polycyclic hydrocarbon; D. McKirdy, pers. comm., 1999). Indeed, microbiological degradation of aromatic hydrocarbons in the natural environment firstly involves transformation of the monocyclic and polycyclic hydrocarbons into aliphatic hydrocarbons and acetate prior to further degradation by other micro-organisms to CO_2 or CH_4 (in anaerobic environments) (Grbic-Galic, 1990).

4.6.3 Gas migration through the crust from its source

A full discussion of gas migration in the upper crust is not in the scope of this project. However, it is necessary to recognise some of the accepted principles and mechanisms behind gas migration from its source to the earth's surface.

It is well established in the petroleum industry that hydrocarbons migrate out of the source rock and into either structural traps or to the earth's surface (Fullagar, 1989). Once trapped, petroleum reservoirs still leak hydrocarbons to the surface through the well-documented processes of hydrocarbon macroseepage (bulk liquid hydrocarbon flow to the surface) and microseepage (light gas [<C6] ascension to the surface; MacElvain, 1969; Horvitz, 1981; Stahl *et al.*, 1981; Jones and Drozd, 1983; Jones, 1984; Horvitz, 1985; Price, 1986; Fullagar, 1989; Heggie, 1989). Therefore, it is reasonable to assume that CO_2 and light hydrocarbons associated with mineralisation also migrate to the surface through microseepagein a similar manner, despite their lower abundance in ore deposits relative to petroleum accumulations.

The detection of predominantly low molecular weight gases in soils above ore deposits is mostly attributed to microseepage (MacElvain, 1969; Price, 1986; Fullagar, 1989). Leythaeuser *et al.*, (1982, 1983), McCarthy and Reimer (1986) and Amundson and Davidson (1990) report that soil gases are detectable at the surface because gases migrate from their origin by diffusion and mass transport. However, Price (1986) dismisses the role of diffusion and mass transport based on observations above petroleum reservoirs. He argues that diffusion of light hydrocarbons through the overlying rocks and soil is too slow for the light hydrocarbons to avoid metabolic degradation by bacteria during their ascent. This notion is supported by Banks and Ghahremani (1987), who found that for ^{222}Rn to be detectable at the surface (half life of 3.82 days), it must migrate rapidly from its source at depth by advective transport, not diffusion. Further to this, diffusion of gases from the source would be spherically dispersive, resulting in a broad, low amplitude anomaly. Soil-gas above structurally-controlled ore deposits anomalies are generally sharp, and confined to a narrow area directly above the mineralised surface (Amanor, 1979; McCarthy and Reimer, 1986; McCarthy *et al.*, 1986; Ball *et al.*, 1990). This suggests that diffusion does not play a major role in soil-gas migration above sulphide mineralisation.

Mass transport (or effusion), contrary to diffusion, would result in surface anomalies with

hydrocarbon concentrations several orders of magnitude higher than those typically observed, with significant concentrations of C_6^+ hydrocarbons at the surface (Price, 1986). It is arguable that few mineral deposits have hydrocarbon species greater than C_6, thus mass transport of gases from a mineral deposit to the soil atmosphere cannot not be dismissed (cf. McCarthy and Reimer, 1986; Amundson and Davidson, 1990). However, as already stated, the principles of hydrocarbon migration above petroleum reservoirs are well known (MacElvain, 1969; Leythaeuser *et al.*, 1982, 1983; Price, 1986; Banks and Ghahremani, 1987; Fullagar, 1989) and should be broadly applicable to gas migration above ore deposits.

MacElvain (1969) and Price (1986) recommend that the ascent of colloidal-sized micro-bubbles through microfractures is a process of Brownian motion. This is because "the small gas bubbles are readily displaced upward by the surrounding moisture at rates up to several millimetres per second, regardless of any sedimentary particles that may intrude the way of their zigzag Brownian path. Such exceedingly small bubbles can quickly ascend hundreds and even thousands of feet (sic) in a manner not available to larger gas bubbles" (MacElvain, 1969). Therefore, fluid pathways for gas migration are presumed to be microfractures (Fullagar, 1989).

4.6.4 Origin of the carbon dioxide and oxygen

Carbon dioxide and oxygen anomalies occur above a variety of different ore deposit styles and are commonly reported (eg., porphyry copper - Hinkle and Dilbert, 1984; Hinkle *et al.*, 1990; Massive Cu-Zn sulphide - McCarthy *et al.*, 1986; late-orogenic, structurally controlled gold - Ball *et al.*, 1990; sediment hosted disseminated gold deposits - Clifton, 1995; sedimentary uranium - Reid and Rasmussen, 1990). The production of CO_2 is generally coeval with the consumption of oxygen, regardless of the processes involved. Therefore, the two gases are discussed together. The strong antithetical relationship of these two gases in the soil atmosphere is reasonably well understood.

4.6.4.1 Origin of the carbon dioxide and oxygen above sulphides

CO_2 above sulphidic ore deposits is attributed to the oxidation of the sulphide minerals by groundwater to form sulphuric acid. The acid subsequently reacts with carbonate minerals to release CO_2 and consume O_2 (Lovell *et al.*, 1983; Hinkle and Dilbert, 1984; Stedman *et al.*, 1984; Peachy *et al.*, 1985; McCarthy *et al.*, 1986; Hinkle *et al.*, 1990). The general reaction for the oxidation of pyrite is as follows (Equation 4.1) (Hinkle *et al.*, 1990):

$$4FeS_2 + 15O_2 + 8H_2O \longrightarrow 2Fe_2O_3 + 8\ H_2SO_4 \qquad \text{(Equation 4.1)}$$

Thus O_2 is consumed during the formation of Fe-oxides and sulphuric acid. The sulphuric acid formed in this reaction attacks carbonate material associated with the ore body and produces CO_2 (Equation 4.2):

$$H^+ + CO_3^{2-} \longrightarrow CO_2 + H_2O \qquad \text{(Equation 4.2)}$$

Investigations by Stedman *et al.* (1984) and Hinkle *et al.* (1990) found that pyrite and other sulphide minerals produce sulphur gases and sulphuric acid in an essentially oxidation reaction that cannot proceed in the absence of air or oxygenated ground water. In general, these authors found that the oxygen content at the oxidation front is often more important than the metallic element content or the sulphide mineral content of the ore body. Stedman *et al.* (1984) and Hinkle *et al.* (1990) conclude that the absence of a CO_2 - O_2 anomaly does not preclude the presence of sulphides, but rather the absence of oxidising sulphides or the absence of adequate pathways for the CO_2 to reach the surface.

The CO_2 - O_2 anomaly above the N75 surface suggests that the sulphidic mineralisation at depth is oxidising and producing CO_2 whilst consuming O_2. Water geochemistry directly above mineralisation at Junction (Table 4.1), indicates that sulphide oxidation is indeed occurring. The lower pH values and higher SO_4 concentrations in the groundwater above the Junction deposit compared to the near neutral pH values and lower SO_4 concentrations in the groundwater from regional bores indicate the presence of oxidising sulphides. Therefore it can be assumed that the CO_2 is originating from dissolving carbonate associated with the alteration zone.

4.6.4.2 Bacterial Production

The production of CO_2 can occur in other ways besides the oxidation of sulphides, and these need to be considered when interpreting soil gas data. Decaying organic matter, oxidising hydrocarbons and root respiration all produce CO_2 at the expense of oxygen (McCarthy and Reimer, 1986; Sleat *et al.*, 1988; Alpers *et al.*, 1990; Amundson and Davidson, 1990; Ball *et al.*, 1990). Plant respiration through roots is a major source of CO_2 production in soils that are covered by a moderately to densely vegetated setting (Deines, 1980; Buyanovsky and Wagner, 1983; Alpers *et al.*, 1990, Amundson and Davidson, 1990). Alpers *et al.* (1990) report that seasonal variations in soil CO_2 concentration can be a result of seasonal variations in photosynthetic activity. Therefore the source of anomalous CO_2 and corresponding O_2 depletion in carbonate-poor soils and rocks can be the result of microbial metabolism of simple organic compounds present in the soil.

One major problem concerning the source of CO_2 is that it is difficult to separate CO_2 sourced from weathering rock processes from CO_2 sourced from root respiration and organic decay (Alpers *et al.* 1990; Amundson and Davidson, 1990). Indeed, Alpers *et al.* (1990) report that root respiration and decaying plant material produce greater CO_2 variations in the soil than oxidising sulphidic mineralisation. These authors base their conclusions on observations made over the same Cu-Zn sulphide ore body at which McCarthy *et al.* (1986) found a clear CO_2 - O_2 anomaly. Alpers *et al.* (1990) did not detect a similar CO_2 - O_2 anomaly. However, they concede that their data is complicated by the effects of rainfall, which appears to have significantly affected the magnitude of the CO_2 anomaly.

McCarthy and Reimer (1986) insist that there is no evidence to suggest that the biological production of CO_2 would be any different in homogeneous soils whether it occurred over the massive Cu-Zn sulphide deposit or beyond it, i.e., it would be laterally homogeneous. Thus, oxidising sulphides and subsequent carbonate dissolution should produce a gas anomaly that is greater than the gas volumes produced by biological activity, because it is an add-on to a relatively widespread homogeneous anomaly.

Fridman (1990) reports that increased concentrations of CO_2 and smaller than usual amounts of O_2 in the soil air probably represent sulphide ores at depth, not local variations in microbiological activity, especially if sulphur gases COS, and/or CS_2 can be detected. This is supported by Sleat *et al.* (1988) who state that microbiological activity in the subsurface is largely controlled by the flux of nutrients (e.g. hydrocarbons and CO_2) into the soil. Therefore, it can be concluded that microbiological activity is not random in a geologically homogeneous environment. Microbiological activity diminishes and the soil gas levels in the area return to background concentrations, if a consistent concentration of nutrients (either CO_2, hydrocarbons or organic matter) is not supplied to the soil. Likely sources for the continuous supply of nutrients (in the form of hydrocarbons and CO_2) may arise from mantle degassing or hydrothermal activity in the deep crust below active fault zones (Fridman, 1990), or oxidising sulphide ore bodies (Lovell *et al.*, 1983; Hinkle and Dilbert, 1984; Stedman *et al.*, 1984; Peachy *et al.*, 1985; McCarthy *et al.*, 1986; Fridman, 1990; Hinkle *et al.*, 1990). Mantle degassing and hydrothermal activity in the Junction area can be dismissed as a realistic nutrient sources.

4.6.4.3 Temperature and moisture levels

Concentrations and fluxes of CO_2 in soils are dependent on soil temperature (Amundson and Davidson, 1990). Studies of the temperature effect on CO_2 production and flux in soils have shown that the fluxing rates increases between 1.5 and 3.0 times for every 10°C increase in temperature between 0° and 50°C (Drobnik, 1962; Whitkamp, 1969, Amundson and Davidson, 1990). Therefore, seasonal, as well as diurnal, temperature changes have been found to strongly affect CO_2 production rates and concentrations in soils (Amundson and Smith, 1988; Amundson *et al.,* 1989). Temperature variations during gas sampling across traverse 6518998 were minimal (range 21.7° to 28.3°C, Table 4.2). Temperature variation across traverse 6519584 were slightly more erratic (range = 10.6° to 24.4°C), due to most of the samples being collected late in the evening and first thing the next morning. However, there does not appear to be any major problems associated with this temperature variation. Therefore, CO_2 - O_2 fluxing in the soil sampled along traverses 6518998 and 6519584 is unlikely to have affected the CO_2 variations noted during the active soil gas survey.

Moisture levels in the soil also effect CO_2 production rates. In dry soils, CO_2 production rates decrease as biological processes are reduced and gaseous exchange occurs readily, resulting in anomalous O_2 and CO_2 responses being diminished (Alexander, 1977; Amundson and Davidson,

1990). Conversely, in wet to saturated soils, gaseous exchange to the atmosphere is completely stopped whilst biological or inorganic processes occur. Saturated soil consumes O_2 and produces CO_2, and so can thereby produce false anomalies. Lower amplitude anomalies or failure to repeat anomalies can also occur immediately after rainfall due to the dissolution of CO_2 (McCarthy *et al.*, 1986; Solomon and Cerling, 1987). Watmuff and Morris (1993) suggest that sampling may be best delayed at least until all free draining water has gone from the soil. Therefore, soil water contents between the permanent wilting point and 60 - 80% saturation are considered ideal for producing consistent soil-gas responses (Alexander, 1977).

Light precipitation did occur at Junction in the week leading up to the soil gas survey. However, the majority of the soil sampled, was not saturated, and was at most, slightly moist. The relatively dry soil at Junction can be explained by the weather patterns recorded for the district (Chapter 1.5.2; Clarke, 1994b). It is not known whether this precipitation had any effect on the rest of the samples from both traverses. If the findings of McCarthy *et al.* (1986) and Solomon and Cerling (1987) are correct for soil gas surveys, it is possible that the anomalies detected at Junction are lower and less defined than those normally present above the N75 surface. However, the soil gas results may not be diminished below normal values. Lovell *et al.* (1983) and Ball *et al.* (1990) report that CO_2 concentrations are generally very much lower in arid areas than in wetter and/or temperate areas, and that consequently anomaly definition increases with increasing aridity.

Point 200 east along traverse 6518998 did have "above average" soil moisture which appears to have resulted in a false CO_2 - O_2 anomaly. The effects of this moisture have been discussed above in section 4.6.1.

4.6.5 Origin of hydrocarbons above mineralisation

Methane and other light hydrocarbons are commonly found above many ore deposits hosted by sedimentary, metamorphic and igneous host rocks (e.g. Mississippi-valley type (MVT) Pb-Zn [Carter and Cazalet, 1984, 1988; Ferguson, 1987, 1988; Mulshaw, 1996], sediment hosted gold [Kesler *et al.*, 1990], late-orogenic, structurally controlled gold [Amanor, 1979], massive Cu-Zn sulphides [McCarthy *et al.*, 1986], and porphyry copper [McCarthy and Reimer, 1986]). However, unlike the well documented origin of CO_2 in the soil atmosphere, CH_4 and other light hydrocarbons occurring above ore deposits (ethane [C_2] to pentane [C_5]) have been theoretically attributed to bacteriological metabolism (Rosaire, 1938; McCarthy and Reimer, 1986; Abraham *et al.*, 1989), and thermal maturation of kerogen during wall rock interaction with the hydrothermal fluid (Douglas *et al.*, 1970; Carter and Cazalet, 1984, 1988; Ferguson, 1987; Kesler *et al.*, 1990) and then, mainly, cursorily dismissed.

Yet hydrocarbons are commonly recorded in carbonate hosted Pb-Zn ± Cu (MVT) deposits (Barton, 1967; McQueen and Powell, 1983; Carter and Cazalet, 1984, 1988; Roedder, 1984;

Giordano, 1985; Ferguson, 1987, 1988; Gize and Barnes, 1987; Etminan and Hoffmann, 1989 and others). They are also known to occur in many other deposit styles, including shale hosted copper deposits (Kelly and Nishioka, 1985; Ho and Mauk, 1996; Landais and Gize, 1997), Carlin-type disseminated gold deposits (Ilchick *et al.*, 1986; Kesler, 1990), Archaean Witwatersrand gold-uranium deposits (Parnell, 1996) and sediment hosted and unconformity type uranium deposits (Hoeve and Sibbald, 1978; Landais *et al.*, 1984; Wenrich, 1985; Landais, 1986; Foster *et al.*, 1990; Landais and Gize, 1997).

The organic matter in these deposits could have played an active or passive role during ore genesis, but, either way, it often results in hydrocarbon accumulation in or around the ore body. Douglas *et al.* (1970), Carter and Cazalet (1984), Goodman (1987), Ferguson (1987) and Kesler *et al.* (1990) report that organic matter may simply undergo in situ thermal maturation during interaction with the hydrothermal fluids. This results in the accumulation or dissipation of organic matter within or around the ore body depending on the nature of the mineralisation and the temperature of formation. Alternatively, Giordano (1985) and Seward and Barnes (1997) report that organometallic complexing is a realistic mechanism for transporting metals to the site of mineralisation. Additionally, Nakashima *et al.* (1984) and Disnar and Sureau (1990) announce that organic matter is an efficient reducing agent for metals and oxidised sulphur species in solution, acting as a trap for migrating metals.

Mineralisation at Junction is clearly not associated with any visible hydrocarbons that were either transported to the site of mineralisation as organic ligands or catagenicaly generated as a result of hydrothermal interaction between the mineralising fluid and the host gabbro. Indeed, efforts to locate traces of graphite that may be indicative of mature hydrocarbons were unsuccessful. The detection of occluded aromatic hydrocarbons in soil samples is interesting and worthy of further investigation. However, the origin of the aromatic hydrocarbons cannot be determined from the mass weights determined by gas chromatography alone, and their presence remains enigmatic.

In many igneous and metamorphic hosted mineral deposits, the presence of a CH_4 soil-gas anomaly is usually accounted for by microbiological activity in the soil under anoxic conditions (McCarthy and Reimer, 1986; Abraham *et al.*, 1989). Therefore, microbial activity is a possible source of the CH_4 in soils above ore deposits. However, methanogenic bacteria are strictly anaerobic organisms. They only occupy anoxic niches in fresh water, soils, aquifers, marine sediments, marshes, swamps and gastrointestinal tracts of animals and insects (Grbic-Galic, 1990; Barns and Nierzwicki-Bauer, 1997). The detection of light hydrocarbons at 50 cm to 100 cm depth in relatively dry, termite-free soil at Junction suggests that the CH_4 did not originate from neither marine sediments, marshes, swamps nor the gastrointestinal tracts of animals and insects.

Methanogenic bacteria use simple organic and inorganic carbon compounds as energy sources, converting them stoichiometrically to CH_4. These carbon sources include CO_2, formate, acetate, di- and tri-methylamine, dimethylsulphide and several alcohols (Madigan *et al.*, 1997; Barns and Nierzwicki-Bauer, 1997). Most methanogenic genera gain energy from the metabolism of CO_2, using H_2 as an electron donor. However, all metabolic reactions can only involve C_1 or C_2 compounds (Whitman *et al.*, 1991). Therefore, due to their requirements for H_2 and a limited number of carbon compounds for growth, methanogens depend on the activities of other organisms to produce these species from complex organic matter (Barns and Nierzwicki-Bauer, 1997).

Methanogens are extreme anaerobes and many are killed quickly by exposure to O_2 (Oremland, 1988). In addition, several methanogens require reduced sulphur for growth and are unable to use oxidised sulfur (Whitman *et al.*, 1991). However, in anaerobic environments suitable for methanogenic metabolism, sulphate reducing bacteria successfully out-compete methanogens for common substrates, such as acetate and H_2 (Oremland and Taylor, 1978). It has been shown that the catabolic enzymes of sulphate-reducing bacteria have higher affinities for acetate and H_2 than methanogenic enzymes (Schonheit *et al.*, 1982; Grbic-Galic, 1990). Therefore, methanogenesis will only occur after most of the sulphate has been used up and the sulphate reducing bacteria population diminishes (Oremland, 1988).

It is unlikely that the light hydrocarbon anomaly above the N75 surface is generated by methanogenic bacteria. Limited geochemical evidence suggests that the ground water aquifer above the Junction deposit is too acidic and aerobic for methanogenic habitation. Oremland, (1988) reports that the presence of free O_2 in ground water aquifers is lethal and Grbic-Galic (1990) found that low pH levels, similar to those measured above the Junction deposit, suppress methanogenic activity. It is likely that any bacteria present at the oxidation front are probably related to one of the sulphide oxidising bacteria such as *Thiobacillus* sp. (Nordstrom and Southam, 1997).

Similarly, the lack of CH_4 or any light hydrocarbons along either traverse apart from above the N75 structure indicates that only aerobic bacteria are present in the near surface soil. This is highlighted at point 200 east along traverse 6518998 where a CO_2 anomaly coincides with an occluded hydrocarbon anomaly (see section 4.6.1). While it is probable that the CO_2 anomaly at this point is related to the unconfirmed presence of the Black Flag Group metasediments, the coincidence of the CO_2 and occluded hydrocarbon anomaly cannot be over-looked. Recent investigations by Grbic-Galic (1990) found that methanogenic bacteria can transform aromatic hydrocarbons to CH_4 and CO_2 in anaerobic environments with the help of other anaerobes. However, the lack of any CH_4 at point 200 east along traverse 6518998 clearly indicates that methanogenic bacteria are not present in the near surface soils or are severely suppressed by the aerobic conditions.

Finally, the presence of higher hydrocarbons (>C_2^+) in soil gas above ore deposits cannot be explained by the presence of methanogenic bacteria in the soil, because C_2^+ hydrocarbons are not ordinarily produced by bacteria. Despite the discovery that certain methanogenic bacteria in anoxic intertidal sediments do form traces of ethane (Oremland, 1981), Oremland *et al.* (1988), reported that trace levels of ethane (C_2H_6) are best produced in anoxic sediment slurries under laboratory conditions where C_2H_6 formation can be stimulated by adding ethanethiol and diethylsulphide to the slurries. It is unlikely that the soil conditions or the compounds needed to form C_2H_6 in the natural environment are present at Junction, and the occurrence of this process can be discounted.

No researchers confidently report that light hydrocarbons trapped in fluid inclusions could be a viable source of the hydrocarbon-soil gas anomalies above igneous or metamorphic host rocks. This is not surprising given that many researchers report that CH_4 and other light hydrocarbon abundances in fluid inclusions are generally less than 1% of the total volatile content in fluid inclusions (Roedder, 1984; Bray *et al.*, 1991; Mernagh and Witt, 1994; Graney and Kesler, 1995; Mernagh, 1996). However, fluid inclusions hosted by gangue minerals that are weathering at the oxidation front are the most likely source of light hydrocarbons in the soil atmosphere above igneous and metamorphic rocks that have no obvious sedimentary associations. CH_4 and trace concentrations of other light hydrocarbons have been reported in fluid inclusions hosted by gangue minerals in many hydrothermal ore deposits, including late-orogenic, structurally-controlled gold deposits occurring in metamorphosed igneous lithologies (Roedder, 1984; Smith and Kesler, 1985; Shepherd *et al.*, 1985; Robert and Kelly, 1987; Clark *et al.*, 1989; Ho *et al.*, and references within, 1990; Bray *et al.*, 1991; Guha *et al.*, 1991; Letnikov and Narseev, 1991; de Ronde *et al.*, 1992; Cassidy and Bennett, 1993; Mernagh and Witt, 1994; Graney and Kesler, 1995; Robert *et al.*, 1995; Mernagh, 1996; Boullier *et al.*, 1998). As stated in section 4.4.2, only small quantities of these gases need to be present in the soil to be detected by passive samplers. Therefore, light hydrocarbons released from fluid inclusions associated with mineralisation during the weathering process should be detectable and define the limits of the alteration associated with that mineralisation.

Graney and Kesler (1995) found that the average gas composition of fluid inclusion fluids in three different late-orogenic, structurally-controlled gold deposits (Sigma, Norbeau and Tadd, Canada) was 14.38, 1.10, 14.05 mol. % CO_2, 16.23, 5.59 and 11.96 mol. % CH_4, and 1.98, 0.32 and 2.31 mol. % $C_nH_{(2n+2)}$ respectively. Similarly, Bray *et al.* (1991) found that volatiles in primary fluid inclusions hosted by tourmaline bordering an Archaean pegmatite cross-cutting a granitic pluton, contained 2.2% CH_4, 0.4% CO_2, 250 ppm C_2H_6, 33 ppm C_3H_8, 11 ppm C_2H_6 and trace amounts of C_4 hydrocarbons. Further to this, Bray *et al.* (1991) also detected up to 13.4% CO_2, 4950 ppm CH_4 and trace C_2H_6 concentrations in late-orogenic, structurally-controlled gold deposits hosted by mafic to ultramafic rocks in the Barberton greenstone belt, South Africa. Therefore, it is anticipated that the weathering of the gangue minerals in these deposits provides

a source of light hydrocarbon gases which can then migrate vertically toward the surface where they can be detected by ultra-sensitive equipment.

The possibility that late-orogenic, structurally-controlled gold deposits may contain and release enough CH_4 and other light hydrocarbons to survive seepage through the overlying lithologies into the overlying soil, where they can be detected in the soil atmosphere, has not been fully tested. However, the presence of light hydrocarbons above the Junction deposit indicates that light hydrocarbon soil-gas technology combined with CO_2 - O_2 soil gas detection techniques may be a viable exploration tool for this mineralisation style. Indeed, it has been shown that combining CO_2 - O_2 soil gas results with light hydrocarbon soil gas results has the ability to screen false soil gas anomalies from those that occur above oxidising sulphidic mineralisation. Therefore, if light hydrocarbon concentrations can be detected in gangue minerals within the Junction deposit at levels that suggest that the results obtained from the passive samplers are related to the mineralisation, soil gas exploration technology may have considerable economic benefits.

CHAPTER FIVE

Fluid inclusion studies

5.1 Introduction

Fluid inclusion investigations are a common geochemical tool used in ore deposit studies. Fluid inclusions are small samples of the fluids that were present in the ore body some time in the past. They can provide data that allow a reconstruction of the fluid that was responsible for mineral precipitation, host-rock alteration, and at Junction, they can indicate the type of fluid that was involved in the gold mineralising process. Fluid inclusions in fault-related veins (such as those at Junction) provide direct information and constraints on the nature of the ore fluid in a mineralised system. Some of this data is not available by any other technique (Ho *et al.*, 1990a, 1990b; Robert *et al.*, 1995). Fluid inclusion characteristics, (determined from microthermometric analyses and laser-Raman spectroscopy) yield data on the types of fluid inclusions present, the temperature and pressure at which mineralisation took place and the density and composition of the fluid that carried solutes to the site of deposition (Roedder, 1984, Roedder and Bodnar, 1997). Interpretation of this data allows a better understanding of the type of ore fluids responsible for transporting fluid solutes, volatiles ± gold and the depositional processes that occurred between these fluids and the host wall rock.

Fluid inclusion data and alteration assemblages associated with late-orogenic, structurally-controlled gold deposits in the Archaean greenstone belts of Western Australia and the Abitibi greenstone belt in Canada, indicate that gold was deposited by a low salinity H_2O-CO_2 ± CH_4 rich, alkaline to near neutral fluid with densities of 0.7 - 0.8 gm/cm^3 (Robert and Kelly, 1987; Ho *et al.*, 1990a, 1990b; Cassidy and Bennett, 1993; Robert *et al.*, 1995; Boullier *et al.*, 1998). Fluid inclusion analysis of other late-orogenic, structurally-controlled gold deposits indicate that bulk salinities were close to, or less than 6 wt % NaCl (Groves *et al.*., 1988; Ho *et al.*, 1990a, 1990b; Boullier *et al.*, 1998), with Na the dominant cation over Ca>K>Mg. Daughter minerals are typically rare. Pressure estimates range from deposit to deposit, but are typically between 0.7 and 4.1 kbar, with most between 1 and 3 kbar (Robert and Kelly, 1987; Sibson *et al.*, 1988; Boullier and Robert, 1992; Boullier *et al.*, 1998). Homogenisation temperatures (Th) indicate that the temperature of entrapment (Tt) for this deposit type range froms 165 - 400°C, with most data clustering between 250 - 300°C. Interpretation indicates that fluid unmixing was relatively common (Robert and Kelly, 1987; Robert *et al.*, 1995).

Research on fluid inclusions in this style of deposit has led to the general acceptance that gold and other solutes were transported by a H_2O-CO_2 bearing fluid. CH_4 is present in most fluid inclusions associated with Archaean late-orogenic, structurally-controlled gold deposits (Robert and Kelly, 1987; Clarke, 1989; Ho *et al.* and references within, 1990a, 1990b; Cassidy and Bennett, 1993; Robert *et al.*, 1995; Boullier *et al.*, 1998). However, its presence can often be below the limit of detection by microthermometry. Raman spectroscopy, quadrupole mass spectrometry, solid phase mass spectrometry and gas chromatography indicate that compositions for carbonic phases in fluid inclusions can range from essentially pure CO_2 to essentially pure CH_4 (Smith and Kesler, 1985; Guha *et al.*, 1991; de Ronde *et al.*, 1992; Mernagh and Witt, 1994; Graney and Kesler, 1995; Mernagh, 1996).

Raman spectroscopy on fluid inclusions from the Mt Charlotte, Sand King and Missouri gold deposits in Western Australia reveal that some fluid inclusions hosted in quartz veining associated with gold mineralisation contain up to 100% CH_4 relative to CO_2 and N_2 (Mernagh and Witt, 1994; Mernagh, 1996). Bulk quartz analyses (ie 1 to 5 gm samples) for liquid phase determination incorporate H_2O in the analysis. This tends to dilute the overall CO_2 and CH_4 values in the sample if specimens contain abundant aqueous secondary fluid inclusions. Nevertheless, Guha *et al.* (1991) report that solid phase mass spectrometry on fluid inclusions from the Sigma gold mine, Canada, contain on average, 55.31 mol. % H_2O, 14.38 mol. % CO_2, 16.23 mol. % CH_4, and 12.08 mol. % N_2, whilst Graney and Kesler (1995) report values approximating 2 mol. % CH_4 relative to the H_2O-CO_2-CH_4 system in fluid inclusions from an unspecified late-orogenic, structurally-controlled gold deposit using similar methods. In comparison, Smith and Kesler (1985) used thermal decrepitation coupled with gas chromatography and found that ore-sample quartz veins in graphitic and carbonaceous material at the Hollinger-McIntyre gold mine, Canada, contain up to 49 mol. % CH4 relative to the H_2O-CO_2-CH_4 system. However, most CH_4 values were below 1.5 mol. % CH_4 in mafic basalts and felsic flows. Adding to this, de Ronde *et al.* (1992) used heated, on-line crushing gas chromatography and determined that mineralised quartz veins from gold mines of the Barberton Greenstone Belt, South Africa contain approximately 90 mol. % H_2O, 10 mol. % CO_2 and 0.06 mol. % CH_4. Clearly CO_2 and CH_4 are ubiquitous with this style of mineralisation. Thus the fluid inclusions in alteration minerals are a likely source for the soil gas anomalies detectable in the soil.

5.1.1 Rationale

The principle aim of this project is to discover the source of the CH_4, CO_2 and other gases that are detectable at the surface in the shallow soil profile. It has been shown that these gases are not related to bacterial activity in the regolith, and that the anomalies only form above the host shear zone. This suggests that the gases are derived from the ore body and its alteration minerals. Exploration using the soil gas detection technique is warranted if it can be proven that these gases are indeed related directly to gold mineralisation. A likely place to look for these gases is in fluid inclusions, because primary and pseudo-primary fluid inclusions represent the original

ore forming solution. Therefore, it is important that all of the main vein types present in the Junction deposit are analysed for their fluid content. This ensures that no unknown gas source is overlooked.

5.1.2 Fluid inclusion theory

Fluid inclusion microthermometry involves freezing and warming a sample under a purpose-built binocular microscope to observe the temperature affects on the fluid trapped inside a fluid inclusion. Freezing and warming runs produce physical changes within a fluid inclusion that correspond to certain chemical compositions. Common ions trapped in fluid inclusions in minerals associated with ore deposits are Na^+, K^+, Ca^{2+}, Mg^{2+}, Cl^-, SO_4^{2-}, CO_3^{2-} and HCO_3^- (Roedder, 1972). Similarly, common gases present in fluid inclusions are CO_2, CH_4, N_2, H_2S and SO_4 (Shepherd *et al.*, 1985). Each of these components have specific physical properties at low temperature which aid in their identification. However, complications arise when two or more of these components are present in the same fluid inclusion, and caution needs to be applied when interpreting these fluid inclusions. Limited leaching experiments on fluid inclusions hosted in quartz veins from late-orogenic, structurally-controlled gold deposits (Ho 1986; Robert and Kelly, 1987) suggest that in terms of atomic abundances, Na is the dominant cation over $Ca \geq K \geq Mg$. CO_2 is ubiquitous with late-orogenic, structurally-controlled gold deposits, and CH_4 is relatively common in many deposits of this style (Smith and Kesler, 1985; Robert and Kelly, 1987; Groves *et al.*., 1988; Ho *et al.*, 1990a and 1990b; Cassidy and Bennett, 1993; Mernagh and Witt, 1994; Robert *et al.*, 1995; Mernagh, 1996; Boullier *et al.*, 1998).

5.1.2.1 Freezing runs

Freezing studies are best used to determine the composition of the phases present in a given fluid inclusion. Fluid inclusions are super-cooled to -190°C (Section 5.2), to initiate the physical changes that correspond to certain chemical compositions.

5.1.2.1.1 Fluid-gas components (CO_2 - CH_4)

Common observations that indicate the presence of CO_2 in fluid inclusions include solidification (freezing) of the liquid between -90°C and -120°C, and melting of this crystal at or very near (below) -56.6°C (Shepherd *et al.*, 1985). The presence of CH_4 can be inferred if a vapour phase is present below -120°C or if the CO_2 invariant point is less than -56.6°C (Roedder, 1984). The presence of CH_4 in a binary gas system with CO_2 leads to a lowering of the temperature for the solid-liquid-vapour invariant point (CO_2 triple point, -56.6°C) (Roedder, 1984). The presence of N_2 and/or H_2S has a similar effect on CO_2 as does CH_4, and Raman spectroscopy is needed to confirm the species present.

5.1.2.1.2 First melt (Tfm) and eutectic temperature (Te)

After freezing the fluid inclusion to -190°C (Section 5.2), the fluid inclusion is slowly warmed. The first appearance of liquid is known as the temperature of first melt (Tfm) (Shepherd *et al.*.,

1985). Tfm often corresponds to the eutectic temperature (Te) where the eutectic is the invariant point determined for the composition of a known component. For example the Te for NaCl-H_2O is -20.8°C, for $CaCl_2$-NaCl-H_2O is -52°C and for CO_2 is -56.6°C.

5.1.2.2.3 Salinity estimates calculated from the melting temperature of fluid hydrates

Following Tfm, the hydrate + ice that is recognisable in the fluid inclusion continues to melt until at some point the hydrate melts, leaving only ice. The salinity of an aqueous fluid inclusion is determined by the final melting temperature of this ice (Tm_{ICE}). Whilst in theory it is possible to estimate the wt% ratios of co-existing electrolytes by their final melt temperature, in practice, recognising the difference between the melting of hydrates within a mass of ice crystals is difficult (Shepherd *et al.*, 1985). For this reason, Tm_{ICE} is calculated as wt% NaCl equivalent. Calculations of wt% NaCl are based on the lowering of Te H_2O-NaCl away from +0.015°C. This lowering effect is directly proportional to the amount of salt in solution (Shepherd *et al.*, 1985). Thus, the more saline the solution trapped in the fluid inclusion, the lower the temperature for Tm_{ICE}. The formation of a CO_2 clathrate in a fluid inclusion during freezing increases the apparent salinity of the solution in that fluid inclusion (see below). Therefore, fluid inclusions that develop clathrates during freezing and warming runs give misleading, elevated salinity values. Such fluid inclusion data is not included in the following discussion.

Salinity values can also be obtained from daughter mineral dissolution temperatures (Shepherd *et al.*, 1985). When halite is present, the salinity of the fluid inclusion is always fixed by the temperature of halite dissolution. Halite dissolution is initiated by slowly heating the fluid inclusion until the halite solid phase dissolves into the liquid phase.

5.1.2.2.4 Salinity estimates calculated from the melting temperature of CO_2 clathrates

The formation of gas hydrates or clathrates in fluid inclusions during the cooling cycle of the microthermometric measurements is typical for most natural fluid systems which include a mixture of H_2O, gases and electrolytes (Collins, 1979). Clathrates complicate phase relationships in the H_2O-salt-gas rich system and cannot be neglected when interpreting Tm data for salinity, composition and density estimates (Bakker *et al.*, 1996). Clathration removes water from the aqueous phase of the fluid inclusion (CO_2 hydrate = CO_2. 5 3/4H_2O) thereby increasing the salinity of the residual solution (Shepherd *et al.*, 1985). The formation of a CO_2 clathrate during freezing invalidates the use of Tm_{ICE} as a measurement of the fluid salinity. However, Tm_{CLATH} is a useful measure of salinity providing that CH_4 or any other gases are not present in the inclusion (Collins, 1979). CH_4, N_2 and other gases commonly form solid solution mixed hydrates with CO_2 and raise the temperature and pressure for Tm_{CLATH} (Hollister and Burruss, 1976). Thus the effect of CH_4 in a mixed CO_2-CH_4 hydrate co-existing with aqueous solution is to counteract the effect of NaCl in the solution (Collins, 1979).

A pure H_2O-CO_2 clathrate melts at +10°C. Assuming the co-existence of other gases is negligible

(as indicated by a shift in $TmCO_2$ significantly below -56.6°C) the presence of NaCl lowers the melting temperature of Tm_{CLATH} proportionate to the amount of NaCl present. Therefore a clathrate that melts above +0.015°C and below +10°C should give a valid estimation of fluid salinity (Shepherd *et al.*, 1985).

5.1.2.2.5 Density calculations for two phase L + V fluid inclusions

The total density of a fluid inclusion (P_{TOT}) is most accurately estimated after the freezing runs have helped to constrain the fluid components within the fluid inclusion. This is because P_{TOT} is dependent on the salinity of the aqueous phase and to a lesser extent, the presence of CO_2. P_{TOT} is calculated from volume and density data of the liquid phase and the density data of the vapour phase using the equation:

$P_{TOT} = pLF + pV\ (1\text{-}F)$ (Equation 5.1; Shepherd *et al.*, 1985)

where F is the degree of fill and is defined as the volumetric proportion of the liquid (VL relative to the total volume of the fluid inclusion [V_{TOT}]):

$F = VL/VL + Vv$ where $VL + Vv = V_{TOT}$ (Equation 5.2; Shepherd *et al.*, 1985)

pL = density of the liquid phase
pV = density of the vapour phase

Therefore, a typical Junction fluid inclusion containing a low to moderately saline (5.5 wt% NaCl) liquid occupying 70% of the fluid inclusions total volume and having a CO_2 density of 0.72 gm/ cm^3 has a fluid density of 0.72 g cm^3:

$$P_{TOT} = 0.72 \times 0.7 + 0.72(1 - 0.7)$$
$$= 0.72$$

5.1.2.2 Heating runs

5.1.2.2.1 Temperature of homogenisation (Th)

Homogenisation involves heating a fluid inclusion sample until the vapour and liquid phase become miscible and form one phase. In H_2O-CO_2 fluid inclusions like those at Junction, three fluid phases (aqueous liquid and CO_2 liquid-vapour) will have two homogenisation temperatures. The lower homogenisation involves the disappearance of one CO_2 phase (L or V) into the other CO_2 phase, whilst the higher homogenisation temperature involves the disappearance of CO_2 into H_2O or H_2O into CO_2 depending on the density of the phases within the fluid inclusion. In general, low density fluid inclusions will homogenise into the vapour phase, whilst high density fluid inclusions will homogenise into the liquid phase. In the high temperature region (CO_2-H_2O homogenisation), the density and thus the internal pressure of the fluid inclusion

determines if the fluid inclusion will decrepitate prior to reaching its true homogenisation temperature.

The temperature at which the CO_2 phases homogenise ($ThCO_2$) is always below the critical point of CO_2 (+31.1°C). The $ThCO_2$ is controlled by the density of the CO_2 phase in the fluid inclusion. A fluid inclusion having less than the critical density of 0.4 gm/cm^3 will homogenise into the vapour state of the CO_2 phase, whereas a fluid inclusion having a greater density than the critical density will homogenise into the liquid state of the CO_2 phase (Shepherd *et al.*, 1985). This is true for pure CO_2 only (H_2O is insoluble in CO_2, and barring the formation of clathrates, the presence of water is independent of CO_2 density; Shepherd *et al.*, 1985). Other gases such as CH_4 and N_2 will raise or lower the critical point of CO_2 and give erroneous data.

The temperature at which all the components within a fluid inclusion homogenise into one phase is called the temperature of total homogenisation (Th) and represents the minimum temperature of entrapment. Th is different to the temperature of entrapment (Tt). Tt is the precise temperature at which the fluid was entrapped. In most cases a pressure correction must be applied to Th to get Tt. An accurate Tt can only be determined if a pressure estimate can be established from an independent source, e.g., geological reconstructions of the depth of formation as determined by mineral assemblages if applicable (Roedder, 1984). If this is possible, a pressure correction can be added to Th to determine Tt (Roedder, 1984).

A number of assumptions regarding the microthermometric data need to be considered before Tt can be determined from Th. These assumptions, listed by Roedder (1984), are summarised here:

- The fluid trapped when the fluid inclusion was healed was a single homogeneous phase. This can be assumed when most fluid inclusions in a sample show approximately the same phase ratio(s).

- The cavity in which the fluid is trapped does not change in volume after sealing. Thermal expansion by later thermal events can lead to permanent stretching of the host mineral, yielding erroneously high Th values. Similarly, thermal contraction on cooling, or dilational change from internal or external pressures may also lead to erroneous Th values.

- Nothing is added or lost from the fluid inclusion after sealing. Decrepitation, leakage and necking down of fluid inclusions result in erroneous Th values because liquid or gas phases present in the original fluid inclusion have been lost, thus changing the original phase composition and pressure of entrapment.

- The affects of pressure are insignificant or are known. Pressure is of significance because it controls the density of the fluids and hence the magnitude of the pressure corrections that must be added to Th to get Tt.

It can be seen from these criteria that calculating the correct Tt from pseudoprimary fluid inclusions from a late-orogenic, structurally-controlled gold deposit is difficult. Robert and Kelly (1987), Boullier and Robert (1992), and Robert *et al.* (1995) have shown Tt is not easily determined for many fluid inclusions in late-orogenic, structurally-controlled gold deposit because trapping mechanisms are controlled by cyclical pressure changes ranging from lithostatic to hydrostatic. Considering the fact that late-orogenic, structurally-controlled gold deposit are hosted in prehnite-pumpellyite to granulite facies metamorphic rocks over a wide range of depths (therefore wide ranging pressures) from epizonal (<6 km) to mesozonal (5 - 11 km) to katazonal (> 10 km) (Hagemann and Ridley, 1993; Brown and Hagemann, 1995), Tt determinations are usually best estimates only.

In the case of two immiscible liquids, changes in pressure and/or temperature cause compositional differences to occur. Pressure and temperature changes result in a parent fluid separating into a high density, more saline liquid and a low density vapour (Shepherd *et al.*, 1985; Robert and Kelly, 1987; Robert *et al.*, 1995). Compositional differences between fluid inclusions trapped in such a seismogenic environment result in fluid inclusions that give erroneous temperature, pressure and density data (Roedder, 1984).

In summary, microthermometric data can only provide constraints on minimum pressures and temperatures of trapping. It is necessary to calculate the isochore consistent with observed data to determine a more accurate temperature and pressure at the time of entrapment (Brown and Hagemann, 1995). However, uncertainties still exist regarding the pressure estimates due to assumptions that must be made of the load conditions. This is true of many late-orogenic, structurally-controlled gold deposit where transient pressure conditions (pressure fluctuations) between hydrostatic and lithostatic fluid pressures might occur, thereby making it difficult to define a single geobarometric gradient (Hagemann *et al.*, 1994).

Roedder and Bodnar (1980) point out that it is difficult to obtain accurate pressure and temperature information from trapped immiscible aqueous and vapour rich fluids. In theory, Th of co-existing water-rich and CO_2-rich fluid inclusions should correspond to Tt. In an efficient heterogeneous adiabatic system, sufficient heat is supplied to the system until the conversion of the homogeneous fluid to liquid and vapour end-members is complete (Roedder, 1984). If it can be shown that a population of fluid inclusions was trapped in such a system simultaneously, and that some of these fluid inclusions homogenise into the vapour state over the same temperature as other fluid inclusions homogenise into the liquid state (Shepherd *et al.*, 1985), then Th = Tt and a pressure estimate may be obtained from them (Roedder, 1984). This scenario is not only difficult to

interpret in late-orogenic, structurally-controlled gold deposit, but is rarely observed in practice. Indeed, contemporaneous populations of fluid inclusions that contained compositional variations from liquid-rich to vapour-rich were found in quartz veins at Junction (see Figure 5.9), but homogenisation of these fluid inclusions into a single phase at the same temperature was not observed.

5.1.2.2.2 Th CO_2

A fluid inclusion at room temperature may appear monophase (L or V) or two-phase (L and V) depending on the density of the entrapped CO_2 phase (Shepherd *et al.*, 1985). At Junction, most CO_2-rich fluid inclusions appear monophase at room temperature, and only appear two-phase with cooling. However, some CO_2-rich fluid inclusions contain both CO_2 liquid and vapour phases at room temperature (see Figure 5.14). In other cases, the vapour phase occupies more than 80% of the fluid inclusion area. These fluid inclusions can be too dark in colour to determine if a liquid and vapour is present, thus appearing monophase (see Figure 5.13).

Homogenisation of the two-phase fluid inclusions below the critical point of CO_2 (+31.1°C) were used to calculate the density of the CO_2 phase. Fluid inclusions that indicated the presence of CH_4, (as indicated by a $TmCO_2$ that is significantly below -56.6°C) were eliminated from the CO_2 density calculations.

5.2 Methods, equipment and procedures

The three main vein types discussed in Chapter 3.6 were analysed for their fluid inclusion properties. All fluid inclusions were supercooled to -190°C using liquid N_2 before slowly warming to the critical temperature of CO_2 (+30.1°C).

Quartz vein samples were selected from a number of underground drives and diamond drill core for fluid inclusion investigation. The samples represent the three most prominent events during which vein formation and sulphide mineralisation occurred. These events are discussed in Chapter 3 and include the pre-gold quartz-molybdenite mineralising event (Mo-type quartz veins), the syn-gold shear zone controlled quartz-pyrrhotite-pyrite mineralising event (syn-gold quartz veins) and the post-gold quartz-carbonate-biotite-pyrrhotite mineralising event (SV-type quartz veins). The majority of the veins analysed represent the gold mineralising event. Quartz veins from this event represent shear and extensional veining within the N25 surface and related hanging wall and foot wall mineralisation.

The analytical techniques used to investigate fluid inclusions include microthermometry and Raman spectroscopy.

All microthermometry was carried out on a REYNOLDS FLUID INC. fluid inclusion heating-freezing stage attached to a Leitz Wetzlar Sm Lux-POL binocular microscope. Temperatures

were recorded to within a tenth of a degree on a Fluid Inc. 410A Trendicator. The temperature of homogenisation (Th) was measured using low heating rates, near Th, of 0.5 to 1.0°C per minute. The temperatures were reproducible to within 1°C for each fluid inclusion. The low temperature measurements were run first to avoid stretching and decrepitation in any sample. Eutectic (first melt) temperature (Tfm) was reproducible to within 2°C. The temperature of final melt (Tm) of the last crystal of ice was measured using heating rates of 1°C a minute. Tm measurements were reproducible to 0.5°C. Freezing measurements were done on each sample before the heating runs to avoid any loss of fluid by decrepitation due to heating, although it is recognised that, possibly, this can lead to stretching as the ice expands slightly. The small size of the fluid inclusion used however, would minimise any likelihood of this occurring. All data is presented in Appendix VI and summarised in Table 5.1 (p. 104).

Twenty-seven doubly polished slabs, 80 to 150 μm thick, were analysed by microthermometry (21 syn gold quartz veins, four SV-type quartz veins and two Mo-type quartz veins). Care was taken during preparation in order not to damage or over heat the plates. Roedder (1984), suggests that in general, the temperature used during sample preparation should be kept below 100°C to avoid decrepitation.

Fluid inclusions were observed in quartz, carbonate (calcite >> dolomite) and albite. However, only fluid inclusions in quartz were analysed by microthermometry. Carbonate and albite are both dominant gangue minerals within the alteration assemblages associated with gold mineralisation. However, the fluid inclusions in these minerals are typically very small (<3μm) (Figure 5.1 and 5.2), although some fluid inclusions up to 12 μm were observed in albite. The small size of these fluid inclusions, together with the opacity and/or the refractive nature of these minerals, preclude any microthermometric analyses being performed.

Laser-Raman spectroscopic data is discussed throughout this chapter to enhance microthermometric results and to confirm compound phases indicated by heating and freezing temperatures obtained during microthermometry. Laser-Raman (or Raman-spectroscopy) was carried out using a Microdil-28 laser-Raman microprobe at the Australian Geological Society Organisation, Canberra, following the technique of Liu and Mernagh (1990). Raman-spectroscopy is discussed in detail in Chapter 6.

5.3 Sample types and related fluid inclusions

The fluid inclusions at the Junction deposit have been classified according to vein generation, and the appearance of the fluid inclusion at room temperature (room temperature = 20°C). Roedder (1984) provides criteria for distinguishing between primary and secondary fluid inclusions. However, for the purpose of this study, isolated or randomly distributed fluid inclusions not obviously related to any healed fracture are considered pseudo-primary. This classification is based on observations by Robert and Brown (1986), Robert and Kelly (1987),

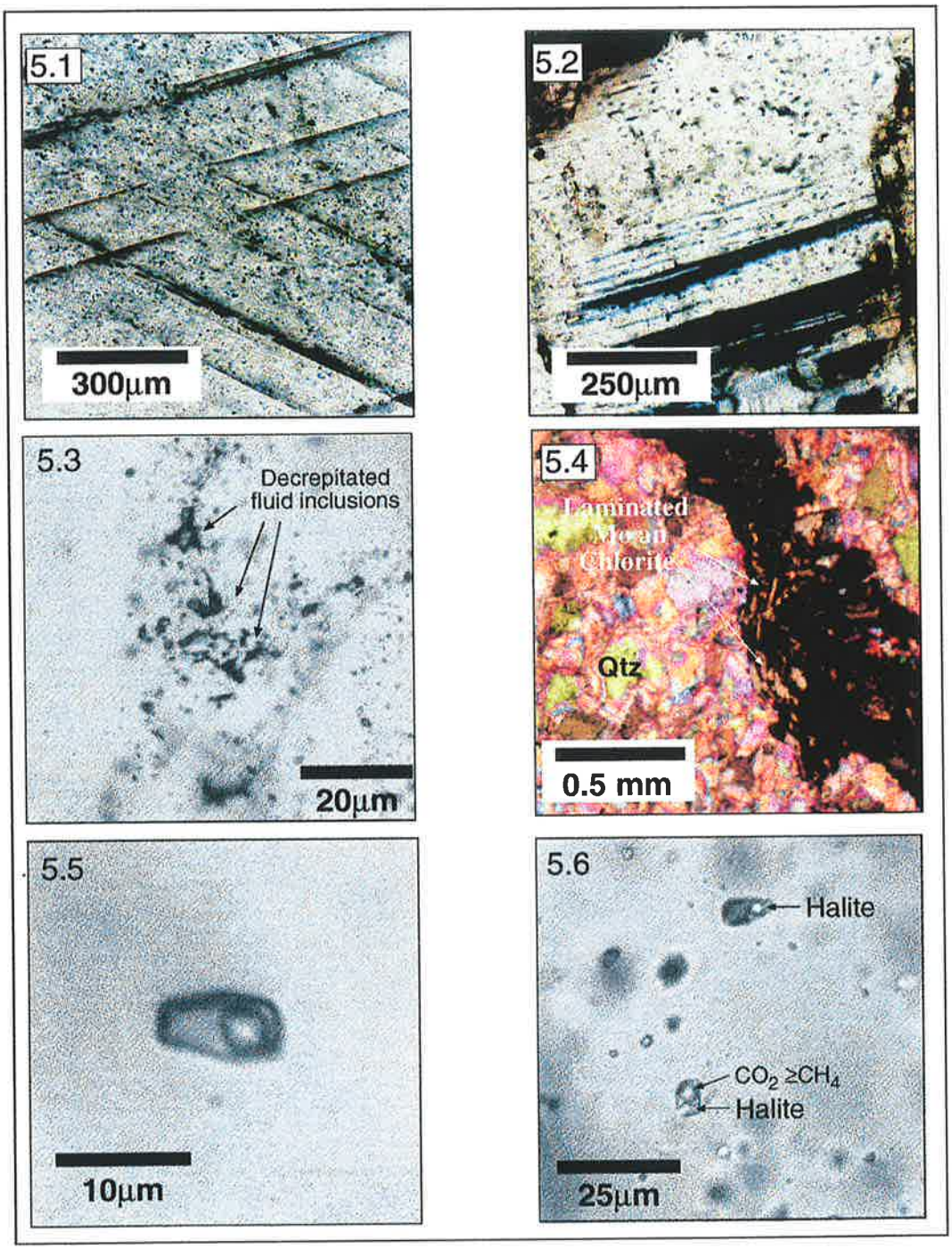


Figure 5.1. Photomicrograph of small (<5µm), but abundant fluid inclusions in calcite.
Figure 5.2. Photomicrograph of tabular fluid inclusions in a twinned albite lath growing near the vein-wall rock margin.
Figure 5.3. Photomicrograph of naturally decrepitated single phase (?carbonic) fluid inclusions occuring at the edge of a deformed quartz grain.
Figure 5.4. Fine grained, strained quartz with sutured margins, typical of Mo-type quartz veins, occurring with co-existing foliated molybdenite.
Figure 5.5. A typical Mo-type fluid inclusion. The vapour phase in these fluid inclusions is around 30 vol. % and not obviously carbonic at room temperature.
Figure 5.6. Mo-type fluid inclusions appear to have trapped a highly saline, H_2O-$CO_2 \geq CH_4$ fluid. Halite daughter minerals are frequently observed in the limited number of samples suitable for analysis. Again notice the constant vapour phase volume.

Ho *et al.*, (1990a, 1990b), Boullier and Robert (1992) and Boullier *et al.* (1998) who note that deformational structures in veins hosted within shear zones show alternating episodes of opening, crystallisation, plastic and/or brittle deformation which indicate that cyclical deformation was an integral part of vein development. It is likely that such cyclical deformation at elevated temperatures has resulted in either re-opening, stretching, necking or decrepitation of primary fluid inclusions within all types of quartz veins and as a result, not a single fluid inclusion can be unambiguously interpreted as primary in origin.

Analytical observations when investigating fluid inclusions incorporate the assumptions that nothing is added or lost from the fluid inclusion after trapping and that the fluid inclusion volume has remained constant. The fluid inclusion is said to have re-equilibrated if either of these assumptions is violated (Roedder, 1984; Vityk, *et al.*, 1994). Decrepitated and leaked fluid inclusions were identified in all quartz examined (Figure 5.3). Fluid inclusions that showed obvious decrepitation or leaking were not used for microthermometric analysis as a loss of fluid had clearly occurred. In some cases, it is possible that fluid inclusions identified as pseudo-primary fluid inclusions are well healed secondary fluid inclusions that have migrated away from the microfracture planes, as suggested by Giles and Marshall (1995). Robert and Kelly (1987) found this to be so for many fluid inclusions that occurred as regularly spaced, three dimensional clusters in the Sigma gold mine, Canada.

5.3.1 Fluid inclusion types in pre-gold Mo-type quartz veins

Fluid inclusions associated with Mo mineralisation are hosted in quartz veins that are cross-cut by all other veins within the Junction mine. This indicates that they formed prior to the main shearing and gold mineralising event. It is not clear how these veins are related to the pre-gold porphyry intrusives (devolatisation products?) or to peak metamorphism in the area. A full interpretation of these veins is not warranted here. However, in terms of the aims of this project, it is important that the phase compositions (specifically the gas phases) of these fluid inclusions be determined.

Molybdenite-bearing quartz veins (Mo-type quartz veins) are poor fluid inclusion hosts. These veins typically display strained quartz grains with undulose extinction and sutured boundaries (Figure 5.4). Fluid inclusions within these veins are nearly always decrepitated and are often too small to analyse by microthermometry. However, on rare occasions (two examples from seven thin sections prepared), pseudoprimary (?primary) fluid inclusions (henceforth known as Mo-type fluid inclusions), interpreted as being representatives of the fluid that formed the Mo-type veins, are preserved in embayments where the effects of recrystalisation were apparently minimised by the surrounding molybdenite-chlorite mineralisation. It is believed that the ductile nature of the molybdenite and chlorite accommodated some of the strain during subsequent deformation, thus preserving some of the original Mo-type quartz and its complement of fluid inclusions. A similar form of preservation is reported by Spry*et al.* (1996) for fluid inclusions

in Mo-bearing quartz veins that were recrystallised at the Golden Sunlight Au-Ag deposit, Montana, USA.

Mo-type fluid inclusions are tabular to slightly rounded in shape. They are predominantly H_20-rich, containing a $CO_2 \geq CH_4$ vapour phase that occupies < 40 vol. %, and may or may not contain a halite daughter mineral (Figures 5.5 and 5.6). Vapour phases of up to 80 vol. % have been observed (Figure 5.7). Two daughter minerals may be present on rare occasions (Figure 5.8). Raman spectroscopy confirmed that halite is a common solid in these fluid inclusions, but was unable to confirm the nature of the second solid present. Fluid inclusion trails are not noticed in the two unstrained samples analysed. However, this small sample population is clearly not representative.

5.3.2 Fluid inclusion types in syn-gold quartz veins

Gold related alteration assemblages at Junction indicate that retrograde rehydration reactions occurred between the Junction Gabbro and a reduced, CO_2-rich, $AuHS_2^-$-bearing, H_2O-dominated fluid. The alteration assemblages vary through the mine according to the mineralogical differences between the zoned gabbro, but alteration always reflects the transition of CO_2 plus gold, S, K and Na into the host rock. This alteration indicates that the vein/lode system formed after peak thermal and burial metamorphism. The alteration assemblage is spatially associated with numerous central and oblique shear veins (henceforth known as shear veins) and horizontal to sigmoidal extensional veins (henceforth known as extensional veins). These vein-types cut across each other indicating that pressure build-up and release associated with movement in a reverse sinistral direction was a continuous and recurring event. That both the shear veins and the extensional veins are preferentially located with gold related alteration in the Junction Shear Zone, indicates that fluid focus was structurally controlled. Given this, it can be assumed that fluid inclusions hosted within these vein types represent samples of the ore fluid responsible for gold deposition.

Shear veins can be distinguished in thin section from extensional veins (aside from other characteristics) on the basis of fluid inclusion morphology. Shear veins have fluid inclusions that display unmixing of a moderately saline H_2O-CO_2 parent fluid. Fluid immiscibility, caused by a drop in pressure associated with seismic rupture along the shear veins, has resulted in fluid inclusions dominated by two distinct end members (Figure 5.9). On the basis of phases present and degree of filling, four optically distinct types of fluid inclusions are identified:

Type A. CO_2 (liquid and vapour)$\pm$ $H_20 \pm CH_4 \pm$ solid,
Type B. CO_2 (liquid and vapour) > $H_20 \pm CH_4 \pm$ solid,
Type C. $H_20 > CO_2$ (liquid and vapour) $\pm CH_4 \pm$ NaCl,
Type D. H_20 - H_2O or CO_2 vapour $\pm$ NaCl.

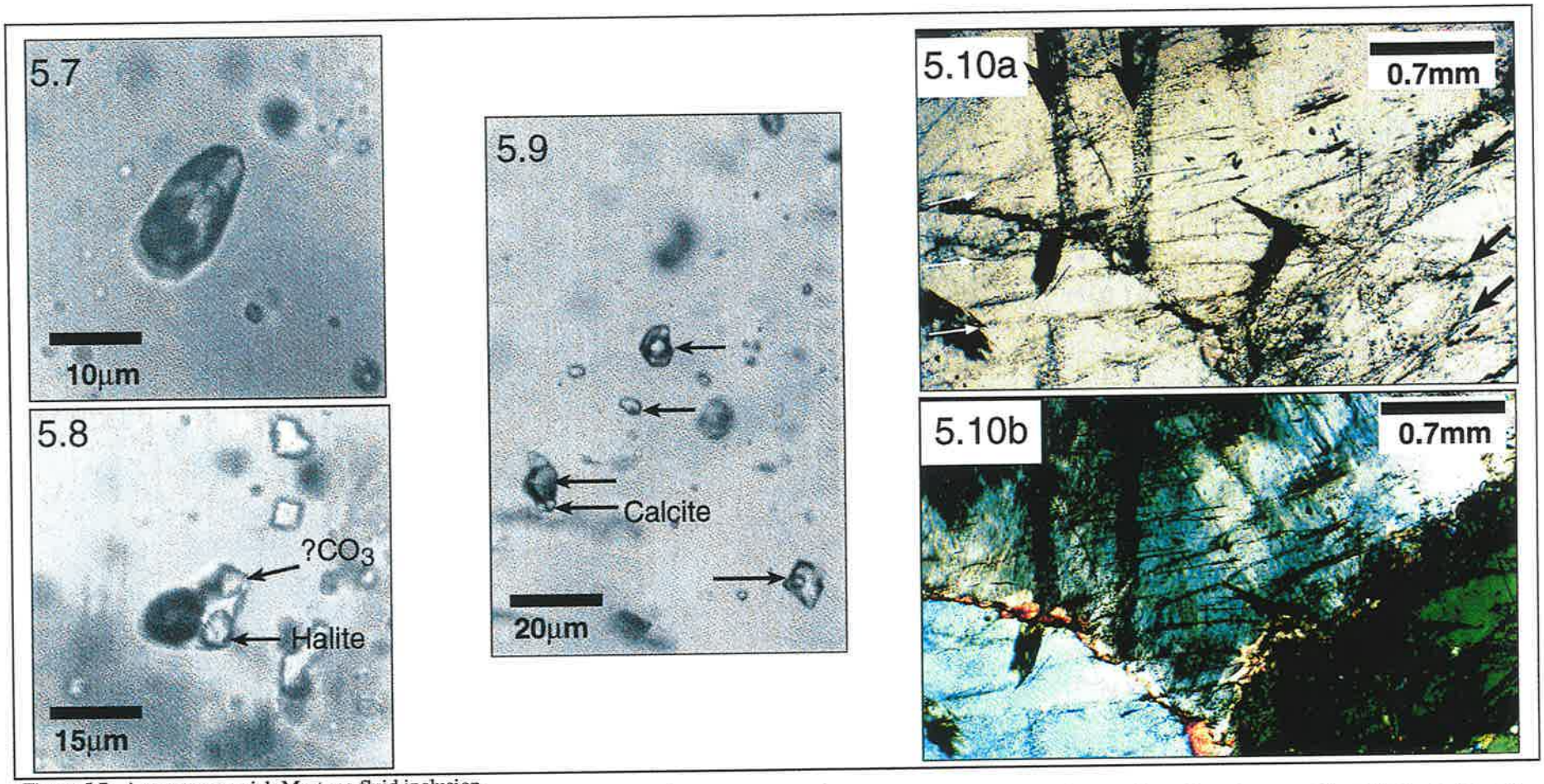


Figure 5.7. A rare vapour rich Mo-type fluid inclusion.
Figure 5.8. Photo micrograph of a carbonic-rich Mo-type fluid inclusion containing a halite daughter mineral and an unidentified carbonate.
Figure 5.9. A three dimentional cluster of fluid inclusions showing classic phase separation in a shear vein. The three largest fluid inclusions in focus have different phase ratios varying from 15 vol. % to 70 vol. % vapour. The largest type B fluid inclusion also contains a rarely seen calcite daughter mineral.
Figure 5.10a and 5.10b. Photomicrographs of fluid inclusion trails in a shear vein in transmitted light (5.10a) and cross polarised light (5.10b). Close inspection of the quartz in this photomicrograph reveals three increments of vein growth and deformation. The green coloured quartz grain (bottom right) is the oldest of the three grains. Fluid inclusion trails are abundant and appear to be randomly orientated. The small black arrows highlight the direction of fluid inclusion trails that terminate at the edge of this quartz grain. The grey coloured quartz grain (upper centre) is second oldest. It contains fewer fluid inclusion trails than the green quartz grain, and two distinct trail orientations can be seen (as indicated by the large black arrows and the small white arrows). One of these sets of fluid inclusion trails can also be seen in the youngest, light blue coloured, quartz grain (indicated by the small white arrows). Fluid inclusion trails in this quartz grain cross cut the other two grains and have one predominant east-west orientation.

A complete spectrum of composition is observed between type A and D fluid inclusions. Fluid inclusion types B and C probably represent these intermediate compositions. The shapes of these fluid inclusions range through rectangular, tabular, rounded and equidimensional. Occasionally fluid inclusions exhibit negative crystal shapes, probably caused by subsequent plastic deformation. Fluid inclusions in shear veins are abundant across all quartz grains and range from 1μm to 20μm (typically 8-12μm) in size. They regularly occur as irregular three dimensional clusters, and trains of CO_2-rich or aqueous rich fluid inclusion trails. In most cases, fluid inclusion trails contain fluid inclusions that have constant liquid to vapour ratios. The trails may cross many quartz grains, or terminate at the edge of a single quartz grain, indicating that early quartz grains co-exist with quartz grains that precipitated later. This is indicated by the orientation of fluid inclusion overgrowths within the quartz grains (Figure 5.10a and 5.10b). Robert and Kelly (1987) note that fluid inclusion trails at the Sigma mine, Canada, sometimes contain fluid inclusions that exhibit various liquid to vapour ratios, but this was not observed at Junction. Three dimensional clusters of fluid inclusions at Junction may have one of two origins. Some of these fluid inclusions are probably the result of earlier, closely spaced fluid inclusion trails of several different orientations that have been transposed during brittle-ductile deformation (Roedder, 1984; Robert and Kelly, 1987), whereas others are possibly primary (Boullier *et al.*, 1998).

Fluid inclusions trapped along healed microfractures often contain constant H_20-CO_2 phase ratios. However, different trails contain fluid inclusions with different phase volumes (e.g. Figures 5.11 and 5.12). Fluid inclusions with constant H_2O-CO_2 phases in the range 40 - 60 vol. % are common and are thought to be close representatives of the original parent fluid which transported the gold to the site of deposition. The presence of this type of fluid inclusion indicates that, for short periods of time during the fracturing of the vein minerals, the P-T conditions were such that the fluid was above the two phase region when the parent fluid was trapped (Robert and Kelly, 1987).

At room temperature (arbitrarily 20°C) type A fluid inclusions consist of a CO_2-dominated phase (vapour ± liquid) with little or no water (Figure 5.13). On rare occasions, these fluid inclusions contain a daughter mineral that has been identified by Raman spectroscopy as either nahcolite ($NaHCO_3$), halite or calcite. CH_4 is often present in variable quantities, as identified by low temperature microthermometry and Raman spectroscopy. These fluid inclusions are common, and are usually found along healed microfractures. Robert *et al.* (1995) found that CO_2-rich fluid inclusions (type A equivalent) are most abundant in shear veins and along subhorizontal planes, parallel to the vein walls. At Junction, CO_2-rich fluid inclusions are equally as common in extensional veins and they do not appear to be constrained to sub-horizontal fluid inclusion trails only. However, it should be acknowledged that fewer thin sections were investigated from

UNIVERSITY OF ADELAIDE LIBRARY

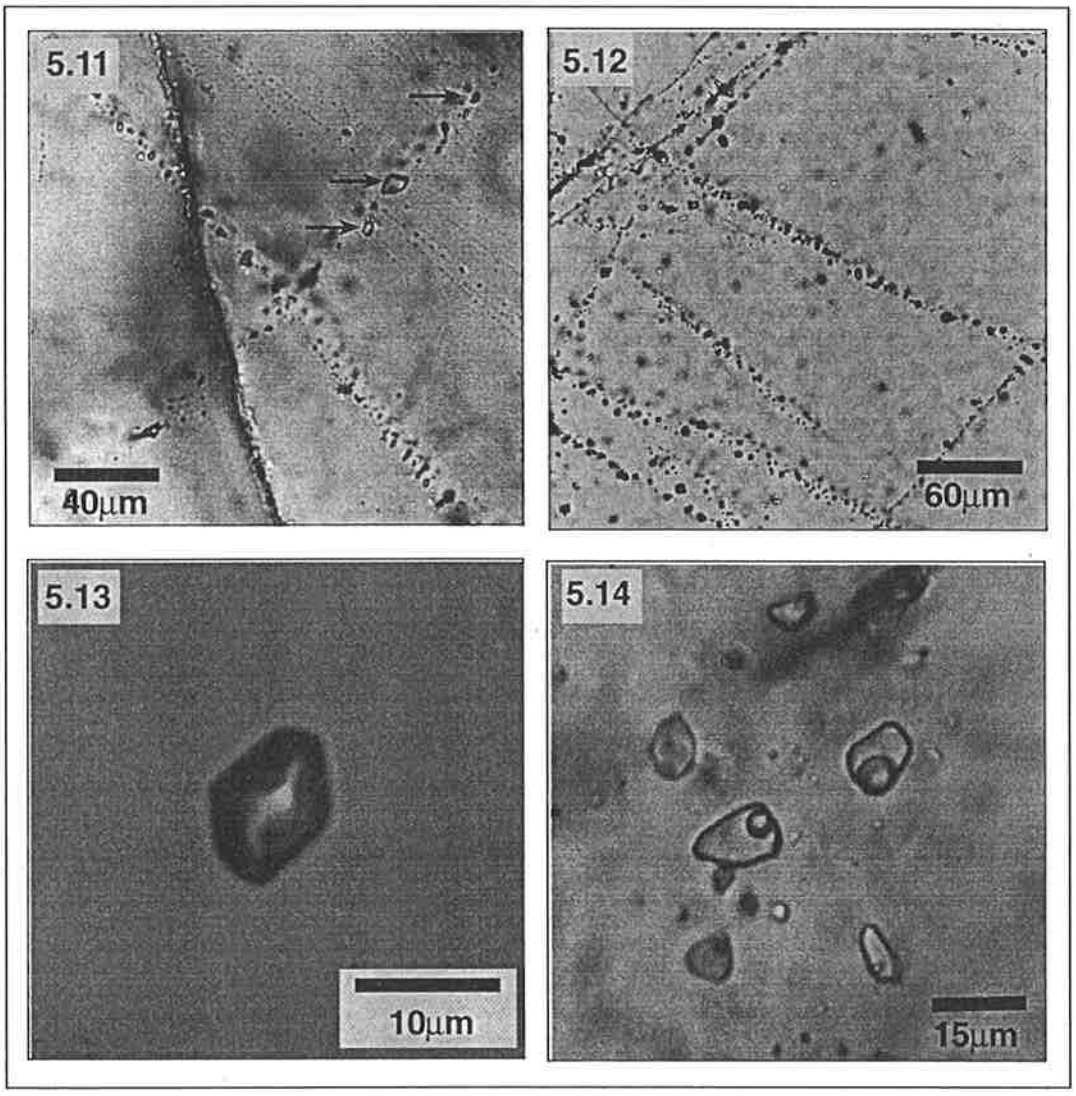


Figure 5.11 Two fluid inclusion trails at almost right angles to each other, both with different phase compositions. The fluid inclusion trail trending from upper right to lower left of the photomicrograph are aqueous two phase fluid inclusions that are up to 8µm across (indicated by arrows). The fluid inclusion trail trending from the upper left corner to lower right corner contains ?vapour only fluid inclusions. However, due to the small (typically < 2µm) size of these fluid inclusions, this can only be inferred from the dark appearance of their composition.

Figure 5.12. Fluid inclusion trails found in a shear vein containing H_2O-CO_2 fluid inclusions (Type B and C) with relatively similar phase ratios.

Figure 5.13. A typical type A fluid inclusion usually found along fluid inclusion trails in extensional quartz-carbonate veins. Although no visual liquid phase is present, it can not be assumed that type A fluid inclusions are 100% $CO_2 \pm CH_4$. A thin, <1µm thick meniscus of liquid forming on the rim of the vapour phase in small (i.e. <5µm) fluid inclusions can occupy a significant percentage of the fluid inclusion. A common characteristic of some type A and type B fluid inclusions is the negative crystal shape (seen here) that the fluid inclusion assumes during plastic deformation.

Figure 5.14. Photomicrograph of two adjacent syn-gold fluid inclusions containing different volumes of a carbonic phase. The fluid inclusion at left is classified as a type D aqueous fluid inclusion because it contains < 20 vol.% vapour, whereas the fluid inclusion to the right is classified as a type C H_2O-CO_2 fluid inclusion because it contains approximately 25 vol% vapour. Volume % calculations are based on visual estimates only.

Junction compared to the number of samples investigated by Robert and Kelly (1987), Boullier and Robert (1992) and Boullier *et al.* (1998), and not all quartz veins were orientated prior to cutting into thin section. Generally, type A fluid inclusions found along healed microfractures are very small (< 2μm), and are not suitable for microthermometry. However, where they occur in three dimensional clusters, they can be up to 10μm in diameter.

At room temperature, type B and C fluid inclusions consist of variable CO_2 and water ratios. The volumetric proportions of CO_2 vary from 20 - 80% (Figures 5.14 and 5.15). CO_2 occurs as liquid and vapour in some fluid inclusions (Figure 5.16). Daughter minerals are rare, but halite and calcite have been identified (Figure 5.17). CH_4 is often present in variable volumes. Type B and C fluid inclusions are equally as common as type A fluid inclusions. They are frequently found as three dimensional arrays, but most commonly they are found along healed microfractures that terminate either within a quartz grain or at the boundary of the quartz grain. Occasionally these fluid inclusion trails cross one or more grain boundaries, indicating that they formed late in the history of that vein (see Figure 5.10a and 5.10b). These fluid inclusions vary in size from <1μm to 20 μm in either the three dimensional array or the fluid inclusion trails.

Type D fluid inclusions are water dominated fluid inclusions (Figure 5.18). These fluid inclusions are common along healed microfractures, but also occur as three dimensional arrays. Type D fluid inclusions are abundant in all shear veins. These fluid inclusions are tabular to rounded, and equidimensional shapes are common. They range in size from <1 μm to 30 μm but are typically around 5 - 8 μm in size. CO_2 may or may not form part of the vapour phase. The presence of CO_2 can only be confirmed by low temperature microthermometric reactions or by Raman spectroscopy, but often its presence can be inferred by the activity or inactivity of the vapour phase at room temperature. Daughter minerals are often present in these fluid inclusions. Halite is the most common species observed, but calcite (or rhodochrosite), nahcolite and siderite have been identified by Raman spectroscopy. In some cases, it is possible that some of these fluid inclusions have undergone some degree of deformation, leakage and rehealing as suggested by Vityk, *et al.* (1994). This may also explain the occurrence of halite daughter minerals in type B and C fluid inclusions.

It is possible that type D fluid inclusions could be mis-identified secondary fluid inclusions not associated with the gold mineralising fluid. However, the aqueous fluid inclusion trails either terminate at, or cut across grain boundaries in all syn-gold vein types. Robert and Kelly (1987) found that many fluid inclusion trails in quartz at the Sigma mine must be associated with the gold transporting fluid because gold flecks are trapped within the fluid inclusions that form the fluid inclusion trails. At Junction however, no gold was found along any fluid inclusion trail, regardless of the phase ratios present. Nevertheless, microthermometric investigations support the premise that most type D fluid inclusions are related to the ore forming fluid. True secondary fluid inclusions are discussed below.

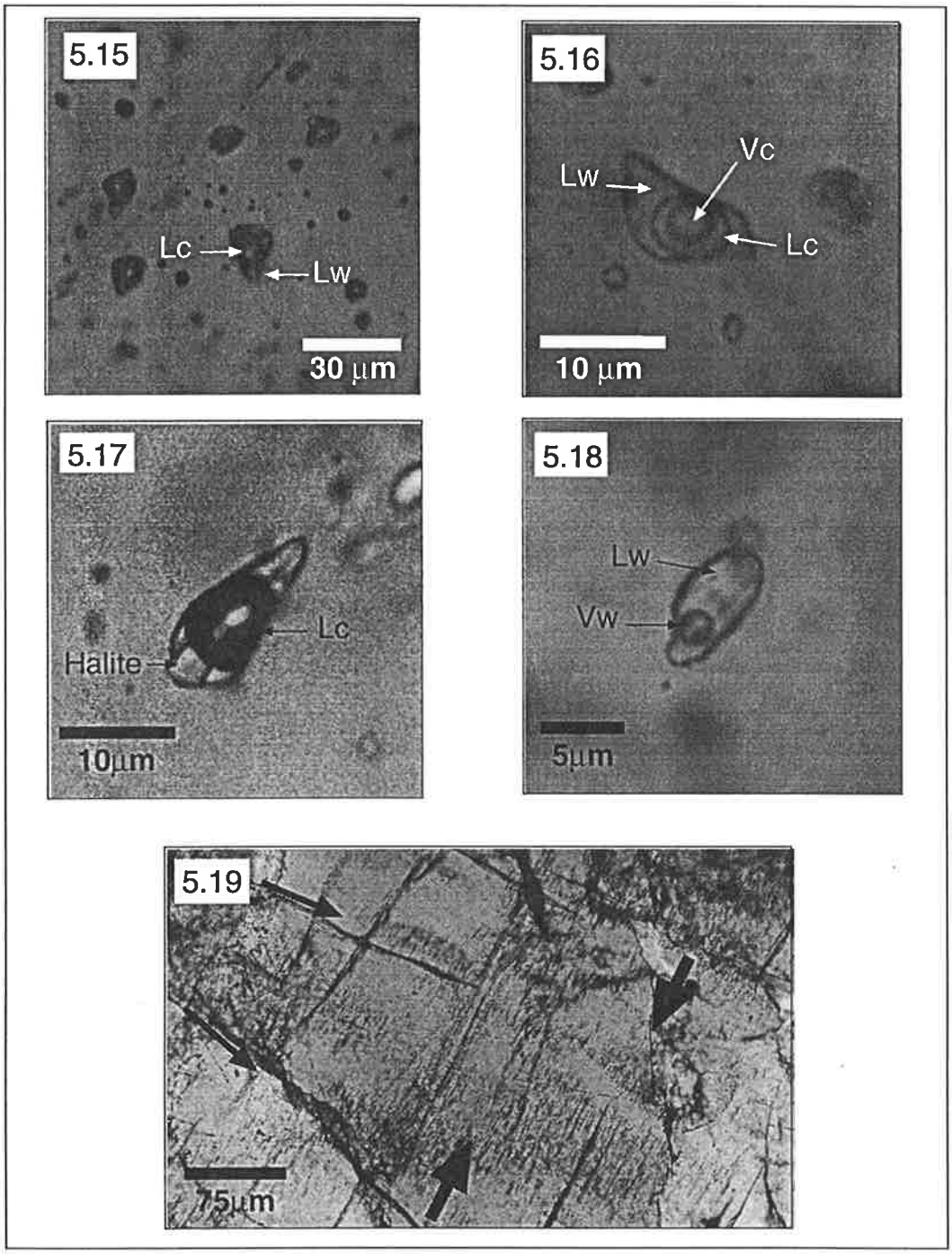


Figure 5.15. Typical type B fluid inclusions displaying >50 vol. % carbonic phase (Lc = liquid CO_2; Lw = liquid water).
Figure 5.16. Type C fluid inclusion at room temperature displaying liquid and vapour $CO_2 \pm CH_4$ phases. (Vc = vapour CO_2; Lc = liquid CO_2; Lw = liquid water).
Figure 5.17. A rare type B fluid inclusion containing > 50 vol. % carbonic phase and a prominent halite daughter mineral (Lc = liquid CO_2).
Figure 5.18. Type D fluid inclusion containing < 20 vol. % vapour phase (Lw = liquid water, Vw = vapour water).
Figure 5.19. Sub-horizontal fluid inclusion trails in an extensional quartz vein. Larger arrows indicate the principle stress direction. Sub-horizontal microfractures open up sub-parallel to the stress direction and sub-parallel to the extensional vein-wall orientation. Fluid inclusion trails can be used as indicators for stress direction and as evidence of extensional vein growth during lithostatic pressure build up. Fluid inclusions trapped along these trails are typically vapour-rich due to the wetting angle of CO_2. Sub-vertical microcracks (smaller arrows) open up during pressure release associated with seismic rupture. Sub-vertical microcracks are sub-parallel to shear vein walls.

Extensional veins host fluid inclusions with relatively consistent liquid-vapour ratios. Fluid inclusions in these veins are typically vapour dominated ($CO_2 \pm CH_4$), but aqueous rich fluid inclusions with rare daughter minerals are not uncommon. Where present, daughter minerals appear to be halite, calcite or nahcolite (based on optical properties and comparisons with daughter minerals identified in fluid inclusions hosted by shear veins). Based on optical observations, fluid inclusions hosted by extensional veins can be classified in the same manner as fluid inclusions hosted by shear veins (i.e. types A to D as described above).

Fluid inclusions hosted by extensional veins are slightly smaller (1μm to 15μm) than those hosted by shear veins. These fluid inclusions are typically tabular or rounded and are rarely equidimensional except where decrepitation is evident. Negative crystal shaped fluid inclusions are slightly more common in this vein type. Fluid inclusions hosted by extensional veins form in small clusters towards the centre of a quartz crystal, or along short (many micrometres) fluid inclusion trails that may or may not cross grain boundaries (Figure 5.19). In regard to the overall population of these fluid inclusions, it is clear that they are less abundant than their counterparts in the shear veins.

The high vapour to liquid ratios exhibited by fluid inclusions in extensional veins inhibit good homogenisation and salinity determinations. However, vapour identification based on the eutectic melting point of CO_2 (-56.6°C) is useful in determining the presence of other gases such as CH_4. In fluid inclusions where CH_4 is not suspected (as determined by the eutectic temperature of CO_2) CO_2 fluid densities can be determined.

5.3.3 Fluid inclusion types in post-gold quartz veins

Post-gold, southeast dipping quartz veins (henceforth known as SV-type quartz veins) cut across all other vein styles and occur in normal fault planes. Quartz grains in these veins are large (several microns to millimetres), clear and undeformed. Similarly, calcite, biotite and pyrrhotite crystals within these veins are large (up to 2 cm) and randomly orientated (see Figures 3.40 and 3.41). These features indicate that SV-type quartz veins post-date the compressional environment present during gold mineralisation. These veins host numerous vapour-rich fluid inclusions (henceforth referred to as SV-type fluid inclusions).

SV-type fluid inclusions are tabular to slightly rounded in shape, but negative crystal shapes are also common. Limited fluid inclusion analyses indicate that vapour dominates over the liquid phase in these fluid inclusions (50 to 100% vapour) and halite daughter minerals are rare (Figure 5.20). Aqueous fluid inclusions are present, but they are not as common as they are in syn-gold shear, or extension veins. Both fluid inclusion types occur as three dimensional arrays, and along healed microfractures. However, there are less healed microfractures present in these vein types than there are in the syn-gold quartz veins.

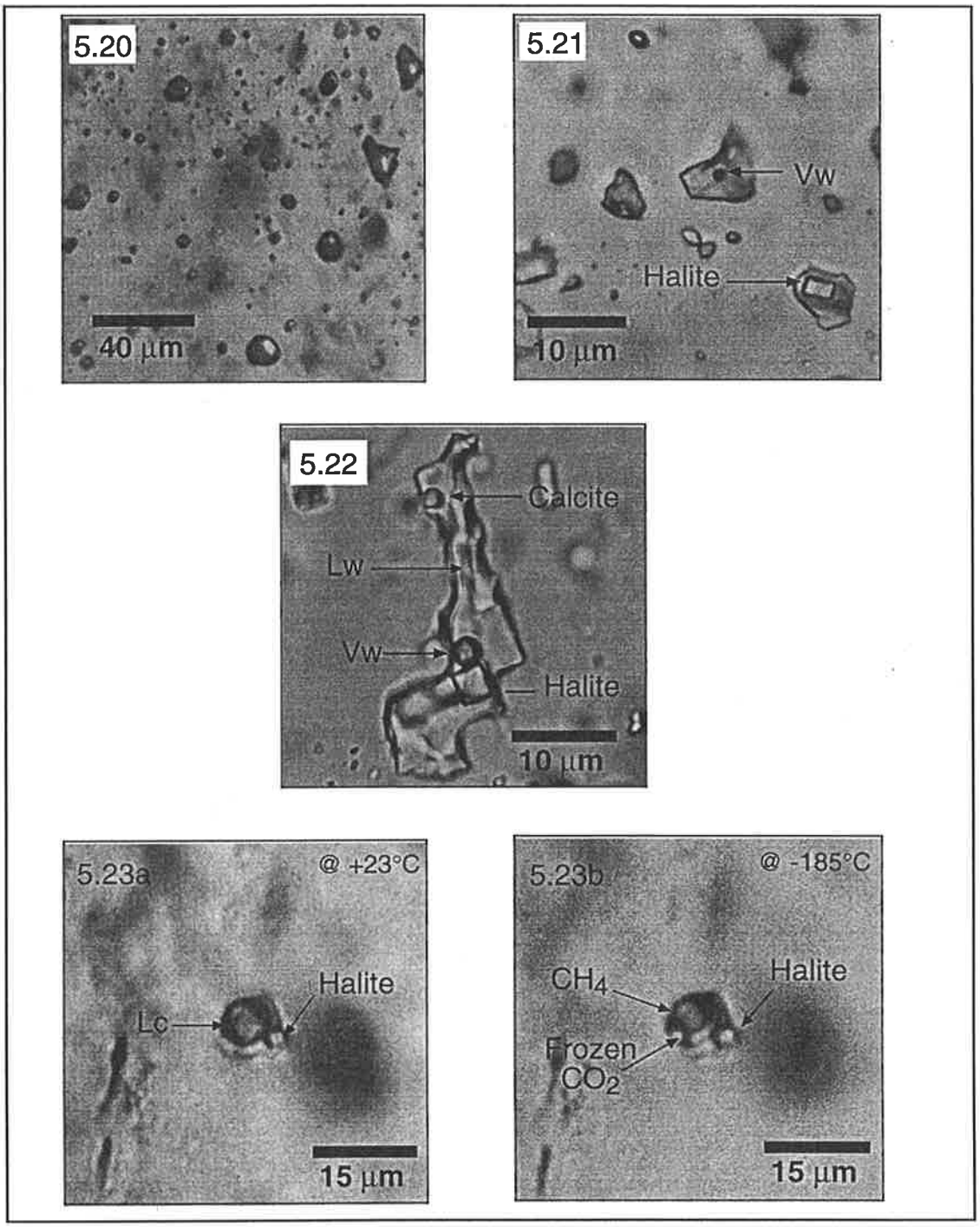


Figure 5.20. Three dimensional array of vapour rich fluid inclusions in a SV-type quartz vein.
Figure 5.21. Aqueous rich, halite bearing secondary fluid inclusions forming a three dimensional cluster (Vw = vapour water).
Figure 5.22. Unusually large, but very typical equi-dimensional secondary fluid inclusion containing two daughter minerals, calcite and halite (Vw = vapour water, Lw = liquid water).
Figure 5.23a and 5.23b. Photomicrographs of the same fluid inclusion taken at +23°C and at -185°C. At the lower temperature a CH_4 vapour phase is clearly present. This behaviour was rarely observed, but Tm_{CO_2} below -56.6°C was regularly observed, as was melting within the frozen vapour phase below -82.1°C (Lc = liquid CO_2).

5.3.4 Secondary fluid inclusions

Many secondary fluid inclusions are optically similar to type D fluid inclusions. However, secondary fluid inclusions are two-phase aqueous fluid inclusions that occur with or without one or more daughter minerals. The presence of these large and occasionally multiple daughter minerals together with their microthermometric behaviour distinguish these fluid inclusions from the type D fluid inclusions. These fluid inclusions almost always occur along fluid inclusion trails cutting across grain boundaries. However, in one sample, they were found to exist as a small cluster within a single quartz grain (Figure 5.21). Secondary fluid inclusions are predominantly small (< 8μm), but on occasion they may be as large as 45 μm in length. Their shape is typically equidimensional, but rounded and tabular secondary fluid inclusions are also common (Figure 5.22).

Secondary fluid inclusions have been found in both the syn-gold quartz veins and the SV-type quartz veins, but their absence from pre-gold Mo-type veins is somewhat enigmatic. It is likely that the small sample population of Mo-type veins examined contributes to this observation.

5.4 Rationale for layout of results and discussion

The different vein types have different levels of importance to this project. This is reflected in the time expended on analysis, interpretation and discussion of the fluid inclusions from different vein types, and is proportional to the importance of that vein type to this project. Fluid inclusions in shear and extensional quartz veins associated with gold mineralisation are the main focus of this part of the project. Their relationship to the transportation and precipitation of gold and their abundance in the mine demands that fluid inclusions in these vein types are examined more thoroughly. Consequently, attention is focussed on the syn-gold shear and extensional veins, and the results from this part of the investigation are discussed first. The results from microthermometry of fluid inclusions in the Mo-type veins and the SV-type veins are discussed in sections 5.6.2 and 5.6.3.

5.5 Understanding the formation of fluid inclusion types in late-orogenic, structurally-controlled gold deposits

Fluid inclusions selected for microthermometry formed either three dimensional clusters within individual quartz (± calcite ± albite) grains or were hosted along fluid inclusion trails that cross cut either one or many grains. Fluid inclusion trails that cut across many crystal boundaries are interpreted by Roedder (1984) as secondary fluid inclusions that form late in the geological history of the mine. However, Robert and Kelly (1987) and Boullier and Robert (1992) note that fluid inclusion trails in the Sigma mine are either aqueous-rich, H_2O-CO_2 mixtures or CO_2-rich fluid inclusions, and that all of these are related to the main gold-mineralising event. Similar fluid inclusion trails are present in the Junction gold mine. Aqueous and CO_2-rich fluid inclusion

trails may cross cut many crystal boundaries, or they may be terminated within or at grain boundaries. These fluid inclusion trails and their different fluid-phase compositions are thought to have formed by pressure fluctuations caused by seismic rupture and lithostatic depressurisation (Robert and Kelly, 1987; Sibson *et al.*, 1988).

5.5.1 The role of seismic rupture and lithostatic depressurisation in controlling phase separation in fluid inclusions

Pressure ± temperature fluctuations caused by seismic rupture and lithostatic depressurisation lead to fluid unmixing and are responsible for the different fluid inclusion types present in the quartz veins hosted in late-orogenic, structurally-controlled gold deposits (Roedder, 1984; Shepherd *et al.*, 1985; Robert and Kelly, 1987; Boullier and Robert, 1992; Robert *et al.*, 1995). Pressure and temperature changes to a parent fluid cause the liquid and vapour phases to become insoluble, leading to unmixing into a separate high density, more saline liquid and a low density, weakly saline vapour (Shepherd *et al.*, 1985; Naden and Shepherd, 1989).

Pressure and temperature fluctuations can be explained by using the fault valve model proposed by Sibson *et al.* (1988). This model involves shear stress variations related to fluid pressure fluctuations. It provides a framework for detailed analysis of the processes accompanying vein development and fluid inclusion entrapment (Boullier and Robert, 1992; Robert *et al.*, 1995). High angle reverse faults, like the one hosting mineralisation at Junction, appear to act as fluid-activated valves capping over-pressured portions of the crust, and promoting large cyclic fluctuations in fluid pressure. Seismic rupture along these faults is triggered by an increase in both fluid pressure and shear stress along the fault (Sibson *et al.*, 1988). The vein systems are therefore inferred to represent rupture-induced nucleation sites within the fault zones. Thus the fluid inclusions entrapped in these veins represent the related cycles in pressure fluctuation.

Boullier and Robert (1992) used experimental studies by Watson and Brenan (1987) to show that the wetting angle of CO_2 and H_2O controls which microfracture orientation each volatile will most likely occupy in each vein type. Sub-horizontal extension veins are characterised by vapour dominated fluid inclusions. These fluid inclusions are a result of fluid pressure reaching supra-lithostatic values. Incremental vertical opening of the sub-horizontal extensional veins and open space filling textures indicate that fluid pressure was high enough to support the rock column above the vein, i.e. fluid pressure was higher than the lithostatic load. Horizontal crack-seal openings and the development of horizontal microcracks (fluid inclusion planes) are features of incremental vertical opening. The fluid inclusion planes represent one of the growth stages of extensional veins during the pre-failure stage of the fault valve model (Figure 5.24; Boullier and Robert, 1992). The textures associated with the incremental vertical opening of the sub-horizontal extensional veins also occur in the shear veins where the extensional veins are connected to shear veins. The parent ore fluid infiltrates these sub-horizontal microfractures that open during extensional growth and remains there, precipitating mineral fibres, until seismic

rupture occurs.

Rupture along the shear vein induces a drop in fluid pressure, resulting in fluid unmixing, and the formation of new sub-vertical microfractures. At this point, the sub-horizontal extension veins collapse (this is estimated to be around 1% or less of the whole thickness of the vein), and are deformed by vertical shortening (Boullier and Robert, 1992). Given that the wetting angle of CO_2 is around 90° and the wetting angle of $H_2O \pm NaCl$ is around 40° (Watson and Brenan, 1987), the CO_2-rich fluid remains in the sub-horizontal microfractures that formed during the formation of the opening of the sub-horizontal extensional veins whereas the H_2O-NaCl fluid is expelled into the sub-vertical microfractures that form during seismic rupture (Boullier and Robert, 1992). Thus, sub-horizontal extensional quartz veins predominantly contain CO_2-rich fluid inclusions, whereas shear veins contain both CO_2-rich and H_2O-rich fluid inclusions. Pressure builds up again when the shear veins are resealed by mineral deposition, thus allowing extensional veins to form once again and to trap vapour rich fluid inclusions.

Boullier and Robert (1992) used this model to explain the generation of different fluid inclusions from a single homogeneous fluid. The fault valve model adequately explains why older growth increments within a vein contain a higher density of fluid inclusions than younger growth increments. Boullier and Robert (1992) found that plastic deformation and rotation of the quartz veins (particularly extensional veins) during subsequent deformation at the Sigma mine, Canada,

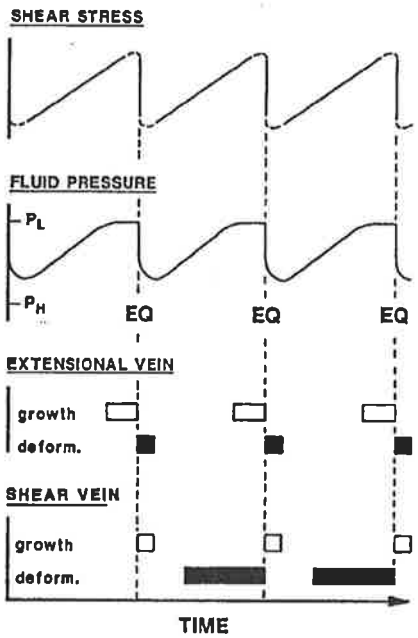


Figure 5.24 Diagram from Boullier and Robert (1992) showing shear stress variations and fluid pressure fluctuations with time, as predicted by the fault-valve model of Sibson *et. al.* (1988). PL, lithostatic pressure; PH, hydrostatic pressure; EQ, earthquake. Growth and deformation stages of the extensional and shear veins are correlated with these variations.

resulted in fluid inclusions containing:

- many different phase ratios and compositions,
- fluid inclusion trails that follow many different orientations, and
- many decrepitated, ruptured and rehealed fluid inclusions.

This can be seen in quartz vein samples collected from Junction (see Figures 5.10a and 5.10b). Further to this, Boullier and Robert (1992) found that shear veins consist of strained to highly deformed quartz grains that have either recrystallised into fluid inclusion-free quartz grains or contain deformed fluid inclusion planes, both of which are cross-cut by younger fluid inclusion planes. This indicates that the microfracturing and subsequent trapping of fluid, occurred intermittently during the whole history of the shear veins. This supports the findings of Robert and Brown (1986) who found that shear vein development comprises alternating episodes of opening, crystallisation and plastic - brittle deformation.

5.6 Results

The results obtained from all of the fluid inclusions studied are summarised in Table 5.1.

5.6.1 Syn-gold quartz veins

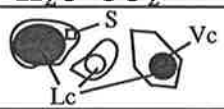
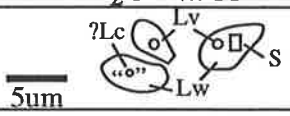
5.6.1.1 Freezing runs

5.6.1.1.1 Fluid solutes

Tfm_{ICE} for fluid solutes at Junction are widely distributed, indicating the presence of ions other than Na^+ in the solution. Many fluid inclusions at the Junction deposit have a Tfm_{ICE} that is below the Te for NaCl-H_2O (-20.8°C), suggesting the presence of K^+ and/or Mg^{2+} and/or Ca^{2+}. Tfm for fluid inclusions from syn-gold quartz veins ranges from -61.5°C to -13.2°C with a peak near -40°C. Type A fluid inclusions did not produce any low temperature solute data. Type B and C fluid inclusions hosted in shear and extensional veins have a Tfm_{ICE} that ranges from -61.5°C to -13.2°C (mean = -32.7°C, standard deviation = 10.2°C, n = 51). Type D fluid inclusions in shear and extensional veins have a Tfm_{ICE} that ranges from -54.4°C to -16.3°C (mean = -36.2°C, standard deviation = 11.0°C, n = 20; Figure 5.25).

The lower temperatures are possibly due to metastable $MgCl_2$ hydrates, and the clustering of data around -30°C to -40°C supports this. However, many fluid inclusions have Tfm below -47°C, indicating the presence of $CaCl_2$.

Experiments by Davis *et al.* (1990) show that fluids containing mixed Ca-Na-Mg solutions, have a Te that is significantly below the equilibrium eutectic of NaCl-H_2O (-20.8°C; Shepherd *et al.*, 1985). For H_2O-$MgCl_2$±NaCl and H_2O-CaCl±$MgCl_2$±NaCl systems, the eutectic

Sample	Type A CO_2 rich	Type B & C H_2O-CO_2	Type D H_2O-NaCl
			
Shear vein	none	Vol.% CO_2 = 20-80 $TmCO_2$ = -66.8 to -56.2°C $ThCO_2$ = 1.2 to 30.1°C Tfm = -61.5 to -18.6°C Tmice = -13.2 to -0.4°C Tmclath = 2.8 to 11.9°C Th = 213.1 to 388.6°C Td = 188.9 to 311.2°C Salinity = 2.1 to 17.1 wt% NaCl eq CO_2 density = 0.6 to 0.92 gm/cm^3	Vol.% CO_2 = 10 - 20 $TmCO_2$ = -58.7 to -56.1°C $ThCO_2$ = +9.8 to +26.1°C Tfm = -54.4 to -16.8°C Tmice = -9.6 to -0.8°C Tmclath = 6.0 to 12.9°C Th = 204.8 to 373.8°C Td = none Salinity = 1.4 to 30.5* wt% NaCl eq. CO_2 density = 0.7 to 0.83 gm/cm^3
Extensional vein	Vol.% CO_2 = 90$^+$ $TmCO_2$ = -57.6 to -56.7°C $ThCO_2$ = -6.6 to +5.2°C Tfm = none Tmice = none Tmclath = none Th = none Td = none Salinity = none CO_2 density = 0.9 to 0.97 gm/cm^3	Vol.% CO_2 = 20-80 $TmCO_2$ = -57.8 to -56.6°C $ThCO_2$ = +1.8 to +27.4°C Tfm = -36.2 to -13.2°C Tmice = -9.3 to -1.2°C Tmclath = 3.6°C Th = 366.6 to 389.9°C Td = 203.3 to 242.2°C Salinity = 2.1 to 13.8 wt% NaCl eq. CO_2 density = 0.75 to 0.91 gm/cm^3 Bulk density = 0.62 to 0.94 gm/cm^3	Vol.% CO_2 = 10 to 20 $TmCO_2$ = -56.9 to -59.2°C $ThCO_2$ = +10.8 to +24.2°C Tfm = -54.4 to -29.8°C Tmice = -23.1 to 0.0°C Tmclath = 22.2°C Th = 201.3 to 347.2°C Td = none Salinity = 0 to 23.3 wt% NaCl eq. CO_2 density = 0.76gm/cm^3
SV-type vein	Vol.% CO_2 = 90$^+$ $TmCO_2$ = -57.7 to -57.1°C $ThCO_2$ = +3.4 to +13.0°C Tfm = none Tmice = none Tmclath = none Th = none Td = none Salinity = none CO_2 density = 0.89 gm/cm^3	Vol.% CO_2 = 20-80 $TmCO_2$ = -58.8 to -56.9°C $ThCO_2$ = -8.1 to +24.4°C Tfm = none Tmice = none Tmclath = 5.0°C Th = 271.1 to 411.4°C Td = none Salinity = 9.0 wt% NaCl eq. CO_2 density = 0.74 to 0.89 gm/cm^3 Bulk density = 0.8 to 0.99 gm/cm^3	none

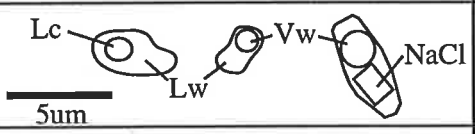
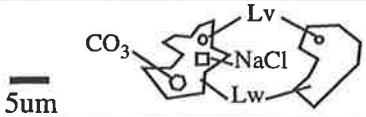
	Mo-type fluid inclusion H_2O-salt ∓ CO_2 ∓ solid	Secondary fluid inclusion H_2O-Salt
		
Mo-type vein	Vol.% CO_2 = 10 to 45 $TmCO_2$ = -62.5 to -58.6°C $ThCO_2$ = 19.5°C Tfm = -53.7 to -23.5°C Tmice = -23.2 to-7.2°C Tmclath = 7.6°C Th = 153.1 to 347.1°C Td = none Salinity = 10.7 to 41.5* wt% NaCl eq. CO_2 density = 0.79 gm/cm^3	Vw% = <5 -15 Tfm = -81.1 to -38.2°C Tmice = -43.0 to -5.7°C Th = 68.9 to 223.4°C Salinity = 8.81 to 33.5 wt% NaCl eq.

Table 5.1. Synthesis of microthermometric data from the four main vein types present in the Junction mine, W.A. $TmCO_2$ = melting temperature of the carbonic phase; $ThCO_2$ = homoginisation temperature of the vapour carbonic phase to the liquid carbonic phase; Tfm = temperature of first melt; Tmice = final melting temperature of ice or hydrate; Tmclath = melting temperature of the carbonic clathrate; Th(L) = homogenisation into the liquid phase; Th(V) = homogenisation temperature into the vapour phase; * = salinity estimated from dissolution temperature of daughter mineral. Lc = liquid CO_2; Lw = liquid water; Vc = vapour CO_2; Vw = vapour water; S = daughter mineral (unspecified); NaCl = halite daughter mineral; CO_3 = carbonate daughter mineral.

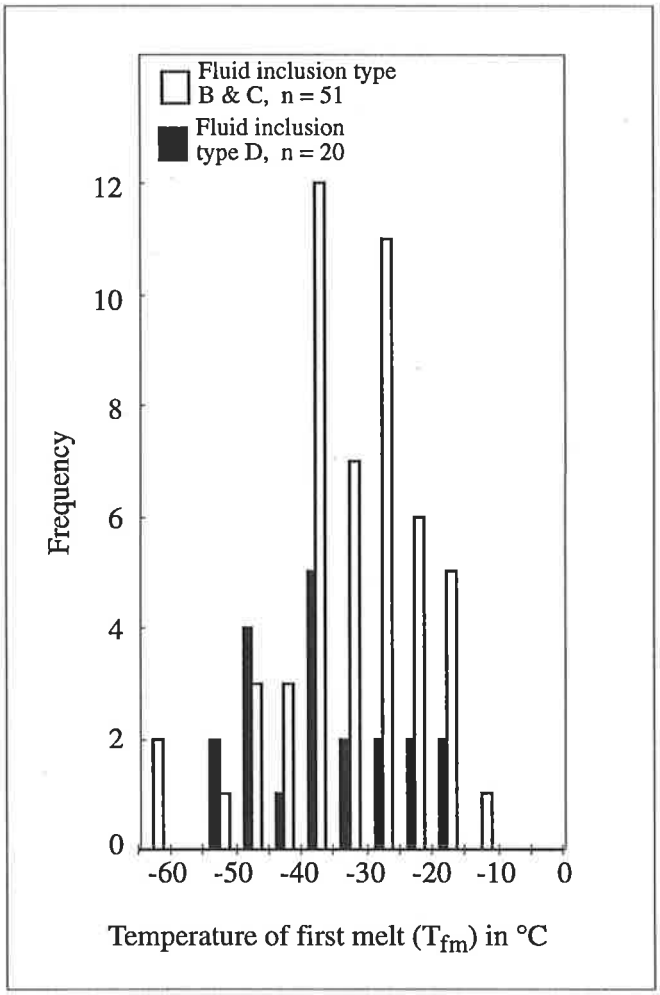


Figure 5.25. Histogram of T_{fm} for type B/C fluid inclusions and type D fluid inclusions. Note the peak shift in type D fluid inclusions towards lower temperatures. This indicates a weak increase in ions other than Na^+ in the fluid in these fluid inclusions.

temperatures are -35°C (first melt range -50°C to -34°C) and -52°C (first melt range -85°C to -47°C) respectively (Shepherd *et al.*, 1985; Davis *et al.*, 1990). Davis *et al.* (1990) observed that for these two systems, first melt temperatures can be significantly depressed, especially in the case of $CaCl_2$ where first melt temperatures may be as low as -80°C. First melting points below -50°C, have been observed for the H_2O-$MgCl_2$± NaCl system, but this is rare (Davis *et al.*, 1990). Such low temperatures would indicate the presence of a metastable salt hydrate.

Raman spectroscopy on a limited number of hydrates formed in fluid inclusions from the Junction mine indicate that Na^+ is the dominant cation species over Ca^{2+} and Mg^{2+}. No K^+ hydrates were identified from the few samples analysed by Raman spectroscopy. However, the presence of KCl is suggested by Tfm near the Te for the H_2O-NaCl-KCl system, i.e. -23.5°C. Hydrate species identified by Raman spectroscopy were $NaCl.2H_2O$ (hydrohalite), $MgCl_2.6H_2O$ or $MgCl_2.12H_2O$ and $CaCl.6H_2O$. In many cases, the presence of $MgCl_2.6H_2O$, and $MgCl_2.12H_2O$

in fluid inclusions is inferred from a broad Raman spectrum which peaks near the $MgCl_2.6H_2O$ and $MgCl_2.12H_2O$ wavelength. However, in some fluid inclusions, the hydrate identified was pure $MgCl_2.6H_2O$ and/or $MgCl_2.12H_2O$. A trace amount of $CaCl.6H_2O$ was detected in only one Type B fluid inclusion, but it formed the dominant hydrate species in many Type D fluid inclusions to further indicate the role of fluid unmixing. Raman spectroscopy also revealed that some gas-rich type A and type B fluid inclusions contained little or no water. This explains the lack of first and final melting temperatures of hydrates in many fluid inclusions.

Nevertheless, it is still not entirely clear which of these solutes travelled in solution with the pregnant ore fluid, and which of them have been enriched and trapped in fluid inclusions as a result of fluid - wall rock interactions. It is suspected that the ore fluid was moderately enriched in Na^+ whilst the Ca^{2+} and Mg^{2+} may have been buffered from the wall rock during fluid-wall rock interactions based on fluid inclusion studies from other late-orogenic, structurally-controlled gold deposits (Smith and Kesler, 1985; Robert and Kelly, 1987; Groves *et al.*, 1988; Clark *et al.*, 1989; Ho *et al.*, 1990a and 1990b; Cassidy and Bennett, 1993; Robert *et al.*, 1995; Boullier *et al.*, 1998) and the number of fluid inclusions that have final melt temperatures below -20.8°C. This interpretation is supported by Bennett and Barker (1992) who show that retrograde metamorphic reactions within thrust zones that cross-cut higher grade metamorphic assemblages in Norway have resulted in the production of chlorite and sericite at the expense of garnet, kyanite, staurolite and hornblende. Their observations show that a range of fluid salinities (27 - 50 wt% NaCl) dominated by Na and Cl, but containing appreciable contents of Ca, K, Fe and Sr, are the direct result of this fluid alteration of the wall rock. At Junction, it is thought that chlorite, forming at the expense of amphibole, and calcite-sulphide-quartz, forming at the expense of titanomagnetite±titanite and ilmenite during high fluid/rock ratios at 215°C to 400°C, resulted in the buffering of Mg and Ca from the wall rock into the original source fluid and was subsequently trapped in the fluid inclusions.

5.6.1.1.2 Daughter minerals

Daughter minerals in late-orogenic, structurally-controlled gold systems are rare (Groves *et al.*, 1988; Ho *et al.*, 1990a and 1990b). However, at Junction, daughter minerals can be found in pseudo-primary fluid inclusions by using a binocular microscope with high magnification and cross-polarised light. Daughter minerals are more common in shear veins than they are in extensional veins. The bright, pale green to pale blue colour associated with halite against the bright, high order pink, green and blue-purple coloured quartz (due to the thickness of the thin section wafer), plus their cubic to rectangular shape make them easy to distinguish under cross-polarised light. On rarer occasions, clear to light orange/brown irregularly-shaped daughter minerals can be found. These cannot be positively identified optically, but carbonate and bicarbonate mineral species have been identified by Raman spectroscopy.

Fluid inclusion types A, B and C rarely contain daughter minerals. However, when they are

present, they are generally very small. Raman spectroscopy has identified the carbonate and bicarbonates daughter minerals calcite or rhodochrosite (calcite and rhodochrosite have the same spectral signal under laser Raman; T. Mernagh pers. comm., 1997), siderite and nahcolite in these fluid inclusions. The origin of these daughter minerals in fluid inclusions containing large CO_2 volumes is unclear. However, it has been demonstrated that some of these fluid inclusions contain minor amounts of $CaCl_2$. Carbonate daughter minerals can form in an environment where CO_2 and Ca^{2+} are at saturation levels, if the partial pressure of CO_2 is high enough, because the supersaturation of Ca^{2+} is extremely low in these conditions (Roedder, 1984).

Type D fluid inclusions occasionally contain one and very rarely two daughter minerals. Fluid immiscibility during pressure fluctuations associated with fault valve reactions (Sibson *et al.*, 1988) led to the enrichment of solutes into the aqueous fluid phase and the development in some fluid inclusions of daughter minerals (Robert and Kelly, 1987). The presence of the carbonate and bicarbonate daughter minerals suggests that the mineralising fluid was neutral to weakly alkaline and possibly contained moderate CO_3^{2-} and HCO_3^{2-}.

5.6.1.1.3 Fluid-gas components (CO_2 - CH_4)

Raman spectroscopy was performed on 75 type A, B, C and D fluid inclusions from syn-gold quartz veins (Chapter 6). However, only CH_4 and CO_2 were identified in all fluid inclusions analysed. No other gases were detected by Raman spectroscopy, although it is likely that N_2 and H_2S/SO_4 are present in some fluid inclusions analysed. Therefore, the following section assumes the presence of CO_2 and CH_4 only.

CO_2 is not restricted to any specific fluid inclusion types at Junction. However, CO_2 clearly dominates type A, B and C fluid inclusions. CO_2 was regularly detected in type D fluid inclusions where the vapour phase occupied at least 10% of the fluid inclusion volume. Instantaneous solidification (freezing = collapsing of the oval to round shape) of the liquid occurs between -91.6°C and -111.0°C. Most of the type A, B and C fluid inclusions freeze close to -99°C. This indicates that the vapour phase observed at room temperature is indeed CO_2. Occasionally, this instantaneous solidification is less spectacular, and with further supercooling another vapour phase becomes apparent. This is interpreted to be CH_4 (Figure 5.23a and 5.23b). Upon freezing some type-D fluid inclusions, the vapour phase expands by as much as 100% before freezing of the liquid phase takes place between -40.3°C and -107.1°C, crushing the vapour phase in the process. The cause of this phenomenon is not well understood, but it is thought that the expansion of the vapour is pressure-induced as freezing results in the formation of ice which lowers the internal pressure of the fluid inclusion, thus allowing the vapour to expand in the newly created area.

Upon warming, most type A, B and C fluid inclusions display melting of the gas phase at or

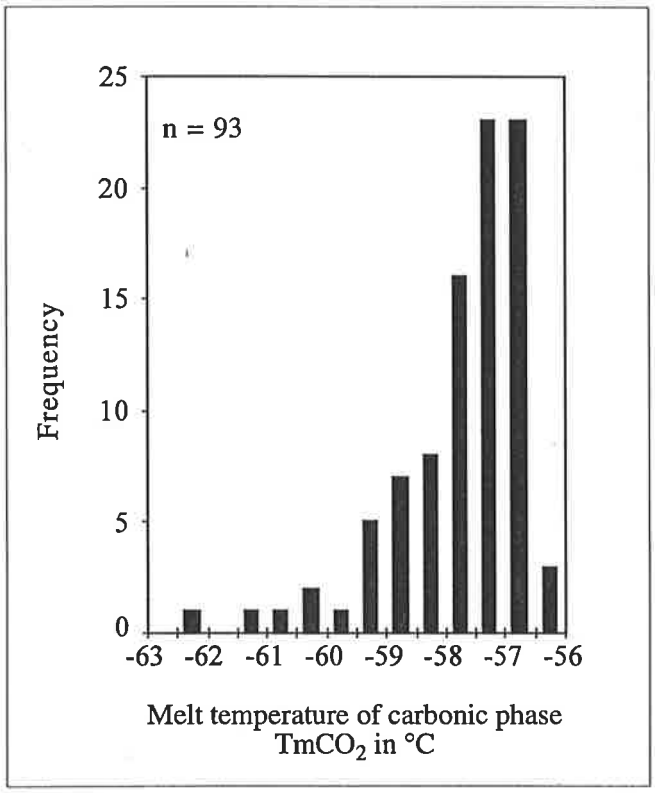


Figure 5.26. Histogram of T_mCO_2 for type A, B, C and D fluid inclusions. The one $TmCO_2$ value of -65.6°C is not plotted here.

near -56.6°C, indicating a CO_2 rich fluid. $TmCO_2$ values range from -55.5°C to -65.6°C (mean = -57.9°C, standard deviation = 1.7°C; n = 93) with a clear peak between -56.5°C and -57.5°C (Figure 5.26). Fluid inclusions with a $TmCO_2$ below that of the CO_2 invariant point indicate the presence of CH_4. In some fluid inclusions, changes in the liquid and vapour phases were observed between -97.6°C and -60.2°C before the melting of CO_2 occurred. This is also interpreted to indicate the presence of CH_4 in these fluid inclusions.

The experimentally-observed but only quantitatively accurate results of Hollister and Burrus (1976) and Burrus (1981) suggest that fluid inclusions that have $TmCO_2$ values between -60°C and -65°C contain 15 - 45 mol. % CH_4 at pressures between 30 and 50 bars. However, the strong partitioning of CH_4 into the vapour phase of CO_2 makes it difficult to estimate the bulk XCH_4 in a fluid inclusion from the temperature of disappearance of the solid CO_2 phase alone (Burruss, 1981). Experimental work by Zhang and Frantz (1992) on synthetic fluid inclusions containing H_2O-CO_2-CH_4 formed between 400°C and 600°C and 1000 and 3000 bars, show that as little 5.5 mol. % CH_4 will give $TmCO_2$ between -60.1°C and -62.9°C if trapped between 2000 and 3000 bars. This is further dependent on the volume of CO_2 present. Therefore, even semi-accurate estimates of the CH_4 volume may be erroneous because $TmCO_2$ is density-dependant. However, modelling of the invariant point data by MacFlinCor software (Brown and Hagemann, 1995) gave close approximations to the qualitative results obtained by Raman spectroscopy.

Raman spectroscopy revealed that some fluid inclusions in syn-gold quartz veins at Junction are CH_4 rich, containing up to 100 mol. % CH_4 in the vapour phase relative to CO_2. However, the majority of fluid inclusions analysed by Raman spectroscopy contain less than 2 mol. % CH_4 relative to CO_2 in the vapour phase. MacFlinCor software calculations estimate that CH_4 ranges from 0.00 to 0.19 mol. % CH_4 relative to CO_2. It can therefore be concluded that the Raman spectroscopy data and the MacFlinCor software calculations tend to favour the findings of Zhang and Frantz (1992), and that small quantities of CH_4 trapped at high pressures give the lower $TmCO_2$ values observed in microthermometry. This suggests that the ore fluid carried only trace amounts of CH_4 in solution. Fluid inclusions that contain up to 100% CH_4 are possibly a result of phase separation due to H_20-CO_2-CH_4 immiscibility (Naden and Shepherd, 1989). However, gas chromatography and elemental analysis coupled with mass spectrometry show levels of CH_4 frequently near 50^+ mol. % in certain positions within both shear and extensional vein types. This is discussed further in Chapters 12 and 13.

5.6.1.1.4 Salinity estimates calculated from the melting temperature of fluid hydrates

The implications that phase separation has on the interpretation needs discussing before the results of the Tm_{ICE} data is discussed. It has been demonstrated that fluid unmixing has occurred at Junction. This has resulted in four different fluid inclusion types, all associated with gold mineralisation, but all containing different phase ratios. Fluid inclusion types A and D are end member products of phase separation. It is therefore expected that type A fluid inclusions will contain no fluid solutes, and that type D fluid inclusions will contain above average concentrations of fluid solutes. If it is assumed that fluid inclusion types B and C are the closest representatives of the original parent ore fluid, then a better estimate of the parent ore fluid salinity should come from the Tm_{ICE} values of fluid inclusion types B and C. Tm_{ICE} data for type B and C fluid inclusions range from -0.8 to -13.2°C (mean = -6.0°C, standard deviation = 3.6°C, n = 29). Salinity estimates calculated from Tm_{ICE} data for type B and C fluid inclusions range from 1.4 wt% NaCl equivalent to 17.08 wt% NaCl equivalent (mean = 8.80 wt% NaCl equivalent, standard deviation = 4.6 wt% NaCl equivalent, n =29) (Figure 5.27).

Tm_{ICE} data for type D fluid inclusions range from 0.0 to -21.3°C (mean = -6.9 °C, standard deviation = 5.2°C, n = 17). These values correspond to fluid salinity estimates that range from 0 to 23.26 wt% NaCl equivalent (mean = 9.6 wt% NaCl equivalent, standard deviation = 6.1 wt% NaCl equivalent, n = 17) (Figure 5.27). A mean value of 8.20 wt% NaCl is obtained if the one outlier value of 23.26 wt% NaCl equivalent is removed from the data set. Either result illustrates that phase separation has not had a major effect on the overall salinity estimates of the type D fluid inclusions.

Assuming that fluid inclusion types B and C are the closest representatives to the homogeneous parent solution responsible for transporting and precipitating gold, the mean estimate should be close to the original parent fluid composition. However, it is important to note that these

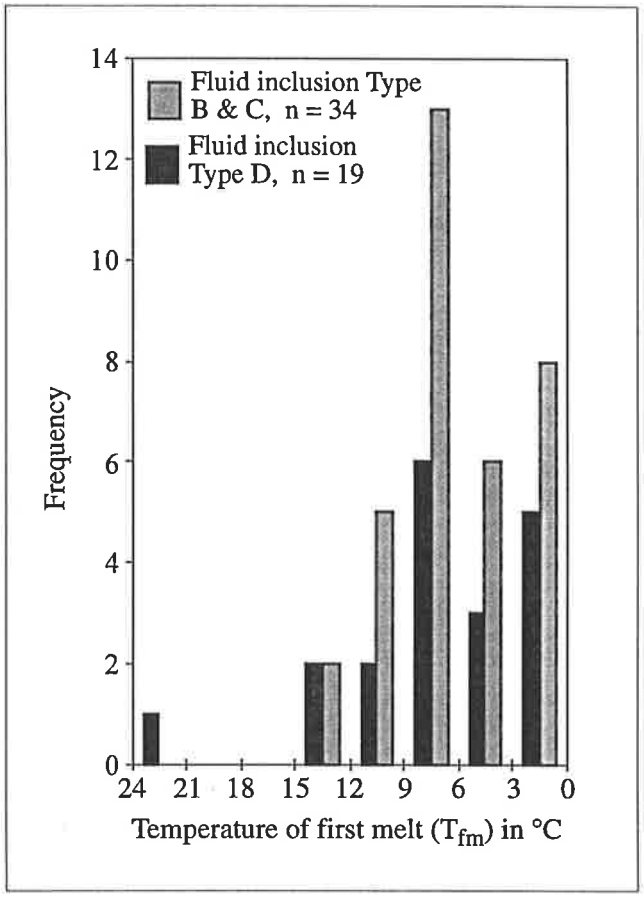


Figure 5.27. Histogram of T_{mICE} for type B/C fluid inclusions and type D fluid inclusions.

values are wt% NaCl *equivalent.*. Fluid inclusions that contain more than one salt component in solution give inaccurate wt% NaCl values. This is because the addition of just small amounts of chlorides lowers the Tm of $NaCl.2H_2O$ from +0.15°C (eg. the addition of KCl lowers the Tm of $NaCl.2H_2O$ from +0.15°C to -2.3°C). Divalent chlorides lower the Tm_{ICE} of $NaCl.2H_2O$ even further. Therefore if the presence of the divalent salts, $CaCl_2$ and $MgCl_2$ is due to wall-rock buffering and they did not form part of the original ore fluid, the mean value for type B and C fluid inclusions may be over estimating the true salinity of the parent fluid that existed prior to phase separation (i.e. the mean value for type B and C fluid inclusions is less than 8.8 wt% NaCl equivalent).

Only one type D fluid inclusion containing a halite daughter mineral was analysed by microthermometry. The dissolution temperature for this halite daughter mineral was 168.9°C. Using the salinity-dissolution plots of Shepherd *et al.* (1985), 168.9°C corresponds to a salinity of 30.5 wt% NaCl equivalent. This compares to the mean value of 8.80 wt% NaCl equivalent and 8.20 wt% NaCl equivalent obtained from type B-C fluid inclusions and type D fluid inclusions respectively.

The presence of a halite daughter mineral in solutions of $CaCl_2$ or $MgCl_2$, does not imply that the solution contains the same amount of NaCl as a saturated fluid in the pure system NaCl-H_2O (≥ 26 wt% NaCl) (Roedder, 1984). This is because the presence of the divalent cations lowers the saturation point of NaCl. An increase in $CaCl_2$ or $MgCl_2$ corresponds to an inverse decrease in NaCl saturation levels. Thus the formation of halite daughter mineral(s) will occur below 26 wt% NaCl (Potter *et al.*, 1977) in the presence of other salts. The presence of other cations introduces complications to these estimates, but, the overall salinity of the fluid inclusion can still be estimated as NaCl wt% equivalent (Shepherd *et al.*, 1985).

5.6.1.1.5 Salinity estimates calculated from the melting temperature of CO_2 clathrates

In fluid inclusions at the Junction mine, clathrates were assumed to be present when the vapour phase of a fluid inclusion was significantly distorted in shape and/or size, or the meniscus between the H_2O solution and vapour appeared slightly indented or exhibited a planar surface indicating the presence of invisible crystals at temperatures above 0°C. Clathrates that formed in fluid inclusions at the Junction mine have a wide Tm_{CLATH} range (2.8°C to 18.2°C). However, by eliminating those fluid inclusions that indicate the presence of CH_4, as indicated by a $TmCO_2$ that is significantly below -56.6°C (i.e. < -57.1°C; Zhang and Frantz (1992) found in their experimental work that some fluid inclusions with 100% CO_2 have an invariant point at -57.0°C even though no other gas was present in their synthetic fluid inclusions) a tight clustering of Tm_{CLATH} is observed between 2.8°C and 6.9°C (mean = 5.3°C, standard deviation = 1.4°C, n = 11). Salinity estimations from these values range between 6.2 and 12.1 wt% NaCl equivalent (mean = 8.1 wt% NaCl equivalent, standard deviation = 1.9 wt% NaCl equivalent, n = 11), and generally agree with the salinity estimations made from Tm_{ICE} values from Type B and C fluid inclusions (mean = 8.8 wt% NaCl equivalent) and Type D fluid inclusions (mean = 8.2 wt% NaCl equivalent).

Salinity estimates for Tm_{ICE} and Tm_{CLATH} from fluid inclusion types B and C are plotted in Figure 5.28.

5.6.1.2 Syn-gold quartz veins - density calculations for the two phase L + V fluid inclusions.

Bulk fluid inclusion densities were calculated using the computer program MacFlinCor (Brown and Hagemann, 1995). Given that type B and C fluid inclusions with vapour phases ranging between 40 and 60 vol. % are believed to be the closest representatives of the parent ore solution (Robert and Kelly, 1987; Ho *et al.*, 1990a and 1990b; Robert *et al.*, 1995, and this study), the range of fluid densities for this fluid inclusion type should approximate the density of the parent ore fluid. Therefore, fluid densities for the parent ore fluid range from 0.62 gm/cm^3 to 0.94 gm/cm^3 with a peak at 0.89 gm/cm^3 (mean = 0.84 gm/cm^3, standard deviation = 0.09 gm/cm^3, n = 21).

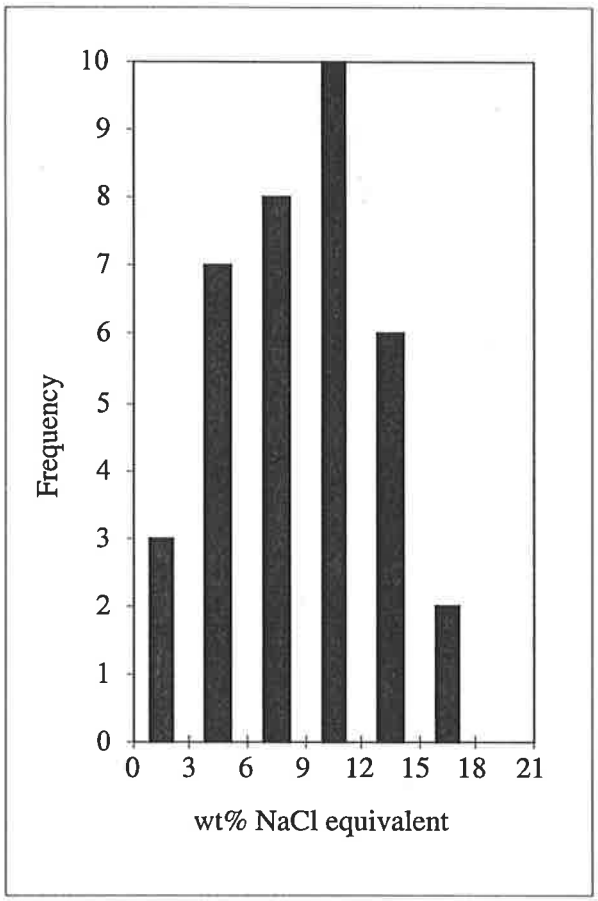


Figure 5.28. Salinity estimates in wt% NaCl equivalent for type B and C fluid inclusions only. Estimates calculated from T_{mICE} and T_{mCLATH} data.

5.6.1.3 Syn-gold quartz veins - homogenisation temperatures

5.6.1.3.1 Th CO_2

CO_2-rich fluid inclusions at Junction homogenise into the liquid state between -6.6°C and 30.1°C with peak distributions at approximately 3°C, 13°C and 25°C (mean = 16°C, standard deviation = 9.8°C, n = 29; Figure 5.29). Homogenisation into the liquid state places the CO_2 density above its critical value of 0.468 gm/cm^3. Estimates for the density of CO_2 at Junction were calculated from CO_2 - density diagrams of Shepherd *et al.* (1985) and range from 0.60 gm/cm^3 to 0.97 gm/cm^3 with peak distributions at approximately 0.92 gm/cm^3, 0.85 gm/cm^3 and 0.72 gm/cm^3 (mean = 0.8 gm/cm^3, standard deviation = 0.09 gm/cm^3, n = 29).

The peak distributions coincide with particular syn-gold fluid inclusions and their vein types. These relationships are illustrated in Figure 5.29. Fluid inclusions that have CO_2 densities peaking near 0.92 gm/cm^3 are predominantly found in type A fluid inclusions in extensional quartz veins only. They indicate that the CO_2 was trapped in these fluid inclusions under high pressure. Three of the 19 type B and C fluid inclusions analysed have densities near 0.9 gm/cm^3, indicating that they too were trapped at high pressures. Two of these are hosted in extensional

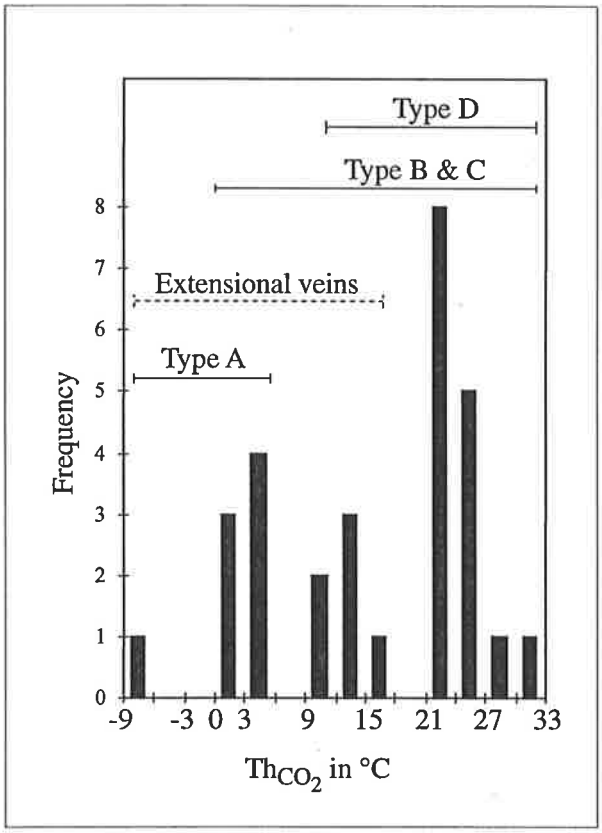


Figure 5.29. Histogram of Th_{CO_2} in °C for all syn-gold fluid inclusion types. Type A fluid inclusions from two extension veins have a narrow and low homogenisation range, indicative of phase separation under lithostaticpressure. Other fluid inclusion types have a broader range of values. Ten of twelve suitable Th_{CO_2} values plot within the range marked Extensional veins.

quartz veins. The remaining peaks at 0.85 gm/cm^3 and 0.72 gm/cm^3 are found in both shear and extensional veins with a weak coincidence between the peak at 0.72 gm/cm^3 and shear veins. Ten of the twelve fluid inclusions suitable for evaluation from five extensional veins have CO_2 densities that are greater than 0.85 gm/cm^3. This indicates that most fluid inclusions trapped in extensional veins were trapped under pressure. This CO_2 density data fits the fault valve model proposed by Sibson *et al.* (1988) and discussed by Boullier and Robert (1992) to describe fluid inclusion formation. The highest CO_2 densities conform to extensional vein growth and thus higher lithostatic pressures, whilst the lowest CO_2 densities conform well with periods of low lithostatic pressure or hydrostatic pressure (Figure 5.24).

5.6.1.3.2 Temperature of total homogenisation and entrapment (Th and Tt)

Th values derived from 60 fluid inclusions associated with gold quartz veins range from 201.3°C to 389.9°C (Figure 5.30). Upon heating, H_2O-CO_2 fluid inclusions often decrepitate prior to homogenisation. However, homogenisation temperatures were obtained for 42 H_2O-CO_2 fluid

inclusions. Total homogenisation into both the liquid and vapour phase has been observed in most samples.

Decrepitation (Td) of many CO_2-bearing fluid inclusions was observed during heating runs. This was mainly noted in the vapour-rich fluid inclusions, but also occurred occasionally in fluid inclusions with less than 25 vol. % vapour. Decrepitation of fluid inclusions is usually the result of the internal pressure within the fluid inclusion exceeding the tensile strength of the brittle host mineral (Roedder, 1984). The basic assumption that the temperature of decrepitation (Td) is approximately equal to Th (Burlinson, 1991) is incorrect because Td is a function of many variables other than Th. However, it can be assumed that Td is the minimum temperature of entrapment for that fluid inclusion.

Type B fluid inclusions generally decrepitate before homogenisation because of their higher CO_2 volume. Eighteen type B fluid inclusions were analysed for Th. Eight of these fluid inclusions decrepitated between 203.3°C and 297.8°C. The other ten type B fluid inclusions homogenised between 213.1°C and 389.9°C. Type C fluid inclusions also have a tendency to decrepitate, but not to the same extent as the type B fluid inclusions. This is because type C fluid inclusions contain < 50 vol. % CO_2. Forty-eight type C fluid inclusions were analysed for Th. Sixteen of these fluid inclusions decrepitated between 188.9°C and 311.2°C. Thirty-two type C fluid inclusions homogenised between 215.3°C and 388.6°C. Collectively, type B and C fluid inclusions homogenise into either the liquid phase or vapour phase between 213.1°C and 389.9°C, with a peak at 300°C ± 15°C (mean = 301.4°C, standard deviation = 23.3°C, n = 42) (Figure 5.30). Only two type B/C fluid inclusions hosted in extensional veins did not decrepitate, and homogenisation into liquid phase occurred at 366.6°C and 389.9°C in these fluid inclusions.

Eighteen type D fluid inclusions were analysed for Th. Type D fluid inclusions have a similar range of homogenisation temperatures to fluid inclusion types B and C (201.3°C to 373.8) (mean = 279.9°C, standard deviation = 50.9°C, n = 18) (Figure 5.30). All but six type D fluid inclusions homogenise into the liquid phase. Dissolution of the one halite daughter mineral observed (ThNaCl) occurred at 168.9°C, well below the final Th for that fluid inclusion at 348.8°C.

Collectively, much of the Th data is supported by temperature estimates from stable isotope analysis of co-existing quartz and calcite. Temperature calculations from ^{18}O stable isotope values of seven samples containing co-existing calcite and quartz give temperature estimates ranging from 190°C to 460°C (mean 345°C; see Chapter 9). However, the mode of values are skewed toward 400°C. This temperature range (near 400°C) is in reasonable agreement with the majority of fluid inclusions analysed by microthermometry given that fluid inclusion homogenisation temperatures are often lower than the isotopic temperature estimates by up to 80°C (Kerrich, 1989).

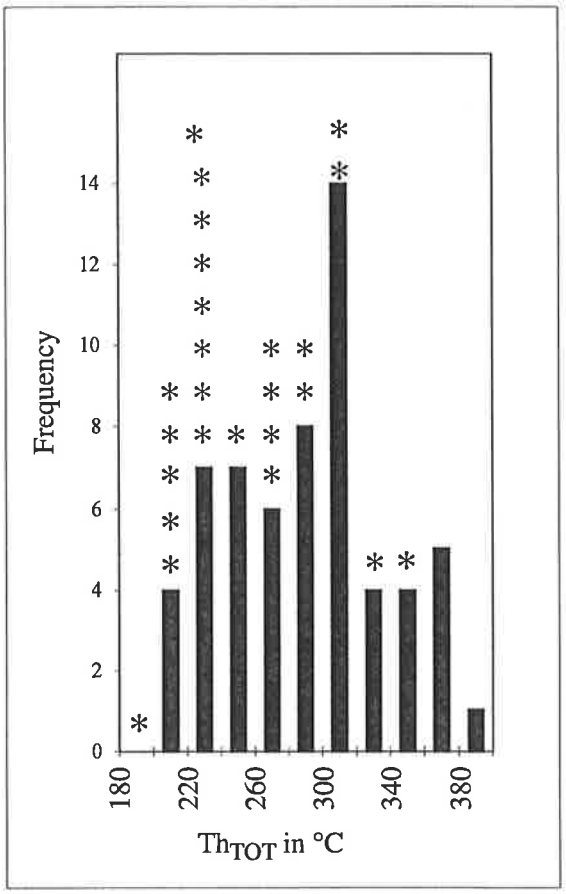


Figure 5.30. Homogenisation and decrepitation (∗) temperatures for all fluid inclusion types in syn-gold quartz veins. Each ∗ represents one decrepitated fluid inclusion.

Th data from some aqueous, type D fluid inclusions do not fit the model range for Archaean, Yilgarn late-orogenic, structurally-controlled gold mineralisation (300°C to 400°C, Ho *et al.*, 1990a and 1990b) and must be explained. Robert and Kelly (1987) were the first to make the connection between the aqueous fluid inclusions and the CO_2-rich fluid inclusions typically associated with this style of gold mineralisation. Although it is unreasonable to assume that none of these fluid inclusions are the secondary type fluid inclusions proposed by Roedder (1984), their fluid composition can be strongly linked to the other three fluid inclusion types (see below).

Robert and Kelly (1987) propose two alternative explanations for the observed low Th of the aqueous fluid inclusions at the Sigma gold mine, Canada. Both theories rely on the fact that after unmixing, the aqueous and CO_2-rich fluids were trapped separately along different fractures. This separate entrapment of two immiscible fluids implies that once isolated in individual fractures, the two fluids are no longer in equilibrium with each other. As a result, the homogenisation temperatures of these fluid inclusions do not represent the temperature of the parent fluid.

The first explanation assumes that homogenisation temperatures of the aqueous fluid inclusions may require a pressure correction (Robert and Kelly, 1987). Fluid inclusions containing no more than a few mole percent of CO_2, and trapped at 2000 bars will require some pressure correction. Using data from Bowers and Hegleson (1983b), Robert and Kelly (1987) imply that a pressure correction of 50°C to 200°C may be applicable to these fluid inclusions, depending on their homogenisation temperature and their CO_2 content. Such pressure corrections result in entrapment temperatures in better agreement with the temperature range obtained from the H_2O-CO_2 inclusions.

The second explanation (Robert and Kelly, 1987) involves CO_2 effervescence from the aqueous fluid as a result of pressure fluctuations at the time of entrapment. The homogeneous fluid must be saturated with respect to CO_2 prior to unmixing and entrapment of the immiscible fluids along different microfractures. The lithostatic pressure decreases and CO_2 begins to exolve from the fluid due to its decreased solubility as an aqueous fluid ascends through the vein system (from point 1 to point 2, Figure 5.31A). This lowers the CO_2 content of the aqueous fluid, but increases its overall salinity. The pressure of the fluids will fluctuate from lithostatic to hydrostatic during seismic rupture due to the tectonic setting of the deposit. This is consistent with the fault valve model proposed by Sibson *et al.* (1988). A rapid and large decrease in fluid pressure (from point 2 to point 3 or 5 depending on the size of the pressure release, Figure 5.31B) makes the CO_2 less soluble, and it effervesces from the aqueous phase, becoming trapped in sub-horizontal microfractures (Boullier and Robert, 1992). The remaining aqueous phase is now purged of its original CO_2, but is trapped along open microfractures. As the fluid within the

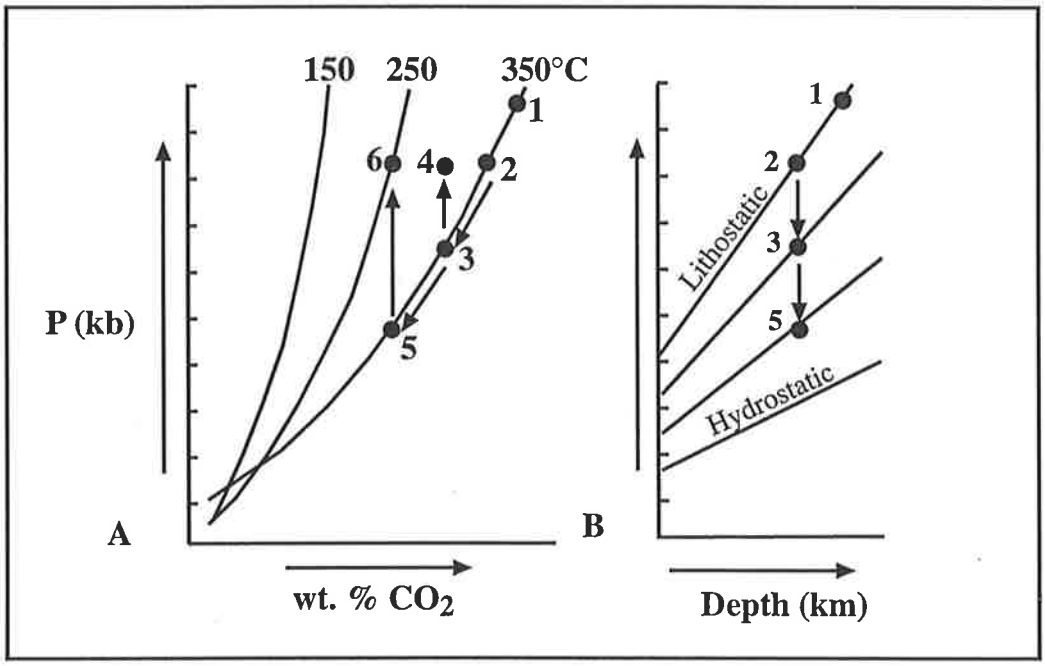


Figure 5.31 A: Solubility of CO_2 in a 20 wt. % NaCl aqueous solution as a function of pressure and temperature (Robert and Kelly, 1987 from data by Takenouchi and Kennedy, 1965). B: Variation of lithostatic and hydrostatic pressures as a function of depth.

shear zone again rises to lithostatic pressure (Sibson *et al.*, 1988; Boullier and Robert, 1992) (point 3 or 5 to points 4 or 6, Figure 5.31A), the remaining aqueous fluid, now under-saturated in CO_2 may become trapped at these lithostatic pressures. If this occurs, then the aqueous fluid will have a homogenisation temperature that is lower than its parent Th. Depending on the size of the pressure decrease associated with the seismic rupture, the volume of CO_2 loss is proportional to the lowering of the aqueous phases new homogenisation temperature. The lowest Th values assume that the aqueous phase is not trapped prior to lithostatic pressure being reached. However, the pressure fluctuations that occur within a shear zone clearly show how a spread of Th data can be obtained.

Alternatively, the Th of type B and C fluid inclusions is thought to be at or below the temperature at which the fluid was trapped in nature due to the presence of other components in the fluid inclusions. The presence of NaCl or other solutes trapped in H_2O-CO_2±CH_4 type B and C fluid inclusions complicates Tt and Pt estimates. Takenouchi and Kennedy (1965) and Bowers and Helgeson (1983a) conclude that the solubility of CO_2 in salt solutions depends on the concentration of that salt. Gehrig (1980) in Bowers and Helgeson (1983a) found that the addition of only 6 wt% NaCl extends the region of immiscibility in the system H_2O-CO_2-NaCl to ≥ 700°C at 500 bars and molar fractions of $CO_2 \leq 0.1$. This infers that a homogeneous solution will unmix into a CO_2-H_2O phase and a H_2O-NaCl phase as soon as the pressure and/or temperature drops below the critical point for that solution. Thus the salinity of the solution controls the solubility of that solution and this will be reflected by the Th of any fluid inclusions that trap this solution.

The ambient wall rock temperature of the deposit is unlikely to vary significantly during vein development, so differences in fluid pressure at different stages in vein development should be recorded as differences in densities in fluid inclusions trapped at different stages (cf. Robert *et al.*, 1995). This is true for fluid inclusions at Junction where type B and C fluid inclusions have lower bulk densities and an overall higher Th than type D fluid inclusions. It can be concluded, therefore, that the wide range of Th values observed is due to the density of the fluid inclusion and not due to the temperature of entrapment. Thus, homogenisation temperatures from fluid inclusions at Junction only indicate the minimum trapping temperature and not Tt.

Further to these observations, Gehrig (1980) and Bowers and Helgeson (1983a) present experimental and thermodynamic calculations for the system H_2O-CO_2-NaCl and note that a fluid containing 6 wt% NaCl relative to H_2O + NaCl, has a two-phase region for an H_2O-CO_2 fluid extending up to 400°C and 2000 bars. This imposes a minimum pressure and a maximum temperature for the fluid inclusions at Junction.

However, further consideration must be paid to the addition or presence of other solutes and vapours present in the fluid inclusions at Junction (e.g. $CaCl_2$ and CH_4). Krader and Frank (1987) found that the addition of NaCl and/or $CaCl_2$ to the H_2O-CH_4-NaCl and H_2O-CH_4-CaCl

systems shifts the CO_2-H_2O or CH_4-H_2O solvus peak to higher temperatures and increases the size of the two phase liquid vapour field. Limited thermodynamic experimental data by Krader and Frank (1987) and Naden and Shepherd (1989) indicate that only small amounts of CH_4 (≤ 5 mol. %) are soluble in aqueous brines over a wide range of pressures and temperatures (up to 3000 bar and 400°C). At temperatures below 400°C, CH_4 solubility is decreased with increased salinity. Thus in similarity with the H_2O-CO_2-NaCl system, at temperatures below 400°C, a parent H_2O-CH_4-NaCl fluid may trap homogeneous end members or unmix to produce and trap immiscible fluids.

Duan *et al.* (1992a, 1992b) present equations of state for mixtures of CH_4-CO_2-H_2O. They found that the addition of CH_4 to the H_2O-CO_2 system substantially affects conditions that influence Th. In particular, the presence of small volumes of CH_4 (≤ 4 vol. %) in the CO_2 phase raises the internal pressure within the fluid inclusion and leads to a lowering of the homogenisation temperature. Zhang and Frantz (1992) found that low concentrations of CH_4 (5.5 mol. %) in the H_2O-CO_2 system has a dominant effect on Th. The presence of CH_4 lowers the slope of the isochores and steepens the liquid-vapour curves, which complicates the determination of the bulk composition of C-O-H fluid inclusions by microthermometry. This in turn leads to erroneous Pt and Tt estimates. The presence of CH_4 in fluid inclusions reduces the usefulness of microthermometry to determining measurements of vapour-liquid homogenisation only.

However, the application of MacFlinCor software (Brown and Hagemann, 1995) incorporates the theoretical and experimental work by Takenouchi and Kennedy (1965), Jacobs and Kerrick, (1981), Bowers and Helgeson (1983a, 1983b), Thiery *et al.* (1994), Van den Kerkhof and Thiery (1994) and others, to model fluid inclusion data to give bulk fluid densities and minimum pressure and temperature estimates. Applying the MacFlinCor program (Brown and Hagemann, 1995) to fluid inclusions relative to the H_2O-CO_2-CH_4-NaCl system, a pressure range of 770 to 4437 bars is obtained from 16 fluid inclusions. However, most fluid inclusions indicate pressures between 1300 and 2900 bars (Appendix VI). This places Junction in the mesozonal (5 - 10 km depth) range of formation.

5.6.2 Pre-gold, Mo-type quartz veins

Ten Mo-type fluid inclusions from two Mo-type quartz veins were analysed by microthermometry. Mo-type fluid inclusions are typically small, tabular to rounded in shape and often contain one or more daughter minerals. They have been described in detail in Section 5.3.1. Only some Mo-type fluid inclusions appear to have any CO_2 present at room temperature, but Raman spectroscopy suggests that all Mo-type fluid inclusions contain minor to significant amounts of CO_2 and CH_4 in the vapour phase. These fluid inclusions and their fluid characteristics are listed in Table 5.1 (p. 104).

5.6.2.1 Freezing runs

5.6.2.1.1 First melt (Tfm), eutectic temperature (Te)

5.6.2.1.1.1 Fluid solutes

Mo-type fluid inclusions have a Tfm that suggests the presence of Na^+, K^+ and/or Mg^{2+} and/or Ca^{2+}. Tfm for the Mo-type fluid inclusions range from -53.7°C to -23.5°C, with a peak forming near -45°C (mean =39.8°C, standard deviation = 9.3°C, n = 10). These temperatures indicate that $CaCl_2$ is a major ion present in solution along with Mg^{2+} and Na^+. H_2O-MgCl±NaCl and H_2O-CaCl±MgCl±NaCl systems have eutectic temperatures at -35°C (first melt range -50°C to -34°C) and -52°C (first melt range -85°C to -47°C) respectively (Shepherd *et al.*, 1985; Davis *et al.*, 1990). Unfortunately, Raman microanalysis on these hydrates was not performed.

5.6.2.1.1.2 Daughter minerals

Daughter minerals in these fluid inclusions are common. In some cases, multiple daughter minerals are present (Figure 5.8). The cubic to rectangular shape of halite makes it easy to distinguish in most fluid inclusions. Raman spectroscopy of the daughter minerals observed confirms the presence of halite. However, other non-halite daughter minerals remain as unidentified carbonate minerals due to their ambiguous spectral signal.

5.6.2.1.1.3 Fluid-gas components (CO_2 - CH_4)

Two of ten fluid inclusions in the Mo-bearing quartz veins froze at -99.7 and -104.2°C indicating that the vapour phase observed at room temperature is probably CO_2. Further to this, four of the ten fluid inclusions melted near -56.6°C confirming that at least some fluid inclusions contain a CO_2-rich fluid. $TmCO_2$ values range from -58.6°C to -62.5°C. All four fluid inclusions have a $TmCO_2$ below that of the CO_2 invariant point, indicating the presence of CH_4. One fluid inclusion displayed melting behaviour at -81.4°C. This is close to the critical point of CH_4, -82.1°C. Laser Raman spectroscopy indicates that some Mo-type fluid inclusions contain considerable CH_4 volumes (19 - 75 mol. %) in the vapour phase.

5.6.2.1.2 Final melt temperature (Tm)

5.6.1.1.2.1 Salinity estimates calculated from the melting temperature of fluid hydrates

Tm_{ICE} data ranges from -7.2°C to -23.2°C (mean = -14.3°C, standard deviation = 4.9°C, n = 9). These values correspond to fluid salinity estimates that range from 10.73 - 24.83 wt% NaCl equivalent (mean = 17.63 wt% equivalent, standard deviation = 4.3 wt% NaCl equivalent, n = 9). Salinity estimates from the dissolution temperature (see below) of two daughter minerals, using the solubility curves of Shepherd *et al.* (1985), are estimated at 41 and 42 wt% NaCl equivalent.

5.6.1.1.2.2 Salinity estimates calculated from the melting temperature of CO_2 clathrates

Only one fluid inclusion formed a CO_2 clathrate which melted at 7.6°C. However, the presence of CH_4 in the vapour phase of this fluid inclusion, indicated by a $TmCO_2$ of -58.6°C, precludes

it from giving an accurate salinity estimate.

5.6.2.2 Homogenisation temperatures

5.6.2.2.1 Th CO_2

One CO_2-rich Mo-type fluid inclusion homogenised into the liquid state at 19.5°C. The presence of CH_4 in this fluid inclusion precludes a CO_2 density calculation from being determined.

5.6.2.2.2 Temperature of total homogenisation and entrapment (Th and Tt)

Eleven Mo-type fluid inclusions were analysed for Th. Homogenisation occurred between 153.1°C and 347.1°C. Most fluid inclusions homogenise at 210°C ± 15°C (mean = 248.1°C, standard deviation = 62.3°C, n = 11). Homogenisation of the vapour into the liquid phase occurred between 153.1°C and 313.7°C. Dissolution of halite daughter minerals in two fluid inclusions occurred at 339.8°C and 347.1°C. In both cases, ThNaCl was greater than Th. Therefore, the homogenisation of temperature of the fluid inclusion was accepted as being ThNaCl.

5.6.2.3 Summary for Mo-type fluid inclusions

Many of the Mo-type fluid inclusions indicate that the fluid transporting the Mo to the site of mineralisation was highly saline. However, the wide range of fluid salinities estimated from these fluid inclusions (10.7 - 41.5 wt% NaCl equivalent) is enigmatic. Mo-type fluid inclusions do not show strong evidence for phase separation/fluid unmixing leading to weakly saline and strongly saline fluid inclusions. Neither do the fluid inclusions show variations in the proportion of vapour present. Limited numbers of fluid inclusions contain weakly variable fluid-vapour ± solid phases, but most have constant compositional phases that do not indicate boiling and fluid unmixing. Given this, it is likely that a pressure correction needs to be applied to obtain the correct Tt. However, the data modelling needed to determine the correct Tt from a H_2O-CO_2-NaCl ± CH_4 solution that has undergone partial or total fluid unmixing is complex, and given the insignificance of these veins to gold mineralisation at Junction, trapping temperatures and pressures will not be considered further.

The Mo-bearing quartz veins are clearly pre-gold mineralisation. It is possible that they could be related to the numerous felsic porphyries that exist throughout the mine. However, a link cannot be made between the two without a detailed study into the Mo mineralisation. Nevertheless, it is interesting to speculate on the relationship between these H_2O-CO_2-NaCl-CH_4 Mo-type fluid inclusions and the gold carrying fluid inclusions that have such similar fluid compositions.

5.6.3 Post-gold, SV-type quartz veins

Fifteen SV-type fluid inclusions from four SV-type quartz veins were analysed by microthermometry. SV-type fluid inclusions are compositionally similar to syn-gold fluid inclusions types and have been classified similarly in Section 5.3.3. All SV-type fluid inclusions

are CO_2-rich or H_2O-CO_2 fluid inclusions. These fluid inclusions correspond to the classification given to syn-gold type fluid inclusions (i.e. type A, B and C) and their fluid characteristics are listed in Table 5.1 (p 104).

5.6.3.1 Freezing runs

5.6.3.1.1 First melt (Tfm), eutectic temperature (Te)

5.6.3.1.1.1 Fluid solutes

No SV-type fluid inclusions formed ice or hydrates upon super-cooling. Therefore no Tfm or Tm data was recorded. One SV-type B fluid inclusion formed a CO_2 clathrate which melted at 5.0°C indicating that a moderately saline liquid phase (9 wt% NaCl equivalent) may have been present.

5.6.3.1.1.2 Fluid-gas components (CO_2 - CH_4)

Vapour-rich SV-type fluid inclusions freeze upon cooling between -93.8°C and -99.6°C, indicating that CO_2 is the dominant vapour phase present. All 15 SV-type fluid inclusions melted near -56.6°C confirming that the vapour-rich fluid inclusions were CO_2-rich. $TmCO_2$ values range from -56.9°C to -58.8°C (mean = -57.5°C, standard deviation = 0.5°C, n = 14). All fluid inclusions have a $TmCO_2$ below that of the CO_2 invariant point, indicating the presence of CH_4. Laser Raman spectroscopy indicates that many SV-type fluid inclusions contain considerable CH_4 volumes (0 - 43 mol. %) in the vapour phase. Estimations of CO_2 : CH_4 ratios using MacFlinCor software (Brown and Hagemann, 1995) on $TmCO_2$ values, indicate that SV-type fluid inclusions contain between 1 and 8% CH_4 relative to CO_2.

5.6.3.2 Homogenisation temperatures

5.6.3.2.1 Th CO_2

CO_2-rich fluid inclusions in the SV-type veins homogenise into the liquid state between -8.1°C and 24.4°C. Eliminating those fluid inclusions that indicate the presence of CH_4 (as indicated by a $TmCO_2$ that is significantly below -56.6°C), estimates of CO_2 densities in SV-type fluid inclusions range from 0.74 gm/cm^3 to 0.89 gm/cm^3.

5.6.3.2.2 Temperature of total homogenisation and entrapment (Th and Tt)

Th of eight SV-type fluid inclusions was determined. Homogenisation occurred between 271.1 and 411.4°C, with a peak at 300 ± 25°C (mean = 314.7°C, standard deviation = 44.7°C, n= 10).

5.6.3.3 Summary on SV-type fluid inclusions

SV-type fluid inclusions are all vapour-rich (>60 vol. % vapour). Aqueous fluid inclusion trails cutting across the quartz grain boundaries are not abundant. It is possible that effervescence and fluid unmixing may have taken place in a similar style to that which formed the vapour-rich fluid inclusions in the syn-gold extension veins (i.e. formation at lithostatic pressure), but the fluid inclusion trails in the SV-type quartz veins are believed to be true secondary fluid

inclusions and vapour-rich fluid inclusion trails are rare.

In the context of this project, further work on the fluid inclusions of this vein type is not warranted, and will not be discussed further.

5.6.4 Secondary fluid inclusions

Secondary fluid inclusions are typically two-phase aqueous fluid inclusions that occur with or without one or more daughter minerals. They almost always occur along planar fluid inclusion trails cutting across grain boundaries and can usually be distinguished from other aqueous fluid inclusions by their typically equidimensional shape.

5.6.4.1 Freezing runs

5.6.4.1.1 First melt (Tfm), eutectic temperature (Te)

5.6.4.1.1.1 Fluid solutes

Secondary fluid inclusions have low Tfm values. Tfm for secondary fluid inclusions range from -81.1°C to -28.2°C, with two peaks forming near -65°C and -40°C (mean = -56.6°C, standard deviation = 14.1°C, n = 42) (Figure 5.32). These temperatures indicate that Ca^{2+} is a dominant ion present in solution along with Na^{+}. H_2O-MgCl ± NaCl and H_2O-CaCl±MgCl±NaCl systems, have eutectic temperatures at -35°C (first melt range -50°C to -34°C) and -52°C (first melt range -85 to -47°C) respectively (Shepherd *et al.*, 1985; Davis *et al.*, 1990) which complements the data from secondary fluid inclusions. First melting points below -50°C have been observed for the H_2O-$MgCl_2$±NaCl system, but this is rare and usually indicates metastable behaviour

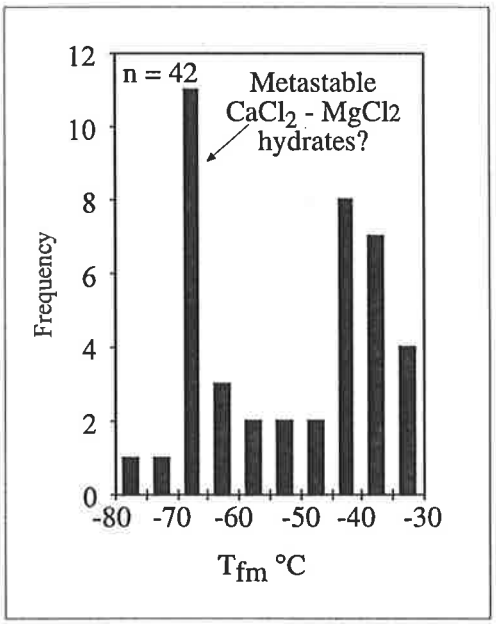


Figure 5.32. Tfm histogram for secondary fluid inclusions. The taller of the two peaks is thought to be due to metastable $CaCl_2$ and/or $MgCl_2$ hydrates.

(Davis *et al.*, 1990). Raman spectroscopy confirms that $CaCl_2$ dominates over NaCl, but neither $MgCl_2$ or KCl were detected. LiCl is known to depress the melting temperature of the aqueous phase to as low as -75°C, but, it too was not detected by laser Raman spectroscopy. Nevertheless, its presence has been noted by Robert and Kelly (1987) in leachate analyses on samples from the Sigma gold mine, Canada.

5.6.4.1.1.2 Fluid-gas components (CO_2 - CH_4)

Secondary fluid inclusions do not contain CO_2 or CH_4. This is confirmed by microthermometric observations and Raman spectroscopy.

5.6.4.2.2 Final melt temperature (Tm)

5.6.4.2.2.1 Salinity estimates calculated from the melting temperature of fluid hydrates

Tm_{ICE} data ranges from -5.7°C to -43.0°C (mean = -23.9°C, standard deviation = 11.4°C, n = 42). Some of these values correspond to fluid inclusions containing one or more daughter minerals. Estimated fluid salinities for secondary fluid inclusions incorporate values estimated from the dissolution temperatures of these daughter minerals and this is discussed below.

5.6.4.3 Homogenisation temperatures

5.6.4.3.1 Temperature of total homogenisation and entrapment (Th and Tt)

Forty-two secondary fluid inclusions were analysed for Th. Homogenisation occurs between 68.9°C and 223.4°C (mean = 139.2°C, standard deviation = 41.7°C, n = 42). Homogenisation

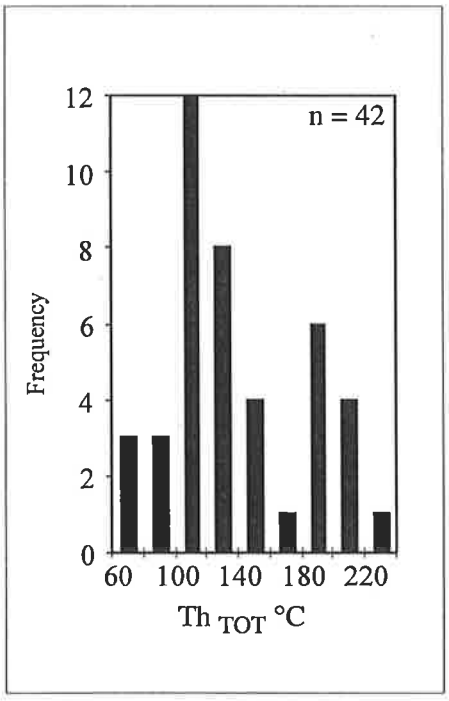


Figure 5.33. Histogram of Th for secondary fluid inclusions showing bimodal distribution. Higher temperature results correspond to ThNaCl.

of the vapour into the liquid phase occurred between 68.9°C and 215.9°C whereas homogenisation by dissolution of halite occurred between 118.9°C and 223.4°C. In most cases, ThNaCl, was greater that Th. In these cases, the Th of the fluid inclusion was accepted as being ThNaCl and these values are incorporated into Figure 5.33. The maximum ThNaCl value provides a minimum trapping temperature for these fluids.

5.6.4.3.1.1 Salinity estimates calculated from the homogenisation temperature of daughter minerals

Daughter minerals in these fluid inclusions are common. In some cases, multiple daughter minerals are present. Halite is the dominant daughter mineral observed in most fluid inclusions, but calcite was found to co-exist with halite occasionally. The cubic to rectangular shape of halite makes it easy to distinguish in most fluid inclusions. Raman spectroscopy of the daughter minerals observed confirms the presence of halite and calcite. As mentioned in section 5.6.1.1.2.1, the presence of a halite daughter mineral in solutions of $CaCl_2$ or $MgCl_2$, does not imply that the solution contained ≥ 26 wt% NaCl, because the presence of the divalent cations lowers the saturation point of NaCl (Roedder, 1984).

Despite the low Tfm data, indicative of $CaCl_2$ and $MgCl_2$ brines, the Tm_{ICE} values are calculated

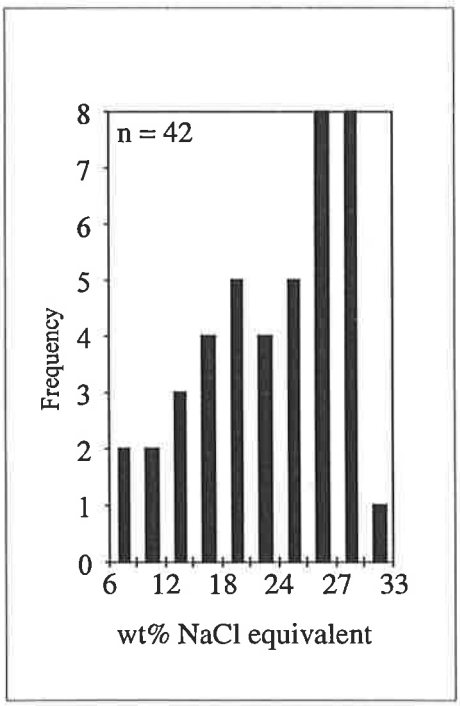


Figure 5.34. Salinity histogram for secondary fluid inclusions combining wt% equivalent data from Tm and ThNaCl results.

as wt% NaCl equivalent for consistency. Salinity estimates from the dissolution temperature of 15 daughter minerals using the solubility curves of Shepherd *et al.* (1985), are in reasonable agreement with the higher wt% NaCl equivalent values estimated from Tm_{ICE}. The combined values TmICE and ThNaCl) range from 8.81 - 33.5 wt% NaCl equivalent. (mean = 23.36 wt% NaCl equivalent, standard deviation = 7.1 wt% NaCl equivalent, n = 42) (Figure 5.34).

5.6.4.4 Discussion on secondary fluid inclusions

Secondary fluid inclusions are present in almost all veins at Junction, the exception being the Mo-type quartz veins. Secondary fluid inclusions show low homogenisation temperatures and a highly (albeit variable) saline - CO_2 free composition. Their Tfm values correspond to a fluid dominated by Ca^{2+}-Na^{+}-Cl^{-}. Fluid inclusions of this nature are common in Archaean lode gold deposits in Western Australia (Clark *et al.*, 1989; Ho *et al.*, 1990a and 1990b) and Canada (Robert and Kelly, 1987; Robert *et al.*, 1995). Recent work on this type of fluid inclusion occurring in Canadian late-orogenic, structurally-controlled gold deposits (Boullier *et al.*, 1998; Field *et al.*, 1998) has distinguished this type of fluid inclusion from the aqueous (type D) fluid inclusions that are believed to be end members of the original gold bearing parent fluid. It can, therefore, be concluded that this type of fluid inclusion is not related to the gold mineralising event. It is likely that the secondary fluid inclusions are the trapped equivalents of evolved basinal brines that have mixed with migrating ground waters and have percolated downward (up to several km) before being trapped. Kyser and Kerrich (1990) found that the composition of the Canadian Shield basement brines percolating into the crust are highly saline. Robert *et al.* (1995) compare these brines with the fluid composition from secondary fluid inclusions in late-orogenic, structurally-controlled gold deposits in the Abitibi greenstone belt. Drill hole samples of groundwater from Kambalda and Junction confirm that highly saline groundwater is present in the district and above the Junction deposit (see Table 4.1, Chapter 4). It is interesting to speculate on the probability of fluid penetration along an extinct shear zone into the crust. Boullier *et al.* (1998) believe that such basinal fluids would have to percolate up to 8 km into the crust at a geothermal gradient of 25°C/km to reach the salinities and temperatures recorded for these fluid inclusions.

5.7 Discussion

Thermometric data support geological observations that four different fluid events (Mo-type, syn-gold type, SV-type and secondary basinal type) were trapped in fluid inclusions in three different vein systems. Disregarding the late secondary fluid inclusions which are not associated with any quartz veining event, it has been demonstrated that CO_2 and CH_4 are present in all vein styles, and therefore all vein types have the potential to be the source of the soil gas anomalies that are detectable at the surface.

Limited numbers of useable fluid inclusions were available for thermometric analysis in two Mo-bearing quartz veins. However, they indicate that a highly saline fluid containing variable

amounts of CO_2 and CH_4 intruded the Junction dolerite after the period of peak metamorphism, but prior to the gold-mineralising event.

Optical observations on fluid inclusions in syn-gold quartz veins suggest that four different fluids have been trapped from a single parent ore fluid as a result of seismic pumping through the Junction shear zone. This is supported by the microthermometric results which show that a continuum exist between the CO_2-rich and the aqueous-rich fluid inclusions and that both fluid inclusion types are end member products of an efficient fluid unmixing process. It can be argued that fluid inclusion types B and C are essentially more evolved samples of the same fluid, and this is not disputed. However, it is noteworthy that type C fluid inclusions are easily distinguished from type B fluid inclusions, based on salinity estimations and vapour to liquid ratios. Therefore, the classification remains.

Based on thermometric data, the four fluids can be summarised as follows:

- a CO_2-rich fluid, containing small amounts of CH_4 (as identified by Raman spectroscopy),
- a CO_2-rich fluid containing small amounts of CH_4, with lesser amounts of low to moderately saline aqueous fluid containing dissolved Na^+, $Mg^{2+} \pm Ca^{2+}$ and Cl^-,
- a moderately saline aqueous fluid containing dissolved Na^+, $Mg^{2+} \pm Ca^{2+}$ and Cl^-, with variable amounts of CO_2 containing small to trace amounts of another gas phase, probably CH_4,
- an aqueous fluid of moderate salinity, containing small amounts of CO_2 ($\pm CH_4$), in which the main dissolved species are $Na > Ca \geq Mg$ and Cl.

Thermometric data indicates that links can be made between type A and type D fluid inclusions. These links are based on compositional similarities between the various fluid inclusion generations. Fluid inclusion types A, B and C can be linked by their CO_2-CH_4 content and (to a lesser extent) their CO_2 homogenisation temperatures. Fluid inclusion types B, C and D can be linked based on their solute compositions and overall Th. Na^+, Mg^{2+}, Ca^{2+} and Cl^- are present in all of these fluid inclusions which collectively homogenise between 201.3°C and 388.6°C. The solute composition and overall Th relationships can be seen on a Th - salinity plot. Figure 5.35 shows that the type B, C and D fluid inclusions all homogenise in the same temperature range, but that their wt% NaCl equivalent salinities roughly vary according to their classification. The vapour-rich type B and type C fluid inclusions have low salinities and plot mostly to the left and centre of the plot, whereas the vapour-poor type D fluid inclusions have higher salinities and plot mostly to the middle and right of the diagram. Type A fluid inclusions did not give Tm data and so their salinity was not determined.

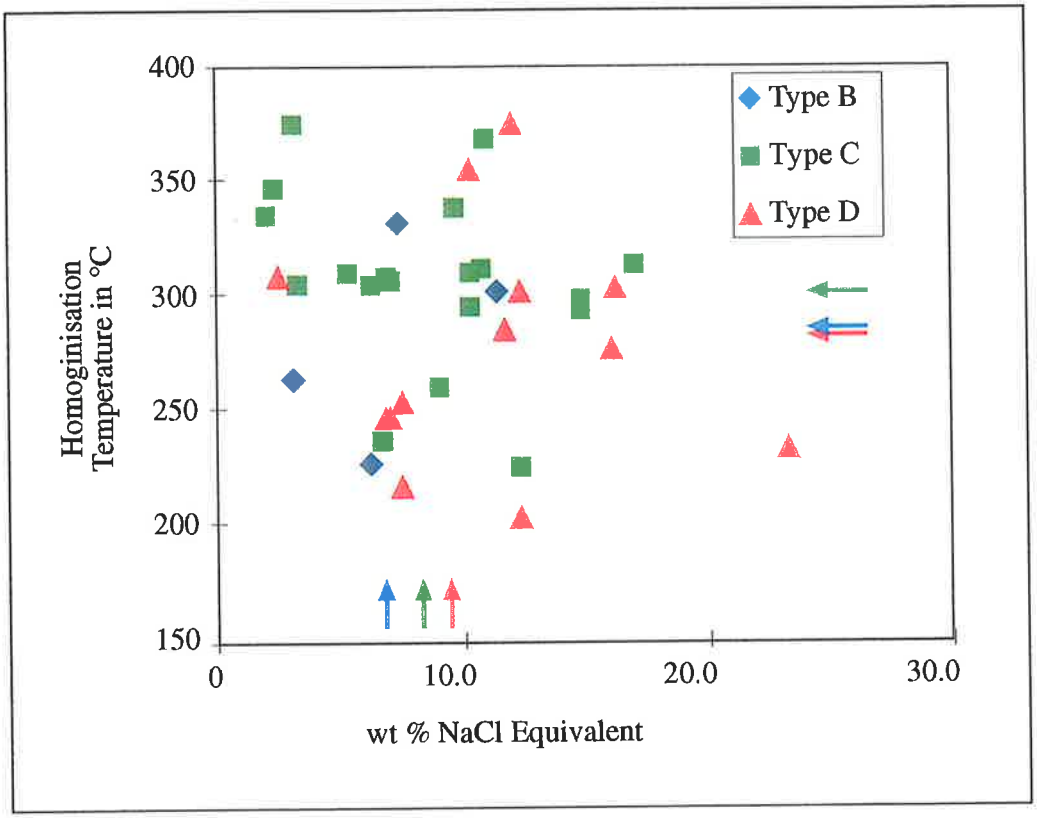


Figure 5.35. Temperature Vs salinity plot for type B, C and D fluid inclusions hosted in syn-gold quartz veins. The plot highlights that there are subtle differences between the fluid inclusion populations that are believed to have originated from a single parent fluid. The small size of the type B fluid inclusion population precludes good definition. However, type B and C fluid inclusions generally have a lower salinity and a higher temperature than type D fluid inclusions indicating that phase separation has probably occurred. Coloured arrows indicate mean values calculated for each fluid inclusion type.

Robert and Kelly (1987) use this compositional continuum shown here by the four fluids to suggest a close genetic relationship exists among these fluids. It can be seen from the different fluid inclusion types that it is probable that there was only one homogeneous fluid source that unmixed and lead to the entrapment of only one fluid type along a given fracture. However, it also indicates that there were four types of fluids circulating in the veins prior to entrapment. This is interpreted to be a result of dynamic fracturing of the vein material under pressure which lead to immiscible phases developing (Boullier and Robert, 1992). Each of the four fluid inclusion types must have formed by fluid immiscibility caused by the cyclical episodes of seismic rupturing. The immiscible fluids were then introduced into microfractures at different times during the fracturing episode. That a single fluid inclusion type is commonly found in different sets of microfractures suggests that fractures form, heal and are decrepitated or cross-cut by later microfractures over a relatively long time interval (Robert and Kelly, 1987; Boullier and Robert, 1992; Robert *et al.*, 1995).

It can be seen from the types of fluid inclusions present that the two end member fluids found in the Junction mine (CO_2-rich and aqueous) are common to many late-orogenic, structurally-controlled gold deposits (Robert and Kelly, 1987; Clark *et al.*, 1989; Ho *et al.*, 1990a and 1990b; Cassidy and Bennett, 1993; Robert *et al.*, 1995; Boullier *et al.*, 1998). They result from unmixing of a parent H_2O-CO_2, low salinity fluid due to pressure drops that occurred at the time of seismic rupture.

This discussion leads to the conclusion that the parent ore fluid at Junction was a CO_2-rich, H_20-NaCl fluid with a fluid density between 0.7 and 0.9 gm/cm^3. It underwent phase separation, due to the immiscible properties of the fluid components below approximately 3000 bars at 350±50°C. These fluid inclusion properties are similar to fluids trapped in fluid inclusions in late-orogenic, structurally-controlled gold deposits around the world (Smith and Kesler, 1985; Robert and Kelly, 1987; Ho *et al.*, 1990a and 1990b; Guha *et al.*, 1991; de Ronde *et al.*, 1992; Boullier and Robert, 1992; Mernagh and Witt, 1994; Graney and Kesler, 1995; Robert *et al.*, 1995; Mernagh, 1996; Boullier *et al.*, 1998).

The fluid inclusions at Junction do not indicate that CH_4 was a major component in the ore forming system. On average, most fluid inclusions analysed by microthermometry contain less than 1 mol. % CH_4 relative to the H_2O-CO_2-CH_4-NaCl system. Indeed, work by Duan *et al.* (1992b) indicates that the deposit would have needed to form above 400°C for significant CH_4 to be present as a soluble phase in the solution. However, some fluid inclusions do show evidence that suggests that CH_4 was locally abundant in some fluid inclusions (indicated by the formation of a vapour phase below -82.4°C) and this is supported by Raman spectroscopy and gas chromatography.

CHAPTER SIX

Laser-Raman spectroscopy

6.1 Introduction

Raman spectroscopy was used in this project to confirm and extend the data obtained during microthermometric investigations (Chapter 5). Raman spectroscopic analysis of chosen, individual fluid inclusions allows non-destructive identification of stoichiometric hydrates (e.g., $NaCl.2H_2O$, $CaCl_2.6H_2O$, $MgCl_2.6H_2O$, $MgCl_2.12H_2O$, $FeCl_3.6H_2O$ and $KCl.MgCl_2.6H_2O$), gases that form in the C-O-H-N-S system and certain daughter minerals (Rosasco and Roedder, 1979; Dubessy *et al.*, 1982; Seitz *et al.*, 1987; Dubessy *et al.*, 1989; Seitz *et al.*, 1996).

Further to the identification of fluid inclusion components in the C-O-H-N-S-hydrate-daughter mineral system, Raman spectroscopy allows the relative molar proportions of a CO_2, CH_4 mixture to be determined (Dubessy *et al.*, 1989; Seitz *et al.*, 1996). This geoanalytical property allows broad comparisons to be made between Raman-spectroscopic data, microthermometric data and gas chromatographic data, thus enhancing gas-fluid composition interpretation.

6.2 Methods, equipment and procedures

Ninety-three fluid inclusions from 21 samples representing the pre-gold Mo-type quartz veins, the syn-gold extensional and shear quartz veins and the post-gold SV-type quartz veins (including three secondary fluid inclusions present in one of the syn-gold vein types) were analysed by Raman spectroscopy. Thin section wafers used for Raman analysis were studied petrographically before being split into sections. Half of the sample was used for microthermometric analysis and the other half was kept for Raman spectroscopy. A complete discussion describing the characteristics of the fluid inclusions in these vein types is given in Chapter 5.3. A brief overview of the fluid inclusions analysed by Raman spectroscopy is given here.

6.2.1 Fluid inclusion types

6.2.1.1 Pre-gold Mo-type quartz veins

Six fluid inclusions from one molybdenite bearing quartz vein were analysed by Raman spectroscopy. Fluid inclusions were carefully selected to ensure their affinity to the molybdenite. All six fluid inclusions contained a fluid phase, a single vapour phase that occupied between 25% and 60% of the fluid inclusion, plus at least one daughter mineral (halite ± an unidentifiable carbonate mineral) (see Figures 5.5, 5.6, 5.7 and 5.8, Chapter 5).

6.2.1.2 Syn-gold extensional and shear veins

Sixty-nine fluid inclusions from 16 syn-gold extension and shear quartz veins were analysed by Raman spectroscopy. The fluid inclusions hosted in these quartz veins usually contained a single vapour phase of various volume, but occasionally a fluid inclusion displayed liquid and vapour CO_2 phases at room temperature and needed warming to its critical point before analysis. Daughter minerals were rare (see Figures 5.9, 5.13, 5.14, 5.16, 5.17 and 5.18, Chapter 5).

6.2.1.3 Post-gold SV-type quartz veins

Thirteen fluid inclusions from three post-gold SV-type quartz veins were analysed by Raman spectroscopy. All of the fluid inclusions analysed from these veins were dominated by a vapour phase (>50% vapour; see Figure 5.20, Chapter 5).

6.2.1.4 Secondary fluid inclusions

Three secondary fluid inclusions from one syn-gold shear vein were analysed by Raman-spectroscopy. Secondary fluid inclusions are optically distinct from most other fluid inclusions, often occurring as two-phase aqueous fluid inclusions with one or more daughter minerals (see Figures 5.21 and 5.22, Chapter 5). These fluid inclusions were analysed by Raman spectroscopy to determine if they contained any CO_2 or CH_4 that may have been unnoticed during routine microthermometric analysis and to identify the multiple daughter mineral species that were present.

6.2.2 Equipment and procedures

Laser-Raman spectroscopy was carried out with a Microdil-28 laser-Raman microprobe at AGSO, Canberra, following the technique of Liu and Mernagh (1990). An Olympus BH-2 microscope with a 100x objective was used, and samples were irradiated with a laser beam about 2μm in diameter at the focus. The laser source is a Spectra Physics 2020 3W argon ion laser, using the 514.5 nm green line as the excitation source. All spectra were recorded using a multichannel detector with the monochromator stepped at 0.5 cm^{-1} intervals and a counting time of 5 or 10 seconds per point. The detectors are linked via an IB10 interface to a Cleveland 286 SP personal computer, with the data being recorded and interpreted into relative molar fractions using software supplied by Dilor Co., Lille, France.

The following spectral windows were used for quantitative analysis: 1375-1395 cm^{-1} (CO_2), 2135-2155 cm^{-1} (CO), 2315-2340 cm^{-1} (N_2), 2570-2630 cm^{-1} (H_2S), 2905-2925 cm^{-1} (CH_4) and 3300-3600 cm^{-1} (all stoichiometric hydrates listed in section 6.1). Daughter minerals were identified by their characteristic Raman spectrum. Gas species and daughter minerals were determined at room temperature whereas hydrates needed to be formed prior to their analysis, requiring the samples to be cooled to -170°C.

6.3 Results

6.3.1 Gas phases confirmed

Raman spectroscopy confirmed the presence of CO_2 and CH_4 in all of the vein types analysed, with good CO_2 and CH_4 peaks obtained from most of the fluid inclusions analysed (Figure 6.1). However, no sulphur gas species, CO or N_2, usually ubiquitous with Archaean, late-orogenic, structurally-controlled gold deposits, were detected.

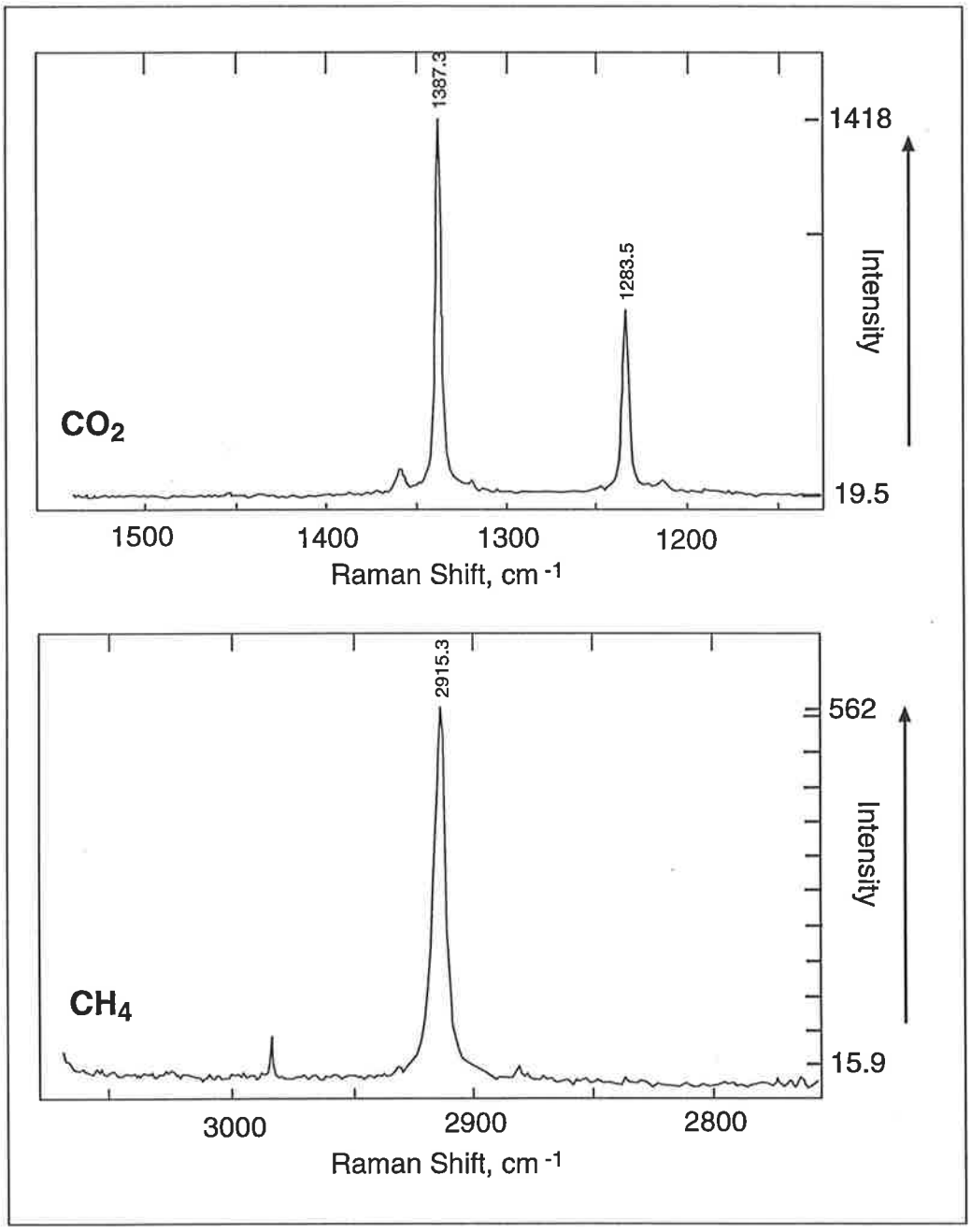


Figure 6.1. An example of the Raman spectra obtained from the vapour phase in a fluid inclusion containing both CO_2 and CH_4.

6.3.1.1 Pre-gold Mo-type quartz veins

The vapour phase of the six pre-gold, Mo-type fluid inclusions contained between 25 and 81% CO_2 (mean = 52% CO_2) and 19 to 75% CH_4 (mean = 48% CH_4; Table 6.1).

Mo-type fluid inclusions

Sample Number	Sample Type	Inclusion type	CO_2	CH_4	% Vapour	Daughter Mineral(s)
1074-66	Mo-type	pseudosecondary	25	75	40	halite/unidentified carbonate
1074-66	Mo-type	pseudosecondary	36	64	35	halite
1074-66	Mo-type	pseudosecondary	37	63	25	
1074-66	Mo-type	pseudosecondary	74	26	65	halite
1074-66	Mo-type	pseudosecondary	60	40	50	halite/unidentified carbonate
1074-66	Mo-type	pseudosecondary	81	19	50	

Table 6.1. Raman spectrocopic data for Mo-type fluid inclusions.

6.3.1.2 Syn-gold extensional and shear veins

The vapour phase of most fluid inclusions in the extensional and shear veins were dominated by CO_2 (mean = 90.93 mol. %, n= 69, relative to CH_4). Fluid inclusions dominated by CH_4 (> 50% CH_4 and up to 100 mol. %) were rare. However, CH_4 concentrations > 10 mol. % relative to CO_2 were not uncommon in some veins (Table 6.2).

6.3.1.3 Post-gold SV-type quartz veins

Raman spectroscopy revealed that the CO_2-CH_4 concentrations in individual fluid inclusions hosted by SV-type quartz veins varied widely from one vein to another. Eight fluid inclusions hosted in samples 1074-131 and 1074-136 contain 99 to 100% CO_2 relative to CH_4 in the vapour phase, whereas five fluid inclusions hosted in sample 1074-93 contain between 57 and 83 mol. % CO_2 relative to CH_4 (Table 6.3).

6.3.1.4 Secondary fluid inclusions

No CO_2, CH_4 or other gas species in the C-O-H-N-S system were detected in the vapour phase of the three secondary fluid inclusions analysed (Table 6.3).

6.3.2 Hydrates and daughter minerals present

Raman spectroscopy on daughter minerals and hydrates that were formed by freezing the fluid inclusions, revealed that fluid inclusions hosted a variety of chloride species and daughter minerals. Carbonate and bicarbonate minerals detected by Raman spectroscopy include calcite and/or rhodochrosite (both have the same spectral signature. However, calcite is the more likely of the two), siderite and nahcolite. Chloride species found to exist were $NaCl.2H_2O$ (hydrohalite), $CaCl_2.6H_2O$ (antarcticite), and $MgCl_2.12H_2O$ (Figure 6.2). No K^+ hydrates were identified

Syn-gold fluid inclusions

Sample number	Sample type	CO_2	CH_4	% Vapour	Daughter mineral(s)	Hydrates present
1074-15	Shear vein	85	15	85	unidentifiable	
1074-15	Shear vein	87	13	75	nahcolite	
1074-28	Shear vein				calcite (?rhodochrosite)	
1074-37	Shear vein	100	0	95		
1074-37	Shear vein	100	0	25		$CaCl_2$
1074-37	Shear vein	100	0	80		
1074-37	Shear vein	100	0	25		
1074-37	Shear vein	100	0	99		
1074-41	Shear vein	27	73	80	siderite	trace $CaCl_2$
1074-43	Extension vein	97	3	40		
1074-43	Extension vein	87	13	45		
1074-43	Extension vein	81	19	65		NaCl
1074-43	Extension vein	98	2	60		
1074-43	Extension vein	100	0	10		$MgCl_2.12H_20$
1074-43	Extension vein	100	0	10		$MgCl_2.12H_20$
1074-43	Extension vein	100	0	15		$MgCl_2.12H_20$
1074-84	Shear vein	93	7	60	calcite (?rhodochrosite)	
1074-84	Shear vein	99	1	65		
1074-84	Shear vein	97	3	50		
1074-84	Shear vein	100	0	65		
1074-84	Shear vein	100	0	100		
1074-105	Extension vein	99	1	70		
1074-105	Extension vein	98	2	95		
1074-105	Extension vein	98	2	50	nahcolite	
1074-105	Extension vein	100	0	25		$CaCl_2$
1074-105	Extension vein	99	1	80		
1074-229	Extension vein	56	44	50		
1074-229	Extension vein	32	68	50	halite	NaCl
1074-229	Extension vein	87	13	100		
1074-229	Extension vein	79	21	100		
1074-233	Extension vein	96	4	90		
1074-233	Extension vein	94	6	90		
1074-233	Extension vein	100	0	40		
1074-233	Extension vein	100	0	40		
1074-233	Extension vein	98	2	100		
1074-233	Extension vein	98	2	40		
1074-236	Extension vein	100	0	100		
1074-236	Extension vein	100	0	90		
1074-236	Extension vein	100	0	100		
1074-236	Extension vein	100	0	100		
1074-240	Extension vein	100	0	100		
1074-240	Extension vein	99	1	100		
1074-240	Extension vein	100	0	100		
1074-240	Extension vein	99	1	90		
1074-240	Extension vein	99	1	100		
1074-243	Extension vein	100	0	100		
1074-243	Extension vein	100	0	25	halite	NaCl
1074-243	Extension vein	99	1	60		
1074-243	Extension vein	100	0	80		
1074-248	Extension vein	100	0	80		
1074-248	Extension vein	100	0	70		
1074-248	Extension vein	100	0	100		
1074-248	Extension vein	98	2	100		
1074-248	Extension vein	99	1	70		
1074-248	Extension vein	94	6	95		
1074-248	Extension vein	97	3	85		
1074-248	Extension vein	97	3	100		
1074-250	Shear vein	86	14	70		
1074-250	Shear vein	29	71	95		
1074-250	Shear vein	0	100	85		
1074-250	Shear vein	37	63	90		
1074-250	Shear vein	79	21	90		
1074-251	Extension vein	88	12	100		
1074-251	Extension vein	94	6	100		
1074-251	Extension vein	100	0	100		
1074-251	Extension vein	96	4	100		
1074-251	Extension vein	99	1	25		$NaCl/CaCl_2$
1074-259	Extension vein	100	0	100		
1074-259	Extension vein	100	0	70		
1074-259	Extension vein	100	0	100		

Table 6.2. Raman spectrocopic data for syn-gold fluid inclusions trapped in shear and extension veins.

from the samples analysed by Raman spectroscopy.

6.3.2.1 Pre-gold Mo-type quartz veins

Raman-spectroscopy on the hydrates formed in the pre-gold Mo-type fluid inclusions revealed that $NaCl.2H_2O$ was the only chloride species present in these fluid inclusions. Daughter minerals found in these fluid inclusions were predominantly identified as halite. However, in fluid inclusions containing two daughter minerals, the second solid could not be positively identified, but its broad spectral signature confined its identification to a carbonate species (Table 6.1).

6.3.2.2 Syn-gold extensional and shear veins

Seven daughter minerals hosted in syn-gold extensional and shear veins were identified by Raman spectroscopy as either halite, calcite (or rhodochrosite), siderite or nahcolite (Table 6.2). Frozen fluid inclusions revealed that the chemistry of individual fluid inclusions was varied and complex. Three hydrate species were found to exist in fluid inclusions hosted by both extensional and shear veins. They were $NaCl.2H_2O$, $CaCl_2.6H_2O$ and $MgCl_2.12H_2O$ (Table 6.2). Trace amounts of $CaCl.6H_2O$ was detected in only one type B fluid inclusion, but it is more predominant in the type D fluid inclusions when it was detected. In one fluid inclusion, two hydrate species were found co-existing in the one fluid inclusion. However, in most of the fluid inclusions analysed, the sharp spectral peaks illustrated in Figure 6.2 were absent or were very broad. The identification of the hydrate was inferred from a broad Raman spectrum which peaked near a recognisable wavelength in these cases. The absence of a spectral peak indicates that the ion-chlorides were absent, whereas a broad spectrum peak indicates that the concentrations of the ion-chlorides were very low (T. Mernagh, pers. comm., 1997).

6.3.2.3 Post-gold SV-type quartz veins

No daughter minerals or hydrates were analysed by Raman-spectroscopy.

6.3.2.4 Secondary fluid inclusions

Raman spectroscopy identified halite and calcite (or rhodochrosite) as the daughter minerals present in the three secondary fluid inclusions analysed (Table 6.3). Frozen secondary fluid inclusions revealed that the chemistry of individual fluid inclusions was complex, but relatively consistent. Sharp spectral peaks (like those illustrated in Figure 6.2) were detected in all three secondary fluid inclusions analysed, revealing the co-existence of $NaCl.2H_2O$ and $CaCl_2.6H_2O$ in each of the fluid inclusions (Table 6.3).

6.4 Discussion

Raman spectroscopy confirms the presence of CO_2 and CH_4 in most of the fluid inclusions, and $NaCl.2H_2O$, $CaCl_2.6H_2O$ and $MgCl_2.12H_2O$ in some of the fluid inclusions analysed from all vein types sampled at Junction. However, the absence of N_2, H_2S and CO from fluid inclusions

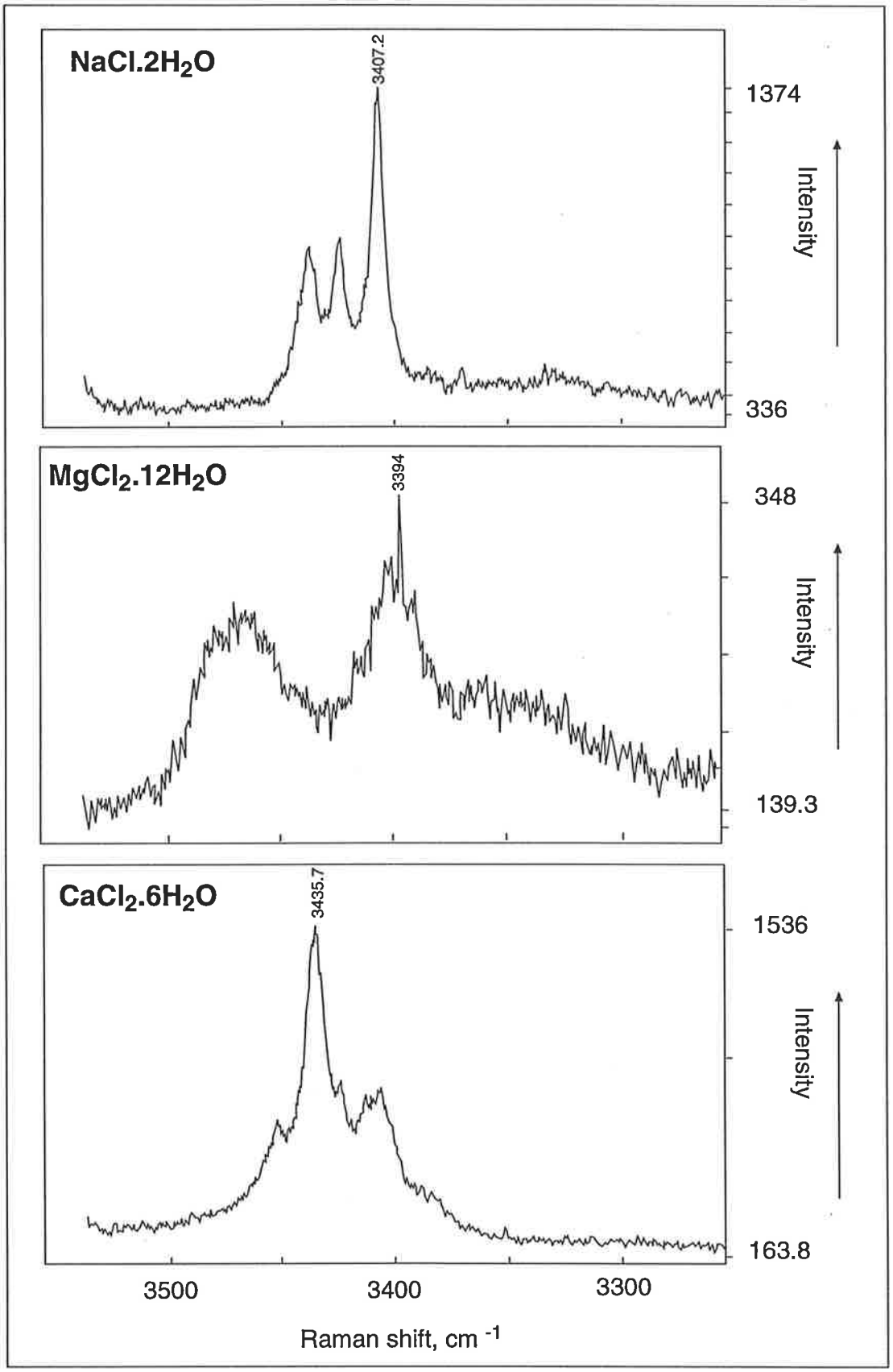


Figure 6.2. An example of the Raman spectra obtained from the liquid phase in different fluid inclusions containing the stoichiometric hydrates $NaCl.2H_2O$, $CaCl_2.6H_2O$, or $MgCl_2.12H_2O$.

SV-type and secondary fluid inclusions.

Sample number	Sample type	Inclusion type	CO_2	CH_4	% Vapour	Daughter mineral(s)	Hydrates present
1074-93	SV-type vein	pseudosecondary	57	43	80		
1074-93	SV-type vein	pseudosecondary	62	38	90		
1074-93	SV-type vein	pseudosecondary	83	17	95		
1074-93	SV-type vein	pseudosecondary	62	38	40		
1074-93	SV-type vein	pseudosecondary	69	31	65		
1074-131	SV-type vein	pseudosecondary	100	0	100		
1074-131	SV-type vein	pseudosecondary	100	0	95		
1074-131	SV-type vein	pseudosecondary	100	0	80		
1074-131	SV-type vein	pseudosecondary	100	0	100		
1074-131	SV-type vein	pseudosecondary	99	1	100		
1074-136	SV-type vein	pseudosecondary	100	0	100		
1074-136	SV-type vein	pseudosecondary	100	0	100		
1074-136	SV-type vein	pseudosecondary	100	0	100		
1074-41		late secondary			<5	halite/calcite(?rhodochrosite)	NaCl
1074-41		late secondary			<5	halite/calcite(?rhodochrosite)	$CaCl_2$/NaCl
1074-41		late secondary			<5	halite/calcite(?rhodochrosite)	CaC_2

Table 6.3. Raman spectrocopic data for SV-type and secondary fluid inclusions.

at Junction, remains enigmatic. Nevertheless, the Raman data support the micothermometric results (Chapter 5) which indicate that a complex C-O-H-salt system is present in many of the fluid inclusions. A thorough discussion of the low temperature behaviour, including the results obtained by the Raman spectroscopic data, is given as needed in that chapter. However, some aspects of the Raman spectroscopy results are not discussed in Chapter 5, and are discussed here.

The detection by Raman spectroscopy of $NaCl.2H_2O$, $MgCl_2.12H_2O$ and $CaCl_2.6H_2O$ hydrates corresponds to microthermometric Tfm values that cluster around -30°C to -40°C and -47°C respectively. The detection of $CaCl.6H_2O$ in particular suggests that Tfm values as low as -75.8°C, recorded during microthermometric analysis, are accurate. Further to this, mixed H_2O-Ca-Na-Mg-Cl solutions suggested in Chapter 5 for eutectic temperatures that fall between -35°C and -52°C are supported by at least one fluid inclusion analysed by Raman spectroscopy that contains both $NaCl.2H_2O$ and $CaCl_2.6H_2O$. However, a larger data base for this interpretation is desirable.

Significant to this project is the finding by Raman-spectroscopy that CO_2 and CH_4 is not restricted to any specific fluid inclusion types at Junction, with the exception of the secondary fluid inclusions. Importantly, it is noteworthy that CH_4-dominated fluid inclusions exist in all vein types analysed, indicating that all veins are potential sources for the CH_4 detectable by passive samplers buried in the soil at the surface.

The detection by Raman spectroscopy of up to 100 mol. % CH_4 (relative to CO_2) in some fluid inclusions (incorporating all Raman data), explains the presence of a vapour phase below -120°C in one syn-gold, type B fluid inclusion (Figure 5.23a and 5.23b, Chapter 5), the unusual "wobbling" behaviour observed in some fluid inclusions at temperatures between -97.6°C and

-60.2°C (Appendix V) and the melting of the gas phase at temperatures as low as -65.6°C, nine degrees below the expected melting point of CO_2.

Further to this, Raman spectroscopy on syn-gold fluid inclusions supports the interpretation in Chapter 5 that most fluid inclusions contain <5.5 mol. % CH_4. Raman spectroscopy reveals that CH_4 values in most fluid inclusions are rarely greater than 5 mol. % relative to CO_2 despite the number of $TeCO_2$ values obtained from microthermometric analysis, that are >2°C below the eutectic point of CO_2, i.e. -56.6°C.

While most fluid inclusions in shear and extensional quartz veins contain >95 mol. % CO_2 relative to CH_4, five fluid inclusions from one quartz shear vein containing flecks of free-gold amongst large, well developed calcite ± dolomite crystals (sample 1074-250), returned CH_4 concentrations that range from 14 - 100% (mean = 53.8 mol. %) relative to CO_2. The proximity of these CH_4-rich fluid inclusions to the large carbonate crystals, prompted a review of the Raman data.

Examination of thin section wafers cut for Raman spectroscopic analysis revealed that the CH_4-dominated (>50 mol. % CH_4) and CH_4-rich (>10 mol. % CH_4) fluid inclusions at Junction, came from veins that were dominated by calcite ± albite >> quartz. Similarly, CH_4-dominated and CH_4-rich fluid inclusions were also found within millimetres of the quartz vein - host rock contact where wall-rock alteration is most intense. These detailed investigations concluded that CH_4-dominated and CH_4-rich fluid inclusions are most likely to be found hosted in quartz that is adjacent to calcite or the wall-rock contact. Alternatively, fluid inclusions hosted in quartz as little as 5 mm away from calcite or the wall-rock contact are likely to contain mixed CO_2:CH_4 ratios, including fluid inclusions that contain 100% CO_2. Finally, fluid inclusions hosted in quartz away from calcite, toward the centre of the quartz vein, contain only CO_2, or are CO_2-dominated fluid inclusions.

This discovery indicates that CO_2 : CH_4 ratios are zoned with respect to the vein wall-rock contact. Further to this, CH_4-rich fluid inclusions hosted in the Mo-type quartz veins and the SV-type quartz veins are also from quartz grains that were within millimetres of the quartz vein - host rock contact. A schematic model for this hypothesis is illustrated in Figure 6.3.

The detection of CH_4-dominated and CH_4-rich fluid inclusions in quartz grains close to calcite crystals, suggests that fluid inclusions hosted in calcite and other fluid inclusion bearing minerals near calcite (e.g. albite and sulphides) may contain many fluid inclusions that are dominated by CH_4. This hypothesis is significant to this project because fluid inclusion-bearing carbonates, feldspars and sulphides, abundant in the gold-bearing Biotite-Carbonate Zone (Chapter 3), weather relatively quickly at an active oxidation front. This makes these minerals a prime source for the light hydrocarbon gases detected in the soil at the surface.

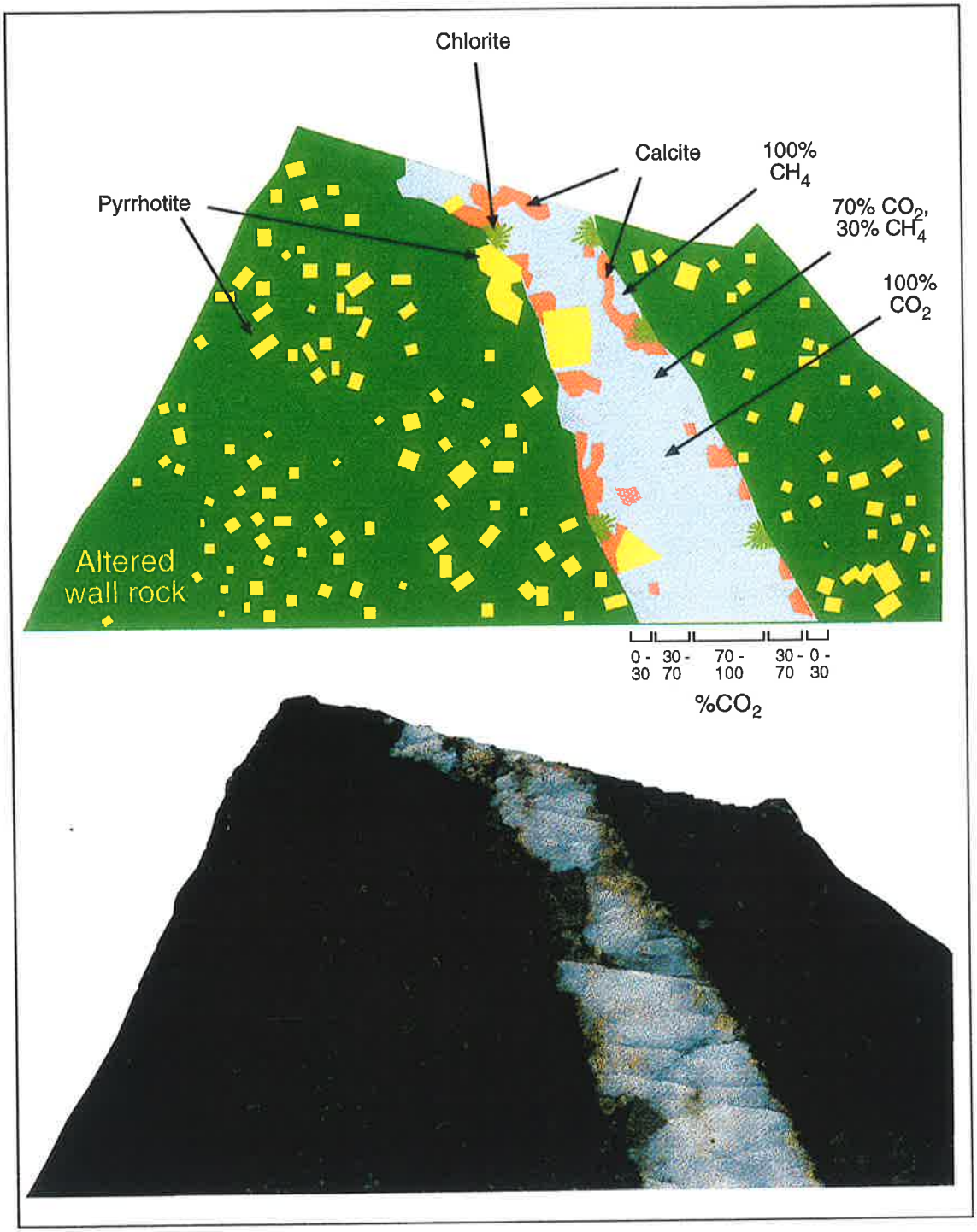


Figure 6.3. A schematic illustration showing the distribution of CO_2 and CH_4 across a typical quartz vein. The illustration is based on the results obtained from Raman-spectroscopic data collected from a quartz-calcite vein sample.

CHAPTER SEVEN

CH_4-bearing fluid inclusions in calcite: a source for the light hydrocarbon soil-gas anomaly

7.1 Introduction to EDTA-gas chromatography

The light hydrocarbon gas anomaly detected in the soil above the Junction deposit is thought to be a primary geochemical signature that is related to gold mineralisation at depth. The sharp, light hydrocarbon peak that occurs immediately above the gold mineralised shear zone, indicates that this anomaly does not originate from a source outside of the shear zone. Instead, the anomaly appears to be related to the weathering of an alteration assemblage associated with gold mineralisation. The probability that the hydrocarbon anomaly in the soil atmosphere is a secondary geochemical signature originating from bacterial metabolism is discussed and dismissed in Chapter 4. Instead, trace to moderate volumes of CH_4 detected in fluid inclusions (Chapters 5 and 6), suggests that the hydrocarbon anomaly originates from the mineralisation itself. This would make the anomaly a primary geochemical signature, a characteristic that enhances the credibility of light hydrocarbons being used as an exploration vector.

Microthermometry and laser-Raman spectroscopy on fluid inclusions within quartz samples from Junction indicate that CH_4 volumes differ from one fluid inclusion to the next with respect to CO_2 (rarely up to 100 mol. % CH_4 and commonly below 1 mol. % CH_4). Indeed, the overall CH_4 content of a given fluid inclusion population within a single quartz vein rarely approaches more than 5 mol. % CH_4. Raman spectroscopy indicates that fluid inclusions with the greatest CH_4 content (with respect to CO_2) are the ones that are closest to the quartz vein - host rock contact. This is where carbonate, biotite, chlorite, albite and sulphide alteration is most intense. Fluid inclusion microthermometry on non-quartz minerals was not performed due to their opacity, and/or internal reflectance of these minerals in >50μm thick wafers. However, fluid inclusions are clearly abundant in carbonates and feldspars (see Figures 5.1 and 5.2, Chapter 5) and Guha *et al.* (1991), Richards and Kerrich (1993) and Hagemann *et al.* (1994) have shown that fluid inclusions are also present in Fe-sulphides in late-orogenic, structurally-controlled gold deposits and other deposit styles. These observations suggest that carbonate, feldspar and other alteration minerals have trapped significant volumes of CH_4 with respect to CO_2 in the vicinity of the quartz vein - host rock contact.

This theory needs confirmation in order to substantiate or dismiss the possibility that the ore deposit contains CH_4 and other light hydrocarbons at concentrations that are high enough to allow at least some CH_4 to migrate to the surface. One appropriate experimental method is to extract the gas from the fluid inclusions in the host and analyse it by gas chromatography.

However, the most common technique for gas extraction from whole rock or quartz vein samples is to heat and/or crush a small weight of sample, thus liberating the light hydrocarbons from mineral surfaces or fluid inclusions as they decrepitate (Andrawes *et al.*, 1984; Smith *et al.*, 1984; Carter and Cazalet, 1985; Kesler *et al.*, 1986; Norman and Sawkins, 1987; Bray *et al.*, 1991; Miller and Pillinger, 1997). The evolved gas is then analysed by gas chromatography. Significantly, both of these extraction techniques have deleterious side effects.

Heating (in most cases as high as 600°C; c.f. Smith *et al.* [1984]; Kesler *et al.* [1986], Miller and Pillinger, [1997]) has been known to alter the original gas composition of the sample by either thermal decomposition or chemical reaction between the compounds present. Andrawes *et al.* (1984) report that Equations 7.1 to 7.3 are the most common chemical reactions that occur during thermal decomposition:

$$H_2O + Fe(II) \rightarrow Fe(III) + H_2 \qquad \text{(Equation 7.1)}$$

$$CH_4 + 2H_2O \rightarrow CO_2 + 4H_2 \qquad \text{(Equation 7.2)}$$

$$CH_4 + H_2O \rightarrow CO + 3H_2 \qquad \text{(Equation 7.3)}$$

This process generates false volatile volumes (thus ratios) in the sample. Further to this, Carter and Cazalet (1985) contend that heat extraction only releases a portion of the total volume of gas in a rock and that the precision of the method is not good. Carter and Cazalet (1985), Ferguson (1987), Disnar (1990), and Miller and Pillinger (1997) also note that heat extraction of gases from rock commonly results in extraneous volumes of gas volatiles being released. These authors maintain that non-indigenous gases evolve from samples that have not been properly decontaminated of machine fluids (drilling oils and lubricants, vehicle-related lubricants and propellants etc.), vegetation or other carbon-bearing (in)organic material. Miller and Pillinger (1997) found that single step heat release of volatiles from quartz grains resulted in $\delta^{13}C$ values that were significantly depleted in ^{13}C. These low values were attributed to the production of $CO_2 \pm CH_4$ by thermal decomposition of an extraneous carbon source that is believed to be present as a carbonaceous film of unknown origin adsorbed on to grain surfaces and along microfractures.

Mechanical crushing of samples is an alternative extraction method that offers the advantage that gas released from fluid inclusions is not contaminated by surficial organic matter. However, relatively low gas yields per sample are common. Further to this, Andrawes and Gibson (1979), Andrawes *et al.* (1984) and Welhan (1988), found that N_2, H_2, CO_2 and CH_4 can be formed

during extended grinding and crushing of blanks, whilst Barker and Torkelson (1975), Andrawes *et al.* (1984), and Mulshaw (1996) report that gases released by crushing techniques, especially CO_2 and hydrocarbons, are prone to adsorption on to the newly generated surfaces of the crushed sample, thus removing some gas from analysis. However, Kazahaya and Matsuo (1985) have shown that these gases can be readily desorbed from the fine grained powder by heating the sample to 200°C to 280°C for a short period.

7.2 Methods and procedures

The mineralogy of the Junction mine lends itself to an alternative gas extraction technique that increases gas yields and minimises volatile degradation and/or extraneous hydrocarbon generation. Hydrocarbon gases were liberated from samples collected at the Junction deposit by dissolving the carbonate fraction of the whole rock in a near neutral solution of ethyl diamine tetra-acetic acid (EDTA). The near neutral EDTA is used because it is able to dissolve carbonate (thus releasing gas from fluid inclusions) without producing unwanted volumes of CO_2. This type of reaction occurs because the active ingredients in EDTA have a strong affinity for the Ca^+ ions, breaking it from its bond with CO_3^-, without the weakly acidic solution breaking the CO_3^- molecule.

Ferguson (1987) reports that the liberation of hydrocarbons by dissolution of carbonate in EDTA is a better technique than the heat extraction technique, and is at least on a par with the grinding or crushing technique. This is because liberation of hydrocarbons from carbonate by EDTA dissolution releases more gas from the same sample than step heating and produces at least as much gas as grinding or crushing. Mulshaw (1996) found that dissolution of carbonate by EDTA liberates higher concentrations of hydrocarbons than both crushing and heat extraction (EDTA liberation: up to 22,000 volume (V) ppm CH_4; crush/grind liberation: up to 15,000 vppm CH_4; heat liberation: up to 1,000 vppm CH_4), but concedes that relative concentrations of light hydrocarbons between samples are similar.

Dissolution of carbonate by EDTA favours the detection of other light hydrocarbons, such as ethane, propane and butane because these gases are neither decomposed by heating at 600°C (Miller and Pillinger, 1997) or adsorbed on to newly generated rock powder (Barker and Torkelson, 1975; Andrawes *et al.*, 1984; Polito, 1993; Mulshaw, 1996). Further to this, contamination by lubricants and/or terrestrial organic matter is eliminated during hydrocarbon extraction by EDTA dissolution because no light hydrocarbons are produced from any organic matter that may be present during the reaction. If machine-related hydrocarbons are present as invisible organic films on mineral surfaces, they are generally the larger and thus heavier aliphatic and aromatic hydrocarbons that do not escape into the head space area that is analysed. The generation of erroneous gas ratios is also eliminated because the technique does not promote any chemical reactions amongst the carbonic gases. However, one significant drawback of the technique is that CO_2 volumes cannot be determined because some CO_2 is produced during the

reaction of carbonate with the acid.

Twenty-eight samples representing the biotite-carbonate zone (BCZ; where gold grades are highest), the proximal-chlorite zone and distal-chlorite zone (PCZ and DCZ; where gold grades are low to negligible), the unaltered gabbro and the post-gold SV-type quartz veins were analysed for their hydrocarbon content. The technique used here is a modification of that offered by Ferguson (1987) and Mulshaw (1996).

Samples were crushed and sieved to >125μm and <1 mm before washing in deionised water to remove any excess rock powder that had attached itself to the sand-sized grains during crushing. The washed grains were dried in an oven at 75°C for 12 to 24 hrs. Approximately 5 gm of sample, weighed to the nearest μg (e.g. 5.2545 gm) was placed in a reaction tube. The reaction tube is similar to the reaction tubes used for off-line extraction of CO_2 from carbonates for stable isotope analysis (Figure 7.1).

Approximately 45 ml of 10% EDTA solution was added to the sample in the reaction tube. The EDTA solution is a mixture of 58% di-sodium salt of EDTA $\{[CH_2N(CH_2COOH).CH_2COONa]_2.2H_2O\}$ and 42% tetra-sodium salt of EDTA $\{[CH_2N(CH_2COONa)_2]_2.2H_2O\}$. This combination gives the solution a pH of 6.85 log units. Solutions with a pH significantly below 6.85 log units dissolve the carbonate too rapidly, producing CO_2 from the host carbonate mineral additional to the CO_2 liberated from the fluid inclusions. Solutions with a pH significantly above 6.85 log units react too slowly with the sample, and prolong the reaction time into weeks instead of days.

The filled reaction tube is fitted to an air tight head piece that has a tap which allows evacuation of air from the head space and a specially built port where a tightly fitted silicone septum is inserted. The silicone septum provides a gas tight seal through which a syringe needle can be inserted to remove an accurate quantity of liberated gas from the head space volume (Figure 7.1). The head piece has a head space volume of 15 ml.

Once assembled, the reaction tube is evacuated of air from the head-space and placed in a stirring bath for 48 hrs. Vibrations generated by the stirring bath plus regular, but gentle agitation by hand promotes faster dissolution of the carbonate in the sample.

The tube is removed from the stirring bath after the 48 hour period and agitated firmly by hand for 3 minutes. This liberates any evolved gas that may be attached to the surface of the remaining grains. A 500μl aliquot of liberated gas is removed from the head space of the reaction tube by a syringe via the silicon septum and immediately injected into the port of the gas chromatograph (GC).

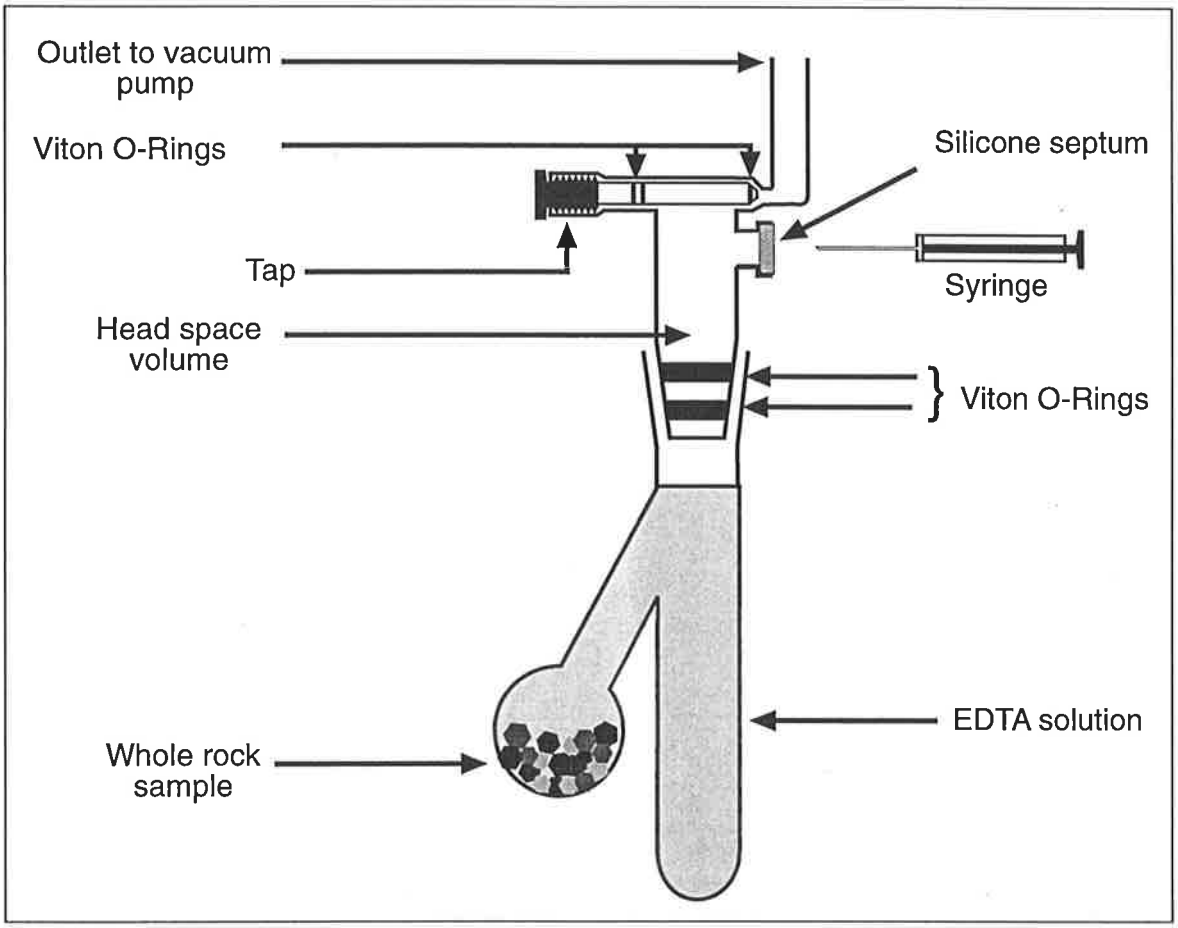


Figure 7.1. Reaction chamber used to dissolve carbonate from whole rock sample. Tap allows the head space air to be removed by vacuum pump. Evolved gas is removed from head space via the silicone septum by a syringe.

The GC used for all analyses was a Perkin Elmer Autosystem GC fitted with a flame ionisation detector (FID). The GC was fitted with a 2 m x 1/8" stainless steel column packed with Unibeads 2S, 60/80 mesh. The detection program was run at 70°C for 10 minutes until all of the sample had passed through the detector. Gas peaks were processed on a MacIntosh computer running software programs Maclab Peaks Vol. 1.3.4 (Noever *et al.*, 1994) and Maclab Charts Vol. 3.3.7 (Macknight *et al.*, 1994).

The raw GC data was converted to CH_4 in volume parts per million (vppm) by standardising the peak area of the sample gas obtained from a 500µl aliquot against the peak area of a standard gas known to contain 100 ppm methane, 100 ppm ethane, 100 ppm propane, 100 ppm butane, 100 ppm pentane and 100 ppm hexane in a nitrogen make up gas (Equation 7.4). The standard was supplied by Scott Specialty gases, USA

Conc. of gas in sample (vppm) = volume area of sample gas / volume area of standard x 100 (Equation 7.4)

It should be noted that the concentration of CH_4 in the 500 µl aliquot removed from the reaction

tube is not representative of the volume of CH_4 released from that sample. This is because different samples contain different quantities of carbonate which release different volumes of hydrocarbons (i.e. a sample containing 0.7 gm of carbonate may release the same amount of CH_4 into the head space area of the reaction tube as a sample that contains only 0.3 gm of carbonate). Therefore, it is important to calculate the total volume of CH_4 released into the head space of the reaction tube and to standardise this volume against the weight of carbonate present in each sample analysed.

The weight of carbonate dissolved in each sample is calculated by measuring the difference between the initial whole rock weight and the post-reaction residue weight. The weighing of the post-reaction residue involves draining the acid solution from the post-reaction residue immediately after the head-space gas has been analysed, rinsing the sample with deionised water and drying the sample at 75°C over-night. The dried residue is weighed and the weight is subtracted from the initial weight of the sample.

The volume of CH_4 released into the head space of the reaction tube is calculated through a series of short equations. Firstly, the weight of CH_4 present in a 500 µl aliquot of standard gas containing 100 ppm CH_4 must be determined (Equations 7.5 and 7.6).

0.05 (vol. of CH_4 at 100 ppm in 500µl aliquot) x

10^{-6}/22.4 (a mole of CH_4 at 0°C and at atmospheric pressure) ⇒ 2.23 nanomoles (Equation 7.5)

Therefore,

2.23 (nanomoles) x 16 (molecular weight of CH_4) ⇒

35.68 ng (weight of CH_4 at 100 ppm in 500 µl aliquot) (Equation 7.6)

This weight of CH_4 at 100 ppm in a 500 µl aliquot is standardised against the vppm CH_4 volume calculated in Equation 7.4 (e.g. 306.66) to give the weight of CH_4 extracted from the head space in the 500µl aliquot (Equation 7.7).

Thus,

35.68ng x 306.66 (vppm CH_4 sample)/100 = 109.42 ng/500 µl aliquot (Equation 7.7)

This value allows calculation of the total volume of CH_4 liberated into the head space, given that the head space volume is constant (15 ml). Therefore, the volume of CH_4 in the 15 ml head-space is equal to 3282.6 ng. Dividing this value by the weight of carbonate that dissolved

in the sample gives the volume of CH_4 released per gm of carbonate dissolved. Thus, if 0.6114 gm of carbonate dissolved from the sample, it would release 5368.86 ng (or 0.54 mg) of CH_4 per gm of carbonate dissolved.

7.3 Results

Samples analysed by EDTA dissolution - gas chromatography (EDTA-GC) are subdivided according to their alteration assemblage and their relationship to gold mineralisation (BCZ, PCZ, DCZ, unaltered gabbro or post gold SV-type quartz veins). Results are summarised in Table 7.1, Figures 7.2 and 7.3, and are presented in full in Appendix VII.

EDTA-GC data

Sample Number	Sample type	Au (ppm)	CH_4 (ppm)	CH_4 /gram carbonate#	C_2H_6 (ppm)	C_2H_6/gram carbonate#
1074-17	BCZ	31	314.84	5368.86	0.42	20.73
1074-36	BCZ	6.9	471.00	8067.83	0.66	31.83
1074-42	BCZ	0.27	346.83	4071.55	0.43	14.21
1074-47	BCZ	4.88	341.96	4502.86	0.89	32.93
1074-84	BCZ		45.84	1408.35	BDL*	
1074-87	BCZ	1.47	526.48	7126.19	1.37	51.94
1074-102	BCZ	0.04	293.86	4517.40	BDL*	
1074-151	BCZ		67.34	958.92		
1074-200	BCZ	15.67	53.86	709.49	BDL*	
1074-204	BCZ		118.82	1801.42		
1074-234	BCZ	7.03	179.81	2217.15	0.34	11.77
1074-252	BCZ	7.6	14.84	316.60		
1074-259	BCZ	10.95	89.66	1067.97	BDL*	
1074-192	PCZ/DCZ		17.88	292.30		
1074-210	PCZ/DCZ	0.07	12.56	163.68		
1074-233	PCZ/DCZ	0.01	13.53	191.77		
1074-237	PCZ/DCZ		8.66	111.91		
1074-240	PCZ/DCZ	0.41	6.85	164.87	BDL*	
1074-241	PCZ/DCZ	0.25	17.77	261.05		
1074-245	PCZ/DCZ	0.26	24.13	311.17		
1074-257	PCZ/DCZ	0.76	7.30	170.43		
1074-35	SV-type		43.51	2928.10		
1074-121	SV-type		23.88	907.34		
1074-264	unaltered gabbro	0.01	1.27	237.28		
1074-272	unaltered gabbro	0.01	1.63	369.43		
1074-275	unaltered gabbro	0.01	1.17	294.17		
1074-276	unaltered gabbro	0.01	1.13	245.09		
1074-277	unaltered gabbro	0.07	10.06	460.25		

Table 7.1. Summary of data collected by EDTA-GC analysis. Hydrocarbon volumes are calculated from volumes of gas liberated from carbonate bearing rock samples associated with mineralisation at the Junction gold deposit.

Weight of sample in ng per gram of carbonate dissolved.
* Below detection limit

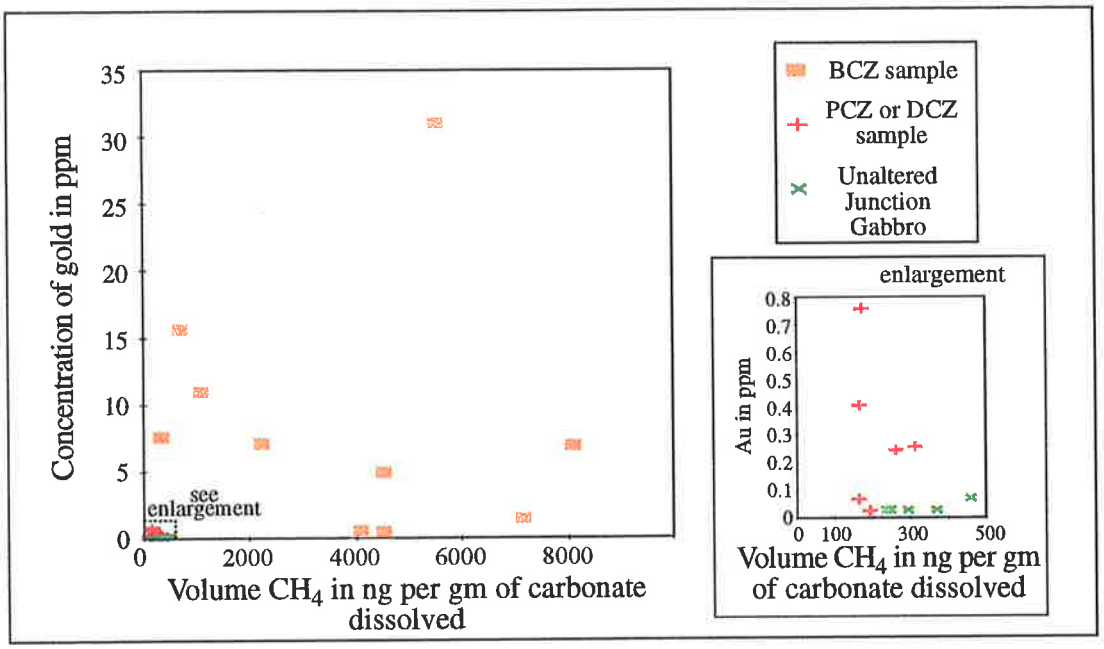


Figure 7.2. Scatter plot comparing the volumes of CH_4 released from one gram of carbonate to the concentration of gold for the same sample.

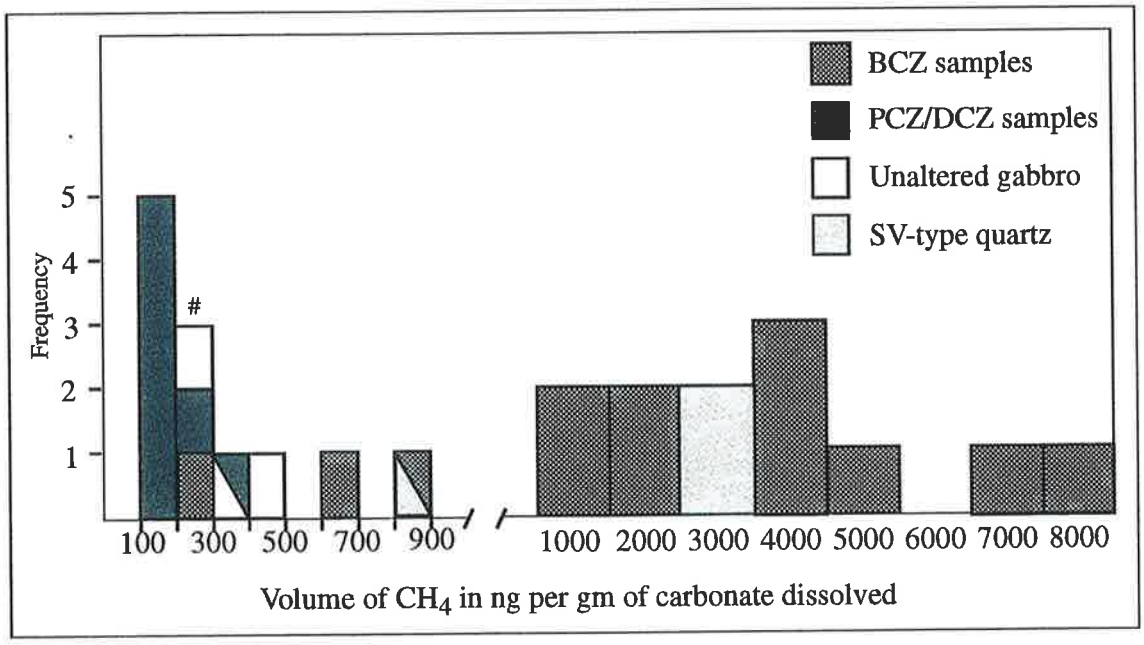


Figure 7.3. Histogram showing the distribution of CH_4 in different sample types analysed from the Junction deposit.

** Note change in horizontal scale!

Note that there are three unaltered gabbro samples that give between 200 and 300 ng of CH_4 per gm of carbonate dissolved, two PCZ/DCZ samples that give between 200 and 300 ng of CH_4 per gm of carbonate dissolved and one BCZ sample that gives between 200 and 300 ng of CH_4 per gm of carbonate dissolved.

Figure 7.2 plots the corrected volume of CH_4 liberated from one gm of carbonate against the gold grade in ppm for that sample. Figure 7.3 is a histogram comparing the volumes of CH_4 liberated from one gm of carbonate from different sample types. Figure 7.2 is slightly incomplete as not all samples were analysed for gold (see Table 7.1).

Thirteen samples representing the syn-gold BCZ, contained between 316 and 8067 ng of CH_4 per gm of carbonate (Figure 7.2 and 7.3) with a mean value of 3252.14 ng of CH_4 per gm of carbonate, n = 13. Minor concentrations of ethane were detected in six of the 13 samples analysed. Trace amounts of ethane, at volumes smaller than the measuring capabilities programed into the GC, were detected in a further four samples. Concentrations of ethane are low and range from 11.53 to 51.91 ng of ethane per gm of carbonate (Table 7.1).

Eight samples representing the syn-gold PCZ and DCZ contain between 111 and 311 ng of CH_4 per gm of carbonate (Figure 7.2 and 7.3), with a mean value of 208.40 ng of CH_4 per gm of carbonate, n = 8. The lower range of values for samples from the BCZ overlap with the upper range of values for samples from the PCZ and DCZ. This may represent samples that were collected from an area where the transition between the BCZ and PCZ was ambiguous. The remaining samples display an obvious distinction between the two populations (Figure 7.3). Ethane is suspected in only one of the samples representing the PCZ and the DCZ. However, the volume of ethane present is below the detection limits of the GC.

Five samples of unaltered gabbro from one drill hole were analysed for their light hydrocarbon content. Four of the five samples contain between 237 and 369 ng of CH_4 per gm of carbonate. One sample (1074-277) is weakly altered, and contains only minor amounts of carbonate. This sample contains 460 ng of CH_4 per gm of carbonate. All of these volumes are similar to or greater than the volumes obtained from the PCZ and DCZ samples. Thus unaltered gabbro samples appear to contain higher volumes of CH_4 than the samples representing the PCZ and the DCZ. Although it can not be unequivocally stated that the unaltered gabbro contains less CH_4 per gm of carbonate than samples from the PCZ and the DCZ, it is unlikely that the unaltered gabbro would contain more CH_4 than the altered PCZ and DCZ samples. It is likely that this discrepancy is amplified by the very small volumes of carbonate present in the unaltered gabbro compounded by the calculations used to estimate the volumes of CH_4 present in each sample. In any case, the trace amounts of carbonate present in the unaltered gabbro and the small quantities of CH_4 present within this carbonate are negligible when compared to the samples from the BCZ. Therefore it is unlikely that the unaltered gabbro could produce the CH_4 anomaly that is detected in the soil atmosphere at the surface.

Two samples representing the post gold, SV-type quartz veins were analysed by EDTA - gas chromatography. Both samples contain large carbonate crystals that are present within the quartz vein. The two samples contain 907 and 2928 ng of CH_4 per gm of carbonate. These values are

similar to and overlap the values obtained from BCZ samples. Their significance to the total CH_4 budget is discussed below. Gold concentrations were not determined for these samples, and so they do not appear in Figure 7.2.

7.4 Discussion

The results indicate that CH_4 and trace amounts of ethane are directly associated with gold mineralisation. The highest CH_4 values correspond to the most intensely altered areas of the BCZ where gold grades are highest. Samples analysed from unaltered and weakly altered gabbro, where gold grades are negligible to sub-economic, contain only minor to negligible volumes of CH_4 (Figure 7.4). These results suggest that the CH_4 detected at the surface by passive samplers, probably originated from fluid inclusions in alteration minerals that are associated with gold mineralisation.

Visual inspection of BCZ hand specimens from CH_4-containing samples indicate that the highest CH_4 values are coincident with carbonate grains that have developed at the margins of the quartz vein - host rock contacts. Lower, but still anomalously high CH_4 values are recorded in samples in altered BCZ gabbro away from the margins of the quartz vein - host rock contacts. This is probably a reflection of fluid inclusion entrapment during carbonate precipitation in open fractures generated by seismic activity (i.e. fracture-vein opening as discussed in Chapter 5). In contrast, carbonate that developed in the host rock as a replacement overgrowth of other minerals trapped fewer fluid inclusions, thus lower volumes of CH_4.

Similar patterns of CH_4 distribution were not noted in samples taken from the proximal and distal chlorite zones (PCZ and DCZ) despite the abundance of vein related carbonate in these samples (e.g. sample 1074-233 is an example of a quartz-carbonate-chlorite vein in the DCZ (see Figure 3.9, Chapter 3), but its CH_4 value is similar to sample 1074-210 which is a wall rock sample within the PCZ [Table 7.1]). Either way, CH_4 volumes are elevated throughout all areas within the BCZ relative to CH_4 levels detected in the PCZ, the DCZ and the unaltered gabbro. These results are schematically illustrated in Figure 7.4.

The association between CH_4 and gold mineralisation is presented in Figure 7.2. It can be seen that samples containing negligible to sub-economic gold grades (< 0.8 ppm Au) contain only minor to negligible volumes of CH_4. In contrast to this, the majority of samples collected from the BCZ contain moderate to high CH_4 volumes and sub-economic (< 0.8 ppm Au) to high (> 3 ppm Au) gold grades. A linear trend between elevated CH_4 volumes and higher gold grades is not observed, nor is it expected. This is because small hand specimens often return gold grades that are not representative of the ore body as a whole. This erratic distribution of gold in hand specimen is known as the "nugget effect" and can be seen when comparing two samples from the BCZ 1074 -17 (31 ppm Au) and 1074-102 (0.04 ppm Au). The lack of a linear trend is further compounded by the wide range of CH_4 volumes released from samples within the

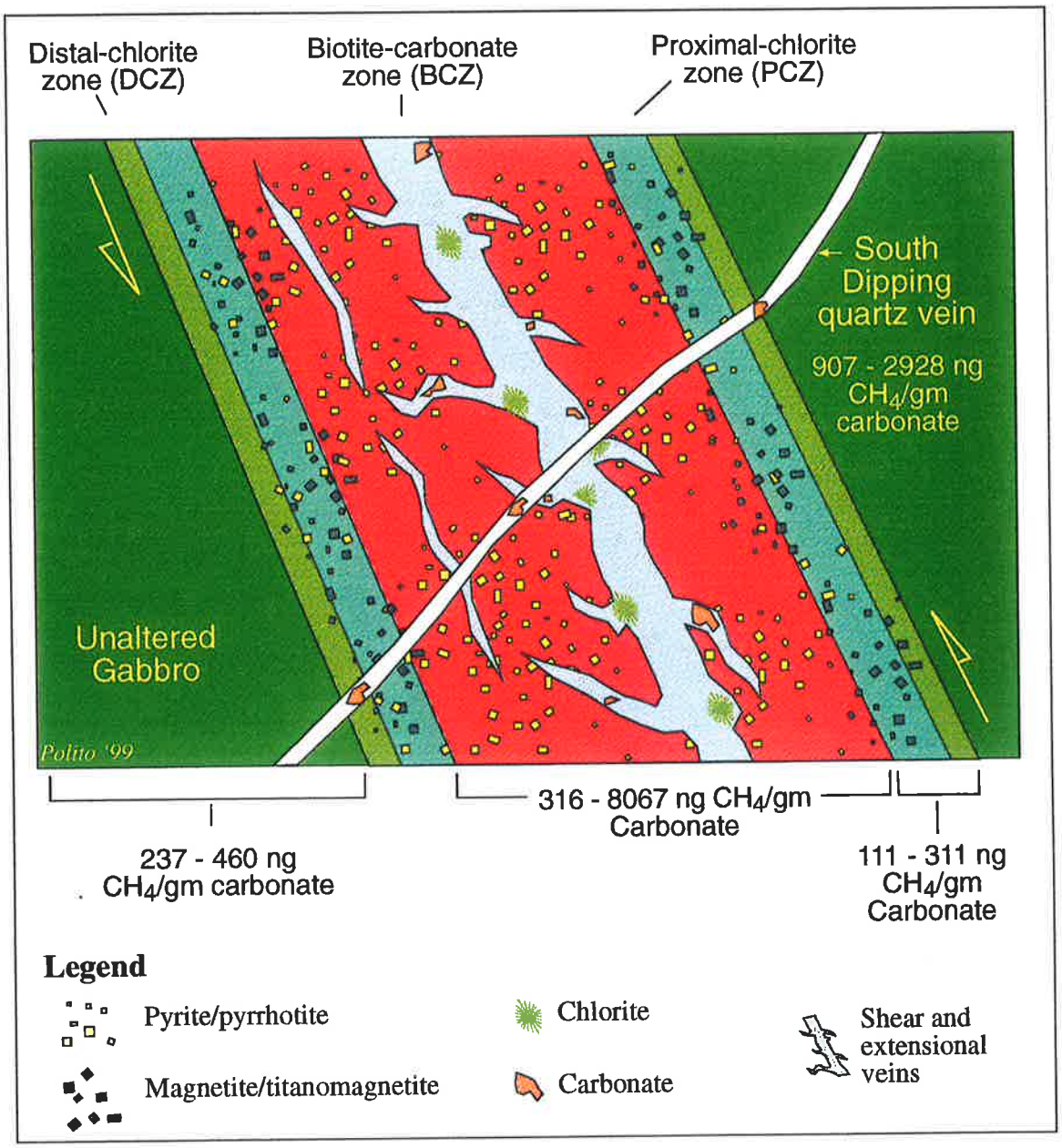


Figure 7.4. Schematic cartoon of CH_4 distribution through the Junction shear zone. The highest CH_4 volumes are concentrated in the BCZ whereas the lowest CH_4 volumes are found in the unaltered gabbro.

BCZ due to the factors discussed above. Nevertheless, the differences between samples from the BCZ and the PCZ-DCZ and unaltered gabbro based on CH_4 volumes and gold concentrations are large enough to conclude that high CH_4 volumes are primarily related to gold mineralisation in the Junction shear zone.

7.4.1 Related work and possible hydrocarbon origin

A similar hydrocarbon distribution to that present at Junction is observed in rock samples collected at the surface at the Ashanti gold deposit, Ghana. Amanor (1979) used heat extraction to liberate hydrocarbons from unaltered metasediments (argillite and metasandstone), calcareous

metasediments related to gold mineralisation and gold-bearing quartz veins. Analyses of samples from outcrops in the vicinity of gold mineralisation at Ashanti detected high levels of CH_4 either side of gold-bearing quartz veins, but low to negligible levels of CH_4 in unaltered host rock. Gold-bearing quartz veins have a negative CH_4 anomaly relative to the adjacent alteration assemblage. Figure 7.5 shows that the highest hydrocarbon volumes at Ashanti do not exceed 400 parts per billion, whereas CH_4 volumes in the BCZ at Junction using the EDTA extraction technique regularly exceed 200 parts per million! This phenomenon is possibly due to the different extraction methods used to extract the hydrocarbons from the two deposits (cf. Mulshaw, 1996).

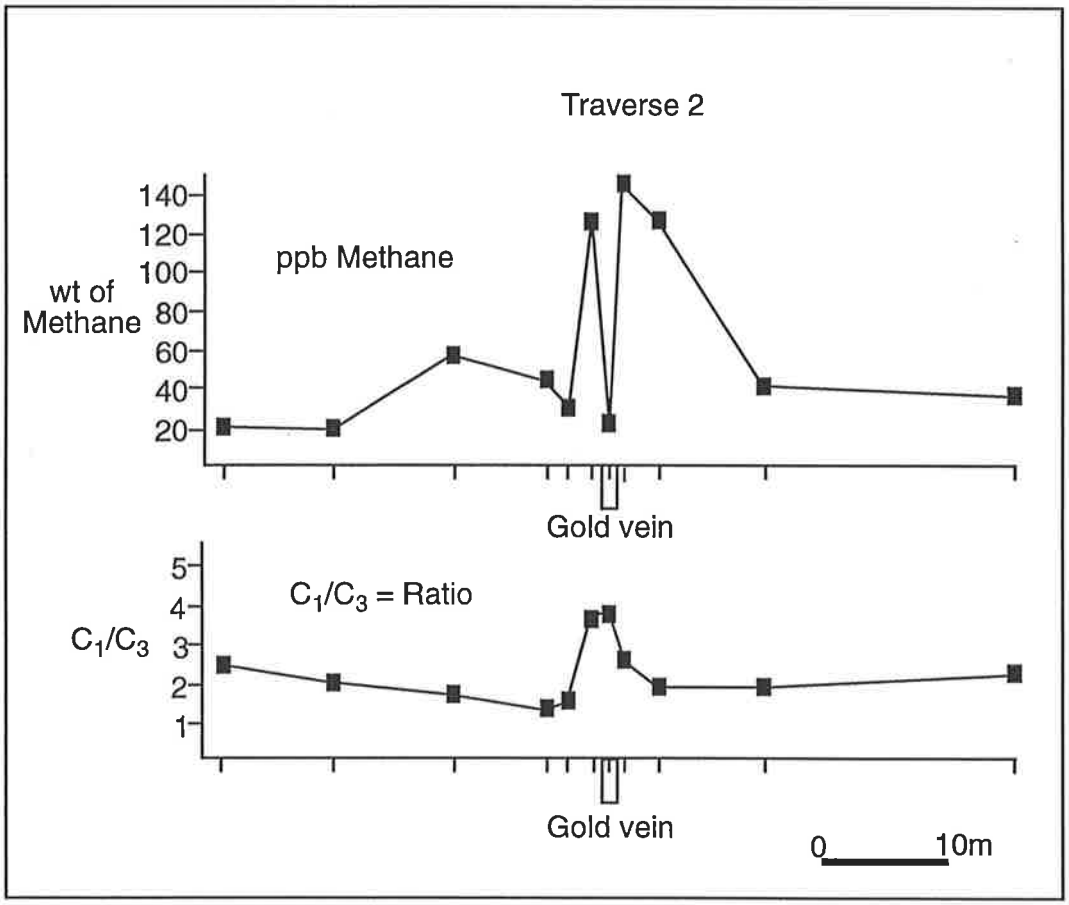


Figure 7.5. Distribution of hydrocarbons across outcropping mineralisation at the Ashanti gold mine, Ghana. Vertical lines on the x-axis indicate sample locations. Samples analysed from Ashanti outcrop at the surface. Therefore they are comparable to the results obtained from fresh rock analysed and discussed in this chapter. Figure taken from Amanor (1979).

Unlike Junction, gold mineralisation in shear zones and quartz veins at Ashanti is hosted in carbonaceous and graphitic metasediments (Oberthur *et al.*, 1996; Mumin *et al.*, 1996). Stable isotope evaluation and fluid inclusion microthermometry indicate that there was extensive interaction between this organic matter with a light $\delta^{13}C$ value and a CO_2-rich hydrothermal fluid (Oberthur *et al.*, 1996). This interaction probably produced the CH_4 volumes observed at Ashanti. No carbonaceous material has been observed at Junction, but similar $CH_4 \pm$ ethane-

generating processes appear to have occurred. However, regardless of the hydrocarbon generation process, the hydrocarbon distribution style in whole rock samples at Ashanti and Junction is identical.

The distribution of hydrocarbons throughout Junction suggests that CH_4 and trace amounts of ethane may be a by product of the interaction of a hot H_2O-CO_2 fluid interacting with an Fe-rich host rock. The process of Fischer-Tropsch hydrocarbon synthesis is investigated further in Chapter 14.

Whilst the in situ synthesis of hydrocarbons at Junction is the most logical origin for these volatiles, their introduction into the ore body after the gold mineralising event can not be over looked. De Ronde *et al.* (1992) found that highly strained quartz sampled from the Three Sisters deposit in the Barberton Greenstone belt, South Africa, contained more H_2O, less CO_2 and noticeably more CH_4 than similar deposit styles that exhibited less strain within the same greenstone belt. Samples with the highest degree of strain contained the largest volume of CH_4. De Ronde *et al.* (1992) suggest that the volume of hydrocarbons present in each deposit is related to the degree of post-mineralisation strain and consequently the amount of fluid overprinting that these samples have endured.

Similarities between the hydrocarbon anomalies at Ashanti and Junction add to the speculation that CH_4 is concentrated in fluid inclusions in the carbonates, feldspars and sulphides within the alteration assemblage and not in the fluid inclusions hosted by quartz. EDTA extraction does not allow CO_2 : CH_4 ratios to be calculated (a data set that would allow direct comparison between EDTA-GC results and heat-crush GC results by other workers [e.g. Andrawes and Gibson, 1979; Smith *et al.*, 1984; Bray *et al.*, 1991, 1992; de Ronde *et al.*, 1992]). However, Bray *et al.* (1991) and Bray and Spooner (1992) found that scheelite from the Hollinger-McIntyre gold quartz-vein system in Canada contained higher volumes of CH_4, thus lower CO_2 : CH_4 ratios than the gold-bearing quartz veins themselves. Further to this, these authors also found that tourmaline crystals immediately external to the Tanco granitic pegmatite, S.E. Manitoba, contained lower CO_2 : CH_4 ratios than quartz vughs found within the pegmatite.

Raman spectroscopy (Chapter 6) supports these findings, revealing that fluid inclusions in quartz immediately adjacent to the quartz vein - host rock contact are enriched in CH_4 with respect to CO_2, whereas fluid inclusions in the quartz vein away from the quartz vein - host rock contact contain only negligible to trace amounts of CH_4 with respect to CO_2 (see Figure 6.3, Chapter 6). If this distribution of hydrocarbons is common around other late-orogenic, structurally-controlled gold deposits similar to Junction, then it is possible that they too contain high volumes of hydrocarbons in their non-quartz alteration assemblage. This also suggests that other late-orogenic, structurally-controlled gold deposits may have a light hydrocarbon anomaly in the soil above their mineralisation. The volume of hydrocarbons present in non-quartz alteration

minerals compared to the volume of hydrocarbons present in quartz vein material has not previously been recognised except for the work of Bray *et al.* (1991) and Bray and Spooner (1992). Therefore the potential of using hydrocarbons as an exploration vector for this style of mineralisation has been overlooked in the past.

It could be argued that post-entrapment decrepitation of fluid inclusions, in a cleavable mineral, preferentially releases one volatile species (such as CO_2) whilst retaining the other (like CH_4). However, this is not supported by Watson and Brenan (1987) or Boullier and Robert (1992), who give detailed accounts of volatile migration and entrapment within fractures as a function of wetting angle properties. These authors show that CO_2 and CH_4 are preferentially trapped along fractures and cleavage planes because of their wetting angle over other volatiles such as water. Therefore, it is likely that if CO_2 was released from a mineral by post-entrapment decrepitation, then CH_4 would also be released. Indeed, Roedder (1984) and Shepherd *et al.* (1985) state that CH_4 has strong partitioning properties with CO_2 and that it is common for CH_4 to dissolve into the liquid CO_2 in fluid inclusions. Further to this, visual inspection of thin sections with carbonate and albite grains clear enough to observe fluid inclusion populations (Figures 5.1 and 5.2) reveals that the ratio of decrepitated to preserved fluid inclusions in the carbonate and albite grains is the same as the ratio observed in quartz grains in the same thin section. Therefore it is not likely that fluid inclusion decrepitation favours the accumulation of one volatile over the other.

It cannot be overlooked that the bulk extraction of volatiles from fluid inclusions in alteration minerals (quartz, carbonates, scheelite and/or feldspars) lacks quality control, given that all fluid inclusion populations, regardless of their association to mineralisation, release volatiles during analysis. This is a key problem with any bulk analysis technique. However, Bray *et al.* (1991) and Bray and Spooner (1992) compared crush-release results from a carefully selected 50 mg quartz wafer, with approximately two gm of quartz chips from the same sample. They found that mol. % values for H_2O, CO_2 and CH_4 are satisfactorily consistent. Further to this, fluid inclusion studies by Robert and Kelly (1987), Bray *et al.* (1991), Robert *et al.* (1995), Boullier *et al.*, (1998) and Field *et al.* (1998) and fluid inclusion results reported in Chapters 5 and 6 show that secondary fluid inclusions that cross-cut quartz veins contain either zero or negligible concentrations of CO_2 and CH_4. Therefore, secondary fluid inclusions at these deposits are not likely to affect the results obtained from bulk extraction analysis.

Unlike the secondary fluid inclusions discussed above and in Chapter 5, it is possible that the post-gold fluids that deposited the SV-type quartz veins, introduced large volumes of hydrocarbons that are not related to gold mineralisation. EDTA-GC analysis, Raman spectroscopy and fluid inclusion microthermometry show that post-gold SV-type quartz veins contain similar concentrations of CH_4 as the syn-gold alteration assemblage. However, alteration selvages around the SV-type quartz veins are not present in either the altered Junction Shear Zone or the unaltered Junction

Gabbro (Chapter 3.6.3), thus, the introduction of volatiles by these veins is believed to be negligible. Gold distribution and alteration minerals that occur near post mineralisation intrusives (e.g. Proterozoic dolerite dykes), are known to be visually affected up to 30 m away from the intruding body (Ellis and Mapleson, 1997). Therefore, carefully selected samples (i.e. away from cross cutting veins known to be post mineralisation and at least 100 m away from post mineralisation intrusives) are required for good geochemical results.

Finally, hydrogen movement into and out of fluid inclusions in quartz as discussed by Mavrogenes and Bodnar (1994) does not appear to affect the volumes of CH_4 present in most fluid inclusions within minerals at Junction. These authors demonstrate that hydrogen can move hundreds of micrometres through quartz in several days when differences in fH_2 and fO_2 outside the fluid inclusion are different to the fH_2 and fO_2 inside the fluid inclusion. However, diffusion of hydrogen into or out of fluid inclusions at Junction is not indicated. The ratios of CH_4 to CO_2 as determined by Raman spectroscopy (Chapter 6) vary from one fluid inclusion to another depending on the proximity of that fluid inclusion to the quartz-vein host-rock contact. Thus, this variability defies the homogeneous gas ratios that may be expected from hydrogen diffusion into or out of the fluid inclusions. Fluid inclusions affected by hydrogen diffusion at Junction should display a relatively consistent ratio of CO_2 : CH_4 through out the deposit, but this is clearly not the case.

7.4.2 Relevance to soil gas anomaly

The results from the EDTA - GC analyses indicate that large volumes of CH_4 and lesser volumes of $C_2H_{(2n+2)}$ are trapped in fluid inclusions in carbonate associated with gold mineralisation (up to 8000 ng per gm of carbonate). It is conceivable that this volume of CH_4 is only a fraction of the total CH_4 budget likely to be present in the ore body and that other non-quartz minerals are likely to contain similar volumes of hydrocarbons. It is envisaged that the light hydrocarbon budget directly related to gold mineralisation is significant and sufficiently large to generate the hydrocarbon anomaly that is detectable at the surface by the passive sampling method discussed in Chapter 4. This hypothesis is based on fluid inclusion populations observed in carbonate and albite, sulphides (Guha *et al.*, 1991; Richards and Kerrich, 1993; Hagemann *et al.*, 1994) and scheelite (Robert and Brown, 1986; Bray and Spooner, 1992) in other late-orogenic, structurally-controlled gold deposits in Western Australia and Canada. The hydrocarbons are trapped in these easily weathered and oxidised minerals. This suggests that the release of significant quantities of CH_4 and other light hydrocarbons from the fresh rock - weathered rock interface into the soil atmosphere is highly likely.

Additions to the soil-gas anomaly by the weathering of carbonates in the post-gold SV-type quartz veins cannot be ruled out. However, whilst EDTA-GC analysis, Raman spectroscopy and fluid inclusion microthermometry reveal that post-gold SV-type quartz veins contain similar concentrations of CH_4 as the syn-gold alteration assemblage, the presence of high CH_4 volumes

in carbonates hosted by SV-type quartz veins is not expected to add significant volumes of CH_4 to the CH_4 budget of the deposit. In fact, considering the small number of SV-type quartz veins that are present throughout the deposit relative to the alteration and veining associated with gold mineralisation (see Figures 3.3a, 3.3b and 3.4), and the quantity of carbonate present in these quartz veins, the total CH_4 budget added to the soil-gas anomaly by the SV-type quartz veins is negligible.

In conclusion, EDTA-GC analysis has identified a primary source for the CH_4 detectable in soil above the ore deposit. CH_4 is predominantly found in minerals only associated with the alteration assemblage containing the highest gold grades. This suggests that CH_4 anomalies detected in soil should only be found above mineralised shear zones that have a similar alteration assemblage to that of Junction. Further to this, the abundance of CH_4 in minerals that are most susceptible to weathering (carbonates, feldspars and sulphides) indicates that continuous emission of light hydrocarbons to the soil atmosphere should occur so long as the ore deposit is oxidising and these minerals are being subject to chemical degradation.

CHAPTER EIGHT

Aliphatic and aromatic hydrocarbons in the biotite-carbonate zone

8.1 Introduction

Occluded aromatic >> aliphatic hydrocarbons are detectable along both of the soil-gas traverses discussed in Chapter 4. However, their origin and relationship to gold mineralisation is enigmatic. Mineralisation at Junction is not associated with any visible organic matter or graphite, thus, the aromatic >> aliphatic hydrocarbons are either contaminants in the soil or they are present in the deposit at very low concentrations, possibly trapped in fluid inclusions.

Light gaseous hydrocarbons, particularly CH_4, are found in fluid inclusions in nearly all metamorphic and igneous hosted ore deposits (Chapter 4.6.5). However, heavier hydrocarbons are rarely recorded in any ore deposit other than the sediment-hosted, Mississippi Valley-type Pb-Zn±Cu deposits, black-shale copper deposits, Carlin-type disseminated gold deposits, Archaean Witwatersrand gold-uranium deposits and various styles of uranium mineralisation (Landais and Gize, 1997).

Organic mass spectrometry coupled with state of the art gas chromatography has the sensitivity to detect picomol volumes of aliphatic and aromatic hydrocarbons by separating compounds that have virtually identical mass spectra (e.g. pentane, hexane and octane) by their boiling point using gas chromatography. Actlabs, Ancaster, Ontario were consulted to determine if any aliphatic and/or aromatic hydrocarbons could be detected in fresh, unweathered ore bearing rock collected from various areas within the biotite-carbonate zone (BCZ). Actlabs were used because of their experience in detecting hydrocarbons adsorbed on to soil and sand particles, and because of their confidence to do the same with unaltered rock chips. To differentiate this method from the GC-MS method discussed in Chapter 12, the organic mass spectrometry - gas chromatography method discussed here is abbreviated to GC-OMS.

8.2 Methods, procedures and materials

Seven chip samples comprising quartz-carbonate vein material and altered gabbro from the BCZ were sent to Actlabs for analysis. This style of analysis (i.e. organic mass spectrometry on metamorphosed igneous rock) had not been conducted before by Actlabs, and "considerable experimentation" was conducted to determine the best sample preparation for this type of analysis. For this reason, Actlabs choose to keep much of the methodology confidential.

Nevertheless, rock chips were washed with acetone prior to analysis to eliminate equipment and fingerprint contamination. The samples were then dried and pulped to <-150 mesh. Approximately 0.2 to 0.25 gm of sample was loaded into a sealed container for passive head-space extraction of hydrocarbons.

The head-space technology used by Actlabs is confidential. However, the technique involved moderate heating and the addition of distilled water to the sample prior to hydrocarbon liberation and extraction. The hydrocarbons desorbed from the sample into the head-space were absorbed on to an activated carbon-coated filament, presumably similar to that used for detecting light hydrocarbon gases in soil above the N75 surface (Chapter 4). The filament was removed after the completion of the extraction technique and heated to its Curie point to release the trapped hydrocarbons. The hydrocarbons were then submitted to the GC-OMS for analysis. The same process was carried out on a quartz blank for analytical control, to determine if any contamination was introduced during the sample preparation method (i.e. acetone or machine introduced impurities).

The results of each sample are processed by a specialised computer program, developed to isolate each response, to subtract the background, to enhance the mass spectra, and to conduct a search against an in-house library of 140,000 compounds (Anonymous, 1996). Specific classes of hydrocarbons found to be common within a sample set were reviewed by Actlabs to determine the most abundant compounds present and if there were any variation in response from one sample to another. Only the most common compounds detected in all samples at significant concentrations were reported by Actlabs.

8.3 Results

Several compounds were detected from the seven samples analysed, including cycloalkanes, n-alkanes, branched alkanes, alkyl benzenes, methyl naphthalenes and alkyl anthracenes. Most of these compounds were at very low concentrations. Twelve compounds detected in significant and variable concentration that were common to all samples were:-

1	?(unidentified compound)	(C_8-C_9, Boiling Point Range [BPR] 126 - 151)
2	?(unidentified compound)	(C_9-C_{10}, BPR 151-174)
3	Dodecanal or Nonenol (aliphatic)	(C_{11}-C_{12}, BPR 196-216)
4	Cyclodecanol (aliphatic)	(C_{12}-C_{13}, BPR 196-216)
5	?(unidentified compound)	(C_{12}-C_{13}, BPR 196-216)
6	Heptadecyne / Undecanal (aliphatic)	(C_{13}-C_{14}, BPR 234-252)
7	Hydroxybiphenyl (aromatic)	(C_{14}-C_{15}, BPR 252-256)
8	?(unidentified compound)	(C_{15}-C_{16}, BPR 266-280)
9	Quinone (aliphatic)	(C_{15}-C_{16}, BPR 266-280)
10	Diethyl Biphenyl / Butylated Hydroxytoluene	(C_{15}-C_{16} BPR 266-280)
11	?(unidentified compound)	(C_{15}-C_{16}, BPR 266-280)
12	Cyclohexene Carboxylic acid (aliphatic)	(C_{16}-C_{17}, BPR 280-292)

Some compounds remain unidentified and others have choices that fit the mass spectra and boiling point range indicated. This is because identification via library spectra matching involves spectral comparisons between compounds detected and spectral patterns of a limited number of known organic compounds. The Actlabs computer library contains only 140,000 of the >2,000,000 organic compounds known to science (Anonymous, 1996). Therefore, very small background matrix differences between spectra in two different samples containing the same compound can result in two or more different library matches. The differences between the compounds identified is not greatly significant for these samples. However, the only way to reliably tell the compounds apart is to purchase both compounds (if available) and analyse them separately for reference (Anonymous, 1996).

8.4 Discussion and research into the atypical hydrocarbons detected

The detection of aliphatic and aromatic hydrocarbons in all of the Junction samples is not trivial given the nature of the host rock. However, investigations into the common hydrocarbons detected by GC-OMS reveal that none of the detected hydrocarbons are indigenous to the rocks analysed.

The Encyclopedia of Chemical Technology (Kroschwitz 1996), reveals that :

- dodecanal (C_{11} - C_{12}, BPR 196-216) is a synthetic alcohol derived from ethylene.

Synthetic alcohols made from this base are used in detergents, perfumes and in the production of plasticisers.

- cyclodecanol (C_{12} - C_{13}, BPR 196 - 216) is a synthetic alcohol-based hydrocarbon manufactured from sebacic acid. Sebacic acid and its derivatives are used in the plastics industry for plasticisers, alkyl resins, polyester resins, polyurethanes and polyamide moulding resins. It is also used in the preparation of dodecanedoic acid.

- heptadecyne (C_{13} - C_{14}, BPR 234 - 252) is an olefin. Higher olefins are used in the synthesis of certain intermediates which are used in the manufacturing of consumer products. The lighter olefins are used as synthetic lubricating oils and in high density polyethylene, as well as in the established areas of special detergents and in the manufacture of poly-vinyl-chloride (PVC) plasticiser alcohols.

- hydroxybiphenyl (C_{14} - C_{15}, BPR 252 - 266) is a synthetic phenolic compound manufactured from the desulfonation of sulfonic acid.

- butylated hydroxytoluene (C_{15} - C_{16}, BPR 266 - 280) is a general purpose antioxidant used in manufacturing plastics, especially low-density polyethylene. With extreme care, it can be used as an antioxidant in plastic used as electrical inhibitors on copper wire.

Significantly, all of the hydrocarbons identified by GC-OMS are synthetically manufactured or refined products of naturally occurring hydrocarbons. References to plastics, detergents and light oils is prolific. This indicates that the hydrocarbons detected by GC-OMS were either blasted into the rocks upon detonation of explosives used in the mine and/or they were introduced into the rocks by earth moving equipment in the form of machine oils, drilling fluids, lubricants or exhaust fumes.

It cannot be concluded that the unidentified aliphatic and aromatic hydrocarbons detected by GC-OMS are also manufactured hydrocarbons that are extraneous to the ore body. However, based on the evidence available, it is unlikely that the remaining unidentified hydrocarbons are indigenous to the Junction shear zone.

The identification of these hydrocarbons in the currently mined N25 surface cannot be directly linked to the predominantly aromatic hydrocarbons detected in the soil above the N75 surface approximately 400 metres east of the N25 surface, primarily because a precise identification of the soil occluded aromatic hydrocarbons is not known (see Chapter 4.6.5). However, it cannot be assumed that all of the aromatic hydrocarbons detected above the N75 surface are indigenous to the soil, or indeed related to alteration associated with gold mineralisation.

CHAPTER NINE

Oxygen isotope analysis

9.1 Introduction

Modern stable isotope geochemistry primarily involves accounting for variations in the isotopic composition of H, C, N, O, Si, and S in a variety of natural substances (Kyser, 1987). The isotopic composition of an element in co-existing phases is mostly influenced by small differences in the thermodynamic properties of the isotopes in these phases (Urey, 1947). The isotopic relationship between two co-existing, but not necessarily equilibrium species (i.e. the parent phase and the daughter phase) is known as the isotopic fractionation factor (Ohmoto and Goldhaber, 1997). The fractionation factor between the parent phase and the daughter phase in hydrothermal ore deposits is primarily a function of temperature (Kyser, 1987).

Stable isotope analyses of quartz and calcite from Junction was undertaken to determine:

- if the quartz and calcite are in isotopic equilibrium with each other,
- to further constrain the temperature of ore deposition, and
- to determine the origin of the ore fluid.

It can be assumed that the quartz and calcite are contemporaneous if it can be concluded that the they are in isotopic equilibrium with each other. It would then follow that the CH_4 detected in the calcite is contemporaneous with the CH_4 and CO_2 detected in the quartz. This is important given that the CH_4 (± light hydrocarbons) detectable in the soil probably originates from the fluid inclusions that would decrepitate during the dissolution of the calcite (+ albite + sulphides) more so than the breakdown of the more durable quartz at the oxidation front.

Further to this, if the quartz and calcite are in isotopic equilibrium with each other, their respective $\delta^{18}O$ values can be used to calculate the temperature of ore formation. The temperature determined from stable isotope pairs is considered to be more accurate, but nevertheless comparable to, the temperature estimates obtained from fluid inclusion microthermometry and mineral equilibria thermodynamics (Ohmoto and Goldhaber, 1997). An accurate temperature

for ore formation is required in the following chapters to not only help constrain the origin of the ore fluid, but to determine the origin of the CH_4 trapped in the fluid inclusions.

Delta^{18}O values are usually determined from quartz, carbonate, feldspar, chlorite, muscovite and biotite in late-orogenic, structurally-controlled gold deposits. The $\delta^{18}O$ values obtained from these minerals are used to identify and/or constrain the origin of the fluids responsible for forming the ore deposit. However, the fractionation of ^{18}O between different minerals is strongly temperature dependent. Therefore, in addition to identifying the origin of the fluid involved in forming a given ore deposit, oxygen isotopic studies may permit the estimation of the ambient fluid temperatures during mineralisation, given that the fractionation of oxygen isotopes between co-existing silicates and other oxygen-bearing ore minerals is a function of temperature alone (Friedman and O'Neil, 1977; and references in Kyser, 1987). Oxygen isotope geothermometry combined with the mineral equilibria temperatures reported in chapter 3 and the fluid inclusion entrapment temperatures reported in chapter 6 should constrain the temperature of ore formation to a narrow window.

Oxygen is abundant in the minerals that form the unaltered host rock in late-orogenic, structurally-controlled gold deposits rock (e.g. amphiboles, micas, feldspar, quartz, carbonates, iron-oxides etc.). However, research on these gold deposits (Kerrich and Fryer, 1979; Golding and Wilson, 1982, 1987; McNeil and Kerrich, 1986; Kerrich, 1987) has revealed that the $\delta^{18}O$ values of vein quartz is independent of the $\delta^{18}O$ of the host rock lithology. Further to this, quartz in the immediately adjacent altered wall rock is isotopically the same as its vein counterparts, but heavier relative to the unaltered host rock (Golding and Wilson, 1983; Golding and Wilson, 1987; Kerrich, 1989; Golding *et al.*, 1990b). Indeed, Golding and Wilson (1983) found a systematic $\delta^{18}O$ enrichment with increased wall rock alteration and gold mineralisation at the Mt Charlotte lode, Kalgoorlie.

Late-orogenic, structurally-controlled gold deposits have relatively uniform $\delta^{18}O$ values that cluster between +12.5 and +16‰ for quartz samples collected from gold-related alteration zones in the Archaean gold deposits, Canada (Kerrich, 1987; Colvine *et al.*, 1988), between +11 and +13.5‰ for quartz samples collected from gold-related alteration zones in the Norseman - Wiluna greenstone belt, Western Australia (Golding and Wilson, 1983, 1987; Golding *et al.*, 1989, 1990a, 1990b; Hagemann *et al.*, 1994) and between +9 and +13.5‰ for carbonate minerals sampled from gold-related alteration zones along the Norseman -Wiluna greenstone belt (references as above). The $\delta^{18}O$ values within each deposit are usually tightly clustered (± 1‰), implying that ambient conditions were consistent throughout successive hydrothermal pulses (Kerrich, 1987).

9.1.1 Application of oxygen isotopes as a geothermometer

The distribution of ^{18}O between mineral pairs is predominantly temperature dependent (Rollinson,

1993). Therefore, the enrichment of $\delta^{18}O$ in one mineral (e.g. quartz) relative to another co-existing mineral (e.g. calcite) can be used to determine the temperature of co-precipitation.

The expression summarising the temperature dependence of oxygen isotopic exchange between a mineral pair is given by Equation 9.1:

$$1000\ln\alpha \text{ mineral}^1\text{-mineral}^2 = A(10^6/T^2) + B \qquad \text{(Equation 9.1)}$$

where T is in °Kelvin and A and B are constants determined experimentally or empirically (Rollinson, 1993). The constant B is often zero and the fractionation factor is a function of $1/T^2$. Rollinson (1993) reports that calcite-mineral ^{18}O exchange is stable to relatively high temperatures. Thus, the best thermometers are between mineral-calcite pairs which show the greatest divergence on a $\ln\alpha$ vs $1/T^2$ diagram. However, Clayton *et al.* (1989) state that carbonate minerals are susceptible to retrograde ^{18}O exchange, and are therefore prone to extensive post-precipitation ^{18}O exchange. This would lead to erroneous temperature estimations.

9.1.1.1 Limitations on oxygen isotope geothermometry

The fractionation factor between two co-existing phases bearing the same isotope, as determined by experimental and theoretical calculations, can be used to determine the temperature at which the two phases were formed. The use of light stable isotopes as geothermometers is only successful in systems that have experienced no post-precipitation alteration of minerals, i.e. there has been no re-equilibration of isotopes. Temperature estimates calculated from the isotopic values of co-existing mineral pairs is considered to be more accurate than homogenisation temperatures of fluid inclusions (Ohmoto, 1986). However, stable isotope temperature estimates are typically in agreement (± 20 - 80°C) with temperature estimates made from fluid inclusion microthermometry (Kerrich, 1987, 1989; de Ronde *et al.*, 1992; Rollinson, 1993; Oberthur *et al.* 1996) and mineral equilibria thermodynamics (Phillips and Groves, 1984; Golding and Wilson, 1987; Clark *et al.*, 1989; McCuaig *et al.*, 1993; Mikucki and Ridley, 1993; Witt *et al.* 1997). Therefore, the use of light stable isotopes as geothermometers has the potential to further constrain the temperature of ore formation.

Successful application of stable isotope geothermometry to ore deposit minerals requires that the following three conditions be satisfied for all mineral pairs:

- the fractionation factors between the mineral pairs are well calibrated and strongly temperature dependent,
- the mineral pairs are in isotopic equilibrium at the time of deposition, and

- the mineral pairs have retained their isotopic composition since formation (Ohmoto, 1986).

Often, these underlying assumptions are not fulfilled, making the application of stable isotope thermometry questionable (Clayton, 1981). Of these three conditions required for the successful application of stable isotope thermometry, the most frequently violated condition is the retention of the original isotopic value since formation. Only in metamorphic rocks where there has been minimal fluid interaction following crystallisation can mineral pairs be used as reliable geothermometers.

Isotopic disequilibrium is most frequently found in slowly cooled rocks and in rocks that have exchanged isotopes with a late, externally-derived fluid. Giletti (1986) showed that in slowly cooling rocks, individual minerals cease to exchange oxygen as they pass through their blocking temperatures. Thus, only the last mineral pair to exchange oxygen will be in equilibrium. Alternatively, Clayton *et al.* (1968) found that retrograde oxygen isotope exchange leads to re-equilibration at temperatures lower than the ambient conditions of mineral-mineral precipitation. In particular, Clayton *et al.* (1968) found that carbonate minerals, particularly calcite, are often subject to retrograde isotope exchange. Kerrich (1987) reports that $\delta^{18}O$ values of dolomites in late-orogenic, structurally-controlled gold deposits are generally more erratic than the restricted range of $\delta^{18}O$ values obtained from co-existing quartz. This results in quartz-dolomite fractionations that are too large to represent isotopic equilibrium, despite textural evidence for their co-precipitation. Calcite tends to experience even more isotopic perturbation than dolomite (Clayton *et al.*, 1968). This suggests that calcite could rarely be used as a geothermometer. This finding, however, is in conflict with the findings of Rollinson (1993).

Isotopic equilibrium can be tested by plotting the values for the sets of mineral-pairs along appropriate isotherms. Minerals from an individual rock which are in isotopic equilibrium should show a smooth trend parallel to the isotherms. Isotopic values that do not plot approximately parallel to the appropriate isotherms are considered to be in disequilibrium (Rollinson, 1993).

9.2 Methods

Care was taken to avoid sampling quartz or carbonate samples within 100m of the two Proterozoic dolerite dykes that cross-cut mineralisation at Junction. Golding *et al.* (1989, 1990a, 1990b) note that some quartz samples at the nearby Victory-Defiance gold mine (ca. 30 km north of Junction) had very heavy and erratic $\delta^{18}O$ values (up to 34‰) that suggest low temperature exchange with a connate or metamorphic fluid. It is interpreted that these values reflect partial to complete isotope exchange during late fluid mobility associated with the intrusion of a Proterozoic dyke through gold mineralisation.

Selected quartz veins were crushed and sieved to a grain size of >63μm < 250μm. The sieved fraction was washed in deionised water to remove rock powder created through the crushing

process. It was then dried at 75°C for 12 - 24 hours. The washed sample was passed through a Franz magnetic separator to remove magnetic particles (chlorite, biotite, pyrrhotite, etc.) that formed part of the vein assemblage. Samples were then bathed in aqua-rega acid solution for 4 hours to remove any excess carbonate material. The sample was then bathed for 30 to 45 seconds in a diluted solution of hydrofluoric acid (HF^-) to etch and remove any remaining albite. This procedure was very effective on these small grain sizes. Albite grains that did not dissolve, were easily broken down by agitating the sample in distilled water in an ultrasonic bath. The suspended albite was easily poured away leaving behind pure quartz. Optical examination under a binocular microscope showed that no albite remained after bathing in HF^-, nor did any pitting or silica-coating of the quartz occur.

Gases for isotopic analysis were prepared using standard techniques (carbonates - McCrea, 1950; quartz - Clayton & Mayeda, 1963). Carbonate mass spectrometry was performed at the Department of Geology and Geophysics, University of Adelaide, South Australia, whereas silicate mass spectrometry was performed at The Department of Geological Sciences, Queens' University, Kingston, Ontario, Canada. All delta notations are relative to Standard Mean Ocean Water (SMOW) for both carbonate and quartz values.

9.3 Results

The $\delta^{18}O$ values were determined from vein- and wall-rock calcite and vein-quartz samples representing the three distinct fluid episodes that reflect pre-, syn- and post-gold mineralisation events.

9.3.1 Pre-gold, Mo-type quartz vein samples

Two Mo-type quartz vein samples gave $\delta^{18}O$ values of +11.8 and +11.9‰ (Figure 9.1).

9.3.2 Syn-gold quartz vein samples

The $\delta^{18}O$ values for 26 biotite-carbonate zone (BCZ) calcite samples range from +9.4 to +12.5‰ (mean = +10.6‰, standard deviation = 0.6‰, n = 26; Figure 9.1). The $\delta^{18}O$ values for seven proximal-chlorite zone and distal-chlorite zone (PCZ and DCZ) calcite samples are statistically identical to the $\delta^{18}O$ values obtained from the BCZ and range between and +9.6 to +12.5‰ (mean = +10.3‰, standard deviation = 0.9‰, n = 7; Figure 9.1).

$\delta^{18}O$ values for 14 quartz vein samples collected from within the BCZ exhibit a narrow range from +11.3‰ to +12.9‰, (mean = +12.3‰, standard deviation = 0.5‰, n = 14), while one quartz vein from the PCZ-DCZ has a value of +11.4‰ (Figure 9.1).

Eleven syn-gold quartz-calcite vein samples were selected for use as stable isotope geothermometers. Temperature estimates were calculated by plotting the $\delta^{18}O$ values for quartz against the corresponding $\delta^{18}O$ values of the co-existing calcite on a graph bearing fractionation curves

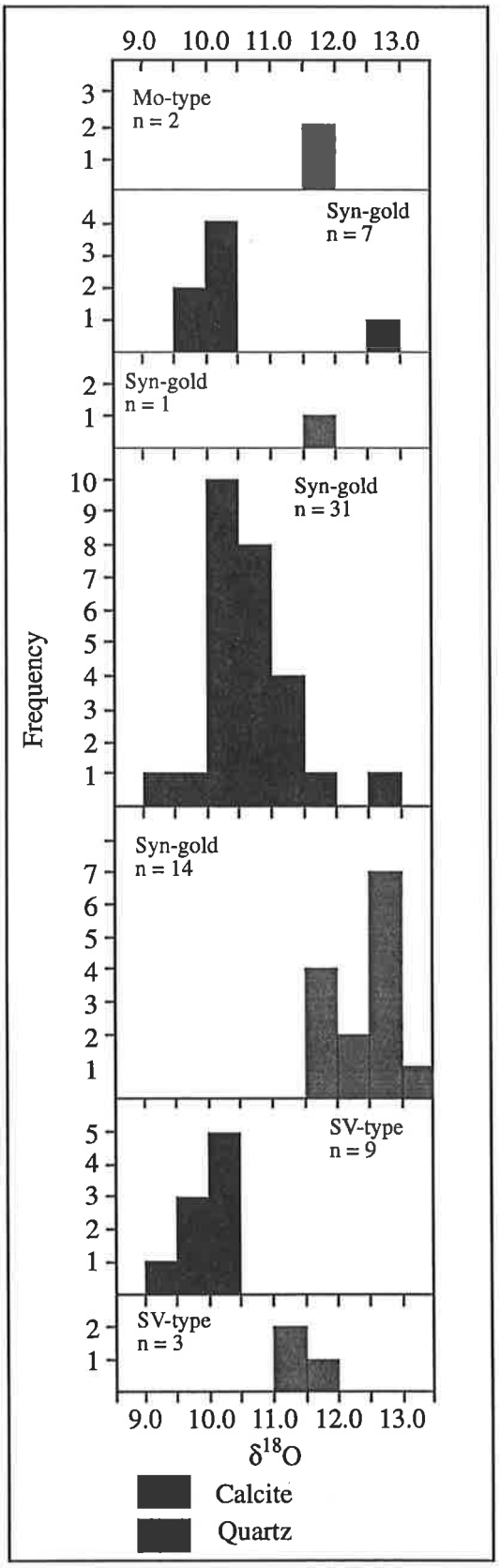


Figure 9.1. Compilation of $\delta^{18}O$ values for Mo-type, syn-gold type and SV-type quartz - calcite veins.

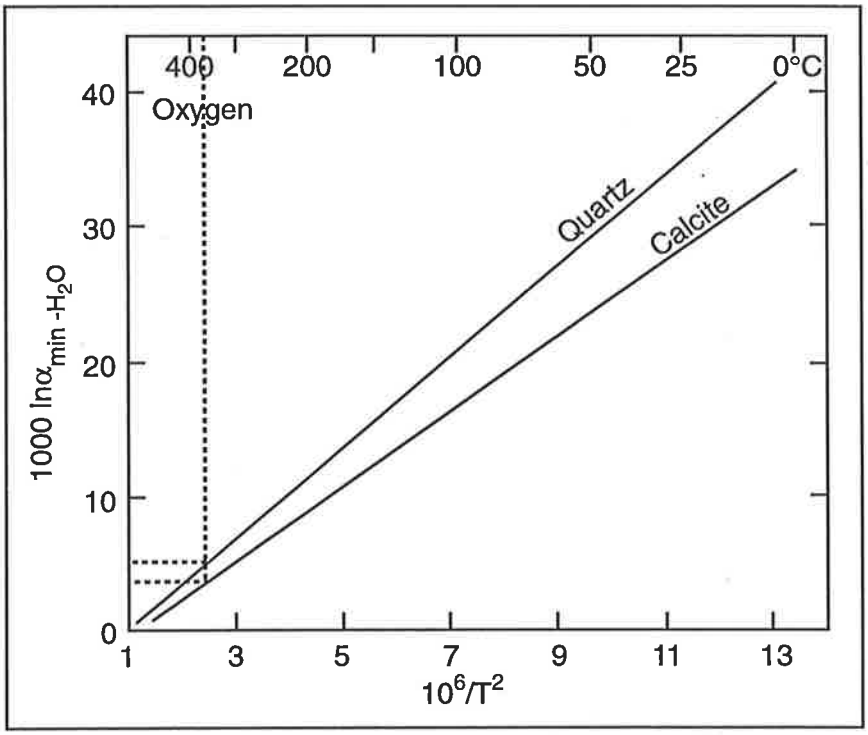


Figure 9.2. Fractionation factors (indicated by dashed lines) for ^{18}O isotopes obtained from quartz and calcite samples from Junction gold mine using relationships between 1000 lna (mineral - H_2O) and $10^6/T^2$ for ^{18}O fractionations (from Kyser, 1987).

based on fractionation factors between quartz and calcite, as illustrated in Kyser (1987) (Figure 9.2).

The temperature estimates for the eleven syn-gold quartz-calcite samples range from 190°C to 460°C (mean = 345°C, standard deviation = 81°C, n =11). However, the mode of values plot near 400°C ± 25°C (Table 9.1).

9.3.3 Post-gold quartz vein samples

The $\delta^{18}O$ values for nine calcite samples from the SV-type quartz veins range from +9.3 to +10.3‰ (mean = +9.9‰, standard deviation = 0.3‰, n = 9), while three quartz samples from the SV-type quartz veins range from +11.1 to +11.6‰ (mean = +11.3‰, standard deviation = 0.2‰, n = 3; Figure 9.1).

Three SV-type quartz-calcite samples were used as isotope geothermometers. Temperature estimates for the three SV-type quartz-calcite samples range from 285°C to 325°C (mean = 303°C, standard deviation = 16, n = 3). These values are in good agreement with the homogenisation

Oxygen isotope geothermometry

Sample Number	Sample Type	$\delta^{18}O$ Calcite	$\delta^{18}O$ Quartz	Geothermometry Temperature
1074-76	BCZ	10.0	12.5	190
1074-84	BCZ	11.2	12.8	320
1074-94	BCZ	10.4	11.8	340
1074-99	BCZ	10.4	11.6	420
1074-105	BCZ	11.8	12.9	460
1074-110	BCZ	10.7	11.9	420
1074-111	BCZ	10.7	12.4	290
1074-114	BCZ	10.6	12.4	280
1074-141	BCZ	10.7	12.0	400
1074-236	BCZ	10.1	11.3	420
1074-251	BCZ	10.2	12.1	260
1074-77	SV- type vein	9.8	11.3	325
1074-130	SV- type vein	9.3	11.1	285
1074-136	SV- type vein	9.7	11.6	300

Table 9.1. Geothermometric pairs and temperature estimates

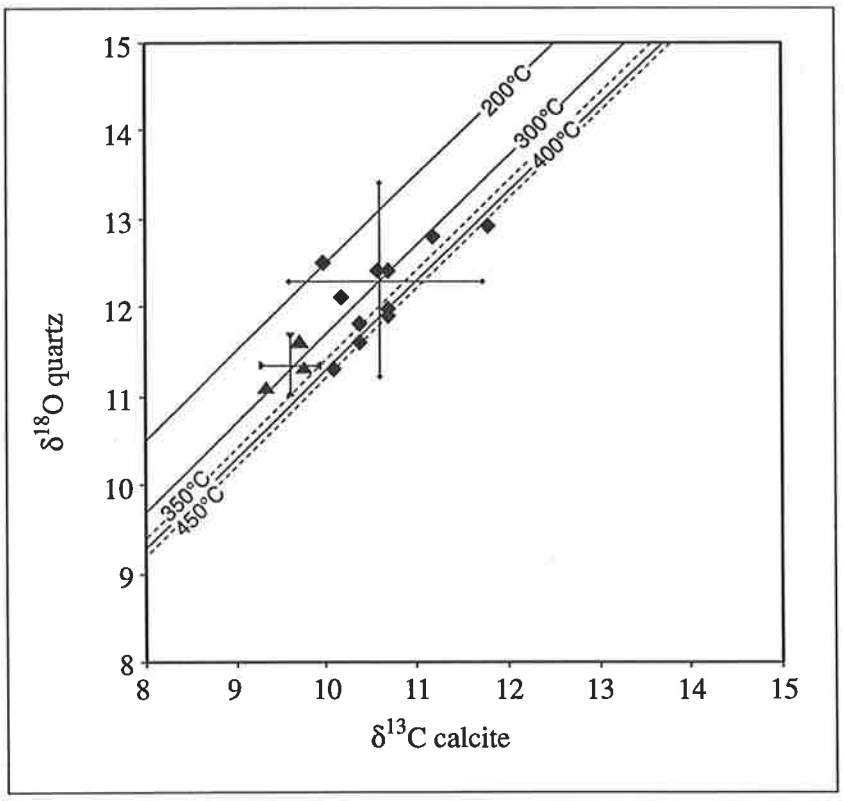


Figure 9.3. Compilation of $\delta^{18}O$ quartz and $\delta^{18}O$ of coexisting calcite for syn-gold quartz-calcite veins and SV-type quartz-calcite veins from the Junction gold mine. Vertical and horizontal bars represent the range of $\delta^{18}O$ values. Their axes cross at the mean $\delta^{18}O$ value for each population. The solid and dashed diagonal lines are temperatures corresponding to appropriate quartz-calcite fractionations constructed from the mineral-water illustrations of Kyser (1987).

temperatures obtained from fluid inclusions trapped in SV-type quartz veins (mean = 314.7°C; Figure 9.3, Table 9.1).

9.4 Discussion

Vein quartz is the most abundant constituent in the alteration assemblages at Junction. Therefore, it is interesting to note that all of the quartz veins analysed (including the Mo-type quartz veins and the SV-type quartz veins) have such a narrow range of $\delta^{18}O$ values over a vertical extent of 700 m. This suggests that all of the quartz was deposited during a relatively narrow temperature and pressure interval from fluid reservoirs with constant $\delta^{18}O$ compositions (Golding and Wilson, 1987). Similarly, the calcite analysed from the relatively barren PCZ-DCZ and the auriferous BCZ zones within the JSZ also have a narrow range. The fact that the $\delta^{18}O$ values of the calcite across the JSZ (incorporating the BCZ, the PCZ and the DCZ) have such a narrow range (9.4 to 12.5‰) supports the premise that oxygen isotopes are strongly influenced by ambient temperatures and not by changes in fugacity (Kerrich, 1989; Taylor, 1997).

The general agreement between temperature estimates from fluid inclusion microthermometry, mineral equilibria thermodynamic calculations and stable isotope geothermometry, plus the uniform range of $\delta^{18}O$ values for both calcite and quartz, indicate that most of the calcite-quartz pairs in the whole rock and vein samples are in isotopic equilibrium with each other.

9.4.1 Oxygen isotope geothermometry

9.4.1.1 Syn-gold quartz vein samples

The temperatures calculated from the syn-gold quartz-calcite pairs (range = 190 - 460°C, mode 400°C ± 25°C), and the syn-gold fluid inclusion homogenisation temperatures (range = 204.8 - 389.9°C, mode = 320°C, see Figure 5.30) have a large range, but, they are nevertheless in agreement. Kerrich (1989) reports that fluid inclusion homogenisation temperatures are often lower than the ^{18}O isotopic temperature estimates by up to 80°C. This is a common phenomenon in late-orogenic, structurally-controlled gold deposits, brought about by the uncertainties involved in selecting the appropriate fluid inclusion entrapment temperature. Ohmoto (1986) supports this statement, reporting that stable isotope geothermometry may give the true temperature of mineralisation, whereas homogenisation temperatures from fluid inclusions generally give the minimum temperature of mineralisation. Therefore, it can be concluded that the upper level temperature estimates obtained from stable isotope geothermometry (>300°C) are probably more accurate than the lower level temperature estimates (< 250°C) for gold mineralisation given that a large proportion of fluid inclusion homogenisation temperatures are greater than 300°C.

Further to this, the higher temperature estimates calculated from the values of co-existing quartz and calcite (340 - 460°C) correspond to the temperature range reported by Witt *et al.* (1997) for gold mineralisation associated with a biotite-calcite-quartz-albite-pyrrhotite±pyrite alteration

assemblage in mafic host rocks. Witt *et al.* (1997) reports that this mineral assemblage forms at mid- to upper greenschist facies metamorphism at approximately 400° ± 25°C. Indeed, it is reported in chapter 3 that the principle gold-bearing zone at Junction (BCZ) is dominated by biotite-calcite-quartz-albite-pyrrhotite±pyrite±rutile±dolomite. Therefore a best estimate of 385 ± 35°C is obtained for the temperature of gold deposition at the Junction deposit based on:

- the geothermometry mode value calculated from stable isotope mineral pairs,
- mineral equilibria thermodynamics applying the data reported by Witt *et al.* (1997) and,
- the mean and mode fluid inclusion homogenisation temperatures that are in agreement (± 20 - 80°C) with stable isotope geothermometry and mineral equilibria thermodynamics, given that fluid inclusions generally give the minimum temperature of mineralisation.

The general agreement between temperature estimates from fluid inclusion microthermometry, mineral equilibria thermodynamic calculations and stable isotope geothermometry, plus the uniform range of $\delta^{18}O$ values for both calcite and quartz, indicate that most of the calcite-quartz pairs in the whole rock and vein samples are in isotopic equilibrium with each other. Only four samples representing the syn-gold quartz-calcite veins indicate that post-precipitation re-equilibration may have occurred, if indeed re-equilibration has occurred at all. These four samples give temperature estimates ranging from 190 - 290°C. Kerrich (1987) reports that disequilibrium between quartz and calcite is often indicated by an enrichment in ^{18}O in the carbonates. However, the $\delta^{18}O$ values for calcite at Junction do not indicate any deviation from the remainder of the $\delta^{18}O$ population (Table 9.1). Therefore, whilst isotopic disequilibrium for these samples cannot be entirely dismissed, it is possible that that the lower temperature estimates are recording a decreasing temperature regime.

9.4.1.2 Post-gold quartz vein samples

A similar interpretation applied to the 11 syn-gold samples can be applied to the three SV-type quartz veins that give isotopic temperature estimates (285 - 325°C). Although the sample population is limited to only three samples, the geothermometry estimates for these SV-type quartz-calcite veins closely overlap fluid inclusion homogenisation temperatures obtained for these veins (mean = 314.7°C). Therefore it can be concluded that the post-gold SV-type veins formed at 300°C ± 25°C, given that the mean fluid inclusion homogenisation temperatures are in agreement (± 20 - 80°C) with the geothermometry estimates and that fluid inclusions generally give the minimum temperature of mineralisation.

9.4.2 The origin of the ore-transporting fluids

9.4.2.1 Pre-gold, quartz vein samples

Fluid inclusion homogenisation temperatures show that the Mo-type quartz veins have formed

at approximately 225°C (Chapter 5.6.2.2.2). However, given that two of the eleven fluid inclusions analysed homogenised at 339°C and 347°C and that fluid inclusions generally give the minimum temperature of mineralisation, it is suggested that the approximate temperature for Mo-type vein precipitation is closer to 340 ± 25°C. The fractionation factor between water-quartz at 340°C is 5.6‰ (Kyser, 1987).

The application of the quartz-water fractionation factor to the Mo-type quartz samples reveals that the $\delta^{18}O$ value of the Mo-type fluid was +5.7 to +5.8‰. This value is the same as the mantle $\delta^{18}O$ value of +5.7‰ (Kerrich, 1989; Rollinson, 1993). However, the $\delta^{18}O$ value of the Mo-type fluid is also bound by the $\delta^{18}O$ range for magmatic and metamorphic reservoirs (Rollinson, 1993) and a single source cannot be determined. The $\delta^{18}O$ values suggest that the Mo-type quartz veins may have originated from mantle fluids mixed with fluids derived from the dewatering of nearby intrusives.

9.4.2.2 Syn-gold quartz vein samples

The fractionation factor between water and calcite at 380°C is 3.6‰ and for water and quartz at 380°C is 5.5‰ (Figure 9.2) (Kyser, 1987). The application of the calcite-water and quartz-water fractionation factor at 380°C, to the mean $\delta^{18}O$ value of BCZ calcite and quartz reveals that the $\delta^{18}O$ value of the ore fluid was 7.0‰ for calcite and 6.8‰ for quartz. Colvine *et al.* (1988) announces that oxygen isotope geothermometry frequently suggests oxygen isotope disequilibrium between carbonate and quartz. However, the $\delta^{18}O$ values obtained from both quartz and calcite at Junction indicate that both quartz and calcite are still in equilibrium and were deposited from a single, homogeneous source.

The mean $\delta^{18}O$ value calculated for the PCZ-DCZ ore fluid is 6.7‰ (calculated from calcite $\delta^{18}O$ values). This is similar to that obtained for BCZ samples. The values from the PCZ-DCZ overlap with those from the BCZ and show no variation across the different alteration zones.

Occasionally, the $\delta^{18}O$ values of calcite and quartz in late-orogenic, structurally-controlled gold deposits clearly reflect the interaction of the parent ore fluid with the host wall rocks (Golding and Wilson, 1987; Golding *et al.*, 1990b). This results in the least altered peripheral zones of the shear zone having a slightly different $\delta^{18}O$ value to the more intensely altered central part of the shear zone. The $\delta^{18}O$ difference at Junction, between the peripheral PCZ-DCZ alteration and the central BCZ alteration, is 0.3‰. The fact that both the calcite and the quartz $\delta^{18}O$ values associated with gold mineralisation do not vary significantly horizontally across the JSZ, or vertically throughout the Junction deposit indicates that either the Junction Gabbro has a $\delta^{18}O$ value that is comparable to the parent ore fluid, or, the parent ore fluid interacted with the host rock at high fluid to wall-rock ratios (Golding and Wilson, 1987; Golding *et al.*, 1990a, 1990b).

The $\delta^{18}O$ data for quartz and carbonate veins and wall rock alteration, indicates that a homogeneous

hydrothermal fluid with a calculated $\delta^{18}O$ value between +6.7‰ and +7.0‰ was responsible for the gold-related veining and the wall rock alteration. This fluid composition is consistent with a magmatic or metamorphic source (Rollinson, 1993). However, a mantle or deep crustal fluid cannot be dismissed (Groves, 1993), and a deeply-sourced primary ore fluid mixing with upper crustal fluid sources as implicated by the crustal continuum model of Groves *et al.* (1992) and Groves (1993) is implied.

9.4.2.3 Post-gold quartz vein samples

The fractionation factor between water and calcite at 340°C is 3.7‰ and for water and quartz at 340°C is 5.6‰ (Kyser, 1987). The application of the calcite-water and quartz-water fractionation factor at 340°C, to the mean $\delta^{18}O$ value of BCZ calcite and quartz reveals that the $\delta^{18}O$ value of the ore fluid was 6.2‰ for calcite and 5.7‰ for quartz.

These values are similar to the mantle $\delta^{18}O$ value of +5.7‰ (Kerrich, 1989; Rollinson, 1993). However, the $\delta^{18}O$ values are also consistent with a magmatic or metamorphic source (Rollinson, 1993) and a single source cannot be determined.

CHAPTER TEN

Stable isotope systematics of carbon in calcite at Junction

10.1 Introduction

Late-orogenic, structurally-controlled gold deposits, particularly within greenschist facies alteration assemblages, are characterised by abundant carbonate (Phillips and Groves, 1984; Golding *et al.,* 1987, 1989, 1990a; Clark *et al.*, 1989; Kerrich, 1987, 1989; Groves, 1993; Mikucki and Ridley, 1993; Robert *et al.*, 1995; Oberthur *et al.*, 1996; Groves *et al.*, 1998; Witt *et al.*, 1998, and this study). Carbon isotope values for all carbon-bearing phases in late-orogenic, structurally-controlled gold deposits (carbonates, CO_2 gas, CH_4 gas) bear particular significance, since the ore forming fluid, characterised by CO_2, is the only source of carbon in an otherwise carbon depleted host rock (Golding *et al.*, 1987, 1989, 1990a; Kerrich, 1987, 1989; McNaughton *et al.*, 1988). Unaltered volcanic rocks of the greenstone sequences are essentially devoid of juvenile carbon, therefore, most carbon in their altered equivalents must have been introduced during alteration (McNaughton *et al.*, 1988). This presumption suggests that stable isotope values from carbonate species are valuable in constraining the source of the hydrothermal fluid which was clearly rich in carbon.

Indeed, stable isotope studies on carbonates resulting from fluid processes in late-orogenic, structurally-controlled gold deposits have been applied largely in the context of tracing the origin of ore forming fluids (Kerrich, 1987, 1989). Previous investigations involving carbon isotope systematics in late-orogenic, structurally-controlled gold deposits have reported median $\delta^{13}C$ values ranging from -8.1‰ to -2.7‰ for carbonates in gold deposits hosted in mafic rocks throughout the Norseman-Wiluna greenstone belt, Western Australia (Groves *et al.*, 1988; McNaughton *et al.*, 1988, 1990 and references therein; Golding *et al.*, 1987, 1989, 1990a and references therein), -9.0‰ to -0.4 ‰ for carbonates in similar gold deposits of the Abitibi greenstone belt, Canada (Kerrich, 1987, 1989 and references therein; Colvine *et al.*, 1988) and -5.9‰ to +0.3‰ for carbonates in similar gold deposits of the Barberton Greenstone Belt, South Africa (de Ronde, 1992). These $\delta^{13}C$ values have not been helpful as source tracers, because of their enigmatic range of values and the many controversial proposals and hypotheses that have been reported.

10.1.1 Carbonate species evaluated at Junction

Extensive carbonate alteration is associated with gold mineralisation within the Junction Shear Zone (JSZ). Calcite is by far the most common carbonate mineral found in the gold mineralised alteration zones (biotite-carbonate alteration zone [BCZ], proximal chlorite zone [PCZ] and the distal chlorite zone [DCZ]) in the Junction deposit, although dolomite and trace ankerite and siderite are known to be present (Chapter 3). Calcite is the only carbonate present in the unmineralised south dipping (SV-type) quartz veins. Calcite in the alteration zone(s) is usually found within the altered wall rock assemblage, making up to 50% of the mineral assemblage in some places. Often this is only apparent when viewed by CL microscopy (Figure 3.16a and 3.16b, Chapter 3). Typically, calcite forms < 20% of the alteration assemblage. Calcite is commonly found on the fringes and tips of quartz veins where it forms euhedral crystals inter-growing with albite, chlorite and sulphides. It does exist toward the centre of quartz veins larger than 5 cm in thickness, but this is rare. Because of the dominance of calcite over other carbonate minerals, $\delta^{13}C$ values were determined from 42 calcite samples and only one dolomite sample.

10.2 Methods

Carbon isotope values were determined from carbonate minerals using the method of McCrea (1950). Samples were initially powdered, and analysed by XRD to identify the carbonate species present. Almost all samples were predominately calcite. Dolomite was regularly identified as a trace to negligible component of the sample, and rarely forms the dominant carbonate species. Where possible, sulphides and other non-carbonate minerals were removed from the sample by Franz electro-magnetic separation. Between 15 mg and 150 mg of pulped sample was needed for the reaction with the 100% phosphoric acid to produce sufficient CO_2 for analysis. This is because the powdered quartz and albite could not be removed from the sample in some cases. Most samples were reacted with phosphoric acid at 25 °C for only four hours. These constraints prevented any traces of dolomite from contaminating the evolved gas. The evolved gas was analysed by a Fissons Optima dual inlet stable isotope ratio mass spectrometer.

Some whole rock samples were known to contain pyrrhotite growing along the cleavage planes of the calcite and albite. The pyrrhotite was impossible to remove from the sample prior to reacting with phosphoric acid. Pyrrhotite is highly reactive with 100% phosphoric acid, producing H_2S that is not easily separated from CO_2 by cryogenic methods. H_2S is a deleterious by-product that leads to poor analytical precision of CO_2 by mass spectrometry. Removal of H_2S from samples was possible by reacting the gas evolved from the whole rock sample with silver phosphate powder.

Gas that evolved from samples containing pyrrhotite was first trapped in a cold finger by liquid nitrogen. Other non-condensable gases were then evacuated from the vacuum line. A tube

containing approximately 1 gm of silver phosphate was then attached to the vacuum line and atmospheric air was evacuated from this tube. The sample gas trapped in the super-cooled cold finger was then warmed to room temperature by a warm water bath and the liquid nitrogen dewar was placed around the tube containing the silver phosphate. The liquid nitrogen dewar was kept around the silver phosphate tube for approximately 5 minutes to ensure maximum adsorption of H_2S by the silver phosphate. The liquid nitrogen dewar was then removed from the tube containing silver phosphate. This tube was then warmed slowly by cool air back to room temperature. The remaining CO_2 gas was then trapped in the cold finger by liquid nitrogen, and the silver nitrate tube was removed from the line. The collection of CO_2 for mass spectrometer analysis then continued as normal.

10.3 Results

10.3.1 $\delta^{13}C$ values for calcite sampled from the JSZ

The $\delta^{13}C$ values for calcite sampled from within the JSZ range from -7.4‰ to -2.5‰ (mean = -5.8‰, standard deviation = 1.4‰, n = 33). All values are presented in Figure 10.1 and listed in Table 11.1, chapter 11. The $\delta^{13}C$ values of the parent CO_2 responsible for depositing carbonate in the JSZ is calculated to have been -2.8‰, based on the calcite-CO_2 fractionation factor of 3.0‰ at 385°C ± 35°C (Kyser, 1987; Ohmoto and Goldhaber, 1997).

Close inspection of $\delta^{13}C$ values in relation to the alteration zones within the JSZ indicate that two distinct $\delta^{13}C$ populations exist. The $\delta^{13}C$ populations can be separated according to their alteration assemblage. Delta^{13}C values collected from the BCZ range from -4.8 ‰ to -7.4 ‰, (mean = -6.5‰, standard deviation = 0.8‰, n = 25; Figure 10.1), whereas the $\delta^{13}C$ values collected from the PCZ and the DCZ range from -2.5 to -4.7 ‰ (mean = -3.4‰, standard deviation = 0.7‰, n = 7; (Figure 10.1). An apparent merging of $\delta^{13}C$ values (e.g. -4.8‰ for one calcite sample in the BCZ and -4.7‰ for one sample in the PCZ) indicates that alteration boundaries are gradational over a number of cm, and possibly up to one m. However, the difference in the mean value for each population is +3.1‰.

The mean $\delta^{13}C$ value of the parent CO_2 responsible for the carbonate precipitated in the BCZ is calculated at -3.5‰, based on the calcite-CO_2 fractionation factor of 3.0‰ for temperatures of 385°C (Figure 10.2; Kyser, 1987; Ohmoto and Goldhaber, 1997). The mean $\delta^{13}C$ value calculated for the CO_2 parent fluid that deposited carbonate in the PCZ and DCZ is -0.4‰, using the same fractionation factor mentioned above.

10.3.2 $\delta^{13}C$ values for calcite sampled from SV-type veins

SV-type calcite was precipitated after gold mineralisation and is only found within the SV-type quartz veins. Delta^{13}C values for SV-type carbonate range from -5.3 to -7.5‰, (mean = 6.9‰, standard deviation = 0.8‰, n = 9; Figure 10.1). Fluid inclusion microthermometry indicates precipitation temperatures close to 300°C. The $\delta^{13}C$ values of the parent CO_2 is calculated to

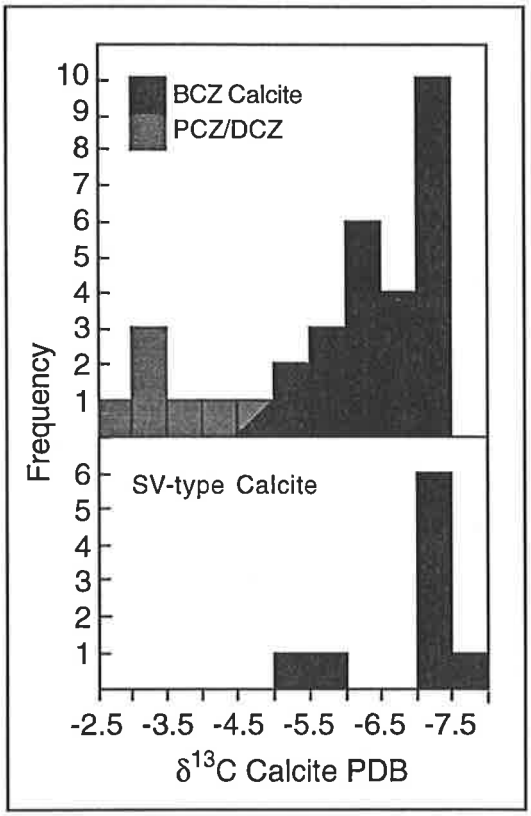


Figure 10.1. Compilation of $\delta^{13}C$ values for Biotite-Carbonate Zone (BCZ) calcite, Proximal-Chlorite Zone/Distal-Chlorite Zone (PCZ/DCZ) calcite and SV-type calcite collected from Junction.

have been -4.9 ‰, based on the calcite-CO_2 fractionation factor of 2‰ at 300°C (see Figure 10.2) (Kyser, 1987; Ohmoto and Goldhaber, 1997).

10.4 Discussion

The $\delta^{13}C$ values for all calcite at Junction are within the range of other carbonate values obtained from all late-orogenic, structurally-controlled gold deposits along the Norseman-Wiluna greenstone belt (Golding *et al.*, 1990a; McNaughton *et al.*, 1990). Specifically, the distribution of $\delta^{13}C$ values for carbonates across the Junction Shear Zone (^{13}C enriched values at the periphery and ^{13}C depleted values toward the centre of the shear zone), are similar to the $\delta^{13}C$ values distributed across the Mt Charlotte gold deposit, Kalgoorlie. The Mt Charlotte gold deposit is hosted in stratigraphically and geochemically similar host rocks to those at Junction (i.e. the granophyric zone of the Golden Mile Dolerite, Mt, Charlotte gold deposit; Golding and Wilson, 1983; Golding *et al.*, 1989, 1990a; McNaughton *et al.*, 1990).

The mean difference in $\delta^{13}C$ values between calcite samples in the BCZ and the PCZ-DCZ (+3.1‰) suggests that the two populations may have been deposited by two different hydrothermal fluids. However, this is not the case at Junction. The only significant difference between the

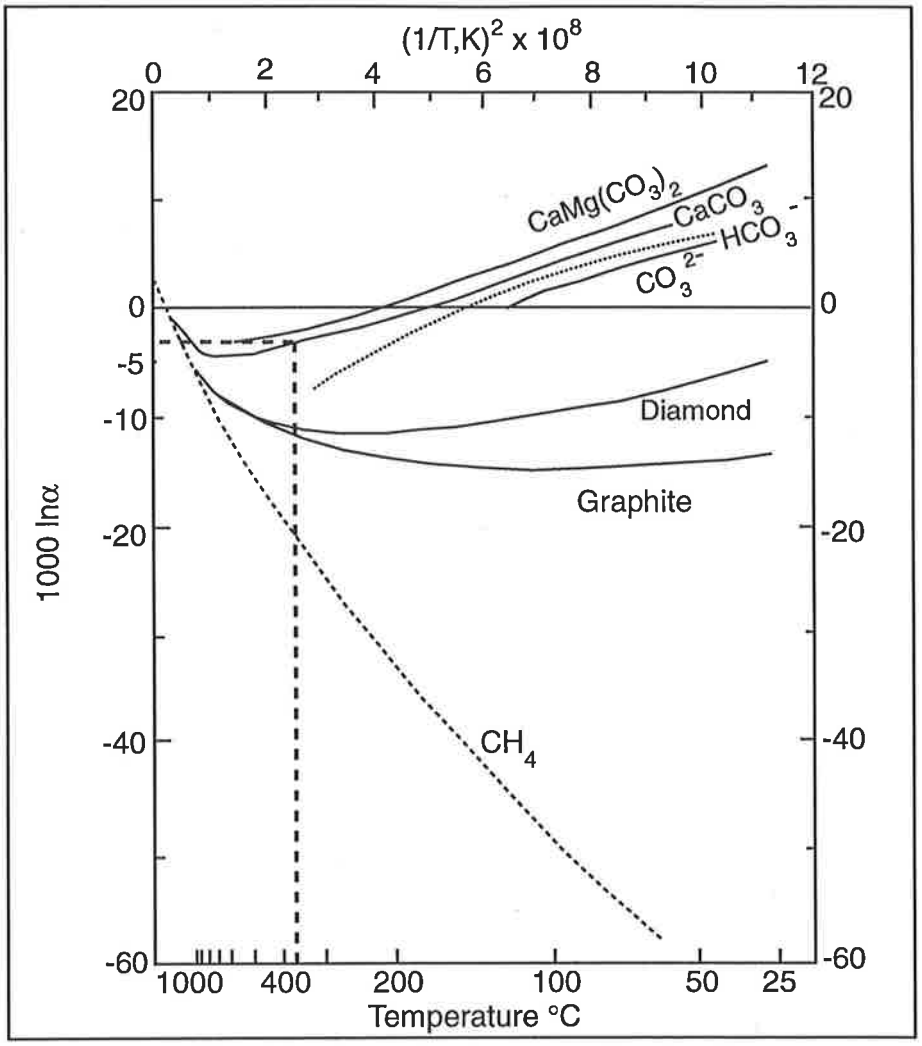


Figure 10.2. The calcite-CO_2 fractionation factor at 385°C is 3.0‰, as illustrated by the dashed line (diagram constructed from illustrations in Kyser, 1987, Ohmoto and Goldhaber, 1997).

alteration zones is that carbonate in the outer PCZ and DCZ is less abundant than that found in the BCZ. The carbonate in the BCZ is petrographically indistinguishable from carbonate in the PCZ and the DCZ in hand specimen and thin section. It forms at the edge of quartz veins and randomly within the host rock assemblage in all alteration zones (Chapter 3). No differences between the two carbonate populations can be seen using cathodoluminescence microscopy. Therefore, both forms of calcite are interpreted to be related to the gold mineralising process, and all calcite hosted within the JSZ is believed to have formed as a result of the ore fluid progressively altering the original host rock.

If the BCZ and the PCZ-DCZ populations were the result of two different fluid sources, the later fluid event would be expected to isotopically overprint the earlier alteration assemblage (Kerrich, 1987). However, this is not the case, despite alteration being pervasive in all alteration zones. Costello (1993), Carey (1994) and this study (Chapter 3) show that mineral zonation associated with gold mineralisation, extending from within the BCZ to the periphery of the DCZ is

gradational and typical of other late-orogenic, structurally-controlled gold deposits (Golding and Wilson, 1983; Phillips and Groves, 1983; Golding *et al.*, 1987, 1989, 1990a; Kerrich, 1989; Neall and Phillips, 1987; Mikucki and Ridley, 1993). The alteration indicates prolonged interaction between a reduced, CO_2-rich fluid interacting with an Fe-rich tholeiitic gabbro. The most intensely sheared and veined section of the Junction shear zone (JSZ), the BCZ understandably contains the most carbonate.

The lower abundance of biotite, albite, sulphides and associated gold grade in the PCZ is a reflection of the limited interaction of the ore fluid with the Junction Gabbro and does not imply a separate fluid altering event. Similarly, the preservation of igneous textures in the DCZ, simply reflects the lack of shearing and permeability in the gabbro in this zone. The alteration assemblages are discussed in detail in Chapter 3, but it is clear from the evidence presented here that the BCZ and PCZ-DCZ were formed from the same fluid over the same period of time. Subsequently, the mean difference of +3.1‰ between the BCZ and the PCZ-DCZ populations are unlikely to be the result of calcite that has precipitated from two separate fluid sources.

10.4.1 The role of Rayleigh stable isotope fractionation

Variations in the $\delta^{13}C$ value of carbonate in late-orogenic, structurally-controlled gold deposits are reported by Kerrich (1989), Golding *et al.* (1990a) and McNaughton *et al.* (1990). At Junction, the $\delta^{13}C$ of calcite varies by up to 5‰ across the JSZ, ranging from -7.4‰ adjacent to quartz veining in the BCZ, to -2.5 ‰ in the altered wall rock in the PCZ-DCZ. The variation is attributed to Rayleigh isotope fractionation during progressive fluid-rock interaction.

Rayleigh isotopic fractionation involves the formation of a daughter species that is not only isotopically distinct from the original parent species, but also results in an antithetical change in the isotopic value of the original parent species. The equilibrium fractionation factor between light stable isotopes is primarily temperature dependent in most ore systems (Kyser, 1987). However, Rayleigh isotopic fractionation between parent and daughter compounds are dependent on variations in the oxygen fugacity of the ore fluids as well as temperature dependence (Ohmoto and Rye, 1979; Ohmoto and Goldhaber, 1997). The effect of pressure is negligible below 10 kbars (Ohmoto and Goldhaber, 1997).

Rayleigh fractionation causes the residual parent species to change its isotopic composition as daughter species formation progresses. The magnitude of change in the isotopic value of the parent species is dependent on:

- the fractionation factor between the parent and daughter species,
- whether or not isotopic equilibrium is established between the parent and daughter species and,

- whether the system is open or closed with respect to the daughter species (Ohmoto and Goldhaber, 1997).

The Junction system is considered to be an open system for isotopic exchange as CO_2 is converted to carbonate and CH_4 in a unidirectional reaction. This implies that the daughter species (CH_4 and carbonate) were continuously removed from the system, causing the parent species (CO_2) to become isotopically more distinct (Ohmoto and Goldhaber, 1997).

The oxidation state of the Junction gold deposit is considered to be favourable for Rayleigh isotope fractionation. Pyrrhotite is the dominant sulphide species present at Junction. Its dominance over pyrite throughout most of the deposit indicates that the oxidation state of the ore body at the time of mineralisation was at or just below the quartz-fayalite-magnetite buffer

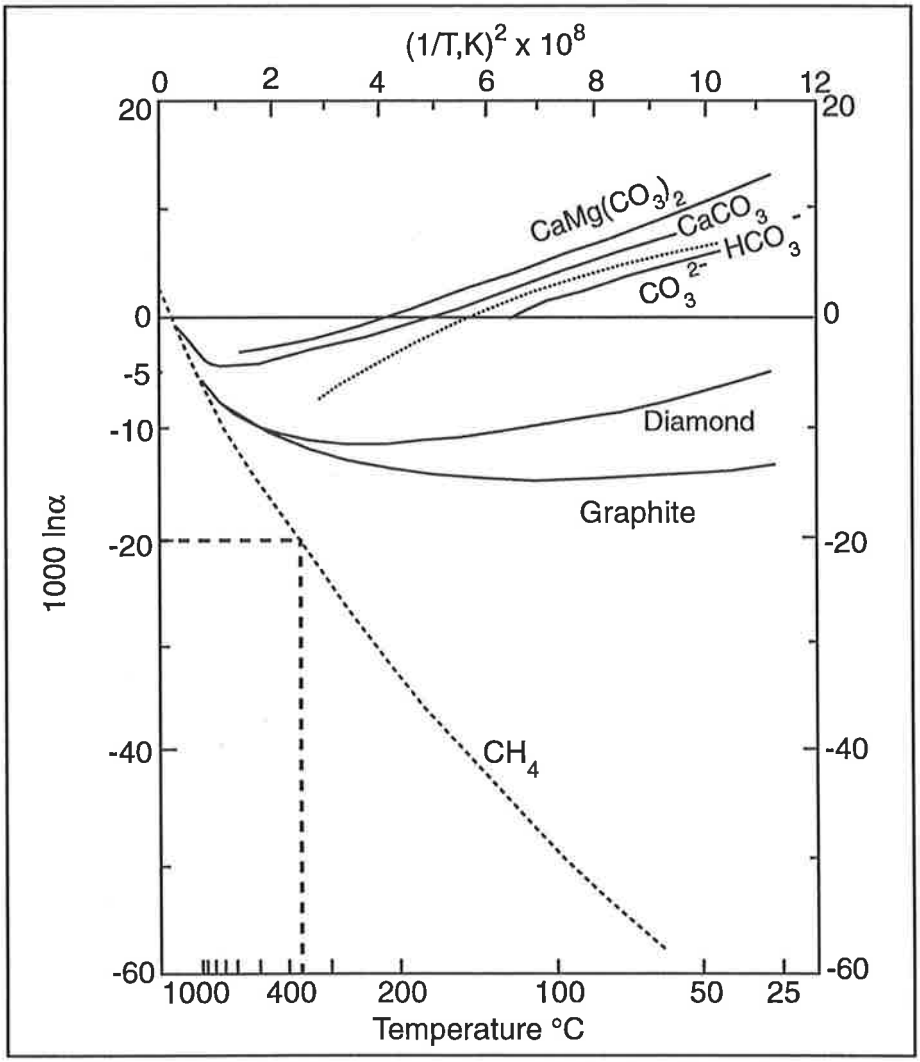


Figure 10.3 The CH_4-CO_2 fractionation factor at 385°C is 20‰, as illustrated by the dashed line. Diagram constructed from illustrations in Kyser (1987) and Ohmoto and Goldhaber (1997).

(QFM). The QFM boundary is approximately co-incident with the CO_2-CH_4 boundary at 350 ± 30°C and 2 kbars (Welhan, 1988; Mikucki and Ridley, 1993). Thus, the presence of pyrrhotite not only suggests a reduced environment, but also indicates the potential for CO_2-CH_4 co-existence.

The presence of CH_4 in the ore forming process is discussed in Chapters 5, 6 and 7. Therein, it is proposed that most of the CH_4 trapped in fluid inclusions at Junction did not travel in the ore forming solution, but instead formed in situ during the reduction of CO_2 to CH_4. The reduction of CO_2 to CH_4 involves a large fractionation of carbon between the two species (20‰ at 385°C {Figure 10.3; Kyser, 1987; Ohmoto and Goldhaber, 1997}). Thus, the fractionation factor between these oxidised and reduced carbon species is large enough to alter the $\delta^{13}C$ of the parent CO_2 as ^{12}C is favourably partitioned to CH_4 (Kyser, 1987; Ohmoto and Goldhaber, 1997).

Colvine *et al.* (1988) and Golding *et al.* (1990a) use this model to propose that carbon isotope fractionation between CO_2 and CH_4 resulted in the progressive depletion of ^{12}C from CO_2 in the hydrothermal fluid and conclude that the heavier $\delta^{13}C$ values for carbonate precipitated in the alteration assemblage is a result of this fractionation. Thus, the lowest $\delta^{13}C$ values for alteration calcite in the JSZ, specifically in the BCZ (-7.4‰), are probably a more accurate reflection of the $\delta^{13}C$ value of the original parent fluid.

The application of Rayleigh isotope fractionation and the subsequent interpretation by Golding *et al.* (1990a) is consistent with the observations made at Junction. The example presented by Golding *et al.* (1990a; Figure 10.4) shows that the isotopic profile of one quartz vein and its gold-bearing alteration halo at the Mt Charlotte gold mine, Kalgoorlie, Western Australia, has a systematic increase in ^{13}C from the centre of the quartz vein (-6‰) to the interface between the bleached pyrite bearing zone and the altered dolerite zone (+6‰) where a narrow pyrrhotitic interface exists. Based on the Rayleigh fractionation model, Golding *et al.* (1990a) attribute the heavier $\delta^{13}C$ values to the conversion of some CO_2 to CH_4 (thus consumption of ^{12}C by CH_4) in the zone associated with pyrrhotite. They imply that the presence of CH_4 and pyrrhotite in the same zone equate to isotopically heavy $\delta^{13}C$ values, whilst the presence of pyrite and the absence of CH_4 equate to isotopically light $\delta^{13}C$ values.

The profile of $\delta^{13}C$ values across the alteration zones at Junction and Mt Charlotte are similar. There is a systematic increase in ^{13}C from the centre of the JSZ (-7.4‰ in the BCZ) to the interface between the DCZ and the unaltered dolerite (-2.5‰) at Junction. The difference between the two deposits is that isotopically light samples from the BCZ at Junction are characterised by their association with abundant pyrrhotite and co-existing high volumes of CH_4 (Figure 10.5a and 10.5b), whereas isotopically heavy samples from the PCZ-DCZ are characterised by their lower concentration of pyrrhotite and low to negligible volumes of CH_4. That parent

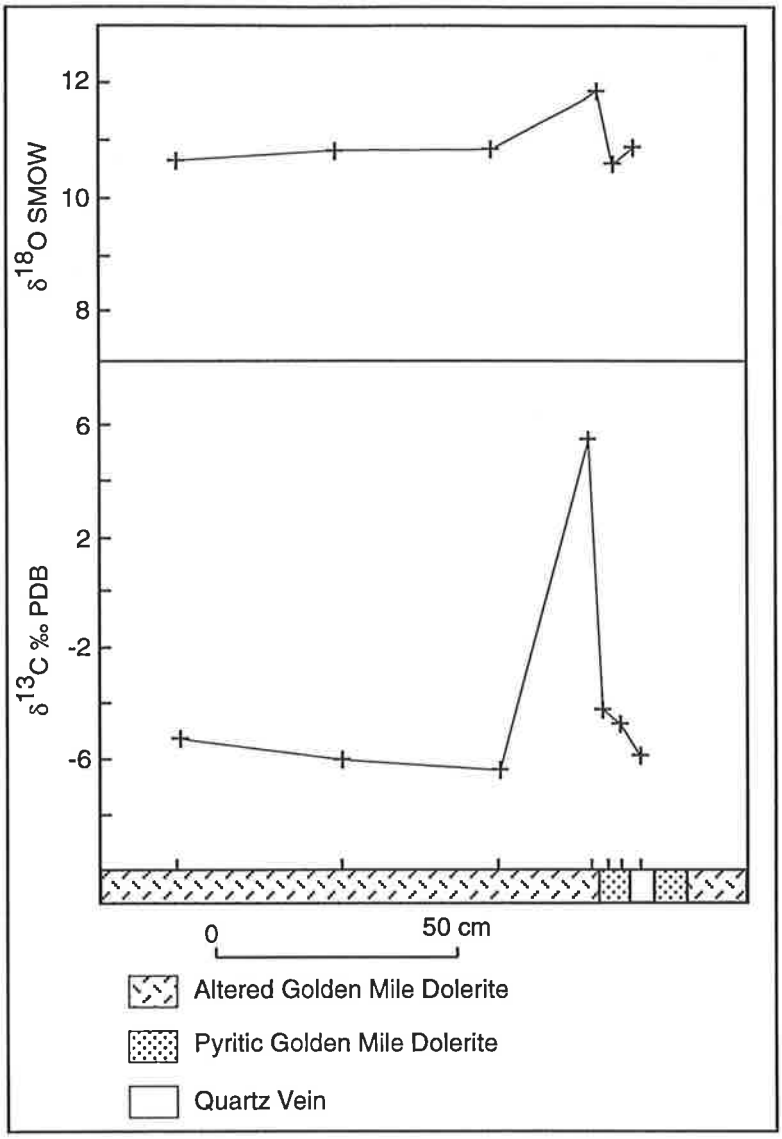
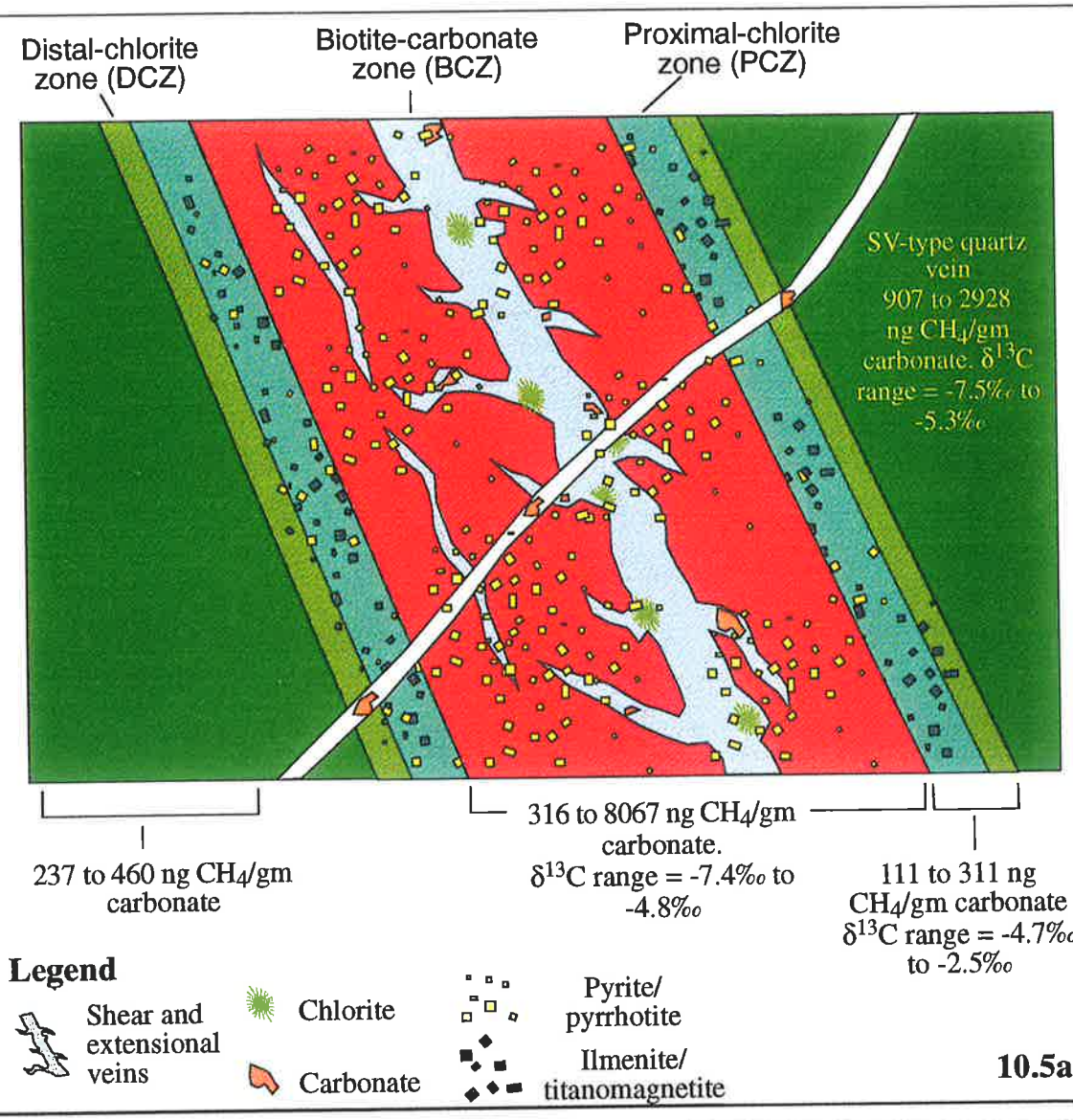


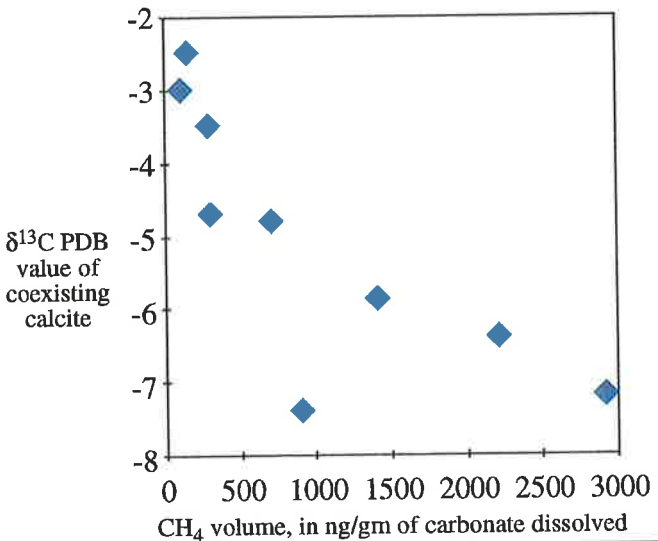
Figure 10.4. The isotopic profile of one quartz vein and its alteration halo at Mt Charlotte shows that heavy carbon and oxygen isotope values are restricted to the pyrrhotitic interface between bleached and altered dolerite (from Golding *et al.*, 1990a). This diagram should be compared to the data presented in Figure 10.5.

CO_2 reacted with the host rock to produce co-existing, isotopically light CH_4 and isotopically light calcite together in the BCZ conflicts with the Rayleigh stable isotope fractionation model.

Rayleigh fractionation between CO_2 and CH_4 remains the suspected mechanism responsible for the variation in $\delta^{13}C$ values of calcite across the JSZ. However, the reduction of CO_2 to CH_4 near the QFM buffer (i.e. in the BCZ) does not appear to affect the $\delta^{13}C$ values of calcite in the immediate area where Rayleigh fractionation supposedly took place. The isotopically heavier CO_2 that resulted from Rayleigh fractionation between CO_2 and CH_4 in a reduced environment (i.e. the BCZ), appears to have been displaced to the periphery of the JSZ where the oxidation state is higher than that in the BCZ and calcite $\delta^{13}C$ values reflect a heavier CO_2 parent. The



10.5a



Sample	$\delta^{13}C$ PDB	CH_4 volume in ng/per gram
1074-35	-7.2	2928.10
1074-84	-5.8*	1408.35
1074-121	-7.4	907.34
1074-192	-3.5	2928.10
1074-200	-4.8	709.49
1074-210	-2.5	163.68
1074-234	-6.4	2217.15
1074-237	-3.0	111.91
1074-245	-4.7	311.17

* 1074-84 is dolomite. Sample corrected to be in equilibrium with calcite at 385°C.

10.5b

Figure 10.5a. Schematic cartoon of CH_4 volumes and $\delta^{13}C$ values for calcite through the Junction shear zone. The highest CH_4 volumes are associated with pyrrhotite in the BCZ and correlate well with the lightest $\delta^{13}C$ values, whereas lower CH_4 volumes in the PCZ/DCZ correlate well with heavier $\delta^{13}C$ values. This correlation is illustrated in Figure 10.5b where it is evident that low CH_4 volumes correlate with heavy $\delta^{13}C$ values. The accompanying table details the samples used. Stable isotope analyses were not completed on samples of unaltered gabbro. This diagram should be compared with Figure 10.4.

mechanisms involved in this process are unclear. The answer probably lies in the processes involved during seismic rupture, (i.e. the porosity of the shear zone during and after rupture, the rate of carbonate precipitation in comparison to the rate of CH_4 production, the mobility of CO_2 in a capped and impermeable shear zone prior to the next phase of seismic activity, phase separation, etc.). Indeed, Golding *et al.* (1989) report that residual CO_2 and late-formed carbonates persistent in the waning stages of mineralisation would be enriched in ^{13}C. However, these processes are beyond the scope of this study and so the questions remain.

Rayleigh isotope fractionation appears to have played a major role in the distinctively different $\delta^{13}C$ values from BCZ calcite compared to the $\delta^{13}C$ values of the PCZ-DCZ calcite at Junction. In these circumstances, the lowest $\delta^{13}C_{(calcite)}$ value measured in a population set is probably the most accurate representation of the $\delta^{13}C_{(CO_2\ parent)}$ value, which, as part of the hydrothermal fluid, reacted with the host rock to precipitate the calcite as an alteration mineral (Colvine *et al.*, 1988). The lowest $\delta^{13}C$ value for calcite in the JSZ is -7.4‰. Therefore, the $\delta^{13}C$ value of the parent CO_2 is estimated to be -4.4‰, based on the fractionation factor of -3.0‰ between CO_2 and calcite at 385°C (Kyser, 1987; Ohmoto and Goldhaber, 1997).

10.4.2 Fluid sources

10.4.2.1 Fluid sources of the JSZ calcite

Volatiles and solutes that travelled in the pregnant hydrothermal fluid have been variously attributed to:

- mantle sources (Colvine *et al.*, 1984; Cameron, 1988, Groves *et al.*, 1992; 1995; Groves, 1993; Deines, 1992),
- modified seawater (Nesbitt *et al.*, 1986; Golding and Wilson, 1987),
- metamorphic devolatisation (Phillips and Groves, 1983; Golding *et al.*, 1987; Kerrich, 1987; Groves and Phillips, 1987) and
- magmatic dewatering (Burrows *et al.*, 1986; Wood *et al.*, 1986a and 1986b; Burrows and Spooner, 1987).

In fact, all of the values determined for the carbonates present in the JSZ (BCZ and PCZ-DCZ) fall within the mantle carbon range (Deines, 1992). However, the exact origin of the hydrothermal fluid remains ambiguous, given that the mean $\delta^{13}C$ value for mantle CO_2 (-5‰; Deines, 1992), overlaps with the $\delta^{13}C$ values of crustal, magmatic and metamorphic fluids ($\delta^{13}C$ values of average crustal rocks = -6 ± 1‰, magmatic rocks = -5 ±1‰ and re-mobilised seawater carbonate = 0 ± 1‰; Nesbitt and Kyser, 1988; Kerrich, 1987; Golding *et al.*, 1987, 1990a; McNaughton *et al.*, 1988). None of these can be considered a unique source for the carbonate associated with

late-orogenic, structurally-controlled gold deposits (Nesbitt and Kyser, 1988).

Theoretically it is possible that a value of -4.4‰ is the result of sea-floor carbonate (mean $\delta^{13}C$ value = 0‰) remobilised during metamorphic devolatisation, mixing with carbon derived from an organic source (mean $\delta^{13}C$ value = -28‰) (e.g. Oberthur *et al.*, 1996). However, few researchers acknowledge this as a dominant process or fluid source, particularly in igneous host-rocks deficient in carbon (Golding *et al.*, 1987, 1990a; Kerrich, 1987; Nesbitt and Kyser, 1988; Groves *et al.*, 1988; McNaughton *et al.*, 1990; de Ronde, 1992).

Burrows *et al.* (1986), Wood *et al.* (1986a and 1986b) and Burrows and Spooner, (1986) suggested that the source for CO_2 in carbonates associated with late-orogenic, structurally-controlled gold deposits was originally magmatic, originating from the outgassing of melts intruded into the crust. However, controversy has surrounded the contributions of magmatic versus metamorphic and crustal versus mantle components of the low-salinity, CO_2-enriched fluids which are widely accepted as the precursors to late-orogenic, structurally-controlled gold deposits (Golding *et al.*, 1989, 1990a; Rock, *et al.*, 1989; Groves *et al.*, 1992, 1995; Groves, 1993).

The co-existence of lamprophyric porphyry intrusives within the Junction ore body (Murphy, 1995) and the predominance of the pre-mineralisation molybdenite-rich quartz veins that are found mostly in the upper levels of the Junction deposit, may be locally significant when considering the source of the ore fluids. Spatial relationships between porphyry intrusives, and gold mineralised shear zone(s) have been noted by other workers in the past (Woodall, 1979; Marmont, 1983; Wood *et al.*, 1986a and 1986b; Rock *et al.*, 1988; Rock *et al.*, 1989; Spry *et al.*, 1996). However, shear zone related carbonation at Junction not only cross-cuts the porphyries and the Mo-type quartz veins, but the volume of these intrusives at Junction is clearly insufficient to account for the volume of the carbonate and gold ore in the alteration halo. Therefore, a direct magmatic source is unlikely.

Colvine (1989), Groves *et al.* (1992) and Groves (1993) recognised that geochemical similarities between all late-orogenic, structurally-controlled gold deposits (ranging from sub-greenschist to granulite facies) can be attributed to volatiles and solutes that have evolved from a deep crustal scale hydrothermal system and/or the mantle. Deep fluid reservoirs include the basal segments of greenstone belts, deep-level intrusive granitoids, mid- to lower-level crustal granitoid-gneisses, mantle lithosphere, and even subducted oceanic lithosphere (Groves, 1993). Radiogenic isotope values (Pb and Sr) implicate fluid evolution from, or in equilibrium with, a number of these reservoirs (Colvine, 1989; Groves *et al.*, 1992; Groves, 1993), but light stable isotopes suggest that complex interactions with upper-level lithologies during fluid advection occurred. Groves *et al.* (1992) and Groves (1993) categorise these findings into their crustal continuum model. This attributes the light stable isotope values in late-orogenic, structurally-controlled gold deposits to complex reactions that occur between deeply-sourced primary fluids and upper-

crustal sequences prior to the final gold deposition in the greenstone lithologies.

The crustal continuum model does not indicate the precise source for the ore forming fluids. It does however, explain the enigmatic $\delta^{13}C$ values common to most late-orogenic, structurally-controlled gold deposits (Groves *et al.*, 1992; Groves, 1993). Therefore, it can be concluded that whereas a $\delta^{13}C$ value of -4.4‰ implicates a deeply sourced fluid common to all gold deposits in the Yilgarn block (Figure 10.6), it is likely that the $\delta^{13}C$ values obtained from the Junction calcite were influenced by other sources, including magmatic dewatering and metamorphic devolatisation for at least a portion of the fluid components. Certainly, Ohmoto and Rye (1979), Kerrich (1987), Nesbitt and Kyser (1988), Deines (1992) and Ohmoto and Goldhaber (1997) caution that $\delta^{13}C$ values of -5 ± 2‰ are difficult to interpret with regard to a carbon source, precisely because mantle fluids interacting with magmatic, sedimentary and metamorphic rocks upon ascent are all characterised by average $\delta^{13}C$ values in this range.

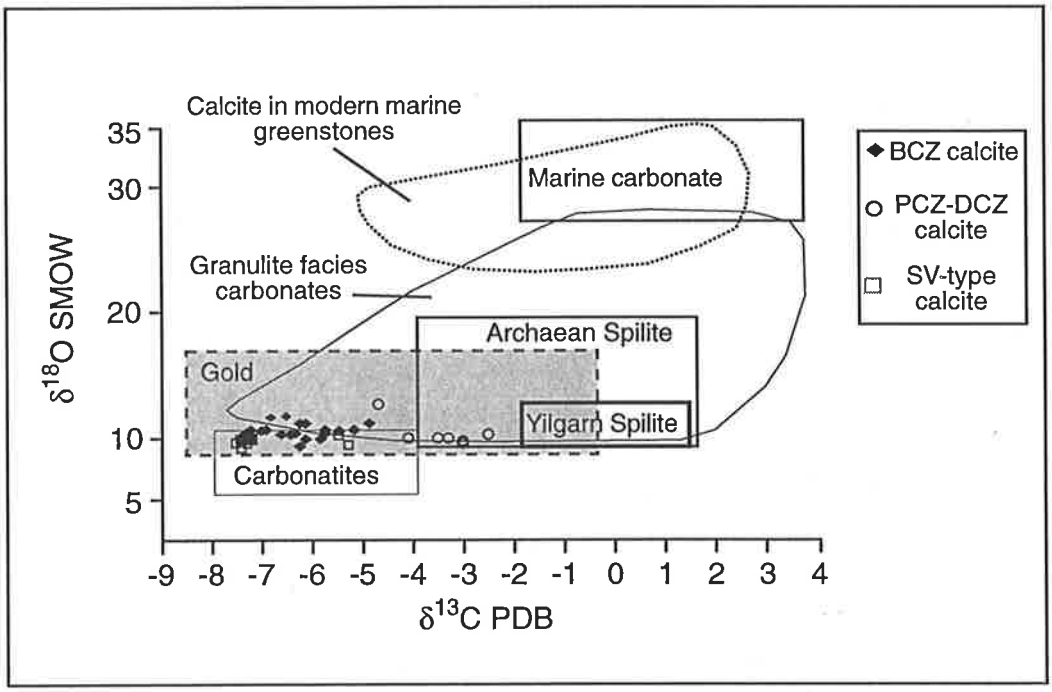


Figure 10.6. The oxygen and carbon isotopic fields of specific fluid reservoirs and the isotope values of calcites from the Junction deposit (oxygen and carbon fields from Kerrich, 1989). All of the $\delta^{13}C$ and $\delta^{18}O$ values obtained from the carbonates collected from the Junction deposit implicate a deeply-sourced fluid common to all gold deposits in the Yilgarn Block.

10.4.2.2 Fluid sources of the SV-type calcite

The $\delta^{13}C$ values for SV-type calcite (-7.5‰ to -5.3‰) overlap the range of $\delta^{13}C$ values determined for calcite in the BCZ (-7.4‰ to -4.8‰). SV-type calcite was precipitated after the main gold mineralisation event and after the resetting of previous $\delta^{13}C$ values may have occurred. However, alteration around the SV-type quartz veins is negligible and no selvages have been noted. Further to this, calcite is the only carbonate present in the SV-type quartz veins, occurring as large crystals growing wholly within the quartz vein. In contrast to this, trace to minor amounts of dolomite and lesser ankerite and siderite have been detected in the JSZ alteration assemblage. Therefore, it does not appear likely that the SV-type quartz veins were the source of carbon in the JSZ. It is also unlikely that fluid percolation into the wall rocks during the formation of the SV-type quartz veins was significant enough to re-set the earlier carbonate isotope values associated with gold mineralisation (cf. O'Neil, 1987). Nevertheless, it is apparent that the SV-type quartz veins formed from a source fluid with the same $\delta^{13}C$ value as the fluid that transported gold to the site of mineralisation. Therefore, interpretation for the origin and source of this parent fluid is the same as that discussed above for carbonates in the BCZ and PCZ-DCZ.

CHAPTER ELEVEN

Stable isotope evaluation of CO_2 in fluid inclusions

11.1 Introduction

One area of light stable isotope research that has received relatively limited investigation is the evaluation and interpretation of stable isotopic values obtained from fluid inclusion gases. Stable isotope evaluation of CO_2 in fluid inclusions has been hampered until recently by the limitation of mass spectrometers and the need for a relatively large sample size (Ohmoto and Goldhaber, 1997). However, new sampling techniques and highly sensitive mass spectrometry now make it possible to measure stable isotope values from very small (picomol) sample sizes (Ohmoto and Goldhaber, 1997; Miller and Pillinger, 1997).

Published $\delta^{13}C$ values of CO_2 (and other carbonaceous components) from fluid inclusion gases are relatively uncommon (based on the volume of literature available: Jackson *et al.*, 1988; Santosh *et al.*, 1995; Oberthur *et al.*, 1996; Miller and Pillinger, 1997; Vasquez *et al.*, 1998). Of these authors, only Santosh *et al.* (1995) and Oberthur *et al.* (1996) report on the $\delta^{13}C$ values obtained from CO_2 extracted from fluid inclusions in late-orogenic, structurally-controlled gold deposits. Recent reports show that the $\delta^{13}C$ values for CO_2 extracted from fluid inclusions overlap the range of values that indicate mantle, magmatic and crustal source reservoirs. These interpretations are similar to those constructed for carbonate $\delta^{13}C$ values from late-orogenic, structurally-controlled gold deposits. Thus, it would appear that fluid inclusion CO_2 has the potential to be used as a reliable source tracer.

CO_2 is a major volatile present in ore forming solutions (Roedder, 1984; Robert *et al.*, 1995; Roedder and Bodnar, 1997; Boullier *et al.*, 1998) and is the only source of carbon in an otherwise carbon-depleted host rock (Golding *et al.*, 1987, 1989, 1990a; Kerrich, 1987, 1989; McNaughton *et al.*, 1988; de Ronde *et al.*, 1992; Groves, 1993). CO_2 is widely accepted as the precursor to carbonatisation in all late-orogenic, structurally-controlled gold deposits (Kerrich, 1987; Golding *et al.*, 1987; McNaughton *et al.*, 1990; Groves, 1993). Fluid inclusion investigations at Junction indicate that CO_2 was the dominant oxidised carbon species in the parent ore fluid. Therefore, isotopic analysis of this trapped CO_2 provides a first hand opportunity to interpret the origin of the primary ore fluid in its original form, given that fluid inclusion volatiles should represent

tiny samples of the original ore fluid (Roedder, 1984; Roedder and Bodnar, 1997). Theoretically, the $\delta^{13}C$ value of CO_2 trapped in the fluid inclusions will have a $\delta^{13}C$ value that reflects the $\delta^{13}C$ value of co-existing carbonate calcite.

11.2 Methods

Extraction of CO_2 from fluid inclusions hosted in quartz veins was carried out to determine the $\delta^{13}C$ value of the CO_2. Selected quartz veins were crushed and sieved to a grain size of >63μm < 1.0 mm. The sieved fraction was washed in deionised water to remove rock powder created through the crushing process. It was then dried at 75°C for 12 - 24 hours. The washed sample was passed through a Franz magnetic separator to remove magnetic particles (chlorite, biotite, pyrrhotite, etc.) that formed part of the vein assemblage. Samples were then bathed in aqua-rega acid solution for 4 hours to remove any excess carbonate material. The remaining sample was now predominantly quartz, but some samples contained minor albite grains. However, the sample was considered to be clean enough for the extraction of CO_2 from fluid inclusions for $\delta^{13}C$ analysis.

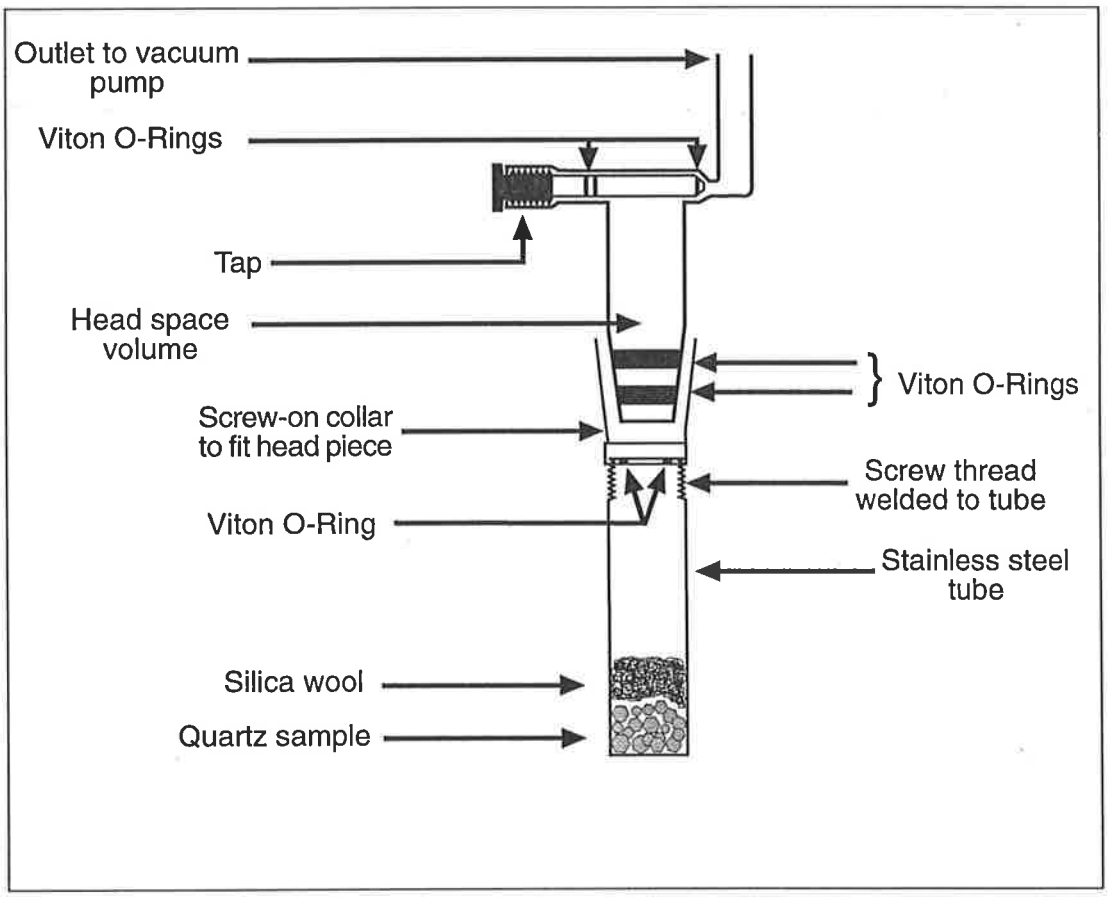


Figure 11.1. Diagramatic representation of the aparatus used to extract CO_2 from quartz. A stainless-steel tube was used to crush the quartz sample. Screw-thread fitted with viton O-rings gives an air tight fit when attached to the screw-on collar. The tap allows the head space air to be removed by vacuum pump. After crushing, the evolved gas is removed from head space through the outlet to the vacuum pump by off-line cryogenic traps. Each stainless steel tube can be used four to six times.

Isotopic analysis of CO_2 from fluid inclusions involved mechanical crushing of quartz and removal of non-condensable volatiles and H_2O from the liberated CO_2 by cryogenic methods. Two grams of sample was loaded into a 9.5 mm diameter tube made from 316 stainless steel. The sample was packed down with silica wool. The tube was specially made to fit an air-tight head piece that had attachments allowing evacuation of air from the tube by the vacuum pump (Figure 11.1). The sample was crushed by hydraulic press at 3000 psi following evacuation of air from the tube. All gases were detached from the newly generated rock powder by heating the stainless steel tube to 150°C with a hot air heat gun. The tube was attached to the vacuum line and the liberated gas was collected using standard cryogenic methods. CO_2 was measured directly by a Fissons Optima mass spectrometer.

Thirty-two samples representing the three mineralisation events (Mo-type quartz veins, syn-gold extensional and shear quartz veins and SV-type quartz veins) were analysed to determine the $\delta^{13}C$ value of the fluid inclusion CO_2 in quartz.

11.3 Results

The fluid inclusions in the pre-mineralisation Mo-type quartz veins released CO_2 which gave $\delta^{13}C$ values that cluster in a tight range from -1.4 and +0.9 ‰ (mean = -0.8‰, standard deviation = 0.8‰, n = 6; Figure 11.2).

The fluid inclusions in the syn-gold quartz veins from within the Biotite-Carbonate Zone (BCZ) released CO_2 with $\delta^{13}C$ values that range between -3.7 and +1.7‰ (mean = -2.2‰, standard deviation = 1.5‰, n = 12; Figure 11.2). Fluid inclusions in four syn-gold quartz veins from the Proximal-Chlorite Zone and the Distal-Chlorite Zone (PCZ-DCZ) released CO_2 which gave $\delta^{13}C$ values ranging between -5.1 and +3.5 ‰ (mean = -1.5‰, standard deviation = 3.1‰, n = 4; Figure 11.2).

Fluid inclusions in ten post mineralisation SV-type quartz veins contain CO_2 which gave $\delta^{13}C$ values ranging between -5.7 and -2.3‰ (mean = -3.7‰, standard deviation = 1.0‰, n = 10; Figure 11.2).

11.4 Discussion

11.4.1 Fluid inclusion CO_2 in Mo-type quartz veins

CO_2 trapped in fluid inclusions in Mo-type quartz veins has a mean $\delta^{13}C$ value of -0.8‰. This value reflects a mixed seawater carbonate - magmatic carbon source for the entrapped CO_2 (Kerrich, 1987; Rollinson, 1993; Ohmoto and Goldhaber, 1997).

Calcite associated with hydrothermal Mo-bearing quartz veins from U.S.A and Canada (porphyry and vein type deposits) has $\delta^{13}C$ values ranging from approximately -10 to -1‰ (Taylor, 1987). The heaviest $\delta^{13}C$ values in these deposits are strongly influenced by wall rock lithologies that

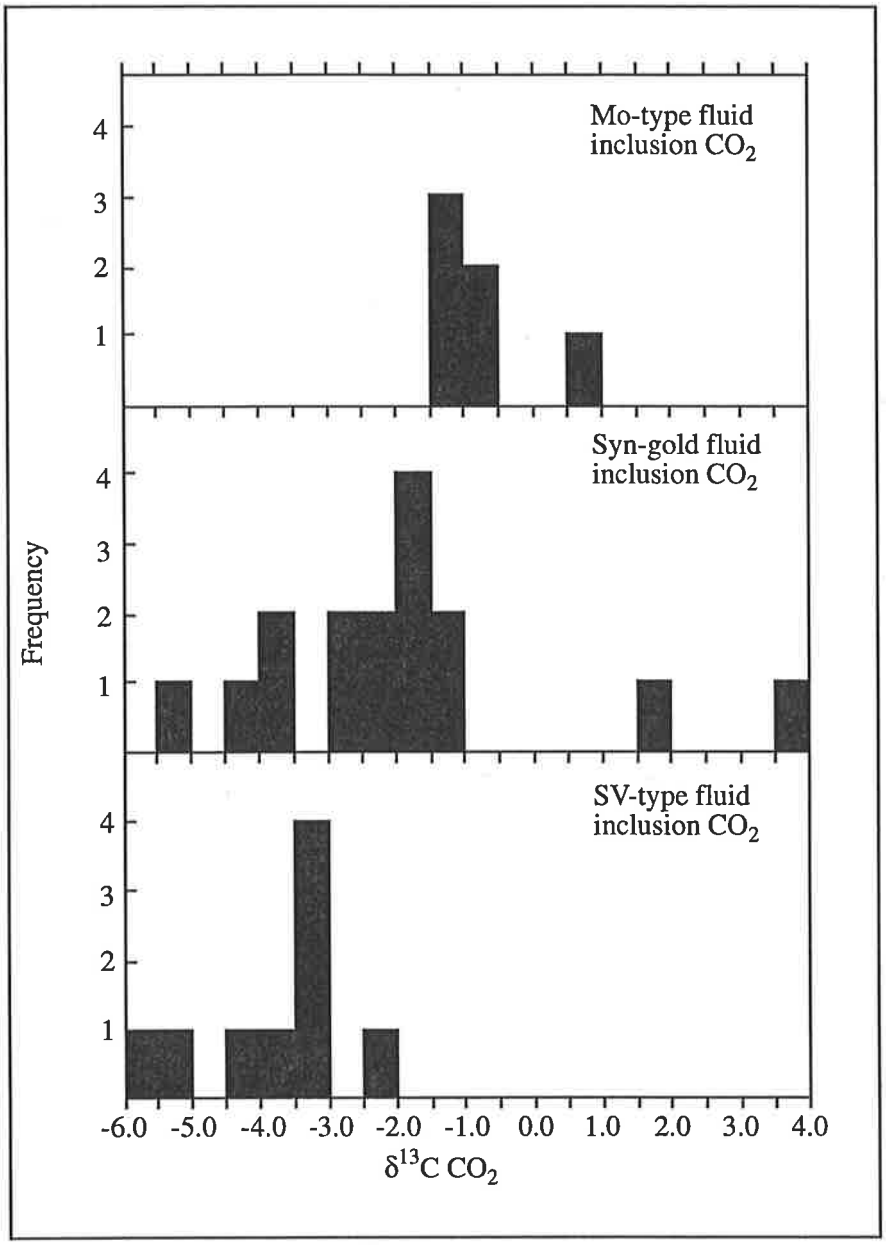


Figure 11.2. Compilation of $\delta^{13}C$ values for Mo-type, Syn-gold type and SV-type fluid inclusion CO_2 extracted from quartz veins and trapped using cryogenic methods.

are dominated by limestone. The majority of $\delta^{13}C$ values obtained from calcite in quartz-carbonate veins hosted in these deposits indicate a mixed mantle - magmatic source for the parent ore fluid (Taylor, 1987), as opposed to the mixed seawater - magmatic carbon source proposed for the $\delta^{13}C_{(CO_2)}$ values extracted from the Junction Mo-type quartz.

The importance of the Mo-type quartz veins at Junction is not considered sufficient to warrant intensive investigation. Nevertheless, the Mo-type quartz veins are unlikely to have originated from fluids that originate from remobilised seawater carbonate, based on the volumes of literature

that associate molybdenum mineralisation with magmatic and mantle fluids, in particular, porphyry intrusives. This view is supported by the oxygen isotope data (Chapter 9) that indicates that the quartz has a mantle and/or magmatic origin, not a reworked seawater carbonate origin.

Further to this, the Mo-type quartz veins at Junction are hosted by the Junction Gabbro and not a carbon bearing metasediment or limestone that could contaminate the original $\delta^{13}C$ value of the parent fluid. Thus, the isotopically heavy $\delta^{13}C$ values obtained from fluid inclusion CO_2 extracted from Mo-type quartz veins at Junction are in disagreement with the calcite $\delta^{13}C$ values and interpretations reported by Taylor (1987) for Mo-bearing porphyry and vein type deposits. Fluid inclusion CO_2, if it were of magmatic origin would be expected to have $\delta^{13}C$ values closer to -3.0‰ (Burrows *et al.*, 1986; Wood *et al.*, 1986a, 1986b; Burrows and Spooner, 1987; Rollinson, 1993; Ohmoto and Goldhaber, 1997).

11.4.2 Fluid inclusion CO_2 in syn-gold quartz veins

The mean $\delta^{13}C$ values for fluid inclusion CO_2 extracted from the quartz veins in the BCZ are in disequilibrium with the mean $\delta^{13}C$ values of the co-existing calcite. Ohmoto and Rye (1979), Kyser (1987) and Ohmoto and Goldhaber (1997), show that isotopic fractionation between hydrothermal calcite and a CO_2-rich parent fluid is between 2.5‰ and 4.0‰ at temperatures between 300 and 450°C. Therefore given that mineralisation occurred at 385 ± 35°C, fluid inclusion CO_2 should be approximately 2.5‰ to 3.5‰ heavier than the co-existing calcite. The mean $\delta^{13}C$ difference between fluid inclusion CO_2 and co-existing calcite is 4.3‰ (range 2.9‰ to 7.4‰) in the BCZ. Similarly, the $\delta^{13}C$ difference between fluid inclusion CO_2 and co-existing calcite in the one PCZ-DCZ sample analysed is 4.1‰ (Table 11.1).

The $\delta^{13}C$ difference between the fluid inclusion CO_2 and co-existing calcite (i.e. $\delta^{13}C$ differences that are > 4.0‰) in some samples is larger than the fractionation values observed between CO_2 and calcite during experimental observations and theoretical calculations (see Figure 10.2, Chapter 10). Santosh *et al.* (1995) interpreted similar results to indicate that the calcite and the CO_2 in the quartz were formed during different fluid events.

Santosh *et al.* (1995) reported on the $\delta^{13}C$ values obtained from CO_2 extracted from fluid inclusions hosted by quartz veins in the Wynad gold deposit, South India, a late-orogenic, structurally-controlled gold deposit. They found that the $\delta^{13}C$ values of CO_2 extracted from fluid inclusions by crushing, were between 3.6‰ and 6.3‰ heavier than $\delta^{13}C$ values obtained from co-existing carbonates (fluid inclusion CO_2, $\delta^{13}C$ = -5.9‰ to -4.1‰, co-existing carbonate $\delta^{13}C$ = -10.5‰ to -9.2‰). These authors suggest the difference in $\delta^{13}C$ values is larger than that expected for equilibrium isotopic fractionation at the temperatures given by microthermometry. Thus, they interpreted this data to mean that the calcite was precipitated from a different fluid to that from which the quartz veins precipitated. The two-stage deposition model proposed by Santosh *et al.* (1995) does not appear to be an appropriate model for Junction.

$\delta^{13}C$ values for coexisting fluid inclusion CO_2 and calcite

Sample	Sample Type	‰$\delta^{13}C_{Calcite}$	‰$\delta^{13}C_{CO_2}$	$\delta^{13}C_{Calcite}$ - $\delta^{13}C_{CO_2}$
1074-64	Mo-type		-1.4	
1074-66	Mo-type		+0.9	
1074-252a	Mo-type		-0.9	
1074-283	Mo-type		-1.3	
1074-284	Mo-type		-1.2	
1074-286	Mo-type		-0.6	
1074-84	Syn-gold BCZ	-5.8#	-2.5	3.3#
1074-94	Syn-gold BCZ	-6.3	-2.2	4.1
1074-99	Syn-gold BCZ	-5.7	+1.7	7.4
1074-105	Syn-gold BCZ	-6.5	-1.9	4.6
1074-111	Syn-gold BCZ	-5.7	-2.8	4.1
1074-141	Syn-gold BCZ	-7.0	-1.9	5.1
1074-149	Syn-gold BCZ		-3.7	
1074-215	Syn-gold BCZ	-5.4	-1.4	4.0
1074-220	Syn-gold BCZ	-7.3	-1.9	5.4
1074-236	Syn-gold BCZ	-7.4	-2.0	5.4
1074-248	Syn-gold BCZ	-7.2	-4.3	2.9
1074-251	Syn-gold BCZ	-7.3	-3.8	3.5
1074-186	Syn-gold PCZ/DCZ		-5.1	
1074-212	Syn-gold PCZ/DCZ		-2.8	
1074-233	Syn-gold PCZ/DCZ		+3.5	
1074-245	Syn-gold PCZ/DCZ	-4.7	-1.5	4.1
1074-25	SV-type	-7.3	-5.3	2.0
1074-35	SV-type	-7.2	-5.7	1.5
1074-52	SV-type	-7.2	-3.6	3.6
1074-77	SV-type	-7.5	-2.3	5.2
1074-94	SV-type		-2.4	
1074-121	SV-type	-7.4	-4.2	3.2
1074-130	SV-type	-7.4	-3.2	4.2
1074-136	SV-type	-7.3	-3.3	4.0
1074-137	SV-type	-5.5	-3.4	2.1
1074-238	SV-type	-5.3	-3.5	1.8

= dolomite sample. Fractionation value calculated for dolomite in equilibrium with calcite at 385°C.

Table 11.1. $\delta^{13}C$ values for fluid inclusion CO_2 with comparisons to co-existing $\delta^{13}C$ values for calcite. $\delta^{13}C_{Calcite}$ - $\delta^{13}C_{CO_2}$ values are the fractionation differences between the calcite and CO_2. These fractionation values indicate that many samples are in disequilibrium with each other.

Petrological and other geochemical data does not support late deposition of carbonate at Junction, or at other nearby gold deposits. In fact, reports by Phillips and Groves (1984), Clark *et al.* (1989), Groves and Phillips (1987), Golding *et al.* (1990a) and Woolrich (1994) support the co-precipitation of carbonate and quartz at the Argo, Victory-Defiance and Hunt gold deposits (10 to 30 km north of Junction, Figure 1.1, Chapter 1). Similarly, Costello (1993), Carey (1994), Gilmore (1996) and this study support the co-precipitation of carbonate and quartz at the Junction deposit.

Cathodoluminescence microscopy (Chapter 3) does indicate that dissolution and re-precipitation of some carbonates occurred during the formation of the Junction deposit. However, the volume of late calcite observed in the Junction Shear Zone is not sufficiently extensive to explain the difference in $\delta^{13}C$ values between the carbonates and the fluid inclusion CO_2. Further to this, $\delta^{18}O$ analyses of co-existing carbonate and quartz indicate that isotopic equilibrium has been retained between the two minerals (Chapter 9). Therefore it can be concluded that deposition of carbonate did not occur at a later stage than the quartz at Junction.

Another interpretation is proposed by Oberthur *et al.* (1996). Many of the $\delta^{13}C$ values for fluid inclusion CO_2 extracted from the BCZ quartz (-5.1‰ to +1.7‰) overlap the range of $\delta^{13}C$ values calculated for the original parent CO_2 (-4.4‰ to -0.4‰; Chapter 10) that deposited the wall-rock and vein calcite. Similar to this observation, Oberthur *et al.* (1996) found that the $\delta^{13}C$ values of fluid inclusion CO_2 extracted from quartz-veins are in approximate agreement with the known isotopic fractionation values between carbonates and CO_2 that form above 250°C ($\delta^{13}C$ fluid inclusion CO_2 values range from -9.5‰ to -15.7‰, compared to $\delta^{13}C$ calcite-dolomite which range from -9.9‰ to -17.0‰). These authors concluded that the fluid inclusion CO_2 and the co-existing carbonate is in approximate equilibrium. However, whilst the range of values appears to be in equilibrium with each other, tabulated data by Oberthur *et al.* (1996) show that none of their values are derived from co-existing samples. This study shows that overlapping ranges from a whole population do not necessarily indicate that equilibrium was attained (see Table 11.1).

An alternative interpretation, mainly overlooked, is the possibility that post-entrapment ^{13}C exchange occurs between CO_2 and other carbonic gases trapped within the fluid inclusions. The most obvious carbonic phase that is known to co-exist with CO_2 in fluid inclusions is CH_4 (Chapters 5, 6 and 7). Post-entrapment re-equilibration will shift the $\delta^{13}C$ value of the CO_2 out of isotopic equilibrium with the co-existing carbonates. Isotopic exchange between co-existing carbonic gases (e.g. CO_2 and CH_4) within the same fluid inclusion occurs, because the conditions of entrapment have changed since mineralisation occurred.

Isotopic exchange between CO_2 and CH_4 is very slow. Indeed, Sackett and Chung (1979) were unable to detect any isotopic exchange between CO_2 and CH_4 at 500°C after 10 days and concluded that exchange between the two species either did not occur or was so slow that it was not experimentally noticeable. However, Harting and Mass (1980) provided the first experimental evidence of isotopic exchange between CO_2 and CH_4 at temperatures of 500 - 600°C. Giggenbach (1982) re-evaluated the experiments of Harting and Mass (1980) and found that the time taken for CO_2 and CH_4 to reach equilibrium is 10^4 years at 400°C and 10^7 years at 300°C. Giggenbach (1982) concluded that isotopic exchange between CO_2 and CH_4 at temperatures below 300°C is extremely slow and unlikely to be attained in natural systems. However, Ohmoto and Lasaga (1982) and Ohmoto (1986) report that the experimental conditions may not apply to hydrothermal

systems and the rates of C isotope exchange between CO_2 and CH_4 probably depends on the concentrations of H_2O, CO_2, CH_4 and H^+ present, as well as on temperature conditions. Ohmoto and Goldhaber (1997) report that two co-existing gas species that are initially out of equilibrium with each other will continue to approach equilibrium at any temperature if they are allowed to co-exist for sufficient time. Thus, it can be assumed that isotopic equilibrium between CO_2 and CH_4 has been on-going within individual fluid inclusions since entrapment.

Mineralisation along the Norseman to Wiluna belt is believed to have ceased approximately 2.6 Ga (Clark *et al.*, 1989; Carey, 1994). This is within error of other precise ages on mineralisation for gold deposits on the Yilgarn Craton (Barnicoat *et al.*, 1991; Wang *et al.*, 1993). It can be concluded that the Junction ore deposit began up-lift and cooling almost immediately after mineralisation ended, given that it formed at a depth of ca. 10 km and that the Kambalda to Norseman area has been near the surface since at least the Late Permian (Clarke, 1994a) and possibly since the Proterozoic (Finkl and Fairbridge, 1979). The almost immediate lowering of the temperature from 385 ±35°C at the time of entrapment implies that CO_2 and CH_4 trapped together in fluid inclusions have been in disequilibrium with each other from the time that mineralisation ceased.

The attainment of isotopic equilibrium between CO_2 and CH_4 is a natural, ongoing process (Ohmoto and Goldhaber, 1997), and proceeds by the reaction:

$$CH_4 + 2H_2O <=> CO_2 + 4H_2$$ Equation 11.1 (Giggenbach, 1982).

The kinetics of the CH_4 - CO_2 isotopic exchange is represented by:

$$^{13}CH_4 + 12CO_2 <=> 12CH_4 + {}^{13}CO_2$$ Equation 11.2 (Harting and Mass, 1980).

The two equations imply that the forward reaction equals the reverse reaction. Thus equilibrium between CO_2 and CH_4 can only be attained at the same time as chemical equilibrium is attained (Ohmoto and Goldhaber, 1997).

A change in temperature from approximately 385 ± 35°C (entrapment temperature 2.6 Ga) to <50°C (near surface temperature) results in a change in the equilibrium fractionation factor between CO_2 and CH_4 from -20‰ to < -58‰ (see Figure 10.3, Chapter 10 for example). Therefore, CO_2 will become isotopically heavier and CH_4 will become isotopically lighter during the re-equilibration process according to the equation of Harting and Mass (1980) and the fractionation factor between CO_2 and CH_4 at temperatures below 385°C. A noticeable shift in $\delta^{13}C$ values for both CO_2 and CH_4 should be observable, assuming the ore body began to cool soon after mineralisation ceased (2.6 Ga), even if isotopic equilibrium is not fully attained in this time (cf. Giggenbach, 1982). Indeed, this appears to be the case where the current $\delta^{13}C$

value for fluid inclusion CO_2 hosted by quartz is heavier than expected and in disequilibrium with co-existing calcite.

Stable isotope geothermometry using co-existing calcite-quartz $\delta^{18}O$ values (Chapter 9), CL microscopy and petrological observations indicate that the quartz and calcite are contemporaneous. Thus, $\delta^{13}C$ values obtained from fluid inclusion CO_2 are an enigma if interpretation insists that the CO_2 in the fluid inclusions has not undergone ^{13}C exchange with some other carbonic phase that must be accessible to the CO_2. That the lightest $\delta^{13}C$ values for calcite in all vein types and alteration zones at Junction do not remotely reflect the $\delta^{13}C$ values obtained from co-existing fluid inclusion CO_2 suggests that the fluid inclusion CO_2 has re-equilibrated with CH_4 in a closed environment over a long period of time.

The $\delta^{13}C$ values obtained from the fluid inclusion CO_2 fit this model. The CO_2 extracted from the fluid inclusions hosted in quartz veins are marginally to moderately heavier than the $\delta^{13}C$ value calculated for the parent CO_2 from the calcite $\delta^{13}C$ values. The differences between the *mean* $\delta^{13}C$ value of fluid inclusion CO_2 and the *mean* $\delta^{13}C$ value calculated from the calcite $\delta^{13}C$ values for the parent CO_2 is 2.2‰ for samples from the JSZ (mean $\delta^{13}C$ value of fluid inclusion CO_2 is -2.2‰, mean $\delta^{13}C$ value of parent CO_2 applying the model of Colvine *et al.* [1988], is -4.4‰). This difference is considered to be the approximate $\delta^{13}C$ shift that has occurred in fluid inclusion CO_2 during the last 2.6 Ga.

The variable shifts in $\delta^{13}C$ values for fluid inclusion CO_2 probably reflect the different populations of fluid inclusions sampled across a given quartz vein. Variations in CO_2 : CH_4 ratios are known to vary across the width of quartz veins in the JSZ (as discussed in Chapter 6 and shown in Figure 6.3). The different concentrations of CO_2 and CH_4 in each fluid inclusion is expected to influence the isotopic exchange potential between the CO_2 and CH_4 (i.e. the less CH_4, H_2O, H^+ trapped in co-existence with CO_2, the less exchange between the two gases is possible, thus, the smaller the $\delta^{13}C$ shift for CO_2).

This model and interpretation does not assume either later deposition, or re-precipitation of the carbonate found in the wall rock as proposed by Santosh *et al.* (1995), but instead proposes that carbon exchange between CO_2 and CH_4 has probably occurred over the 2.6 Ga period since entrapment. The model does not dismiss the effect of Rayleigh isotope fractionation during the ore forming process. Indeed, Rayleigh fraction remains the proposed mechanism for the calcite $\delta^{13}C$ variations across the JSZ (-7.4‰ to -2.5‰). Thus, the model presented here not only adequately explains the $\delta^{13}C$ values obtained from the alteration calcite and the $\delta^{13}C$ variations observed for fluid inclusion CO_2, but it also suggests that a reinterpretation of results may be required for data collected and discussed by Jackson *et al.* (1988), Santosh *et al.* (1995), Oberthur *et al.* (1996) and Vazquez *et al.* (1998).

11.4.3 SV-type quartz veins

A similar state of disequilibrium exists for the SV-type quartz veins, where only four of the nine $\delta^{13}C$ values indicate fluid inclusion CO_2 - vein calcite equilibrium. CO_2 in equilibrium with co-existing calcite in the SV-type quartz veins should have a $\delta^{13}C$ difference close to 2.0‰, based on fractionation factors calculated using temperature estimates obtained by microthermometry (300°C). Instead, the $\delta^{13}C$ difference between the fluid inclusion CO_2 and its co-existing calcite ranges from 1.5 to 5.2‰ (mean = 3.2‰). Therefore, the interpretation presented in section 11.4.2 above, is applicable to the SV-type veins, and it can be concluded that CO_2 - CH_4 re-equilibration has occurred in these veins also.

11.4.4 Concluding remarks

It can be concluded that the Mo-type quartz veins discussed in Section 11.4.1, once had a much lighter $\delta^{13}C$ value than that presently indicated, if one applies the interpretation presented in Section 11.4.2 to the $\delta^{13}C$ values obtained from CO_2 extracted from Mo-type quartz veins. Raman-spectroscopy and limited fluid inclusion microthermometry show that large volumes of CH_4 are present in some fluid inclusions trapped in the Mo-type veins (Chapter 6). Therefore, isotopic fractionation between co-existing CO_2 and CH_4 is assumed. The application of the mean $\delta^{13}C$ shift suggested for the syn-gold quartz veins (2.2‰) to the original $\delta^{13}C$ of fluid inclusion CO_2 trapped in fluid inclusions hosted by the Mo-type quartz veins (-0.8‰) reveals that the Mo-type quartz veins possibly formed from a fluid that contained CO_2 with a $\delta^{13}C$ value closer to -3.0‰. This value suggests a possible mantle origin with a distinct magmatic - crustal influence (Burrows *et al.*, 1986; Wood *et al.*, 1986a and 1986b; Deines, 1992; Rollinson, 1993; Ohmoto and Goldhaber, 1997). This interpretation fits the Mo-type style of mineralisation discussed by Taylor (1987) better than the reworked seawater carbonate origin suggested in section 11.4.1.

In conclusion, the results of this work indicate that the role of CH_4 in fluid inclusions has previously been overlooked, resulting in a misinterpretation of fluid inclusion $\delta^{13}C$ values. This misinterpretation of $\delta^{13}C$ values has in turn led to the incorrect interpretation of paragenetic sequences and therefore a misunderstanding of the formation of these ore deposits and their fluid sources.

CHAPTER TWELVE

Coupled gas chromatography and stable isotope mass spectrometry

12.1 Introduction

Carbon isotope values for all carbon bearing phases in late-orogenic, structurally-controlled gold deposits (e.g. carbonates, CO_2 gas, CH_4 gas) bear particular significance, since the ore forming fluid, characterised by CO_2, is the only source of carbon in an otherwise carbon depleted host rock (Golding *et al.*, 1987, 1989; Kerrich, 1987, 1989; McNaughton *et al.*, 1988). Therefore, co-existing carbon-bearing phases are expected to be in isotopic equilibrium with each other at the time of gold mineralisation. However, stable isotope values obtained from CO_2-rich fluid inclusions in quartz at Junction are in disequilibrium with the stable isotope values of co-existing calcite. This leads to the conclusion that the calcite has either been re-equilibrated since its precipitation, or that it is not related to the quartz-hosted CO_2-rich fluid inclusions (cf., Santosh *et al.*, 1995; Oberthur *et al.*, 1996). However, oxygen isotope analysis incorporating stable isotope geothermometry, using co-existing calcite-quartz $\delta^{18}O$ values (Chapter 9) and CL microscopy coupled with other petrological observations (Chapter 3) indicate that the quartz and calcite are contemporaneous. Thus, it is proposed that post-entrapment ^{13}C exchange has occurred between CO_2 and CH_4 (Chapter 11) resulting in the $\delta^{13}C$ value of the fluid inclusion CO_2 shifting out of isotopic equilibrium with the co-existing carbonates.

Fluid inclusion investigations often refer to the presence of CH_4 in the fluid inclusions trapped in late-orogenic, structurally-controlled gold deposits (e.g. Smith and Kesler, 1985; Robert and Kelly, 1987; Clark *et al.*, 1989; Ho *et al.*, 1990 and references within; Guha *et al.* 1991; de Ronde *et al.*, 1992; Cassidy and Bennett, 1993; Mernagh and Witt, 1994; Graney and Kesler, 1995; Robert *et al.*, 1995; Mernagh, 1996; Boullier *et al.*, 1998; this study). Therefore, it is possible that re-equilibration between co-existing CO_2 and CH_4 within individual fluid inclusions is responsible for the CO_2 - calcite disequilibrium observed.

Confirmation that CO_2 and CH_4 have been approaching equilibrium for the past 2.6 Ga, can be obtained by calculating the original $\delta^{13}C$ values of CO_2 and CH_4. The $\delta^{13}C$ value taken as the parent CO_2 that led to the deposition of calcite in the JSZ (incorporating all values from the BCZ, PCZ and the DCZ) is -4.4‰ (Chapter 10.4.1). The isotopic fractionation factor between CO_2 and CH_4 at 385°C is ca. 20‰ (Figure 10.3, Chapter 10; Kyser, 1987; Ohmoto and Goldhaber,

1997). Therefore, the isotopic value of CH_4 at the time of ore formation would be -24.4‰, assuming that the CO_2 and CH_4 were in equilibrium with each other at the time of entrapment. Post-entrapment re-equilibration of CO_2 and CH_4 at low temperatures is indicated if $\delta^{13}C$ deviations from these values are shown.

12.1 Methods

The $\delta^{13}C$ values of co-existing CO_2 and CH_4 can be measured using gas chromatography coupled with stable isotope mass spectrometry (GC-MS). GC-MS involves the separation of carbon-bearing gases by gas chromatography and the subsequent isotopic analysis of these carbon bearing gases by mass spectrometry.

Selected quartz veins were crushed and sieved to a grain size of >63μm and < 250μm. The sieved fraction was washed in deionised water to remove rock powder created through the crushing process. It was then dried at 75°C for 12 - 24 hours. The washed sample was passed through a Franz magnetic separator to remove magnetic particles (chlorite, biotite, pyrrhotite, etc.) that were part of the vein assemblage. Samples were then bathed in aqua-rega acid solution for 4 hours to remove any excess carbonate and non-magnetic sulphide material. Trace amounts of albite were not always removed from the sample. If it had been necessary, a process involving washing the sample in hydrofluoric acid could have been used. However, the small quantities of albite in the sample do not effect the quality of the results.

Gases were released from the fluid inclusions by the mechanical crushing of the quartz ± albite grains. Five grams of sample was loaded into a 9.5 mm diameter tube made from 316 stainless steel. The sample was packed down with silica wool. The tube was specially made to fit an air-tight head piece that had attachments allowing evacuation of air from the tube by the vacuum pump (Figure 12.1). The air in the tube was first evacuated and then the sample was crushed by hydraulic press at 3000 psi.

All of the gases released by crushing were detached from the newly-generated rock powder by heating the stainless steel tube to 150°C with a hot-air heat gun. A sub-sample of the liberated gas was removed from the head space of the tube by a 100μm syringe and injected into a Hewlett Packard Model 5890 Series II gas chromatograph fitted with a Poraplot-Q coated Chromapack plot fused silica 25MXO.32MM column. The GC was fitted with a 1m long pre-column used to cryo-focus the gases when the sample was injected into the injection port. Cryo-focusing enhanced the separation of CH_4 from CO_2 by exploiting the wide differences in their melting point properties. The gases were separated in the GC column, and then passed through a GC Combustion Interface which has an oxidiser and a reduction column. The oxidiser and reduction column converts all of the carbon-bearing gases to CO_2 for mass spectrometric analysis. The mass spectrometer used was a Finnigan Mat 252 with continuous-flow technology.

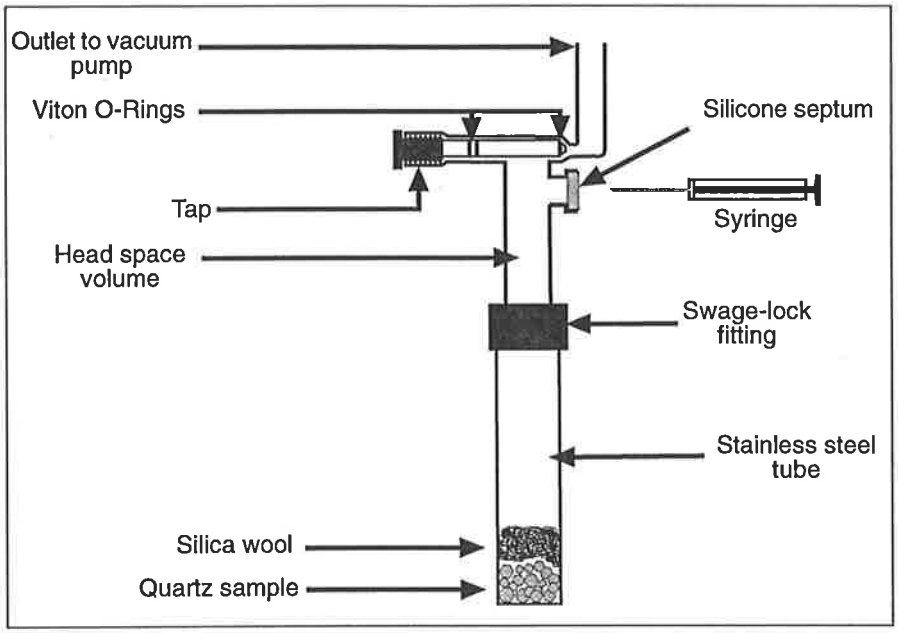


Figure 12.1. Diagramatic representation of the aparatus used to extract CO_2 from quatrz. A stainless-steel tube was used to crush the quartz sample. The tap allows the head space air to be removed by vacuum pump. Evolved gas is removed from head space via the silicone septum by a syringe.

12.3 Results

The method of GC-MS applied to samples from the Junction mine was able to measure the volume of all carbon bearing gas phases (CO, CO_2, CH_4, C_2H_6, $CnH_{[2n+2]}$) likely to be trapped in fluid inclusions and at the same time measure the $\delta^{13}C$ value of those gases. Fifteen samples representing the three main mineralisation events (Mo-type veins, syn-gold veins and SV-type veins) were analysed. All fifteen samples had only CO_2 and CH_4 as the gases detected. The data obtained is presented in Table 12.1.

12.3.1 Pre-gold Mo-type quartz vein samples

Four pre-mineralisation Mo-type quartz veins were crushed and analysed. The ratios of CO_2:CH_4 ranged from 0.59 to 0.97. The $\delta^{13}C$ values for Mo-type CO_2 range from -10.4‰ to -2.4‰ and $\delta^{13}C$ values for Mo-type CH_4 range from -34.7‰ to -32.8‰.

12.3.2 Syn-gold quartz vein samples

Nine syn-gold quartz veins from within the JSZ have CO_2: CH_4 ratios that range from 0.29 to 0.99. The $\delta^{13}C$ values for syn-gold CO_2 range from -10.4‰ to +1.1‰ (mean = -5.0‰, standard deviation = 3.0‰, n = 9). The $\delta^{13}C$ values for syn-gold CH_4 range from -50.5 to -35.2‰ (mean =-42.4‰, standard deviation = 5.2‰, n = 9).

12.3.3 Post-gold SV-type quartz vein samples

The two post mineralisation SV-type quartz veins that were analysed have CO_2 to CH_4 ratios of 0.9 and 0.99. The $\delta^{13}C$ values for SV-type CO_2 are -3.8‰ and -0.6‰. The $\delta^{13}C$ values for SV-type CH_4 are -39.5‰ and -35.6‰.

$\delta^{13}C$ values for fluid inclusion CO_2 determined by the off-line technique compared with $\delta^{13}C$ values for CO_2 and CH_4 determined by GC-MS methods

Sample	Sample type	Off-line fluid inclusion ‰$\delta^{13}C_{CO_2}$	‰ $\delta^{13}C_{CO_2}$	Voltage amplitude	Peak area	Estimated CO_2 volume	‰ $\delta^{13}C_{CH_4}$	Voltage amplitude	Peak area	Estimated CH_4 volume	‰ Calcul. $\delta^{13}C\Sigma$	‰ EA-MS $\delta^{13}C\Sigma$
1074-252a	Mo-type	-0.9	-10.4	1.33	0.62	97.0	-34.7	0.05	0.49	3.0	-21.6	-28.2
1074-283	Mo-type	-1.3	-2.4	6.5	25.7	97.0	-32.8	0.10	0.70	3.0	-3.2	-7.8
1074-284	Mo-type	-1.2	-10.2	1.1	6.3	61.0	-34.7	0.60	4.00	39.0	-19.7	-8.2
1074-286	Mo-type	-0.6	-9.1	0.9	4.0	59.0	-32.8	0.40	2.80	41.0	-18.9	-6.7
1074-41	Syn-gold BCZ	—	-7.0	0.99	4.7	94.0	-43.5	0.04	0.30	6.0	-9.2	-26.7
1074-43	Syn-gold BCZ	—	-7.1	1.4	6.0	95.0	-35.3	0.04	0.30	5.0	-8.4	-17.7
1074-84	Syn-gold BCZ	-2.5	-1.6	10.7	51.4	87.0	-50.5	1.52	8.00	13.0	-8.2	-9.4
1074-99	Syn-gold BCZ	+1.7	+1.1	4.7	35.2	88.0	-35.2	0.82	4.87	12.0	-3.4	-10.5
1074-111	Syn-gold BCZ	-2.8	-7.4	0.80	9.4	99.0	-49.1	0.01	0.07	1.0	-13.1	-6.3
1074-149	Syn-gold BCZ	-3.7	-3.6	2.68	33.8	98.0	-40.5	0.09	0.76	2.0	-4.7	-12.1
1074-229	Syn-gold BCZ	—	-10.4	1.9	1.9	29.0	-38.8	4.30	21.70	71.0	-36.5	-18.6
1074-212	Syn-gold PCZ/DCZ	-2.8	-5.0	1.9	8.7	96.0	-45.8	0.06	0.40	4.0	-6.8	-13.0
1074-245	Syn-gold PCZ/DCZ	-1.5	-1.9	4.8	21.2	95.0	-40.9	0.20	1.20	5.0	-3.9	-5.6
1074-93	SV-type	-2.4	-0.6	4.2	17.0	90.0	-35.6	0.30	1.90	10.0	-3.7	-13.7
1074-136	SV-type	-3.3	-3.8	2.34	30.1	99.0	-39.5	0.03	0.18	1.0	-4.0	-12.0

Table 12.1. $\delta^{13}C$ values of coexisting fluid inclusion CO_2 determined by off-line crushing and cryogenic trapping of CO_2 tabulated for comparison with the $\delta^{13}C$ values for CO_2 and CH_4 as determined by GC-MS methods. $\delta^{13}C\Sigma$ values were calculated using mass balance equations and compared to coexisting $\delta^{13}C\Sigma$ values determined by EA-MS analysis. All $\delta^{13}C$ values are relative to PDB. Underlined values - are discussed in section 12.4.

12.4 Discussion

12.4.1 Interpretation of $\delta^{13}C$ values

The results obtained from Raman-spectroscopy (Chapter 6) and EDTA-GC analysis (Chapter 7) are supported by the fact that only CO_2 and CH_4 were detected by GC-MS. There is no correlation between the CO_2 volumes detected and the $\delta^{13}C$ values obtained in any of the samples analysed. This indicates that the isotopic variations are not due to sample size and that the $\delta^{13}C$ values represent the true isotopic signature of the fluid. However, the $\delta^{13}C$ values of fluid inclusion CO_2 collected and analysed by the off-line crushing and cryogenic trapping technique (Chapter 11) are often different to the $\delta^{13}C$ values of fluid inclusion CO_2 determined by GC-MS (Table 12.1).

The samples that registered voltage amplitudes greater than 1.9 volts on the mass spectrometer during GC-MS analysis gave $\delta^{13}C_{(CO_2)}$ values that correlate with the $\delta^{13}C$ values determined from fluid inclusion CO_2 obtained by the off-line crushing and cryogenic collection technique. These samples are underlined in Table 12.1. The first conclusion arrived at is that the variation in isotopic values may be due to the size of the sample that goes through the mass spectrometer. However, the CO_2 standard that was automatically injected into the GC-MS system at the start of each analysis, registered a maximum amplitude of 1.3 volts and returned consistent $\delta^{13}C$ values (10.1±0.1‰ from > 50 runs). Indeed, experimental runs, using the same mass spectrometer employed for the GC-MS analyses, show that the mass spectrometer is accurate to ±0.2‰ at amplitude levels as low as 0.15 volts. Therefore, the $\delta^{13}C$ values obtained from CO_2 determined by GC-MS are **not** influenced by the size of the sample passing into the mass spectrometer.

The reason for these voltage related values is an enigma. The light $\delta^{13}C$ values of CO_2 (-7‰ to -10.4‰) are lower than the minimum $\delta^{13}C$ value calculated for the parent CO_2 (-4.4‰) and the values obtained by off-line crushing and cryogenic trapping technique (Chapter 11). Contamination by air through the swage-lock fittings used to attach the stainless-steel tube to the head-piece (Figure 12.1) is one possible source of the isotopically light CO_2. The lightest $\delta^{13}C$ values for fluid inclusion CO_2 (-7‰ to -10.4 ‰) are close to the $\delta^{13}C$ value of CO_2 in the earth's atmosphere, i.e. -8‰ (Kyser, 1987). The abundance of CO_2 in the earth's atmosphere is approximately 300 ppm. Therefore, the $\delta^{13}C$ value of fluid inclusion CO_2 would be swamped by the $\delta^{13}C$ value of atmospheric CO_2 if contamination did occur, given the extremely small volume of CO_2 released from the fluid inclusions within five grams of quartz. The $\delta^{13}C$ value of CH_4 injected into the GC-MS system (-32.8‰ to -50.5‰) neither supports nor discounts this theory. The $\delta^{13}C$ value of atmospheric CH_4 is -41‰ (Kyser, 1987), but CH_4 only accounts for approximately 3 to 4 ppm of atmospheric air. Thus, the $\delta^{13}C$ value obtained for CH_4 injected into the GC-MS system may simply indicate mixing between fluid inclusion CH_4 and atmospheric CH_4, given the low but variable volumes of CH_4 expected to be released from fluid inclusions with respect to CO_2 and other fluid inclusion volatiles, if contamination did occur.

However, if contamination by air did occur, the voltage amplitude detected by the GC-MS would be significantly larger than the voltage amplitudes detected for uncontaminated samples. Thus, the results remain enigmatic, unless every sample is considered to be contaminated. Therefore, the samples analysed by GC-MS with CO_2 $\delta^{13}C$ values that are lower than -4.4 ± 1.0‰ (the estimated value of the parent CO_2 that precipitated the calcite in the Junction Shear Zone) are considered to be an inaccurate representation of the fluid inclusion CO_2.

Eight of the 15 samples analysed by GC-MS are considered to be accurate based on their voltage amplitudes and their $\delta^{13}C$ values being near or heavier than -4.4 ± 1.0‰. These samples gave $\delta^{13}C$ values that are comparable with the $\delta^{13}C$ values obtained from fluid inclusion CO_2 extracted from quartz by the off-line crushing and cryogenic trapping technique (Chapter 11).

12.4.1.1 Pre-gold Mo-type quartz vein samples

Only one of the four Mo-type quartz vein samples is considered to have given an accurate $\delta^{13}C$ value. Sample 1074-283 released 97% CO_2 relative to CH_4. The CO_2 has a $\delta^{13}C$ value of -2.4‰. This value is comparable with the $\delta^{13}C$ value of fluid inclusion CO_2 obtained from the off-line crushing and cryogenic trapping technique (-1.4‰, Table 12.1). Therefore the $\delta^{13}C$ value of the co-existing CH_4 is considered to be accurate. The $\delta^{13}C$ value of the co-released CH_4 is -32.8‰.

The lack of carbonate associated with the Mo-type quartz veins prevents determination of the $\delta^{13}C$ value of the parent fluid. However, it is proposed that the Mo-type parent fluid contained CO_2 with a $\delta^{13}C$ value of approximately -3.0‰, based on estimates calculated in Chapter 11. Therefore, the corresponding $\delta^{13}C$ value estimated for Mo-type CH_4 is -24.0‰ at the time of entrapment (fractionation factor between CO_2 and CH_4 at 340°C = 21‰), based on the estimated $\delta^{13}C$ value of the Mo-type CO_2 in the parent fluid and the fluid inclusion homogenisation temperatures for this vein type (ca. 340°C).

The measured fractionation factor between the co-existing CO_2 and CH_4 in the one Mo-type quartz vein is 30.4‰ ($\delta^{13}C$ value of CH_4 - $\delta^{13}C$ value of CO_2), i.e. 5.9‰ greater than the expected $\delta^{13}C$ value if CO_2-CH_4 re-equilibration did not occur. The $\delta^{13}C(CH_4)$ value equates to a temperature of ca. 220°C when applied to the CO_2 and CH_4 fractionation curve (Figure 12.2). This is well below the ca. 340°C determined from homogenisation temperatures of halite daughter minerals in the Mo-type fluid inclusions. Consequently, the shift in the $\delta^{13}C$ value of CH_4 can be taken to indicate that re-equilibration has occurred between CH_4 and CO_2. Therefore, it can be assumed that the $\delta^{13}C$ value for Mo-type CO_2 is heavier now than it was at the time of entrapment.

12.4.1.2 Syn-gold quartz vein samples

Five of the nine syn-gold quartz vein samples analysed are considered to have given accurate $\delta^{13}C$ values (underlined in Table 12.1). These samples released between 87 and 99% CO_2 relative to CH_4. The CO_2 has $\delta^{13}C$ values ranging from -5.0‰ to +1.1‰. These values are comparable with the $\delta^{13}C$ values obtained from fluid inclusion CO_2 by the off-line crushing and cryogenic trapping technique. The $\delta^{13}C$ values of the co-released CH_4 range from -50.5‰ to -35.2‰.

The fractionation factor between the co-existing CO_2 and CH_4 in these syn-gold quartz veins ranges from -36.3‰ to -48.9‰ ($\delta^{13}C$ value of CH_4 - $\delta^{13}C$ value of CO_2). These fractionation factors equate to a temperature of ca. 90°C to 175°C when applied to the CO_2 and CH_4 fractionation curve (Figure 12.1). This temperature range is well below the calculated temperature of formation and entrapment estimated from fluid inclusion microthermometry, ca. 385°C. The shift in the $\delta^{13}C$ value of CH_4 from ca. -24.4‰ (the estimated isotopic value of CH_4 at the time of ore formation, see section 12.1) to as low as -50.5‰, indicates that re-equilibration has occurred between CH_4 and CO_2. This indicates that the $\delta^{13}C$ value of the syn-gold CO_2 in fluid inclusions must be heavier now than it was at the time of entrapment.

12.4.1.3 Post-gold SV-type quartz vein samples

A similar interpretation can be applied to the two SV-type quartz veins that contain 90% and 99% CO_2 relative to CH_4 and have $\delta^{13}C$ values of -3.8‰ and -0.6‰ for CO_2 and -39.5 and -35.6‰ for CH_4. Delta^{13}C values of SV-type calcite (lowest value = -7.5‰), indicate that the parent CO_2 in the hydrothermal fluid had a $\delta^{13}C$ value of -4.5‰ (applying the method of Colvine *et al.* [1988] and the fractionation between CO_2 and calcite at 300°C = 3.0‰; Ohmoto and Goldhaber, 1997). Thus, co-existing CH_4 must have had a $\delta^{13}C$ value of -28.5‰, given the fractionation between CO_2 and CH_4 at 300°C is -24‰ (Ohmoto and Goldhaber, 1997). The fractionation factors indicated by GC-MS for the co-existing CO_2 and CH_4 (-35.0‰ and -35.3‰), indicate re-equilibration, and correlate with temperatures of 180°C, well below the temperature of entrapment as indicated by fluid inclusion microthermometry (Figure 12.1).

12.4.2 Application of mass balance equations to the GC-MS results

Mass balance equations of the analysed CO_2 and CH_4 cannot be used to discriminate the accuracy of any samples. This is because variations in the sum total of the CO_2 and CH_4 $\delta^{13}C$ values in the fluid inclusions ($\delta^{13}C\Sigma$) may only reflect the volumes of CH_4 relative to CO_2 in the sample. The volumes of CO_2 (87 - 99%; Table 12.1) relative to CH_4 in the bulk samples of quartz determined by GC-MS (and considered to be accurate) reflect the volumes of CO_2 relative to CH_4 determined by Raman-spectroscopy. Raman-spectroscopy and EDTA-GC analysis (Chapters 6 and 7) have shown that CH_4 volumes vary across the profile of a quartz vein, with the CO_2:CH_4

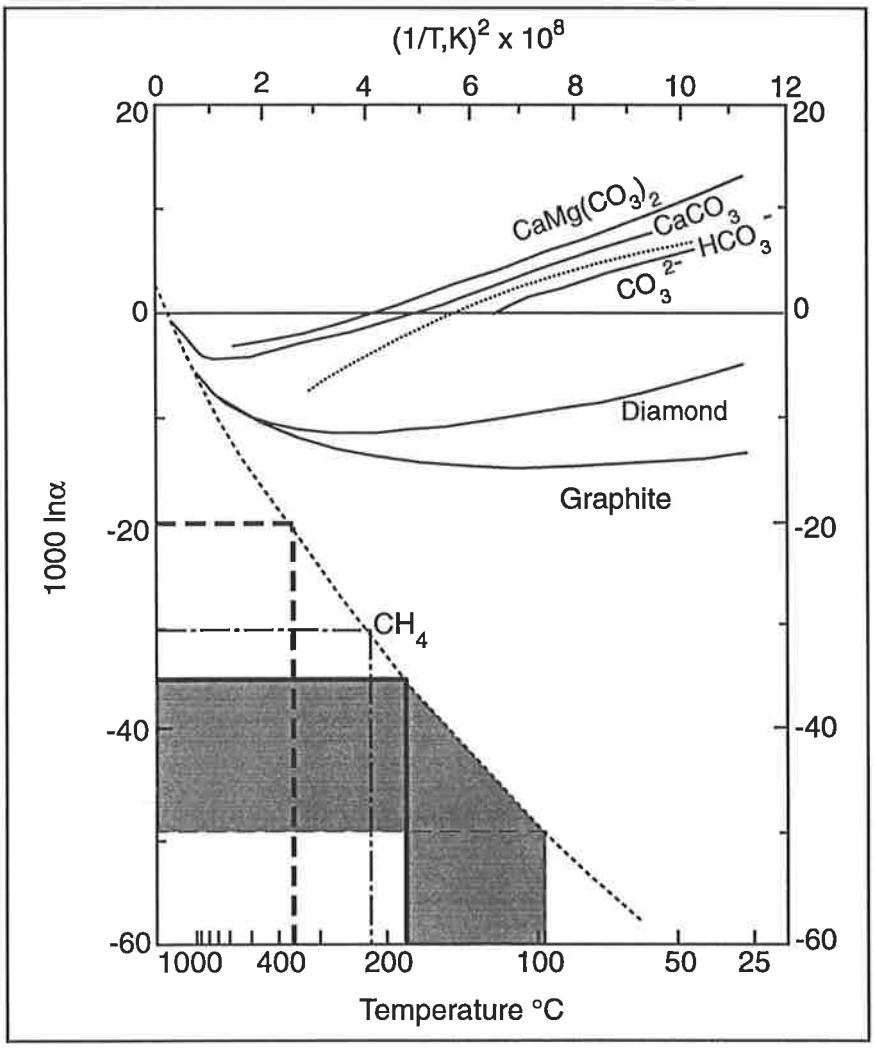


Figure 12.2. The stable isotope fractionation factor between co-existing CO_2 and CH_4 in the one Mo-type quartz vein analysed is 30.4‰. This equates to a temperature of 220°C (dot-dash line —·—·). Stable isotope fractionation factors between co-existing CO_2 and CH_4 in syn-gold quartz veins range from 36.3‰ to 48.9‰. This equates to a temperature range of ca. 90 - 175°C (outlined by shaded area), which is well below the stable isotope fractionation factor of 20‰ estimated for CO_2 and CH_4 at ca. 350°C (thick dashed line). The stable isotope fractionation factor between coexisting CO_2 and CH_4 in the SV-type quartz veins analysed is 35.0‰ and 35.3‰. This equates to a temperature of 175°C (thick solid line).

ratios lowest at the edges of the quartz vein at the contact with the host rock. Thus, it is possible that the variation in CO_2 and CH_4 ratios reflects the position of the analysed sample within the quartz vein.

Mass balance equations combine the volumetric proportions of the CO_2 and CH_4 (calculated from the peak areas registered by the mass spectrometer) with the $\delta^{13}C$ values of each gas, in

order to determine the $\delta^{13}C\Sigma$ of the original parent fluid. This is done using Equation 12.1:

$$\delta^{13}C\Sigma = \delta^{13}C\,(CO_2)x(\text{area } CO_2/\text{area of } CO_2 + \text{area of } CH_4) + \delta^{13}C\,(CH_4)x(\text{area } CH_4/\text{area of } CO_2 + \text{area of } CH_4) \quad \text{(Equation 12.1)}$$

Mass balance calculations applied to all samples analysed by GC-MS show that the $\delta^{13}C\Sigma$ values vary from sample to sample (-36.5‰ to -3.2‰, Table 12.1). However, mass balance calculations applied to the samples with stable isotope values considered to be accurate show that the $\delta^{13}C\Sigma$ value of individual samples are:

- -3.2‰ for the one Mo-type quartz vein,
- -3.2‰ to -6.8‰ for the five syn-gold quartz veins, and
- -3.7‰ to -4.0‰ for the two post-gold, SV-type quartz veins.

These values are close to the $\delta^{13}C$(parent CO_2) values estimated from $\delta^{13}C$(calcite) values for the primary CO_2 in the parent hydrothermal fluids:

- -3.0‰ for the Mo-type quartz veins,
- -4.4‰ for the syn-gold quartz veins, and
- -4.5‰ for the post-gold SV-type quartz veins.

The fractionation factors between CO_2 and CH_4, for all of the samples considered to be analytically correct, suggest that equilibrium between the two gases has not been reached for the near surface temperature of 50°C. The range of differences in the $\delta^{13}C$ values between the CO_2 and CH_4 in the samples analysed is 30.4‰ to 48.9‰. These fractionation factors represent a significant shift in the $\delta^{13}C$ values estimated for CH_4 and CO_2 at 300°C (25‰) and 385°C (20‰). However, a fractionation factor of approximately 58‰ would be needed to indicate equilibrium between CO_2 and CH_4 at 50°C.

The calculated fractionation factors imply that isotopic equilibrium has not been attained. However, this apparent isotopic disequilibrium between CO_2 and CH_4 can be attributed to either one or a combination of two processes. Giggenbach (1982) theoretically calculated that isotopic equilibrium between CO_2 and CH_4 takes 10^{10} years at temperatures below 200°C. The Junction ore body formed approximately $2.6x10^9$ years ago (Carey, 1994). Giggenbach (1982) concludes that isotopic exchange between CO_2 and CH_4 at temperatures below 300°C is extremely slow

and unlikely to be attained in natural systems. However, as stated briefly in Chapter 11.4, Ohmoto and Lasaga (1982) and Ohmoto (1986) suggest that theoretical and experimental conditions may not apply to hydrothermal systems. They hypothesise that the rates of carbon isotope exchange between CO_2 and CH_4 depend on the concentrations of H_2O, CO_2, CH_4 and H^+ present in each fluid inclusion, as well as the temperature conditions prevailing since mineralisation ceased. Therefore, it is possible that equilibrium between CO_2 and CH_4 has been reached in fluid inclusions containing suitable concentrations of H_2O, CO_2, CH_4 and H^+, but not in others where the critical relative ratios between these molecules does not exist.

The reason that samples analysed by GC-MS indicate disequilibrium between CO_2 and CH_4 is that exceptions to the aforementioned scenarios may occur. The most likely exception would involve cases where CO_2 and CH_4 cannot exchange carbon isotopes with each other simply because only one of the gases was trapped, i.e. without the other. Raman spectroscopy on individual fluid inclusions shows that many fluid inclusions are CO_2-rich, and that some contain 100% CO_2. There are considerably fewer fluid inclusions that containing 100% CH_4, although there are some. These fluid inclusions obviously cannot change their $\delta^{13}C$ value. Further to this, the variable shifts in $\delta^{13}C$ values for CO_2 and CH_4 may also reflect the volume of water present in these fluid inclusions (Ohmoto and Goldhaber, 1997). Water is needed to promote isotopic exchange (Equations 11.1 and 11.2, Chapter 11). Therefore, bulk gas analyses on quartz chips will give variable $\delta^{13}C$ values for CO_2 and CH_4 depending on the number of fluid inclusions present that have retained their original $\delta^{13}C$ values either due to the solitary existence of one of the gases in a fluid inclusion, or the volume of water present in the fluid inclusion. Thus, fluid inclusions without any water phase will be precluded from any isotopic alteration.

12.4.3 Concluding remarks

In conclusion, the analyses of quartz veins for the volumetric determination of fluid inclusion CO_2 and CH_4 and their respective $\delta^{13}C$ values by GC-MS have shown that GC-MS evaluation supports the finding of Raman-spectroscopy and EDTA-GC analysis. Further to this, GC-MS analysis suggests that the heavier $\delta^{13}C$ values obtained for fluid inclusion CO_2 by off-line crushing and cryogenic trapping are mostly a result of isotopic re-equilibration between fluid inclusion CO_2 and CH_4 at temperatures below the entrapment temperature, and not necessarily due to re-precipitation/re-equilibration of calcite by a geochemically distinct fluid after syn-gold precipitation.

GC-MS evaluation has also aided in the understanding of, and thus the interpretation of, the $\delta^{13}C$ values of fluid inclusion CO_2. The GC-MS evaluation has revealed that post-entrapment re-equilibration does occur in individual fluid inclusions, resulting in the $\delta^{13}C$ values of CO_2 becoming heavier at the same time as the $\delta^{13}C$ values of CH_4 become lighter. This discovery shows that fluid inclusion CO_2 and vein-wall rock calcite are not likely to be in equilibrium if CH_4 is present along with CO_2 in the fluid inclusions. Therefore, previous interpretations by

Santosh *et al.* (1995), who conclude that the fluid inclusion CO_2 in quartz was deposited by a different fluid source to that which deposited the vein-wall rock calcite, can be dismissed. This is a significant break-though in the interpretation of stable isotope geochemistry for mineral exploration.

CHAPTER THIRTEEN

Coupled elemental analysis - mass spectrometry

13.1 Introduction

Fluid inclusion microthermometry, laser-Raman microanalysis and GC-MS, indicate that CO_2 is the principle gas trapped in fluid inclusions at Junction. This is supported by many workers who report on fluid inclusions in late-orogenic, structurally-controlled gold deposits (Roedder, 1984; Robert and Brown, 1986; Boullier *et al.*, 1992; Robert *et al.*, 1995; Ho *et al.*, 1990; etc). However, EDTA-GC analysis and Raman-spectroscopy suggest that CH_4 volumes may exceed CO_2 volumes in fluid inclusions at the edges of quartz veins near the host-rock contact. CH_4 volumes in fluid inclusions hosted by gangue minerals at Junction are important when considering the source of the light hydrocarbons detected in the soil atmosphere above gold mineralisation.

An elemental analyser (EA) is used to determine the concentrations of C, N and S in a given sample. Therefore, an EA coupled with a highly sensitive mass spectrometer (EA-MS) can be used to determine the concentrations of CO_2 and CH_4 in a small sample of non-carbon bearing material (e.g. quartz). Elemental analysis involves instantaneously combusting a sample at very high temperatures (ca 1600°C), thus converting all of the compounds present in the sample into individual elements. The concentrations of these elements can then be determined by the EAs detectors. The element of interest can be isotopically analysed when the EA is coupled with a mass spectrometer. The isotopic values obtained by EA-MS can then be applied to mass balance equations to determine the volumes of CO_2 and CH_4 in each sample.

It has been established in Chapters 5, 6 and 12 that CO_2 and CH_4 are trapped in fluid inclusions in quartz at variable concentrations. Further to this, it has been shown that these two gases are rarely in isotopic equilibrium with each other once the entire ore system begins to cool down. However, it is reasonable to assume that carbon trapped in fluid inclusions at the time of mineral precipitation cannot escape from the fluid inclusion unless decrepitation and/or leakage occurs. Indeed this is the basic premise of fluid inclusion microthermometry. Therefore, the evaluation of carbon in a non-carbonate mineral (such as quartz) by EA-MS measures the sum total of carbon in a sample, i.e. the $\delta^{13}C\Sigma$ value.

The $\delta^{13}C\Sigma$ value of a sample must reflect the $\delta^{13}C$ values of the individual carbon bearing species present in fluid inclusions and pore spaces within the sample. Thus, the $\delta^{13}C$ values of the CO_2 and co-existing CH_4 in a quartz sample, together with the volumes of each gas in that sample, will influence the $\delta^{13}C\Sigma$ value determined by EA-MS assuming that CO_2 and CH_4 are the only source of carbon in the sample.

The $\delta^{13}C\Sigma$ value obtained from a non-carbonate mineral by EA-MS allows a reconstruction of the CO_2 and CH_4 ratio when applied to mass balance equations, so long as the temperature of entrapment is known, and the original isotopic value for one of the carbon-bearing species in the ore fluid can be established. Therefore, EA-MS provides a quick and accurate method of determining the CO_2 and CH_4 ratios in small specially selected samples. The determination of the CO_2 and CH_4 ratios in these hand picked samples of quartz is important, given that the CO_2 and CH_4 ratios vary across different parts of the quartz vein, and that quartz, being the most abundant gangue mineral in the Junction deposit, is a potentially major CH_4 reservoir for the soil gas anomaly detectable in the soil atmosphere.

Thus, EA-MS supports and expands on the data obtained in Chapters 5, 6 and 12.

13.2 Methods

Selected quartz veins were crushed and sieved to a grain size of >63μm < 250μm. The sieved fraction was washed in deionised water to remove rock powder created through the crushing process. It was then dried at 75°C for 12 - 24 hours. The washed sample was passed through a Franz magnetic separator to remove magnetic particles (chlorite, biotite, pyrrhotite, etc.) that formed part of the vein assemblage. Samples were then bathed in aqua-rega acid solution for 4 hours to remove any excess carbonate material. The sample was then bathed for 30 to 45 seconds in a diluted solution of hydrofluoric acid (HF-) to etch and remove any remaining albite. This procedure was very effective on these small grain sizes. Albite grains that did not dissolve, were easily broken down by agitating the sample in distilled water in an ultrasonic bath. The suspended albite was easily poured away leaving behind pure quartz. Optical examination under a binocular microscope showed that no albite remained after bathing in HF-.

Sixty to 75 mg of the dried sample was carefully weighed into a tin capsule and sealed by crimping the opening of the capsule. The samples were then loaded into an automated carousel on a continuous flow Carlo Erba Model NCS-1500 elemental analyser. The automated carousel drops each sample individually into a chamber where it is flushed with helium to remove any air contamination prior to combustion. The sample is combusted at approximately 1600°C. The element of interest is then separated from the rest of the combusted sample by its mass weight and passed through a Combustion Interface which has an oxidiser column and a reduction column to convert the elements to oxides before it flows into the mass spectrometer. The mass spectrometer is a Finnigan Mat 252 with continuos flow technology.

13.3 Results

Forty-five samples from three quartz vein generations were analysed by EA-MS to determine the $\delta^{13}C\Sigma$ value of the carbon-bearing fluids trapped in the fluid inclusions.

13.3.1 EA-MS analyses on pre-gold Mo-type quartz veins

The EA-MS analyses on pre-mineralisation, Mo-type quartz chips gave $\delta^{13}C\Sigma$ values of between -28.2‰ and -6.7‰ (mean = -14.1‰, standard deviation = 8.7‰, n = 6; Table 13.1, Figure 13.1).

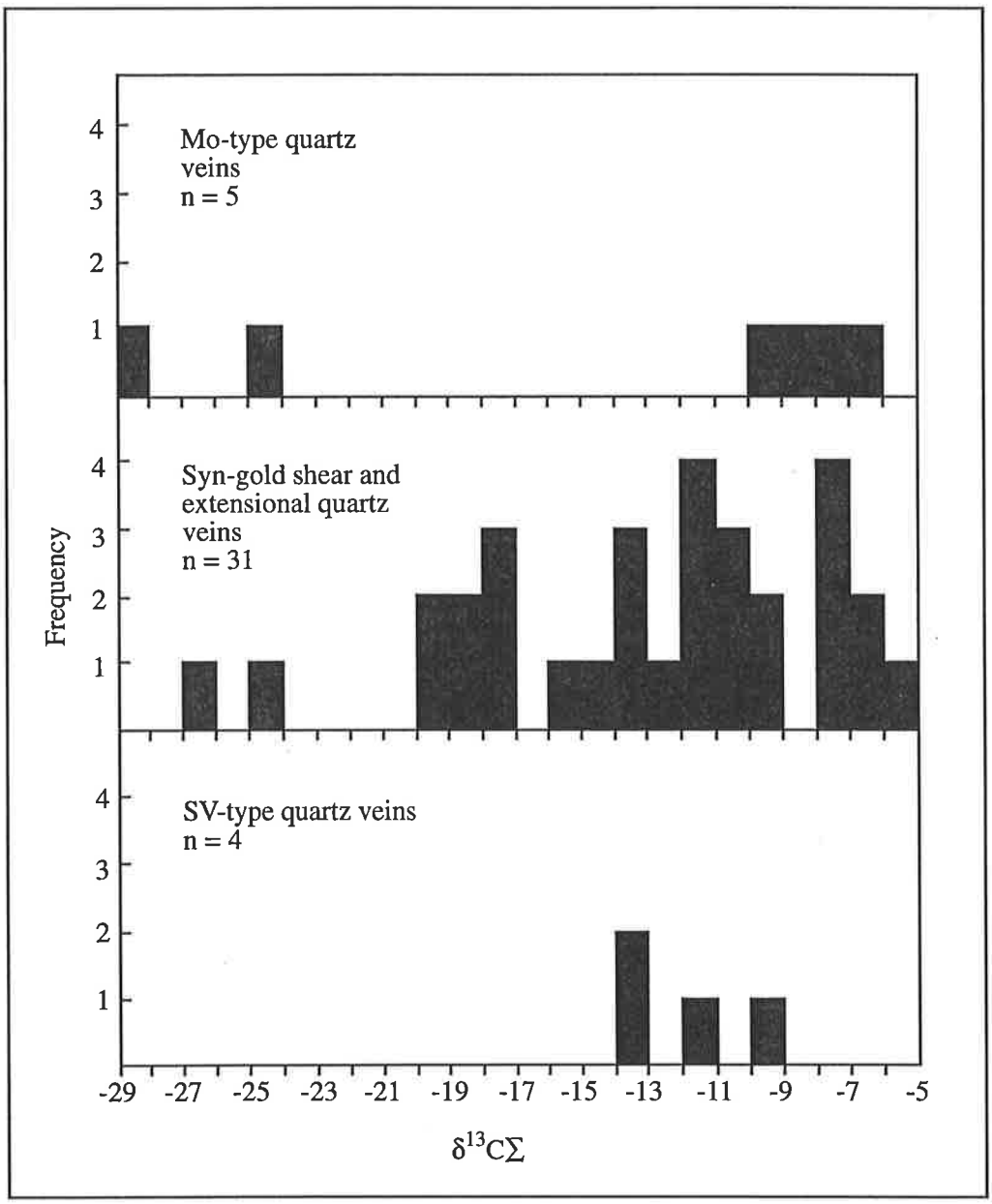


Figure 13.1. Compilation of $\delta^{13}C\Sigma$ values for Mo-type, syn-gold type and SV-type carbonic fluid (CO_2 and CH_4) extracted from quartz veins by combustion in an elemental analyser and determined by mass spectrometry.

EA-MS values ($\delta^{13}C\Sigma$), estimated CO_2 and CH_4 volumes, corresponding CH_4 volumes calculated from GC-MS data and Raman-spectroscopic data

Sample	Sample Type	$\delta^{13}C\Sigma$ ‰	% CO_2	% CH_4	Corresponding % CH_4 volumes determined by GC-MS	Corresponding % CH_4 volumes determined by laser-Raman
1074-64	Mo-type	-24.3	1	99	—	48.0
1074-66	Mo-type	-9.4	71	29	—	—
1074-252a	Mo-type	-28.2	0.0	100	3.0	—
1074-283	Mo-type	-7.8	81.5	18.5	3.0	—
1074-284	Mo-type	-8.2	76.5	23.5	39.0	—
1074-286	Mo-type	-6.7	85	15	41.0	—
1074-41	Syn-gold BCZ	-26.7	00.0	100	6.0	—
1074-43	Syn-gold BCZ	-17.7	35	65	5.0	9.3
1074-74	Syn-gold BCZ	-24.5	1	99	—	—
1074-76	Syn-gold BCZ	-7.8	85.5	14.5	—	—
1074-84	Syn-gold BCZ	-9.5	77	23	13.0	2.2
1074-94	Syn-gold BCZ	-11.9	65	35	—	—
1074-97	Syn-gold BCZ	-10.5	72	28	—	—
1074-99	Syn-gold BCZ	-10.5	72	28	12.0	—
1074-105	Syn-gold BCZ	-7.2	88.5	11.5	—	1.2
1074-110	Syn-gold BCZ	-10.3	73	27	—	—
1074-111	Syn-gold BCZ	-6.3	93	7	1.0	—
1074-114	Syn-gold BCZ	-9.1	79	21	—	—
1074-119	Syn-gold BCZ	-6.0	94.5	5.5	—	—
1074-134	Syn-gold BCZ	-14.0	54.5	45.5	—	—
1074-141	Syn-gold BCZ	-11.8	65.5	34.5	—	—
1074-149	Syn-gold BCZ	-12.1	64	46	2.0	—
1074-215	Syn-gold BCZ	-18.3	33	67	—	—
1074-220	Syn-gold BCZ	-7.4	87.5	12.5	—	—
1074-224	Syn-gold BCZ	-17.6	35.5	64.5	—	—
1074-226	Syn-gold BCZ	-15.1	49	51	—	—
1074-227	Syn-gold BCZ	-14.4	52.5	47.5	—	—
1074-229	Syn-gold BCZ	-18.6	31.5	68.5	71.0	36.5
1074-236	Syn-gold BCZ	-11.2	68.5	31.5	—	0.0
1074-240	Syn-gold BCZ	-11.5	67	33	—	0.6
1074-241	Syn-gold BCZ	-7.9	85	15	—	—
1074-248	Syn-gold BCZ	-13.5	57	43	—	0.0
1074-251	Syn-gold BCZ	-17.1	38	62	—	0.6
1074-252	Syn-gold BCZ	-19.5	27	73	—	—
1074-253	Syn-gold BCZ	-13.1	59	41	—	—
1074-279	Syn-gold BCZ	-6.9	90	10	—	—
1074-282	Syn-gold BCZ	-19.9	25	75	—	—
1074-212	Syn-gold PCZ/DCZ	-13.0	59.5	40.5	4.0	—
1074-233	Syn-gold PCZ/DCZ	-12.3	63	37	—	—
1074-245	Syn-gold PCZ/DCZ	-5.6	96.5	3.5	5.0	—
1074-257	Syn-gold PCZ/DCZ	-15.7	45	55	—	—
1074-77	SV-type	-13.7	67.5	32.5	—	—
1074-93	SV-type	-13.7	67.5	32.5	10.0	33.4
1074-130	SV-type	-9.8	83	17	—	—
1074-136	SV-type	-12.0	74	26	1.0	0.0

Table 13.1. EA-MS values ($\delta^{13}C\Sigma$) together with the estimated CO_2 and CH_4 volumes calculated using Equation 13.1 and the appropriate fractionation factors for CO_2 and CH_4 at different temperatures. Corresponding CH_4 volumes in % are calculated from GC-MS data and Equation 12.1, Chapter 12 and Raman-spectroscopic data, Chapter 6.

13.3.2 EA-MS analyses on syn-gold quartz veins

The EA-MS on syn-gold quartz chips from the BCZ have $\delta^{13}C\Sigma$ values of between -6.0‰ and -26.7‰ (mean = -13.2‰, standard deviation = 5.2‰, n = 31; Table 13.1, Figure 13.1). The four PCZ-DCZ quartz vein samples have $\delta^{13}C\Sigma$ values that range from -5.6‰ to -15.7‰ (mean = -11.7‰, standard deviation = 3.7‰, n = 4; Table 13.1, Figure 13.1).

13.3.3 EA-MS analyses on post-gold SV-type quartz veins

The EA-MS on the post-gold, SV-type quartz chips have $\delta^{13}C\Sigma$ values that range from -9.8‰ to -13.7‰ PDB (mean = -12.3‰, standard deviation = 1.6‰, n = 4; Table 13.1, Figure 13.1).

13.3.4 Calculation of CO_2 and CH_4 ratios from the EA-MS $\delta^{13}C\Sigma$ values

The $\delta^{13}C$ values for calcite collected from the mineralised BCZ show that the CO_2-rich parent fluid had a $\delta^{13}C$ value near -4.4‰ (Chapter 10). The EA-MS analyses of the carbonic fluids within the fluid inclusions in the quartz veins were much lower than -4.4‰ (the mean $\delta^{13}C\Sigma$ values of the BCZ quartz veins is -13.2‰), suggesting that another carbonic species must be present (possibly CH_4 and/or CO). Raman-spectroscopy, GC-MS and fluid inclusion microthermometry indicate that methane is the likely source for the lower $\delta^{13}C\Sigma$ values obtained.

Mass balance calculations use Equation 13.1 to determine the respective volumes of CO_2 and CH_4 present in a sample. Equation 13.1 incorporates known $\delta^{13}C$ values for CO_2 (determined from calcite-CO_2 fractionation factors) and the fractionation factor between CO_2 and CH_4 at a given temperature (determined by either fluid inclusion microthermometry or stable isotope geothermometry):

$$\delta^{13}C\Sigma = X(CO_2) \,.\, \delta^{13}C\,(CO_2) \quad + \quad X(CH_4) \,.\, \delta^{13}C(CH_4\{CO_2 + CO_2\text{-}CH_4 \text{ fractionation @ a pre-determined T°C}\}) \qquad \text{(Equation 13.1)}$$

where $\delta^{13}C\Sigma$ is determined by EA-MS, $X(CO_2)$ and $X(CH_4)$ are the volumes of CO_2 and CH_4 present in the sample and $\delta^{13}C\,(CO_2)$ and $\delta^{13}C\,(CH_4)$ are the isotopic values for CO_2 and CH_4 respectively.

Given that the $\delta^{13}C$ value of the parent CO_2 responsible for depositing carbonate in the BCZ at approximately 385±35°C is -4.4‰, the $\delta^{13}C$ value of co-existing CH_4 is -24.4‰ (fractionation factor between CO_2 and CH_4 at 385°C equalling ca. 20‰ [Kyser, 1987]), thus, when $\delta^{13}C\Sigma$ = -13.2‰:-

$$-13.2 = X(CO_2) \; . \; (-4.9) \; + \; X(CH_4) \; . \; (-4.9 + -20)$$

then $$-13.2 = X(CO_2) \; . \; (-4.9) \; + \; X(CH_4) \; . \; (-24.9)$$

which gives $X(CO_2) = 58.5\%$ and

$$X(CH_4) = 41.5\%$$

Applying equation 13.1 to the two $\delta^{13}C\Sigma$ end members obtained from quartz chips sampled from the syn-gold quartz veins by EA-MS, gives CH_4 volumes that range from 4.5% ($\delta^{13}C$ = -5.6 ‰) to 100% ($\delta^{13}C$ = -26.7 ‰) relative to CO_2 in the same sample (Table 13.1). Thus, $\delta^{13}C\Sigma$ values determined by EA-MS that fall between these two end members represent a mix of CO_2 - CH_4 (Figure 13.2).

The fractionation factor between CO_2 and CH_4 in the Mo-type quartz veins and the SV-type quartz veins is different to the fractionation factor used for the syn-gold quartz veins because fluid inclusion homogenisation temperatures and isotope geothermometry indicate that these vein types formed at 340°C and 300±25°C respectively. Therefore, the fractionation factor for CO_2 and CH_4 at 340°C is 21‰ and at 300°C is 25‰ (Kyser, 1987). Application of Equation 13.1 to the $\delta^{13}C\Sigma$ values obtained from the six Mo-type quartz veins gives CH_4 volumes that range from 15% to 100% relative to CO_2 (based on a parent fluid $\delta^{13}C$ CO_2 value of -3.5‰), whereas the four SV-type quartz veins analysed give CH_4 volumes that range from 17% to 32.5% relative to CO_2 (based on a parent fluid $\delta^{13}C$ CO_2 value of -5.5‰).

13.4 Discussion

Many of the values obtained are significantly lighter than expected if the only carbon source in the ore forming fluid was CO_2. Table 13.1 shows that the volume of CH_4 estimated to be present in most samples analysed by EA-MS is much higher than the volumes determined by Raman-spectroscopy and gas chromatography. Raman-spectroscopy indicates that a few fluid inclusions contain up to 100% CH_4 and GC-MS shows that some samples contain up to 91% CH_4. However, the majority of fluid inclusions/samples analysed by these methods contain less than 5% CH_4 with respect to CO_2 (i.e. CO_2 = 95+%). Further to this, Raman-spectroscopy and EDTA-GC analysis show that samples that do contain high levels of CH_4 occur at the edge of the quartz vein - host-rock contact where the wall rock alteration is the most intense.

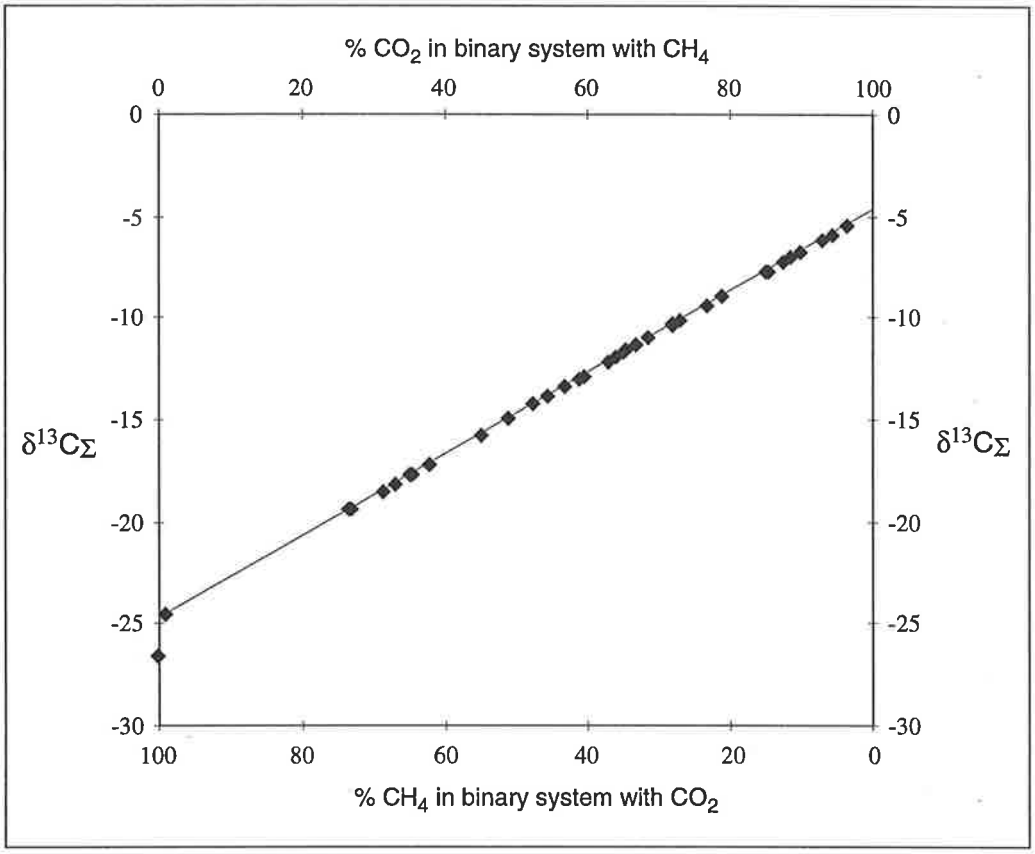


Figure 13.2. The $\delta^{13}C\Sigma$ values determined by EA-MS (Table 13.1) for syn-gold samples plotted along the equilibrium curve for CO_2 and CH_4 assuming mineralisation occurred at 385°C. The fractionation factor between CO_2 and CH_4 at this temperature is ca. 20‰. The $\delta^{13}C$ value calculated for the CO_2 in the parent fluid is 4.4‰ (Chapter 10). This value governs the positioning of the equilibrium curve on the graph. The relative volume of CO_2 and CH_4 in each sample analysed by EA-MS can be read directly from the graph according to the position that each samples' value plots along the equilibrium curve.

The EA-MS $\delta^{13}C\Sigma$ values indicate that most of the samples analysed either contain high levels of CH_4, or sample contamination by another carbon source that has a very light $\delta^{13}C$ value has occurred. Mapping of underground drives (Figures 3.3a, 3.3b and 3.4, Chapter 3) and re-evaluation of drill hole logs shows that not all samples collected came from the edge of a quartz vein where CH_4 values are known to be highest. Further to this, comparisons made between data collected from samples that were analysed by EA-MS, GC-MS and Raman-spectroscopy show the estimated volume of CH_4 present in a quartz vein analysed by EA-MS is higher than levels of CH_4 detected by GC-MS or Raman spectroscopy. Contamination by late secondary fluid inclusions is unlikely as fluid inclusion microthermometry and Raman-spectroscopy show that no CO_2 or CH_4 is present in these fluid inclusions.

Miller and Pillinger (1997) present data showing that instantaneous heat decrepitation (or single step heat extraction) of fluid inclusion gases from quartz at ca. 600°C is characterised by CO_2 having a $\delta^{13}C$ value around -25‰. Further to this, Miller and Pillinger (1997) found that the $\delta^{13}C$ value of CO_2 became more negative as the volume of the quartz sample was reduced. The

low $\delta^{13}C$ value was neither attributed to the fluid inclusion CO_2, nor to CO_2 released from an empty extraction tube (i.e. the system blank). Miller and Pillinger (1997) and Mattey *et al.* (1989), suggest that thermal degradation of surficial organic contamination of unknown origin is the most probable source for the low $\delta^{13}C$ values.

Miller and Pillinger (1997) recommend the multiple-stepped heat extraction technique of fluid inclusion gases in order to obtain greater accuracy for the $\delta^{13}C$ value of the fluid inclusion CO_2. These authors found that the use of the multiple-stepped heat extraction technique up to 300°C removes the surficial contaminants with their low $\delta^{13}C$ values, resulting in the CO_2 released above 300°C having a significantly heavier $\delta^{13}C$ value that is a more accurate value for the fluid inclusion CO_2. The work of Miller and Pillinger (1997) suggests that the single-step, instantaneous combustion technique used for small quartz samples at 1600°C during EA-MS analysis is the likely explanation for the consistently low $\delta^{13}C\Sigma$ values obtained from Junction samples.

Great care was taken to remove all surface contamination. Notwithstanding, organic mass spectrometry coupled with gas chromatography (Chapter 8), detected low levels of extraneous synthetic hydrocarbons in all samples analysed. The most common of the acyclic and cyclic hydrocarbons detected (dodecanol, cyclododecanol, heptadecyne, hydroxybiphenyl and butylated hydroxytoluene) are used to manufacture plasticisers, resins, detergents and light oils commonly used in lubricants explosives and drilling fluids (Kroschwitz, 1996). Therefore it is likely that these hydrocarbons were blasted or forced into the rock during mine-related rock blasting or during drilling with high pressure fluids. This carbon source was not isotopically analysed. However, organic hydrocarbons with similar mass weights typically have light $\delta^{13}C$ values (ca. -20‰ to -35‰) (Faure, 1986) and their presence adequately explains the $\delta^{13}C\Sigma$ values obtained by EA-MS analysis.

That the extraneous hydrocarbon contamination was still not removed during routine sample preparation, even though this included washing the crushed sample in aqua-rega acid, hydrofluoric acid and acetone and ultrasonic bathing in deionised water before drying in an oven at 75°C, indicates that heat-removal of these hydrocarbons (cf., Miller and Pillinger, 1997) may be the only option available when trying to obtain a reliable data set. The detection of these hydrocarbons in every sample analysed by organic mass spectrometry - gas chromatography suggests that all samples collected from Junction are contaminated. Therefore the reliability of the results obtained from EA-MS is in question. It is unlikely that some of the CH_4 volumes indicated by EA-MS analyses could go undetected by both Raman-spectroscopy and GC-MS. Therefore, even though EA-MS is obviously a powerful analytical tool, the discovery of a serious contamination source does undermine the usefulness of the EA-MS results. Therefore, all EA-MS results need to be considered with caution.

Miller and Pillinger (1997) report that mechanical crushing has the advantage that gas release

from sources other than fluid inclusions are minimal. Thus, results obtained during GC-MS analysis and off-line crushing and CO_2 trapping by cryogenic traps are not suspected to be contaminated.

CHAPTER FOURTEEN

Origin of CH_4 in the Junction gold deposit

14.1 Introduction: what are the currently proposed origins for the light hydrocarbons?

CO_2, CH_4, other light hydrocarbons ($C_nH_{[2n+2]}$), CO, H_2S and N_2 are commonly reported gases present in fluid inclusions associated with late-orogenic, structurally-controlled gold mineralisation (Roedder, 1984; Wood *et al.*, 1986a and 1986b; Ho *et al.*, 1990a and 1990b; Bray and Spooner, 1991; Graney and Kesler, 1995; Mernagh and Witt, 1994). CO_2 is the dominant gas species trapped in fluid inclusions, while CH_4, CO, H_2S and N_2 are usually at much lower and variable concentrations in this deposit style. This observation is true for fluid inclusions at Junction, where Raman-spectroscopy, gas chromatography and fluid inclusion microthermometry show that fluid inclusions hosted in shear and extensional veins are dominated by CO_2, and lower, but variable concentrations of CH_4.

Significantly, microthermometry and Raman-spectroscopy (Chapters 5 and 6) indicate that CH_4 concentrations in fluid inclusions (with respect to CO_2), are erratic from one fluid inclusion to another (regularly above 10 mol. % CH_4). However, the CH_4 content of a given fluid inclusion population within a single quartz vein rarely exceeds 5 mol. % with respect to CO_2. However, quartz-hosted fluid inclusions containing anomalously high CH_4 concentrations are regularly encountered at, or near, the quartz vein - host rock contact where carbonate, chlorite and albite alteration is most intense (Chapter 6). Further to this, EDTA-gas chromatography indicates that calcite found near the quartz vein - host rock contact contains up to 8067 μg CH_4 and 52 μg C_2H_6 per gm of carbonate (Chapter 7). This suggests that other alteration minerals near the quartz vein - host rock contact (e.g. feldspars, scheelite and sulphides) may also trap a considerable portion of the the deposit's CH_4 budget.

CH_4 accumulation near the quartz vein - host rock contact is possibly a result of fluid immiscibility (cf. Boullier and Robert, 1992; Robert *et al.*, 1995). Indeed, Naden and Shepherd (1989), present results from fluid unmixing experiments to show that CH_4 has a large immiscibility field which is responsible for the development of CO_2 and CH_4-rich fluid inclusions. In fact, only small (<5 mol. %) amounts of CH_4 are soluble in aqueous brines up to 3 kbars and 400°C, whereas

significantly more CO_2 (up to 15 mol. %) is soluble under the same conditions (Naden and Sheppherd, 1989).

The large field of CH_4 fluid immiscibility indicates that CH_4-rich fluid inclusions will form during fluid unmixing initiated by relatively low concentrations of CH_4 as the fluid approaches 400°C and 3 kbars. The restricted solubility of CH_4 in an aqueous brine suggests that very little fluid-wall rock interaction is required to initiate fluid unmixing (Naden and Shepherd, 1989). The relative solubility of CO_2 is much higher than CH_4 at elevated temperatures and pressures. Therefore, the extent of the reaction needed to initiate unmixing of CO_2 is that much greater (Naden and Sheppherd, 1989). Given these parameters, late-orogenic, structurally-controlled gold deposits that formed below 400°C and 3 kbars, could not have transported more than 5 mol. % CH_4 to the site of deposition. Thus, the presence of CH_4-rich fluid inclusions at Junction, indicate either very efficient fluid unmixing, or the production of CH_4 at the site of mineralisation during fluid-wall rock reactions.

If fluid unmixing is the suspected mechanism responsible for CH_4-rich fluid inclusions at Junction, CH_4-rich fluid inclusions should be detected across the entire width of the quartz vein. That Raman-spectroscopy only detected CH_4-rich fluid inclusions near the quartz vein - wall rock interface suggests that the CH_4-rich fluid inclusions were not produced by fluid unmixing of the ore transporting fluid. Instead, it is likely that the CH_4 was produced during fluid - wall rock reactions involving a CO_2-rich fluid and H_2 derived from a number of sources including H_2O and the $Au(HS)_2^-$ (or $HAu[HS]_2$) complex. These are both commonly cited components of late-orogenic, structurally-controlled gold ore fluids (Seward, 1973; Neall and Phillips, 1987; Naden and Shepherd, 1989; Seward and Barnes, 1997).

The origin of CH_4 in non-sedimentary metallic ore deposits is generally attributed to the thermal maturation of organic matter - kerogen, hydrogenation of graphite, or more commonly, degassing of hydrocarbons from the mantle (Hunt, 1979; Giggenbach, 1982; Tissot and Welte, 1984; Gold, 1984; Roedder, 1984; Arnorsson and Gunnlaugsson, 1985; Capaccioni *et al.*, 1995). Welhan (1988) announces that the principle sources of CH_4 in hydrothermal fluids are:

- thermal breakdown of complex hydrocarbons at moderate to high temperature (>100°C) (biogenic source),
- biological production, principally by bacteria at low (< 200°C) temperatures (biogenic source),
- outgassing of juvenile carbon as CH_4, similar to that of juvenile He, via high-temperature hydrothermal systems (abiogenic source) and/or,

- inorganic synthesis in reactions at high temperatures (>300 °C), involving CO_2 and H_2 or other C-H molecules which maybe derived from various sources (abiogenic source).

Abiogenesis is not the favoured origin for CH_4 found in hydrothermal systems. Many workers favour an organic origin for CH_4 and other $C_nH_{(2n+2)}$ hydrocarbons in hydrothermal fluids (Giggenbach, 1982; Roedder, 1984; Arnorsson and Gunnlaugsson, 1985; Capaccioni *et al.*, 1995). These authors suggest that thermogenically produced CH_4 detected in hydrothermal fluids formed as the hydrothermal fluid passed through continental crust consisting of multiple rock types, including sequences of sedimentary material containing organic matter, kerogen, or graphite.

Organic matter, including graphite is not known to occur in the Junction Gabbro, nor is it found in the alteration assemblage of the JSZ. Its absence precludes hydrocarbons forming as a result of hydrogenation of elemental carbon. However, graphite is known to occur in the metasedimentary formations of the Black Flag Group. The Black Flag Group is the volcaniclastic sedimentary sequence of rock that hosts the Junction Gabbro. It is possible that CH_4 was produced in the Black Flag Group metasediments during the ascension of a gold-bearing hydrothermal fluid. However, given the immiscible nature of CH_4 in hydrothermal fluids (c.f. Naden and Shepherd, 1989), it is unlikely that any CH_4 which may have formed in the Black Flag Group metasediments travelled through to the Junction Gabbro before unmixing occurred. Instead, CH_4 produced in the Black Flag Group metasediments would have unmixed almost immediately, possibly resulting in the precipitation of some gold at or near the graphite bearing metasediments. Further to this, the zonation of gases in the quartz veins cannot be explained by the external generation of CH_4 relative to the Junction Gabbro.

Abiogenesis is suspected as the principle source of CH_4 in high temperature volcanic rock-dominated mid-ocean ridge (MOR) systems (Welhan, 1988). Indeed, research in MOR systems (Welhan and Craig, 1979; Cheminee *et al.*, 1991; German *et al.*, 1994; Ishibashi *et al.*, 1994) has shown that CH_4 and other $C_nH_{(2n+2)}$ hydrocarbons are always present at variable concentrations in these sediment-free environments. Welhan (1988) and Ishibashi *et al.* (1994) found that MOR CH_4 has an unusually heavy isotopic signature ($\delta^{13}C$ range -20‰ to -1‰ [PDB]), indicative of an inorganic origin. Thermogenically produced CH_4 generally has a $\delta^{13}C$ value < -25‰ and bacterially produced CH_4 is mostly < -60‰ (PDB) (Ohmoto and Goldhaber, 1997). The distinction that CH_4 can be produced abiogenically is significant when evaluating ore systems such as that at Junction where CH_4 is thought to have evolved in situ during wall rock alteration.

The ubiquitous existence of CH_4, H_2 and other $C_nH_{(2n+2)}$ hydrocarbons in hydrothermal fluids, usually dominated by the gases, CO_2 and H_2S (both typically comprise 90 - 99% of the total dissolved gas), have led to suggestions that gas-gas and gas-mineral reactions are responsible for the presence of these light hydrocarbons (Petersilie, 1963, 1970; Konnerup-Madsen *et al.*,

1979; Konnerup-Madsen, 1988; Welhan, 1988; Salvi and Williams-Jones, 1992, 1997). These workers propose that large volumes of CH_4 result from the interaction of CO_2 reacting with H_2 formed during mineral alteration processes in an iron-oxide-catalysed Fischer-Tropsch type synthesis reaction.

14.2 CH_4 formation by Fischer-Tropsch synthesis

It is proposed that most of the CH_4 found in the Junction deposit formed by Fischer-Tropsch type synthesis (FTTS) reactions. FTTS is an industrial process where petroleum is produced from carbon monoxide or carbon dioxide and hydrogen gases reacting on a metallic iron or iron-oxide catalyst (Szatmari, 1989). The process is used at an industrial scale to make synthetic hydrocarbon oils.

Early workers (Robinson, 1963; Friedel and Sharkey, 1963) applied the reactions of FTTS to the generation of large oil reserves. However, FTTS has since been suspected in natural but inorganic geological samples to explain phenomena such as the presence of aliphatic hydrocarbons in the Orguel and Murray carbonaceous chondrite meteorites (Studier *et al.*, 1968, 1972), carboxylic acids, hydrocarbons and amino acids found in the Murchison meteorite (Reisse and Mullie, 1993), and CH_4 through to alkanes in silica-undersaturated alkalic igneous systems and peralkaline granites (Konnerup-Madsen, 1988; Salvi and Williams-Jones, 1992, 1997).

The basic reaction in FTTS is the highly exothermic hydrogenation of CO and the slightly endothermic hydrogenation of CO_2 (Anderson, 1984; Roper, 1983; Szatmari, 1989). The formation of CH_4 from CO_2 is a two step process. CO must be formed first and is then hydrogenated to CH_4 and other hydrocarbons (Weatherbee and Bartholomew, 1984). FTTS involves breaking the carbon - oxygen bond, and replacing the oxygen with a carbon-carbon carbon bond or a carbon-hydrogen bond (Szatmari, 1989). The catalyst needed for this reaction is a Group VIII metal (iron, cobalt, nickel, ruthenium, rhodinium, palladium, osmium, iridium, platinum) in its native or oxide form (Madon and Taylor, 1981; Roper, 1983; Anderson, 1984; Salvi & Williams-Jones, 1997). Fischer-Tropsch type synthesis reactions could occur naturally in the presence of wustite or magnetite (Anderson, 1984).

Reisse and Mullie (1993) propose that Fischer-Tropsch type synthesis may start from two

precursors, C and C^+, and suggest the following series of reactions to explain the presence of carboxylic acids, hydrocarbons and amino acids that are found in the Murchison meteorite that fell to earth in 1969:

$C^+ + H_2$ -------> $CH_2^+ + hv$ (Equation 14.1)

$C + H_3^+$ -------> $CH^+ + H_2$ (Equation 14.2)

$CH^+ + H_2$ -------> $CH_2^+ + H$ (Equation 14.3)

$CH_2^+ + H_2$ -------> $CH_3^+ + H$ (Equation 14.4)

$CH_3^+ + H_2$ -------> $CH5^+ + hv$ (Equation 14.5)

$CH_3^+ + e$ -------> $CH_2 + H$ (Equation 14.6)

$CH_3^+ + e$ -------> $CH^+ H_2$ (Equation 14.7)

$CH_5^+ + e$ -------> $CH_4 + H$ (Equation 14.8)

$C^+ + CH_4$ -------> $C_2H_3^+ + H$ (Equation 14.9)

$CH_3^+ + CH_4$ -------> $C_2H_5^+ + H_2$ (Equation 14.10)

Salvi and Williams-Jones (1997) simplify the reactions, and propose that CH_4 and other light hydrocarbons found in silica-undersaturated alkalic igneous systems and peralkaline granites are produced when hydrothermal fluids interact with a Group VIII metal in its native or oxide form by the disequilibrium reactions:

$$nCO + (2n + 1)H_2 = C_nH_{(2n+2)} + H_20 \quad \text{(Equation 14.11)}$$

$$nCO_2 + (3n + 1)H_2 = C_nH_{(2n+2)} + H_20 \quad \text{(Equation 14.12)}$$

Whilst hydrocarbon chains may form and result in complex hydrocarbons mixtures (Anderson, 1984; Szatmari, 1989; Reisse and Mullie 1993), lighter hydrocarbons, (particularly CH_4) are favoured in higher temperature (≥400°C) environments (Anderson, 1984; Salvi and Williams-Jones, 1997). Therefore, CH_4 is usually the most abundant hydrocarbon in number, but not necessarily in volume weight (Statterfield and Huff, 1982; Szatmari, 1989). These findings are supported by Salvi and Williams-Jones (1997), who found that the Strange Lake pegmatites contained low C_2H_6:CH_4 ratios.

14.3 Application of FTTS to the Junction fluids

Fischer-Tropsch type synthesis is the probable mechanism for the presence of CH_4 and trace ethane volumes detected in fluid inclusions (Raman-spectroscopy) and carbonates (EDTA-GC analysis) found in most samples collected from the biotite-carbonate-zone of the Junction deposit. Geological and geochemical data show that the Junction Shear Zone was primed for hydrocarbon generation by Fischer-Tropsch type synthesis during the mineralisation process.

Fluid inclusion homogenisation temperatures, petrological - SEM investigations and oxygen

stable isotope studies show that gold deposition at Junction formed in the 350°C - 410°C range in the titanomagnetite-ilmenite dominated zones of the Junction Gabbro. It is proposed that the introduction of a hot, reduced ore fluid (cf., Phillips and Groves, 1984; Groves *et al.*, 1984; Neall and Phillips, 1987; Colvine *et al.*, 1988; Kerrich, 1989; Naden and Shepherd, 1989; Seward and Barnes, 1997) resulted in a lowering of the fO_2 to levels at or just below the QFM buffer at the site of mineralisation (Chapter 3.5.3.1). The fO_2 values estimated for the BCZ indicate that mineralisation occurred at or just below the CO_2:CH_4 boundary (fO_2 = 10-31 at 350°C and 2 kbars [Mikucki and Ridley, 1983; Witt *et al.*, 1997]), thus promoting CH_4 and ethane generation. This hypothesis supports the observation that CH_4 is concentrated at the edges of the quartz veins where fluid access to iron-oxide bearing gabbro was greatest. Lesser access to the gabbro by the hydrothermal fluids resulted in negligible CH_4 being generated and trapped toward the centre of the quartz veins.

CHAPTER FIFTEEN

Summary of the main findings and general discussion

15.1 The main findings

The results from this project show that soil-gas anomalies involving CO_2-O_2 and light hydrocarbons exist above the mineralised N75 surface at Junction. Further to this, investigations found that these anomalies are sourced directly from the mineralisation itself. Thus, the relationship between the gas composition detected in the soil-atmosphere and the gas composition associated with gold mineralisation has been established. The important results acquired from each analytical technique used to uncover these characteristics are discussed at the end of each chapter. Thus, only a few of the important interpretations are reiterated here in a summarised version.

15.1.1 The soil-gas anomalies

CO_2-O_2 anomalies detectable by active sampling methods above the N75 surface provide a clear indication that the narrow, sulphide-carbonate bearing shear zone is oxidising at depth and can be located from the surface. However, CO_2 is the commonest gas component associated with decomposing carbonates. Thus, the CO_2-O_2 anomalies only indicate that carbonate is dissolving to release CO_2 and consume O_2. The detection of light hydrocarbon gas anomalies by passive samplers that are co-incident with the CO_2-O_2 anomalies above both of the traverses, indicate that hydrocarbons are the "finger print-type" characteristic that have the potential to differentiate between a soil-gas anomaly associated with unmineralised, but oxidising carbonates and a soil-gas anomaly that originates from oxidising carbonates associated with gold mineralisation.

The detection of co-incidental CO_2 and light hydrocarbon anomalies are strong advocates against the possibility that the anomalies are simply the result of microbiological activity in the soil or in the shear zone. Firstly, methanotrophic and methanogenic bacteria cannot productively co-exist in the same environment given their respective sensitivities to oxygen (or the lack thereof), and secondly, it is unlikely that ethane, and impossible that C_3^+ hydrocarbons are produced by bacteria.

The detection of the aromatic >> aliphatic hydrocarbons adsorbed on to soil particles (occluded hydrocarbons) above the N75 surface do not support the CO_2 - light hydrocarbon anomalies.

Indeed, occluded hydrocarbon anomalies along both traverses are off-set both up and down dip from the CO_2 - light hydrocarbon anomalies. This inconsistency fails to enhance the use of occluded hydrocarbons as a detection vector for late-orogenic, structurally-controlled gold deposits. The identification of synthetic hydrocarbons in the currently mined N25 surface (Chapter 8) cannot be directly linked to the predominantly aromatic hydrocarbons detected in the soil above the N75 surface approximately 400 metres east of the N25 surface. This is primarily because a precise identification of the soil occluded aromatic hydrocarbons is not known (see Chapters 4 and 8 for discussion). However, it cannot be assumed that all of the aromatic hydrocarbons detected above the N75 surface are indigenous to the soil, or indeed related to alteration associated with gold mineralisation.

The light hydrocarbons detected in the soil above the N75 surface are indeed a potential "finger print-type" characteristic that would make soil-gas detection technique a viable exploration tool for late-orogenic structurally-controlled gold deposits. However, the source of these light hydrocarbons must be linked to the ore deposit itself. Investigations into the geology of the ore deposit show that the light hydrocarbons do originate from the oxidising ore body.

15.1.2 The light hydrocarbon gas - gold relationship

Fluid inclusion investigations using microthermometry, Raman spectroscopy and gas-chromatography show that CH_4 and trace amounts of ethane are present in the fluid inclusions associated with gold mineralisation at Junction. Microthermometric analysis indicates that many fluid inclusions have a $TmCO_2$ below that of the CO_2 invariant point, thus indicating the presence of CH_4. However, microthermometry does not indicate that CH_4 was a major component in the ore forming system. On average, most fluid inclusions analysed by microthermometry contain less than 1 mol. % CH_4 relative to the H_2O-CO_2-CH_4-NaCl system. Experimental calculations by Zhang and Frantz (1992) indicate that the $TmCO_2$ values obtained from fluid inclusions at Junction infer that most fluid inclusions contained <5.5 mol. % CH_4. This concentration is supported by calculations made using the MacFlinCor software of Brown and Hagemann (1995) which estimates that CH_4 volumes in individual fluid inclusions range from 0.00 to 0.19 mol. % CH_4 relative to CO_2. Further to this, Raman spectroscopy shows that the majority of fluid inclusions analysed contain < 2 mol. % CH_4 relative to CO_2 in the vapour phase.

Significantly, Raman spectroscopy reveals that some fluid inclusions in the syn-gold quartz veins at Junction are CH_4-rich, containing up to 100 mol. % CH_4 in the vapour phase relative to CO_2. Notably, Raman spectroscopy indicates that CH_4 is zoned within the quartz veins, with the highest concentrations of CH_4 detected at the edge of the quartz vein - host rock contact within the biotite-carbonate zone (BCZ). This observation has not previously been reported in veins from this style of mineralisation and indicates that CH_4 probably formed insitu as a result of CO_2 interacting with an Fe-rich rock in a Fischer Tropsch-type synthesis reaction.

Thin section petrography clearly indicates that the calcite and albite found at the edge of these quartz veins contain numerous fluid inclusions that probably trapped similar concentrations of CH_4 to that detected by Raman spectroscopy in adjacent quartz grains. This hypothesis is supported by EDTA-GC results which found that the calcite that formed at the edge of the quartz veins in the BCZ contains high levels of CH_4 and trace amounts of ethane. Other light hydrocarbons (C3+) were not detected by this method, possibly because of the high detection limits used, but work by Graney and Kesler (1995) and Bray and Spooner (1992) indicate that such hydrocarbons do exist in trace amounts in late-orogenic, structurally-controlled gold deposits in Canada. The EDTA-GC results have identified the best primary source for the CH_4 detectable in soil above the ore deposit. That the CH_4 and trace ethane is predominantly found in the minerals associated with the alteration assemblage containing the highest gold grades suggests that light hydrocarbon anomalies detected in soil should only be found above mineralised shear zones that have a similar alteration assemblage to that of Junction.

The $\delta^{18}O$ values determined for co-existing calcite and quartz indicate that the quartz and calcite are still in isotopic equilibrium with each other. This supports the fact that the calcite analysed by the EDTA-GC technique was contemporaneous with the adjacent quartz veins. This finding is confirmed by CL microscopy. CL investigations show that the calcite was fractured and deformed during brittle-ductile deformation associated with the shearing and gold deposition event. However, the later Fe-depleted calcite that rims and fills the voids between the fractured calcite precipitated during the following fluid pulse into the shear zone, and not during a much later fluid event. Thus, the CH_4-rich fluid inclusions that were found to exist in the calcite adjacent to the quartz veins must have been trapped at the same time as the precipitation of the adjacent quartz veins during the deposition of gold in the Junction deposit.

Significantly, it is conceivable that the volume of CH_4 in the calcite-hosted fluid inclusions is only a fraction of the total CH_4 budget likely to be present in the Junction ore body, given that other adjacent, non-quartz minerals (e.g. albite, sulphides and scheelite) are likely to contain similar volumes of hydrocarbons. The abundance of CH_4 in these minerals that are most susceptible to weathering (carbonates, feldspars and sulphides) indicate that continuous emission of light hydrocarbons to the surface should occur so long as the ore deposit is oxidising and these minerals are being broken down.

Further to the findings by microthermometry, Raman spectroscopy and EDTA-GC analyses, stable isotope investigations of the carbonates and fluid inclusion gases support the fact that CH_4 is present in the deposit now, and was probably formed insitu as gold deposition occurred. The $\delta^{13}C$ values of the calcite provided the opportunity to calculate the original $\delta^{13}C$ value of the parent CO_2 that formed part of the hydrothermal fluid and the $\delta^{13}C$ values were used to constrain the parent hydrothermal fluid to known fluid reservoirs. However, the range of $\delta^{13}C$(calcite) values that occur across the Junction Shear Zone indicate that Rayleigh isotope

fraction must have occurred as CH_4 was being formed insitu within the BCZ.

The fact that the CO_2 trapped in quartz-hosted fluid inclusions was found to be in disequilibrium with the calculated value for the original parent fluid was significant to this part of the project. This does not unequivocally indicate that the calcite and quartz were deposited from two different fluid sources, but instead, it suggests that another carbon-bearing gas species (i.e. CH_4) was probably trapped in many of the fluid inclusions with the CO_2, and that the two gases have since re-equilibrated over the 2.6 Ga that they have been trapped together. Indeed, gas-chromatography coupled with isotope mass spectrometry show that this is probably the case.

Gas-chromatography coupled with isotope mass spectrometry shows that the $\delta^{13}C$ values of co-existing CO_2 and CH_4 are no longer in isotopic equilibrium. The CO_2 has become isotopically heavier at the same time as the CH_4 has become isotopically lighter. This is the expected outcome in fluid inclusions where the two gases have shared an enclosed environment for almost 2.6 Ga. The results are significant because they challenge previous interpretations by workers who conclude that similar results indicate that the fluid inclusion CO_2 in quartz was deposited by a different fluid source to that which deposited the vein-wall rock calcite. This is a significant break though in the interpretation of stable isotope geochemistry for mineral exploration because quartz veins with CO_2 that is isotopically in disequilibrium with co-existing carbonates may be indicating the presence of CH_4 in the fluid inclusions and as such, the area being investigated may be an excellent prospect for gold ore deposition.

A comparative study between the $\delta^{13}C$ values of the fluid inclusion CH_4 and the $\delta^{13}C$ values of the soil-gas CH_4 was not completed as part of this project. However, future studies in this area may choose to do this. Further to this, it is unfortunate that the EAMS data does not support the gas-chromatography - isotope mass spectrometry results because of a probable contamination by synthetic hydrocarbons that were probably introduced during mining operations at Junction.

The results summarised here do not indisputably link the light hydrocarbons detected in the soil to the hydrocarbons detected in the fluid inclusions hosted in the alteration minerals associated with gold mineralisation, particularly quartz and calcite, although it is highly likely that this is so. However, CH_4 ($\pm C_nH_{(2n+2)}$) is known to also be present in fluid inclusions hosted in Mo-type and SV-type quartz veins, and therefore, these veins are also potential sources for the light hydrocarbons detected in the soil. Nevertheless, it can be concluded that the relative abundance of these veins compared to the volume of veins and the alteration halo associated with the syn-gold mineralisation event preclude the Mo- and SV-type veins from being a genuine source for the soil-gas anomalies that are present. Certainly, the late secondary fluid inclusions which are not associated with any quartz veining event, can be disregarded as a source of the soil-gas anomalies because it has been demonstrated that CO_2 and CH_4 are not present in these fluid

inclusions.

Further to this, the absence of lignite in Cainozoic sediments in the Junction area, and the lack of evidence to support the presence of an active microbiological community preclude both of these media from being the source for the soil-gas hydrocarbon anomaly. Similarly, the occluded hydrocarbons cannot be considered to be an origin for the light hydrocarbon soil-gas anomalies. This is because the two classes of hydrocarbon do not overlap along either traverse as co-incidental anomalies. It would be expected that the two classes of hydrocarbons would form a co-incidental anomalous peak if the light hydrocarbons were sourced from the breakdown of the heavier hydrocarbons.

15.2 Implications of this study

On the basis of the observations summarised above, it can be concluded that the Junction gold deposit is a remarkable test-case that indicates that soil-gas geochemistry is a successful exploration vector in the Kambalda area. The detection of the soil-gas anomaly above the N75 surface has particular significance to the exploration for similar styles of gold mineralisation around Junction, Kambalda, the Yilgarn Craton and beyond. Indeed, Witt (1993) lists a number of layered and differentiated mafic and ultramafic sills in the Menzies to Kambalda area alone that host gold mineralisation similar in style to the mineralisation at Junction. This indicates that soil-gas geochemistry similar to that at Junction should not be restricted to the mafic sills of the Kambalda area. In fact, given that most late-orogenic, structurally-controlled gold deposits on the Yilgarn Craton are hosted in mafic and ultramafic lithologies (Groves *et al.,* 1988, 1990), and most of these have broadly similar alteration assemblages (including fluid inclusion geochemistry) to that at Junction (Phillips and Groves, 1983; Neall and Phillips, 1987; Groves *et al.,* 1988, 1990; Mikucki *et al.*, 1990; Mikucki and Ridley, 1993; Witt *et al.*, 1997), soil-gas geochemistry has application across the entire Yilgarn Craton.

However, there will always be cases where soil-gas geochemistry will not detect all styles of mineralisation, especially if they are not presently oxidising. A non-oxidising ore body will not produce any gas halo at all, and ore deposits that do not contain light hydrocarbons in fluid inclusions hosted by the gangue minerals will not be detected using hydrocarbon detection techniques.

Finally, the results from this project suggest that soil-gas geochemical exploration for late-orogenic, structurally-controlled gold deposits, may be a preferred method for explorers in areas where transported cover and deeply leached bedrock render useless the traditional metal-in-soil trace element geochemistry. Indeed, soil-gas geochemistry is able to detect the buried N75 surface where traditional metal-in-soil trace element geochemistry twice failed. This fact is significant to the exploration geologist because it shows that soil-gas anomalies can pin-point the position of a shear zone of limited width, whereas other exploration methods give much

broader anomalies. However, it is for this reason that soil-gas geochemistry is not the first choice exploration vector for the regional explorationist.

Nevertheless, in cases where geophysical and geochemical anomalies are too dispersed to delineate with precision the primary site of the buried ore deposit, soil-gas geochemistry may improve the likelyhood of success in the task of selecting future drilling sites. Indeed, in every individual case, success can only be enhanced by combining soil-gas surveying with various types of geochemical and geophysical prospecting methods. However, there will always be cases where soil-gas geochemistry may have special "stand alone" application.

References

Abraham L. D., Westlake K., Mackie R. I., Putterill J. F., and Baecker A. A. W. (1989) Methanogenesis and sulfate reduction in timber and drainage water from a gold mine. *Geomicrobiology Journal* **7**, 167-183.

Alexander M. (1977) *Introduction to Soil Microbiology*. 2nd edition. John Wiley and Sons. New York

Alpers C. N., Dettman D. L., Lohmann K. C., and Brabec D. (1990) Stable isotopes of carbon dioxide in soil gas over massive sulphide mineralisation at Crandon, Wisconsin. *Journal of Geochemical Exploration* **38**, 69-86.

Amanor J. A. (1979) The geology of the Ashanti gold mines and implications for exploration. Unpublished MSc thesis, Imperial College, University of London.

Amundson R. G. and Smith V. S. (1988) Annual cycles of physical and biological properties in an uncultivayed and irrigated soil in the San Joaquin Valley of California. *Journal of Agriculture, Ecosystems and Environment* **20**, 195-208.

Amundson R. G. and Davidson E. A. (1990) Carbon dioxide and nitrogenous gases in the soil atmosphere. *Journal of Geochemical Exploration* **38**, 13-41.

Amundson R. G., Chadwick O. A., and Sowers J. M. (1989) A comparison of soil climate and biological activity along an elevation gradiant in the eastern Mojave Desert. *Oecologia* **80**, 395-400.

Anderson R. B. (1984) *The Fischer-Tropsch Synthesis*. Academic Press. New York.

Andrawes F. F. and Gibson E. K., Jr. (1979) Release and analysis of gases from geological samples. *American Mineralogist* **64**, 453 - 463.

Andrawes F., Holzer G., Roedder E., Gibson E. K. J., and Oro J. (1984) Gas chromatographic analysis of volatiles in fluid and gas inclusions. *Journal of Chromatography* **302**, 181 - 193.

Anonymous. (1996) Unpublished Technical Report to WMC Resources. ACTLABS, Unpublished Technical Report to WMC Resources.

Archibald N. J. (1985) The stratigraphic and tectonic-metamorphic history of the Kambalda-Tramways Area, Western Australia. WMC Resources, (KNO) Unpublished Internal Report. **K/2889**.

Archibald N. J., Bettenay L. F., Bickle M. J., and Groves D. I. (1981) Evolution of Archaean

crust in the Eastern Goldfields Province of the Yilgarn Block, Western Australia. *Archaean Geology: Second International Symposium*, Perth, pp. 491 - 504.

Arnorsson S. and Gunnlaugsson E. (1985) New gas geothermometers for for geothermal exploration - Calibration and application. *Geochimica et Cosmochimica Acta* **49**, 1307 - 1325.

Bakker R. J., Dubessy J., and Cathelineau M. (1996) Improvements in clathrate modelling: I. The H_2O-CO_2 system with various salts. *Geochimica et Cosmochimica Acta* **60**, 1657 - 1681.

Balkau J. (1989) Exploration History of the Junction Gold Orebody. WMC Resources, (KNO) Unpublished Internal Report. **K/3190**.

Ball T. K., Crow M. J., Laffoley N., Piper D., and Ridgway J. (1990) Application of soil-gas geochemistry to mineral exploration in Africa. *Journal of Geochemical Exploration* **38**, 103-115.

Banks P. O. and Ghahremani D. T. (1987) Fracture control of radon leakage, Moreland Hills, Ohio; implications for shale gas exploration. *Shell Nachrichten* **3 (1),** 40 - 55.

Barker C. and Torkelson B. E. (1975) Gas adsorption on crushed quartz and basalt. *Geochemica et Cosmochimica Acta* **39**, 212 - 218.

Barley M. E., Groves D. I., Hallberg J. A., Libby J. W., and McNaughton N. J. (1990a) Geology and Late-Archaean tectonic evolution of the Yilgarn Craton. In (ed. S. E. Ho, Groves, D.I. and Bennett, J.M.), *Gold deposits of the Archaean Yilgarn Block, Western Australia: Nature genesis and exploration guides* **23**, pp. 19 - 30. Geology Department (Key Centre) and University Extension, The University of Western Australia. Nedlands.

Barley M. E., Groves D. I., and McNaughton N. J. (1990b) Regional hydrothermal alteration in greenstone belts. In (ed. S. E. Ho, Groves, D.I. and Bennett, J.M.), *Gold deposits of the Archaean Yilgarn Block, Western Australia: Nature genesis and exploration guides* **20,** pp. 55 - 57. Geology Department (Key Centre) and University Extension, The University of Western Australia. Nedlands.

Barnicoat A. C., Fare R. J., Groves D. I., and McNaughton N. J. (1991) Synmetamorphic lode-gold deposits in high grade Archaean settings. *Geology* **19**, 921-924.

Barns S. M. and Nierzwicki-Baur S. A. (1997) Microbial diversity in ocean, surface and subsurface environments. In (ed. B. J.F. and K. H. Nealson), *Geomicrobiology: interactions between microbes and minerals*, Reviews in Mineralogy, 35 - 79. The Mineralogical Society of America. Washington.

Barton P. B. J. (1967) Possible role of organic matter in the precitation of the Mississippi Valley ores. In (ed. J. S. Brown), Genesis of the stratiform lead-zinc-barite-fluorite deposits in carbonate rocks, Economic Geology Monograph 3, 371 - 378.

Bavington O. A. and Keays R. R. (1978) Precious metal values from interflow sedimentary rocks from the komatiite sequence at Kambalda, Western Australia. *Economic Geology* **42**, 1151 - 1163.

Beard J. S. (1979) Phytogeographic Regions. In (ed. J. Gentilli), *Western Landscapes*. 107-120. University of Western Australia Extension Service Publication.

Bennett D. G. and Barker A. J. (1992) High salinity fluids: the result of retrograde metamorphism in thrust zones. *Geochimica et Cosmochimica Acta* **56**, 81 - 95.

Boullier A.-M. and Robert F. (1992) Paleoseismic events recorded in the Archaean gold-quartz vein networks, Val d'Or Abitibi, Quebec. *Journal of Structural Geology* **14**, 161-179.

Boullier A.-M., Firdaous K., and Robert F. (1998) On the significance of aqueous fluid inclusions in gold-bearing quartz vein deposits from the Southeastern Abitibi Subprovince (Quebec, Canada). *Economic Geology* **93**, 216-223.

Bowers T. S. and Helgeson H. C. (1983a) Calculations of the thermodynamic and geochemical consequences of nonideal mixing in the system H_2O-CO_2-NaCl on phase relations in geological systems: Equations of state for H_2O-CO_2-NaCl fluids at high pressure and temperature. *Geochimica et Cosmochimica Acta* **47**, 1247 - 1275.

Bowers T. S. and Helgeson H. C. (1983b) Calculations of the thermodynamic and geochemical consequences of nonideal mixing in the system H_2O-CO_2-NaCl on phase relations in geological systems: Metamorphic equilibria at high pressures and temperatures. *American Mineralogist* **68**, 1059 - 1075.

Bray C. J. and Spooner E. T. C. (1992) Fluid inclusion volatile gases by gas chromatography with photoionization/microthermal conductivity detectors: Applications to magmatic MoS_2 and other H_2O-CO_2 and H_2O-CH_4 fluids. *Geochimica et Cosmochimica Acta* **56**, 261-272.

Bray C. J., Spooner T. C., and Thomas A. V. (1991) Fluid inclusion volatile analysis by heated crushing, on-line gas chromatography; application to Archaean fluids. *Journal of Geochemical Exploration* **42**, 167-192.

Brown P. E. and Hagemann S. G. (1995) MacFlinCor and its application to fluids in Archaean lode-gold deposits. *Geochimica et Cosmochimica Acta* **59**, 3943 - 3952.

Burlinson K. (1991) Decrepitation in gold exploration. A case history from the Cotan prospect, N.T. *Journal of Geochemical Exploration* **42**, 143 - 156.

Burrows D. R. and Spooner E. T. C. (1987) Generation of a magmatic H_2O-CO_2 fluid enriched in Mo, Au and W within an Archaean sodic granodiorite stock, Mink Lake, Northwestern Ontario. *Economic Geology* **82**, 1931 - 1957.

Burrows D. R., Wood P. C., and Spooner E. T. C. (1986) Carbon isotope evidence for a magmatic origin for Archean gold-quartz vein ore deposits. *Nature* **321**, 851-854.

Burruss R. L. (1981) Phase equilibria in the C-O-H-S fluid inclusions. In (ed. L. S. Hollister and M. L. Crawford), *Fluid inclusions: applications to petrology* . 39 - 74. Mineralogical Association of Canada Short Course Handbook.

Butt C. R. M. (1981) The nature and origin of the lateritic weathering mantle, with particular reference to Western Australia. In (ed. H. A. Doyle, J. E. Glover, and D. I. Groves), *Geophysical prospecting in deeply weathered terranes* **6**, pp. 11 - 29. Geology Department and University Extension, The University of Western Australia. Nedlands.

Butt C. R. M. (1989) Genesis of lateritic and supergene gold deposits in the Yilgarn Block, Western Australia. In (ed. R. R. Keays, W. R. H. Ramsay, and D. I. Groves), *Econoic Geology, Monograph 6. The geology of gold deposits: The perspective in 1988.* 460 - 470. New Haven.

Butt C. R. M., Hart M. K. W., and Gole M. J. (1985) Gases and trace elements in soils at the North Silver Bell Deposit, Pima County, Arizona - Discussion. *Journal of Geochemical Exploration* **24**, 129 - 138.

Buyanovsky G. A. and Wagner G. H. (1983) Annual cycles of carbon dioxide levels in soil air. *Soil Science Society of America Journal* **47**, 1139 - 1145.

Cameron E. M. (1988) Archean gold: relation to granulite formation and redox zoning in the crust. *Geology* **16**, 109-112.

Cameron E. M. (1989) Derivation of gold by oxidative metamorphism of a deep ductile shear zone: Part I. Conceptual model. *Journal of Geochemical Exploration* **31**, 135 - 147.

Campbell I. H. and Hill R. I. (1988) A two-stage model for the formation of the granite-greenstone terranes of the Kalgoorlie-Norseman area, Western Australia. *Earth and Planetary Science Letters* **90**, 11-25.

Capaccioni B., Martini M., and Mangani F. (1995) Light hydrocarbons in hydrothermal and magmatic fumeroles: hints of catalytic and thermal reactions. *Bulletin of Volcanology* **56**, 593-600.

Carey M. L. (1994) Petrography and Geochemistry of Selected Sills from the Kambalda-Kalgoorlie Region, W.A. Unpublished Honours thesis, Australian National University.

Carter J. S. and Cazalet P. C. D. (1984) Hydrocarbon gases in rocks as pathfinders for mineral exploration. *Prospecting in areas of glaciated terrane (Glasgow Symposium),* London, pp. 11 - 20.

Carter J. S. and Cazalet P. C. D. (1985) The potential for using hydrocarbon gases in rocks as pathfinders for mineral exploration. Mercury Hydrocarbons Ltd., Unpublished report for the EEC.

Carter J. S., Cazalet P. C. D., and Ferguson J. (1988) Light hydrocarbon gases and mineralisation.

In (ed. J. Buissonnas and P. Omenetto), Mineral Deposits within the European community 406 - 427. Springer-Verlag. Heidelberg.

Cassidy K. F. and Bennett J. M. (1993) Gold mineralisation at the Lady Bountiful Mine, Western Australia: an example of a granitoid-hosted Arcaean lode-gold deposit. *Mineralium Deposita* **28**, 388 - 408.

Chacko T., Mayeda T. K., Clayton R. N., and Goldsmith J. R. (1991) Oxygen and carbon isotope fractionations between CO_2 and calcite. *Geochimica et Cosmochimica Acta* **55**, 2867 - 2882.

Cheminee J. L., Stoffers P., McMurty G., Richnow H., Puteanus D., and Sedwick P. (1991) Gas-rich submarine exhalations during the 1989 eruption of Macdonald Seamount. *Earth and Planetary Science Letters* **107**, 318-327.

Claoue- Long J. C., Compston W., and Cowden A. (1988) The age of the Kambaldagreenstones resolved by ion-microprobe: implications for Archaean dating methods. *Earth and Planetary Science Letters* **89**, 239 - 259.

Clark M. E. (1987) The geology of the Victory gold mine, Kambalda, Western Australia. Unpublished PhD thesis, Queens' University, Canada.

Clark M. E., Archibald N. J., and Hodgson C. J. (1986) The structural and metamorphic setting of the Victory gold mine, Kambalda, Western Australia. In (ed. A. J. MacDonald), *Gold '86*, 243 - 254. Konsult International Inc. Willowdale, Ontario.

Clark M. E., Carmichael N. J., Hodgson C. J., and Fu M. (1989) Wall-rock alteration, Victory gold mine, Kambalda, Western Australia. In (ed. R. R. Keays, W. R. H. Ramsay, and D. I. Groves), *Economic Geology Monograph 6. The Geology of Gold deposits: The Perspective in 1988,* 445-459.

Clarke J. D. A. (1988) The Junction soil anomalies. WMC Resources,(KNO) Unpublished Internal Memorandum. **CON 665**.

Clarke J. D. A. (1989) Nature and significance of spicular sediments in Lake Lefroy. WMC Resources, (KNO) Unpublished Internal Report. **K/3125**.

Clarke J. D. A. (1993) Stratigraphy of the Lefroy and Cowan palaeodrainage channels, Western Australia. *Journal of the Royal Society of Western Australia* **76**, 13 - 23.

Clarke J. D. A. (1994a) Evolution of the Lefroy and Cowan palaeodrainage channels, Western Australia. *Australian Journal of Earth Sciences* **41**, 55-68.

Clarke J. D. A. (1994b) Geomorphology of the Kambalda region, Western Australia. *Australian Journal of Earth Sciences* **41**, 229-239.

Clarke J. D. A. (1994c) Lake Lefroy, a palaeodrainage playa in Western Australia. *Australian Journal of Earth Science* **41**, 417 - 427.

Clarke J. D. A. and Chenoweth L. (1996) Classification, genesis and evolution of ferruginous surface grains. *AGSO Journal of Australian Geology and Geophysics* **16**, 213 - 221.

Clayton R. N. (1981) Isotopic thermometry. In (ed. R. C. Newton, A. Navrotsky, and B. J. Wood), *Thermodynamics of minerals and melts*. 85 - 109. Springer-Verlag. New York.

Clayton R. N. and Mayeda T. K. (1963) The use of bromine pentafluoride in the extraction of oxygen from oxides and silicates for isotopic analysis. *Geochimica et Cosmochimica Acta* **27**, 53 - 106.

Clayton R. N., Muffler L. J. P., and White D. E. (1968) Oxygen isotope study of calcite and silicates of the River Ranch No.1 well, Salton Sea geothermal field, California. *American Journal of Science* **266**, 968-979.

Clayton R. N., Goldsmith J. R., and Mayeda T. K. (1989) Oxygen isotope fractionation in quartz, albite, anorthite and calcite. *Geochimica et Cosmochimica Acta* **53**, 725 - 733.

Clifton C. G. (1984) Interpretation of soil-gas data (CO_2, CS_2, COS, SO_2, H_2S). Preliminary Report II. Exploration research laboratories, Corvallis, Unpublished lecture series notes.

Clifton H. E. (1995) Sedimentary facies and high resolution sequence stratigraphy of Pleistocene valley-fill/esturine deposits, Willapa Bay, Washington. *Association of American Petroleum Geologists Bulletin* **79**, 1725 - 1726.

Collins P. L. F. (1979) Gas hydrates in CO_2-bearing fluid inclusions and the use of freezing data for estimation of salinity. *Economic Geology* **74**, 1435 - 1444.

Colvine A. C. (1989) An empirical model for the formation of Archaean gold deposits. Products of final cratonisation of the Superior Province, Canada. In (ed. R. R. Keays, W. R. H. Ramsay, and D. I. Groves), *Economic Geology, Monograph 6, The Geology of Gold Deposits: The Perspective in 1988*. 37-53.

Colvine A. C., Andrews A. J., Cherry M. E., Durocher M. E., Fyon A. J., Lavigne M. J., Macdonald A. J., Marmont S., Poulsen K. H., Springer J. S., and Troop D. G. (1984) *An integrated model for the origin of Archean lode gold deposits.* Ontario Geological Survey, Open File Report. **5524**.

Colvine A. C., Fyon J. A., Heather K. B., Marmont S., Smith P. M., and Troop D. G. (1988) *Archaean lode-gold deposits in Ontario.* Ontario Geological Survey. Miscellaneous Paper 139. Toronto

Costello J. (1993) Alteration assemblages - Junction. WMC Resources,(KNO) Unpublished Technical Report. **003.**

Costello J. (1994) Junction Deeps - mineralogy and alteration study: TD2312 Intersection. WMC Resources, (KNO) Unpublished Technical Note. **93/003.**

Cowden A. and Archibald N. J. (1985) Stratigraphy of the Kambalda-Kalgoorlie Archaean

greenstone terrane, Western Australia. *Australian Journal of Earth Science* **31**, 200 - 213.

Cowden A. (1986) Geological legends. WMC Resources, (KNO) Unpublished Internal report. **K/2968**.

Cowden A. (1988) Emplacement of komatiitis lava flows and associated nickel sulphide deposits at Kambalda, Western Australia. *Economic Geology* **83**, 436 - 442.

Cowden A. and Archibald N. J. (1987) Massive sulphide fabrics at Kambalda and their relevance to the inferred stability of monosulphide solid-solution. *Canadian Mineralogist* **25**, 37 - 50.

Cowden A. and Roberts D. E. (1990) Komatiite hosted nickel sulphide deposits, Kambalda. In (ed. F. E. Hughes), *Geology of the ineral deposits of Australia and Pupua New Guinea*, 567 - 581. The Australasian Institute of Mining and Metallurgy. Melbourne.

Davis D. W., Lowenstein T. K., and Spencer R. J. (1990) Melting behaviour of fluid inclusions in laboratory-grown halite crystals in the systems NaCl-H_2O, NaCl-KCl-H_2O, NaCl-$MgCl_2$-H_2O and NaCl-$CaCl_2$-H_2O. *Geochimica et Cosmochimica Acta* **54**, 591 - 601.

de Ronde C. E., Spooner E. T. C., de Witt M. J., and Bray C. J. (1992) Shear zone-related, Au quartz vein deposits in the Barberton Greenstone Belt, South Africa: Field and petrographic characteristics, fluid properties, and light stable isotope geochemistry. *Economic Geology* **87**, 366 - 402.

Deer W. A., Howie R. A., and Zussman J. (1993) An introduction to the rock forming minerals. 2nd edition. Longman Scientific and Technical. London

Deines P. (1980) The isotopic composition of reduced organic carbon. In (ed. J. Fritz and C. H. Fontes), *Handbook of Environmental Isotope Geochemistry,* 329-406. Elsevier. Amsterdam.

Deines P. (1992) Mantle carbon: concentration, mode of occurrence, and isotopic composition. In (ed. M. Schidlowski, S. Golubic, M. M. Kimberley, D. McKirdy, and P. A. Trudinger), *Early organic evolution implications for mineral and energy resources.* 133 - 145. Springer-Verlag. Heidelburg.

Deines P., Gurney J. J., and Harris J. W. (1984) Associated chemical and carbon isotopic composition variations in diamonds from Finsch and Premier kimberlite. South Africa. *Geochimica et Cosmochimica Acta* **48**, 325-342.

Disnar J. R. and Gauthier B. (1988) Exploration for concealed orebodies by the analysis of volatile organic compounds contained in surface rocks: Treves Zn-Pb deposit (Gard, France). *Journal of Geochemical Exploration* **30**, 179 - 196.

Disnar J. R. and Sureau J. F. (1990) Organic matter in ore genesis: progress and perspectives. *Organic geochemistry* **16**, 577 - 599.

Disnar J. R. (1990) Volatile hydrocarbons in Ba-Zn-Pb ore genesis: analysis and use in mineral exploration. *Journal of Geochemical Exploation* **38**, 205 - 224.

Donnelly T. H., Lambert I. B., Oehler D. Z., Hallberg J. A., Hudson D. R., Smith J. W., Bavinton O. A., and Golding L. (1977) A reconnaissance study of stable isotope ratios in Archaean rocks from The Yilgarn Block, Western Australia. *Journal of the Geological Society of Australia* **24**, 409 - 420.

Douglass A. G., Eglinton G., and Henderson W. (1970) Thermal alteration of the organic matter in sediments. In (ed. G. D. Hobson and G. C. Speers), *Advances in organic geochemistry,* 369 - 388. Pergamon Press. Oxford.

Drobnik H. (1962) The effect of temperature on soil respiration. *Folia Microbiology* **7**, 132-140.

Duan Z., Moller N., and Weare J. H. (1992a) An equation of state for the CH_4-CO_2-H_2O system: I. Pure Systems from 0 - 1000°C and 0 - 8000 bar. *Geochimica et Cosmochimica Acta* **56**, 2605 - 2617.

Duan Z., Moller N., and Weare J. H. (1992b) An equation of state for the CH_4-CO_2-H_2O sytem: II. Mixtures from 50 - 1000°C and 0 - 1000 bar. *Geochimica et Cosmochimica Acta* **56**, 2619 - 2631.

Dubessy J., Audeoud D., Wilkins R., and Kosztolanyi C. (1982) The use of the Raman microprobe mole in the determineation of the electrolytes dissolved in the aqueous phase of fluid inclusions. *Chemical Geology* **37**, 137-150.

Dubessy J., Poty B., and Ramboz C. (1989) Advances in C-O-H-N-S fluid geochemistry based on micro-Raman spectrometric analysis of fluid inclusions. *European Journal of Mineralogy* **1**, 517 - 534.

Dunsmore H. E. and Shearman D. J. (1977) Mississippi Valley-type lead-zinc ore bodies: a sedimentary and diagenetic origin. *Proceedings of the forum on oil and ore in sediments,* Imperial College, London, pp. 189 - 201.

Dyck W. (1976) The use of helium in mineral exploration. *Journal of Geochemical Exploration* **5**, 10 - 13.

Ellery S. and Watts D. (1996) WMC St Ives Gold. Junction North Surface Geology. WMC Resources.(KNO) Unpublished map. 1: 7500

Ellis P. and Mapleson D. (1997) Alteration around a Proterozoic dyke at the Junction mine, and its effect on gold mineralisation. WMC Resources, (KNO) Unpublished Techical Report. **TSIG 028**.

Etminan H. and Hoffmann C. F. (1989) Biomarkers in fluid inclusions: A new tool in constraining source regimes and its implications for the genesis of Mississippi Valley-type deposits. *Geology* **17**, 19-22.

Faure G. (1986) *Principles of Isotope Geology*. 2nd edition. John Wiley and Sons. New York

Ferguson J. (1987) A possible role for light hydrocarbons in Pb/Zn mineral exploration. *Mineralogical Magazine* **51**, 527 - 533.

Ferguson J. (1988) The nature and origin of light hydrocarbon gases associated with mineralisation in the Northern Pennines. *Marine and Petroleum Geology* **5**, 378 - 384.

Field P. M., Kerrich R., and Kyser T. K. (1998) Characteristics of Barren Quartz Veins in the Proterozoic La Ronge Domain, Saskatchewan, Canada: A Comparison with Auriferous Counterparts. *Economic Geology* **93**, 602-616.

Finkl C. W. and Fairbridge R. W. (1979) Palaeogeographic evolution of a rifted cratonic margin: S.W. Australia. *Palaeogeography, Palaeoclimatology, Palaeoecology* **26**, 221-252.

Foster C. B., Robbins E. I., and Bone Y. (1990) Organic tissues, graphite, and hydrocarbons in host rocks of the Rum Jungle Uranium Field, northern Australia. *Ore Geology Reviews* **5**, 509-523.

Fridman A. I. (1990) Application of naturally occurring gases as geochemical pathfinders in prospecting for endogenic deposits. *Journal of Geochemical Exploration* **38**, 1-11.

Friedel R. A. and Sharkey A. G. J. (1963) Alkanes in natural and synthetic petroleums: comparison of calculated and actual compositions. *Science* **129**, 1203 - 1205.

Friedman I. and O'Neil J. R. (1977) Compilation of stable isotope fractionation factors of geochemical interest. *U.S. Geological Survey, Professional Paper*. **440-KK**.

Fullagar P. K. (1989) *Petroleum exploration by geochemical and geophysical detection of vertical migration*. WMC Resources,Petroleum Exploration Society of Australia unpublished course notes.

Gee R. D., Baxter J. L., Wilde S. A., and Williams I. R. (1981) Crustal development in the Yilgarn Block, Western Australia. *Geological Society of Australia Special Publication* **7**, 43 - 56.

Gee R. D., Myers J. S., and Trendall A. F. (1986) Relation between Archaean high-grade gneiss and granite-greenstone terrane in Western Australia. *Precambrian Research* **33**, 87 - 102.

Gehrig M. (1980) Phasengleichgewichte und pVT-Daten ternarer Mischungen aus Wasser, Kohlendioxid und Natriumchlorid bis 3 kbar und 550°C. Hochshul Verlag. Freiburg.

German C. R., Briem J., Chin C., Danielsen M., Holland S., James R., Jonsdottir A., Ludford E., Moser C., Olafsson J., Palmer M. R., and Rudnicki R. L. (1994) Hydrothermal activity on the Reykjanes Ridge: the Steinaholl vent-field at 63°06'N. *Earth and Planetary Science Letters* **121**, 647-654.

Giggenbach W. F. (1982) Carbon-13 exchange between CO_2 and CH_4 under geothermal conditions.

Geochimica et Cosmochimica Acta **46**, 159-165.

Giles A. D. and Marshall B. (1995) Fluid inclusion studies on a multiply deformed metamorphosed volcanic-associated massive sulphide deposit. *Economic Geology* **89**, 803 - 919.

Giletti B. J. (1986) Diffusion effects on oxygen isotope temperatures of slowly cooled igneous and metamorphic rocks. *Earth and Planetary Science Letters* **77**, 218 - 228.

Gilmore P. J. (1996) A structural, geochemical and geotechnical analysis of the Junction Pit, St Ives gold Mines, Western Australia. unpublished Honours thesis, University of Newcastle.

Giordano T. H. (1985) A preliminary evaluation of organic ligands and metal-organic complexing in Mississippi Valley-type ore solutions. *Economic Geology* **80**, 96 - 106.

Gize A. P. and Barnes H. L. (1987) The organic geochemistry of two Mississippi Valley-type lead-zinc deposits. *Economic Geology* **82**, 457 - 470.

Golding S. D. and Wilson A. F. (1982) Geochemical and stable isotopic studies of the Crown and Mararoa reefs, Norseman, Western Australia. *Revista Brasileira de Geociencias* **12**, 445 - 456.

Golding S. D. and Wilson A. F. (1983) Geochemical and stable isotope studies at the No. 4 lode, Kalgoorlie, Western Australia. *Economic Geology* **78**, 438-450.

Golding S. D. and Wilson A. F. (1987) Oxygen and hydrogen isotope relations in Archean gold deposits of the Eastern Goldfields Province, Western Australia: constraints on the source of Archean gold-bearing fluids. In (ed. S. E. Ho and D. I. Groves), *Recent Advances in Understanding Precambrian Gold Deposits* **11**, pp. 703-713. Geology Department and University Extension, University of Western Australia.

Golding S. D., Groves D. I., McNaughton N. J., Barley M. E., and Rock N. M. S. (1987) Carbon isotopic composition of carbonates from contrasting alteration styles in supracrustal rocks of the Norseman-Wiluna belt, Yilgarn Block, Western Australia: their significance to the source of Archean auriferous fluids. In (ed. S. E. Ho and D. I. Groves), *Recent Advances in Understanding Precambrian Gold Deposits* **11**, pp. 215-238. Geology Department and University Extension, University of Western Australia.

Golding S. D., McNaughton N. J., Barley M. E., Groves D. I., Ho S. E., and Rock N. M. S. (1989) Arcaean carbon and oxygen reservoirs: Their significance for fluid sources and circulation paths for Archaean mesothermal gold deposits of the Norseman-Wiluna Belt, Western Australia. In (ed. R. R. Keays, W. R. H. Ramsay, and D. I. Groves), *Economic Geology Monograph 6, The geology of gold deposits: The perspective in 1988,* 376 - 388.

Golding S. D., Clark M. E., Keele R. A., Wilson A. F., and Keays R. R. (1990a) Geochemistry of Archaean epigenetic gold deposits in the Eastern Goldfields Province, Western Australia. In (ed. H. K. Herbert and S. E. Ho), *Stable isotopes and fluid processes in*

mineralisation **23**, Geology Department and University Extension, The University of Western Australia. Nedlands.

Golding S. D., Barley M. E., Cassidy K. F., Groves D. I., Ho S. E., Hronsky J. M. A., McNaughton N. J., Sang J. H., and Turner J. V. (1990b) Source of ore fluid and ore components: Oxygen and hydrogen studies. In (ed. S. E. Ho, Groves, D.I. and Bennet, J.M.), *Gold deposits of the Archaean Yilgarn Block, Western Australia: Nature Genesis and exploration guides* **20**, pp. 252 - 258. Geology Department (Key Centre) and University Extension, The University of Western Australia. Nedlands.

Goodman S. (1987) The relationship between light hydrocarbons and carbonate petrology - a study from the Mendip Hills. *Geological Journal* **22**, 371 - 382.

Graney J. R. and Keslar S. E. (1995) Gas composition of fluid in ore deposits: Is there a relation to magmas? In (ed. J. F. H. Thompson), *Magmas, Fluids and Ore Deposits, Mineralogical Association of Canada Short Course Series* **23**, pp. 221-245. Victoria.

Grbic-Galic D. (1990) Methanogenic Transformation of aromatic hydrocarbons and phenols in groundwater aquifers. *Geomicrobiology Journal* **8**, 167-200.

Gresham J. J. and Loftus-Hills G. D. (1981) The geology of the Kambalda Nickel field, Western Australia. *Economic Geology* **76**, 1373 - 1416.

Groves D. I. (1993) The crustal contiuum model for late-Archaean lode-gold deposits of the Yilgarn Block, Western Australia. *Mineralium Deposita* **28**, 366-374.

Groves D. I. and Phillips G. N. (1987) The genesis and tectonic control on Archean gold deposits of the Western Australian Shield - a metamorphic replacement model. *Ore Geology Reviews* **2**, 287-322.

Groves D. I., Phillips G. N., Ho S. E., Henderson C. A., Clark M. E., and Woad G. M. (1984) Controls on distribution of Archaean hydrothermal gold deposits in Western Australia. In (ed. R. P. Foster), *Gold '82: The Geology, Geochemistry and Genesis of Gold Deposits* 689-712. Z.A. Balkema. Rotterdam.

Groves D. I., Golding S. D., Rock N. M. S., Barley M. E., and McNaughton N. J. (1988) Archean carbon reservoirs and their relevance to the source for gold deposits. *Nature* **332**, 254-257.

Groves D. I., Knox-Robinson C. M., Ho S. E., and Rock N. M. S. (1990) An overview of Archaean lode-gold deposits. In (ed. S. E. Ho, D. I. Groves, and J. M. Bennett*), Gold deposits of the Archaean Yilgarn Block, Western Australia: Nature Genesis and exploration guides.* **20**, pp. 2 - 19. Geology Department (Key Centre) and University Extension, The University of Western Australia. Nedlands.

Groves D. I., Barley. M.E., Barnicoat A. C., Cassidy K. F., Fare R. J., Hagemann S. G., Ho S. E., Hronsky J. M. A., Mikucki E. J., Muellar A. G., McNaughton N. J., Perring C. S.,

Ridley J. R., and Verncombe J. R. (1992) Sub-greenschist to granulite hosted Archaean lode-gold deposits of the Yilgarn Craton: A depositional continuum from deep sourced hydrothermal fluids in crustal-scale plumbing systems. In (ed. J. E. Glover and S. E. Ho), *The Archaean; terranes, processes and metallogeny: proceedings volume for the third international Archaean symposium.* **22**, pp. 325-338. Geology Department (Key Centre), University Extension, University of Western Australia.

Groves D. I., Ridley J. R., Bloem E. M. J., Gebre-Mariam M., Hronsky J. M. A., Knight J. T., McNaughton N. J., Ojala J., Vielreicher R. M., Holyland P. W., and McCuaig T. C. (1995) Lode-gold deposits of the Yilgarn Block: products of Late-Archaean crustal scale overpressured hydrothermal systems. *Journal of Geological Society of London, Special Publication* **95**, 155 - 172.

Groves D. I., Goldfarb R. J., Gebre-Mariam M., Hagemann S. G., and Robert F. (1998) Orogenic gold deposits: A proposed classification in the context of their crustal distribution and relationship to other gold deposit types. *Ore Geology Reviews* **13**, 7 - 27.

Guha J., Keslar S. E., and Jones H. D. (1991) Fluid characteristics of vein and altered wall rock in Archaean mesothermal gold deposits. *Economic Geology* **86**, 667-684.

Hagemann S. G. and Ridley J. R. (1993) Hydrothermal fluids in epi- and katazonal crustal levels in the Archaean - Implications for P-T-X-t evolution of lode-gold mineralisation. An international conference on crustal evolution, metallogeny and exploration of the Eastern Goldfields. Extended Abstracts, 123-130.

Hagemann S. G., Gebre-Mariam M., and Groves D. I. (1994) Surface-water influx in shallow-level Archaean lode-gold deposits in Western Australia. *Geology* **22**, 1067-1070.

Hand J. (1996) Mineralised volcanic and sedimentary environments in the Eastern Goldfields. Unpublished PhD progress report to WMC Resources.

Harting P. and Maass I. (1980) Neue Ergebnisse zum Kohlenstoff - Isotopenaustausch im System CH_4 - CO_2. In (ed. Mitteilungen zur 2. Arbeitstagung "Isotope in der natur". November 1980, 13 - 24. Leipzig.

Heggie D. (1989) Offshore detection of vertical migration of hydrocarbons. Unpublished report by the PESA 1989 Special Lecturer.

Hein K. A. A., Carey M., Sugden T. J., and Stone B. (1996) The stratigraphy of the Kambalda-St Ives area: workshop notes. WMC Resources, (KNM) Unpublished Technical Report. **229**.

Hinkle M. E. and Dilbert G. A. (1984) Gases and trace elements in soils at the North Silver Bell deposit, Pima County, Arizona. *Journal of Geochemical Exploration* **20**, 323 - 336.

Hinkle M. E., Ryder J. L., Stutley S. J., and Botinelly T. (1990) Production of sulphur gases and

carbon dioxide by synthetic weathering of crushed drill cores from the Santa Cruz porphyry copper deposit near Casa Grande, Pinal County, Arizona. *Journal of Geochemical Exploration* **38**, 43 - 68.

Ho E. S. and Mauk J. L. (1996) Relationship between organic matter and copper mineralisation in the Proterozoic Nonesuch Formation, northern Michigan. *Ore Geology Reviews* **11**, 71 - 88.

Ho E. S., Meyers P. A., and Mauk J. L. (1990) Organic geochemical study of mineralisation in the Keweenan Nonesuch Formation at White Pine, Michigan. *Organic Geochemistry* **16**, 229 - 234.

Ho S. E. (1986) A fluid inclusion study of Archaean gold deposits of the Yilgarn Block, Western Australia. unpublished PhD thesis, The University of Western Australia.

Ho S. E., Groves D. I., and Phillips G. N. (1990a) Fluid inclusions in quartz veins associated with Arcaean gold mineralisation: clues to ore fluids and ore depositional conditions and significance to exploration. In (ed. H. K. Herbert and S. E. Ho*), Stable isotopes and fluid processes in Mineralisation* **23**, pp. 35 - 50. Geology Department and University Extension, The University of Western Australia. Nedlands.

Ho S. E., Bennett J. M., Cassidy K. F., Hronsky J. M. A., Mikucki E. J., and Sang J. H. (1990b) Nature of ore fluid, and transportational and depositional conditions: Fluid inclusion studies. In (ed. S. E. Ho, D. I. Groves, and J. M. Bennett), *Gold deposits of the Archaean Yilgarn Block, Western Australia: Nature Genesis and exploration guides* **20**, pp. 198 - 211. Geology Department (Key Centre) and University Extension, The University of Western Australia. Nedlands.

Hodgson C. J. (1989) The structure of shear-related, vein type gold deposits: A review. *Ore Geology Reviews* **4**, 231 - 273.

Hoeve J. and Sibbald T. I. I. (1978) On the genesis of the Rabbit Lake and unconformity type uranium deposits in Northern Saskatchewan, Canada. *Economic Geology* **73**, 1450 - 1473.

Holland C. L. (1995) Visitors guide to the Junction gold mine: Version One. WMC Resources, (KNO) Unpublished Technical Report. **010**.

Hollister L. S. and Burruss R. C. (1976) Phase equilibria in fluid inclusions from the Khtada Lake metamorphic complex. *Geochimica et Cosmochimica Acta* **40**, 163 - 175.

Horvitz L. (1939) On geochemical prospecting. *Geophysics* **4**, 210 -225.

Horvitz L. (1945) Recent developments in geochimical prospecting for petroleum. *Geophysics* **10,** 487 - 493.

Horvitz L. (1954) Near surface hydrocarbons and petroleum accumulation at depth. *American Institutre of Mining and Metallurgical Engineers, Transactions* **199**, 1205 - 1209.

Horvitz L. (1972) Vegetation and geochemical prospecting for petroleum. *American Association of Petroleum Geologists Bulletin* **56**, 925 - 940.

Horvitz L. (1981) Hydrocarbon geochemical prospecting after forty years. In (ed. B. M. Gottlieb), *Unconventional methods in exploration for petroleum and natural gas II.* 83-95. Southern Methodist University Press. Dallas.

Horvitz L. (1985) Geochemical exloration for petroleum. *Science* **229** (4716), 821-827.

Hunt J. M. (1979) Petroleum geochemistry and geology. Freeman. San Francisco.

Illchick R. P., Brimhall G. H., and Schull W. H. (1986) Hydrothermal maturation of indigenous organic matter at the Alligator Ridge gold deposit, Nevada. *Economic Geology* **81**, 113 - 130.

Ishibashi J.-I., Wakita H., Nojiri Y., Grimaud D., Jean-Baptisie P., Gamo T., Auzende J.-M., and Urabe T. (1994) Helium and carbon geochemistry of the hydrothermal fluids from the North Fiji Basin spreading ridge (southwest Pacific). *Earth and Planetary Science Letters* **128**, 183-197.

Jackson D. H., Mattey D. P., and Harris N. B. W. (1988) Carbon isotope coposition of fluid inclusions in charnockites from southern India. *Nature* **333**, 167 - 168.

Jacobs G. K. and Kerrick D. M. (1981) methane: an equation of state with application to the ternary system H_2O-CO_2-CH_4. *Geochemica et Cosmochimica Acta* **45**, 607-614.

Jones V. T. (1984) Overview of geochemical exploration technology. Exploration Technologies, Unpublished notes for a short course on Geochemical Technology.

Jones V. T. and Drozd R. J. (1983) Prediction of oil or gas potential by near-surface geochemistry. *American Association of Petroleum Geologists, Bulletin* **67**, 932 - 952.

Kazahaya K. and Matsuo S. (1985) A new ball-milling method for extraction of fluid inclusions from minerals. *Geochemistry Journal* **19**, 45 - 54.

Keiffer S. W. (1982) Thermodynamics and lattice vibrations of minerals; 5. Applications to phase equilibria, isotopic fractionation and high pressure thermodynamic properties. *Reviews in Geophysics* **20**, 827 - 849.

Kelly W. C. and Nishioka G. K. (1985) Precambrian oil inclusions in late veins and the role of hydrocarbons in copper mineralization at White Pine, Michigan. *Geology* **13**, 334-337.

Kerrich R. (1983) *Geochemistry of gold deposits in the Abitibi greenstone belt.* Canadian Institute of Mining, Special Paper **27**.

Kerrich R. (1987) The stable isotope geochemistry of Au-Ag vein deposits in metamorphic rocks. In (ed. T. K. Kyser), *Stable Isotope Geochemistry of Low-Temperature Fluids*, Mineralogical Association of Canada Short Course, **13**, pp. 287-336.

Kerrich R. (1989) Shear zone hosted mesothermal gold deposits; a review of geochemical

evidence on the sources of fluids and solutes. In (ed. J. T. Bursnall), *Mineralization and Shear Zones.* 129 - 194. Geological Association of Canada Short Course Notes, **6**.

Kerrich R. and Fryer B. J. (1979) Archean precious-metal hydrothermal systems, Dome Mine, Abitibi Greenstone Belt: Part II. REE and oxygen isotope relations. *Canadian Journal of Earth Sciences* **16**, 440-458.

Kesler S. E. (1990) Soil and rock gas geochemistry. *Journal of Geochemical Exploration* **38**, vii - viii.

Kesler S. E. and Gardner M. J. (1986) Factors effecting sulphur gas anomalies in overburden. *Journal of Geophysical Research* **91**, 12339 - 12342.

Kesler S. E., Haynes P. S., Creech M. Z., and Gorman J. A. (1986) Application of fluid inclusion and rock-gas analysis in mineral exploration. *Journal of Geochemical Exploration.* **25**, 201 - 215.

Kesler S. E., Gerdenich M. J., Steininger R. C., and Smith C. (1990) Dispersion of soil gas around micron gold deposits. *Journal of Geochemical Exploration* **38**, 117 - 132.

Klessig P. J. (1984) History and geology of the Aligator Ridge gold mine, White Pine County, Nevada. *Exploration for ore deposits of the North American Cordillera.* Association of Exploration Geochemists 1984 Regional Symposium, FT2-27 to FT2-35.

Konnerup-Madsen J., Larsen E., and Rose-Hansen J. (1979) Hydrocarbon rich inclusions in minerals from the alkaline Ilimaussaq intrusion, South Greenland. *Bulletin of Mineralogy* **102**, 642-653.

Krader T. and Franck E. U. (1987) The ternary systems H2O-CH4-NaCl and H2O-CH4-CaCl to 800K and 250MPa. *Ber Bunsenges Physical Chemistry* **91**, 627 - 634.

Kreulen R. (1987) Thermodynamic calculations of the C-O-H system applied to fluid inclusions: Are fluid inclusions unbiassed samples of ancient fluids? *Chemical Geology* **61**, 56-64.

Kroschwitz J. I. (1996) Encyclopedia of Chemical Technology. John Wiley and Sons. New York.

Kyser T. K. (1987) Equilibrium fractionation factors for stable isotopes. In (ed. T. K. Kyser), *Stable Isotope Geochemistry of Low Temperature Fluids*, Mineralogical Association of Canada Short Course, **13**, pp. 1-84.

Kyser T. K. and Kerrich R. (1990) Geochemistry of fluids in tectonically active crustal region. In (ed. B. E. Nesbitt), *Fluids in tectonically active regimes of the continental crust*, Mineralogical Association of Canada Short Course, **18**, pp. 133 - 230. Nepean.

Landais P. (1986) Geochemical analyses of the organic matters associated with the breccia pipes in the Grand Canyon area. *Geological Society of America Program.*, **389**.

Landais P. and Gize A. P. (1997) Organic matter in hydrothermal ore deposits. In (ed. H. L. Barnes), *Geochemistry of hydrothermal ore deposits*, 3rd edition, pp. 613 - 655. John Wiley and Sons. New York.

Landais P., Monthioux M., and Meunier J. D. (1984) Importance of the oxidation maturation pair in the evolution of humic coals. *Organic Geochemistry* **7**, 249 - 260.

Laubmeyer G. (1933) New geophysical prospecting method, especially for hydrocarbon strata. *Petroleum* **29**, 1 - 4.

Lesher C. M. and Arndt N. T. (1995) REE and Nd isotope geochemistry, petrogenesis and volcanic evolution of contaminated komatiites at Kambalda, Western Australia. *Lithos* **34**, 127 - 157.

Letnikov F. A. and Narseev A. F. (1991) Use of fluid inclusion gas surveys for the assesment of lode deposits (with reference to gold and tungsten deposits). *Journal of Geochemical Exploration* **42**, 133 - 142.

Leythaeuser D., Schaefer R. G., and Yukler A. (1982) Role of diffusion in primary migration of hydrocarbons. *American Association of Petroleum Geologists Bulletin* **66**, 408 - 429.

Leythaeuser D., Schaefer R. G., and Pooch H. (1983) Diffusion of light hydrocarbons in the subsurface sedimentary rocks. *American Association of Petroleum Geologists Bulletin* **67**, 889 - 895.

Lindgren W. (1933) *Mineral Deposits*. 4th edition. McGraw Hill. New York and London

Liu L. G. and Mernagh T. P. (1990) Phase transitions and Raman spectra of calcite at high pressures and room temperature. *American Mineralogist* **75**, 801 - 806.

Lovell J. S., Hale M., and Webb J. S. (1983) Soil air carbon dioxide and oxygen measurements as a guide to concealed mineralisation in semi-arid and arid regions. *Journal of Geochemical Exploration* **19**, 305-317.

MacElvain R. (1969) Mechanics of gaseous ascension through a sedimentary column. In (ed. W. B. Heroy), *Unconventional methods in exploration for petroleum and natural gas* 15 - 28. Southern Methodist University Press. Dallas.

Macknight M., Noever T., Warrington B., Bromley P., and Hamel M. (1994) Maclab Charts.

Madigan M. T., Martinko J. M., and Parker J. (1997) Biology of microorganismsPrentice Hall. Upper Saddle River, New Jersey.

Madon R. J. and Taylor W. F. (1981) Fischer-Tropsch synthesis on precipitated iron catalyst. *Journal of Catalysis* **69**, 32 - 43.

Marmont S. (1983) The role of felsic intrusions in gold mineralisation. In (ed. A. C. Colvine), *The geology of gold in Ontario,* Miscellaneous Paper, **110**, pp. 38 - 47. Ontario Geological Survey. Toronto.

Marshall D. J. (1989) Cathodoluminescence of geological materials Unwin, Hyman. Boston, London

Mattey D. P., Exley R. A., and Pillinger C. T. (1989) Isotopic composition of CO_2 and dissolved carbon species in basalt glass. *Geochimica et Cosmochimica Acta* **53**, 2377 - 2386.

Matthews A. and Beckinsale R. D. (1979) Oxygen isotope equilibration systematics between quartz and water. *American Mineralogist* **64,** 232-240.

Mauk J. L. and Hieshima G. B. (1992) Organic matter and copper mineralization at White Pine, Michigan, U.S.A. In (ed. P. A. Meyers, L. M. Pratt, and B. Nagy) *Geochemistry of Metalliferous Black Shales, Chemical Geology* **99**, 189-211.

Mavrogenes J. A. and Bodnar R. J. (1994) Experimental evidence and geological implications of hydrogen movement into and out of fluid inclusions in quartz. *Geochimica et Cosmochimica Acta* **59**, 3987 - 3995.

McCarthy J. H. and Reimer G. M. (1986) Advances in soil gas exploration for natural resources. *Journal of Geophysical Research* **91**, 12327 - 12338.

McCarthy J. H., Lambe R. N., and Dietrich J. A. (1986) A case study of soil gases as an exploration guide in glaciated terrane - Crandon massive sulphide deposits, Wisconsin. *Economic Geology* **81**, 1408 - 1420.

McCrea J. M. (1950) On the isotopic chemistry of carbonates and a palaeotemperature scale. *Journal of Chemical Physics* **18**, 849 - 857.

McCuaig T. C., Kerrich R., Groves D. I., and Archer N. (1993) P-T-t deformation-fluid characteristics of lode-gold deposits: Evidence from alteration systematics. In (ed. D. R. Lentz), *Alteration and Alteration Processes Associated with Ore-forming systems* 339-379. Geological Association of Canada, Short Course Notes.

McNaughton N. J., Turner J. V., Golding S. D., and Groves D. I. (1988) Carbon in carbonated ultramafic rocks of the Norseman-Wiluna belt: further implications for the source of carbon in Archaean mesothermal gold deposits. In (ed. S. E. Ho and D. I. Groves), *Advances in understanding Precambrian gold deposits.* **12**, pp. 195 - 208. Geology Department (Key Centre) and University Extension, The University of Western Australia. Nedlands.

McNaughton N. J., Barley M. E., Cassidy K. F., Golding S. D., Groves D. I., Ho S. E., Hronsky J. M. A., Sang J. H., and Turner J. V. (1990) Source of ore fluid and ore components: Carbon isotope studies. In (ed. S. E. Ho, D. I. Groves, and J. M. Bennett), *Gold deposits of the Archaean Yilgarn Block, Western Australia: Nature Genesis and exploration*

guides. **20**, Geology Department (Key Centre) and University Extension, The University of Western Australia. Nedlands.

McNeil A. M. and Kerrich R. (1986) Archean lamprophyric dykes and gold mineralization, Matheson, Ontario: the conjunction of LIL-enriched mafic magmas, deep crustal structures and Au concentration. *Canadian Journal of Earth Sciences* **23**, 324-342.

McQueen R. W. and Powell T. G. (1983) Organic geochemistry of the Pine Point ore field and region, Northwest Territories, Canada. *Economic Geology* **78**, 1 - 25.

Mernagh T. P. and Witt W. K. (1994) Early, methane-rich fluids and their role in Archaean gold mineralisation at the Sand King and missouri deposits, Eastern Goldfields Province, Western Australia. *12th Australian Geological Convention - Geoscience Australia - 1994 and Beyond,* Perth, pp. 284.

Mernagh T. P. (1996) Gold mineralisation at Mt Charlotte: Evidence for fluid oxidation from fluid inclusions. *13th Australian Geological Convention - Geoscience for the community,* Canberra, pp. 292.

Mikucki E. J. and Ridley J. R. (1993) The hydrothermal fluid of Arcaean lode-gold deposits: Constraints on its composition inferred from ore and wallrock alteration assemblages over a spectrum of metamorphic grades. *Mineralium Deposita* **28**, 469-481.

Mikucki E. J., Groves D. I., and Cassidy K. F. (1990) Alteration patterns: wallrock alteration in sub-amphibolite facies gold deposits. In (ed. S. E. Ho, D. I. Groves, and J. M. Bennett), *Gold deposits of the Archaean Yilgarn Block, Western Australia: Nature Genesis and exploration guides.* **20**, pp. 60 - 78. Geology Department (Key Centre) and University Extension, The University of Western Australia. Nedlands.

Miller M. F. and Pillinger C. T. (1997) An appraisal of stepped heating release of fluid inclusion CO_2 for isotopic analysis: A preliminary to d13C characterisation of carbonaceous vesicles at the nanomole level. *Geochimica et Cosmochimica Acta* **61**, 193 - 205.

Mol A., Finn D., and Hein K. A. A. (1996) Observations and interpretations of structures a the Junction gold mine, St Ives Goldfields, Kambalda. WMC Resources, (KNM) Technical Report. **021**.

Mulshaw S. C. (1996) A critical evaluation of the use of hydrocarbon gases in rocks as a pathfinder for base-metal mineralisation in Shannonbridge, central Ireland. *Journal of Geochemical Exploration* **56**, 265 - 277.

Mumin A. H., Fleet M. E., and Longstaffe F. J. (1996) Evolution of hydrothermal fluids in the Ashanti gold belt, Ghana: Stable isotope geochemistry of carbonates, graphite, and quartz. *Economic Geology* **91**, 135 - 148.

Murphy T. E. (1995) An investigation into the petrology and geochemistry of the felsic to intermediate intrusions within the Junction gold mine, Kambalda Western Australia;

and their relationship to gold mineralisation. unpublished Honours, University of Technology.

Myers J. S. and Hickman A. H. (1990) Pilbara and Yilgarn Craton - regional geology and mineralisation. In (ed. F. E. Hughes), *Geology of the mineral deposits of Australia and Papua New Guinea* 129 - 133. Australiasian Institute of Mining and Metallurgy. Melbourne.

Naden J. and Shepherd T. J. (1989) Role of methane and Carbon dioxide in gold deposition. *Nature* **342**, 793 - 795.

Nakashima S., Disnar J. R., Perruchot A., and Trichet J. (1984) Experimental study of mechanisms of fixation and reduction of uranium by sedimentary organic matter under diagenetic or hydrothermal conditions. *Geochimica et Cosmochimica Acta* **48**, 2321 - 2329.

Neall F. B. and Phillips G. N. (1987) Fluid-wall rock interaction in an Archean hydrothermal gold deposit: a thermodynamic model for the Hunt Mine, Kambalda. *Economic Geology* **82**, 1679-1694.

Nelson D. R. (1995) Compilation of SHRIMP U-Pb zircon geochronology data, 1994. Western Australian Geological Survey Records. **1995/3**.

Nesbitt B. E. and Kyser T. K. (1988) The origin of carbon in Archean lode gold deposits. *Nature* **14**, 506 - 509.

Nesbitt B. E., Murrowchick J. B., and Muehlenbachs K. (1986) Dual origin of lode-gold deposits in the Canadian Cordillera. *Geology* **14**, 506-509.

Newman C. (1993) Junction geological update. WMC Resources, (KNM) Unpublished Internal Report. **217**.

Noever T., Macknight M., Warrington B., Bromley P., and Brown R. (1994) Maclab Peaks.

Nordstrom D. K. and Southam G. (1997) Geomicrobiology of sulphide mineral oxidation. In (ed. B. J.F. and K. H. Nealson), *Geomicrobiology: interactions between microbes and minerals*, 361 - 390. Mineralogical Society of America, Reviews in Mineralogy Washington.

Norman D. I. and Sawkins F. J. (1987) Analysis of volatiles in fluid inclusions by mass spectrometry. *Chemical Geology* **61**, 1-10.

O'Neil J. R. (1987) Preservation of H, C and O isotopic ratios in the low temperature environment. In (ed. T. K. Kyser), *Stable Isotope Geochemistry of Low Temperature Fluids*, Mineralogical Association of Canada Short Course Notes, **13**, 85 - 128.

O'Neil J. R. and Taylor H. P. J. (1967) The oxygen isotope and cation exchange chemistry of feldspars. *American Mineralogist* **52**, 1414 - 1437.

O'Neil J. R., Clayton R. N., and Mayeda T. K. (1969) Oxygen isotope fractionation in divalent

metal carbonates. *Journal of Chemical Physics* **51**, 5547-5558.

Oakes B. W. and Hale M. (1987) Dispersion patterns of carbonyl sulphide above mineral deposits. *Journal of Geochemical Exploration* **28**, 235 - 249.

Oberthur T., Mumm A. S., Vetter U., Simon K., and Amanor J. A. (1996) Gold mineralisation in the Ashanti Belt of Ghana: Genetic Constraints of the stable isotope geochemistry. *Economic Geology* **91**, 289 - 301.

Ohmoto H. (1986) Stable isotope geochemistry of ore deposits. In (ed. J. W. Valley, H. P. J. Taylor, and J. R. O'Neil), *Stable Isotopes in High Temperature Geological Processes* 491-560. Mineralogical Society of America Reviews in Mineralogy.

Ohmoto H. and Rye R. O. (1979) Isotopes of sulphur and carbon. In (ed. H. L. Barnes), *Geochemistry of Hydrothermal Ore Deposits*, 2nd edition 509-567. John Wiley and Sons. New York.

Ohmoto H. and Lasaga A. C. (1982) Kinetics of reactions between aqueous sulphates and sulphides in hydrothermal systems. *Geochimica et Cosmochimica Acta* **46**, 1727 - 1745.

Ohmoto H. and Goldhaber M. B. (1997) Sulphur and carbon isotopes. In (ed. H. L. Barnes), *Geochemistry of hydrothermal ore deposits*, 3rd edition, 517 - 612. John Wiley and Sons. New York.

Oremland R. S. (1981) Microbial formation of ethane in anoxic esturine sediments. *Applied Environmental Microbiology* **42**, 122 - 129.

Oremland R. S. (1988) Biogeochemistry of methanogenic bacteria. In (ed. A. J. B. Zehnder), *Biology of anaerobic organisms* 641-705. Wiley. New York.

Oremland R. S. and Taylor B. F. (1978) Sulphate reduction and methanogenesis in marine sediments. *Geochimica Cosmochimica Acta* **42**, 209-214.

Oremland R. S., Whiticar M. J., Strohmair F. E., and Kiene R. P. (1988) Bacterial ethane formation from reduced, ethylated sulphur compounds in anoxic sediments. *Geochimica et Cosmochimica Acta* **52**, 1895 - 1904.

Parnell J. (1996) Phanerozoic analogues for carbonaceous matter in Witwatersrand ore deposits. *Economic Geology* **91**, 55 - 62.

Peachey D., Nicholson R. A., and Ball T. K. (1985) Discussion on use of carbon dioxide and oxygen in soil gases to detect hidden orebodies. Institute of Mining and Metallurgy *Transactions*, **93**, B201 - B203.

Peden R. (1997) 30,000E, 59851N to 30,000E, 62149N longitudinal map of the Junction Mine: Junction to June 1997, N25 Surface drill intersections. WMC Resources.(KNO) unpublished Map. 1:2000

Perring C. S. and McNaughton N. J. (1992) The relationship between Arcaean gold mineralisation and spatially associated minor intrusions at Kambalda and Norseman gold camps, Western Australia: Lead Isotope evidence. *Mineralium Deposita* **27**, 10 - 22.

Perring C. S., Rock N. M. S., Golding S. D., and Roberts D. E. (1989) Criteria for recognition of metamorphosed or altered lamprophyres: a case study from the Arcaean of Kambalda, Western Australia. *Precambrian Research* **43**, 215 - 237.

Petersilie I. A. (1963) Organic matters in igneous and metamorphic rocks of the Kola Peninsula. In (ed. A. P. Vinogradov), *Chemistry of the Earth's crust.* 178-184.

Petersilie I. A. and Sorensen H. (1970) Hydrocarbons gases and bitumenous substances in rocks from the Illimaussaq alkaline intrusion, South Greenland. *Lithos* **3**, 59-76.

Phillips G. N. (1986) Geology and alteration in the Golden Mile, Kalgoorlie. *Economic Geology* **81**, 779-808.

Phillips G. N. and Groves D. I. (1983) The nature of Archean gold fluids as deduced from gold deposits of Western Australia. *Journal of the Geological Society of Australia* **30**, 25-39.

Phillips G. N. and Groves D. I. (1984) Fluid access and fluid wall-rock interactionin the genesis of the Archaean gold-quartz vein deposit at Hunt Mine, Kambalda, Western Australia. In (ed. R. P. Foster), *Gold '82: The geology, geochemistry and genesis of gold deposits* 389 - 416. A.A. Balkema. Rotterdam.

Polito, P.A. (1993) The geology and geochemistry of the Moorowie copper mine, Northern Flinders Ranges, South Australia. Unpublished Honours thesis. University of Adelaide.

Potter R. W., Clynne M. A., and Brown D. L. (1977) Freezing point depression of aqueous sodium chloride solutions. *Economic Geology* **73**, 284 - 285.

Price L. C. (1986) Primary petroleum migration from shales with oxygen rich organic matter. *Journal of Petroleum Geology* **47**, 28 -36.

Ramsay J. G. and Huber M. I. (1983) The Techniques of Modern Structural Geology, Volume 1: Strain Analysis Academic Press. Orlando.

Reddel C. (1995) Kambalda Region. WMC Resources.(KNO) unpublished map.

Reid A. R. and Rasmussen J. D. (1990) The use of soil-gas CO_2 in the exploration for sulphide bearing breccia pipes in Northern Arizona. *Journal of Geochemical Exploration* **38**, 87 - 101.

Reimer G. M. (1986) Helium soil-gas survey of the Aurora Uranium deposit, McDermitt Caldera Complex, Oregon. *Journal of Geophysical Research* **91**, 12,355 - 12,358.

Reisse J. and Mullie F. (1993) On the origins of organic matter in carbonaceous chondrites. *Pure and Applied Chemistry* **65**, 1281-1292.

Richards J. P. and Kerrich R. (1993) Observations of zoning and fluid inclusions in pyrite using a transmitted infrared light microscope. *Economic Geology* **88**, 716 - 723.

Richet P., Bottinga Y., and Javoy M. (1977) A review of hydrogen, carbon, nitrogen, pxygen, sulphur and chlorine stable isotope fractionation among gaseous molecules. Annual *Reviews in Earth and Planetary Science* **5**, 65 - 110.

Rimstidt J. D. (1997) Gangue mineral transport and deposition. In (ed. H. L. Barnes), *Geochemistry of hydrothermal ore deposits.* 3rd edition, pp. 487 - 516. John Wiley and Sons. New York.

Robert F. and Brown A. C. (1986) Archaean gold bearing quartz veins at the Sigma mine, Abitibi greenstone belt, Quebec. Part 1. Geological relations and formation of the vein system. *Economic Geology* **81**, 578-592.

Robert F. and Kelly W. C. (1987) Ore-forming fluids in Archean gold-bearing quartz veins at the Sigma Mine, Abitibi greenstone belt, Quebec, Canada. *Economic Geology* **82**, 1464-1482.

Robert F., Poulsen K. H., and Dube B. (1994) Structural analysis of lode gold deposits in deformed terranes. Geological Survey of Canada. Ottawa.

Robert F., Boullier A., and Firdaous K. (1995) Gold-quartz veins in metamorphic terranes and their bearing on the role of fluids in faulting. *Journal of Geophysical Research* **100**, 12,861-12,879.

Roberts D. E. (1987) The Golden Mile Dolerite at Junction. WMC Resources,Unpublished Internal memorandum. KNO file, **KJ/3/G**.

Roberts D. E. and Elias M. (1990) Gold deposits of the Kambalda-St Ives region. In (ed. F. E. Hughes), *Geology of the mineral deposits of Australia and Papua New Guinea* 479 - 491. The Australiasian Instititute of Mining and Metallurgy. Melbourne.

Robinson R. (1963) Duplex origin of petroleum. *Nature* **199**, 113 - 114.

Rock N. M. S. (1988) Gold, lamprophyres, and porphyries: What does their association mean? In (ed. R. R. Keays, Ramsay, W.R.H. and Groves, D.I.), *Economic Geology Monograph 6, The Geology of gold deposits: The perspective in 1988.* 609 - 625.

Rock N. M. S., Hallberg J. A., Groves D. I., and Mather P. J. (1988) Archaean lamprophyres in the gold fields of the Yilgarn Block, Western Australia: new indications of their widespread distribution and significance. In (ed. S. E. Ho and D. I. Groves), *Advances in understanding Precambrian gold deposits* **12**, pp. 245 - 275. Geology Department and University Extension, The University of Western Australia.

Roddick J. C. (1984) Emplacement and metamorphism of Archaean mafic volcanics at Kambalda, Western Australia - geochemical and isotopic constraints. *Geochimica et Cosmochimica Acta* **48**, 1305 - 1318.

Roedder E. (1972) The composition of fluid inclusions. USGS Professional Paper **440**.

Roedder E. (1984) *Fluid inclusions*. Mineralogical Society of America, Reviews in Mineralogy. Bookcrafters, Inc. Michigan

Roedder E. and Bodnar R. J. (1980) Geologic pressure determinations from fluid inclusion studies. *Annual Review. Earth and Planetary Science* **8**, 263 - 301.

Roedder E. and Bodnar R. J. (1997) Fluid Inclusion studies of hydrothermal ore deposits. In (ed. H. L. Barnes), *Geochemistry of hydrothermal ore deposits.* 3rd edition, pp. 657 - 698. John Wiley and Sons. New York.

Rollinson H. (1993) *Using geochemical data: evaluation, presentation, interpretation.* John Wiley and Sons. New York

Roper M. (1983) Fischer-Tropsch synthesis. In (ed. W. Keim), *Catalysis in C1 Chemistry,* 41-88. Dordrecht.

Rosaire E. E. (1938) Shallow stratigraphic variations over Gulf Coast structures. *Geophysics* **3**, 96 - 115.

Rosasco G. J. and Roedder E. (1979) Application of a new Raman microprobe spectrometer to nondestructive analysis of sulphate and other ions in individual phases in fluid inclusions in minerals. *Geochimica et Cosmochimica Acta* **43**, 1907 - 1915.

Sackett W. and Chung H. M. (1979) Experimental confirmation of the lack of carbon isotope exchange between methane and carbon dioxides at high temperatures. *Geochimica et Cosmochimica Acta* **43**, 273 - 276.

Salvi S. and Williams-Jones A. E. (1992) Reduced orthomagmatic C-O-H-NaCl fluids in the Strange Lake rare-metal granitic complex, Quebec/Labrador, Canada. *European Jouranal of Mineralogy* **4**, 1155-1174.

Salvi S. and Williams-Jones A. E. (1997) Fischer-Tropsch synthesis of hydrocarbons during sub-solidus alterationof the Strange Lake peralkaline granite, Quebec/Labrador, Canada. *Geochimica et Cosmica Acta* **61**, 83-99.

Santosh M., Nadeau S., and Javoy M. (1995) Stable isotopic evidence for the involvement of mantle-derived fluids in Wynad gold mineralisation, South India. *Journal of Geology* **103**, 718 - 728.

Schonheit P., Kristjansson J. K., and Thauer R. K. (1982) Kinetic mechanism for the ability of sulphate reducers to out-compete methanogens for acetate. *Journal of Archaea Microbiology* **132**, 295-288.

Seitz J. C., Pasteris J. D., and Wopenka B. (1987) Characterisation of CO_2-CH_4-H_2O fluid inclusions by microthermometry and laser Raman microprobe spectrometry: Inferences for clathrate and fluid equilibria. *Geochimica et Cosmochimica Acta* **51**, 1651 - 1664.

Seitz J. C., Pasteris J. D., and Chou I.-M. (1996) Raman spectroscopic characterisation of gas mixtures. II. Quantitative composition and pressure determination of the CO_2-CH_4 system. *American Journal of Science* **296**, 577 - 600.

Seward T. M. (1973) The complexes of gold and the transport of gold in hydrothermal ore solutions. *Geochimica et Cosmochimica Acta* **37**, 377 - 390.

Seward T. M. and Barnes H. L. (1997) Metal transport by hydrothermal ore fluids. In (ed. H. L. Barnes), *Geochemistry of hydrothermal ore deposits*, 3rd edition, pp. 435 - 486. John Wiley and Sons. New York.

Shepherd T. J., Rankin A. H., and Alderton D. H. M. (1985) *A practical guide to fluid inclusion studies*. Blackie and Sons publishers. New York

Sibson R. H. (1990) Faulting and fluid flow. In (ed. B. E. Nesbitt), *Fluids in tectonically active regimes of the continental crust,* Mineralogical Association of Canada Short Course, **18**, 93 - 132.

Sibson R. H., Robert F., and Poulsen K. H. (1988) High angle reverse faults, fluid-pressure cycling and mesothermal gold-quartz deposits. *Geology* **16**, 551 - 555.

Sleat R. and von der Dick H. (1989) Soil microbial hydrocarbon-oxidising activities as a tool for oil and gas prospecting - a new approach. *IGT Symposium, New Orleans, USA*.

Smith T. J. and Kesler S. E. (1985) Relation of fluid inclusion geochemistry to wallrock alteration and lithogeochemical zonation at the Hollinger-McIntyre gold deposit, Timmins, Ontario. *Canadian Institute of Mining and Metallurgy Bulletin* **78**, 35-46.

Smith T. J., Cloke P. L., and Kesler S. E. (1984) Geochemistry of fluid inclusions from the MacIntyre-Hollinger gold deposit, Timmins, Ontario, Canada. *Economic Geology* **79**, 1265 - 1285.

Smith R. E. and Anand R. R. (1990) Geochemical Exploration. In (ed. S. E. Ho, D. I. Groves, and J. M. Bennett), *Gold deposits of the Archaean Yilgarn Block, Western Australia: Nature Genesis and exploration guides.* **20**. Geology Department (Key Centre) and University Extension, The University of Western Australia. Nedlands.

Sokolov V. A. (1935) Summary of the experimental work of the gas survey (in Russian). *Neftyanoye Khoziaistvo* **27**, 28 - 34.

Sokolov V. A. (1959) Investigations into direct oil detection methods. *5th World Petroleum Congress, Proceedings,* New York, pp. 667 - 687.

Solomon D. K. and Cerling T. E. (1987) The annual carbon dioxide cycle in a montane soil: observations, modelling and implications for weathering. *Water Resources Research* **23**, 2257-2265.

Spry P. G., Paredes M. M., Foster F., Truckle J. S., and Chadwick T. H. (1996) Evidence for a

genetic link between gold-silver telluride and porphyry molybdenum mineralization at the Golden Sunlight Deposit, Whitehall, Montana: Fluid inclusion and stable isotope studies. *Economic Geology* **91**, 507-526.

Stahl W., Faber E., Carey B. D., and Kirksey D. L. (1981) Near-surface evidence of migration of natural gas from deep reservoirs and source rocks. *American Association of Petroleum Geologists, Bulletin* **65**, 1543 - 1550.

Statterfield C. and Huff G. A. J. (1982) Carbon number distribution of Fischer-Tropsch products formed on an iron catalyst in a slurry reactor. *Journal of Catalysis* **73**, 187 - 197.

Stedman D. H., Creech M. Z., Cloke P. L., Kesler S. E., and Gardner M. J. (1984) Formation of CS2 and COS from decomposition of metal sulphides. *Geophysical Research Letters* **11**, 858 - 860.

Studier M. H., Hayatsu R., and Anders E. (1968) Origin of organic matter in early solar system - I. Hydrocarbons. *Geochimica et Cosmochimica Acta* **32**, 151 - 173.

Studier M. H., Hayatsu R., and Anders E. (1972) Origin of organic matter in early solar system - V. Further studies of meteorite hydrocarbons and a discussion of their origin. *Geochemica et Cosmochimica Acta* **36**, 189 - 215.

Sugden T., Stanko H., and Bannerman B. (1995) Solid geology of the Kambalda Area, Western Australia incorporating the stratigraphic column for the Kambalda - Tramways corridor. WMC Resources.(KNO) unpublished Map. 1:50,000

Swager C. and Griffin T. J. (1990) An early duplex in the Kalgoorlie - Kambalda greenstone belt, Eastern Goldfields Province, Western Australia. *Precambrian Research* **48**, 63 - 73.

Swager C. P., Witt W. K., Griffen T. J., Ahmat A. L., Hunter W. M., McGoldrick P. J., and Wyche S. (1992) Late-Archaean granite greenstonesof the Kalgoorlie terrane, Yilgarn Craton, Western Australia. In (ed. S. E. Ho, D. I. Groves, and J. M. Bennett), *Gold deposits of the Archaean Yilgarn Block, Western Australia: Nature Genesis and Exploration Guides,* 107 - 122. Geology Department (Key Centre) and University Extension, University of Western Australia. Nedlands.

Szatmari P. (1989) Petroluem formation by Fischer-Tropsch synthesis in plate tectonics. *American Association of Petroluem Geologists Bulletin* **73**, 989-998.

Takenouchi S. and Kennedy G. C. (1965) The solubility of carbon dioxide in NaCl solution at high temperatures and pressures. *American Journal of Science* **263**, 445 - 454.

Taylor C. H., Kesler S. E., and Cloke P. L. (1982) Sulphur gases produced by the decomposition of sulphide minerals: Application to geochemical exploration. *Journal of Geochemical Exploration* **17**, 165 - 185.

Taylor H. P. J. (1987) Stable isotope geochemistry of ore forming fluids. In (ed. T. K. Kyser),

Stable Isotope Geochemistry of Low Temperature Fluids, Mineralogical Association of Canada Short Course Notes, **13**, 337 - 419.

Taylor H. P. (1997) Oxygen and hydrogen isotope relationships in hydrothermal mineral deposits. In (ed. H. L. Barnes), *Geochemistry of hydrothermal ore deposits,* 3rd edition, 229 - 302. John Wiley and Sons. New York.

Thiery R., van den Kerkhof A. M., and Dubessy J. (1994) vX properties of CH_4-CO_2 and CO_2-N_2 fluid inclusions: modelling for T < 31 °C and P < 400 bar. *European Journal of Mineralogy* **6**, 753 - 771.

Tissot B. P. and Welte D. H. (1984) *Petroleum formation and occurrence*. 2nd edition. Springer. Berlin

Urey H. C. (1947) The thermodynamic properties of isotopic substances. *Journal of the Chemical Society* **20,** 562 - 581.

van den Kerkhof A. M. and Thiery R. (1994) Phase transitions and density calculations in the CO_2-CH_4-N_2 system. In (ed. B. De Vivo and M. L. Frezzottii), *Fluid inclusions in minerals: Methods and applications,* 171 - 190. VPI Press.

Vaughan D. J. and Craig J. R. (1997) Sulphide ore mineral stabilities, morphologies, and intergrowth textures. In (ed. Barnes), *Geochemistry of hydrothermal ore deposits*, 3rd edition, 367 - 434. John Wiley and Sons. New York.

Vazquez R., Vennemann T. W., and Kesler S. E. (1998) Carbon and oxygen isotope halos in the Host Limestone, El Mochito Zn-Pb-(ag) Skarn massive sulphide-oxide deposit, Honduras. *Economic Geology* **93**, 15 - 31.

Veevers J. J. (1984) *Phanerozoic Earth History of AustraliaClarendon Press*, Oxford. London

Viellanave J. (1997) Hydrocarbon sampling and analysis for mineral exploration. TEG Rocky Mountain, Denver Colarado,Unpublished technical report to WMC Resources.

Vityk M. O., Bodnar R. J., and Schmidt C. S. (1994) Fluid inclusions as tectonothermobarometers: relation between pressure-temperatre history and reequilibration morphology during crustal thickening. *Geology* **22**, 731 - 734.

Vratislav H., Klaus S., and Vladimir B. (1997) Contrasting chemistry and H, O, C isotope composition of greenschist facies, Hercynian and Alpine metamorphic fluids (Western Carpathians). *Chemical Geology* **136**, 281-293.

Wang L. G., McNaughton N. J., and Groves D. I. (1993) An overview of the relationship between granitoid intrusions and gold mineralisation in the Archaean Murchison Province, Western Australia. *Mineralium Deposita* **28**, 482 - 494.

Watmuff I. G. and Morris B. J. (1993) Soil air carbon dioxide and oxygen measurement as an aid to exploration for concealed sulphide mineralisation in South Australia - a practical

assesment. *AusIMM Centenary Conference*, Adelaide, pp. 63 - 72.

Watson E. B. and Brenan J. M. (1987) Fluids in the lithosphere. 1. Experimentally determined wetting characteristics of CO_2-H_2O fluids and their implications for fluid transport, host-rock physical properties and fluid inclusion formation. *Earth and Planetary Science* **85**, 497 - 515.

Weatherbee G. D. and Bartholomew C. H. (1984) Hydrogenation of CO_2 on Group VIII metals - IV.Specific activities and selectivities of silica-supported Co, Fe, and Ru. *Journal of Catalysis* **87**, 352 - 362.

Welhan J. A. (1988) Origins of methane in hydrothermal systems. *Chemical Geology* **71**, 183 - 198.

Welhan J. A. and Craig H. (1979) Methane and hydrogen in East Rise hydrothermal fluids. *Geophysical Research Letters* **6**, 829 - 832.

Wenrich K. J. (1985) Mineralisation of Breccia pipes in northern Arizona. *Economic Geology* **80**, 1722 - 1735.

Whitkamp M. (1969) Cycles of temperature and carbon dioxide evolution from litter and soil. *Ecology* **50**, 922-924.

Whitman W. B. (1985) Methanogenic bacteria. In (ed. C. R. Woese and R. S. Wolfe), *The Bacteria,* 3-84. Academic Press. New York.

Whitman W. B., Bowen T. L., and Boone D. R. (1991) The methanogenic bacteria. In (ed. A. Balows, H. G. Truper, M. Dworkin, W. Harder, and K. J. Schleifer), *The Prokaryotes,* 719 - 767. Spinger-Verlag. New York.

Witt W. K. (1992) Gold deposits of the Kalgoorlie - Kambalda - St Ives area, Western Australia. Geological Survey of Western Australia unpublished report, **1992/15**.

Witt W. K. (1993) Lithological and structural controls on gold mineralisation in the Archaean Menzies - Kambalda area, Western Australia. *Australian Journal of Earth Science* **40**, 65 - 86.

Witt W. K. and Vanderhor F. (1998) Diversity within a unified model for Archaean gold mineralisation in the Yilgarn Craton of Western Australia: An overview of the late-orogenic, structurally-controlled gold deposits. *Ore Geology Reviews* **13**, 29 - 64.

Witt W. K., Knight J. T., and Mikucki E. J. (1997) A synmetamorphic lateral fluid flow model for gold mineralisation in the Archaean Southern Kalgoorlie and Norseman Terranes, Western Australia. *Economic Geology* **92**, 407-437.

Witt W. K., Hickman A. H., Townsand D., and Preston W. A. (1998) Mineral Potential of the Archaean Pilbara and Yilgarn Cratons, Western Australia. *AGSO Journal of Geology and Geophysics* **17**, 201 - 221.

Wood P. C., Burrows D. R., and Spooner E. T. C. (1986a) Au-quartz vein and intrusion-hosted Cu-Au-Ag-Mo mineralization, Hollinger-McIntyre Mines, Timmins, Ontario: geological characteristics, structural examination, igneous and hydrothermal alteration geochemistry, and light stable isotope (hydrogen and oxygen) geochemistry. Ontario Geological Survey Miscellaneous Paper 130, p. 56-80,

Wood P. C., Burrows D. R., Thomas A. V., and Spooner E. T. C. (1986b) The Hollinger-McIntrye Au-quartz vein system, Timmins, Ontario, Canada: geologic characteristics, fluid properties and light stable isotope geochemistry. *Proceedings of Gold '86, Toronto*, pp. 56-80.

Wood S. A. (1996) The role of humic substances in the transport and fixation of metals of economic interest (Au, Pt, Pd, U, V). *Ore Geology Reviws* **11**, 1 - 31.

Woodall R. (1979) Gold - Australia and the world. In (ed. J. E. Glover and D. I. Groves), *Gold mineralisation1* - **3**. Geology Department and University Extension Service, The University of Western Australia, Publication. Nedlands.

Woolrich N. K. (1994) The Stratigraphy and gold mineralisation of the Argo Tertiary palaeochannel at Kambalda, Western Australia. unpublished Honours thesis, Curtin University of Technology.

Zhang Y. and Frantz J. D. (1992) Hydrothermal reactions involving equilibrium between minerals and mixed volatiles: 2. Investigations of fluid properties in the CO_2-CH_4-H_2O system using synthetic fluid inclusions. *Chemical Geology* **100**, 51 - 72.

Zheng Y.-F. and Hoefs J. (1993) Carbon and Oxygen isotopic covariations in hydrothermal calcites. *Mineralium Deposita* **28**, 79 - 89.

Appendices

Appendix I:	Sample numbers and drill hole/ drive sampled	A1.1
Appendix II:	Labelled SEM images	A2.1
Appendix III:	Electron microprobe traverse results: Sample 1074 - 50	A3.1
	Electron microprobe traverse results: Sample 1074 - 91	A3.2
	Electron microprobe traverse results: Sample 1074 - 226	A3.3
	Electron microprobe traverse results: Sample 1074 - 237	A3.4
Appendix IV:	X-ray diffraction results	A4.1
Appendix V:	Junction soil-gas survey results over the N75 surface	A5.1
Appendix VI:	Fluid inclusion database	A6.1
Appendix VII:	EDTA-Gas chromatography database	A7.1

Appendix I. Sample numbers and drill hole / drive sampled

University Sample Number	WMC Sample Number	Drill Hole Number	Drill hole sample interval or drive location
1074-000			Argo open pit
1074-001			Argo open pit
1074-002			Argo open pit
1074-003			Argo open pit
1074-004			Argo open pit
1074-005			Argo open pit
1074-006			Argo open pit
1074-007			Argo open pit
1074-008			Argo open pit
1074-009			Argo open pit
1074-010			Revenge u-ground
1074-011			Revenge u-ground
1074-012			Revenge u-ground
1074-013			402-3 / Zone 2
1074-014			402-3 / Zone 2
1074-015			402-3 / Zone 2
1074-016			402-3 / Zone 2
1074-017			502-1A / Zone 3
1074-018			512-1 X-cut. Z4
1074-019			512-1 X-cut. Z4
1074-020			502-1B / Zone 3
1074-021			502-1 X-cut. Z3
1074-022			403-3 Sth / Z3 - Z4
1074-023			403-3 Sth / Z3 - Z4
1074-024			Unknown location
1074-025			405-3 Nth / Zone 4
1074-026			405-3 Nth / Zone 4
1074-027			405-3 Nth / Zone 4
1074-028			201-2 Sth / Zone 4
1074-029			202-2 Sth / Zone 3
1074-030			202-2 Sth / Zone 3
1074-031			402-3 Sth / Zone 2
1074-032			402-3 Sth / Zone 2
1074-033			402-3 Sth / Zone 2
1074-034			402-3 Sth / Zone 2
1074-035			502-1B / Zone 3
1074-036			405-2 Nth / Zone 4
1074-037			405-2 Nth / Zone 4
1074-038			405-4 Nth / Zone 4
1074-039			405-4 Nth / Zone 4
1074-040			405-4 Nth / Zone 4
1074-041			405-4 Nth / Zone 4
1074-042			202-0 Slot/ Zone 3
1074-043			202-0 Slot/ Zone 3
1074-044			202-0 Slot/ Zone 3
1074-045			202-0 Slot/ Zone 3
1074-046			202-0 Slot/ Zone 3
1074-047			202-0 Slot/ Zone 3

University Sample Number	WMC Sample Number	Drill Hole Number	Drill hole sample interval or drive location
1074-048			No Sample
1074-049			301-3-54Sth / Z4
1074-050			301-3-54Sth / Z4
1074-051			402-3 Nth / Zone 2
1074-052			403-3 Sth / Zone 4
1074-053			403-3 Sth / Zone 4
1074-054			403-3 Sth / Zone 4
1074-055			403-3 Sth / Zone 4
1074-056			301-2-62 Nth/ Z4
1074-057			301-2-62 Nth/ Z4
1074-058			No Sample
1074-059			No Sample
1074-060			No Sample
1074-061			No Sample
1074-062			No Sample
1074-063			No Sample
1074-064			No Sample
1074-065			405-1 / Zone 4
1074-066			405-1 / Zone 4
1074-067			405-1 / Zone 4
1074-068			405-1 / Zone 4
1074-069			405-1 / Zone 4
1074-070			502-1-25 / Zone 3
1074-071			No Sample
1074-072			No Sample
1074-073			No Sample
1074-074			No Sample
1074-075			502-1-25 / Zone 3
1074-076			502-1-25 / Zone 3
1074-077			502-1-25 / Zone 3
1074-078			502-1-25 / Zone 3
1074-079			502-1-25 / Zone 3
1074-080			502-1-25 / Zone 3
1074-081			502-1-25 / Zone 3
1074-082			502-1-25 / Zone 3
1074-083			502-1-25 / Zone 3
1074-084			502-1-25 / Zone 3
1074-085			502-1-25 / Zone 3
1074-086			502-1-25 / Zone 3
1074-087			502-1-25 / Zone 3
1074-088			502-1-25 / Zone 3
1074-089			
1074-090			
1074-091			502-1-25 / Zone 3
1074-092			502-1-25 / Zone 3
1074-093			502-1-25 / Zone 3
1074-094			502-1-25 / Zone 3
1074-095			502-1-25 / Zone 3
1074-096			502-1-25 / Zone 3
1074-097			502-1-25 / Zone 3

University Sample Number	WMC Sample Number	Drill Hole Number	Drill hole sample interval or drive location
1074-099			502-1-25 / Zone 3
1074-100			502-1-25 / Zone 3
1074-101			502-1-25 / Zone 3
1074-102			502-1-25 / Zone 3
1074-103			502-1-25 / Zone 3
1074-104			502-1-25 / Zone 3
1074-105			502-1-25 / Zone 3
1074-106			502-1-25 / Zone 3
1074-107			
1074-108			502-1-25 / Zone 3
1074-109			502-1-25 / Zone 3
1074-110			405-1 / Zone 4
1074-111			405-1 / Zone 4
1074-112			405-1 / Zone 4
1074-113			405-1 / Zone 4
1074-114			405-1 / Zone 4
1074-115			405-1 / Zone 4
1074-116			405-1 / Zone 4
1074-117			405-1 / Zone 4
1074-118			405-1 / Zone 4
1074-119			405-1 / Zone 4
1074-120			405-1 / Zone 4
1074-121			405-1 / Zone 4
1074-122			405-1 / Zone 4
1074-123			405-1 / Zone 4
1074-124			405-1 / Zone 4
1074-125			405-1 / Zone 4
1074-126			405-1 / Zone 4
1074-127			405-1 / Zone 4
1074-128			405-1 / Zone 4
1074-129			405-1 / Zone 4
1074-130			405-1 / Zone 4
1074-131			405-1 / Zone 4
1074-132			405-1 / Zone 4
1074-133			405-1 / Zone 4
1074-134			405-1 / Zone 4
1074-135			405-1 / Zone 4
1074-136			405-1 / Zone 4
1074-137			405-1 / Zone 4
1074-138			405-1 / Zone 4
1074-139			405-1 / Zone 4
1074-140			405-1 / Zone 4
1074-141			405-1 / Zone 4
1074-142			405-1 / Zone 4
1074-143			405-1 / Zone 4
1074-144			405-1 / Zone 4
1074-145			
1074-146			405-1 / Zone 4
1074-147			405-1 / Zone 4
1074-148			405-1 / Zone 4

University Sample Number	WMC Sample Number	Drill Hole Number	Drill hole sample interval or drive location
1074-150			405-1 / Zone 4
1074-151			502-1-25 / Zone 3
1074-152			502-1-25 / Zone 3
1074-153			
1074-154			
1074-155			
1074-156			
1074-157			502-1-25 / Zone 3
1074-158			
1074-180	68815	JT5-18	2.2 - 2.35m
1074-181	68816	JT5-18	21.3 - 21.4m
1074-182	68817	JT5-18	127.0 - 127.08m
1074-183	68818	JT5-36	13.8 - 13.85m
1074-184	68819	JT5-36	28.35 - 28.45m
1074-185	68820	JT5-36	67.0 - 67.2m
1074-186	68821	JT5-36	79.0 - 79.12m
1074-187	68822	JT5-36	131.25 - 131.39m
1074-188	68823	JT5-36	155.4 - 155.55m
1074-189	68824	JT4-194	30.25 - 30.50m
1074-190	68825	JT4-198	22.24 - 22.44m
1074-191	68826	JT4-198	21.2 - 21.4m
1074-192	68827	JT5-41	10.1 - 10.2m
1074-193	68828	JT5-41	1.5 - 1.6m
1074-194	68829	JT5-42	0.45 - 0.55m
1074-195	68830	JT5-39	7.7 - 7.9m
1074-196	68831	JT5-39	15.25 - 15.32m
1074-197	68832	JT4-195A	17.6 - 17.8m
1074-198	68833	JT5-18	15.3 - 15.35m
1074-199	68834	JT5-18	103.5 - 103.7m
1074-200	68835	JT4-144	0.35 - 0.45m
1074-201	68836	JT4-144	2.1 - 2.3m
1074-202	68837	JT5-52	127.4 - 127.7m
1074-203	68838	JT5-52	85.75 - 85.8m
1074-204	68839	JT3-112	44.7 - 44.9m
1074-205	68840	JT3-112	69.4 - 69.45m
1074-206	68841	JT3-112	107.3 - 107.5m
1074-207	68842	JT5-54	13.2 - 13.3m
1074-208	68843	JT2-73	47.3 - 47.45m
1074-209	68844	JT2-73	48.35 - 48.45m
1074-210	68845	JT2-127	73.9 - 74m
1074-211	68846	JT2-127	75.75 - 75.8m
1074-212	68847	JT2-127	85.3 - 85.55m
1074-213	68848	JT2-136	31.5 - 31.7m
1074-214	68849	JT2-136	39.5 - 39.7m
1074-215	68850	JT4-31	31.15 - 31.3m
1074-216	68851	JT4-31	85.5 - 85.55m
1074-217	68852	JT4-31	87.5 - 87.7m
1074-218	68853	JT4-46	134.1 - 134.2m
1074-219	68854	JT4-46	134.8 - 135m
1074-220	68855	JT4-52	43.15 - 43.3m

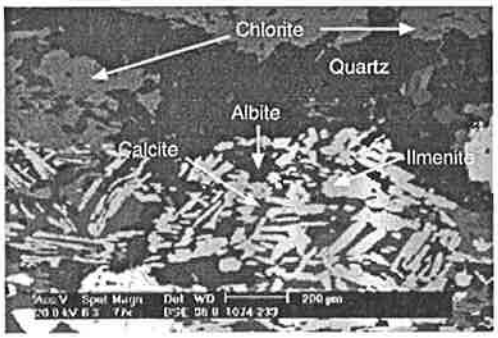
University Sample Number	WMC Sample Number	Drill Hole Number	Drill hole sample interval or drive location
1074-222	68857	JT4-52	45.8 - 46m
1074-223	68858	JT4-53	57.7 - 57.9m
1074-224	68859	JT4-53	66.7 - 66.8m
1074-225	68860	JT4-53	68.8 - 69m
1074-226	68861	JT2-73	48.9 - 49m
1074-227	68862	JT4-80	122.2 - 122.4m
1074-228	68863	JT4-80	124.3 - 124.5m
1074-229	68864	TD2805	689.8 - 689.85m
1074-230	68865	TD2805	694.6 - 694.7m
1074-231	68866	TD4083	447.5 - 447.65m
1074-232	68867	TD4084	518.3 - 518.5m
1074-233	68868	TD5684	985.1 - 985.2m
1074-234	68869	TD2808	626 - 626.5m
1074-235	68870	TD2809	628.15 - 628.25m
1074-236	68871	TD2836	442.3 - 442.5m
1074-237	68872	TD2836	475.5 - 475.6m
1074-238	68873	TD2836	485.8 - 485.9m
1074-239	68874	TD2842	643.2 - 643.4m
1074-240	68875	TD2842	644.6 - 644.8m
1074-241	68876	TD2844	511.1 - 511.2m
1074-242	68877	TD2844	511.5 - 511.7m
1074-243	68878	TD2844	524.2 - 524.4m
1074-244	68879	TD2844	525 - 525.2m
1074-245	68880	TD1478	127.5 - 127.75m
1074-246	68881	TD1478	174.5 - 174.6m
1074-247	68882	TD1498	176.1 - 176.2m
1074-248	68883	TD1498	175.75 - 175.85m
1074-248	68883	TD1498	175.75 - 175.85m
1074-249	68884	TD1506	68.8 - 69m
1074-250	68885	TD1506	66.8 - 67m
1074-251	68886	TD1506	85.6 - 85.8m
1074-251	68886	TD1506	85.6 - 85.8m
1074-252	68887	TD1507	86.1 - 86.4m
1074-252A	68887	TD1507	86.1 - 86.4m
1074-253	68888	TD1511	93.5 - 93.65m
1074-254	68889	TD1511	95.4 - 95.55m
1074-255	68890	TD1511	98.5 - 98.55m
1074-256	68891	TD2239A	540 - 540.15m
1074-257	68892	TD2239A	540.8 - 541m
1074-258	68893	TD2967	293.7 - 293.75m
1074-259	68894	TD2967	296 - 296.1m
1074-260	68895	TD2967	298.2 - 298.35m
1074-261	68896	TD2836	468.8 - 468.9m
1074-262	68897	TD2836	461 -461.2m
1074-263	68898	TD2836	336.8 - 337m
1074-264	68899	TD2836	403.8 - 403.9m
1074-265	68900	TD2836	377.9 - 378m
1074-266	57284	TD2836	347.0 - 347.15m
1074-267	57285	TD2836	330.8 - 330.9m
1074-268	57286	TD5684	970.9 - 971m

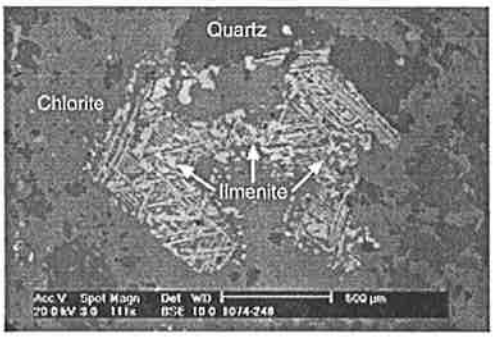
Appendix 3.1 Junction Samples

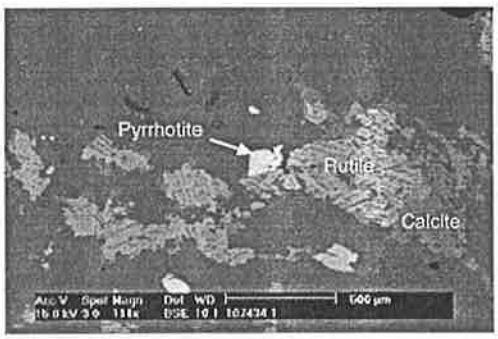
University Sample Number	WMC Sample Number	Drill Hole Number	Drill hole sample interval or drive location
1074-270	57288	TD5684	958.8 - 959m
1074-271	57289	TD5684	935.2 - 935.4m
1074-272	57290	TD5684	907.1 - 907.25m
1074-273	57291	TD5684	859.6 - 859.8m
1074-274	57292	TD1506	157.0 - 156.8m
1074-275	57293	TD1506	144.0 - 144.1m
1074-276	57294	TD1506	121.3 - 121.4m
1074-277	57295	TD1506	99.1 - 99.2m
1074-278	57296	TD1506	72.5 - 72.8m
1074-279	57297	TD2158	186.7 - 186.9m
1074-280	57298	TD2158	187.1 - 187.2m
1074-281	57299	TD2158	188.25 - 188.35m
1074-282	57300	TD2202	125.0 - 125.2m
1074-282		TD2202	
1074-283	JP174402		501-4 acc (F23)
1074-284	JP174403		611-0 acc (F23)
1074-285	JP174404		501-3 refuge (F23)
1074-286	JP167891		401-1-100N

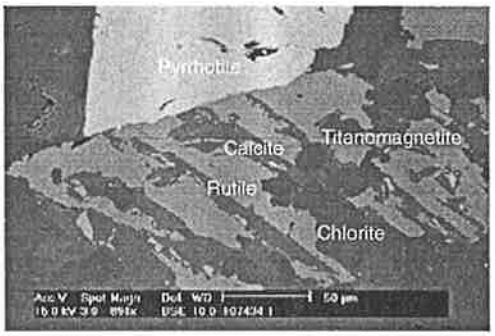
Appendix 3.1 Junction Samples

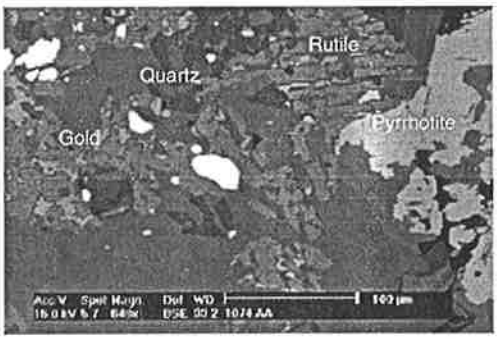
Appendix II. Labelled SEM images.

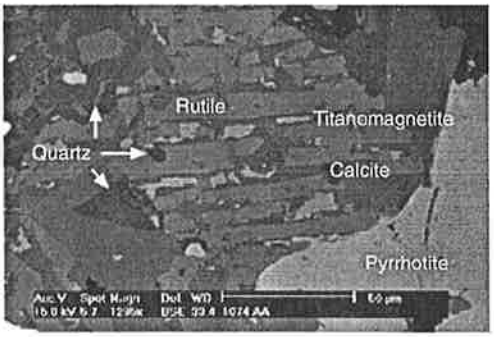


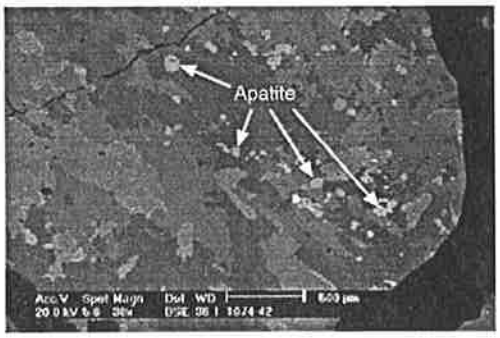


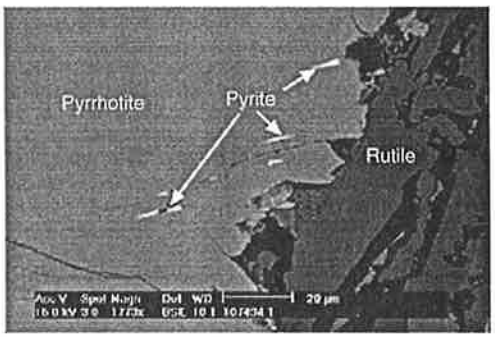










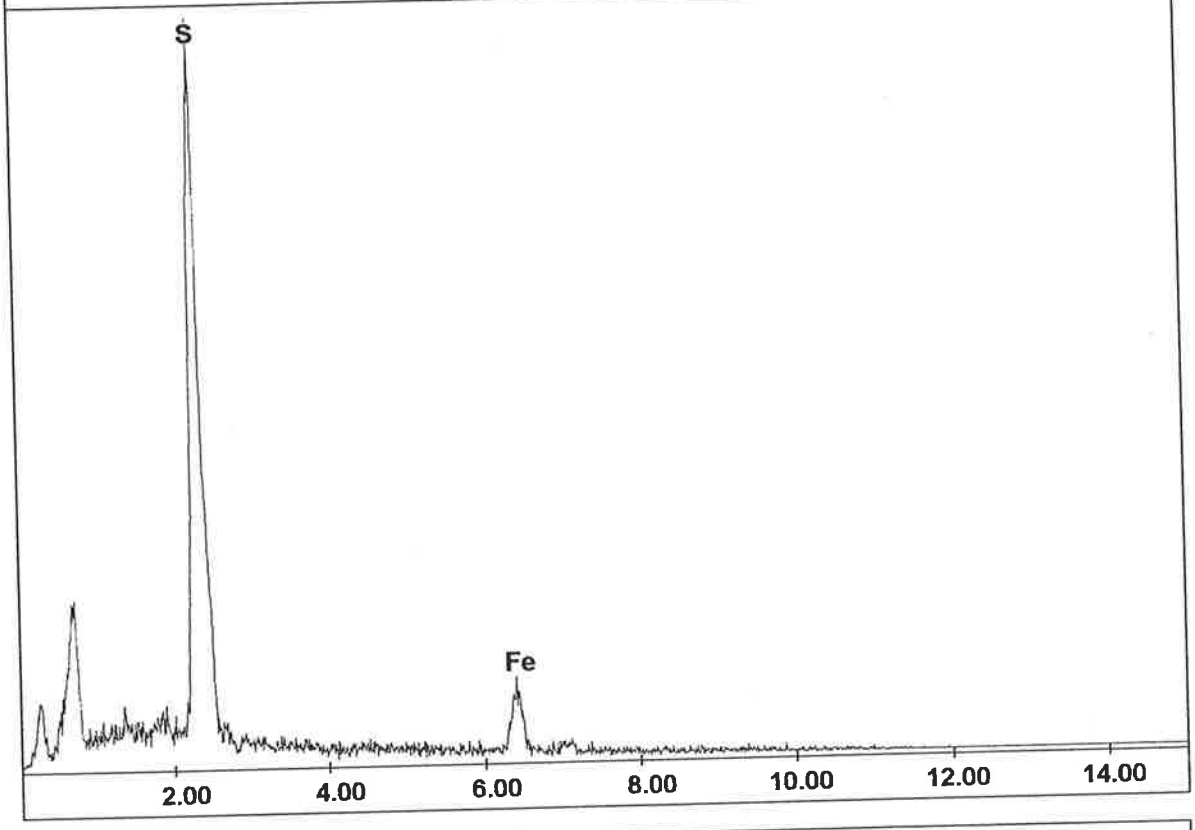


Untitled:5 — Pyrite

Label:1074-34 Pyrite

kV:15.0 Tilt:0.0 Take-off:35.0 Det Type:SUTW+ Res:151 Tc:20

FS : 620 Lsec : 50 8-Oct-98 11:46:31



EDAX ZAF Quantification (Standardless)
Element Normalized

Element	Wt %	At %	K-Ratio	Z	A	F
S K	64.34	75.86	0.6081	1.0395	0.9080	1.0014
FeK	35.66	24.14	0.3230	0.9208	0.9839	1.0000
Total	100.00	100.00				

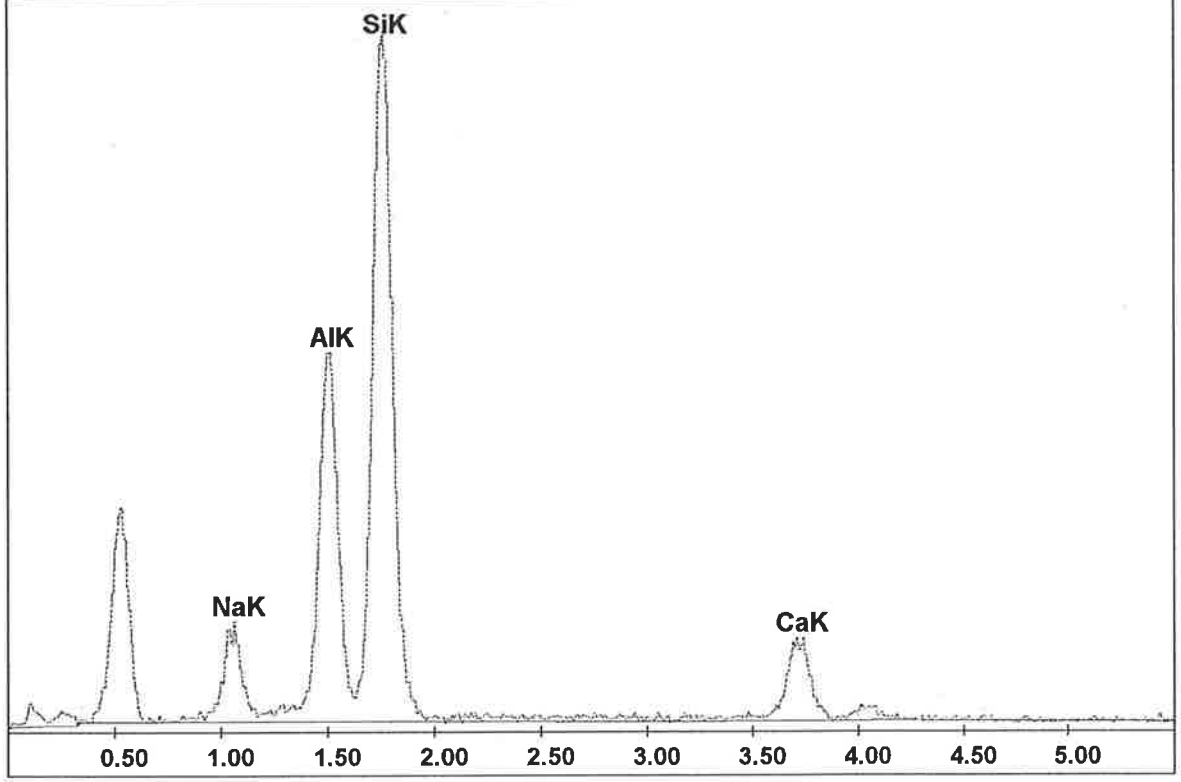
Element	Net Inte.	Bkgd Inte.	Inte. Error	P/B
S K	117.78	4.56	1.33	25.83
FeK	14.38	1.02	3.86	14.10

Albite

Label:1074-233

kV:20.0 Tilt:0.0 Take-off:36.7 Det Type:SUTW+ Res:138 Tc:40

FS : 1654 Lsec : 30 12-Oct-98 10:10:33



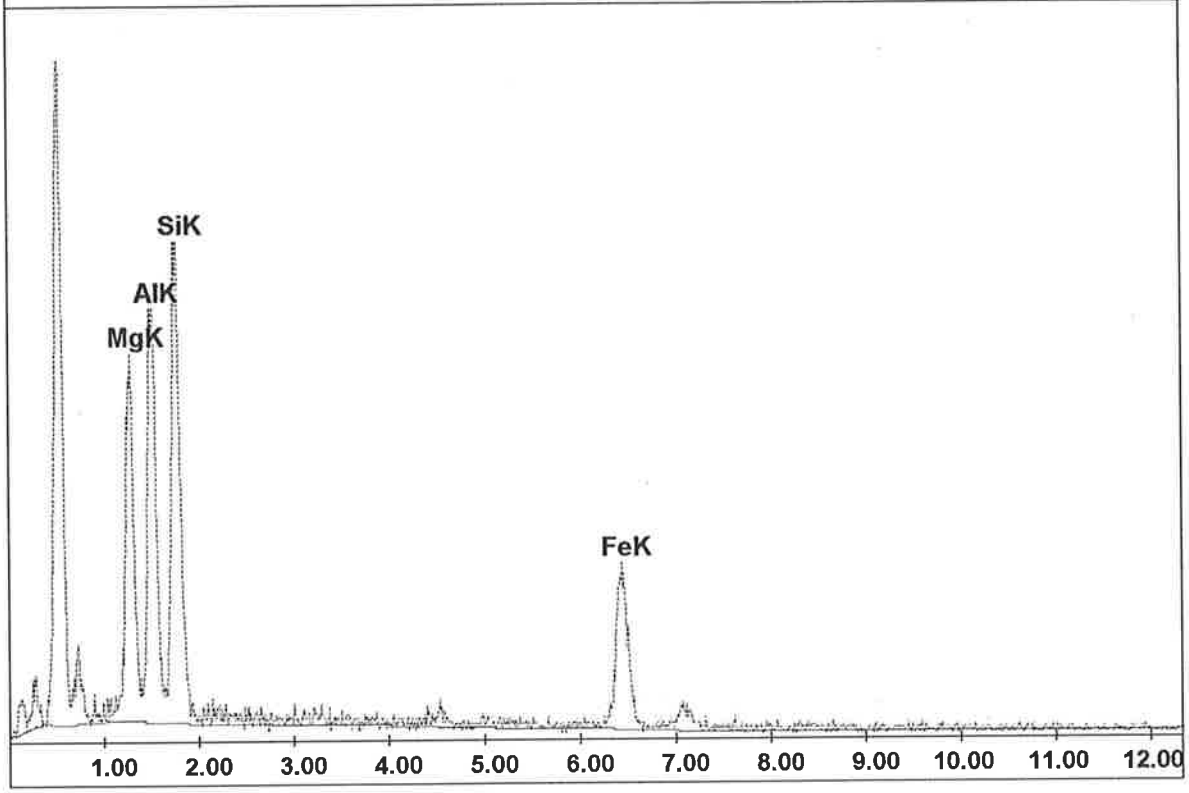
EDAX ZAF Quantification (Standardless)
Oxides

Element	Wt %	At %	K-Ratio	Z	A	F
Na2O	6.75	7.27	0.0205	0.9619	0.4245	1.0045
Al2O3	25.08	16.43	0.0876	0.9571	0.6827	1.0104
SiO2	61.57	68.45	0.1901	0.9850	0.6701	1.0005
CaO	6.59	7.85	0.0417	0.9560	0.9249	1.0000
Total	100.00	100.00				

Chlorite

Label:1074 AA 6

kV:15.0	Tilt:0.0	Take-off:36.7	Det Type:SUTW+	Res:138	Tc:40
FS : 419		Lsec : 30		8-Oct-98	10:01:06



EDAX ZAF Quantification (Standardless)
Oxides

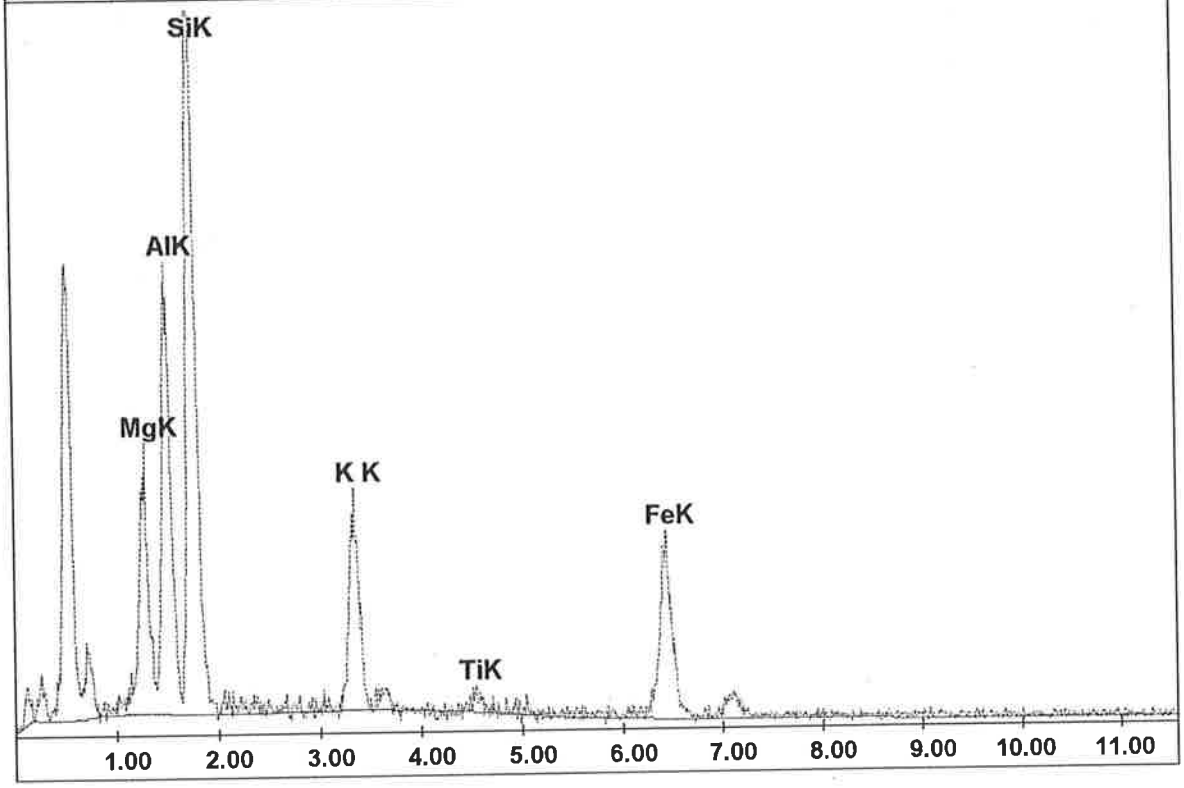
Element	Wt %	At %	K-Ratio	Z	A	F
MgO	16.01	30.84	0.0551	1.0096	0.5632	1.0035
Al2O3	21.32	16.24	0.0702	0.9795	0.6328	1.0031
SiO2	27.88	36.02	0.0895	1.0061	0.6822	1.0003
Fe2O3	34.79	16.91	0.2143	0.8784	1.0025	1.0000
Total	100.00	100.00				

Biotite

Label:1074 AA 3

kV:15.0 Tilt:0.0 Take-off:36.7 Det Type:SUTW+ Res:138 Tc:40

FS : 448 Lsec : 30 8-Oct-98 09:50:59



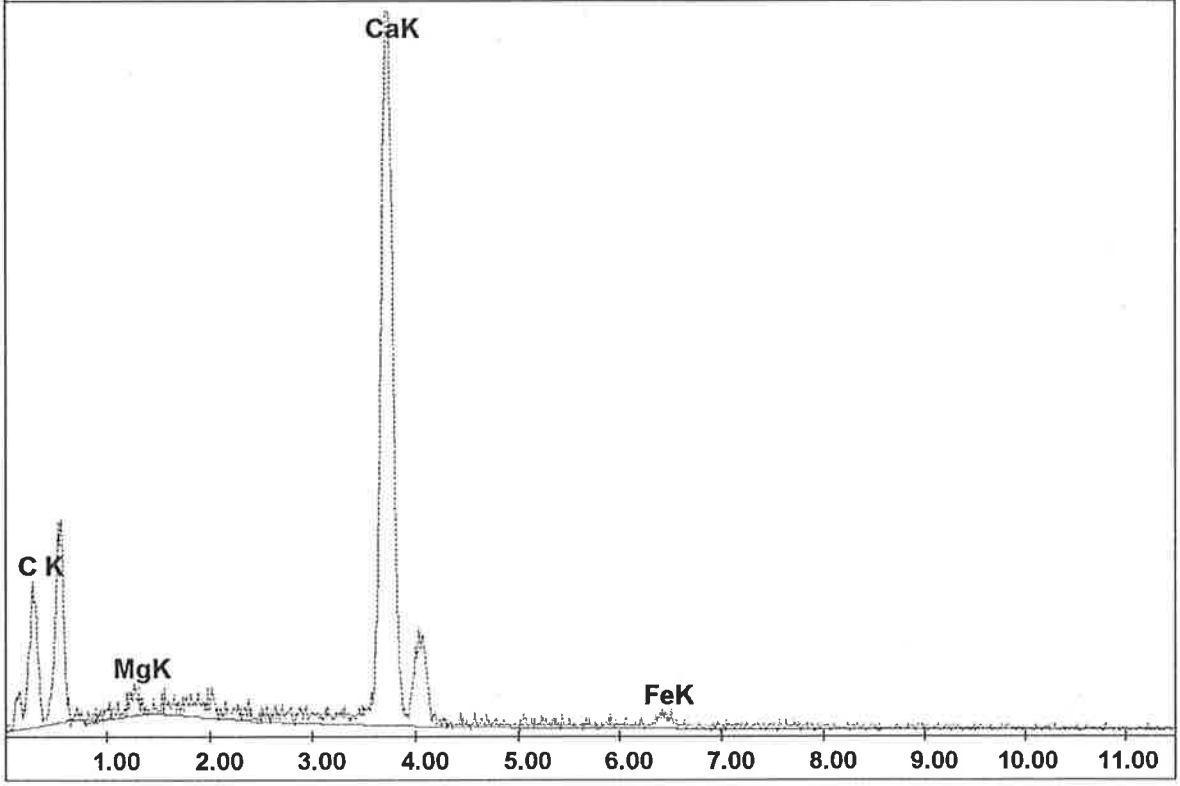
EDAX ZAF Quantification (Standardless)
Oxides

Element	Wt %	At %	K-Ratio	Z	A	F
MgO	8.89	17.64	0.0307	1.0109	0.5642	1.0039
Al2O3	16.55	12.98	0.0571	0.9808	0.6612	1.0045
SiO2	34.26	45.61	0.1160	1.0077	0.7181	1.0010
K2O	7.84	6.66	0.0589	0.9544	0.9421	1.0056
TiO2	1.67	1.68	0.0089	0.8877	0.9772	1.0218
Fe2O3	30.79	15.42	0.1892	0.8798	0.9986	1.0000
Total	100.00	100.00				

Calcite

Label:1074 AA Calcite

kV:15.0	Tilt:0.0	Take-off:36.7	Det Type:SUTW+	Res:138	Tc:40
FS : 538		Lsec : 30		8-Oct-98	09:53:29



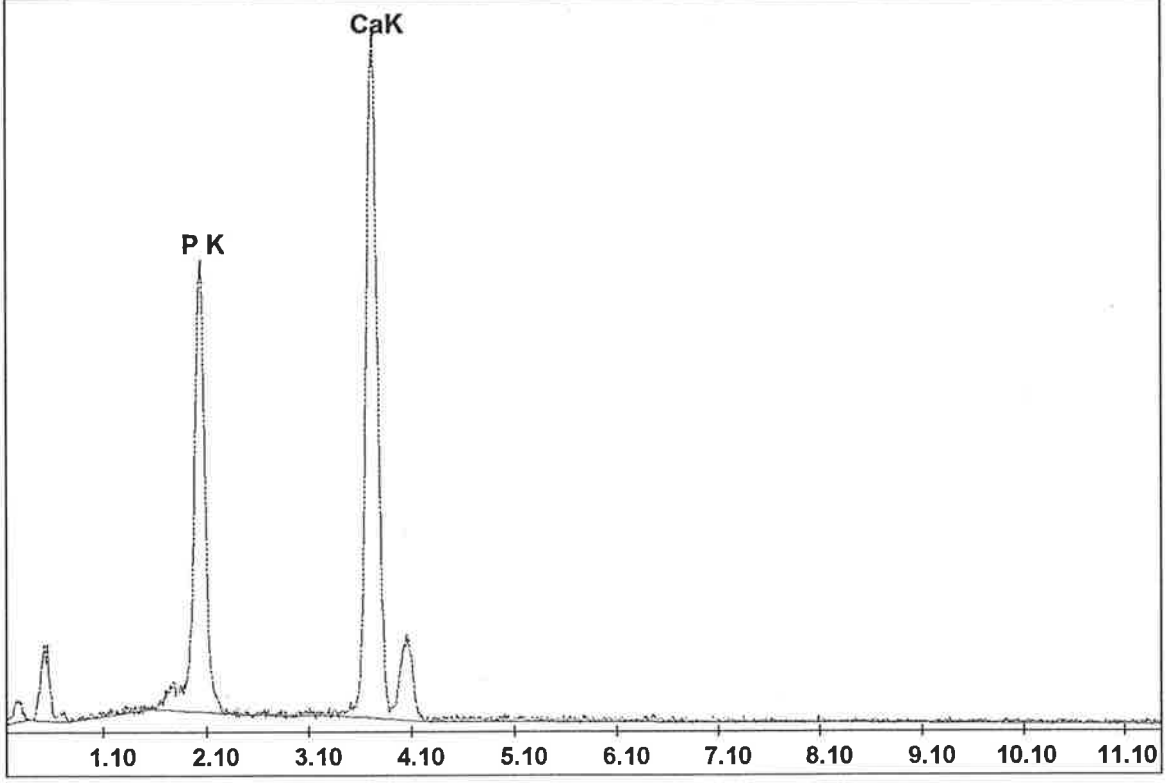
EDAX ZAF Quantification (Standardless)
Oxides

Element	Wt %	At %	K-Ratio	Z	A	F
CO2	42.08	48.97	0.0553	1.0498	0.4586	1.0009
MgO	1.33	1.69	0.0046	0.9840	0.5819	1.0011
CaO	52.65	48.08	0.3588	0.9479	1.0048	1.0011
Fe2O3	3.94	1.26	0.0232	0.8545	0.9866	1.0000
Total	100.00	100.00				

Apatite

Label:1074-248

kV:20.0	Tilt:0.0	Take-off:36.7	Det Type:SUTW+	Res:138	Tc:40
FS : 1739		Lsec : 30		12-Oct-98	10:00:03

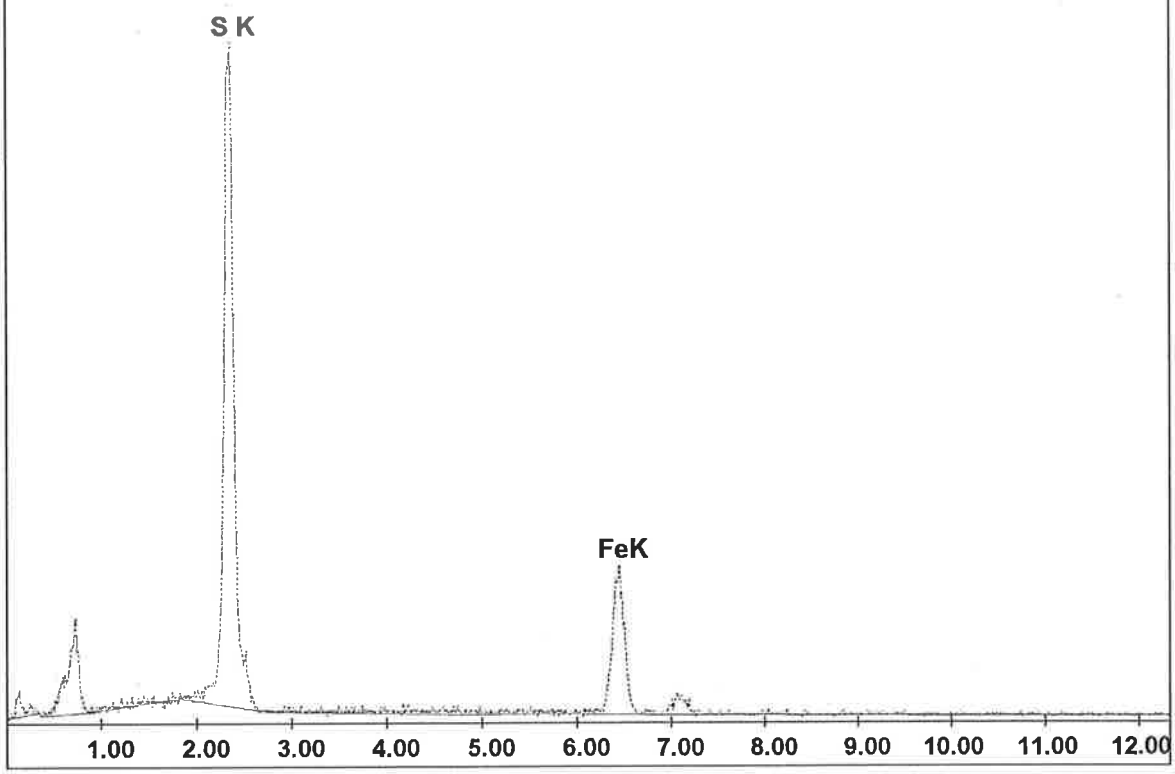


EDAX ZAF Quantification (Standardless)
Oxides

Element	Wt %	At %	K-Ratio	Z	A	F
P2O5	42.29	22.45	0.1514	0.9632	0.8428	1.0106
CaO	57.71	77.55	0.3840	0.9700	0.9598	1.0000
Total	100.00	100.00				

Element	Net Inte.	Bkgd Inte.	Inte. Error	P/B
P K	306.57	13.00	1.06	23.58
CaK	533.37	8.70	0.80	61.31

Pyrrhotite					
Label:1074 AA 7					
kV:15.0	Tilt:0.0	Take-off:36.7	Det Type:SUTW+	Res:138	Tc:40
FS : 1057		Lsec : 30		8-Oct-98	10:07:56



EDAX ZAF Quantification (Standardless)
Element Normalized

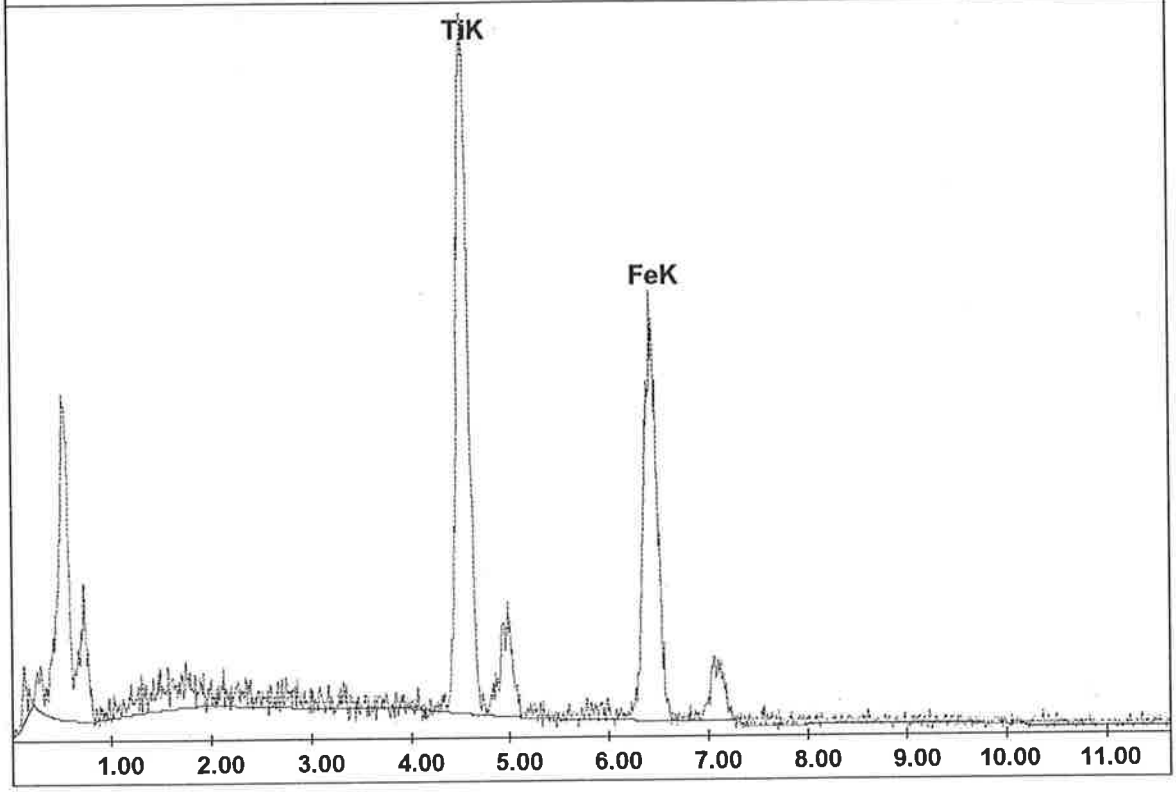
Element	Wt %	At %	K-Ratio	Z	A	F
S K	45.43	59.19	0.4202	1.0626	0.8687	1.0020
FeK	54.57	40.81	0.5086	0.9423	0.9890	1.0000
Total	100.00	100.00				

Element	Net Inte.	Bkgd Inte.	Inte. Error	P/B
S K	280.90	6.53	1.10	42.99
FeK	78.03	2.00	2.09	39.02

Ilmenite

Label:1074 AA 2

kV:15.0	Tilt:0.0	Take-off:36.7	Det Type:SUTW+	Res:138	Tc:40
FS : 370		Lsec : 30		8-Oct-98	09:45:27



EDAX ZAF Quantification (Standardless)
Oxides

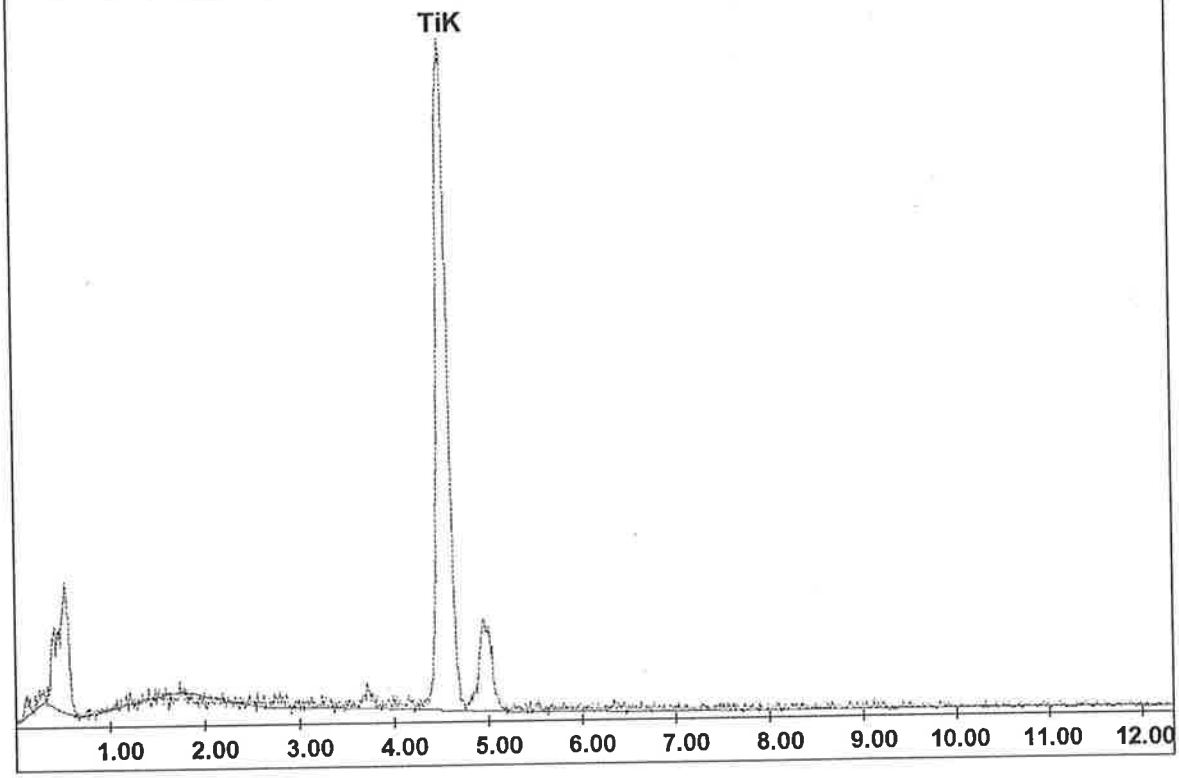
Element	Wt %	At %	K-Ratio	Z	A	F
TiO2	44.61	61.69	0.2577	0.9333	0.9969	1.0355
Fe2O3	55.39	38.31	0.3540	0.9271	0.9858	1.0000
Total	100.00	100.00				

Element	Net Inte.	Bkgd Inte.	Inte. Error	P/B
TiK	122.60	4.33	1.68	28.29
FeK	80.30	2.50	2.07	32.12

Rutile

Label:1074 AA Rutile

kV:15.0	Tilt:0.0	Take-off:36.7	Det Type:SUTW+	Res:138	Tc:40
FS : 630	Lsec : 30			8-Oct-98	09:58:13



EDAX ZAF Quantification (Standardless)
Oxides

Element	Wt %	At %	K-Ratio	Z	A	F
TiO2	100.00	100.00	0.5564	0.9232	1.0054	1.0000
Total	100.00	100.00				

Element	Net Inte.	Bkgd Inte.	Inte. Error	P/B
TiK	200.47	2.27	1.30	88.44

Appendix III. Sample 1074-50 - Electron microprobe traverse results

Point number	O	Ca	Mg	Mn	Fe	Total	Fe:Mn
1	45.49	14.00	4.45	0.18	13.32	77.43	76.10
2	46.80	41.69	0.00	0.72	1.31	90.52	1.81
3	49.48	38.11	0.51	0.59	1.78	90.46	2.99
4	50.05	26.27	5.43	0.09	1.26	83.11	13.41
5	45.49	34.92	1.03	0.70	2.45	84.59	3.52
6	50.28	41.71	0.00	0.42	0.69	93.11	1.65
7	51.90	37.59	1.15	0.21	0.23	91.07	1.08
8	51.96	39.43	0.19	0.13	0.14	91.85	1.11
9	51.00	42.02	0.00	0.09	0.12	93.23	1.28
10	47.97	41.21	0.00	0.40	0.96	90.54	2.39
11	48.46	41.25	0.10	0.56	1.58	91.96	2.85
12	47.68	41.46	0.04	0.50	1.15	90.82	2.31
13	44.91	41.25	0.44	0.66	2.02	89.27	3.07
14	44.10	40.81	0.63	0.61	2.25	88.41	3.69
15	46.38	40.70	0.57	0.59	2.51	90.74	4.28
16	29.19	0.16	7.70	0.03	15.69	52.77	603.62
17	50.89	39.53	0.27	0.52	1.70	92.92	3.26
18	47.23	40.11	0.41	0.58	1.95	90.29	3.36
19	44.10	40.68	0.57	0.59	1.93	87.87	3.25
20	50.64	38.36	0.48	0.56	1.73	91.76	3.08

Values are given as bulk percentages minus carbon (±silica)

Appendix III. Sample 1074-91 - Electron microprobe traverse results

Point number	O	Ca	Mg	Mn	Fe	Total	Fe:Mn
1	48.86	19.93	7.99	0.52	10.13	87.43	0.07
2	55.18	19.10	7.73	0.44	8.84	91.29	0.06
3	49.64	20.25	10.17	0.60	6.27	86.93	0.06
4	6.47	17.20	10.46	0.62	7.16	41.91	0.06
5	50.47	20.09	9.62	0.63	6.28	87.10	0.07
6	49.29	20.16	10.35	0.63	5.97	86.40	0.06
7	6.04	13.22	11.13	0.60	5.65	36.65	0.05
8	49.39	20.12	9.95	0.74	6.70	86.89	0.07
9	47.86	19.54	7.40	0.43	10.98	86.21	0.06
10	50.13	19.85	8.91	0.72	6.60	86.20	0.08
11	50.10	20.23	9.99	0.65	6.39	87.36	0.06
12	50.50	20.31	10.01	0.75	6.00	87.55	0.07
13	47.90	19.81	10.22	0.66	5.78	84.36	0.06
14	17.60	5.64	3.53	0.32	30.33	57.42	0.09
15	49.41	19.51	7.61	0.43	10.17	87.12	0.06
16	55.89	14.78	6.74	0.43	7.38	85.22	0.06
17	47.12	19.26	8.22	0.41	9.71	84.72	0.05
18	9.57	16.59	3.34	0.29	10.09	39.89	0.09
19	37.21	18.91	5.35	0.58	7.88	69.93	0.11
20	50.08	19.83	7.89	0.44	10.24	88.48	0.06
21	48.76	19.75	8.27	0.46	9.73	86.97	0.06
22	10.82	27.79	3.81	0.46	4.38	47.25	0.12
23	49.82	18.67	5.27	0.40	8.31	82.47	0.08
24	51.57	38.02	0.21	0.59	1.63	92.01	2.82
25	47.08	19.72	7.78	0.88	9.52	84.98	0.11
26	45.95	19.11	7.14	0.37	11.89	84.46	0.05
27	44.76	19.16	7.50	0.38	11.63	83.42	0.05
28	44.50	19.19	0.35	0.28	1.67	66.00	0.81
29	58.64	29.09	0.41	0.49	1.73	90.36	1.18
30	28.72	34.74	0.29	0.61	1.56	65.92	2.08

Values are given as bulk percentages minus carbon (±silica)

Appendix III. Sample 1074-226 - Electron microprobe traverse results

Point number	O	Ca	Mg	Mn	Fe	Total	Fe:Mn
1.00	46.03	41.44	0.51	0.58	1.98	90.55	3.42
2.00	46.64	41.55	0.57	0.64	2.02	91.43	3.14
3.00	47.01	41.12	0.59	0.60	2.16	91.47	3.61
4.00	47.59	40.88	0.61	0.56	2.16	91.81	3.83
5.00	47.64	40.32	0.64	0.63	2.10	91.33	3.33
6.00	47.24	40.99	0.67	0.66	2.36	91.92	3.57
7.00	47.10	40.81	0.65	0.61	2.36	91.52	3.87
8.00	47.01	41.05	0.64	0.63	2.28	91.62	3.61
9.00	47.31	40.93	0.65	0.60	2.05	91.54	3.39
10.00	47.58	38.35	0.29	0.53	1.23	87.98	2.30
11.00	48.71	40.48	0.46	0.55	1.71	91.91	3.11
12.00	47.58	40.59	0.60	0.57	1.91	91.26	3.33
13.00	47.63	40.08	0.61	0.54	2.01	90.86	3.71
14.00	48.16	40.16	0.63	0.66	2.09	91.70	3.15
15.00	48.16	40.13	0.63	0.60	2.05	91.57	3.42
16.00	47.91	39.89	0.61	0.56	2.07	91.04	3.70
17.00	47.75	40.20	0.59	0.57	2.14	91.25	3.73
18.00	47.08	39.82	0.64	0.61	2.06	90.20	3.37
19.00	47.49	40.03	0.61	0.60	2.11	90.83	3.53
20.00	47.66	40.25	0.60	0.55	2.12	91.18	3.85
21.00	47.14	40.07	0.60	0.62	2.09	90.53	3.40
22.00	48.84	39.32	0.59	0.59	2.02	91.36	3.44
23.00	46.99	40.27	0.60	0.55	2.15	90.57	3.89
24.00	47.76	39.82	0.61	0.65	2.21	91.05	3.42
25.00	47.34	39.77	0.59	0.57	1.96	90.23	3.46
26.00	48.09	40.06	0.60	0.61	2.10	91.45	3.45
27.00	47.65	40.12	0.62	0.55	2.21	91.16	3.99
28.00	47.49	39.59	0.63	0.58	2.06	90.35	3.59
29.00	49.86	37.50	0.59	0.59	1.93	90.46	3.30
30.00	47.88	39.68	0.65	0.60	2.02	90.85	3.36
31.00	47.75	39.74	0.63	0.62	2.12	90.86	3.44
32.00	47.27	39.53	0.63	0.64	2.02	90.08	3.17
33.00	48.11	37.87	0.56	0.59	1.68	88.82	2.85
34.00	47.67	39.75	0.66	0.62	2.10	90.78	3.41
35.00	49.35	39.57	0.37	0.52	1.53	91.34	2.95
36.00	50.48	39.73	0.00	0.47	1.02	91.71	2.18
37.00	49.44	39.49	0.16	0.59	1.44	91.11	2.46
38.00	47.08	39.69	0.62	0.67	2.26	90.31	3.39
39.00	48.51	39.43	0.40	0.55	1.68	90.57	3.06
40.00	48.75	38.50	0.82	0.65	1.98	90.71	3.05

Values are given as bulk percentages minus carbon (±silica)

Appendix III. Sample 1074-237 - Electron microprobe traverse results

Point number	O	Ca	Mg	Mn	Fe	Total	Fe:Mn
1.00	51.52	36.39	0.27	0.26	1.28	89.72	4.84
2.00	51.96	37.12	0.24	0.29	1.32	90.93	4.63
3.00	51.33	36.89	0.21	0.27	1.29	89.99	4.74
4.00	51.20	36.94	0.22	0.35	1.26	89.97	3.59
5.00	50.99	37.03	0.20	0.34	1.34	89.89	3.96
6.00	70.71	0.05	0.00	0.00	0.00	70.76	0.00
7.00	55.59	0.05	0.00	0.03	0.04	55.70	0.00
8.00	51.51	36.87	0.23	0.28	1.29	90.18	4.58
9.00	51.42	36.92	0.23	0.33	1.27	90.17	3.86
10.00	50.31	35.67	0.25	0.28	1.34	87.85	4.79
11.00	51.17	37.05	0.27	0.32	1.38	90.18	4.34
12.00	51.39	37.27	0.24	0.31	1.37	90.58	4.45
13.00	59.95	24.12	0.13	0.19	0.77	85.17	4.12
14.00	66.08	0.03	0.00	0.00	0.01	66.12	0.00
15.00	45.07	0.00	0.00	0.00	0.00	45.07	0.00
16.00	54.31	0.01	0.01	0.00	0.01	54.33	0.00
17.00	51.50	0.01	0.01	0.02	0.00	51.54	0.00
18.00	44.09	0.00	0.00	0.00	0.01	44.10	0.00
19.00	68.28	0.02	0.00	0.00	0.00	68.31	0.00
20.00	48.93	36.49	0.00	0.21	0.52	86.14	2.53
21.00	50.07	37.86	0.30	0.20	0.30	88.72	1.52
22.00	48.85	39.03	0.00	0.19	0.13	88.20	0.68
23.00	49.42	38.95	0.01	0.19	0.11	88.68	0.55
24.00	49.79	38.79	0.00	0.24	0.09	88.91	0.36
25.00	51.14	38.41	0.07	0.35	0.20	90.17	0.58
26.00	51.44	38.37	0.09	0.32	0.23	90.45	0.73
27.00	67.03	0.10	0.00	0.00	0.02	67.15	0.00
28.00	60.20	0.04	0.01	0.01	0.01	60.28	0.00
29.00	67.58	9.55	0.00	0.07	0.08	77.28	1.18
30.00	50.94	37.43	0.06	0.35	1.15	89.93	3.34

Values are given as bulk percentages minus carbon (±silica)

Appendix IV. X-ray diffraction results

Sample number	Dominant mineral	Sub-dominant mineral	Minor mineral	Minor/Trace mineral	Trace mineral
1074-16	Calcite	Albite	Quartz	Chlorite*	Dolomite
1074-25	Calcite	Chlorite*	Quartz	Dolomite	
1074-35	Calcite	Quartz	Dolomite		
1074-36	Dolomite	Calcite	Chlorite*	Quartz	
1074-37	Dolomite	Calcite	Quartz	Chlorite*	Biotite
1074-42	Calcite	Dolomite	Chlorite*	Quartz	
1074-43	Quartz	Albite	Chlorite*	Calcite	
1074-46	Chlorite*	Calcite	Quartz	Biotite	
1074-47	Calcite	Biotite	Chlorite*		
1074-51	Calcite				
1074-52	Calcite	Quartz	Chlorite*	Dolomite	
1074-93	Quartz	Calcite	Biotite	Albite	Chlorite*
1074-94	Quartz	Biotite	Calcite	Chlorite*	
1074-130	Quartz	Calcite			
1074-136	Quartz	Calcite	Dolomite		
1074-192	Quartz	Calcite	Albite	Biotite	
1074-210	Calcite	Chlorite*	Quartz	Albite	
1074-220	Quartz	Calcite	Chlorite*	Biotite	Albite
1074-224	Biotite	Chlorite*	Calcite	Quartz	Albite
1074-226	Biotite	Albite	Calcite	Chlorite*	Quartz
1074-227	Biotite	Chlorite*	Quartz	Albite	Calcite
1074-233	Calcite	Quartz	Biotite	Amphibole#	Chlorite*
1074-236	Biotite	Quartz	Calcite	Albite	Chlorite*
1074-240	Albite	Calcite	Quartz	Amphibole#	Chlorite*
1074-241	Biotite	Chlorite*	Calcite	Albite	Quartz
1074-253	Calcite	Chlorite*	Biotite	Albite	Quartz
1074-257	Albite	Biotite	Chlorite*	Calcite	

Chlorite* = Clinochore species
Amphibole# = Tremolite species

Appendix V

Junction survey lines over the N75 structure

July-August, 1997.

LINE 6518998 NORTH

6518998N, 389962E, or 0m East/West
Creamy-brown loamy soil with calcrete nodules. Hole sited on salt bush plain with scattered acacia and occasional eucalyptus. Soil is generally bare, but may be covered by lichen or leaf and tree litter in places. This site is approx. 2m from large eucalyptus. Sampler buried at 40 cm above indurated calcrete surface.

6518998N, 5mW
Creamy-brown loamy soil with calcrete nodules. Hole sited on salt bush plain with scattered acacia and occasional eucalyptus. Soil is generally bare, but may be covered by lichen or leaf and tree litter in places. This site is approx. 2m from large eucalyptus. Sampler buried at 40cm.

6518998N, 10mW
Creamy-brown loamy soil with calcrete nodules. Hole sited on salt bush plain with scattered acacia and occasional eucalyptus. Soil is generally bare, but may be covered by lichen or leaf and tree litter in places. This site is approx. 2m from large eucalyptus. Sampler position just to the edge of a graded track, bulldozed approx. 5 years ago and used infrequently. Sampler buried approximately 20cm deep due to near surface quartz vein (? part of sub outcropping N75) and near a 1m tall eucalyptus sapling.

6518998N, 50mW
Brown loamy soil with calcrete nodules at base and rare to occasional ferric nodule. No intervening sites due to disturbances owing to access track and bund wall (2m high soil wall built around open pits for flood protection). Hole sited on salt bush plain with scattered acacia and occasional eucalyptus. Sampler buried at 30cm.

6518998N, 5mE
Brown sandy loam with calcrete nodules toward base. Scattered quartz chips throughout (from N75 surface?). Vegetation is salt bush plain with scattered acacia and occasional eucalyptus. Sampler buried at 30cm.

6518998N, 10mE
Brown sandy loam with calcrete nodules toward base. Scattered quartz chips throughout (from N75 surface?). Vegetation is salt bush plain with scattered acacia and occasional eucalyptus. Sampler buried at 30cm.

6518998N, 15mE
Brown sandy loam with calcrete nodules toward base. Scattered quartz chips throughout. Vegetation is salt bush plain with scattered acacia and occasional eucalyptus. Sampler buried at 25cm.

6518998N, 20mE
Brown sandy loam with calcrete nodules toward base. Scattered quartz chips throughout. Vegetation is salt bush plain with scattered acacia and occasional eucalyptus. Sampler buried at 30cm.

6518998N, 30mE
Brown sandy loam with calcrete nodules toward base. Scattered quartz chips throughout. Sampler buried at 30cm next to small acacia.

6518998N, 40mE
Brown sandy loam with calcrete nodules toward base. Scattered quartz chips throughout.

at 40cm.

6518998N, 50mE
Brown sandy loam with calcrete nodules toward base. Scattered quartz chips throughout. Vegetation is salt bush plain with scattered acacia and occasional eucalyptus. Sampler buried at 40cm.

6518998N, 60mE
Brown sandy loam with calcrete nodules toward base. Scattered quartz chips throughout. Vegetation is salt bush plain with scattered acacia and occasional eucalyptus. Sampler buried at 40cm.

6518998N, 80mE
Brown sandy loam with calcrete nodules toward base. Scattered quartz chips throughout. Vegetation is salt bush plain with scattered acacia and occasional eucalyptus. Sampler buried at 40cm. Site near, but not on, old drill site which has since been rehabilitated.

6518998N, 100mE
Orange alluvial sandy loam approximately 50 cm deep lying over indurated calcrete. Old drill site nearby. Sampler buried at 60 cm.

6518998N, 150mE
Orange alluvial sandy loam approximately 50 cm deep lying over indurated calcrete. Old drill site nearby. Sandy loam to 60 cm, sampler buried at 70cm.

6518998N, 200mE
Orange alluvial sandy loam approximately 50 cm deep lying over indurated calcrete. Old drill site nearby. Vegetation changes very slightly. Salmon gums (eucalyptus species) grow here. This may be due to a change in the underlying geology (Black Flag volcanogenic sediments instead of Junction Gabbro [gold host rock]).

LINE 6519584 NORTH

6519584N, 389498E, or 0m East/West
Reddish alluvial loam with rare ferric nodules. Soil is calcareous at base. Surrounding soil surface covered by salt bush, scattered acacia and occasional eucalyptus. Soil is rarely covered by lichen or leaf and tree litter in places. Sampler buried at 80cm.

6519584N, 6(six)mW
Reddish alluvial loam with rare ferric nodules. Soil is calcareous at base. Surrounding soil surface covered by salt bush, scattered acacia and occasional eucalyptus. Soil is rarely covered by lichen or leaf and tree litter in places. Sampler buried at 80cm.

6519584N, 10mW
Surface covered by salt bush, scattered acacia and occasional eucalyptus. Reddish alluvial loam with scattered ferric nodules. Soil is calcareous at base. Sampler buried at 90cm

6519584N, 15mW
Surface covered by salt bush, scattered acacia and occasional eucalyptus. Reddish alluvial loam with scattered ferric nodules. Soil is calcareous at base. Sampler buried at 80cm.

6519584N, 30mW
Surface covered by salt bush, scattered acacia and occasional eucalyptus. Reddish alluvial loam with scattered ferric nodules. Soil is calcareous at base. Sampler buried at 80cm.

6519584N, 50mW
Reddish alluvial loam with ferric nodules and scattered quartz lag. Indurated calcrete at base. Sampler buried at 30cm.

6519584N, 5mE
Orange-brown, sandy alluvial loam for 40cm, underlain by creamy-brown calcareous loam. Immediate area covered by dense leaf and twig litter. Sampler buried close to large Salmon Gum at 40cm.

6519584N, 10mE
Mostly as above, leaf and twig litter not as abundant, sampler buried at 80 cm.

6519584N, 15mE
Bare lichen covered soil. Soil surface covered by salt bush, scattered acacia and occasional eucalyptus. Orange-red sandy alluvial loam with minor quartz and ferric nodules. Calcareous loam at base of hole. Sampler buried at 80 cm.

6519584N, 21m (twenty-one) E
Bare lichen covered soil. Soil surface covered by salt bush, scattered acacia and occasional eucalyptus. Orange-red sandy alluvial loam with minor quartz and ferric nodules. Calcareous loam at base of hole. Sampler buried at 80 cm.

6519584N, 30mE
Bare lichen covered soil. Soil surface covered by salt bush, scattered acacia and occasional eucalyptus. Orange-red sandy alluvial loam with minor quartz and ferric nodules. Calcareous loam at base of hole. Sampler buried at 80 cm.

6519584N, 40mE
Mostly are lichen covered soil. Soil surface covered by salt bush, scattered acacia and occasional eucalyptus. Orange-red sandy alluvial loam with minor quartz and ferric nodules. Calcareous loam at base of hole. Sampler buried at 80 cm., no calcareous loam at base of hole.

6519584N, 60mE
Mostly are lichen covered soil. Soil surface covered by salt bush, scattered acacia and occasional eucalyptus. Orange-red sandy alluvial loam with minor quartz and ferric nodules. Calcareous loam at base of hole. Sampler buried at 90 cm., no calcareous loam at base of hole.

6519584N, 80mE
Mostly are lichen covered soil. Soil surface covered by salt bush, scattered acacia and occasional eucalyptus. Orange-red sandy alluvial loam with minor quartz and ferric nodules. Calcareous loam at base of hole. Sampler buried at 80 cm.

6519584N, 100mE
Reddish-brown sandy alluvial loam with minor ferric nodules. Calcareous loam at base of hole. Area slightly disturbed by vehicle tracks of unknown age. Sampler buried at 90cm.

6519584N, 150mE
Soil geology and vegetation as above. Sampler located at edge of a moderately used track which skirts the local bund wall. Sampler buried at 80cm.

6519584N, 200mE
Soil geology and vegetation as above. Carbonate nodules at base, Sampler buried at 80 cm. ****Due to local rainfall during the period that the sampler was buried, the soil was waterlogged at this site only****

Appendix VI. Fluid inclusion database

Sample Number	Sample Type	Fluid Inclusion Type	Phases @ 20°C	% Vapour	Fluid Inclusion Type	XCO2	Freezing temperature °C	Low T° Melt	Tfm	TmCO$_2$	Tm	Wt.% NaCl equiv.	Tm Clath.	Wt.% NaCl equiv.	Wt% NaCl equiv. Summary	ThCO2	CO$_2$ density	Wt% CO$_2$	CO$_2$:CH$_4$ - CO$_2$	CO$_2$:CH$_4$ - CH$_4$	XH$_2$O	XCO$_2$	XCH$_4$	Bulk Density	Th	Homog° State	Th$_{NaCl}$	MacFlinCor Pressure (bar)
1074-17	Extn Vein	Pseudo Pri.	L & V	95	A	0.73	-98.9			-56.7						3.8	0.9	0.94	0.992	0.008				0.9				
1074-17	Extn Vein	Pseudo Pri.	L & V	95	A	0.73	-97.9			-56.8						1.2	0.92	0.94	0.99	0.01				0.91				
1074-17	Extn Vein	Pseudo Pri.	L & V	95	A	0.73	-98.7			-56.8						4.9	0.9	0.94	0.99	0.01				0.89				
1074-17	Extn Vein	Pseudo Pri.	L & V	95	A	0.73	-99.1			-56.9						5.2	0.9	0.94	0.99	0.01				0.88				
1074-17	Extn Vein	Pseudo Pri.	L & V	95	A	0.73	-99.7			-57.6						1.3	N.A.	0.94	0.97	0.03				0.88				
1074-54	Extn vein	Pseudo Pri.	V	95	A	0.73	-93.5	-78.8		-57						-6.6	0.97	0.94	0.99	0.01				0.94				
1074-15	Shear Vein	Pseudo Pri.	L & 2V	50	B	0.23	-98.2		-23.8	-58.2	-0.4	0.71	6.60	6.20	6.20	15.7	N.A.	0.44	0.94	0.06	0.75	0.21	0.010	0.89	225	V into L		1682
1074-15	Shear Vein	Pseudo Pri.	L & 2V	50	B	0.23	-97.8	-60.2	-29.5	-58.1	-1.8	3.06			3.06	14.3	N.A.	N.A.	0.94	0.06	0.75	0.23	0.010	0.90	262	V into L		1964
1074-15	Shear Vein	Pseudo Pri.	L & 2V	80	B	0.5	-100.8		-26.1	-62.1	-4.6	7.31			7.31	19.8	N.A.	N.A.			0.56	0.28	0.130	0.56	330	V into L		770
1074-26	Extn Vein	Pseudo Pri.	L & 2V	50	B	0.23	-98.6	-81.3		-57.1						30.2			0.98	0.02				0.79	390	V into L		
1074-27	Shear Vein	Pseudo Pri.	L & 2V	50	B	0.23	-99.1	-82.4	-35.3	-56.3			11.80	N.A.	N.A.	25.1	0.72	N.A.	1.00	0.00	0.80	0.20	0.000	0.85	297.8#	L into V		2155®
1074-31	Shear-Extn	Pseudo Pri.	L & 2V	80	B	0.7		-90.2		-56.7						30.1	0.6	0.7			0.77	0.23	0.000	0.63	267.8#	L into V		588®
1074-41	Shear Vein	Pseudo Pri.	L & V	70	B	0.4		(-80.1)		-65.6											0.53	0.47	0.000		373	V into L		
1074-44	Shear-Extn	Pseudo Pri.	L & V	50	B	0.23				-57.2						2.2	N.A.	0.48	0.98	0.02				0.89	213	L into V		1613
1074-44	Shear-Extn	Pseudo Pri.	L & 2V	50	B	0.23	-98	-72.8		-58.3						10.2	N.A.	0.46	0.94	0.06				0.93	254.6#	L into V		
1074-44	Shear-Extn	Pseudo Pri.	L & 2V	60	B	0.3	-97.9	-72.7		-57.1						11.8	0.86	0.56	0.98	0.02				0.91	210.1#	L into V		
1074-46	Breccia	Pseudo Pri.	L & 2V	60	B	0.3	-96.2		-35.2	-57.5	-7.8	11.46			11.46	16.1	N.A.	N.A.	0.97	0.03	0.65	0.31	0.010	0.90	300	L into V		2321
1074-50	Extn vein	Pseudo Pri.	L & V	55	B	0.27	-97.9			-56.8						12	0.85	0.51	0.995	0.005				0.91	238.3#	L into V		
1074-50	Extn vein	Pseudo Pri.	L & V	60	B	0.3	-92.2	(-91.8)		-56.7						5.9	0.89	0.57	0.997	0.003				0.93	203.3#	L into V		
1074-50	Extn vein	Pseudo Pri.	L & V	60	B	0.3	-94	(-97.6)		-56.8						1.8	0.91	0.57	0.995	0.005				0.94	203.3#	L into V		
1074-56	Shear Vein	Pseudo Pri.	L & 2V	55	B	0.27	-96.2			-57.5			6.90	N.A.		25.8	N.A.	N.A.	0.96	0.04	0.75	0.23	0.010	0.81	252	V into L		1328
1074-56	Shear Vein	Pseudo Pri.	L & 2V	60	B	0.3	-96.6	-73.7	-50.3	-57.5			6.20	N.A.		29.4	N.A.	N.A.	0.96	0.04	0.77	0.21	0.010	0.68	330	L into V		905
1074-105	Shear-Extn	Pseudo Pri.	L & 2V	70	B	0.4	-96.2			-58.8						9.7	N.A.	N.A.						N.A.	229.8#	L into V		
1074-105	Shear-Extn	Pseudo Pri.	L & 2V	70	B	0.4	-97.8			-58.6						9.1	N.A.	N.A.						N.A.	230	L into V		
1074-14	Extn Vein	Pseudo Pri.	L & V	20	C	0.07	-97.6		-13.2	-56.6	-1.2	2.07			2.07	22.6	0.75	0.15			0.92	0.08	0.000	0.95				
1074-15	Shear Vein	Pseudo Pri.	L & V	25	C	0.09			-24		-7.9	11.58			11.58										304.2#	L into V		
1074-15	Shear Vein	Pseudo Pri.	L & V	30	C	0.12			-26		-1.9	3.23			3.23										303	L into V		
1074-15	Shear Vein	Pseudo Pri.	L & V	35	C	0.14			-19.2		-3.2	5.26			5.26										308	L into V		
1074-15	Shear Vein	Pseudo Pri.	L & V	25	C	0.09		-89.6		-58.8																		
1074-15	Shear Vein	Pseudo Pri.	L & 2V	20	C	0.07	-101.3	-111	-25.4	-61.2	-6.4	9.73			9.73	19.3	N.A.	N.A.						N.A.	337	V into L		
1074-15	Shear Vein	Pseudo Pri.	L & 2V	45	C	0.19	-101.4		-23.1	-60.2	-1.2	2.07			2.07	19.2	N.A.	0.39	0.81	0.19				0.91	334	V into L		
1074-15	Shear Vein	Pseudo Pri.	L & 2V	25	C	0.09	-96.2	-77.2	-30.1	-61	-1.4	2.41			2.41	22.7	N.A.	0.2						0.93	346	V into L		
1074-16	Shear Vein	Pseudo Pri.	L & 2V	30	C	0.12	-109.1		-39.2	-56.7	-7.2	10.73			10.73	13.6	N.A.	N.A.			0.84	0.12	0.002	1.00	309	V into L		3250
1074-16	Shear Vein	Pseudo Pri.	L & V	20	C	0.07	-106.9	-88.7	-18.6	-57.2			11.90	N.A.	N.A.	-46.4									307	L into V		
1074-16	Shear Vein	Pseudo Pri.	L & V	20	C	0.07	-108.1		-19.1				10.90	N.A.	N.A.										226	V into L		
1074-16	Shear Vein	Pseudo Pri.	L & V	35	C	0.14	-106.8	-94.2	-19.8		-2	3.39			3.39										279.1#	L into V		
1074-16	Shear Vein	Pseudo Pri.	L & V	20	C	0.07	-100.8		-37.8	-57.1	-6.3	9.6			9.60	11.6	0.86	N.A.			0.89	0.08	0.002	1.02	224.7#	L into V		2602®
1074-17	Extn Vein	Pseudo Pri.	L & V	25	C	0.09			-33.1		-9.3	13.8			13.80										242.1#	L into V		
1074-17	Extn Vein	Pseudo Pri.	L & V	35	C	0.14	-96.2																		222.4#	L into V		
1074-22	Shear-Extn	Pseudo Pri.	L & V	40	C	0.16		-71.4	-34.4		-1.8	3.06			3.06										373	L into V		
1074-22	Shear-Extn	Pseudo Pri.	L & 2V	30	C	0.12	-103.3		-39.6	-57.2	-3.6	5.86			5.86	24.8	N.A.	N.A.			0.87	0.11	0.003	0.93	222.6#	L into V		1840®
1074-22	Shear-Extn	Pseudo Pri.	L & V	20	C	0.07	-98.8	-76.2	-28.7	-57.5	-7.7	11.34			11.34	7.8	N.A.	N.A.			0.88	0.08	0.002	1.04				
1074-22	Shear-Extn	Pseudo Pri.	L & V	20	C	0.07			-27.4		-8.6	12.39			12.39										224	V into L		
1074-22	Shear-Extn	Pseudo Pri.	L & V	30	C	0.12	-99.5	-93.2		-56.5						27	0.69	0.22						0.91				
1074-22	Shear-Extn	Pseudo Pri.	L & V	25	C	0.09		-80.1		-56.9						24.4	0.72	0.19						0.93				
1074-22	Shear-Extn	Pseudo Pri.	L & V	30	C	0.12	-97.6			-60.1						24.2	N.A.	0.23						0.91				
1074-22	Shear-Extn	Pseudo Pri.	L & V	20	C	0.07			-23.4		-4.2	6.74			6.74										235	L into V		
1074-22	Shear-Extn	Pseudo Pri.	L & V	45	C	0.19		-76.3	-26.2	-59.5			6.20	N.A.	N.A.	20.6			0.81	0.19				0.91	311.2#	L into V		
1074-22	Shear-Extn	Pseudo Pri.	L & 2V	40	C	0.16	-94.2		-33.2	-59.5			7.30	N.A.	N.A.	30.1	N.A.	N.A.	0.83	0.17				0.89	307	V into L		
1074-22	Shear-Extn	Pseudo Pri.	L & V	20	C	0.07			-42.4	-59.5	-5.2	8.14	6.20	N.A.	N.A.	20.6					0.94	0.05	0.005	0.92	301	V into L		2047
1074-26	Extn Vein	Pseudo Pri.	L & 2V	35	C	0.14	-98.6	-84.3	-36.2	-57.1			3.60	11.00	11.00	30.3									367			
1074-26	Extn Vein	Pseudo Pri.	L & V	25	C	0.09		(-108.6)		-57.8						27.4	N.A.	0.18						0.92				
1074-27	Shear	Pseudo Pri.	L & V	25	C	0.09	-101.1	-61.1	-48	-57.1			6.60	6.20	6.20	1.2	0.92	N.A.							303	L into V		
1074-27	Shear	Pseudo Pri.	L & V	20	C	0.07				-57.9			9.40	N.A.	N.A.	24.2	N.A.	N.A.										
1074-31	Shear-Extn	Pseudo Pri.	L & V	30	C	0.12	-95.2		-29.8	-56.7	-6.4	9.73	4.90	9.00	9.00	12.6	0.86	N.A.			0.84	0.13	0.001	1.00	258	V into L		2970
1074-36	Shear-Extn	Pseudo Pri.	L & V	25	C	0.09	-91.6			-56.6						24	0.72	0.19						0.93				
1074-36	Shear-Extn	Pseudo Pri.	L & V	25	C	0.09	-99.6		-19.8	-57.7	-3.8	6.16			6.16	21.9	N.A.	N.A.			0.89	0.08	0.004	0.96				

Sample Number	Sample Type	Fluid Inclusion Type	Phases @ 20°C	% Vapour	Fluid Inclusion Type	XCO2	Freezing temperature °C	Low T° Melt	Tfm	$TmCO_2$	Tm	Wt.% NaCl equiv.	Tm Clath.	Wt.% NaCl equiv.	Wt% NaCl equiv. Summary	ThCO2	CO_2 density	Wt% CO_2	CO_2:CH_4 - CO_2:CH_4 - CO_2	CH_4	XH_2O	XCO_2	XCH_4	Bulk Density	Th	Homog° State	Th_{NaCl}	MacFlinCor Pressure (bar)
1074-40	Shear	Pseudo Pri.	L & V	45	C	0.19	-92.6		-32.6		-12	15.76	18.50												256	V into L		
1074-40	Shear	Pseudo Pri.	L & V	40	C	0.16	-92.6	(-86.3)	-33.1		-13	17.08			17.08										312	V into L		
1074-41	Shear	Pseudo Pri.	L & V	35	C	0.14		(-89.8)		-66.8															301	V into L		
1074-41	Shear	Pseudo Pri.	L & V	20	C	0.07		-79.8																	264.1#	L into V		
1074-44	Shear-Extn	Pseudo Pri.	L & V	25	C	0.09			-36.2	-57.6	-10	14.15			14.15	-7.5					0.84	0.11	0.003	1.07	203.5#	L into V		2794®
1074-44	Shear-Extn	Pseudo Pri.	L & 2V	45	C	0.19	-98			-58.3						9.1	N.A.	0.42						0.8	271.9#	L into V		
1074-45	Shear-Extn	Pseudo Pri.	L & 2V	20	C	0.07	-102.6		-38.6	-57.4	-6.8	10.24			10.24	22.6	N.A.	N.A.			0.90	0.06	0.002	0.99	293	L into V		2952
1074-45	Shear-Extn	Pseudo Pri.	L & 2V	20	C	0.07	-98.8		-37.6	-57.4	-7.8	11.46	7.20	N.A.	N.A.	24.2	N.A.	N.A.			0.91	0.06	0.002	0.96	188.9#	L into V		
1074-45	Shear-Extn	Pseudo Pri.	L & 2V	35	C	0.14	-97.7	-72.8	-27.1	-57.8			4.80	N.A.	N.A.	19.3	N.A.	N.A.							262	L into V		
1074-45	Shear-Extn	Pseudo Pri.	L & 2V	40	C	0.16	-94.4	-77.8	-27	-57.9	-6.2	9.49			9.49				0.94	0.06				0.7	224.1#	L into V		
1074-45	Shear-Extn	Pseudo Pri.	L & 2V	20	C	0.07	-99.4		-43.4	-57.7			7.80	N.A.	N.A.	16.1	N.A.	N.A.							287	L into V		
1074-45	Shear-Extn	Pseudo Pri.	L & 2V	35	C	0.14	-98.2		-40.3	-57.8			7.70	N.A.	N.A.	16.6	N.A.	N.A.							287	L into V		
1074-46	Breccia	Pseudo Pri.	L & V	20	C	0.07	-96.8	-91		-59.4						24.5	N.A.	0.15						0.94				
1074-46	Breccia	Pseudo Pri.	L & 2V	25	C	0.09	-96.3			-57.6						24.4	N.A.	N.A.						0.93	389	V into L		
1074-46	Breccia	Pseudo Pri.	L & V	40	C	0.16		-93.2	-46.2	-57.7	-13	16.89			16.89	10.3	N.A.	N.A.	0.96	0.04	0.76	0.18	0.007	0.81	216.8#	L into V		2375®
1074-50	Extn vein	Pseudo Pri.	L & V	20	C	0.07	-98.1	-75.2		-57						23.3	0.75	0.15						0.95				
1074-50	Extn vein	Pseudo Pri.	L & V	20	C	0.07	-96.2	(-83.2)		-57						14.3	0.84	0.17						0.97				
1074-56	Shear	Pseudo Pri.	L & V	20	C	0.07			-60.1	-57.1	-6.8	10.24			10.24	-18.6		N.A.			0.87	0.09	0.001	1.06	308	L into V		4401
1074-56	Shear	Pseudo Pri.	L & 2V	25	C	0.09			-61.5	-56.8			6.20	7.00	7.00	26.2	0.72	N.A.							305	L into V		
1074-56	Shear	Pseudo Pri.	L & 2V	25	C	0.09	-35.8		-48.2	-57.5			6.50	N.A.	N.A.	28.1	N.A.	N.A.							280.1#	L into V		
1074-56	Shear	Pseudo Pri.	L & 2V	20	C	0.07			-30.9	-56.2			6.30	6.90	6.90	28.6	0.64	N.A.							306	L into V		
1074-56	Shear	Pseudo Pri.	L & 2V	45	C	0.19			-36.2	-57			6.10	N.A.	N.A.	25.2	0.72		0.98	0.02				0.68	230.1#	L into V		
1074-56	Shear	Pseudo Pri.	L & V	20	C	0.07	-96			-57.6			10.60	N.A.		21.4	N.A.	N.A.										
1074-56	Shear	Pseudo Pri.	L & V	25	C	0.09	-96.2	-67.7		-57.1			2.80	12.10	12.10	21.4	0.77	N.A.										
1074-84	Shear	Pseudo Pri.	L & 2V	30	C	0.12	-96.3		-38.7	-57.4			6.00		14.87	10.9									291	L into V		
1074-84	Shear	Pseudo Pri.	L & 2V	25	C	0.09	-98.1		-28.9	-59.6	-11	15.27	6.60	N.A.		21.2	N.A.	N.A.			0.93	0.05	0.008	0.89	284	V into L		1519
1074-84	Shear	Pseudo Pri.	L & 2V	25	C	0.09	-97.6		-22.8	-58.4	-2.8	4.65			4.65	28	N.A.	N.A.							221#	L into V		
1074-84	Shear	Pseudo Pri.	L & 2V	20	C	0.07	-98.1	(-78.4)	-22.8	-58.7			8.10	N.A.		28.1	N.A.	N.A.							223	V into L		
1074-84	Shear	Pseudo Pri.	L & 2V	45	C	0.19	-98.6		-30.1	-58.4			8.40	N.A.		21.3	N.A.	N.A.	0.93	0.07				0.62	255	L into V		
1074-13	Shear Vein	Pseudo Pri.	L & V	10	D				-28.3	-56.8			6.30	6.90	6.90	20.3									245	V into L		
1074-13	Shear Vein	Pseudo Pri.	L & V	10	D				-37.1				12.90	N.A.	N.A.										277	V into L		
1074-14	Extn Vein	Pseudo Pri.	L & V	15	D		-97.4	-65.1		-57.6	-1.5	2.57			2.57	21.1	N.A.	0.12			0.94	0.05	0.002	0.97				
1074-15	Shear Vein	Pseudo Pri.	L & V	15	D			(-66.4)	-16.8		-4.7	7.45			7.45										252	L into V		
1074-16	Shear Vein	Pseudo Pri.	L & 2V	15	D		-107.8		-38.7	-57.6	-6.9	10.36			10.36	9.8	N.A.	N.A.			0.91	0.06	0.002	1.04	353	V into L		4437
1074-17	Extn Vein	Pseudo Pri.	L & V	10	D				-29.8		-8.6	12.39			12.39										201	L into V		
1074-22	Shear-Extn	Pseudo Pri.	L & V	15	D				-22.4	-56.6	-4.3	6.88			6.88										243	L into V		
1074-22	Shear-Extn	Pseudo Pri.	L & V	10	D		-101.1		-36.4	-58.7	-7.8	11.46													205	V into L		
1074-26	Extn Vein	Pseudo Pri.	L & V	10	D			-67.3	-45.6	-56.9	-21	23.26			23.26										232	V into L		
1074-26	Extn Vein	Pseudo Pri.	L & V	15	D			Wouldn't Freez																	347	V into L		
1074-27	Shear	Pseudo Pri.	L & V	10	D				-34.1	-57	-4.4	7.02	6.30	6.90	6.90	13.5	0.83	N.A.			0.94	0.04	0.001	1.02				
1074-27	Shear	Pseudo Pri.	L & V	15	D			-66	-39.9		-33														278	L into V		
1074-31	Shear-Extn	Pseudo Pri.	L & V	10	D		-96.7			-56.7						17.6	0.8	0.08						0.98				
1074-31	Shear-Extn	Pseudo Pri.	L & V	10	D		-97.6	-66.3		-57.2						15.1	N.A.	0.08						0.98				
1074-31	Shear-Extn	Pseudo Pri.	L & V & S	10	D		-36.5	-87.5	-46.9		-9.6	N.A.	6.30	N.A.	30.5*										349	V into L	169	
1074-36	Shear-Extn	Pseudo Pri.	L & V	15	D		-83	-67.3	-20.6	-57.5	-0.8	1.4			1.40	23.1	N.A.	0.11			0.95	0.05	0.002	0.95				
1074-36	Shear-Extn	Pseudo Pri.	L & V	10	D		-91.8		-16.3	-56.8	-1.5	2.57			2.57	23.5	0.75	0.07			0.96	0.03	0.000	0.98				
1074-40	Shear	Pseudo Pri.	L & V	10	D			-79.2	-58.6		-8.3	12.05			12.05										374	V into L		
1074-46	Breccia	Pseudo Pri.	L & V	10	D		-96.8			-57.6						21.4	N.A.	0.08						0.98				
1074-46	Breccia	Pseudo Pri.	L & 2V	15	D		-96.8		-47.8	-56.7			6.00	7.50	7.50	26.1	0.7	N.A.							215	V into L		
1074-50	Extn vein	Pseudo Pri.	L & V	10	D				-36.7		-8	11.7			11.70										284	L into V		
1074-50	Extn vein	Pseudo Pri.	L & V	10	D				-35.6		-8.5	12.28			12.28										300	L into V		
1074-50	Extn vein	Pseudo Pri.	L & V	15	D		-97.1	-73.6		-57						22.2	0.76	0.11						0.96				
1074-54	Extn vein	Pseudo Pri.	L & V	15	D				-51.9		-12	16.24			16.24										302	V into L		
1074-54	Extn vein	Pseudo Pri.	L & V	10	D				-54.4		-12	16.05			16.05										275	V into L		
1074-54	Extn vein	Pseudo Pri.	L & 2V	15	D				-48		-1.5	2.57			2.57										306	V into L		
1074-233	Extn vein	Pseudo Pri.	L & V	10	D		-99.6		-33.1	-58.3	-9.7	13.62			13.62	24.2	N.A.	N.A.			0.93	0.02	0.002	1.03				
1074-233	Extn vein	Pseudo Pri.	L & V	10	D		-80.6	(-87.7)	-43	-59.2	0	0			0.00	10.8	N.A.	0.08			0.96	0.03	0.003	0.97				
1074-233	Extn vein	Pseudo Pri.	L & V	15	D		-97.6	(-86.2)		-58.4						13.2	N.A.	0.13						0.97				
1074-20	South Vein	Pseudo Pri.	L & V	40	SV-type C	0.16				-58.8						12.6	N.A.	0.36	0.92	0.08	0.81	0.19		0.94	389	V into L		
1074-20	South Vein	Pseudo Pri.	L & V	40	SV-type C	0.16				-58.1						-8.1	N.A.	0.39	0.95	0.05	0.79	0.21		0.99	411	V into L		
1074-25	South Vein	Pseudo Pri.	L & 2V	70	SV-type B	0.4	-95.6			-57.4						23.5	N.A.	0.63	0.97	0.03				0.82	302	V into L		

Sample Number	Sample Type	Fluid Inclusion Type	Phases @ 20°C	% Vapour	Fluid Inclusion Type	XCO2	Freezing temperature °C	Low T° Melt	Tfm	$TmCO_2$	Tm	Wt.% NaCl equiv.	Tm Clath.	Wt.% NaCl equiv.	Wt% NaCl equiv. Summary	ThCO2	CO_2 density	Wt% CO_2	CO_2-CH_4 - CO_2	CO_2-CH_4 - CH_4	XH_2O	XCO_2	XCH_4	Bulk Density	Th	Homog* State	Th_{NaCl}	MacFlinCor Pressure (bar)
1074-25	South Vein	Pseudo Pri.	L & 2V	60	SV-type B	0.3	-96.3	-90.1		-56.9			5.00	9.00	9.00	23.4	0.75	N.A.	0.99	0.01	0.66	0.31	0.002	0.87	313	V into L		
1074-25	South Vein	Pseudo Pri.	L & 2V	60	SV-type B	0.3	-93.8			-57.1						23.6	0.74	0.52	0.98	0.02				0.84	292	V into L		
1074-25	South Vein	Pseudo Pri.	L & 2V	70	SV-type B	0.4	-96.1			-57.4						23.6	N.A.	0.63	0.97	0.03				0.82	271	V into L		
1074-29	South Vein	Pseudo Pri.	V	90	SV-type A	0.72	-99.6			-57.6						3.4	N.A.	0.89	0.97	0.03				0.92				
1074-29	South Vein	Pseudo Pri.	V	95	SV-type A	0.73	-97.6			-57.1						7.1	0.89	0.94	0.98	0.02				0.89				
1074-29	South Vein	Pseudo Pri.	V	90	SV-type A	0.72	-98.1			-57.3						7.5	N.A.	0.89	0.98	0.02				0.9				
1074-29	South Vein	Pseudo Pri.	V	95	SV-type A	0.73	-98.6			-57.3						4.7	N.A.	0.94	0.98	0.02				0.9				
1074-29	South Vein	Pseudo Pri.	V	95	SV-type A	0.73	-96.2			-57.7						13	N.A.	0.94	0.96	0.04				0.86				
1074-29	South Vein	Pseudo Pri.	L & V	25	SV-type C	0.09	-99.6			-57.1															284	V into L		
1074-93	South Vein	Pseudo Pri.	L & V	20	SV-type C	0.07			-49.8		11.8														278	V into L		
1074-66	Mo Vein	Pseudo Pri.	L & V	30	Mo-type C		-39.4		-40.6	-61.5	-10	14.36			14.36										216	V into L		
1074-66	Mo Vein	Pseudo Pri.	L & V	30	Mo-type C		-41.2		-42.4	-59.8	-9.8	13.72			13.72										314	V into L		
1074-66	Mo Vein	Pseudo Pri.	L & V & S	30	Mo-type C																				308	V into L	347	
1074-66	Mo Vein	Pseudo Pri.	L & V & S	15	Mo-type D		-104.2	-81.4	-41.3	-62.5	-12	15.76			15.76										306	V into L	340	
1074-66	Mo Vein	Pseudo Pri.	L & V	10	Mo-type D		-38.6		-38		-7.2	10.73			10.73										153	V into L		
1074-284	Mo Vein	Pseudo Pri.	L & V	10	Mo-type D				-47.1		-23	24.83			24.83										208	V into L		
1074-284	Mo Vein	Pseudo Pri.	L & V	15	Mo-type D				-29.8		-16	19.37			19.37										211	V into L		
1074-284	Mo Vein	Pseudo Pri.	L & V	20	Mo-type C				-53.7		-21	22.91			22.91										303	V into L		
1074-284	Mo Vein	Pseudo Pri.	L & V	45	Mo-type C		-99.7		-30.1	-58.6			7.60	N.A.		19.5	0.79	N.A.						N.A.	224	V into L		
1074-284	Mo Vein	Pseudo Pri.	L & V	10	Mo-type D		-47		-51.6		-16	19.6			19.60										205	V into L		
1074-284	Mo Vein	Pseudo Pri.	L & V	10	Mo-type D		-44.8		-23.5		-14	17.43			17.43										209	V into L		
1074-13	Shear	Secondary	L & V	15	D				-54.4		-7.6	11.22			11.22										121	V into L		
1074-14	Extn Vein	Secondary	L & V	5	D		-65.3		-46.2		-20	22.31			22.31										184	V into L		
1074-14	Extn Vein	Secondary	L & V	5	D		-66.2		-45.8		-22	23.97			23.97										112	V into L		
1074-14	Extn Vein	Secondary	L & V	5	D		-66.5		-56.3		-16	19.45			19.45										99.1	V into L		
1074-14	Extn Vein	Secondary	L & V	8	D		-66.5		-63.1		-16	19.29			19.29										115	V into L		
1074-26	Extn Vein	Secondary	L & V & S	5	D		-89.6		-74.6		-39	N.A.			31.1*										103	V into L	183	
1074-26	Extn Vein	Secondary	L & V & S	5	D		-96.7		-73.5		-36	N.A.			30.9*										104	V into L	181	
1074-26	Extn Vein	Secondary	L & V & S	5	D		-69.9		-69.9		-25	N.A.			30.9*										98.8	V into L	181	
1074-26	Extn Vein	Secondary	L & V	5	D		-90.4		-63.8		-26	26.7			26.7										93.6	V into L		
1074-26	Extn Vein	Secondary	L & V & S	5	D		-94.6		-70.8		-26	N.A.			30.5*										93.1	V into L	170	
1074-26	Extn Vein	Secondary	L & V	8	D		-92.5		-72.6		-24	25.61			25.61										118	V into L		
1074-26	Extn Vein	Secondary	L & V	15	D		-58.6		-41.2		-23	24.63			24.63										216	V into L		
1074-40	Shear	Secondary	L & V & S	5	D		-95.9		-73.5		-40	N.A.			28.7*										105	V into L	123	
1074-40	Shear	Secondary	L & V & S	5	D				-81.1		-43	N.A.			28.4*										77.1	V into L	119	
1074-40	Shear	Secondary	L & V & S	5	D				-76.6		-39	N.A.			29.2*										138	V into L	143	
1074-41	Shear	Secondary	L & V & S	8	D		-90.2		-73.6		-40	N.A.			32*										136	V into L	206	
1074-41	Shear	Secondary	L & V & S	5	D		-87.9		-73.2		-39	N.A.			31.8*										104	V into L	195	
1074-41	Shear	Secondary	L & V & S	5	D		-107.1		-72.8		-36	N.A.			30.1*										152	V into L	154	
1074-41	Shear	Secondary	L & V & S	15	D		-81.2		-72.8		-38	N.A.			29.1*										184	V into L	138	
1074-41	Shear	Secondary	L & V & S	10	D				-53.5		-34	N.A.			29.1*										167	V into L	136	
1074-41	Shear	Secondary	L & V	10	D				-45.6		-34	31.99			31.99										153	V into L		
1074-44	Shear-Extn	Secondary	L & V	8	D		-40.3		-40.3		-5.8	8.95			8.95										117	V into L		
1074-45	Breccia	Secondary	L & V	8	D		-50.1		-41.2		-14	17.61			17.61										129	V into L		
1074-45	Breccia	Secondary	L & V	5	D		-50.2		-38.2		-17	20.3			20.3										132	V into L		
1074-45	Breccia	Secondary	L & V	5	D		-50.2		-38.3		-12	15.76			15.76										118	V into L		
1074-45	Breccia	Secondary	L & V	15	D		-47.1		-47.1		-12	16.24			16.24										117	V into L		
1074-45	Breccia	Secondary	L & V	15	D		-53.8		-48.8		-13	17.26			17.26										137	V into L		
1074-50	Extn vein	Secondary	L & V	10	D		-58.6		-38.5		-24	25.58			25.58										215	V into L		
1074-50	Extn vein	Secondary	L & V	5	D		-78		-39.3		-21	23.47			23.47										117	V into L		
1074-56	Shear	Secondary	L & V	10	D		-72		-58.8		-26	26.85			26.85										191	V into L		
1074-56	Shear	Pseudo Pri.	L & V	10	D		-55.5		-48.6		-40	36.86													230	V into L		
1074-84	Shear	Secondary	L & V	5	D		-78.6		-45.6		-18	20.75			20.75										118	V into L		
1074-84	Shear	Secondary	L & V	5	D		-72.1		-47.8		-9.8	13.72			13.72										147	V into L		
1074-84	Shear	Secondary	L & V	5	D		-79.2		-43.6		-19	21.61			21.61										98.7	V into L		
1074-84	Shear	Secondary	L & V	5	D		-78.6		-45.6		-18	20.75			20.75										118	V into L		
1074-20	South Vein	Secondary	L & V	8	SV-type D				-54.6		-11	14.97			14.97										127	V into L		
1074-20	South Vein	Secondary	L & V	15	SV-type D		-78		-39.1		-7.3	10.86			10.86										200	V into L		
1074-25	South Vein	Secondary	L & V	5	SV-type D				-42.6		-8.5	12.28			12.28										78	V into L		
1074-25	South Vein	Secondary	L & V	5	SV-type D				-43.2		-7.8	11.46			11.46										72.5	V into L		
1074-25	South Vein	Secondary	L & V	5	SV-type D				-43.6		-5.7	8.81			8.81										68.9	V into L		
1074-25	South Vein	Secondary	L & V	5	SV-type D				-69.8		-27	27.02			27.02										113	V into L		
1074-93	South Vein	Secondary	L & V & S	5	SV-type D				-71		-37	N.A.			33.5*										62.9	V into L	223	
1074-93	South Vein	Secondary	L & V & S	5	SV-type D				-70.4		-37	N.A.			28.8*										73.8	V into L	129	
1074-93	South Vein	Secondary	L & V & S	5	SV-type D				-67.3		-38	N.A.			28.8*										73.6	V into L	129	

* = wt.% NaCl calculated from ThNaCl, # = fluid inclusion decrepitated, ® = pressure estimated from decrepitation temperature

Appendix VII. EDTA-Gas chromatography data base

Sample number	Sample type	Weight initial grams	Weight final grams	Weight dissolved grams	EDTA volume mls	Head space volume	Area of CH_4 in 500µl sample	Area of CH_4 for Std. = 100 ppm	Estimated concentration CH_4 in ppm	Estimated vol. of CH_4 (ng) per 500µl sample	Total volume of CH_4 (ng) per gram of calcite	Au ppm	Area of C_2H_4 in 500µl	Area of C_2H_4 for Std. = 100 ppm	Estimated concentration C_2H_4 in ppm	Estimated vol. of C_2H_4 (ng) per 500µl	Total volume of C_2H_4 (ng) per gram of
1074-17	BCZ	5.5354	4.924	0.6114	45	30	849.15	276.90	306.66	109.42	5368.86	31	15.65	529.07	2.96	0.37	18.35
	Extension Vein	5.5354	4.924	0.6114	45	30	871.80	276.90	314.84	112.34	5512.07	31	17.68	529.07	3.34	0.42	20.73
1074-36	BCZ	5.5337	4.9088	0.6249	45	30	1304.20	276.90	471.00	168.05	8067.83	6.9	27.74	529.07	5.24	0.66	31.83
	Extension Vein	5.5337	4.9088	0.6249	45	30	1282.10	276.90	463.02	165.21	7931.12	6.9	27.36	529.07	5.17	0.65	31.39
1074-42	BCZ	4.2586	3.3468	0.9118	45	30	805.20	234.18	343.84	122.68	4036.46	0.27	15.50	511.69	3.03	0.40	13.03
	Extension Vein	4.2586	3.3468	0.9118	45	30	812.20	234.18	346.83	123.75	4071.55	0.27	16.90	511.69	3.30	0.43	14.21
1074-47	BCZ	6.1696	5.3567	0.8129	45	30	772.56	233.75	330.51	117.92	4352.01	4.88	35.94	519.1	6.92	0.89	32.93
	Extension Vein	6.1696	5.3567	0.8129	45	30	799.34	233.75	341.96	122.01	4502.86	4.88	26.81	519.1	5.16	0.67	24.56
1074-84	BCZ	1.2085	0.8601	0.3484	35	30	115.70	252.40	45.84	16.36	1408.35		BDL	517.81	n.d	n.d	n.d
	Shear Vein	1.2085	0.8601	0.3484	35	30	112.30	252.40	44.49	15.88	1366.97		BDL	517.81	n.d	n.d	n.d
1074-87	BCZ	5.3508	4.56	0.7908	45	30	1232.90	234.18	526.48	187.85	7126.19	1.47	53.60	511.69	10.48	1.37	51.96
	Breccia	5.3508	4.56	0.7908	45	30	1214.20	234.18	518.49	185.00	7018.11	1.47	49.90	511.69	9.75	1.28	48.37
1074-102	BCZ	4.5678	3.8715	0.6963	50	30	741.70	252.40	293.86	104.85	4517.40	0.04	BDL	517.81	n.d	n.d	n.d
	Breccia	4.5678	3.8715	0.6963	50	30	639.81	252.40	253.49	90.45	3896.83	0.04	BDL	517.81	n.d	n.d	n.d
1074-151	BCZ	5.2372	4.4855	0.7517	40	30	134.80	234.18	57.56	20.54	819.67		n.d	511.69	n.d	n.d	n.d
	Shear Vein	5.2372	4.4855	0.7517	40	30	157.70	234.18	67.34	24.03	958.92		n.d	511.69	n.d	n.d	n.d
1074-200	BCZ	6.5343	5.7217	0.8126	45	30	125.90	233.75	53.86	19.22	709.49	15.67	BDL	519.1	n.d	n.d	n.d
	Extension Vein	6.5343	5.7217	0.8126	45	30	120.69	233.75	51.63	18.42	680.13	15.67	BDL	519.1	n.d	n.d	n.d
1074-204	BCZ	5.2881	4.5821	0.706	45	30	329.00	276.90	118.82	42.39	1801.42		n.d	529.07	n.d	n.d	n.d
	Extension Vein	5.2881	4.5821	0.706	45	30	302.80	276.90	109.35	39.02	1657.96		n.d	529.07	n.d	n.d	n.d
1074-234	BCZ	5.5295	4.6614	0.8681	45	30	497.90	276.90	179.81	64.16	2217.15	7.03	13.96	529.07	2.64	0.33	11.53
	Extension Vein	5.5295	4.6614	0.8681	45	30	466.12	276.90	168.34	60.06	2075.64	7.03	14.25	529.07	2.69	0.34	11.77
1074-252	BCZ	6.8779	6.376	0.5019	45	30	34.70	233.75	14.84	5.30	316.60	7.6	n.d	519.1	n.d	n.d	n.d
	Extension Vein	6.8779	6.376	0.5019	45	30	33.70	233.75	14.42	5.14	307.47	7.6	n.d	519.1	n.d	n.d	n.d
1074-259	BCZ	6.7555	5.8569	0.8986	45	30	182.13	233.75	77.92	27.80	928.13	10.95	BDL	519.1	n.d	n.d	n.d
	Extension Vein	6.7555	5.8569	0.8986	45	30	209.57	233.75	89.66	31.99	1067.97	10.95	BDL	519.1	n.d	n.d	n.d
1074-192	PCZ/DCZ	5.2134	4.5586	0.6548	30	30	34.57	236.40	14.62	5.22	239.05		n.d	526.29	n.d	n.d	n.d
	Zone 2	5.2134	4.5586	0.6548	30	30	42.27	236.40	17.88	6.38	292.30		n.d	526.29	n.d	n.d	n.d
1074-210	PCZ/DCZ	5.0357	4.2141	0.8216	45	30	26.10	236.40	11.04	3.94	143.84	0.07	n.d	526.29	n.d	n.d	n.d
	Zone 2	5.0357	4.2141	0.8216	45	30	29.70	236.40	12.56	4.48	163.68	0.07	n.d	526.29	n.d	n.d	n.d
1074-233	PCZ/DCZ	5.446	4.6908	0.7552	40	30	30.01	252.40	11.89	4.24	168.52	0.01	n.d	517.81	n.d	n.d	n.d
	Zone 4	5.446	4.6908	0.7552	40	30	34.15	252.40	13.53	4.83	191.77	0.01	n.d	517.81	n.d	n.d	n.d
1074-237	PCZ/DCZ	5.8291	5.0007	0.8284	45	30	21.65	252.40	8.58	3.06	110.83		n.d	517.81	n.d	n.d	n.d
	alteration	5.8291	5.0007	0.8284	45	30	21.86	252.40	8.66	3.09	111.91		n.d	517.81	n.d	n.d	n.d
1074-237	Re-run	5.8658	4.9166	0.9492	45	30	44.10	276.90	15.93	5.68	179.60		n.d	529.07	n.d	n.d	n.d
1074-240	PCZ/DCZ	5.0046	4.5597	0.4449	45	30	16.20	236.40	6.85	2.45	164.87	0.41	BDL	526.29	n.d	n.d	n.d
	Extension Vein	5.0046	4.5597	0.4449	45	30	15.20	236.40	6.43	2.29	154.70	0.41	BDL	526.29	n.d	n.d	n.d
1074-241	PCZ/DCZ	5.0931	4.3646	0.7285	45	30	42.00	236.40	17.77	6.34	261.05	0.25	n.d	526.29	n.d	n.d	n.d
	Extension Vein	5.0931	4.3646	0.7285	45	30	42.00	236.40	17.77	6.34	261.05	0.25	n.d	526.29	n.d	n.d	n.d
1074-245	PCZ/DCZ	5.8176	4.9876	0.83	45	30	56.40	233.75	24.13	8.61	311.17	0.26	n.d	519.1	n.d	n.d	n.d
	Zone 1	5.8176	4.9876	0.83	45	30	49.53	233.75	21.19	7.56	273.27	0.26	n.d	519.1	n.d	n.d	n.d

Sample number	Sample type	Weight Initial grams	Weight Final grams	Weight Disolved grams	EDTA volume mls	Head Space volume	Area of CH4 in 500µl sample	Area of CH_4 for Std. = 100 ppm	Estimated concentration CH4 in ppm	Estimated vol. of CH4 (ng) per 500µl sample	Total volume of CH4 (ng) per gram of calcite	Au ppm	Area of C_2H_4 in 500µl sample	Area of C_2H_4 for Std. = 100 ppm	Estimated concentration C_2H_4 in ppm	Estimated vol. of C_2H_4 (ng) per 500µl sample	Total volume of C_2H_4 (ng) per gram of calcite
1074-257	PCZ/DCZ	5.1474	4.6891	0.4583	50	30	17.25	236.40	7.30	2.60	170.43	0.76	n.d	526.29	n.d	n.d	n.d
	Zone 2	5.1474	4.6891	0.4583	50	30	16.30	236.40	6.90	2.46	161.04	0.76	n.d	526.29	n.d	n.d	n.d
1074-35	Post Min.	0.8382	0.3924	0.4458	45	30	307.80	252.40	121.95	43.51	2928.10		n.d.	517.81	n.d	n.d	n.d
	Sth Vein	0.8382	0.3924	0.4458	45	30	280.86	252.40	111.28	39.70	2671.82		n.d.	517.81	n.d	n.d	n.d
1074-121	Post Min.	5.0301	4.2407	0.7894	40	30	140.00	234.18	59.78	21.33	810.64		n.d.	511.69	n.d	n.d	n.d
	Sth Vein	5.0301	4.2407	0.7894	40	30	156.70	234.18	66.91	23.88	907.34		n.d.	511.69	n.d	n.d	n.d
1074-264	Unalt'ed	5.2393	5.0788	0.1605	40	30	8.51	277.70	3.06	1.09	204.37	0.01	n.d	524.92	n.d	n.d	n.d
	Gabbro	5.2393	5.0788	0.1605	40	30	9.88	277.70	3.56	1.27	237.28	0.01	n.d	524.92	n.d	n.d	n.d
1074-272	Unalt'ed	5.3874	5.2551	0.1323	45	30	12.68	277.70	4.57	1.63	369.43	0.01	n.d	524.92	n.d	n.d	n.d
	Gabbro	5.3874	5.2551	0.1323	45	30	11.35	277.70	4.09	1.46	330.68	0.01	n.d	524.92	n.d	n.d	n.d
1074-275	Unalt'ed	5.099	4.9795	0.1195	45	30	7.34	277.70	2.64	0.94	236.75	0.01	n.d	524.92	n.d	n.d	n.d
	Gabbro	5.099	4.9795	0.1195	45	30	9.12	277.70	3.28	1.17	294.17	0.01	n.d	524.92	n.d	n.d	n.d
1074-276	Unalt'ed	5.2781	5.1397	0.1384	45	30	8.80	277.70	3.17	1.13	245.09	0.01	n.d	524.92	n.d	n.d	n.d
	Gabbro	5.2781	5.1397	0.1384	45	30	8.80	277.70	3.17	1.13	245.09	0.01	n.d	524.92	n.d	n.d	n.d
1074-277	Unalt'ed	5.3884	4.7324	0.656	45	30	75.12	277.70	27.05	9.65	441.39	0.07	n.d	524.92	n.d	n.d	n.d
	Gabbro	5.3884	4.7324	0.656	45	30	78.33	277.70	28.21	10.06	460.25	0.07	n.d	524.92	n.d	n.d	n.d